78817

SCIENTIFIC NOTEBOOK 115E

BY

Charles B. Connor

SCIENTIFIC NOTEBOOK 115E

BY

Charles B. Connor

Southwest Research Institute
Center for Nuclear Waste Regulatory Analyses
San Antonio, Texas

Notebook #115E

Development of Radiation Boundary Condition

Chuck Connor

C. B. Connor

Two-dimensional models in metra/mutliflo have been developed to model the cooling of the Tolbachik dike. These models are affected by radiative boundary conditions at the surface. The goal is to write a simple 1D model with a radiative boundary condition to test the Multiflo code.

1.0 Introduction

One of the problems we have encountered in modeling the cooling of the Tolbachik dike is the boundary condition at the surface. It is clear that this boundary is somewhat insulating from field observations. For instance, snow buried by one meter of scoria does not melt during the summer at Tolbachik, and near surface ground temperatures are very warm over the dike, even though the surface temperature is very cold compared to the scoria temperatures. Thus a constant temperature surface boundary condition tends to cool the near-surface scoria much faster than observed.

Ozisik, M.N., 1989, Boundary value problems in Heat Conduction, Dover publications, New York, 504 pp., presents a boundary value problem involving time-dependent heat conduction through a slab with one insulated boundary and one radiative boundary. Here, rather than a radiative boundary, I use a constant temperature boundary condition.

$$\frac{\partial^2 T}{\partial x^2} = \frac{1}{\alpha}\frac{\partial T}{\partial t}$$

where T is temperature in °K, t is time in seconds, x is distance in m, and alpha is the thermal diffusivity in m^2/s. This applies within the slap at time greater than 0.

At the constant temperature boundary, x = 0, T = constant at t > 0.

and

$$\frac{\partial T}{\partial x} = \frac{\sigma\varepsilon}{-\kappa}(T^4 - T_a^4)$$

where sigma is the Stephan-Boltzmann constant 5.6696e-8W/m^2, epsilon is the emissivity (0-1), and kappa is the bulk thermal conductivity of the rock. Ta is the atmospheric temperature in °K.

As an Example:

FIGURE 1. Illustration of the boundary value problem.

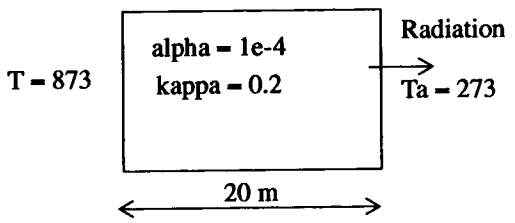

The following TrueBasic code is used to model the 1D boundary conditions

```
•dim temp(0:20,0:1000)
•open #1: name "temp.out", create newold
•erase #1
•
•let alpha = 1e-4
•let stephan = 5.6696e-8
•let emissivity = 0
•let atmos_temp = 273
•
•let time_step = 3600
•let z_step = 1
•let kappa = 0.2
•
•
•print stephan*emissivity/(-kappa)
•
•for z = 0 to 20
•let temp(z,0) = 273
•next z
•
```

```
•let sigma = alpha*time_step/(z_step)^2
•
•
•for t = 0 to 999
•let temp(0,t) = 873
•for z = 1 to 19
•
•let temp(z,t+1) = (1-2*sigma)*temp(z,t) + sigma*(temp(z-1,t) + temp(z+1,t))
•
•next z
•let temp(20,t+1) = 0.01 * (stephan*emissivity/(-kappa) * (temp(20,t)^4 -
atmos_temp^4)) + temp(19,t+1)
•let temp(0,t+1) = 873
•next t
•
•set window 0,20,0,873
•for z = 0 to 20
•plot z,temp(z,10);
•next z
•plot
•
•for z = 0 to 20
•plot z,temp(z,20);
•next z
•plot
•
•for z = 0 to 20
•plot z,temp(z,500);
•next z
•plot
•
•for z = 0 to 20
•plot z,temp(z,1000);
•next z
•plot
•
•for z = 0 to 20
•print #1: z,temp(z,10),temp(z,50),temp(z,500)
•next z
•plot
•
•end
```

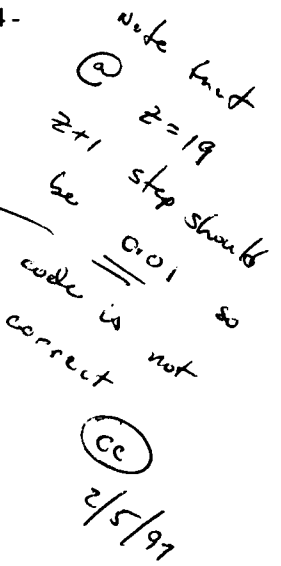

The above code was run for various emissvities (epsilon) between 0 and 1. The following figure (Figure 2, "Temperatures in the 1D slab as a function of time.," on page 4) is a graph of the results of this code. At comparatively short times (t = 10 or 50 hrs), the temperature profile does not depend on the emissivity because the radiative boundary at distance = 20 m is not playing a role. At 500 hours, the results depend on the value of the emissivity. For emissivity = 1, the problem has reached a steady state with the "sur-

face temperature" being about 375°K, hotter than would be expected for a constant temperature boundary. For the emissivity = 0 case, the profile has not reached a steady state. Heat will continue to build in the slab until a temperature of 873°K is reached throughout the block. These two results encompass the range of solutions.

So, it is clear for the 1D solution that temperature profile are significantly changes for the radiative boundary condition, depending on the value of the emissivity chosen.

FIGURE 2. Temperatures in the 1D slab as a function of time.

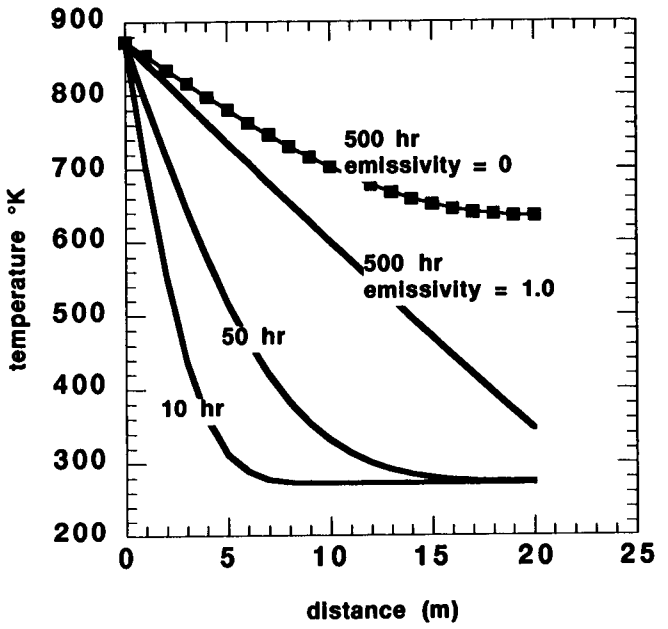

White, F.M., 1984, Heat Transfer, Addision-Wiley Publishing, Reading, MA, 588 pp., reports the emissivity for several materials. For brick and concrete, the emissivity is between 0.75 and 0.9, for soil the emissivity is 0.93-0.96. So, for scoria, the emissivity is likely similar to these materials.

February 6, 1997
Acct #20-5708-461

Development of a 2D Radiation Boundary Condition

Chuck Connor

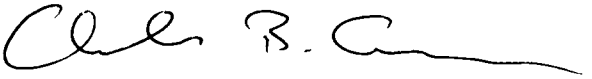

Two-dimensional models in metra/mutliflo have been developed to model the cooling of the Tolbachik dike. These models are affected by radiative boundary conditions at the surface. The goal is to write a simple 2D model with a radiative boundary condition to test the Multiflo code.

1.0 Introduction

In 2D, heat transfer through the slab is governed by:

$$\frac{\partial^2 T}{\partial x^2} + \frac{\partial^2 T}{\partial z^2} = \frac{1}{\alpha}\frac{\partial T}{\partial t}$$

where T is temperature in °K, t is time in seconds, x is distance in m, z is depth in m, and alpha is the thermal diffusivity in m^2/s. This applies within the slab at time greater than 0.

At the constant temperature boundary, x = 0, T = constant at t > 0.

and

$$\frac{\partial T}{\partial z} = \frac{\sigma\varepsilon}{-\kappa}(T^4 - T_a^4)$$

where sigma is the Stephan-Boltzmann constant 5.6696e-8W/m^2, epsilon is the emissivity (0-1), and kappa is the bulk thermal conductivity of the rock. Ta is the atmospheric temperature in °K.

As an Example:

FIGURE 1. Illustration of the 2D boundary value problem.

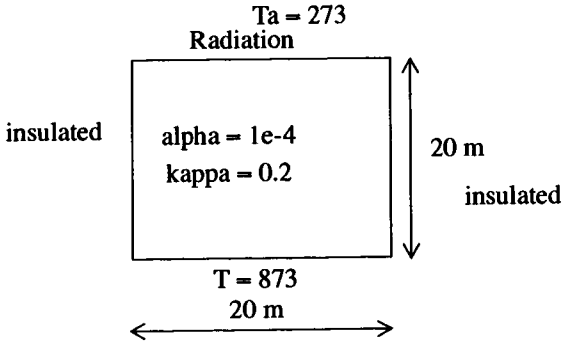

The following code is an explicit finite difference code to solve the radiation boundary problem. The code assumes a fixed grid node spacing in the x-direction and allows variable grid node spaing in the z direction. This is important because the radiation boundary condition is only numerically stable for very short grid spacing. Because of this short grid spacing requirement, run times for this code are very long, even with few grid nodes! An Implicit numerical scheme would be better.

```
•DIM temp(0:20,0:20), new_temp(0:20,0:20), dist(0:20)
•
•OPEN #1: name "temp.out", create newold
•ERASE #1
```

```
•
•LET alpha = 1e-6
•LET stephan = 5.6696e-8
•LET emissivity = 0.9
•LET atmos_temp = 273
•
•
•LET time_step = 1000
•LET z_step = 1
•LET x_step = 1
•LET kappa = 0.2
•
•
•PRINT stephan*emissivity/(-kappa)
•
•
•!initial conditions
•FOR z = 1 to 20
•   FOR x = 0 to 20
•      LET temp(x,z) = 273
•   NEXT x
•NEXT z
•
•FOR x = 0 to 20
•   LET temp(x,0) = 873
•NEXT x
•
•FOR z = 0 to 10
•   LET dist(z) = z*1.5
•NEXT z
•FOR z = 11 to 20
•   LET dist(z) = dist(z-1) + .1
•NEXT z
•
•LET z_step = .1
•
•LET sigma = alpha*time_step/(z_step)^2
•PRINT sigma
•GET KEY dum
•
•FOR t = 0 to 10000
•
•   FOR z = 1 to 19
•      FOR x = 1 to 19
•
•         LET t1 = temp(x,z)
•         LET t2 = temp(x,z+1)
•         LET t3 = temp(x+1,z)
•         LET t4 = temp(x,z-1)
•         LET t5 = temp(x-1,z)
```

```
•       LET d1 = dist(z-1)
•       LET d2 = dist(z)
•       LET d3 = dist(z+1)
•       LET d12 = d1+(d1+d2)/2
•       LET d23 = d2+ (d2+d3)/2
•
•       LET dum1 = (t3-2*t1+t5)/x_step^2
•       LET dum2 = ((t2-t1)/(d3-d2) - (t1-t4)/(d2-d1))*1/(d23-d12)
•       LET new_temp(x,z) = alpha*time_step*(dum1+dum2) + t1
•
•       !let new_temp(x,z) = sigma*(t2 + t3 + t4 + t5) + (1-4*sigma)*temp(x,z)
•
•    NEXT x
•  NEXT z
•
•
•
•  !recalculate new temperatures at boundaries
•
•
•  !radiation boundary condition at the surface
•  FOR x = 0 to 20
•     !print temp(x,20)
•     !let new_temp(x,20) = 273
•     !if x = 1 then
•     !let dum = temp(x,20)^4
•     !print dum, dum - atmos_temp^4
•     !end if
•
•     LET new_temp(x,20) = 0.01 * stephan*emissivity/(-kappa) * (temp(x,20)^4 -
atmos_temp^4) + temp(x,19)
•
•
•  NEXT x
•
•  !constant temperature boundary at the base
•  FOR x = 0 to 20
•     LET new_temp(x,0) = 873
•  NEXT x
•
•  !insulated boundary at the side walls
•  FOR z = 1 to 19
•     LET new_temp(0,z) = 2*sigma*temp(1,z) + (1-2*sigma)*temp(0,z)
•     LET new_temp(20,z) = 2*sigma*temp(19,z) + (1-2*sigma)*temp(20,z)
•  NEXT z
•
•  MAT temp = new_temp
•
•NEXT t
•
```

```
•
•SET WINDOW 0,25,0,873
•LET x = 0
•FOR z = 0 to 20
•   PLOT dist(z), temp(x,z);
•NEXT z
•PLOT
•
•SET COLOR "cyan"
•LET x = 5
•FOR z = 0 to 20
•   PLOT dist(z), temp(x,z);
•NEXT z
•PLOT
•
•SET COLOR "green"
•LET x = 10
•FOR z = 0 to 20
•   PLOT dist(z), temp(x,z);
•NEXT z
•PLOT
•
•SET COLOR "red"
•LET x = 20
•FOR z = 0 to 20
•   PLOT dist(z), temp(x,z);
•NEXT z
•PLOT
•
•MAT PRINT #1: temp
•END
•
•
```

A vertical temperature profile through the slab looks like this:

873	652.435	478.369	368.25	311.151
286.335	277.112	274.13	273.28	273.063
273.012	273.011	273.01	273.008	273.007
273.006	273.006	273.005	273.004	273.003
273.003				

variation in temperature at the surface along the length of the slab is less than 0.1°K, so it is clear that the code is slow but stable.

February 7, 1997
Acct #20-5708-461

Investigation of Aeromagnetic Anomaly East of Repository

Chuck Connor

A magnetic anomaly on the east side of the repository is investigated by making profiles of individual E-W trending flight lines across it.

1.0 Introduction

Aeromagnetic anomalies in the Yucca Mountain region are often produced by faults and basalts buried at shallow depths. A sharpnegative aromagnetic anomaly is located on the east side of the reposiotry at Forty Mile wash. Here, I simply look at the data across this anomaly to better understand its character and to determine if additional ground magnetic surveys are warranted.

The following unnumbered color print on the next page shows the location of this anomaly.

TABLE 1. Magnetic Data on East-West line across the anomaly

Easting	Northing	Magentics (nT)
554647	4071750	51719
554607	4071760	51719
554567	4071760	51720
554527	4071760	51721
554488	4071758	51720

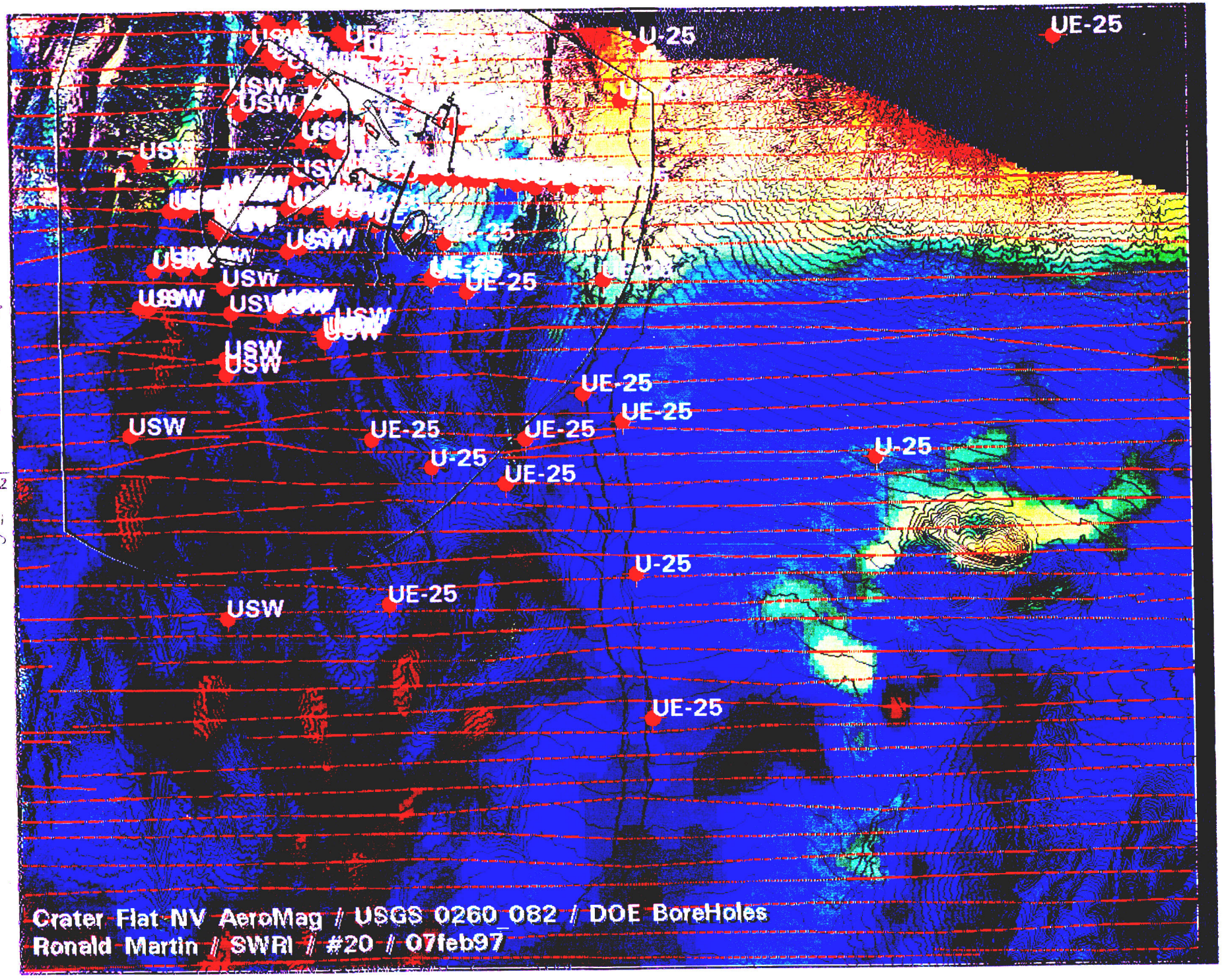
UE-25
U-25
USW
Crater Flat NV AeroMag / USGS 0260_082 / DOE BoreHoles
Ronald Martin / SWRI / #20 / 07feb97

Easting	Northing	Magentics (nT)
554448	4071759	51721
554408	4071760	51722
554369	4071761	51724
554329	4071762	51725
554289	4071763	51725
554250	4071764	51726
554210	4071765	51724
554170	4071766	51723
554131	4071767	51724
554091	4071770	51723
554051	4071770	51723
554012	4071770	51723
553972	4071770	51722
553932	4071770	51723
553893	4071770	51723
553853	4071770	51723
553813	4071770	51722
553773	4071780	51721
553734	4071780	51719
553694	4071780	51719
553654	4071780	51718
553615	4071780	51715
553575	4071780	51713
553535	4071780	51711
553496	4071780	51710
553456	4071780	51709
553416	4071780	51709
553377	4071790	51708
553337	4071790	51707
553297	4071790	51708

Easting	Northing	Magentics (nT)
553257	4071790	51708
553218	4071790	51708
553178	4071790	51707
553138	4071790	51703
553099	4071790	51698
553059	4071790	51692
553019	4071790	51686
552980	4071800	51680
552940	4071796	51676
552900	4071797	51672
552861	4071798	51669
552821	4071799	51666
552781	4071800	51664
552742	4071801	51661
552702	4071802	51660
552662	4071803	51659
552623	4071804	51656
552586	4071800	51656
552550	4071800	51654
552514	4071800	51646
552477	4071800	51640
552441	4071800	51631
552405	4071800	51625
552368	4071800	51618
552332	4071800	51615
552296	4071800	51613
552260	4071800	51612
552223	4071800	51610
552187	4071800	51611
552151	4071800	51613

Easting	Northing	Magentics (nT)
552114	4071800	51620
552078	4071800	51629
552042	4071800	51641
552006	4071800	51654
551969	4071800	51669
551933	4071800	51683
551897	4071800	51696
551860	4071800	51704
551824	4071800	51708
551788	4071800	51706
551751	4071800	51699
551715	4071803	51687

FIGURE 1. Profile across Yucca Mountain and the Anomaly

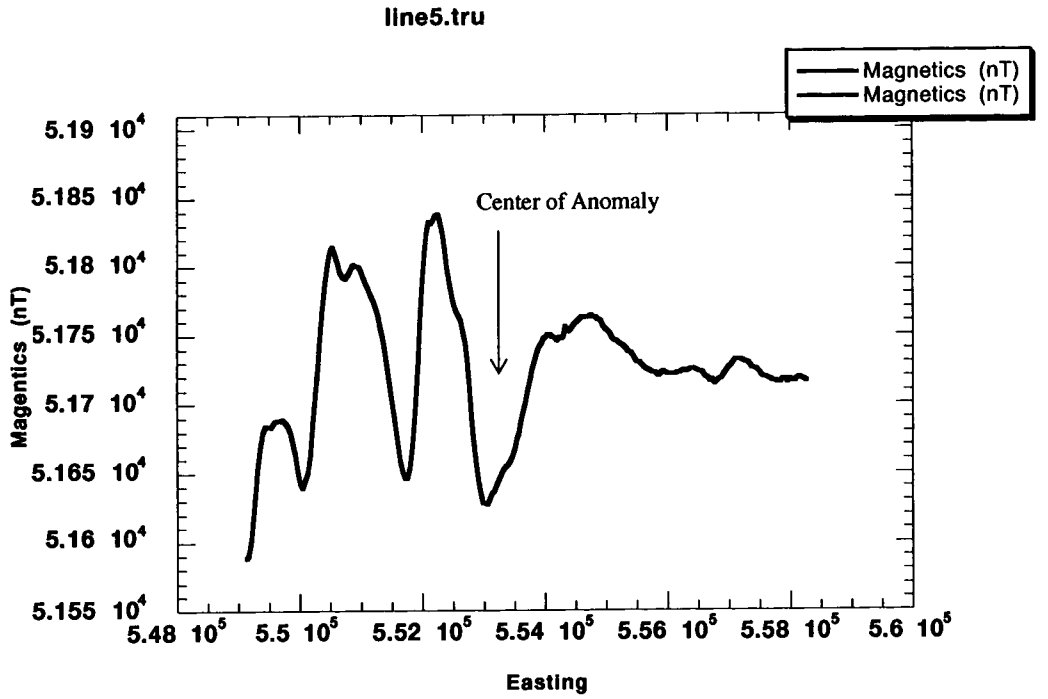

The following are a series of profiles acoss the anomaly. Starting south of the anoamly and working north. Line 4 is at the anoamly peaak, based on the aeromagnetic data.

FIGURE 2.

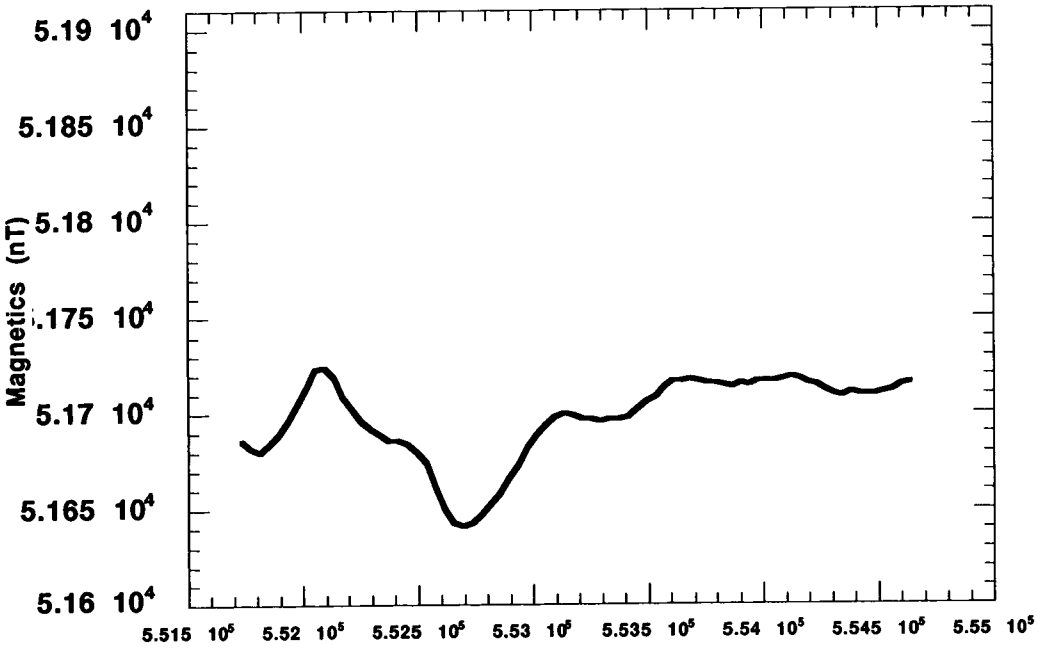
Line 1
Magnetics (nT)
5.19 10^4
5.185 10^4
5.18 10^4
5.175 10^4
5.17 10^4
5.165 10^4
5.16 10^4
5.515 10^5
5.52 10^5
5.525 10^5
5.53 10^5
5.535 10^5
5.54 10^5
5.545 10^5
5.55 10^5

FIGURE 3.

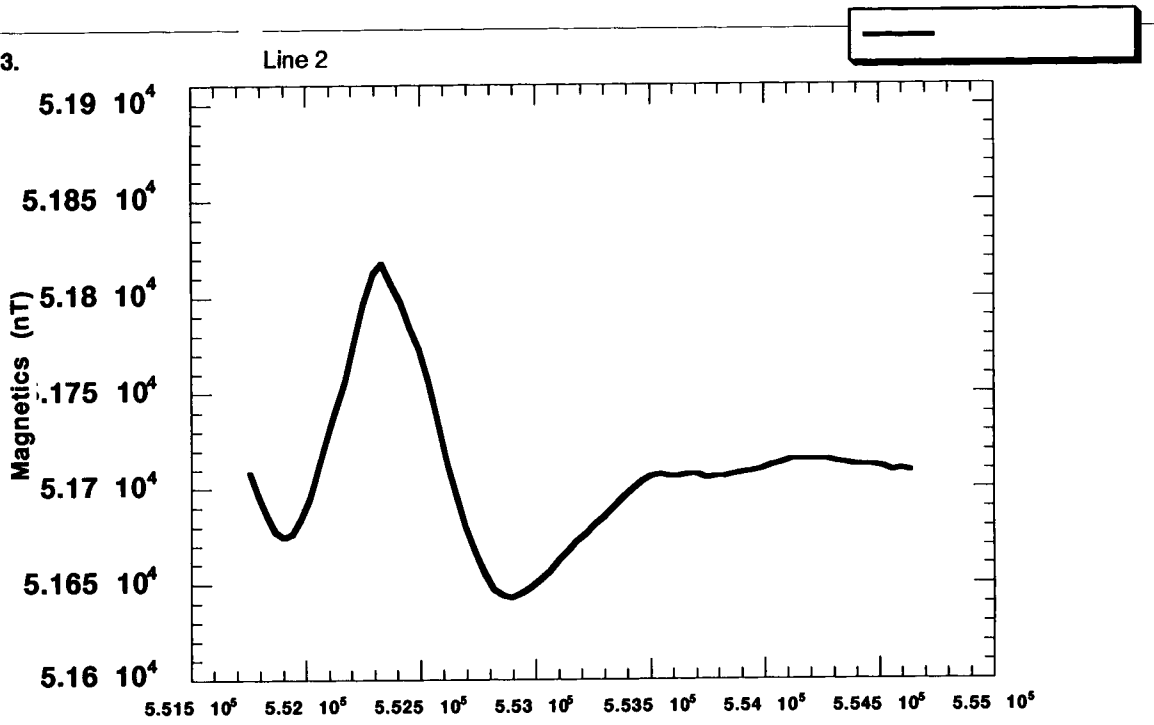

FIGURE 4.

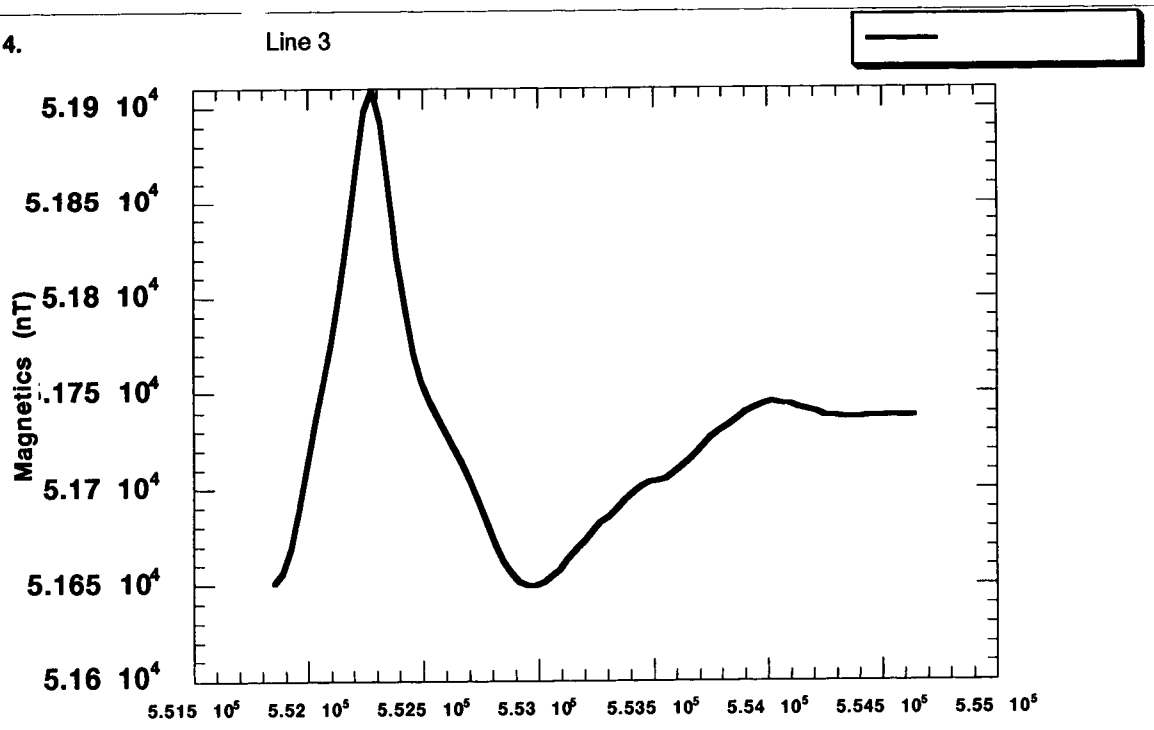

FIGURE 5.

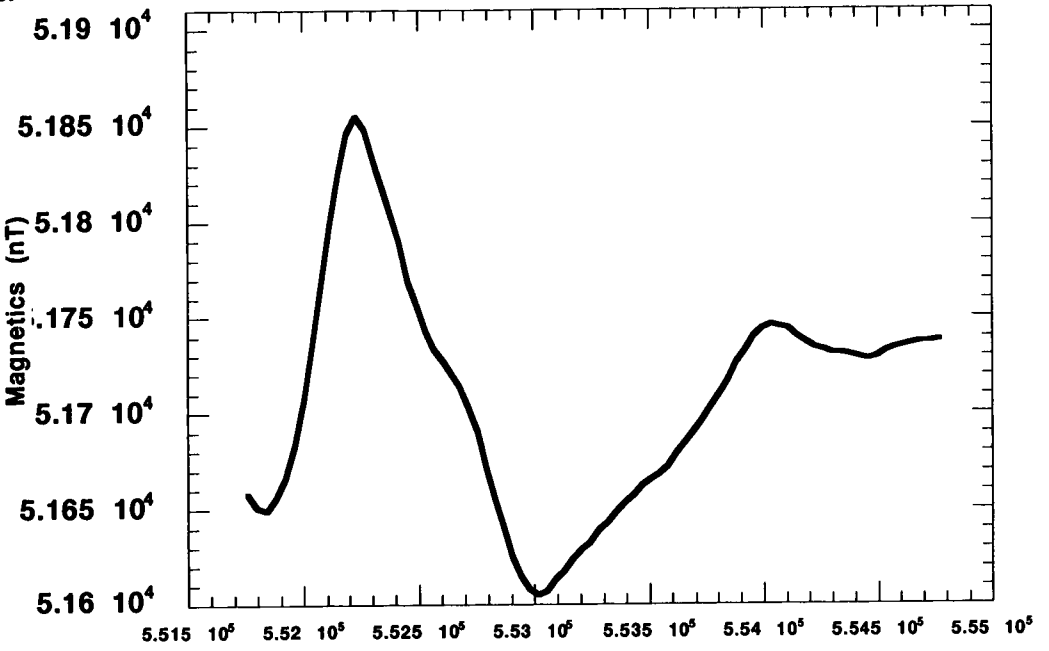

FIGURE 6.

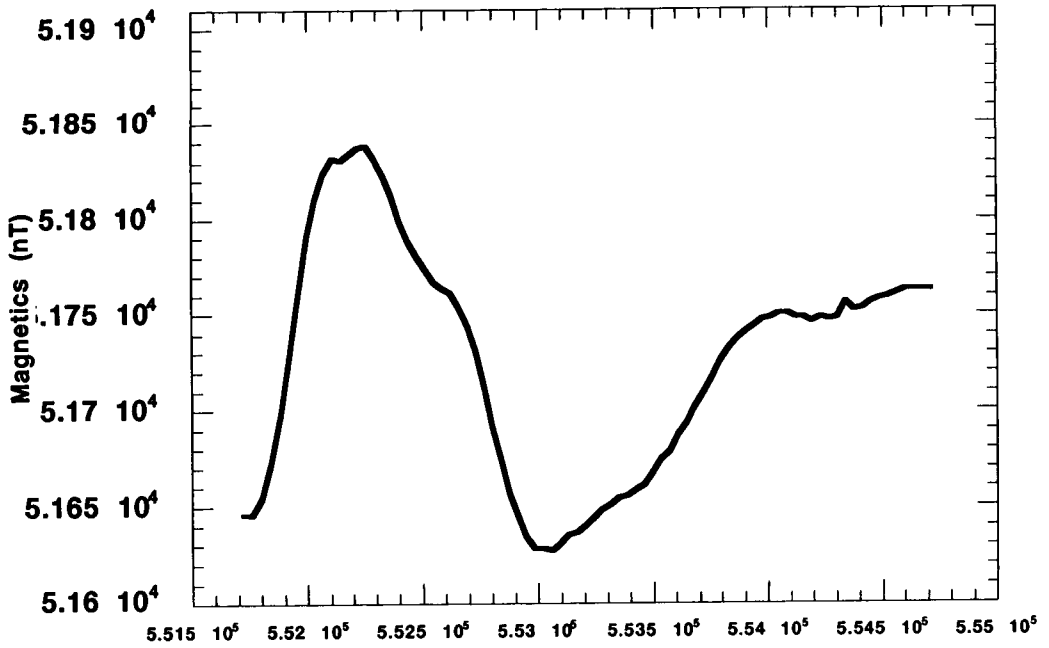

FIGURE 7.

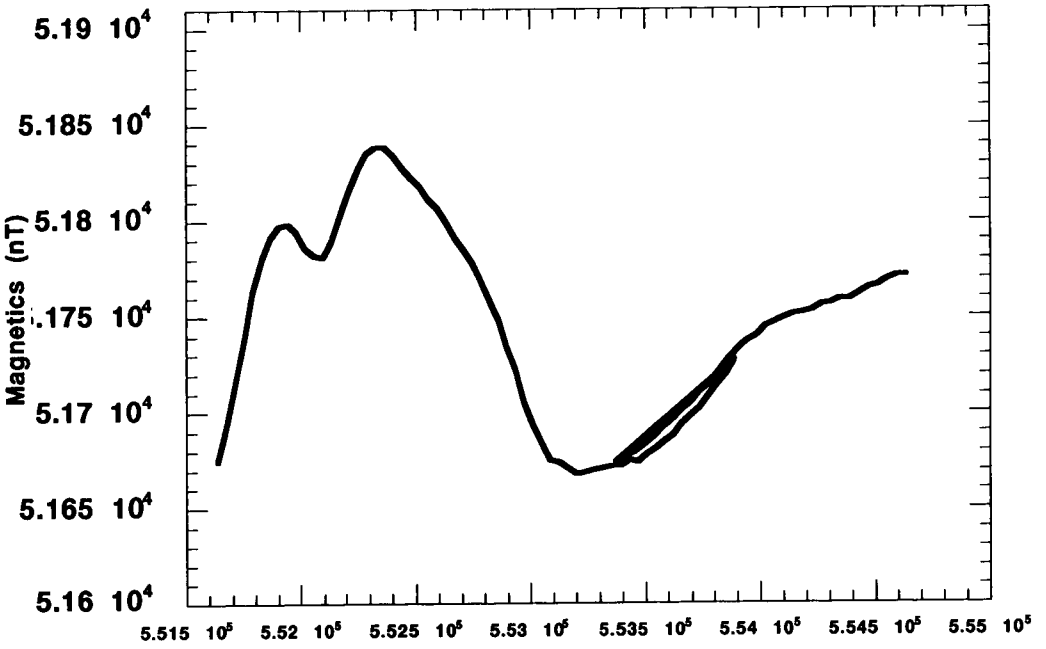

FIGURE 8.

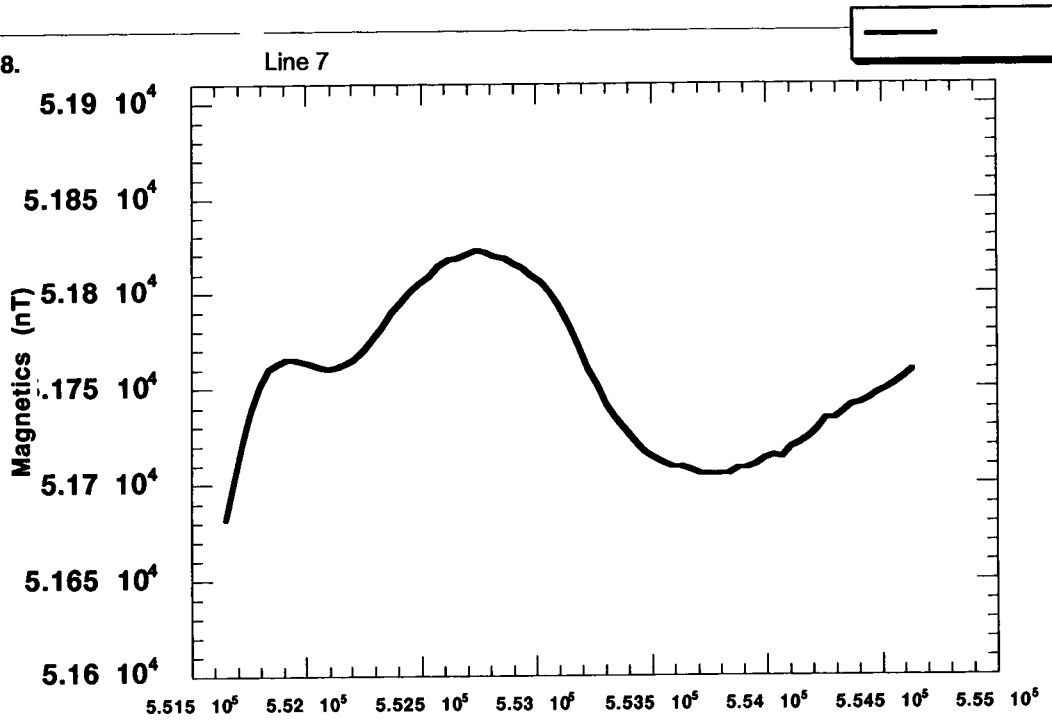

FIGURE 9.

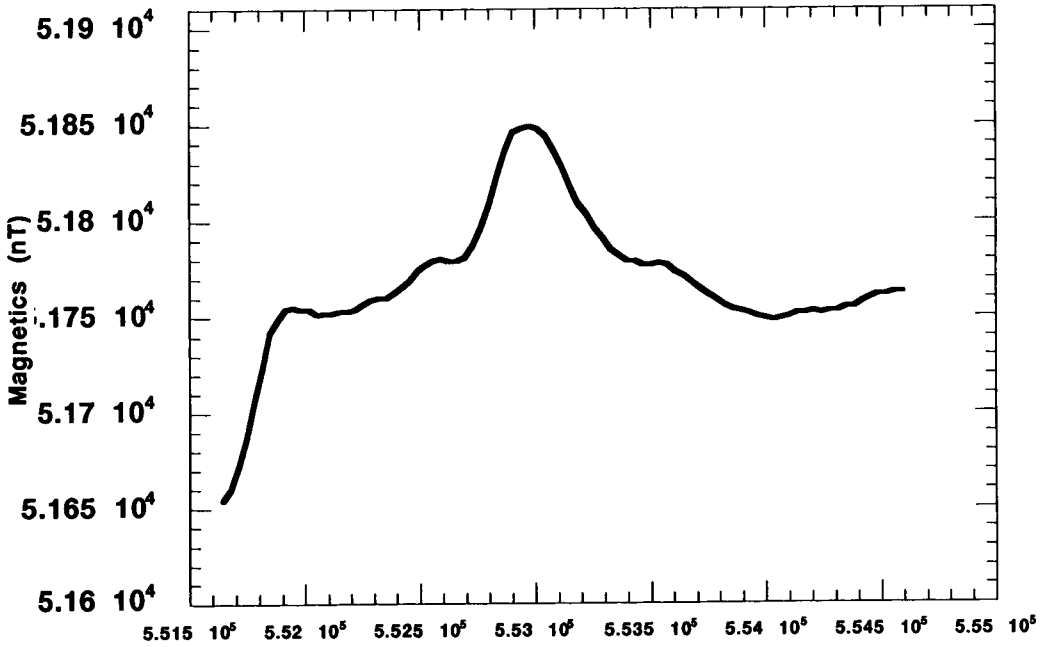

Some general observations of the above profiles are:

The negative anomaly may simply be caused by a fault on the west side of Forty Mile Wash

At its maximum (Lines 4 and 5) the anomaly looks additivr. This means that more than one body may be producing the anomaly.

Based on observation of these profiles, it looks like the anomaly is produced by a shallow fault scarp or dike and not by a buried cone or volcanic vent or lava flow.

There is no page 11 of 11.

Procedure for Sampling Aeromagnetic Lines

Chuck Connor

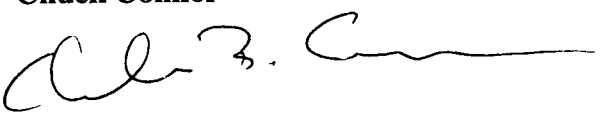

A magnetic anomaly on the east side of the repository is investigated by making profiles of individual E-W trending flight lines across it.

1.0 Introduction

Looking at longer lines across the anomaly east of the repository area.

Arc Info puts out point coverages that look like:

```
•Arcedit: |> list <|
•        9080
•AREA                =      0.000
•PERIMETER           =      0.000
•FMW_ZMANY#          =       9080
•FMW_ZMANY-ID        =    *******
•CHAR_IDX            =  0160E1111477
•Z00                 =    31614.90
•Z0                  =      776.00
•XUTM                =    551732.56
•YUTM                =   4072247.75
•Z1                  =      356.00
•Z2                  =     3600.00
•Z3                  =    51686.00
•Z4                  =    51970.03
•Z5                  =    51566.23
•XLONG               =      -116.83
•YLAT                =       36.64
•        9081
•AREA                =      0.000
•PERIMETER           =      0.000
```

```
•FMW_ZMANY#          = 9081
•FMW_ZMANY-ID        = *******
•CHAR_IDX          = 0160E1111477
•Continue? I>> y <<I
•Z00             =   31615.40
•Z0              =    776.00
•XUTM              =   551772.56
•YUTM              =  4072245.75
•Z1              =    350.00
•Z2              =    3600.00
•Z3              =   51682.00
•Z4              =   51970.20
•Z5              =   51566.23
•XLONG             =    -116.83
•YLAT            =     36.64
•       9082
```

This file is translated using the following trueBasic code

```
•open #1: name "long5_5.raw"
•open #2: name "long5_5.tru", create newold
•erase #2
•
•Print #2:" ";" ";"East";" ";"North";" ";"Fl_Ele";" ";"Magnetics";" ";"DEM"
•Do while more #1
•
•line input #1: lin$
•let tag$ = lin$[2:5]
•if tag$ = "XUTM" then print #2: val(lin$[33:42]),
•if tag$ = "YUTM" then print #2: val(lin$[32:42]),
•if tag$ = "Z1  " then print #2: val(lin$[34:42]),
•if tag$ = "Z3  " then print #2: val(lin$[34:42]),
•if tag$ = "ZELE" then print #2: val(lin$[34:42])
•
•loop
•end
```

And the output file looks like this:

```
•  East North Fl_Ele Magnetics DEM
• 548331.     4.0712e+6     400      51707      1227.06
• 548366.     4071206      421      51708      1221.97
• 548402.     4.07121e+6    446       51706      1226.91
• 548437.     4.07121e+6    478       51704      1232.3
• 548472.     4.07121e+6    523       51702      1229.33
• 548507.     4071211      554      51700      1216.74
• 548543.     4.07121e+6    592       51698      1203.67
```

• 548578.	4.07121e+6	585	51694	1190.94
• 548613.	4071215	607	51688	1179.92
• 548648.	4.07122e+6	562	51682	1169.18
• 548683.	4.07122e+6	494	51675	1161.1
• 548718.	4.07122e+6	494	51668	1155.67
• 548754.	4.07122e+6	494	51662	1150.4
• 548789.	4.07122e+6	523	51660	1145.17
• 548824.	4.07122e+6	523	51658	1142.79
• 548859.	4071224	494	51661	1142.61
• 548894.	4.07123e+6	494	51667	1143.98
• 548930.	4.07123e+6	472	51675	1148.44
• 548965.	4071228	456	51683	1157.84
• 549000	4.07123e+6	417	51691	1173.85

Where the columns are:

- Easting (meters)
- Northing (meters)
- Flight Elevation avove the ground surface (Feet)
- Total Magnetic Field (nanoTeslas)
- Terrain elevation above Sea Level (meters)

The file is then out out into a graphing package and Magnetics and elevation information is plotted against Easting (these flight lines run E-W).

February 8, 1997
Acct #20-5708-461

Investigation of Aeromagnetic Anomaly East of Repository 2

Chuck Connor

A magnetic anomaly on the east side of the repository is investigated by making profiles of individual E-W trending flight lines across it.

1.0 Introduction

Looking at longer lines across the anomaly east of the reposiotry area.

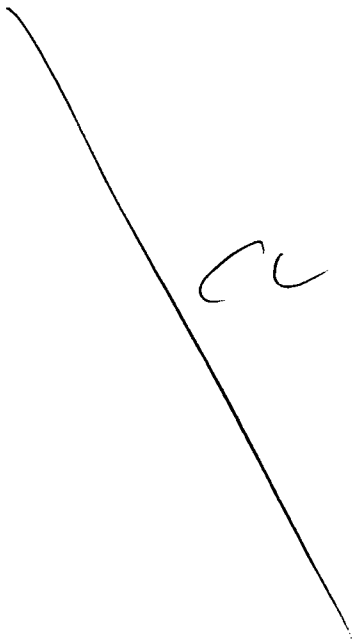

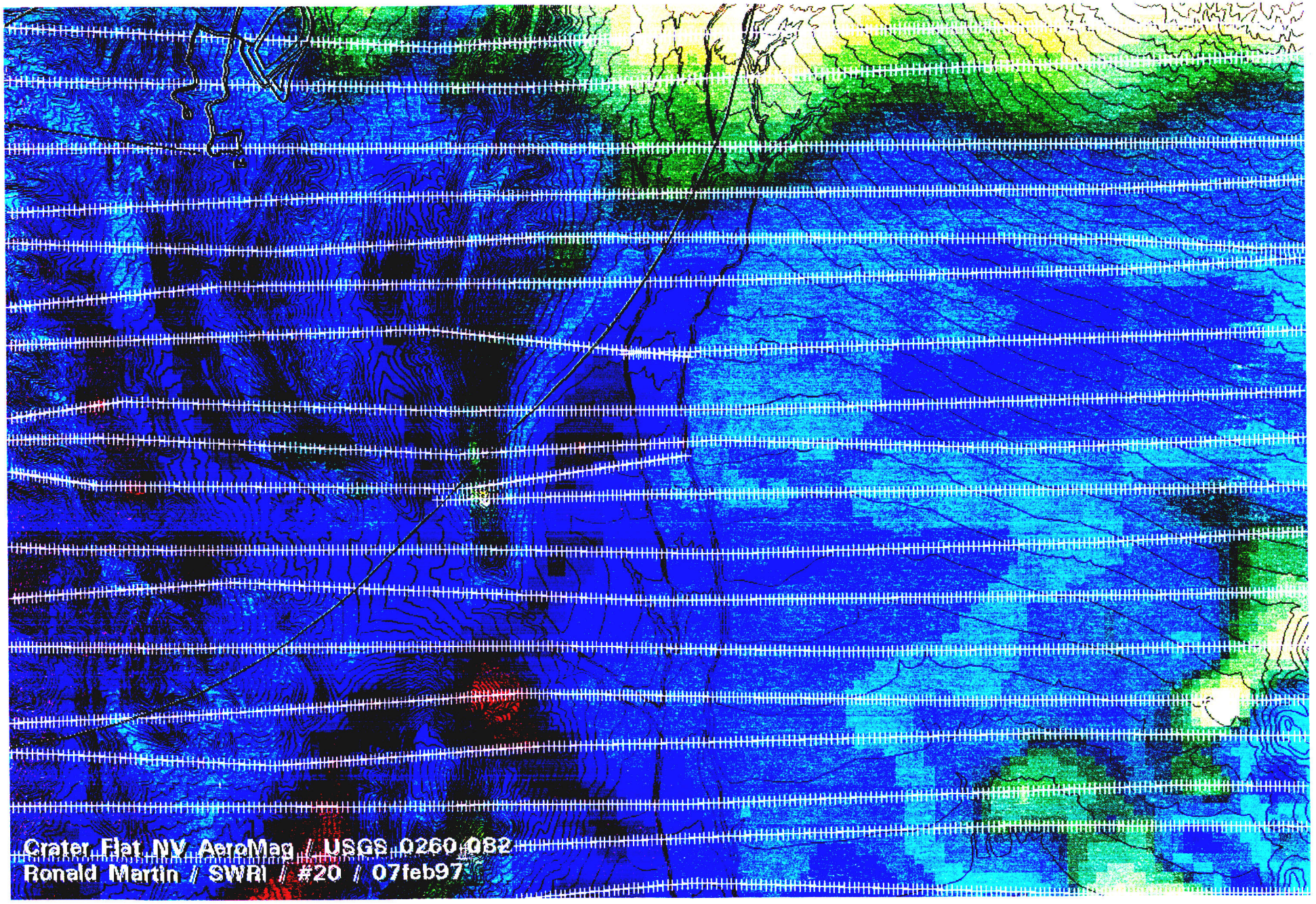
Crater Flat NV AeroMag / USGS 0260 082
Ronald Martin / SWRI / #20 / 07feb97

FIGURE 1. Line 2 - magnetics bold , DEM - thin line

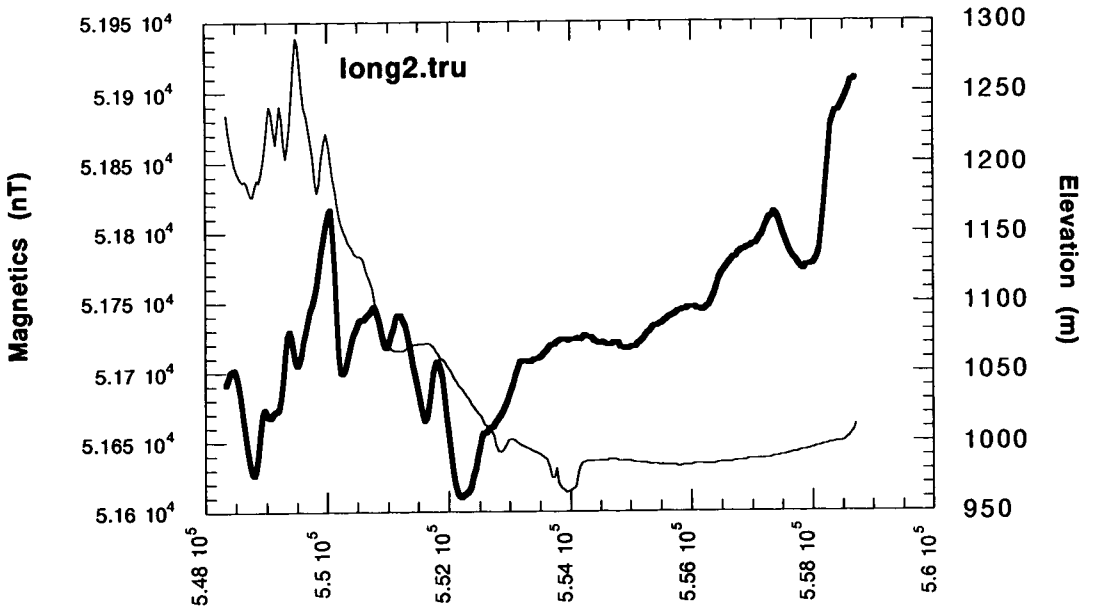

FIGURE 2. Flight Elevation for Line 2

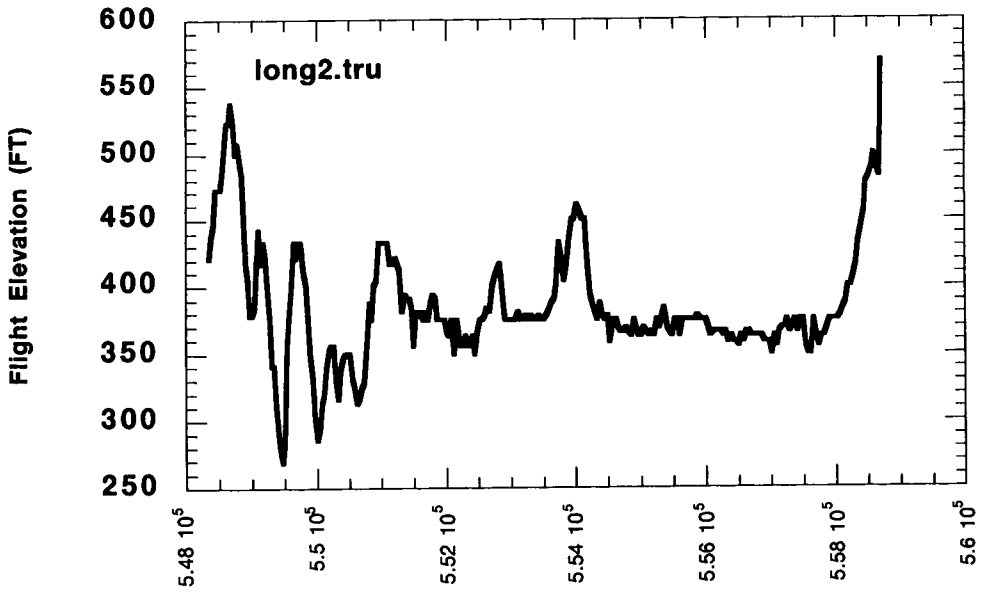

FIGURE 3. Line 3. magnetics - bold, DEM - thin line

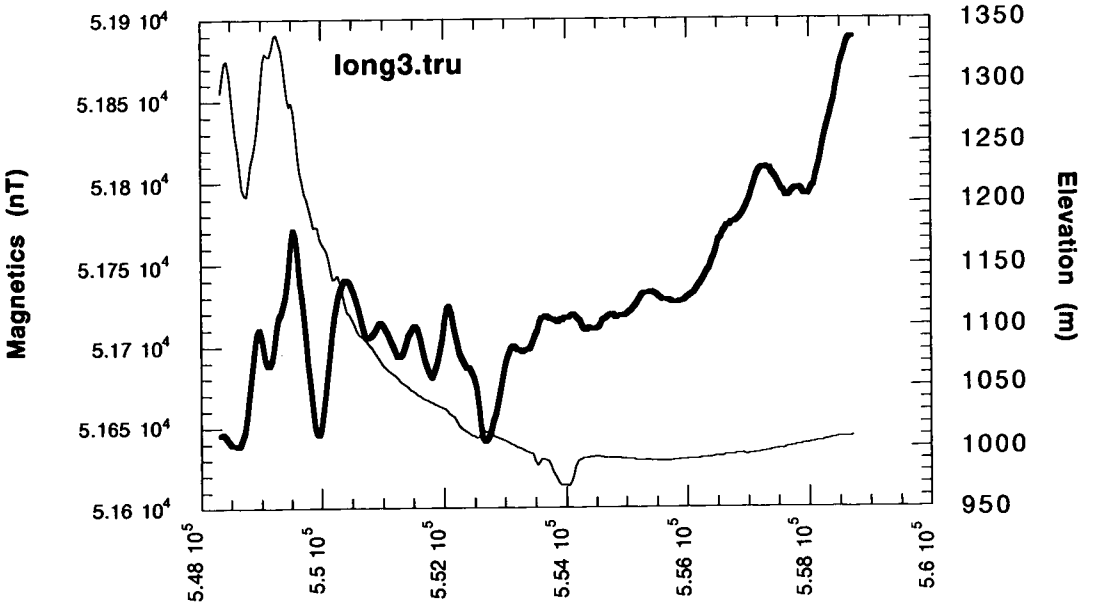

FIGURE 4. Flight Elevation line 3

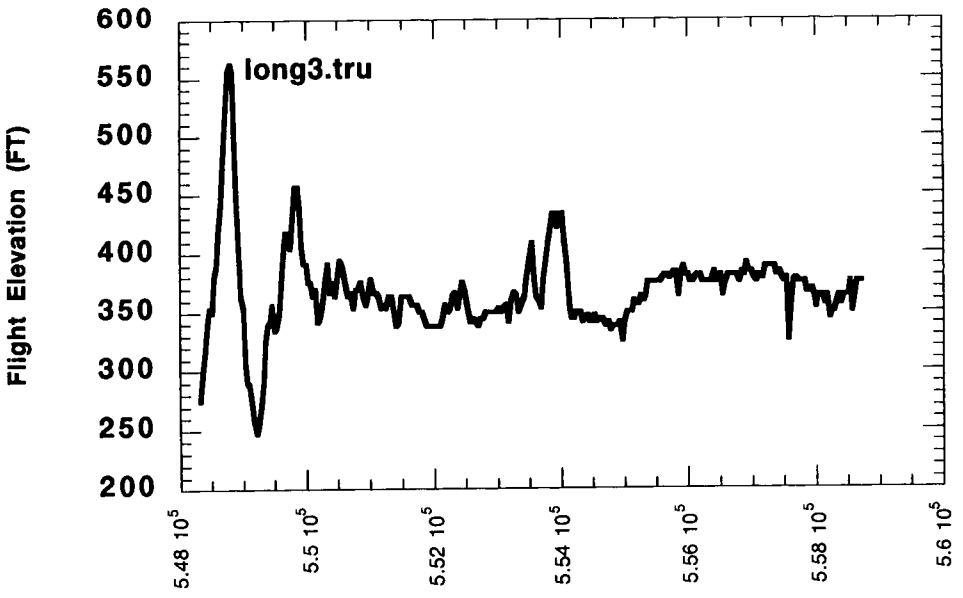

FIGURE 5. Line 4

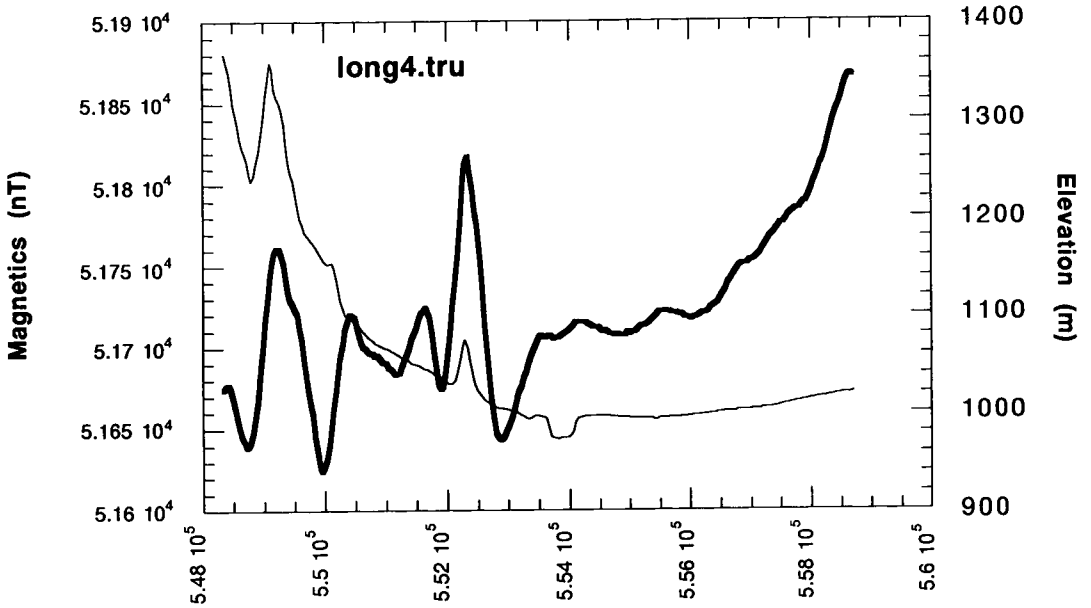

FIGURE 6. Flight Elevation - line 4

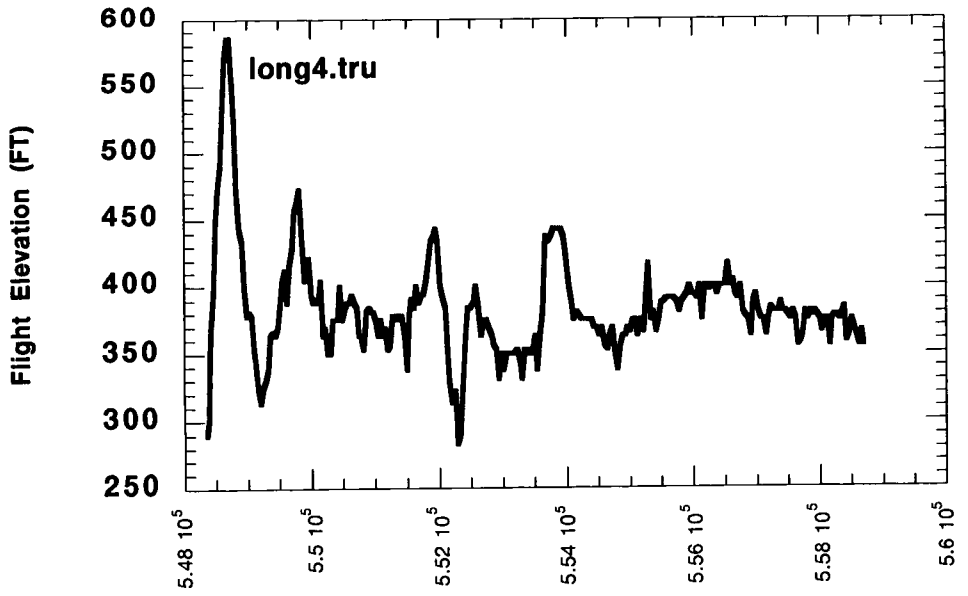

FIGURE 7. Line 5

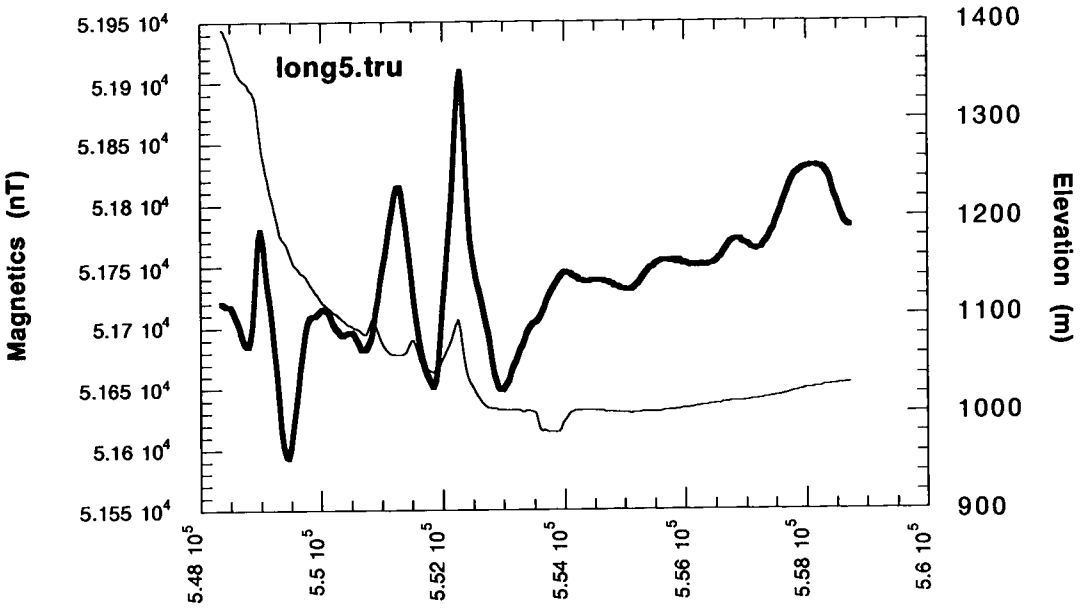

FIGURE 8. Flight Elevation line 5

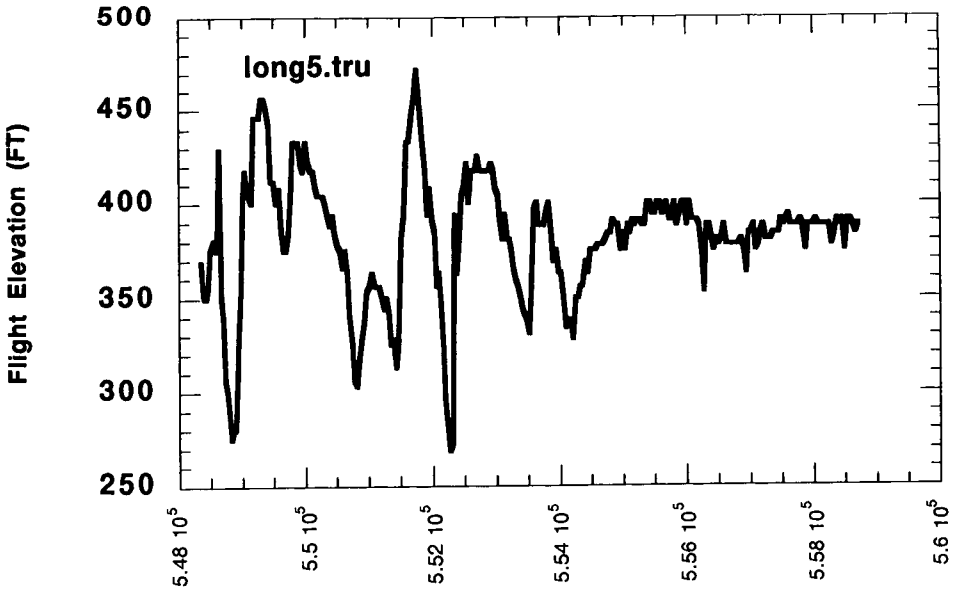

FIGURE 9. Line 6

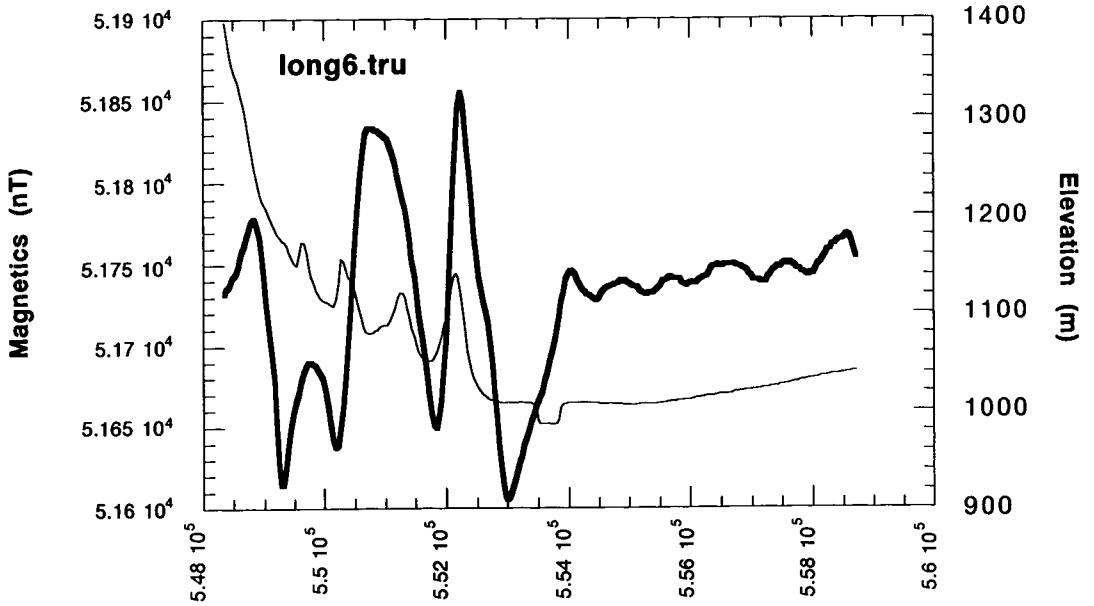

FIGURE 10. Flight elevation line 6

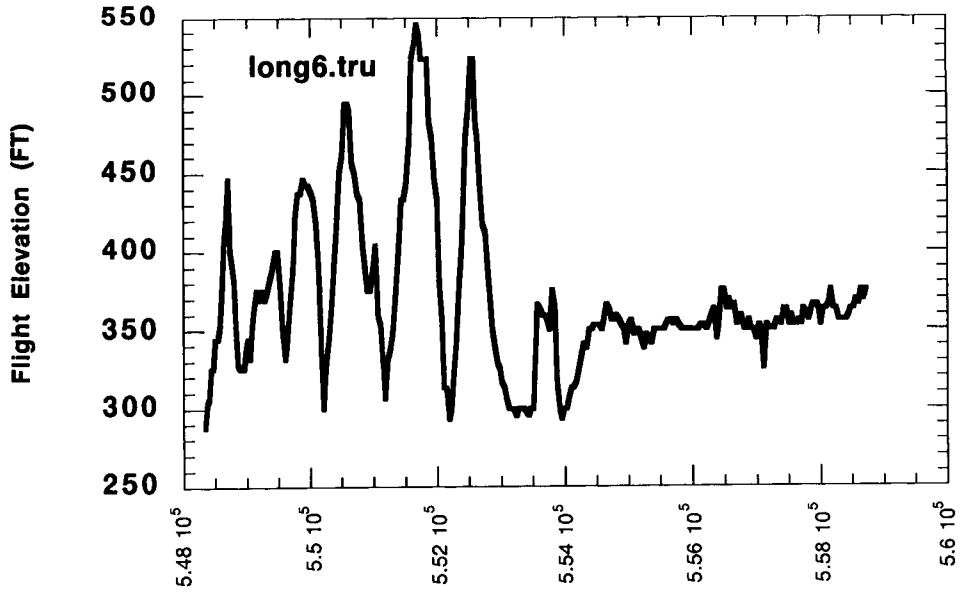

FIGURE 11. Line 7

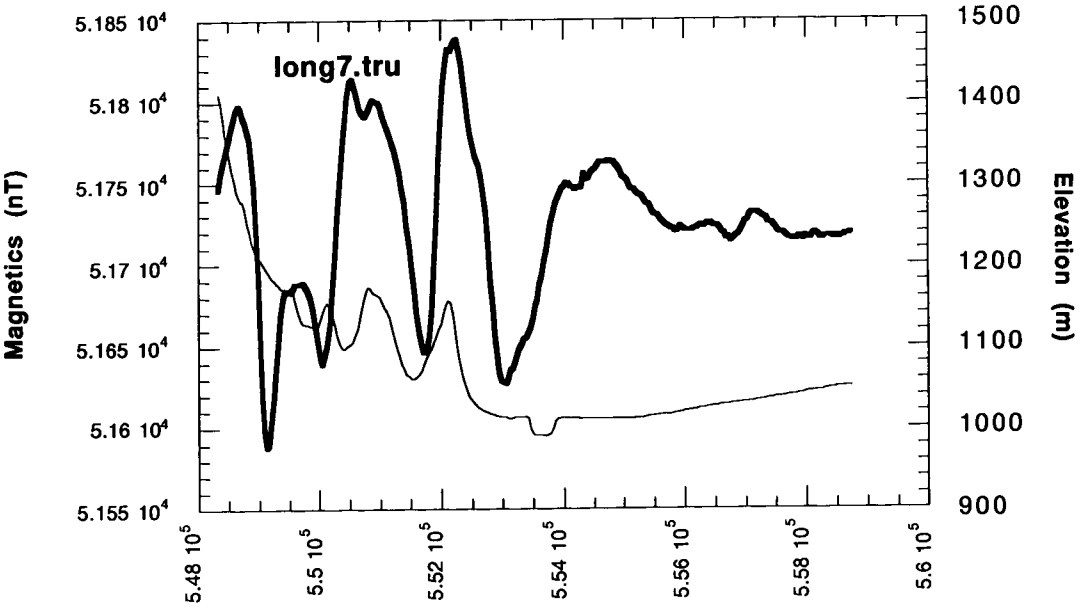

FIGURE 12. flight elevation line 7

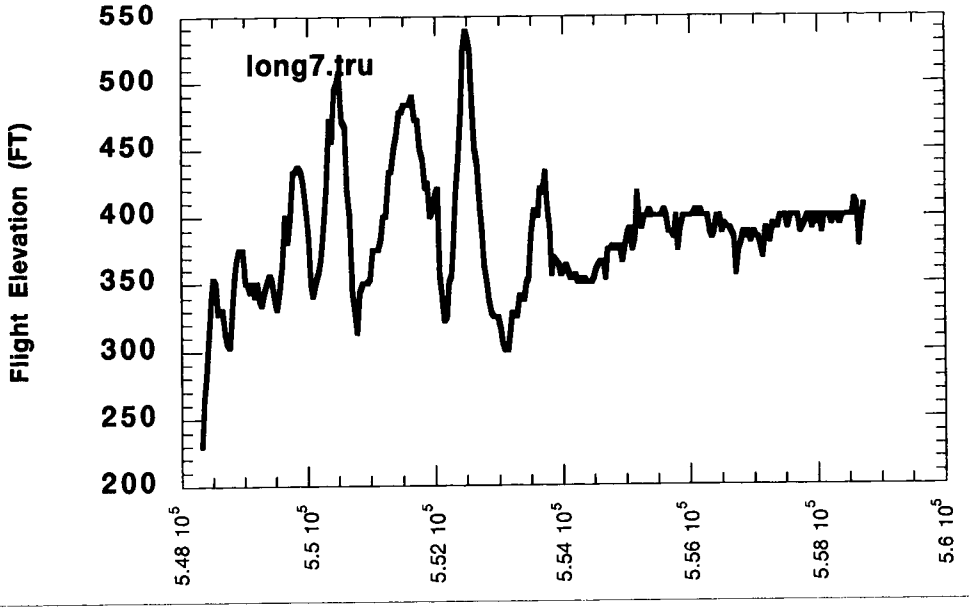

FIGURE 13. Line 8

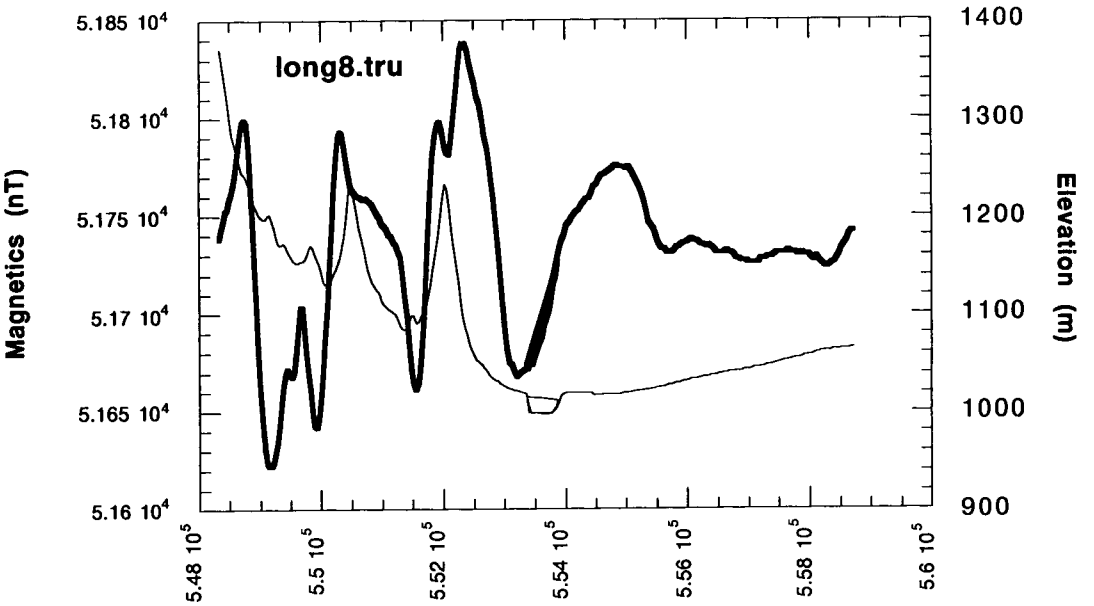

FIGURE 14. flight elevation line 8

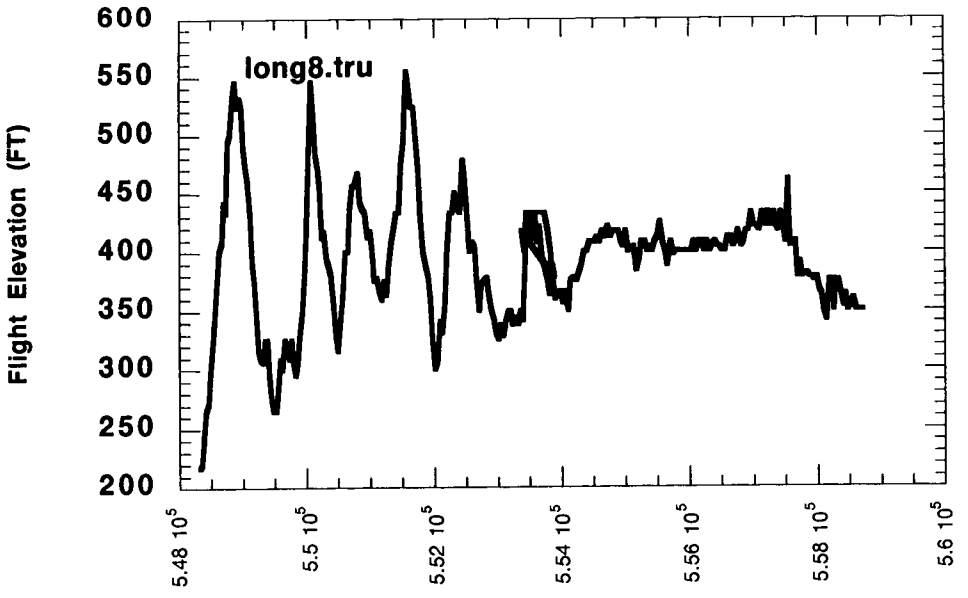

FIGURE 15. Line 9

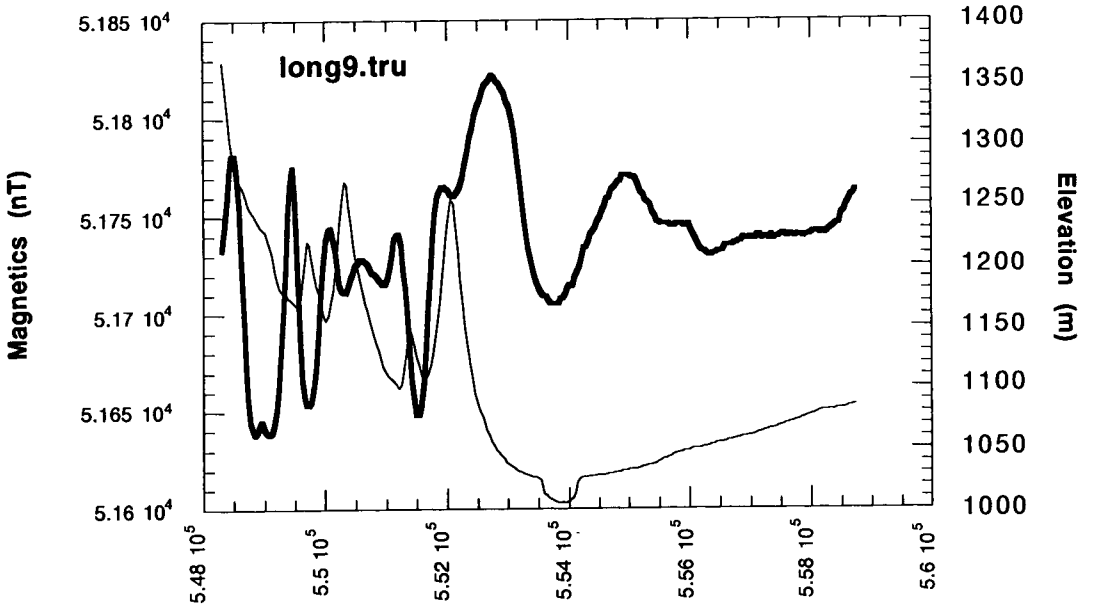

FIGURE 16. flight elevation line 9

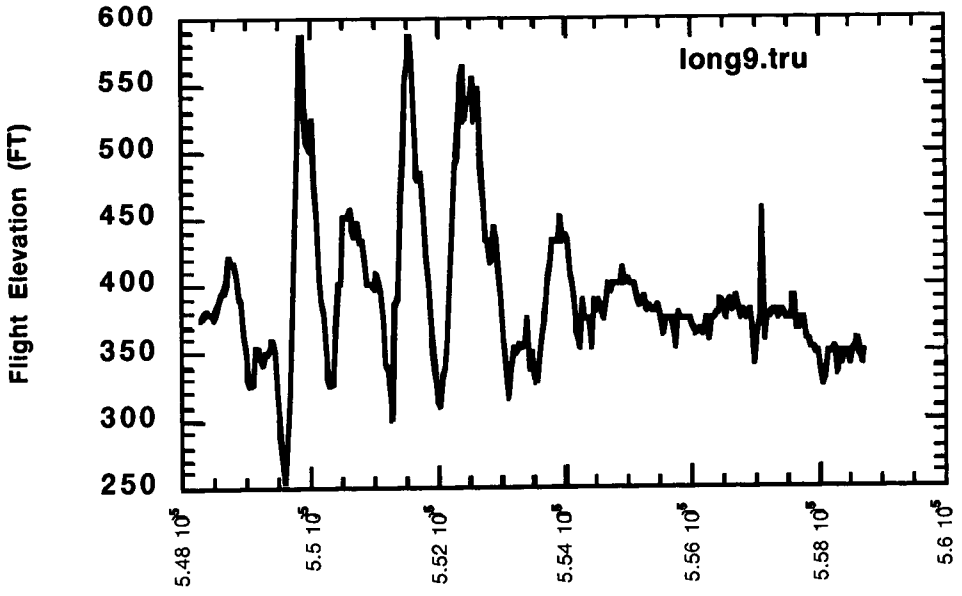

FIGURE 17. Line 10

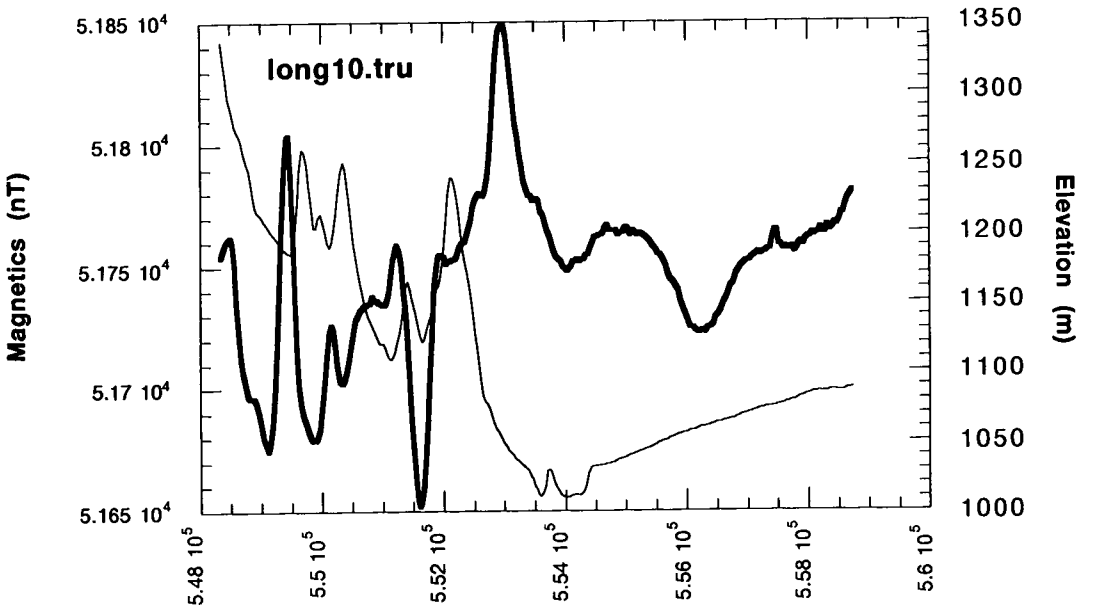

FIGURE 18. flight elevation line 10

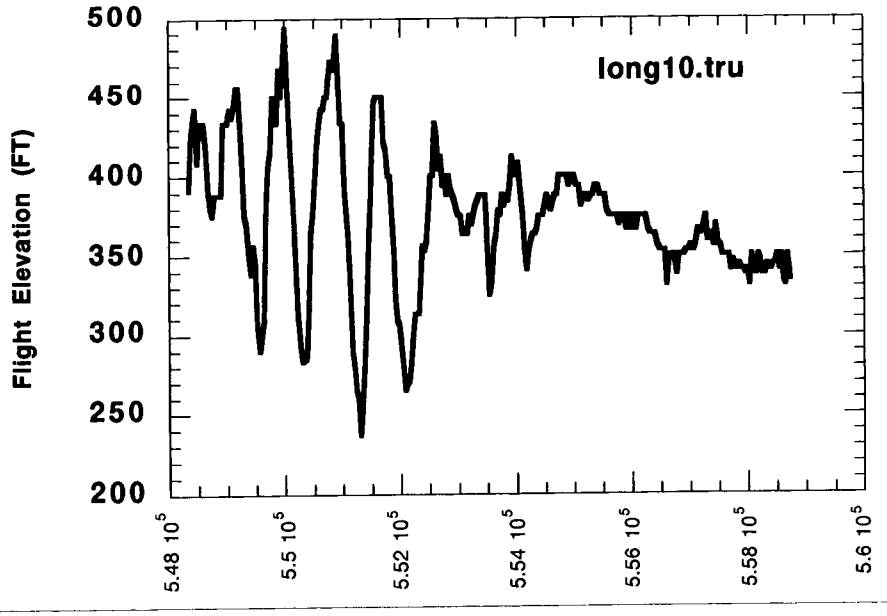

FIGURE 19. Line 11

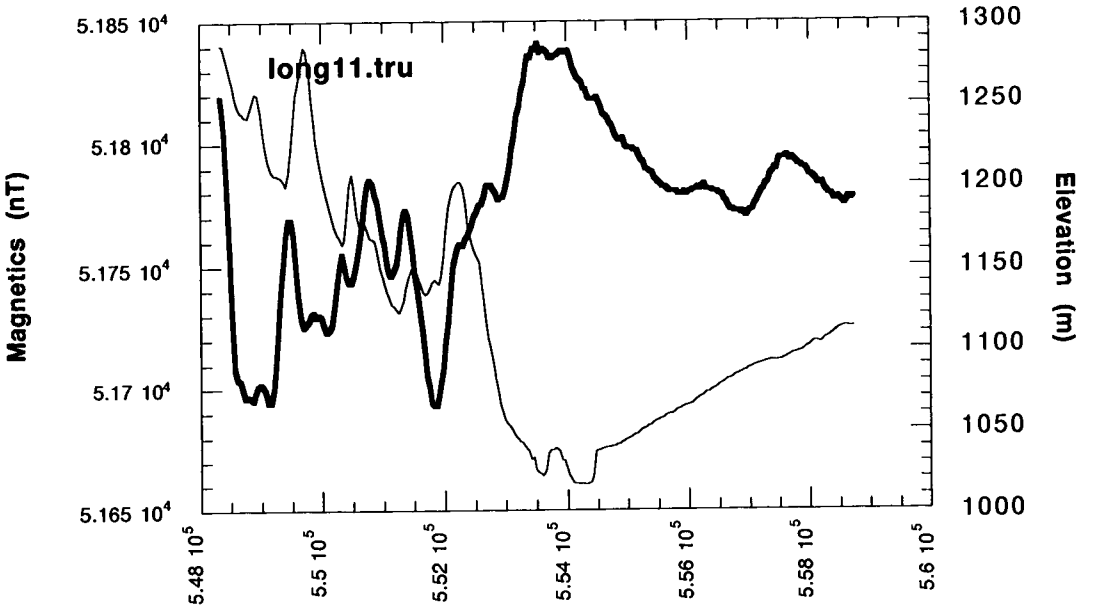

FIGURE 20. flight elevation line 11

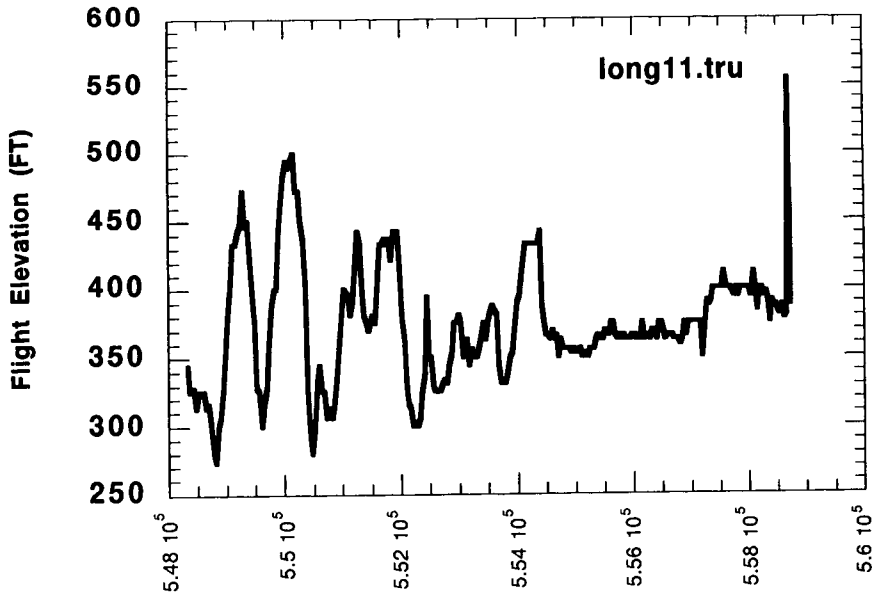

FIGURE 21. Line 12

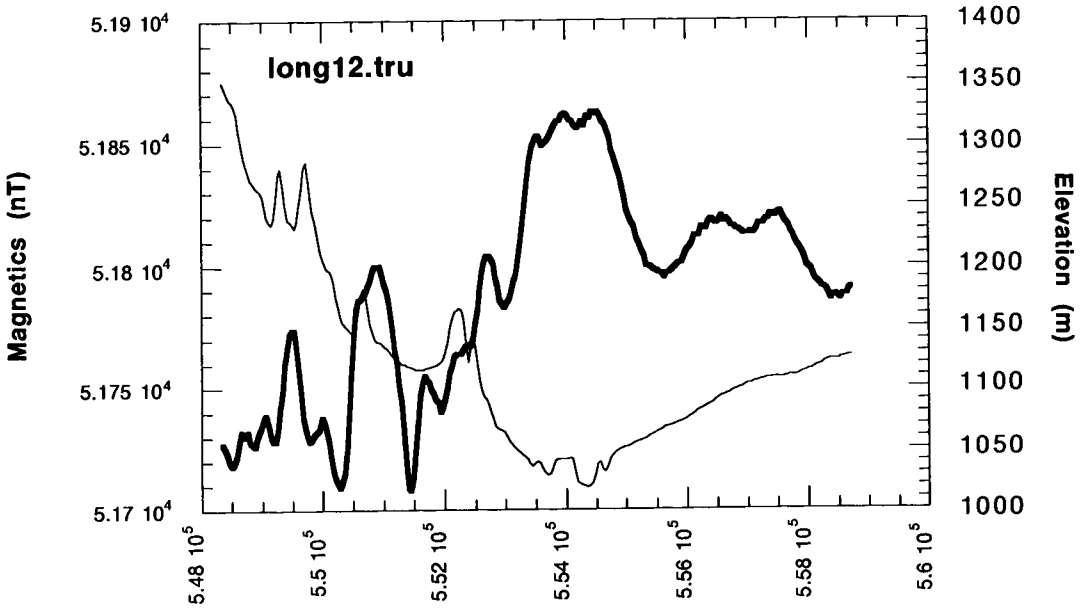

FIGURE 22. flight elevation line 12

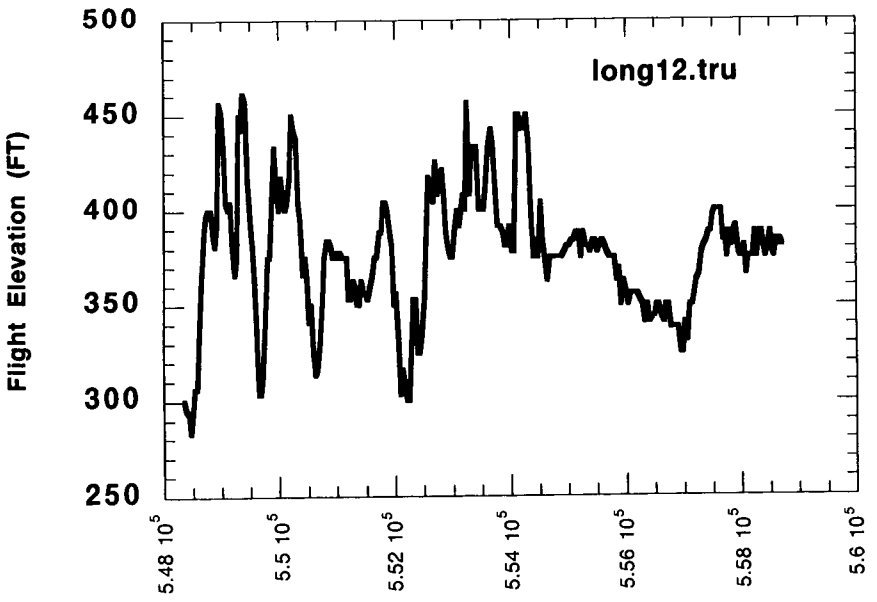

FIGURE 23. Line 13

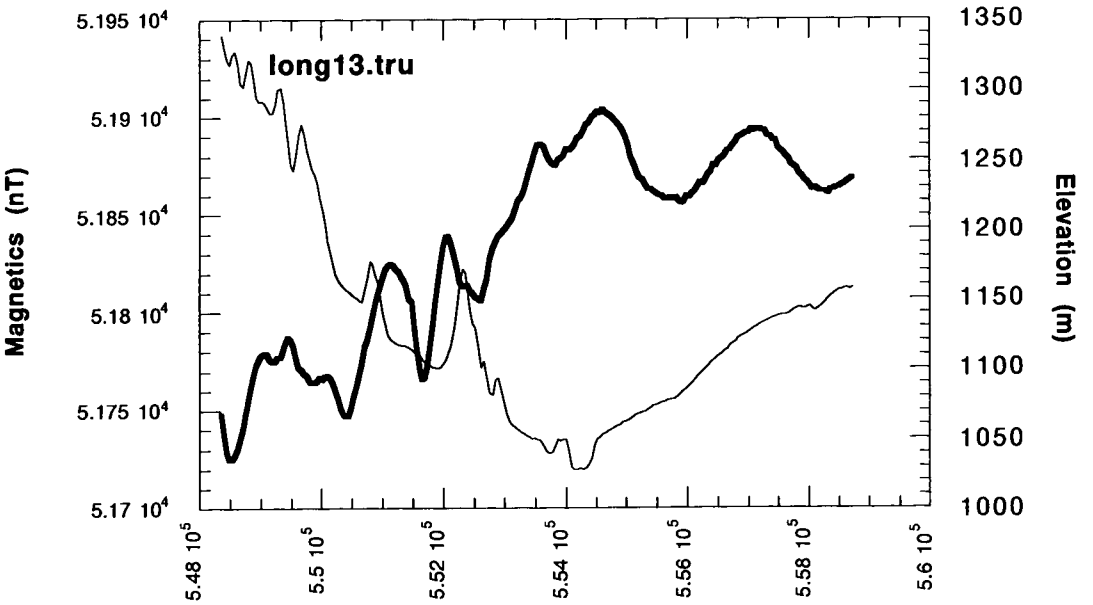

FIGURE 24. Flight elevation line 13

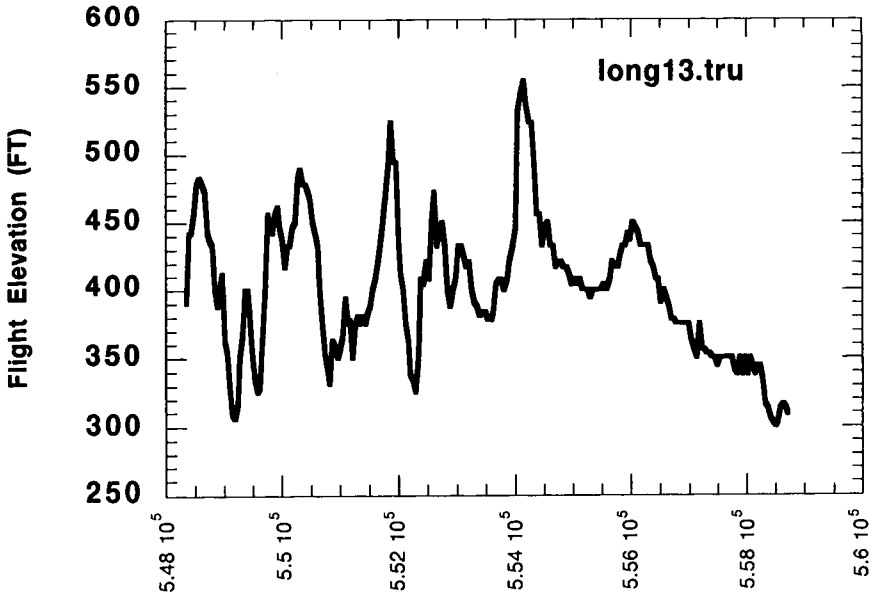

Modeling the Change in Slopes of cinder cones

Chuck Connor

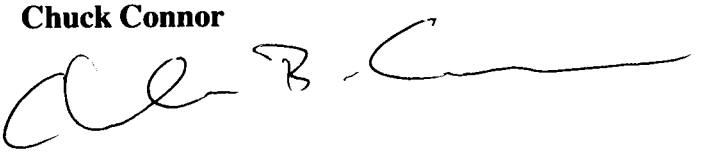

The diffusion equation in radial coordinates is used to model the change in slope of a cinder cone with time. This is useful in estimiating how well cones can be dated based on geomorphology. FM Conway will apply this in the San Francisco volcanic field.

1.0 Introduction

Cinder cones erode by diffusion and advection. Over time, scoria on the cone slopes creeps downslope as a diffusive process. Wash also occurs on cone slopes. Wash tends to develop gulleys and remove material from the base of the cone, but does little to change the slope of the cone over time (except locally in gulleys). Chang in slope over time is basically governed by creep. One way to express the change in height of a cone with time is using the diffusion equation.

$$\frac{\partial^2 h}{\partial r^2} + \frac{1}{r}\frac{\partial h}{\partial r} = \frac{1}{\alpha}\frac{\partial h}{\partial t}$$

Where h is the height of the cone, r is the radial distance from the center of the cone, t is time since the cone formation, and alpha is creep. This partial differential equation is solved using a finite difference approximation.

The following TrueBasic code solves the equation using finite differences:

```
•!generalized diffusion in one -dimension
•
•open #2: name "erodo.out", create newold
•erase #2
•
•dim mtx(100), new_h(100), slope (20000,2)
```

```
•
•let timleng = 1.5e6
•let timstep = 200
•let creep = 0.004
•let del_r = 10
•let totalpts = 100
•
•open #1: screen 0.2,0.8,0.2,0.8
•set window 0,1000,0,880
•
•!set up the cone geometry
•for x = 1 to 9
•let mtx(x) = 100 + x*del_r * sin(30*pi/180)
•next x
•
•for x = 10 to 100
•let mtx(x) = mtx(9) - (x*del_r - 9*del_r)*sin(35*pi/180)
•if mtx(x) < 0 then let mtx(x) = 0
•next x
•
•!plot the cone profile
•for x = 1 to 100
•plot x*del_r, mtx(x);
•next x
•plot
•
•
•!run simulation
•
•for timer = 1 to timleng step timstep
•
•for cont1 = 2 to totalpts-1
•let dum1 = (mtx(cont1+1) - 2*mtx(cont1) + mtx(cont1-1))/del_r^2
•let dum3 = (mtx(cont1-1)-mtx(cont1))/del_r
•
•let new_h(cont1) = creep*timstep*(dum1 + dum2) + mtx(cont1)
•next cont1
•
•let new_h(1) = new_h(2)
•let new_h(totalpts) = new_h(totalpts-1)
•
•mat mtx = new_h
•
•!plot
•!let count = 0
•!for x = 1 to 100
•!plot x*del_r, mtx(x);
•!next x
•!plot
•!end if
```

```
•
•let count = count + 1
•if count = 100 then
•
•let kount = kount + 1
•let slope(kount,1) = timer
•
•let max_slope = -1e10
•for xcount = 2 to 100
•
•let sloper = new_h(xcount-1) - new_h(xcount)
•if sloper > max_slope then let max_slope = sloper
•next xcount
•let slope(kount,2) = atn(max_slope/del_r)*180/pi
•print timer,slope(kount,2)
•let count = 0
•end if
•next timer
•
•for x  = 1 to kount
•print#2: slope(x,1),slope(x,2)
•next x
•
•end
```

Output from this code is the maximum slope of the cinder cone as a function of time in years.

For these simulations it is assumed that the cone has an outer slope of about 30°. The distance step in the calculations is 10 m and the time step in the calculations is 200 yr. Calculations are made out to 1 km from the cone center and for a total time period of 1.5 million years. It is assumed that the cone is radially symetric. Processes like cone breqaching are not considered.

2.0 Results

The creep coefficient alpha was varied from 0.004 m2/yr to 0.016 m2/yr. Profiles for this range of creep coeffiecients were calculated and maximum slope of the cone was calculated at each time step. These curves were compared to maximum slope bs. age data provided by Mike Conway.

FIGURE 1. Comparison of the diffusion model with maximum slopes on radiometrically dated cones,

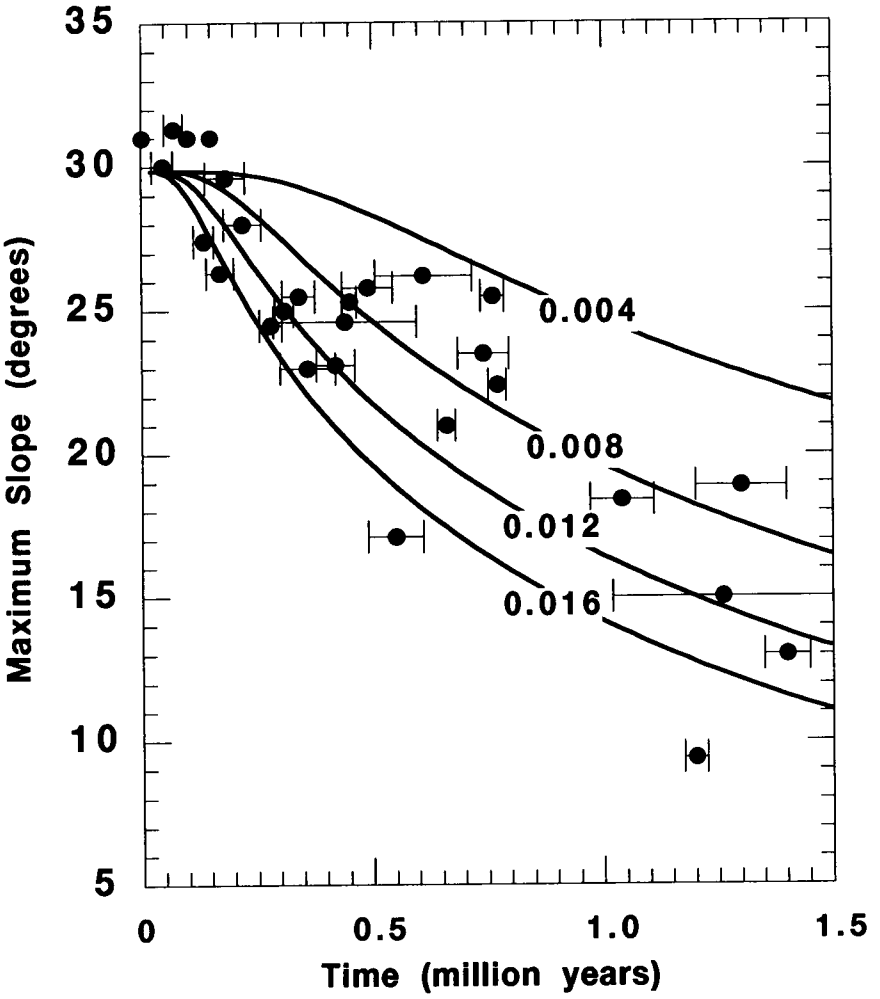

using coefficients of diffusion from 0.004 m2/yr to 0.016 m2/yr.

This range of diffusivities bound the data well. High diffusivites (e.g., 0.016 m2/yr) might be associated with cones that lack agglutination and consist of relatively fine grained scoria. Low diffusivities might be associated with cones that are either partially agglutinated or have relatively coarse scoria.

3.0 Conclusions

Cones of a given age may have widely varying maximum slopes due to variation in creep (associated with physical characher of cone scoria).

For the data, creeps between 0.004 and 0.016 m2/yr describe the range of slopes for different aged cones. A creep of about 0.01 m2/yr minimized the standard error.

A minimum age for cones seems to fall out rather well. For example, cones with max slopes less then 20° are not younger than 0.5 Ma.

It would be worthwile looking at the nature of scoria in the cones dated to determine if the degree of agglutination or grainsize varies well with creep. If this is the case, ages deduced from the maximum slope could be more precise than indicated by the full range.

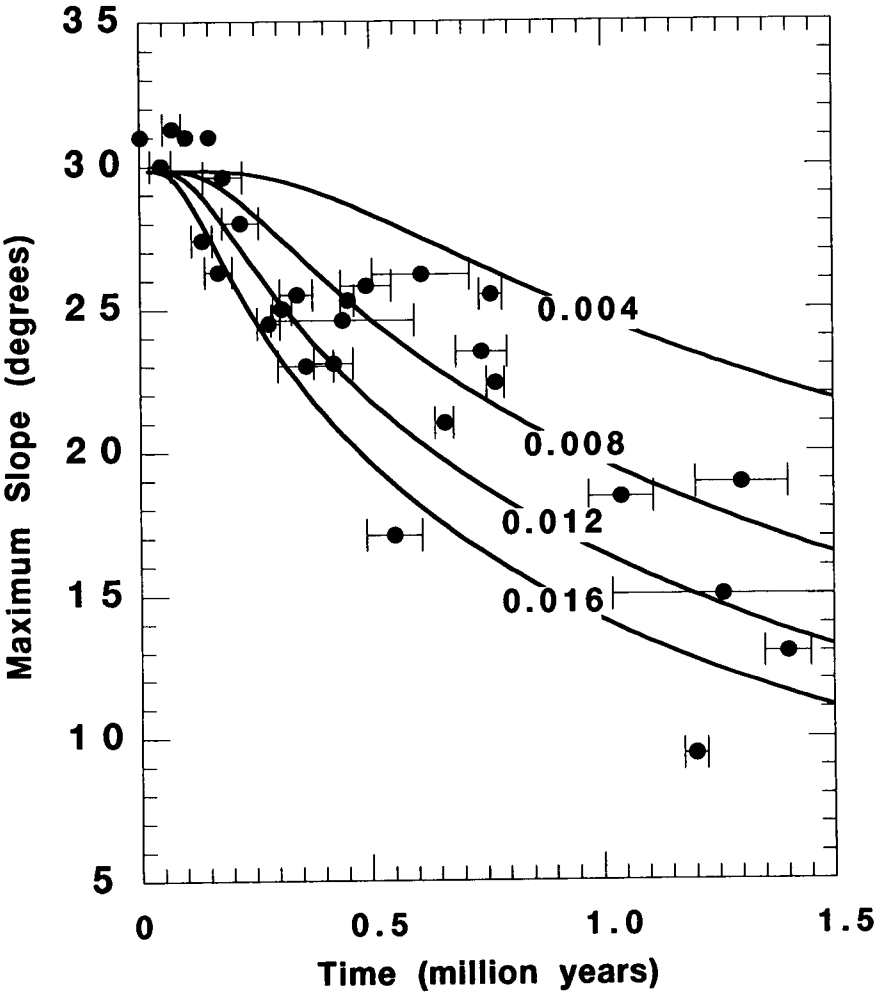
35
30
25
20
15
10
5
0
0.5
1.0
1.5
Maximum Slope (degrees)
Time (million years)
0.004
0.008
0.012
0.016

cc:Mail for: charles connor

Subject: Sci Notebook
From: Larry McKague 4/16/97 16:38
To: Charles Connor

"I have reviewed this scientific notebook and find it in general compliance with QAP-001 and there is sufficient technical information so that another qualified individual could repeat the activity.
(signed) _____ Element (date)"

H. Lawrence McKague
4/17/97

8/17

SCIENTIFIC NOTEBOOK 115E

BY

Charles B. Connor

SCIENTIFIC NOTEBOOK 115E

BY

Charles B. Connor

Southwest Research Institute
Center for Nuclear Waste Regulatory Analyses
San Antonio, Texas

SCIENTIFIC NOTEBOOK

CHUCK CONNOR

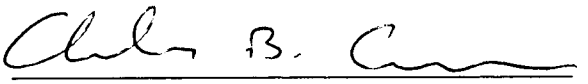

PROJECT

IGNEOUS ACTIVITY

PROJECT NUMBER 20-1402-461

October, 1997 - APRIL,1998

PARTS IN THIS NOTEBOOK:

Scientific Notebook
Project: 20-1402-461

Chuck Connor CC
December 31, 1997

Aero Magnetic Anomalies and Volcanism

IA staff have evaluated the significance of aeromagnetic anomalies in the YMR that may represent buried basaltic volcanoes. These aeromagnetic anomalies were identified by studying aeromagnetic maps in the site region and comparing these data with Landsat TM , topographic, and geologic databases within a geographic information system. The search area included Crater Flat, western Jackass Flat, and the Amargosa Valley near Yucca Mountain. The search area did not extend north of the southern edge of the Timber Mountain caldera or west of the Bare Mountain fault, or the southern projection of this fault into the Amargosa Valley.

Criteria for identifying these target anomalies on the aeromagnetic map were:

1) Occur in areas of alluvial sedimentation (bedrock not exposed)

2) Have amplitudes and wavelengths comparable to previously studied anomalies, such as Steve's pass anomaly, Northern cone anomaly, and the three aeromagnetic anomalies associated with Amargosa Valley aeromagnetic anomaly A.

These criteria were applied qualitatively by interpretation of the maps and images. At this point, more sophisticated map processing, such as wavelength filtering and related anomaly enhancement techniques have not been performed.

A total of 29 target anomalies were identified by applying these criteria. It is possible to rank the quality of these anomalies on a relative scale, a practice commonly followed in exploration using magnetic data. These 29 anomalies are in addition to previously recognized aeromagnetic anomalies associated with basalts, including aeromagnetic anomalies A-E and the normal polarity anomaly mapped in southern Crater Flat.

Ten of the anomalies are of highest quality, meaning that they have characteristics on the aeromagnetic map which are very similar to those anomalies we have identified previously. These are anomalies with amplitudes on the order to 60-200 nT, clear dipolar signatures, and which occur in isolation. It is expected that ground magnetic mapping of these sites has a reasonable high potential of identifying the large amplitude, short-wavelength anomalies associated with basalt in the Yucca Mountain region and may provide insight into structural controls on volcanism in the area. Because of their amplitudes and wavelengths on the aeromagnetic maps of the region, these anomalies are likely to be associated with shallowly buried rocks and therefore are more likely to be among the youngest basaltic features buried in the area. Only two of these anomalies have amplitudes and wavelengths comparable to the five aeromagnetic anomalies previously identified by the U.S. Geological Survey.

Ten anomalies are of slightly less robust character. Frequently, these anomalies have comparable amplitudes and wavelengths to the highest quality anomalies, but occur in areas where the magnetic data are generally more complex, usually

due to shallow basement. For example, a strong normal polarity anomaly occurs near Forty Mile wash west of Lathrop Wells. This anomaly would be of highest quality except that tuff in this area is shallow and also carries a strong magnetic signature, producing anomalies of nearly comparable amplitude. Thus, the causative body for this anomaly may be tuff. Other anomalies have reasonably good signatures but occur in high gradient areas, such as along fault blocks. Finally, some of these anomalies have smaller amplitudes or very short wavelengths (less than 0.5 km) compared to the highest quality anomalies.

The remaining 9 anomalies are possible targets, but because of anomaly shape, wavelength or amplitude are less likely to result from buried basalt.

Considering all 29 anomalies, the majority of these anomalies are located in Crater Flat and the Amargosa Desert. Most of these anomalies occur near areas where volcanoes have been previously mapped. Exceptions are: two high quality anomalies in northern Crater Flat, north of Northern cone; one high quality and one intermediate quality anomaly near Forthy Mile wash, north of US95; two intermediate quality and one low quality anomalies east of the Yucca Mountain block in Jackass Flat; and several anomalies east of anomaly B in the Amargosa Desert, possibly associated with the Miocene Stealth Basalt. Some other patterns of volcanism persist in the aeromagnetic anomalies. Anomalies tend to cluster and anomalies tend to produce NE-trends in vent distribution, similar to those observed in the mapped volcanoes of the YMR.

CNWRA staff are of the opinion that none of these anomalies should be included in probability models of the volcanic hazard at the proposed repository site until these anomalies are investigated further using ground magnetic surveys as a fast and inexpensive means of assessing each anomaly in detail. However, it is appropriate to investigate the potential impact of these new data on volcanic hazard assessments by assuming that all or some of these anomalies result from buried basaltic volcanoes not previously recognized or incorporated in probabilistic models.

The impact of these potential volcanoes on volcanic hazard was assessed using probability models previously published by CNWRA staff. These are nonhomogeneous Poisson probability models that calculate probability solely on the basis of the distribution of past volcanic events. An Epanachnikov kernel model was used because this is a relatively straightforward model with few underlying assumptions. Probability of volcanism occurring within a 5.2 km repository foot print was calculated. Dike length, dike width, and geometry of the disrupted zone are not considered in these models. Structural controls not considered in these models. The resulting models tend to yield comparatively low probability values because these features are not considered.

Briefly, the Epanechnikov model calculates probability of volcanism within a small area of interest by mapping a smoothing kernel about the locations of past volcanic activity. This kernel distributes probability about the volcano based on a smoothing parameter. Short smoothing parameters result in comparatively high probability zones close to existing volcanoes; long smoothing parameters result

in lower probability values that are more broadly distributed. Application of the Epanechnikov models results in the probability of volcanic disruption of a 1 km2 area at the center of the repository, given that a volcanic event occurs. A Poisson model is then used to estimate the probability of this event using a 10,000 yr time period of interest, a 5.2 km^2 area, and the recurrence rate of volcanism.

Previous CNWRA studies investigated the affects of changing smoothing parameters on probability of disruption of the repository using two data sets and smoothing parameters between 0 and 30 km. The clustering characteristics of cinder cones in the vicinity of the proposed repository indicate that smoothing parameters between 18 and 25 km best capture the distribution of past volcanism.

As a base case, the probability of disruption was calculated without using the additional aeromagnetic anomalies and assuming a recurrence rate of volcanism of 18 volcanoes in five million years. For this model, probabilities are zero at smoothing distances less than 8 km because this is the distance from the repository to Northern Cone, the closest mapped volcano to the repository. The probability goes through a maximum at a smoothing parameter of 18 km. The annual probability of disruption using a smoothing parameter of 18 km and a recurrence rate of 18 volcanoes in five million years is 1.2 x 10-8 /yr.

Including the aeromagnetic anomalies has two affects on this base case probability estimate. First, probabilities are much greater at smoothing distances less than 15 km. This is due to the presence of aeromagnetic anomalies in Forthymile Wash. Second, adding the 29 aeromagnetic anomalies to the 18 mapped volcanoes yields a recurrence rate of 47 volcanoes in five million years. At smoothing distances less than 15 km, probabilities increase by one order of magnitude or more. The change in probability is less dramatic at longer smoothing distances. For example, at a smoothing distance of 10 km the probability changes from 2 x 10-9 /yr to 2 x 10-8 /yr. At a smoothing distance of 18 km, the probability changes from 1.2 x 10-8 /yr to 3.1 x 10-8/yr when aeromagnetic anomalies are incorporated into the hazard analysis.

The change in probability is very sensitive to changes in the assumed regional recurrence rate. For example, suppose that five of the aeromagnetic anomalies represent volcanoes that are Quaternary in age. This assumption may be reasonable because several of the anomalies are located in areas of very high sedimentation. For example, the Steve's Pass anomaly, mapped during April field work, is located in an area of high sedimentation, is located along the Quaternary Crater Flat volcano alignment, and is reversely magnetized, as are all of the approximately 1 million year old basalts in Crater Flat. Under these circumstances, a better estimate of the recurrence rate is on the order of 15 volcanoes per million years, resulting in probabilities of volcanic disruption of 5 x 10-8/yr at a smoothing distance of 18 km.

Other types of probability models have given higher probabilities of volcanic disruption of the site. For example, some CNWRA models integrate gravity-gradient data, sensitive to the location of faults with large displacements, with

nonhomogeneous probability maps. Probabilities were calculated using the same recurrence rates given above and weighting gravity gradient and nonhomogeneous probability models equally. Probabilities of 5.3 x 10-8 /yr of site disruption were calculated using this structural model, not considering the aeromagnetic anomalies. The probability of volcanic disruption increased to 2 x 10-7/ yr when aeromagnetic anomalies were included in the model and a recurrence rate of 15 volcanoes per one million years was used.

Therefore, preliminary interpretation of these data and models indicates that inclusion of aeromagnetic anomalies increases probability by factors of 2 to 10, with the greatest increase seen in models that yield low probabilities. In addition, many of these volcanic centers are located well outside the volcanic source zones identified in the DOE Probabilisitc Volcanic Hazards Assessment elicitation. Simple expansion of these source zones to include the 29 possible basaltic centersalso would result in the inclusion of the repository within most of these zones. Therefore, inclusion of these volcanoes would likely impact the DOE Probabilisitc Volcanic Hazards Assessment probability calculations.

One fundamental result of this analysis is that it provides guidance about which anomalies have the largest potential impact on probability and, as a result, should receive high priority in further field invesitgations. These include the anomalies in the Forty mile wash, which are of variable quality and several anomalies in southern Crater Flat and the Amargosa desert, which because of their wavelengths, amplitudes, and positions in the basin may be shallowly buried in an area of rapid sedimation and, therefore, are possibly young.

Scientific Notebook
Project 20-1402-461

Chuck Connor CC
January, 1998

CNWRA Ground Magnetic Surveys in the Yucca Mountain Region, Nevada (1996-1997)

S. L. Magsino, C.B. Connor, B.E. Hill, J.A. Stamatakos, P.C. La Femina, D.A. Sims, and R.H. Martin

(Note: color figures are not contained in this notebook)
(Note: All data related to this milestone are contained on the CDROM accompanying report CNWRA98-001)

Executive Summary

The purpose of this Intermediate Milestone is to deseminate ground magnetic data collected by Center for Nuclear Waste Regulatory Analyses staff (CNWRA) in the Yucca Mountain region (YMR) between April, 1996 and June, 1997. These data were collected to support the U.S. Nuclear Regulatory Commission (NRC) in the analysis of volcanic and tectonic hazards to the proposed high-level radioactive waste repository at Yucca Mountain.

Data from fourteen surveys in the YMR are contained on a CD ROM attached to this report. These data are formatted as Arc/Info export files, text data files, postscript files showing magnetic maps of each survey area, and text files describing each survey. This CD ROM can be read by most computers. Nevertheless, the easiest and fastest way to read this CD ROM is to use a UNIX operating system.

1 INTRODUCTION

Yucca Mountain, the proposed site of the first high-level radioactive waste repository in the United States, lies within a central Basin and

Range Province of the North American Cordillera. This region is geologically active and the area about Yucca Mountain is no exception. During the Quaternary, the YMR has been the site of small volume basatic volcanic eruptions, faulting, and historical seismicity. This activity suggests that geologic hazards associated with the tectonic setting of Yucca Mountain must be assessed, as further volcanic eruptions and faulting at the site pose a risk of noncompliance of the site with environmental standards designed to protect the public health and safety during the performance period of the repository.

The U.S. Nuclear Regulatory Commission (NRC) has identified several key technical issues (KTIs) related to geologic hazards at the site. These KTIs include the Igneous Activity (IA) KTI, concerned primarily with volcanic hazards to the proposed respository and the Structural Deformation and Seismicity (SDS) KTI, primarily concerned with the faulting and seismicity in the site region during the perfomance period of the repository. Many of the technical activities related to these KTIs during 1996-1997 are described in Hill et al. (1997) and Stamatakos et al. (1997).

The purpose of this report is to make available ground magnetic data collected in the YMR by staff of the Center for Nuclear Waste Regulatory Analyses (CNWRA) between 1996 and 1997. These data were collected to support resolution of the IA and SDS KTIs. During 1996 and 1997, CNWRA staff conducted fourteen separate ground magnetic surveys in the YMR. Locations of these surveys are shown in Figure 1-1.

2 CD ROM Disk

A CD ROM disk accompanies this report. This CD contains ground magnetic data collected in the YMR of Nevada by the CNWRA staff. Data from fourteen surveys are included in this CD ROM disk. They are:

1) Crater Flat (1996)
2) Alice (1997)

3) Amargosa Desert (1996)
4) Baby Huey (1997)
5) Jackass Flat (1997)
6) Kane Spring (1997)
7) Northern Forty Mile Wash (1997)
8) Northern Cone (1996)
9) Porkchop (1997)
10) Solitario Canyon (1997)
11) Southern Crater Flat (1997)
12) Steve's Pass (1997)
13) SW Northern Cone (1997)
14) Windy Wash (1997)

A separate directory exists for each survey. Each directory contains the following:

- An Arc/info (v. 7.0.2) export file (*.e00) with raw data, drift corrected data, international geomagnetic reference field (IGRF) corrected data, and dates and times of data collection. These files can be accessed by creating a workspace within Arc/info and running the import command.

- A *.dat file contain the Northing, Easting, and IGRF corrected data in an x,y,z format. This file can be read by most word processing programs.

- An encapsulated postscript file (*.ps) with a map of the data gridded and contoured using EarthVision. This postscript file can be opened using Ghostview, Showcase, or similar postscript readers installed on UNIX operating systems.

- A directory contents explaining within which coordinate system (e.g., UTM, NAD 83) the survey was conducted, the names of the files within that directory, and details about the Arc/info coverages. This file can be read by most word processing programs.

The CD ROM disk can be read using UNIX, Windows NT, and MacIntosh operating systems. For full use of the data contained on this disk, it is recommended that a UNIX operating system be used and ARC/Info workspaces be created for each of the Arc/Info export files. If Arc/Info is not available, it is possible to read the *.dat files as simple text files. These text files can be used to plot, grid, and contour the data sets in packages like Geosoft Oasis Montaj, Surface III, Surfer, Geophysical Mapping Tools, and Earthvision.

3 METHODS

3.1 Data Collection

The ground magnetic surveys were conducted using a Geometrics model G-858 optically-pumped cesium-vapor magnetometer. This magnetometer provides data repeatability in areas of high magnetic gradient and is capable of collecting data at a much greater sampling rate than many other types of magnetometers. Magnetic readings were made with the G-858 at one or two second intervals. Sensor height was approximately 1 m above the ground surface for all surveys.

The magnetometer was interfaced to a differential global positioning system (DGPS), which collected position information every second. Real time differential corrections were made on position data and sent, via RS232 cable, as a string in National Marine Electronics Association (NMEA) protocol to the magnetometer and stored with magnetic measurements. The base station for these surveys included a proton-precession magnetometer (Geometrics model G-856), set to continuously record diurnal variation in the magnetic field, and the DGPS base station, consisting of a GPS receiver and telemetry.

3.2 Drift Corrections/Data Reduction

Positional information was reduced to true map coordinates by positioning

the DGPS base station at known benchmarks or by tying the base station to benchmarks in the region by DGPS surveying. Magnetic readings, time, position, and elevation were stored in the magnetometer memory and downloaded to a laptop computer at regular intervals.

Ground magnetic values presented in this report use drift corrected values from which the international geomagnetic reference field (IGRF) has been subtracted. An example of typical diurnal variation is shown in Figure 3-1. Diurnal variation from one day to the next was accounted for by comparing data collected at the same location on different days. After drift correction, the IGRF corrected value was calculated for each station (Malin and Barrachlough,1981).

3.3 Data Resolution

Although error associated with the cesium-vapor magnetometer is on the order of 0.1 nT, total error in the surveys is typically 1 nT due to position error. Error may be as much as 10 nT in areas of high magnetic gradient, as in areas of basalt cover. Error is introduced to the magnetic data in four ways:

- Change in instrument sensitivity
- Diurnal variation in the magnetic field
- Error in the GPS location
- Survey technique.

Change in instrument sensitivity refers to change in the value of the magnetic field measured by the magnetometer, exclusive of external factors. Instrument drift in magnetometers is very low, << 0.1 nT/day. Change in instrument sensitivity was monitored during most surveys by sampling the magnetic field at up to seven wooden stakes located in close proximtiy to one another. Readings were collected at each of these stakes in rapid succession and the difference between readings at successive stakes calculated. These difference values were compared before and after surveys were made. In all cases, it was determined that differences

changed by less than 0.9 nT.

Diurnal variation in the Earth's magnetic field results from changes in conductivity of the upper atmosphere during the day. These temporal changes are on the order of 30-50 nT and vary in amplitude over distances of100 km or more. Therefore, it is necessary to montior diurnal variations in the intensity of the magnetic field using a base station located at the survey site. Drift observed at the base station is subtracted from the field observations. Error is introduced into this drift correction because drift is interpolated between readings at the base station. Maximum rates of change in the magnetic field during these surveys was < 0.004 nT/s with 95 percent confidence. Thus, at a three minute sampling rate, interpolation error is most likely maximum at 90 s and could be as much as 0.36 nT. This assumes that maximum rates of change in the magnetic field are well represented by the variance in observations. Sampling was not conducted during magnetic storms, which produce greater rates of change in the magnetic field.

The ground resolution of the DGPS varies among the surveys. For three surveys conducted in 1996, Crater Flat, Northern Cone, and Amargosa Anomaly A, radio technical commission for maritime services (RTCM) DGPS corrections were made. RTCM data quality yields a horizontal postion ± 5 m of actual location 95 percent of the time. The remaining eleven surveys were completed using radio technical - twenty centimeter (RT-20) DGPS resolution. GPS positions are ± 20 cm of actual location 95 percent of the time in RT-20 surveys.

Several conditions occassionally occur during survey that dilute the precision of DGPS measurments. Loss of communication between one or more satellites and the GPS receiver (loss of lock) occasionally results in position errors. Since the status of the telemetry network is displayed on the GPS receiver during surveying, data are not collected during loss of lock. Momentary loss of lock not noticed by the DGPS operator during data collection is easily recognized during post-processing within a geographic information system (GIS) and such data are deleted. Upsets in the radio

telemetry between the base station and the survey party can also result in positional errors. These errors can also be noted in the field, during data collection, or during post-processing.

Additional positional error results from survey technique. Collection of ground magnetic data requires one person to carry the magnetometer and a second person carrying the DGPS receiver and antenna. Thus the magnetometer sensor and the DGPS antenna are separated by a distance of 3-4 m during the survey. This offset distance is necessary to avoid biasing the magnetic readings with the small magnetic field associated with the DGPS equipment. Because the person carrying the magnetometer walks in front of the person carrying the DGPS antenna, offset in the position information is partly corrected by correlating magnetic readings with DGPS readings collected 1-2 seconds after the magnetic readings are collected. Nevertheless, a total postion error resulting from survey design may be as much as 4 m. Combining this error with error resulting from the DGPS postion, magnetic features such as the boundaries of buried lava flows are located within ±9 m for the RTCM surveys and ±4.2 m for the RT-20 surveys.

Postion errors influence the absolute error in magnetic values depending on the local magnetic gradient. Typical local magnetic gradients are 0.1 to 1.0 nT /m. Thus a ±9 m postion error results in a error in the magnetic value at a given map location of 0.9 to 9.0 nT. Therefore, maximum errors on these surveys is considered to be 10 nT, except on very near-surface basaltic lava flows, on which the magnetic gradients can be much steeper.

4 AREAS SURVEYED

The fourteen magnetic surveys each consist of 3,000 to 70,000 magnetic measurements. Line spacing varied between 25-500 m, depending on the wavelength and complexity of observed anomalies.

4.1 1996 Crater Flat Survey

Crater Flat (Figure 1-1) is a structural half-graben where small-volume basaltic volcanism has repeatedly occurred since large-volume silicic volcanism ended during the mid-Miocene. Deposition of young alluvial sediments has partially or completely buried volcanoes in the southern part of the basin, obscuring the volcanic history of the area. Two Quaternary cinder cones, the Little Cones, are exposed in the northern portion of the survey area, with lava outcrops extending approximately 400 m south of the Little Cones. The survey area covers approximately 6 km^2 immediately surrounding and south of the Little Cones between UTM coordinates (533500, 4066000) and (536500, 4070000). Figure 4-1 is a magnetic anomaly map showing gridded and contoured results of the ground magnetic survey. The Little Cones (Figure 4-1) and surrounding lava flows are seen as short-wavelength, very high-frequency predominantly negative anomalies on the map. Magnetic data indicate the buried flows extend approximately 1 km beyond flows exposed at the surface. These flows are buried 15-30 m beneath a nearly featureless alluvial plane (Connor, et al., 1997). So, rather than being incongruously small volcanic features compared to nearby cones, the Little Cones and their lava flows exemplify the final stages of inundation and burial of two young cinder cones in an actively subsiding basin (Stamatakos, et al., 1996). The magnetic map also shows a striking positive anomaly approximately 2 km south of the Little Cones. This anomaly had been previously observed on aeromagnetic maps (Kane and Bracken, 1983; Langenheim, 1995). The anomaly has a peak-to-peak amplitude of 1100 nT, with positive and negative peaks separated by 750 m. The negative portion of this anomaly is truncated by anomalies associated with the Little Cone Lava flows. The polarity, size, and symmetrical nature of this anomaly indicate it is caused by an older, completely buried volcano. A third prominent magnetic feature was discovered near outcrops of Miocene basalt. This feature is a linear magnetic anomaly extending from the southern end of the survey area to the north-northwest for approximately 500 m (Figure 4-1). The anomaly is probably caused by a shallow dike associated with the Miocene basalts (Connor et al., 1997).

4.2 Amargosa "Anomaly A" Survey (1996)

Five anomalies were identified in Amargosa Valley by Langenheim, et al. (1993) as potential buried volcanoes or related igneous features. Of these anomalies, Amargosa "Anomaly A" (Figure 4-2) is the most complex and difficult to interpret from aeromagnetic maps. "Anomaly A" is of great interest because of its proximity to the Lathrop Wells cinder cone, the youngest volcano in the Yucca Mountain region, and because it is the closest of the Amargosa Valley anomalies to the proposed repository site. With these factors in mind, we completed a ground magnetic survey of "Anomaly A" to constrain its origin and to better resolve its distribution in the subsurface. The survey area covers approximately 20 km^2 within UTM coordinates 543500E, 4051000N and 547000E, 4060000N. The map of magnetic data collected over Amargosa "Anomaly A" delineates three separate anomalies associated with shallowly buried, reversely magnetized rock (Figure 4-2). These anomalies are distributed over 4.5 km on a northeast trend, and each has an amplitude of 70-150 nT. The identification of the northeast trend of "Anomaly A" is a key result of this survey. The trending is similar to the alignment of five Quaternary cinder cones in Crater Flat and to the Sleeping Butte cinder cones, a Quaternary vent alignment 40 km to the northeast. Although the age of the Amargosa Valley alignment is not known, it suggests that development of northeast-trending cone alignments is a pattern of volcanism that has persisted through time in the Yucca Mountain region and supports the idea that future volcanism may exhibit a similar pattern (Smith et al., 1990). Although the character of these anomalies can be partially resolved with aeromagnetic data (Langenheim, et al., 1993), trenchant details emerge from the ground magnetic survey are important to volcanic hazard analyses and tectonic studies of the region. Such details include the character of the southernmost anomaly, which has a smaller amplitude than those to the north but is nonetheless distinctive, and the northeast-trending structure within the negative portion of the central anomaly, which mimics the overall trend of the alignment. The ground magnetic data also enhance the small positive anomalies north of each of the three larger amplitude negative anomalies, reinforcing the interpretation that "Anomaly A" is produced by coherent basalt edifices with strongly

reversed remanent magnetizations (Connor, et al., 1997).

This survey was extended north of highway U.S. 95 as far as the southern outcrops of the lava flows from Lathrop Wells volcano (Figure 4-3). Short-wavelength anomalies on northern part of this map are a result of normally magnetized lavas from Lathrop Wells. A +70 nT anomaly is located south of these lavas. This anomaly is roughly circular in shape and approximately 1 km in diameter. This anomaly may result from an isolated block of buried tuff or basalt.

4.3 Northern Cone Survey (1996)

Northern Cone, located in Crater Flat approximately 8 km from the repository site, is the closest Quaternary volcano to Yucca Mountain. Its proximity to the site of the proposed repository makes the structural setting of Northern Cone of particular interest in volcanic hazard assessment. Surveying was conducted primarily along east-west trending lines 100 m apart over rugged alluvial topography. The survey area covered approximately 5 km^2 immediately surrounding Northern Cone. Gridded and contoured ground magnetic data over the Northern Cone area are presented in figure 4-4. The magnetic anomaly map is superimposed over topography, roads and mapped faults (Frizzel and Schulters, 1990). Northern Cone consists of approximately 0.4 km^2 of highly magnetized (10-20 Am^{-1}) lava flows, near-vent agglutinate, and scoria aprons resting on a thin alluvial fan. Large-amplitude, short-wavelength anomalies were observed over the cone.

No evidence of northeast-trending structures were discovered that could directly relate Northern Cone to the rest of the Quaternary Crater Flat cinder cone alignment. Instead, prominent linear anomalies surrounding Northern Cone trend nearly N-S and have amplitudes of up to 400 nT. These anomalies likely result from offsets in underlying tuff across faults extending beneath the alluvium (Connor, et al., 1997). The relationship between faults and Northern Cone is clear when the ground magnetic map is compared with topographic and fault maps (Frizzell and

Schulters, 1990; Faulds et al., 1994). The north-trending anomalies at Northern Cone roughly coincide with mapped faults just north of the survey area that have topographic expression resulting from large vertical displacements. These mapped faults and the faults inferred from the magnetic map are all oriented north to north-northeast, trends favorable for dilation and dike injection in the current stress state of the crust. Thus the Northern Cone magnetic survey further supports the idea that volcanism on the eastern margin of Crater Flat was localized along faults (Connor, et al., 1997).

4.4 Steve's Pass Survey (1997)

The Steve's Pass Survey was conducted over a 27 km^2 area immediately south of Bare Mountain and Steve's Pass. Other than a few outcrops of quartz latite lavas and tuff, the area is completely covered with alluvium. The complex nature of aeromagnetic anomalies over the area, including the highest amplitude aeromagnetic anomaly along the Quaternary Crater Flat volcano alignment makes this area particularly interesting.

Figure 4-5 is a ground magnetic anomaly map of the survey area. Notable features include a linear northwest-southeast trending ground magnetic anomaly truncating two N trending, curvilinear anomalies. Stamatakos, et al. (1997), describe the first of these anomalies as part of an active first-order fault extending from south of Beatty, Nevada to southernmost Bare Mountain and bending southward along the western edge of the Amargosa gravity trough. Stamatakos et al. (1997) and Slemmons (1997) named this fault the Carrara Fault. The magnetic expression of the Carrara Fault is most apparent in the features it offsets. A -1700 nT anomaly with a horizontal distance of 400 m between positive and negative peaks lies along the Carrara Fault, where this fault truncates a N-trending curvilinear anomalies. The amplitude and wavelength of this -1700 nT anomaly is consistent with buried basaltic lavas in the area and is interpreted to be a buried basaltic volcanic center, the Carrara Fault Basalt. This anomaly is elongated parallel to the trend of the fault. Some rotation or displacement may have occurred given the geometry of the

magnetic anomaly.

A smaller anomaly with peak-to-peak amplitude of 1700 nT, and horizontal distance between peaks of 50 m is located 400 m south of the Carrara Fault Basalt. The anomaly is also caused by a reversely magnetized body. No apparent displacement or rotation of this body has occurred. This, and the Carrara Fault Basalt, lie in alignment with 1.0 Ma basaltic cones in Crater Flat, also reversely magnetized, extending the Crater Flat volcanic alignment to 16 km in length.

The above mentioned N-trending curvilinear anomalies have similar length and trend, but opposite polarities, and are both truncated at the Carrara Fault. The western curvilinear anomaly is results from normally magnetized rock, has a peak-to-peak amplitude of 950 nT, and extends at least 2.5 km south of the Carrara Fault, probably continuing beyond the survey area. Parallel to this anomaly, approximately 1200 m to the east, is an anomaly with a peak-to-peak amplitude of 750 nT, produced by reversely magnetized rock. Both anomalies bend northeast approximately 1 km south of the Carrara Fault anomaly. Both anomalies are asymmetric in cross-section in the southern part of the map and become more symmetric as they curve to the north, possibly a result of the changing trend of the anomalies with respect to magnetic north. If these anomalies represent faults, the change in symmetry may be caused by greater throw on the faults in the north, closer to the Carrara Fault. Stamatakos et al. (1997) suggest these parallel anomalies are produced by the edges of a faulted blocks of highly magnetized Miocene silicic tuff or porphyry flows.

A third magnetic anomaly possibly produced by buried basalt lies in the southeastern part of the survey area and is detailed in figure 4-6. This is a symmetric reverse magnetic anomaly with a peak-to-peak amplitude of 360 nT separated by a horizontal distance of 150 m. The causative body is buried completely within alluvium and has a shape similar to a vertical cylinder, such as might result from erosion of a volcanic neck. This body is either of basaltic origin or a block of tuff which has slid off from hills to the north. This latter interpretation requires, however, that no

rotation of the tuff block occurred during transport to its present location.

The complex positive anomaly pattern observed in the northeast portion of figure 4-5 are related to Miocene quartz latite lava flows which crop out in the northern part of the map. Displacement in these anomalies is possibly caused by the Carrara Fault.

4.5 Alice Survey (1997)

The Alice survey area covers 0.5 km^2 in Forty-mile Wash, just east of Alice Ridge between UTM coordinates 554200E,4078600N and 554800E, 4080400N. The area is characterized by somewhat rough alluvial topography and is bounded on east and west by ignimbrite outcrops. This area was chosen for detailed investigation because aeromagnetic anomalies indicated the possible presence of basalts.

The most obvious feature on the ground magnetic map is a complex, high amplitude, negative anomaly in the central part of the survey area (Figure 4-7). Peak-to-peak amplitude of the anomaly is 800 nT, and the horizontal distance between positive and negative peaks is 200 m. The rest of the map is characterized by complex anomalies with amplitudes up to 200 nT of varying wavelength. Because of the nature of the anomalies and the presence of ignimbrite or tuff outcrops on either side of Forty-mile Wash, we attribute these anomalies to the presence of tuff beneath the alluvium. The "noisy" character of some contour lines are caused by randomly oriented blocks of magnetized rock within the alluvium. Some of the anomalies on this map may be caused by basaltic rocks, but ground magnetic data indicate that a shallowly buried volcanic center is not present in this area.

4.6 Northern Forty-mile Wash Survey (1997)

The Northern Forty-mile Wash survey was conducted over a 1 km^2 area

within Forty-mile Wash, northeast of Alice Ridge. The survey area is 700 m north of the northern boundary of Alice survey and is located between UTM coordinates 554200E, 4081100N and 555500E, 4082300N. The area is characterized by rugged alluvial topography bounded on both sides of the wash with rhyolitic ignimbrites. Like the Alice survey, this area was also chosen for detailed investigation because of aeromagnetic anomalies indicative of the possible presence of basalts. Anomalies in this area (Figure 4-8)large-amplitude and short-wavelength and complex in map pattern. Amplitudes range from 900 to 1500 nT, somewhat larger than the anomalies mapped near Alice Ridge, but are of similar wavelength (approximately 200 m peak-to-peak). As in theAlice Ridge area, these anomalies are attributed to ignimbrite beneath the alluvium.

4.7 Jackass Flat Survey (1997)

The Jackass Flat survey was conducted within Jackass Flat, an alluvial fan with very little topographic relief. The survey covered a 1.8 km^2 area between UTM coordinates 555400E,4072000N and 556400E, 4073800N. This investigation took place to determine the nature of an isol;ated aeromagnetic anomaly within this alluvial fan. The survey consisted of five N-S traverses spaced 200 m apart. The most obvious feature on the resulting ground magnetic map (figure 4-9) is a long wavelength, -50 nT anomaly. The observed ground magnetic anomaly has none of the magnetic character of a shallow basalt, nor does it resemble the magnetic anomaly shown on aeromagnetic maps. The causative body of the ground magnetic anomaly is interpreted to be a deep feature, possibly related to topography of the magnetic basement. Reexamination of the aeromagnetic anomaly suggests that it is an artifact caused by error in flight line position, and does not represent a geologic body.

4.8 Kane Spring Survey (1997)

The Kane Spring Survey covers a 2.5 km^2 area in Jackass Flat, west of Little Skull Mountain between UTM coordinates 554800E, 4062600N and

(556600E, 4065200N. The area is covered with alluvium with little topographic gradient. The area was investigated because of complex aeromagnetic anomalies along the N-trending Gravity Fault, north of aeromagnetic anomaly "B" (Langenheim, 1993). No surface expression of the Gravity Fault exists in the region. The ground magnetic anomaly map (figure 4-10) is dominated by a NNE-trending anomalies with a peak-to-peak amplitudes of approximately 150 nT. These anomalies are likely the result of offset of reversely magnetized ignimbrites across a west dipping N-trending normal fault. No evidence of shallow buried basalt was found in the Kane Springs area.

4.9 Baby Huey Survey (1997)

The Baby Huey Survey covers a 2 km^2 area located in the Amargosa Desert, southwest of Bare Mountain, between UTM coordinates 526200E, 4059800N and 527600E, 4062000N. This area was investigated to better delineate an aeromagnetic anomaly. The aeromagnetic anomaly was of particular interest because it is located along the southwest extension of the Crater Flat Quaternary cinder cone alignment. The survey was conducted over flat alluvium. The main feature on the resulting ground magnetic map (figure 4-11) is an oval shaped, 80 nT positive anomaly. Magnetic contrast on the southeastern edge of the anomaly is more abrupt where it is immediately adjacent to a very low amplitude (20-30 nT), N-trending structure transecting the length of the map. The positive anomaly may represent a block of ignimbrite displaced on a fault. Based on the horizontal magnetic gradient of the anomaly, the tuff may be thinning to the north or, displacement on the fault is greater in the north. There is no indication of shallowly buried basalt in this area.

4.10 Windy Wash Survey (1997)

The Windy Wash survey covers an 8 km^2 area within Windy Wash, adjacent to Yucca Mountain. This area was investigated in order to characterize the relationship between Pliocene Basalts in southern Crater Flat and geologic structures, such as the Crater Flat and Windy Wash faults. The survey covers the area between UTM coordinates 541200E, 4068200N and

543800E, 4070200N. This area consists of Pliocene basalts exposed on the Windy Wash and Crater Flat footwalls, separated by relatively flat alluvium. The magnetic map (figure 4-12) shows a complex pattern of short-wavelength, large-amplitude anomalies associated with exposed basaltic lavas and the Crater Flat and Windy Wash faults. The Crater Flat fault manifests itself as a 1000 nT anomaly produced by offset of reversely magnetized basalt in the western half of the map area. Basalt outcrops on the Crater Flat footwall are characterized by extremely high horizontal magentic gradients. Similarly, the Windy Wash fault appears on the eastern edge of the map as a N-S trending,1000 nT anomaly, most conspicuous at the edge of the lava outcrop.

The Crater Flat footwall basalts extend 600-1000 m east of the Crater Flat fault, based on the frequency and character of mapped anomalies. East of the buried basalts, the wavelength of magnetic anomalies increases abruptly, indicating an increase in the thickness of alluvium. Furthermore, the rocks buried at these greater depths are normally magnetized. This is best seen at the north edge of the lava flow along a WNW-trending lineament which indicates the position of the north edge of the rock unit. These data indicate the existence of a normally polarized body, basalt or tuff, located tens of meters below the Windy Wash alluvium. This finding suggests that the basalts exposed along the Windy Wash and Crater Flat Faults are not part of the same lava flow. The WNW-trending lineament may indicate the position of an additional fault, or mark the northern edge of a normally polarized lava flow.

4.11 Southwest Northern Cone

The Southwest Northern Cone survey covers a 1 km^2 area, approximately 2.5 km southwest of Northern Cone and 3 km north of Black Cone. The survey was located between UTM coordinates 537200E, 4076600N and 539000E, 4078600N. Surveying was conducted along a grid of north-south and east-west trending lines spaced 200 m apart over alluvial topography to characterize a magnetic anomaly discerned on aeromagnetic maps. Numerous low-amplitude, short-wavelength features over the map reflect

the presence of randomly-oriented highly-magnetized rock within the alluvium. Prominent in the center of the resulting ground magnetic map (Figure 4-13) is an anomaly with a peak to peak amplitude of 250 nT and a horizontal distance between peaks of 600 m. The most striking feature of this anomaly is the relationship between the positive and negative portions of the anomaly. The positive portion of the anomaly is of similar magnitude to, but higher horizontal gradient than, the negative portion of the anomaly, and appears to be wrapped around the northeast corner of the negative portion of the anomaly. This anomaly is the result of a buried body of reversely magnetized rock, likely basalt or tuff, that is tilted or thins to the northwest. This magnetized body may have also rotated in a clockwise direction since acquiring remanent magnetization.

4.12 Solitario Canyon Survey (1997)

The Solitario Canyon Survey was conducted over the Solitario Canyon Fault in order to map the magnetic anomalies associated with a known basaltic dike. Surveying was done within UTM coordinates 547100E, 4079400N and 547450E, 4081000N. The dike, exposed in a trench in the northwestern most part of the survey area, is dated to be 10.6 Ma and is approximately 3 m wide where exposed in the trench. Intermittent basalt outcrops were located up to 200 m south of the trench. The anomaly associated with this dike is reversely polarized, has a very short wavelength, and a peak to peak amplitude of approximately 800 nT (Figure 4-14). Transecting the entire length of the ground magnetic map is a north-south trending, short wavelengh, reversely polarized anomaly with an amplitude of approximately 300 nT. Intermmitently over this anomaly, paricularly notable in the southeast corner of the map, are areas of higher wavelength, similar in character to that produced by the known basaltic dike. The entire north-south structure has a wavelength and amplitude consistent with a basaltic dike and may represent a dike within the the Solitario Canyon Fault. The anomaly, however, may be produced solely by the fault.

4.13 Southern Crater Flat (1997)

The 1997 Southern Crater Flat survey was conducted in the deepest part of the Southern Crater Flat Basin, east of the 1996 Crater Flat Survey. The area covers approximately 2.8 km^2 between UTM coordinates 535800E, 4065400N and 537800E, 4067400N. Surveying was done along primarily N-trending lines spaced 200 m apart over flat alluvium. This area was chosen for detailed investigation to characterize ambiguous aeromagnetic anomalies mapped in two previous surveys across this area. The resulting ground magnetic map (Figure 4-14) shows several long-wavelength anomalies with amplitudes of between 70 and 150 nT. These anomalies are likely caused by structures within the magnetic basement and are not the result of near surface features.

4.14 Porkchop Survey (1997)

Two roughly N-trending traverses were conducted within northern Crater Flat. These traverses were done to ascertain whether an aeromagnetic anomaly located over this area is of volcanic origin. The eastern ground magnetic profile, Figure 4-15, is approximately 3.5 km long. This profiles shows a normally polarized anomaly having a peak-to-peak amplitude of 420 nT and a horizontal distance of 1200 m. This profile is characteristic of that produced by a horizontal body of magnetized rock beneath the surface. Figure 4-16 shows the resulting ground magnetic profile of the western traverse. The traverse is approximately 3 km long. The southern half of the survey is relatively smooth with a symmetrical 200 nT, reversely polarized anomaly with a horizontal distance of 150 m between peaks. The northern half of the survey is characterized by higher frequency, very high amplitude anomalies associated with exposed ignimbrite.

5 Summary

Fourteen ground magnetic surveys were conducted in the YMR between

April 1996 and June, 1997 by CNWRA staff. These surveys identified faults and buried volcanoes in the YMR, data required in order to complete the evaluation of geologic hazards at the proposed Yucca Mountain high-level radioactive waste repository.

6 References

Connor, C.B., S. Lane-Magsino, J.A. Stamatakos, R.H. Martin, P.C. La Femina, B.E. Hill, and S. Lieber. 1997. Magnetic surveys help reassess volcanic hazards at Yucca Mountain, Nevada. Eos, Transactions of the American Geophysical Union 78(7): 73, 75-78.

Hill, B.E., C.B. Connor, and J.S. Trapp. 1996. Igneous Activity. NRC High-Level Radioactive Waste Program Annual Progress Report, Fiscal Year 1996. CNWRA 96-01A. San Antonio, TX: Center for Nuclear Waste Regulatory Analyses: 2-1-2-32.

Kane,

Langenheim, V.E., and D.A. Ponce. 1995. Depth tooPre-Cenozoic basement in southwest Nevada. Proceedings of the Sixth Annual International Conference on High-Level Radioactive Waste Management. La Grange Park, IL: American Nuclear Society: 129-131.

Langenheim, V.E., K.S. Kirchoff-Stein, H.W. Oliver. 1993. Geophysical investigations of buried volcanic centers near Yucca Mountain, southwestern Nevada. Proceedings of the Fourth Annual International Conference on High-Level Radioactive Waste Management. La Grange Park, IL: American Nuclear Society: 1,840-1,846.

Stamatakos, J.A., C.B. Connor, B.E. Hill, S. L. Magsino, and D.A. Ferrill. 1997. The Carrara Fault in southwestern Nevada revealed from detailed gravity and magnetic results: Implications for seismicity, volcanism, and tectonics near Yucca Mountain, Nevada. Eos, Transactions of the American

Geophysical Union,

Slemmons, D.B. 1997. Carrara Fault, in southwestern Nevada from paleoseismic, geologic, and geophysical evidence: Implications to the earthquake hazards and tectonics near Yucca Mountain, Nevada. Eos, Transactions of the American Geophysical Union,

Chuck Connor CC
October, 1997

- DOE's definitions of igneous events will be acceptable provided that they are defined consistently throughout the safety case. Intrusive and extrusive events should be distinguished and their probabilities estimated separately. Definitions in current use for extrusive volcanic events include formation of a new volcano (Crowe et al., 1982; Connor and Hill, 1995), an episode of eruptive activity at a new or existing volcano following an extended period of quiescence (Ho et al., 1991; Smith and Bradshaw, 1994), and mappable eruptive units, each being an assemblage of volcanic products with internal stratigraphic features that indicate a cogenetic origin and eruption from a common vent (Condit and Connor, 1996). Definitions of intrusive events include injection of single igneous dikes and formation of dike swarms (Delaney and Gartner, 1994).

Technical Basis

It is critical to provide a formal defintion of the igneous or volcanic event used to describe recurrence rate in any volcanic hazard analysis model. The definition used for igneous or volcanic events will affect the results of the probability analysis, and therefore must be used consistently throughout the analysis. Furthermore, it is critical to account for differences in event definition when comparing the results of different probabilistic volcanic hazard analyses.

Definitions of volcanic and igneous events include:

- Individual mappable eruptive units
- Episodes of vent or vent alignment formation
- Occurrence of an igneous intrusion

- Volcanic eruption and accompanying dike injection.

As discussed in the following, these volcanism in the YMR can be categorized using each of these definitions but with varying degrees of confidence. The probabilities resulting from applications of these differenct definitions will be different, and the consequences of these events on repository performance are different.

Definitions of volcanic events vary widely in the literature (Condit and others, 1989a; Bemis and Smith, 1993; Delaney and Gartner, 1994; Lutz and Gutmann, 1995; Connor and Hill, 1995). Ideally, volcanic events would correspond to eruptions. Unfortunately, subsequent geologic processes often obliterate evidence of previous eruptions from the geologic record (e.g., Walker, 1993). Consequently, volcanic events have been defined as mappable eruptive units, each unit being an assemblage of volcanic products having internal stratigraphic features that indicate a cogenetic origin and eruption from a common vent (Condit and Connor, 1996). A simple definition that can be applied to young cinder cones, spatter mounds, and maars is based on morphology: an individual edifice represents an individual volcanic event (Connor and Hill, 1995). In older, eroded systems, such as Pliocene Crater Flat, evidence of the occurrence of vents, such a near-vent breccias or radial dikes, is required. One important advantage of this definition of volcanic events is that it is based on geological and geophysical mapping, and not based on geochronological data. Therefore, this definition can be applied with greater confidence than others which require geochronological data. Volcanic hazard analyses using this definition for volcanic events assumes that all mapped volcanic units occur as independent

events. The resulting probability estimate is for direct disruption of the proposed repository by volcanic eruption (e.g., Connor and Hill, 1995).

However, several edifices can form during a single, essentially continuous, eruptive episode. For example, three closely spaced cinder cones formed during the 1975 Tolbachik fissure eruption (Tokarev, 1983; Magus'kin et al., 1983). In this case, the three cinder cones represent a single eruptive event, that is distributed over a larger area than is represented by a single cinder cone. The three 1975 Tolbachik cinder cones have very different morphologies, and erupted adjacent to three older (late? Holocene) cinder cones (Braytseva et al., 1983). Together this group forms a 5 km-long N-trending alignment. Without observing the formation of this alignment, it would likely be difficult to resolve the number of volcanic events represented by these six cinder cones if the number of volcanic events was defined as the number of eruptions. This type of eruptive activity results in uncertainty in the number of volcanic events represented by individual volcanoes, even where these volcanoes are well-preserved.

Additional mapping in other volcanic fields has indicated that some cinder cone alignments develop over long periods of time during multiple episodes of volcanic eruption (Connor and Condit, 1992; Conway et al., 1997), particularly where there is fault control on the locations of basaltic vents. For example, Conway et al. (1997) found that the northern segment of the Mesa Butte Fault Zone, San Francisco volcanic field, Arizona, repeatedly served as a pathway for magma ascent for at least 1 m.y., resulting in the formation of a cinder cone alignment (Figure ***). Isochron

dates reported in Conway et al. (1997) indicate that volcanism along the northern Mesa Butte Fault was episodic and successive episodes were separated in time by as much as 400 k.y. (Figure ***). Additionally, spatial patterns of volcanism along the Mesa Butte alignment were apparently independent of field-wide trends, evinced by the large lateral shifts in volcanic loci between successive episodes. These observations help clarify trends observed in the development of young, potentially active volcanic alignments. For example, the largely Holocene Craters of the Moon Volcanic Field shows similar eruption patterns characterized by multiple episodes of magmatism and frequently shifting loci of volcanism along the Great Rift (Kuntz et al., 1986), albeit on a time scale of thousands of years. This behavior contrasts sharply with eruption patterns of other short-lived fissure eruptions, such as the Laki fissure eruption (Thordarson and Self, 1993), or the Tolbachik erupton of 1975. Observations of episodic volcanism along the Mesa Butte Fault indicate independent magmatic episodes may recur along structures even following periods of quiescence lasting 100 ka or more. Thus alignments, such as the Amargosa magnetic anomaly A alignment can not be considered to represent single volcanic events *a priori.*

Paleomagnetic and radiometric dating of the Quaternary Crater Flat cinder cones (Figure ***) suggest that these cinder cones may have formed during a relatively brief period of time (< 100,000 yr), and therefore, like the Tolbachik alignment, may represent a single eruptive event. Evidence from aeromagnetic and ground magnetic surveys (Langenheim et al., 1993; Connor et al., 1997) suggests that buried volcanoes exist in southern Crater Flat along this alignment. Therefore the alignment may have reactivated through time, in a manner similar to the Mesa Butte volcano

alignment.

Effectively, defining aligned volcanoes of similar ages as single volcanic events reduces both the total number of volcanic events in the region and the regional recurrence rate. However, the area affected by the entire cone alignment is much greater than the areas impacted by individual cinder cones, and this affect must be propoagated through the volcanic hazard analysis.

Experimentation with changes the definition of a volcanic event from indidivual cinder cones to cone alignments has indicated that this change has little affect on the probability of disruption of the repository because the increased area affected by volcanic events offsets the reduction in the regional recurrence rate (Connor and Hill, 1995). Hazard analyses made using this definition of volcanic events also estimate the probability of direct dsruption of the proposed repository. Primary uncertainties in this estimate will result from estimation of the number and distribution of volcanic vents along alignments.

Some of the geochemical variation present at some YMR Quaternary volcanoes has been interpreted to represent reactivation of individual volcanoes after more than 10,000 yr quiescence (Wells et al., 1990; Crowe et al., 1992b; Bradshaw and Smith, 1994). However, results from paleomagnetic studies appear to contradict this interpretation (Champion, 1991; Turrin et al., 1991), and cast doubt on the likelihood that cinder cones in the YMR have reactivated long after their original formation (Whitney and Shroba, 1991; Wells et al., 1991; 1992; Turrin et al., 1992). Given the

possibility of cinder cone reactivation, the number of volcanoes present in the YMR may underestimate the rate of volcanic eruptions that will occur in the future in the YMR. However, in the context of volcanic hazards for the proposed repository, the spatially dispersed character of volcanism gives rise to hazards, rather than the reactivation of an existing cinder cone. Thus, reactivation of cinder cones would be interesting as a gauge of overall activity in the volcanic system, but is not necessarily related to rates of new volcano formation.

Igneous events differ from volcanic events in that igneous events must encompass the intrusive and extrusive components of igneous activity. Generally, the number of mapped igneous dikes is not considered to be a reasonable definition of igneous events because multiple dikes are often injected into the shallow crust during single episodes of ignous intrusion. Furthermore, individual dikes frequently coalese at lower stratigraphic levels. For example, Delaney and Gartner (1994) mapped approximately 1,700 individual dikes in the Pliocene San Rafael volcanic field, Utah. These dikes are associated with approximately 60 breccia zones and volcanic buds, that are interpreted to the the roots of volcanic vents which have eroded away. Based on their mapping the the San Rafael volcanic field, Delaney and Gartner (1994) suggested that approximately 175 episodes of intrusion resulted in the emplacement of the 1,700 dikes and 60 volcanic vents, but also indicated that this grouping of mapped units was a subjective process.

In the YMR, the number of Plio-Quatrnary igneous events is unknown, but, based on analogy with the San Rafeal volcanic field, may be a factor of two or more greater

than the number of volcanic events. Studies in the YMR by Ratcliff et al. (1994) and Crater Krough and Valentine (1995) have demonstrated that Miocene basaltic igneous intrusions stagnated within several hundred meters of the surface without erupting. These basaltic dikes and sills are mapped in Miocene tuffs, similar in character and composition to those of Yucca Mountain. Thus, probability estimates based on the number of igneous events would encompass both direct disruption of the repository with transport of waste into the accessible environment during a volcanic eruption, and the indirect effects of volcanism, such as canister failure during dike or sill intrusion. Primary uncertainty in a probability estimate based on this definiton of igneous event would result from uncertainty in the recurrence rate of igneous intrusions.

Finally, it is possible to define an igneous event in terms of the subsurface area disrupted by the intrusion of magma during a volcanic event. For example, numerous dikes in the San Rafael volcanic field were injected laterally through the shallow subsurface for hundreds of meters away from volcanic vents during volcanic eruptions. Uncertainties resulting from this definition of igneous events includes estimate of probable lengths and widths of dike zones associated with the formation of vents and the locations of vents along these dike zones.

Chuck Connor CC
Nov, 1997

Acceptance Criteria 3

Estimates of the probability of volcanic disruption of the proposed repository by igneous activity must be consistent with patterns of past igneous activity in the region and in other comparable volcanic fields. Patterns in the distribution and timing of cinder cone volcanism in the YMR are similar to patterns identified in other, often more voluminous volcanic fields. These spatial patterns include:

- Shifts in the locus of volcanic activity through time
- Vent clusters
- Vent alignments and correlation of vents and faults

Each of these spatial patterns is reviewed in this section, with emphasis on the nature of these spatial patterns in the YMR and how these compare with spatial patterns in cinder cone volcanism observed in other basaltic volcanic fields. This comparison is followed by a discussion of how these spatial patterns in volcanic activity can be used to calibrate and test probabilistic volcanic hazard models for disruption of the proposed repository.

4.4.3.1 Shifts in the location of basaltic volcanism

Spatial variation in recurrence rate of volcanism in the YMR are shown by shifts in the locus of basaltic volcanism from east to west since the cessation of caldera-forming volcanism in the Miocene Southern Nevada Volcanic Field (Crowe and Perry, 1989). Comparable shifts have occurred in many other volcanic fields. In the Coso Volcanic Field, California, Duffield et al.

(1980) found that basaltic volcanism has taken place in essentially two stages. Eruption of basalts occurred over a broad area in what is now the northern and western portions of the Coso Volcanic Field from approximately 4 to 2.5 Ma. In the Quaternary the locus of volcanism shifted to the southern portion of the Coso field. Condit et al. (1989) noted the tendency for basaltic volcanism to gradually migrate from west to east in the Springerville Volcanic Field between 2.5 and 0.3 Ma. Other examples of continental basaltic volcanic fields in which the location of cinder cone volcanism has migrated include the San Francisco Volcanic Field, Arizona (Tanaka et al., 1986), the Lunar Crater Volcanic Field, Nevada (Foland and Bergman, 1992), the Michoacán-Guanajuato Volcanic Field, Mexico (Hasenaka and Carmichael, 1985), and the Cima Volcanic Field, California (Dohrenwend et al., 1984; Turrin et al., 1985). In some areas, such as the San Francisco and Springerville Volcanic Fields, migration is readily explained by plate movement (Tanaka et al., 1986; Condit et al., 1989; Connor et al., 1992). In other areas, the direction of migration or shifts in the locus of volcanism does not correlate with the direction of plate movement. In either case, models developed to describe the recurrence rate of volcanism or to predict locations of future eruptions in volcanic fields need to be sensitive to these shifts in the location of volcanic activity.

Generally, sensitivity to these shifts in the locus of volcanism can be accomplished by weighting more recent (e.g., Pliocene and Quaternary) volcanic events more heavily than older (e.g., Miocene) volcanic events. However, shifts in the locus of volcanism also introduce uncertainty into the probabilistic hazard assessment. For example, in the Cima volcanic field, < 1.2 Ma basaltic vents are located south of older volcanic vents (Dohrenwend et al., 1984; Turrin et al., 1985), suggesting that probability models based on the distribution of older vents would not have forecast the location of subsequent eruptions adequately. In the Springerville volcanic field, large scale shifts in the locus of volcanism accompanied a geochemical change in the basalts, from tholeiites and transitional basalts to more alkalic basalts, suggesting that a change in petrogenesis signaled

shifts in the locus of volcanism (Condit and Connor, 1996). Fortunately, the affects of large scale shifts in the locus of volcanism on probability models are mitigated by the long time scales (>0.25 m.y.) on which these shifts appear to occur in other volcanic fields.

4.4.3.2 Vent Clustering

Crowe et al. (1992a) and Sheridan (1992) noted that basaltic vents appear to cluster in the YMR. Connor and Hill (1995) performed a series of analyses of volcano distribution that yielded several useful observations about the nature of volcano clustering in the region. First, vents form statistically significant clusters in the YMR. Spatially, volcanoes less than 5 Ma form four clusters, the Crater Flat and Amargosa Valley Clusters overlapping somewhat due to the position of Lathrop Wells volcano and the three aeromagnetic anomaly A vents. Second, a volcanic event located at the repository would be spatially part of, albeit near the edge of, the Crater Flat Cluster, rather than forming between or far from clusters in the YMR. Third, three of the four clusters contain Quaternary basalt, indicating that these clusters are long-lived and provide some indication of the likely areas of future volcanism.

Cinder cones are known to cluster within many volcanic fields (Heming, 1980; Hasenaka and Carmichael, 1985; Tanaka et al., 1986; Condit and Connor, 1996). Spatial clustering can be recognized through field observation, or through the use of exploratory data analysis or cluster analysis techniques (Connor, 1990). Clusters identified using the latter approach in the Michoacán-Guanajuato and the Springerville Volcanic Fields were found to consist of 10 to 100 individual cinder cones. Clusters in these fields are roughly circular to elongate in shape with diameters of 10 to 50 km. The simplest explanation for the occurrence, size, and geochemical differences between many of these clusters is that these areas have higher magma supply rates from the mantle. Factors affecting magma pathways through the upper crust, such as fault distribution, appear to have little

influence on cluster formation (Connor, 1990; Connor and Condit, 1994). In some volcanic fields, such as Coso, the presence of silicic magma bodies in the crust may influence cinder cone distribution by impeding the rise of denser mafic magma (Eichelberger and Gooley, 1977; Bacon, 1982), resulting in the formation of mafic volcano clusters peripheral to the silicic magma bodies.

Basaltic vent clustering has a profound affect on estimates of recurrence rate of basaltic volcanism. For example, Condit and Connor (1996) found that recurrence rate varies by more than two orders of magnitude across the Springerville volcanic field due to the spatio-temporal clustering of volcanic eruptions. In the YMR, Connor and Hill (1995) identified variations in recurrence rate of more than one order of magnitude from the Amargosa Desert to southern Crater Flat due to the clustering Quaternary volcanism. In contrast, probability models based on a homogeneous Poisson density distribution will overestimate the likelihood of future igneous activity in parts of the YMR far from Quaternary centers and underestimate the likelihood of future igneous activity within and close to Quaternary volcano clusters.

4.4.3.3 Vent alignments and correlation of vents and faults

Tectonic setting, strain-rate and fault distribution all may influence the distribution of basaltic vents within clusters, and sometimes across whole volcanic fields (Nakamura, 1977; Smith et al., 1990; Parsons and Thompson, 1991; Takada, 1994). Kear (1964) discussed local vent alignments, in which vents are the same age and easily explained by a single episode of dike injection, and regional alignments, in which vents of varying age and composition are aligned over distances of 20 to 50 km or more. Numerous mathematical techniques have been developed to identify and map vent alignments on different scales, including the Hough transform (Wadge and Cross, 1988), two-point azimuth analysis (Lutz, 1986), and frequency-domain map filtering techniques (Connor,

1990). Regional alignments identified using these techniques are commonly colinear or parallel to mapped regional structures. For example, Draper et al. (1994) and Conway et al. (1997) mapped vent alignments in the San Francisco Volcanic Field which are parallel to, or colinear with, segments of major fault systems in the area. About 30% of the cinder cones and maars in the San Francisco Volcanic Field are located along these regional alignments (Draper et al., 1994). Lutz and Gutmann (1995) identified similar patterns in the Pinacate Volcanic Field, Mexico. Although alignments can clearly form due to episodes of dike injection (Nakamura, 1977) and therefore are sensitive to stress orientation (Zoback, 1989), there are also examples of injection along pre-existing faults (e.g., Kear, 1964; Draper et al., 1994; Conway et al., 1997).

Smith et al. (1990) and Ho (1992) define NNE-trending zones within which average recurrence rates exceed that of the surrounding region. These zones correspond to cinder cone alignment orientations, including Quaternary Crater Flat and the Sleeping Buttes, that Smith et al. (1990) and Ho (1992) hypothesize may occur as a result of structural control. Recent geophysical surveys of Aeromagnetic Anomaly A provide further evidence of the significance of NE trending alignments in the YMR (Connor et al., 1997). The ground magnetic map of data collected over Aeromagnetic Anomaly A delineates three separate anomalies associated with shallowly buried, reversely magnetized rock (Figure Amargosa A). These anomalies are distributed over 4.5 km on a NE trend, each having an amplitude of 70-150 nT. Although these features can be partially resolved with aeromagnetic data (Langenheim et al., 1993), trenchant details emerge from the ground magnetic survey that are important to probabilistic volcanic hazard analyses and tectonic studies of the region. Such details include the character of the southernmost anomaly, which has a smaller amplitude than those to the north but is nonetheless distinctive, and the NE-trending structure within the negative portion of the central anomaly, which mimics the overall trend of the alignment (Figure Amargosa A). The ground magnetic data also enhance the small positive anomalies north of each of the three larger amplitude negative anomalies, reinforcing the interpretation that Aeromagnetic Anomaly A is

produced by coherent basalt edifices with strongly reversed remanent magnetizations.

Figure Amargosa A. Ground magnetic map of Aeromagnetic Anomaly A showing three aligned anomalies, interpreted to be produced by a buried alignment of three volcanoes. Contour interval is 10 nT.

A key result of this survey is identification of the NE trend of the anomalies, quite similar to the alignment of five Quaternary cinder cones in Crater Flat (Figure CFBAS), and to the Sleeping Butte cinder cones, a Quaternary vent alignment 40 km to the northeast. Although the age of the Amargosa Valley alignment is at present uncertain, it suggests that development of NE-trending cone alignments is a pattern of volcanism that has persisted through time in the Yucca Mountain region and supports the idea that future volcanism may exhibit a similar pattern (Smith et al., 1990).

Other ground magnetic surveys provide further evidence of the localization of cinder cones on faults (Stamatakos et al, 1997; Connor et al., 1997). Northern Cone is located in Crater Flat, approximately 8 km from the repository site, and is the closest Quaternary volcano to Yucca Mountain. Its proximity to the site of the proposed repository makes the structural setting of Northern Cone of particular interest to volcanic hazard assessment. Northern Cone consists of approximately 0.4 km^2 of highly magnetized (10–20 Am^{-1}) lava flows, near-vent agglutinate, and scoria aprons resting on a thin alluvial fan. Large-amplitude, short-wavelength magnetic anomalies were observed over the cone. No evidence of NE-trending structures were discovered that could directly relate Northern Cone to the rest of the Quaternary Crater Flat cinder cone alignment. Instead, prominent linear anomalies surrounding Northern Cone trend nearly N-S and have amplitudes of up to 400 nT (Figure Northern). These anomalies likely result from offsets in underlying tuff across faults extending beneath the alluvium.

Figure Northern. Northern Cone is located in the central part of the map, as indicated by high-

amplitude, short-wavelength anomalies. North-south trending anomalies are interpreted to be produced by faults which displace tuff beneath the alluvial cover.

The relationship between faults and Northern Cone is clarified when the ground magnetic map is compared with topographic and fault maps (Frizzell and Schulters, 1990; Faulds et al., 1994). The N-trending anomalies at Northern Cone roughly coincide with mapped faults immediately north of the survey area that have topographic expression resulting from large vertical displacements. These mapped faults and faults inferred from the magnetic map are all oriented N to NNE, trends favorable for dilation and dike injection in the current stress state of the crust. Thus, the Northern Cone magnetic survey provides further support for the idea that volcanism on the eastern margin of Crater Flat was localized along faults.

Thus, there is ample evidence to suggest that patterns in basaltic volcanic activity are influenced by the stress state of the crust and by fault patterns. This influence includes the development of NE-trending volcanic alignments and the localization of vents along faults. Smith et al. (1990) noted that the occurrence of NE-trending alignments is particularly important because much of the Quaternary volcanic activity in the region has occurred southwest of the repository site. Furthermore, faults bound and penetrate the repository block that have a similar map pattern to those faults which have hosted volcanism at Northern Cone and Lathrop Wells. Probability models for igneous disruption of the repository need to account for these trends.

4.4.3.4 Summary

Cumulatively, previous studies of volcanism in the YMR and elsewhere indicate that models describing the recurrence rate, or probability, of basaltic volcanism should reflect the clustered

nature of basaltic volcanism and shifts in the locus of basaltic volcanism through time. Models also should be amenable to comparison with basic geological data, such as fault patterns and neotectonic stress information, which impact vent distributions on a comparatively more detailed scale.

Chuck Connor CC
October 1997

4.4.4 Criteria 4

Probability models for volcanic disruption of the proposed repository rely on a set of parameters to bound the recurrence rates and magnitudes of igneous events. Use of values or ranges for these parameters must be justified using geologic data and analyses. In the following, parameters related to:

- Temporal recurrence rate of volcanism
- Spatial recurrence rate of volcanism
- Magnitude of volcanic and igneous events

are discussed and evaluated.

4.4.4.1 Temporal Recurrence Rate

Probability models rely on estimates of the expected regional recurrence rate of volcanism in the YMR in order to calculate the probability of future disruptive volcanic activity. Previous estimates have relied on past recurrence rates of volcanism as a guide to future rates of volcanic activity. This approach has yielded estimates of regional recurrence rate between 1 and 12 volcanic events per million years (v/my) (e.g., Ho, 1991; Ho et al., 1991; Crowe et al., 1992; Margulies et al., 1992; Connor and Hill, 1995), with various definitions of volcanic event accounting for at least part of this range.

The simplest approach to estimate regional recurrence rate is to average the number of volcanic

events that have occurred during some time period of arbitrary length. For instance, Ho et al. (1991) average the number of volcanoes that have formed during the Quaternary (1.6 m.y.) to calculate the recurrence rate. Through this approach they estimate an expected recurrence rate of 5 v/my. Crowe et al.(1982) averaged the number of new volcanoes over a 1.8 million year period. Crowe et al. (1992) consider the two Little Cones to represent a single volcanic event, and therefore conclude that there are seven Quaternary volcanic events in the region. This lowers the estimated recurrence rate to approximately 4 v/my. The probability of a new volcano forming in the YMR during the next 10,000 yr is 4-5 percent, assuming a recurrence rate of between 4 and 5 v/my.

An alternative approach is the repose time method (Ho et al., 1991). In this method, a recurrence rate is defined using a maximum likelihood estimator (Hogg and Tanis, 1988) that averages events over a specific period of volcanic activity:

$$\lambda_t = \frac{(E-1)}{(T_o - T_y)}$$

where E is the number of events, T_o is the age of the first event, T_y is the age of the most recent event, and λ_t is the estimated recurrence rate. Using eight Quaternary volcanoes as the number of events, E, and 0.1 Ma for the formation of Lathrop Wells, the estimated recurrence rate depends on the age of the first Quaternary volcanic eruption in Crater Flat. Using a mean age of 1.0 Ma yields an expected recurrence rate of approximately 8 v/my. However, the ages of Crater Flat volcanoes are currently estimated at approximately 1.0±0.2 Ma (Table ***). Therefore, the expected recurrence rate is between approximately 6 and 10 v/my. Of course, using different

definitions of volcanic events leads to different estimates of recurrence rate. For example, using the formation of vents and vent alignments during the Quaternary, E = 3 and the recurrence rate is 2–3 v/my. The repose time method has distinct advantages over techniques that average over an arbitrary period of time because it restricts the analysis to a time period that is meaningful in terms of volcanic activity. In this sense it is similar to methods applied previously to estimate time-dependent relationships in active volcanic fields (Kuntz et al., 1986).

Ho (1991) applied a Weibull-Poisson technique (Crow, 1982) to estimate the recurrence rate of new volcano formation in the YMR as a function of time. Ho (1991) estimates $\lambda(t)$ as:

$$\lambda(t) = \left(\frac{\beta}{\theta}\right)\left(\frac{t}{\theta}\right)^{\beta-1}$$

where t is the total time interval under consideration (such as the Quaternary), and β and θ are intensity parameters in the Weibull distribution that depend on the frequency of new volcano formation within the time period, t. In a time-truncated series, β and θ are estimated from the distribution of past events. In this case there are $n = 8$ new volcanoes formed in the YMR during the Quaternary. β and θ are given by (Ho, 1991):

$$\beta = \frac{n}{\sum_{i=1}^{n} \ln\left(\frac{t}{t_i}\right)}$$

and

$$\theta = \frac{t}{n^{1/\beta}}$$

where t_i refers to the time of the i^{th} volcanic event. If β is approximately equal to unity, there is little or no change in the recurrence rate as a function of time and a homogeneous Poisson model would provide an estimate of regional recurrence rate quite similar to the nonhomogeneous Weibull-Poisson model. If $\beta > 1$ then a time trend exists in the recurrence rate and events tend to occur more frequently with time. If $\beta < 1$, new volcanoes form less frequently over time and the magmatic system may be waning.

Where few data are available, such as in analysis volcanism in the YMR, the value of β can be strongly dependent on the period t and the timing of individual eruptions. Ho (1991) analyzed volcanism from 6 Ma, 3.7 Ma, and 1.6 Ma to the present and concluded that volcanism is developing in the YMR on time scales of t = 6 Ma and 3.7 Ma, and has been relatively steady, β = 1.1, during the Quaternary.

Uncertainty in the ages of Quaternary volcanoes has a strong impact on recurrence rate estimates calculated using a Weibull-Poisson model. For example, if mean ages of Quaternary volcanoes are used (Table ***) and t = 1.6 Ma then, as Ho (1991) calculated, β = 1.1 and the probability of a

new volcano forming in the region within the next 10,000 yr is approximately 5 percent. This agrees well with recurrence rate calculations based on simple averaging of the number of new volcanoes that have formed since 1.6 Ma.

Crowe et al. (1995) have pointed out that the Weibull-Poisson model is strongly dependent on the value of t, and suggested that t should be limited to the time since the initiation of a particular episode of volcanic activity. This has an important effect on Weibull-Poisson probability models. If mean ages of Quaternary volcanoes are used and t = 1.2 Ma, the probability of a new volcano forming in the next 10,000 years drops from 5 percent to 2 percent, and $\beta < 1$, indicating waning activity. Alternatively, if volcanism was initiated along the alignment approximately 1.2 Ma, but continued through 0.8 Ma, the expected recurrence rate is again close to 5 v/my and the probability of new volcanism in the YMR within the next 10,000 yr is about 5 percent (t = 1.2 Ma). The confidence intervals calculated on $\lambda(t)$ are quite large in all of these examples due to the few volcanic events (n=8) on which the calculations are based (Connor and Hill, 1993).

Cumulatively, these analyses suggest that a broad range of recurrence rates should be considered, regardless of the definition of volcanic event used. Many recurrence rate models depend on additional information to estimate recurrence rates of volcanism. Bacon (1982) observed that cumulative erupted volume in the Coso Volcanic Field since about 0.4 Ma is remarkably linear in time. Successive eruptions occur at time intervals that depend on the cumulative volume of the previous eruptions. This linear relationship was used by Bacon (1982) to forecast the timing of future eruptions and to speculate about processes, such as strain rate, that may govern magma supply and output in the Coso Volcanic Field. Kuntz and others (1986) successfully applied a

volume-predictable model to several areas on the Snake River Plain, where recurrence rates of late Quaternary volcanism are much higher than in the Coso Volcanic Field but cumulative volumetric rate of basaltic magmatism is nonetheless linear in time. Condit and Connor (1996) discovered volume eruption rates were relatively constant in the Springerville volcanic field between 1.2 and 0.3 Ma, but that the number of cone forming eruptions varied in time, in conjunction with changes in petrogenesis. These relationships between eruption volume, petrogenesis, strain rate, and frequency of volcanic events observed in other volcanic fields suggests that recurrence rate estimates in the YMR may be further refined.

4.4.4.2 Spatial Recurrence Rate

Early models assessing the probability of future volcanism in the YMR and the likelihood of a repository-disrupting igneous event relied on the assumption that Plio-Quaternary basaltic volcanoes are distributed in a spatially uniform random manner over some bounded area (e.g., Crowe et al., 1982; Crowe et al., 1992a; Ho et al., 1991; Margulies et al., 1992). However, as discussed in Section 4.4.3, patterns in the distribution and age of basaltic volcanoes in the YMR make the choice of these bounded areas somewhat subjective. For example, Smith et al. (1990) and Ho (1992) define NNE-trending zones within which average recurrence rates exceed that of the surrounding region. These zones correspond to cinder cone alignment orientations that Smith et al. (1990) and Ho (1992) hypothesize may occur as a result of structural control. Such narrow zones lead to comparatively high estimates of spatial recurrence rate and probability of volcanic disruption of the repository site. Using bounded areas that are large compared to the current distributions of cinder cone clusters results in relatively low estimates of spatial recurrence rate. Ho (1992) argued that under these circumstances, using narrow bounding areas which include the repository give

conservative estimates of probability of volcanic disruption.

Alternatively, spatial recurrence rate can be estimated using models which explicitly account for volcano clustering. Three spatial and spatio-temporal nearest-neighbor models were presented by Connor and Hill (1995) to describe clustering of basaltic volcanism in the YMR. This approach features several characteristics of nearest-neighbor methods which make them amenable to volcano distribution studies and hazard analysis in areal volcanic fields. First, volcanic eruptions, such as the formation of a new cinder cone, are discrete in time and space. Using nearest-neighbor methods, the probability surface is estimated directly from the location and timing of these past, discrete volcanic events. As a result, nearest-neighbor models are sensitive to the patterns generally recognized in cinder cone distributions. Furthermore, the resulting probability surfaces are continuous, rather than consisting of abrupt changes in probability that must be introduced in spatially homogeneous models. Continuous probability surfaces can be readily compared to other geologic data, such as fault location, that may influence volcano distribution. Nearest-neighbor methods also eliminate the need to define areas or zones of volcanic activity as is required by all spatially homogeneous Poisson models.

Past volcanic activity can be used to estimate parameters used in these nonhomgeoneous Poisson probability models for disruption of the proposed repository. This is particularly important in modeling the distribution of volcanism in the YMR because of vent clustering. As discussed previously (Section 4.4.3), vent clustering results in dramatic changes in spatial recurrence rate across the YMR. In order to model clustering and use these models in probabilistic volcanic hazard analysis, it is necessary to estimate parameters used in the models. One approach to parameter estimation is to use observed volcano distributions as a basis for comparison. This parameter

estimation can be done formally if appropriate models are used.

One method of estimation of the spatial recurrence rate of volcanic events in the YMR and the probability of future volcanic events uses kernel functions (Silverman, 1986; Lutz and Gutmann, 1995; Connor and Hill, 1995; Condit and Connor, 1996). In volcanic hazard analysis, the kernel function must be estimated and used to deduce the probability density function. Several types of kernels, including Gaussian and Epanechnikov kernels, are discussed by Silverman (1986). All multivariate kernels have the property:

$$\int_{\mathbb{R}} \mathrm{K}(\mathbf{x})\, d\mathbf{x} = 1$$

where K(**x**) is the kernel function, and **x** is an n-dimensional vector. A Gaussian kernel function for 2D spatial data is:

$$\mathrm{K}(x,y) = \frac{1}{2\pi} \exp\left\{-\frac{1}{2}\left[(x-x_v)^2 + (y-y_v)^2\right]\right\}$$

where in the kernel is calculated for at a point x,y and the center of the kernel, in this case the volcano location is x_v, y_v. If the kernel is normalized using the smoothing parameter, h, then the kernel function is a Gaussian function and h is equivalent to the standard deviation of the

distribution

$$K(x,y) = \frac{1}{2\pi h^2} \exp\left\{-\frac{1}{2}\left[\left(\frac{x-x_v}{h}\right)^2 + \left(\frac{y-y_v}{h}\right)^2\right]\right\}$$

If x and y locations are on a rectangular grid, the probability density function based on the distribution of n volcanoes is

$$\hat{p}(x,y) = \frac{1}{n \Delta x \Delta y} \sum_{i=1}^{n} K(x,y)$$

where Δx and Δy are grid spacing in the x and y directions, respectively. The above equations can be used to estimate spatial recurrence rate of volcanism, or the probability of volcanic disruption of the proposed repository site, given a volcanic eruption in the region. The results of this probability estimate depend on h. One approach to bounding uncertainty in the probability estimates resulting from this calculation is to evaluate probability using a wide range of h (Connor and Hill, 1995). Alternatively, the effectiveness of the kernel model and optimal values of h can be deduced from the distribution of nearest-neighbor distances between existing volcanoes. For example, the 2D Gaussian kernel model can be compared with the distribution of nearest-neighbor distances between existing volcanoes by recasting the kernel function in polar coordinates:

$$K(r,\theta) = \frac{2}{h(2\pi)^{\frac{3}{2}}} exp\left[-\frac{1}{2}\left(\frac{r^2}{h^2}\right)\right]$$

where r is distance from the nearest-neighbor volcanic event. The cumulative probability density function then becomes

$$\hat{f}(R) = \int_0^{2\pi}\int_0^{R} \frac{2}{h(2\pi)^{\frac{3}{2}}} exp\left[-\frac{1}{2}\left(\frac{r^2}{h^2}\right)\right] dr d\theta$$

where $\hat{f}(R)$ is the expected fraction of volcanic events within a distance R of their nearest-neighbor volcanic event.

Distance to nearest-neighbor volcanic event in the YMR varies depending on the definition used for volcanic event. Treating all vents as individual volcanic events, the mean distance to nearest-neighbor volcanic event is 3.8 km with a standard deviation of 5.8 km. However, some vents such as SW and NE Little Cones are quite closely spaced and may be treated as single volcanic events. Treating vents spaced more closely than 1 km as single volcanic events, the mean distance to nearest-neighbor volcanic event increases to 5.0 km and the standard deviation to 5.9 km.

Alternatively, volcanic events can be defined in terms of vents and vent alignments. In this definition, Quaternary Crater Flat volcanoes are taken as a single event, as is Pliocene Crater Flat. Using this definition, mean distance to nearest-neighbor volcanic event increases to 7.0 km, with a standard deviation of 6.4 km.

The observed fraction of volcanoes erupted at a given nearest-neighbor distance or less is compared with a Gaussian kernel model with standard deviations of 3–7 km in Figure (kernel model). A Gaussian kernel model with h=5 km reasonably describes the expected distance to nearest-neighbor volcano, particularly between 5 and 10 km. Smaller values, such as h = 3 km, model the distribution of individual vents at distances less than 4 km, but do not model vent distribution well at distances greater than 4 km. For instance, the h = 3 km model predicts that 95 percent of all volcanoes will be located at nearest-neighbor distances less than 6 km, but 15 to 40 percent of all volcanoes in the YMR are located at greater distances than this, depending on the definition of volcanic events used. The h=7 km model tends to slightly overestimate the number of volcanoes at nearest-neighbor distances greater than 8 km. Thus, the h = 5 km model best describes the over all distribution of vents and vent pairs for use in evaluation of hazards at the repository, located approximately 8 km from the nearest Quaternary volcano. This is slightly less than the standard deviation of the observed distribution because Buckboard Mesa, located 25 km from its nearest-neighbor, is an outlier in the observed volcano distribution and increases the variance.

Figure kernel model. Comparison of observed fraction of volcanoes within a given distance of their nearest-neighbor volcano with Gaussian kernel models calculated using *h* = 3 km, 5 km, and 7 km. Observed curves include all vent (open squares), all vents or vent pairs more closely spaced then 1 km (solid

circles), and vents and vent alignments (open circles). Buckboard Mesa (BB) is an outlier in the distribution as it is approximately 25 km from its nearest neighbor. The center of the repository site is located 8.2 km from Northern Cone, the nearest Quaternary volcano.

Vents and vent alignments have fewer nearest-neighbors at distances less than 4 km than expected if this distribution is modeled using a Gaussian kernel (Figure kernel model). Rather, this distribution can be modeled using a simple modification of the Gaussian kernel to account for a mean offset of the probability density function from zero:

$$\hat{f}(R) = \int_0^{2\pi} \int_0^{R} \frac{2}{h(2\pi)^{\frac{3}{2}}} exp\left[-\frac{1}{2}\left(\frac{(r-\bar{x})^2}{h^2}\right)\right] dr d\theta$$

where $\bar{x}$ is the mean offset. Incorporating a mean offset of 5–7 km and h = 3 km results in an improved fit between the observed distribution of distance to nearest-neighbor volcanic events and the Gaussian kernel model (Figure Gaussian Cluster). The need for this mean offset arises because vent alignments are more widely spaced than individual vents. However,the variance does not increase significantly as a result of this increased spacing when vent alignments are considered as single volcanic events. This comparatively low variance suggests that there is a characteristic nearest-neighbor distance of 5–10 km in the YMR for volcanic events defined as vents or vent alignments.

Figure Gaussian Cluster. Comparison of observed fraction of volcanic events within a given distance of their nearest-neighbor volcanic event with Gaussian kernel models calculated using h = 3 km and $\bar{x}$ = 5 and 7 km. Observed curves include vents and vent alignments (open circles) as single volcanic events, calculated from the center of the vent alignment. Buckboard Mesa (BB) is an outlier in the distribution as it is approximately 25 km from its nearest neighbor.

This analysis indicates that volcanic event distribution can be modeled using a Gaussian kernel with h = 5–7 km provided that volcanic events are defined as individual vents or vent pairs. When vent alignments are considered as individual volcanic events the Gaussian kernel needs to be modified to include an offset distance. Thus, model testing indicates that the types of kernels and parameters used within each kernel to evaluate probability should vary with the definition of volcanic event.

The Epanechnikov kernel function is widely used to estimate spatial recurrence rate in basaltic volcanic fields (Lutz and Gutmann, 1995; Connor and Hill, 1995; Condit and Connor, 1996) and may be tested in a similar manner as the Gaussian kernel function. The Epanechnikov kernel in 2D Cartesian coordinates is:

$$\mathrm{K}(x,y) = \frac{2}{\pi h^2}\left\{1-\left[\left(\frac{x-x_v}{h}\right)^2+\left(\frac{y-y_v}{h}\right)^2\right]\right\}$$

where

$$\sqrt{(x-x_v)^2+(y-y_v)^2} \leq h$$

and

$$K(x,y) = 0$$

otherwise. In polar coordinates this kernel function becomes

$$K(r,\theta) = \frac{3}{4\pi h}\left[1-\left(\frac{r^2}{h^2}\right)\right], \quad r \leq h.$$

The cumulative probability density function is then:

$$\hat{f}(R) = \int_0^{2\pi}\int_0^{R} \frac{3}{4\pi h}\left[1-\left(\frac{r^2}{h^2}\right)\right] dr d\theta, \quad R \leq h.$$

As was accomplished with the Gaussian kernel, the cumulative probability density function for the Epanechnikov kernel can be compared with the observed fraction of volcanoes erupted at a given nearest-neighbor distance or less for various values of h (Figure Epanechnikov). This comparison

that an Epanechnikov kernel function with h = 10 km best models the distribution of distance to nearest-neighbor volcanic event, if volcanic events are defined as vents or vent pairs. If volcanic events are defined as vents or vent alignments, 15 km < h < 18 km better approximately the distribution of distances to nearest-neighbor volcanic events, given the current distribution of volcanoes. Comparing the Epanechnikov and Gaussian kernel models suggests that the Gaussian kernel models better fit the observed distribution than Epanechnikov distributions, particularly at distances greater than 6 km. The difficulty fitting the observed distributions with the Epanechnikov kernel function results from truncation of this distribution at distances greater than h.

Figure epanechnikov. Comparison of observed fraction of volcanoes within a given distance of their nearest-neighbor volcano with Epanechnikov kernel models calculated using *h* = 5 km, 10 km, and 18 km. Observed curves include all vent (open squares), all vents or vent pairs more closely spaced then 1 km (solid circles), and vents and vent alignments (open circles). Buckboard Mesa (BB) is an outlier in the distribution as it is approximately 25 km from its nearest neighbor. The center of the repository site is located 8.2 km from Northern Cone, the nearest Quaternary volcano.

Testing models against observed distributions also leads to a natural definition of conservatism. For example,the distance between the proposed repository and its nearest-neighbor Quaternary volcano is 8.2 km. A Gaussian kernel function with h = 7 km clearly is conservative because a greater fraction of volcanic events occur at nearest-neighbor distances less than 8.2 km than predicted by the model, whereas a Gaussian kernel function with h = 3 km is not conservative (Figure kernel model). Similarly, probability models based on Epanechnikov kernel functions and h > 10 km are

conservative where volcanic events are defined as vents and vent pairs, and h > 18 km where volcanic events are defined as vents and vent alignments.

4.4.4.3 Magnitude of igneous events

4.4.4.4 Summary

Scientific Notebook
Project 20-1402-461

Chuck Connor
October ,1997

4.4.4.3 Area Affected by Igneous Events

The area affected by igneous events varies with the definition of igneous event (Section 4.4.2). Where igneous events are defined in terms of individual, mappable eruptive units, the resulting probability estimate is for direct disruption of the proposed repository and release of inventory into the accessible environment. The probability of such a volcanic event disrupting the repository inventory depends on the area of repository potentially disrupted by flow of magma through the subsurface conduit of the volcano as the eruption develops. Observations at cinder cones in the process of formation (e.g., Luhr and Simkin, 1993; Fedotov, 1983; Doubik et al., 1996) indicate that these eruptions are initiated by dike injection at comparatively low ascent velocities, on the order of 1 m per second, which can deform an area of the ground surface several hundred meters in length. However, basaltic eruptions quickly localize into vent areas as the eruption progresses and magma flow velocities increase to around 100 m/s. Hill (1996) reviewed literature on subsurface areas disrupted by basaltic volcanoes analogous to past volcanic eruptions in the YMR. Based on this review and data collected at Tolbachik volcano, Russia, Hill concluded that typical subsurface conduit diameters are between 1 m and 50 m at repository depths. However, where vent conduits are exposed in the San Rafael volcanic field (Delaney and Gartner, 1994), conduit diameters are often on the order of 100 m. Therefore, areas disrupted by vent formation, potentially leading to the release waste into the accessible environment, are on the order of 0.01 km^2 or less. Conservatively, such a volcanic event centered within 50 m of the repository boundary may result in transport of waste to the surface.

Using this approach, the probability of a volcanic eruption through the repository, given an eruption, can be approximated from the effective area of the repository, A_e:

$$P[\ \textit{eruption through repository} | \textit{eruption centered at } x,y] = \begin{cases} 1, \textit{ if } x,y \in A_e \\ 0, \textit{ otherwise} \end{cases}$$

where the effective area, A_e, is the area of the repository and the region about the repository within one conduit radius of the repository boundary (Geomatrix, 1996).

Other definitions of igneous events result in the need for more complex analyses of the area affected because these events have length and orientation (Sheridan, 1992; Geomatrix, 1996). In these cases, probability density functions must be estimated for both the length and orientation of igneous events. Geomatrix (1996) gave the probability that an event centered on a given location will result in intersection of an igneous intrusion with the repository. This probability can be expressed as:

$$P\left[L \geq l_r,\ \phi_1 \leq \Phi \leq \phi_2\right] = \int_{l_r}^{\infty} \int_{\phi_1}^{\phi_2} f_L(l) \cdot f_\Phi(\phi)\, d\phi dl$$

where phi is the azimuth of the igneous event with respect to north, with phi1 and phi2 representing the range of azimuths which would result in intersection with the repository, given an igneous event centered on x,y a distance l_r from the repository boundary. The probability that the

igneous event length, L, will exceed l_r at an azimuth between phi1 and phi2 depends on the probability density functions $f_L(l)$ and $f_{phi}(phi)$ for igneous event half-length and azimuth, respectively.

This characterization of area affected by igneous events must be further modified depending on the type of event considered. Defining igneous events as volcanic vents or vent alignments may result in an estimate of the probability of volcanic disruption of the repository, if the frequency of vent formation along the alignment is included in the calculation. The length of the vent alignment is taken as the distance between the centers of the first and last volcanoes in the alignment. For example, the length of the Amargosa Desert Aeromagnetic Anomalies "A" alignment of three vents is 4.0 km. The length of the Quaternary Crater Flat alignment of five vents is 11.2 km, based on the distance between SW Little Cone and Northern Cone. Six vents occur along the 3.6 km Pliocene Crater Flat alignment. Average vent density along these alignments is on the order of 0.5-2.0 vents/km. This vent density suggests that if an alignment defined by the distance between the first and last vents in the alignment intersects the repository, it should be assumed that a vent will form within the repository boundary as a result of this intersection.

Uncertainty increases considerably when the functions $f_L(l)$, and $f_{phi}(phi)$ are introduced because these functions must be estimated from limited YMR geologic data. If the igneous event is development of a vent or vent alignment, mapped vent locations are useful in constraining the functions f(phi) and f(l). Considering Plio-Quaternary volcanism in the YMR, six igneous events consist of the formation of isolated vents, and four igneous events resulted in the formation of vent alignments. Of these four vent alignments, two are less than 4 km long, the Pliocene Crater Flat vents and the Sleeping Butte vent pair. The Amargosa Desert Aeromagnetic Anomaly "A" alignment is slightly longer than 4 km. The Quaternary Crater Flat alignment, one of the youngest and most important volcanic events in the YMR, is also the longest alignment, approximately 11 km long. Although these data provide an idea of the range of alignment lengths possible in the YMR, they are not sufficient to estimate a probability distribution for vent alignment lengths, $f_L(l)$.

Draper et al (1994) mention that approximately 30 percent of the vents in the San Francisco volcanic field form alignments, and the remaining vents are isolated and appear to have formed during independent episodes of volcanic activity. This value appears to be comparable to the ratio of vent alignments to individual vents in the YMR. Data on vent alignment lengths from other volcanic fields suggests that vent alignments may be considerably longer than the Quatenary Crater Flat alignment. For example, Connor et al. (1992) identified vent alignments > 20 km in length in the Springerville volcanic field, AZ. Vent alignments of comparable or greater length have been identified in the Michoacan-Guanajuato volcanic field, Mexico (Wadge and Cross, 1988; Connor, 1990), the Pinacate volcanic field, Mexico (Lutz and Gutmann, 1995). Smith et al. (1990) suggested that alignments may be up to 20 km long, with a lower probability of 40 km long alignments, based on mapping in the Lunar Crater, Reveille Range, and San Francisco volcanic fields. However, none of these authors developed distributions for vent alignment lengths in these areas. Furthermore, it is not clear that the conditions for vent alignment formation and factors controlling vent alignment length are comparable between these different regions and the YMR.

As a result, it is difficult to estimate the distribution function for $f_L(l)$ for vents and vent alignment formation, due to a lack of data. Given these caveats, the probability density function for event length can be expressed as:

Chuck Connor CC

$$f_L(l) = \begin{cases} \frac{1}{2}, & l = 0 \\ \frac{U[l_{min}, l_{max}]}{2}, & l > 0 \end{cases}$$

By this definition, 50 percent of igneous events have zero length and only disrupt the repository if they fall within the effective area of the repository. The remaining 50 percent of igneous events form alignments which affect areas up to a distance l_{max} from the point x,y. This percentage assigned to zero-length igneous events is a source of uncertainty in probability estimates and is not well constrained by available data. The probability density function is construed to be a uniform random distribution between l_{min} and l_{max} because the distribution of alignment lengths is so poorly known. Under these circumstances a uniform random distribution likely yields a reasonably conservative probability estimate.

Using this definition of $f_L(l)$, probability estimates of intersection of the repository, given an event at x,y, will not be strongly dependent on l_{min} compared to l_{max}. The value of lmax can be chosen as 5.6 km, taking the Quaternary Crater Flat alignment as the maximum alignment half-length. However, given observations in other volcanic fields, l_{max} may be 20 km or more.

The distribution function for azimuth of alignments or dike zones, f_{phi}(phi) is better constrained by the data on vent alignments, regional stress distribution and the orientations of high-dilation tendency faults. Three of the alignments in the YMR trend 020° to 030°, perpendicular to the least principle horizontal compressional stress in the region, approximately 028° (e.g., Morris et al., 1993). Under these circumstances, fphi(phi) may vary over a narrow range. For example,

$f_\Phi(\phi) = U[020°, 035°]$.

Alternatively, fphi(phi) near the repository may respond to the distribution of fault orientations (Figure faults), if ascending magmas tend to exploit faults as low-energy pathways to the surface (Conway et al., 1997; Jolly and Sanderson, 1997).

Figure Faults. Distribution of fault segments with respect to fault azimuth. This distribution is weighted by fault segment length. Near the repository, fphi(phi) may vary as a function of this distribution of fault orientations if ascending magmas follow fault planes to the surface.

Other definitions of igneous events attempt to capture the probability of igneous intrusions intersecting the repository boundary (Sheridan 1992; Geomatrix, 1996). Igneous intrusions commonly form anastomosing networks a shallow levels in the crust, forming multiple dike segments at a given structural level (e.g., Gartner and Delaney, 1994). Consequently, a term may be added to equation *** to account for the width of igneous events, such as the width of the dike swarm formed during igneous intrusion:

$$P\left[L \geq l_r,\ \phi_1 \leq \Phi \leq \phi_2,\ W \geq w_r\right] = \int_{l_r}^{\infty}\int_{\phi_1}^{\phi_2}\int_{w_r}^{\infty} f_L(l)\cdot f_\Phi(\phi)\cdot f_W(w)\,dw\,d\phi\,dl$$

where $f_W(w)$ is a probability density function describing the half-width of the igneous event, which may be a significant fraction of the half-length, and w_r is the shortest distance to the repository boundary perpendicular to the event azimuth, for a given azimuth and event length. Numerous individual dikes, dike segments, and sills may be located within this zone. Little is known about the distribution fW(w). In Pliocene Crater Flat, the half-width of the dike swarm appears to be on the order of 200 m. In contrast, Gartner and Delaney (1994) mapped dike zones up to 5 km wide (W = 2.5 km) in the San Rafael volcanic field.

Given the spatial density of these igneous features, it is conservative to consider intersection of the area defined by equation *** with the effective repository area as resulting in igneous disruption of the site. It is emphasized that this definition of an igneous event does not necessarily result in direct transport of radioactive waste to the surface by erupting magma.

4.4.4.4 Summary

Probability estimates for volcanic disruption of the proposed repository depend on accurate estimation of parameters used to model temporal and spatial recurrence rates, and magnitudes of igneous events. Estimation of these parameters is hampered by the comparatively few events in the YMR and because such parameter distributions are not widely estimated for other basaltic volcanic fields. In many instances, even the shapes of probability distributions for individual parameters are poorly known.

The numbers of parameters that must be estimated and the uncertainties associated with parameter estimation change with the definition of igneous event. Igneous events defined as individual, mappable eruptive vents involves the least parameter estimation. Temporal recurrence rate of such YMR igneous events has been 8 volcanic events during the last 1 m.y. Connor and Hill (1995) suggested that future recurrence rates of this type of event may be between 2 and 10 volcanic events/m.y. A distribution function for the probability of temporal recurrence rate within this range has not been estimated and use of this range does not assume a central tendency. Spatial recurrence rate, if estimated using kernel functions, can be estimated from distance between nearest-neighbor vents. This comparison suggests that the smoothing parameter, h, used in these functions will yield reasonably conservative values for h≥5 km for Gaussian kernel functions and h≥10 km for Epanechnikov kernel functions. Of all types of igneous events, those defined as individual, mappable eruptive vents are the simplest to interpret in terms of area affected by volcanic activity. Essentially, igneous events centered within the effective area of the repository disrupt a subsurface area o the repository of < 0.01 km^2 and those centered outside this area do not disrupt the inventory. Thus, uncertainties associated with the probability of repsository disruption type of igneous event largely are related to uncertainty in estimation of reasonably conservative values for temporal recurrence rate.

Defining igneous events as vents and vent alignments reduces the temporal recurrence rate. Only three YMR vent and vent–alignment forming eruptions have occurred since 1 Ma. Thus, reasonably conservative values for temporal recurrence rate may be on the order of 3-5 igneous

events/m.y., understanding that there remains significant uncertainty associated with this estimate of temporal recurrence rate. For spatial models, the smoothing parameter, h, must increase because the distance between near-neighbor events increases. Experimentation suggests that $h \geq 18$ km may be sufficiently conservative for Epanechnikov models, based on this igneous event definition. Application of the Gaussian kernel function indicates $h \geq 9$ km is conservative, or use of small values of h (e.g., h = 3 km) with offset distances of x = 5 km are reasonably conservative. Use of the vent and vent alignment definition of igneous events introduces probability density functions associated with the length and azimuth of the alignment, which must be estimated in order to calculate the probability of disruption of the repository. Vent alignment azimuth and length can be estimated from existing vent alignments in the YMR and additional data, such as principle stress orientations in the shallow crust. Probability density functions such as equations *** and *** may be used for these parameters. However, it is noted that based on limited available data, it is untenable to estimate reasonably conservative distributions for YMR vent alignment length. Under these circumstances, it is appropriate to explore the sensitivity of igneous event probability estimates to vent alignment length and orientation.

Additional uncertainty is introduced by defining igneous events as igneous intrusions. For example, the lengths of these intrusions cannot be estimated directly from data available for Plio-Quaternary volcanoes in the YMR, other than these lengths are likely greater than the lengths of vent alignments. In addition, the probability density function for the widths of igneous intrusions, which normally consist of multiple individual dikes, should be estimated but is poorly known.

As a result of these technical concerns, DOE and NRC have not yet reached agreement on the appropriate range of volcanic and intrusive probability estimates to use in performance assessment. Staff conclude, however, that a 1×10^{-7} annual probability of volcanic disruption provides a reasonably conservative value for use in performance assessment. Further analysis of the probability of volcanic disruption of the site is not warranted until completion of consequence analyses and risk assessment. Reassessment of probabilities may not be necessary if conservative consequence analyses demonstrate that risks associated with volcanic disruption of the proposed repository are sufficiently low to assure public health and safety. Finally, Staff acknowledge that quantitative volcanic hazard assessment is a rapidly developing field. Changing techniques in this discipline and the related areas of geophysical and geological site characterization may necessitate revision of these probability estimates.

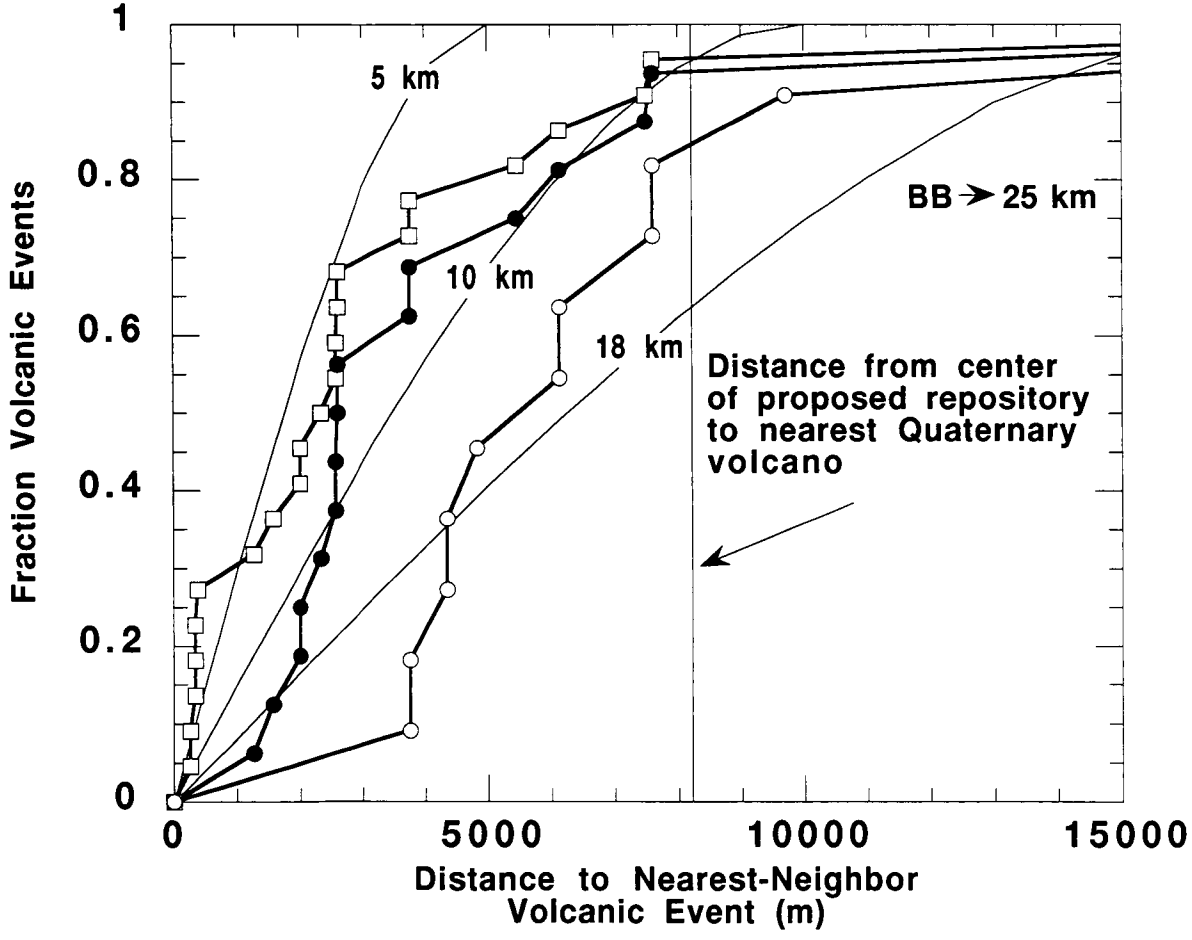
1
0.8
0.6
0.4
0.2
0
Fraction Volcanic Events
5 km
10 km
18 km
BB ➔ 25 km
Distance from center of proposed repository to nearest Quaternary volcano
0
5000
10000
15000
Distance to Nearest-Neighbor Volcanic Event (m)

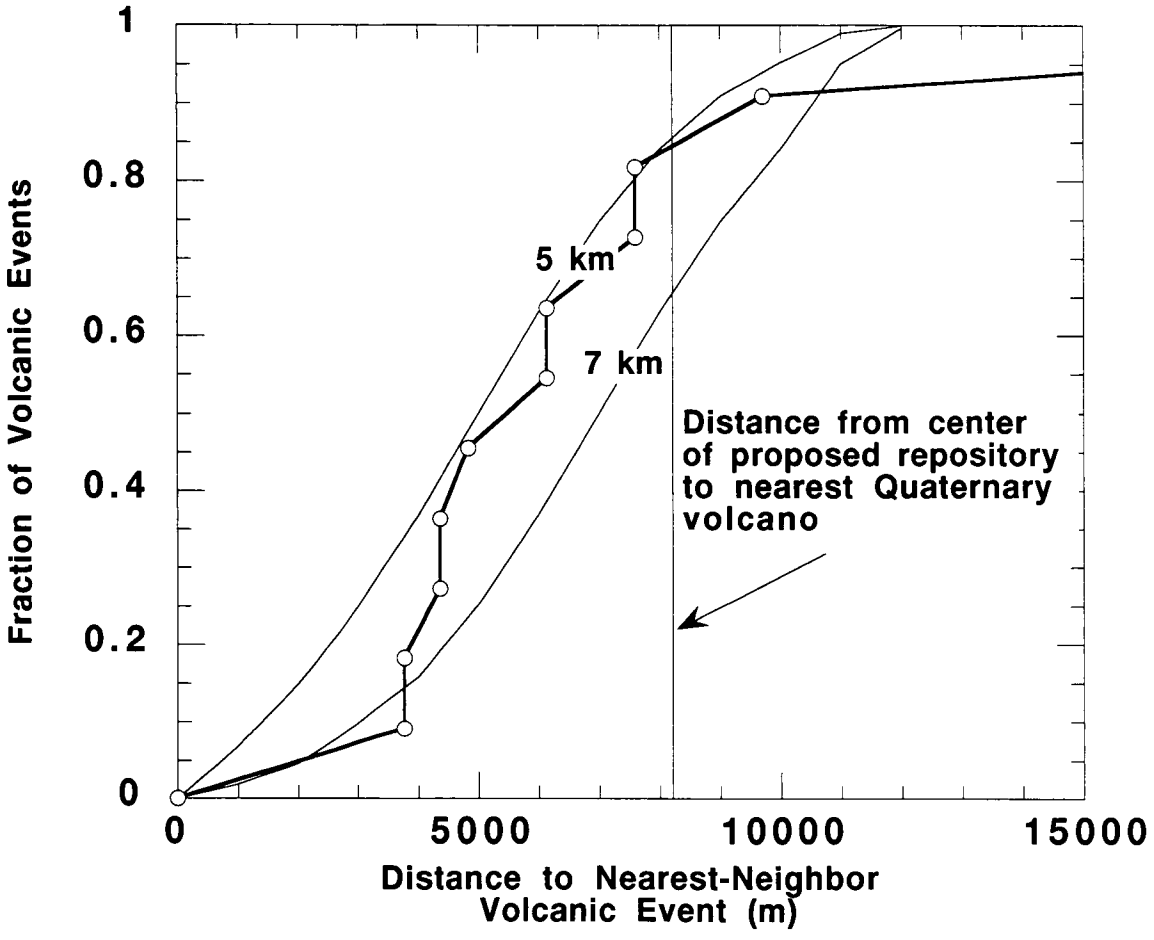
Fraction of Volcanic Events
1
0.8
0.6
0.4
0.2
0
0
5000
10000
15000
Distance to Nearest-Neighbor Volcanic Event (m)
5 km
7 km
Distance from center of proposed repository to nearest Quaternary volcano

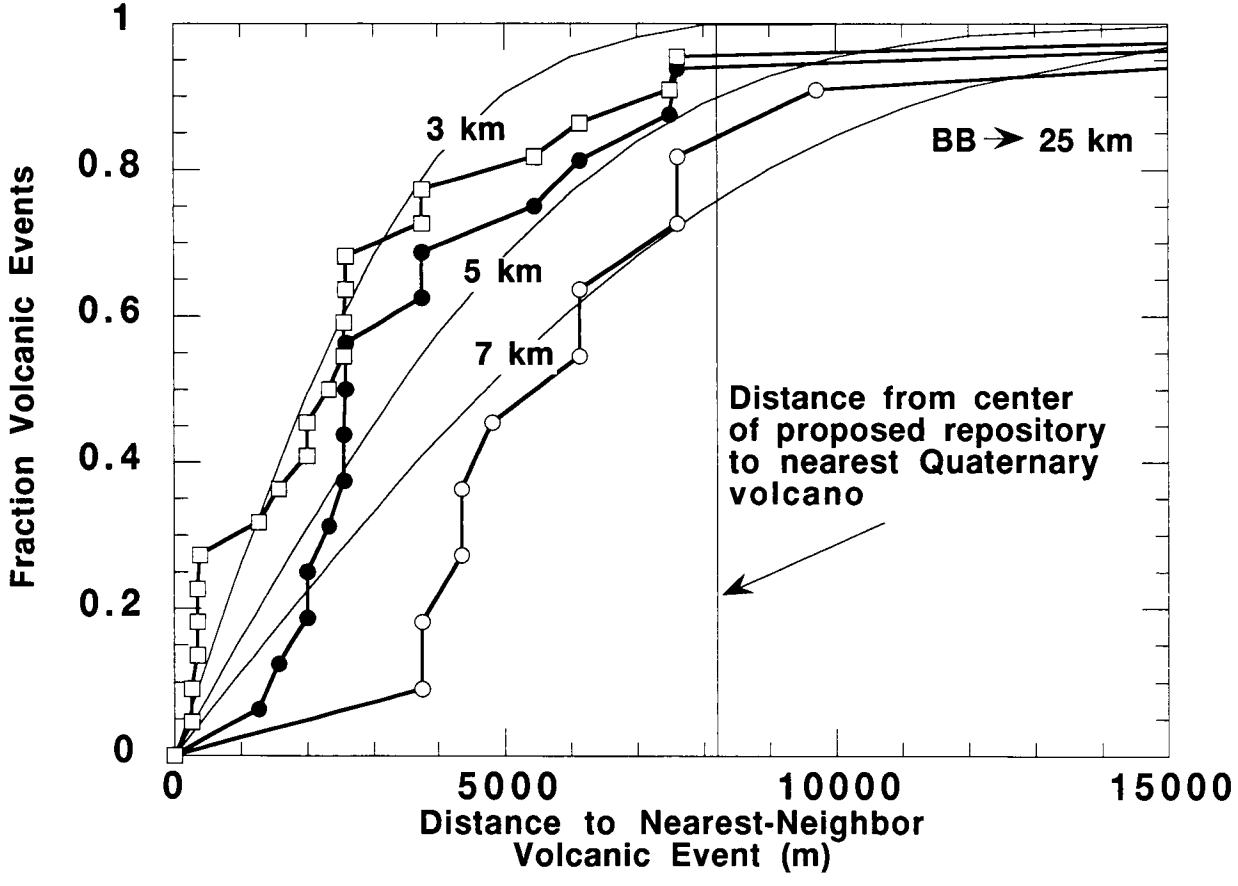
Fraction Volcanic Events
1
0.8
0.6
0.4
0.2
0
0
5000
10000
15000
Distance to Nearest-Neighbor Volcanic Event (m)
3 km
5 km
7 km
BB → 25 km
Distance from center of proposed repository to nearest Quaternary volcano

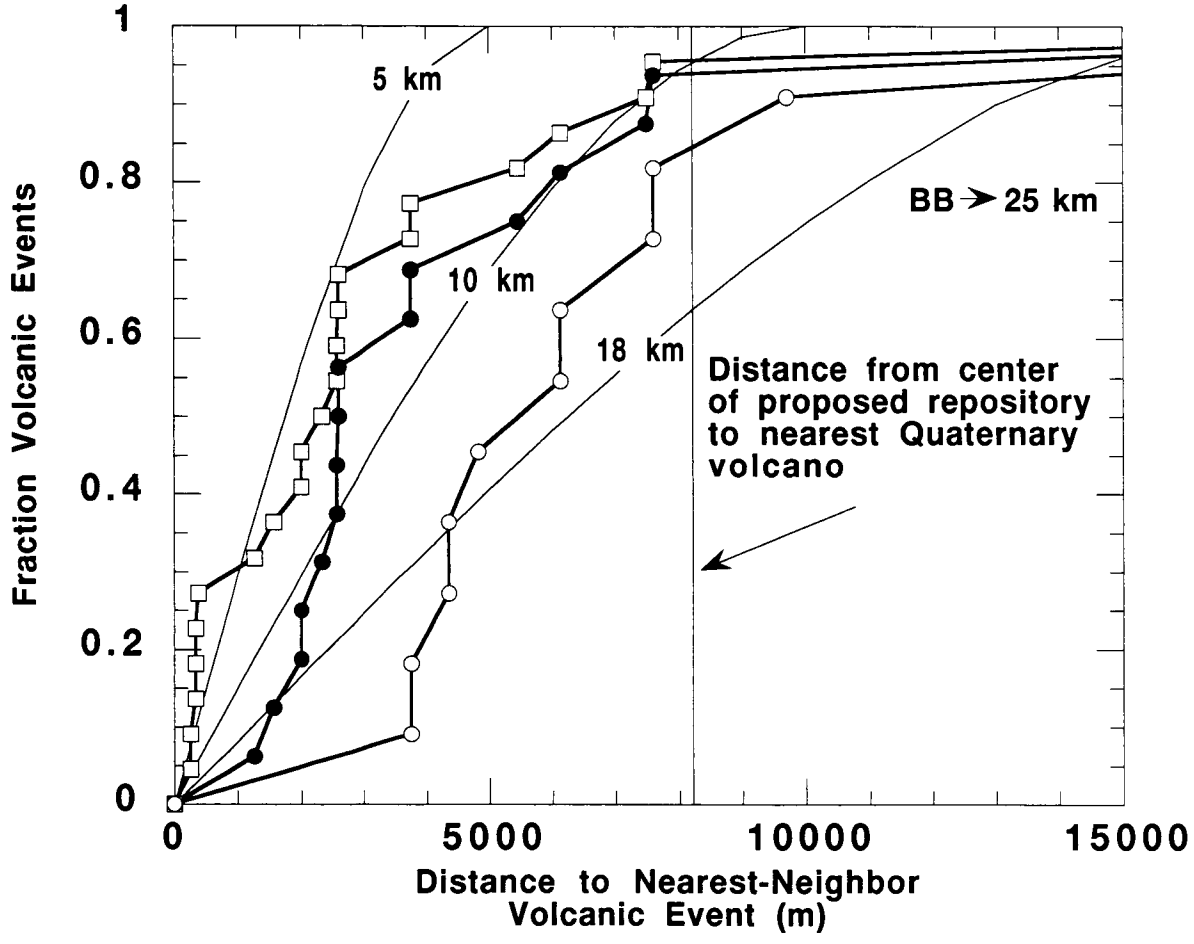
1
0.8
0.6
0.4
0.2
0
Fraction Volcanic Events
5 km
10 km
18 km
BB ➔ 25 km
Distance from center of proposed repository to nearest Quaternary volcano
0
5000
10000
15000
Distance to Nearest-Neighbor Volcanic Event (m)

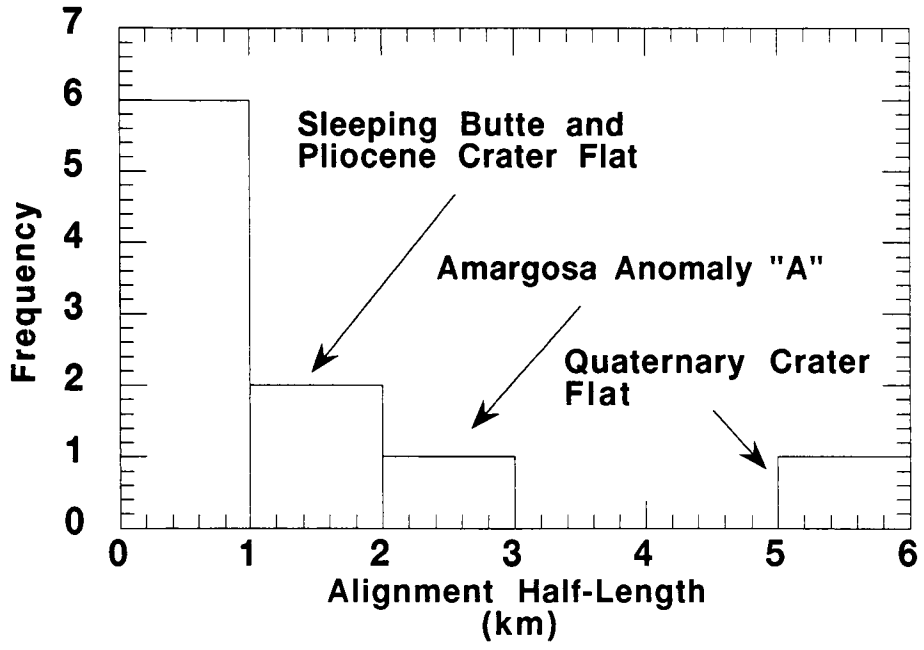
Frequency
0
1
2
3
4
5
6
7
Sleeping Butte and
Pliocene Crater Flat
Amargosa Anomaly "A"
Quaternary Crater
Flat
0
1
2
3
4
5
6
Alignment Half-Length
(km)

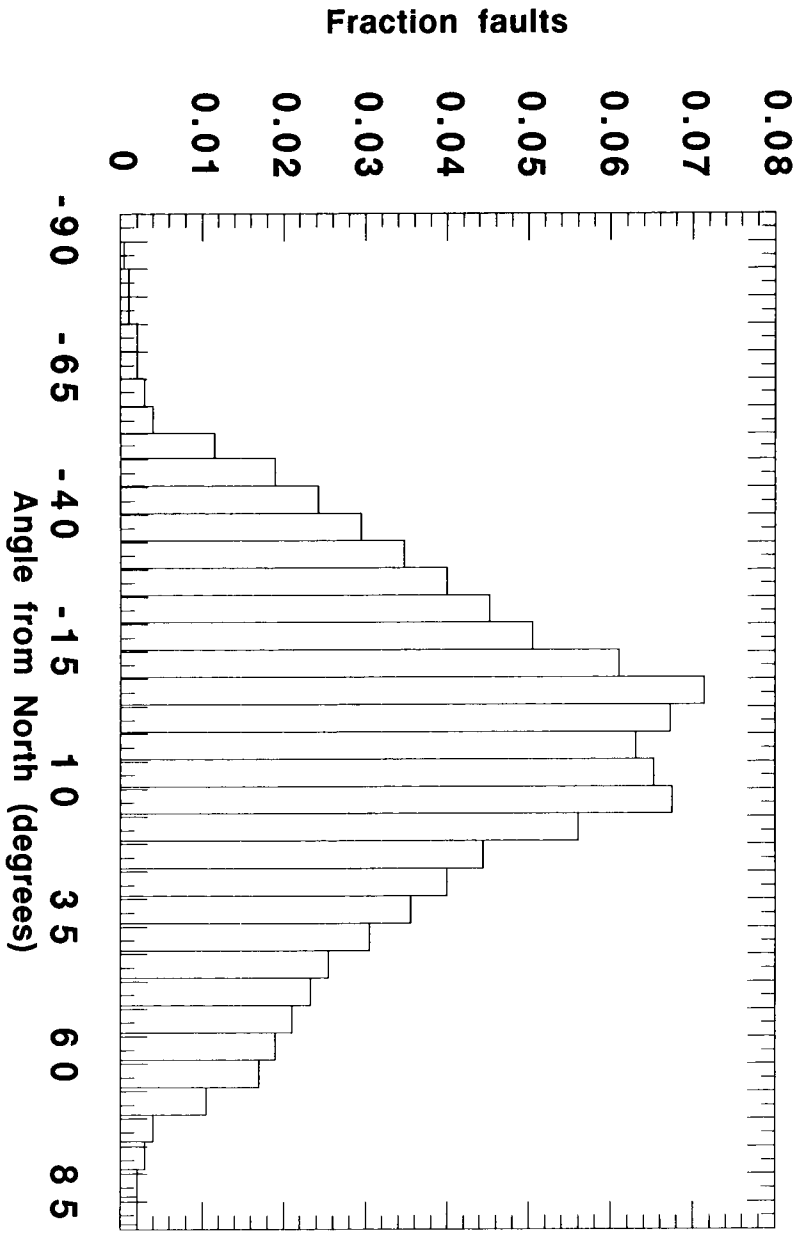
Fraction faults
0
0.01
0.02
0.03
0.04
0.05
0.06
0.07
0.08
-90
-65
-40
-15
10
35
60
85
Angle from North (degrees)

Scientific Notebook
Project 20-1402-461

Chuck Connor CC
October, 1997

The following is mathematics code used to calculate the solutions to gaussian and epanechnikov kernel functions in polar coordinates.

Written by Chuck Connor

Program:

```
h=5.0
Integrate[2/(h*Sqrt[2]*Sqrt[Pi]*Pi*2)*Exp[-0.5*((r/h)^2)],
{r,-2,2},{t,0,Pi}]
N[%,4]
5.
(0.2198 + 0. I) Sqrt[2]
0.3108 + 0. I
h=3.0
mean = 5.0
lim = 15.0
Integrate[2/(h*Sqrt[2]*Sqrt[Pi]*Pi*2)*Exp[-0.5*(((r-mean)/h)^2)],
{r,-lim,lim},{t,0,Pi}]
N[%,4]
3.
5.
15.
0.706803  Sqrt[2]
0.9996
Print ["Epanechnikov kernel in polar coordinates"]
h=5.0
lim = 4.0
Integrate[3/(4*h*Pi)*(1-(r/h)^2),
{r,-lim,lim},{t,0,Pi}]
N[%,4]
Epanechnikov kernel in polar coordinates
5.
```

4.
0.944
0.944

Scientific Notebook
Project 20-1402-461

Chuck Connor CC
October, 1997

4.4.5 Acceptance Criteria 5

Low recurrence rate basaltic volcanic activity in the Basin and Range occurs where magmas are generated by decompression of fertile mantle during crustal extension (e.g., Bacon, 1982; McKenzie and Bickle, 1988). Magma ascent through the crust is enhanced by crustal structures produced by extension, leading to correlation between basaltic volcanism and structure across a range of scales, from the superposition of individual faults and vents to the occurrence of entire volcanic fields at the margins of extensional basins (Connor, 1990; Parsons and Thompson, 1991; Conway et al., 1997). Volcanic hazard analysis of the proposed repository must quantify these often complex geological relationships probabilistically.

The relationship between structure and volcanism has been used to suggest both higher and lower probabilities of volcanic disruption of the repository than are predicted using spatio-temporal patterns in vent distribution (Connor and Hill, 1995). Smith et al. (1991) suggested a narrow NE-trending structurally controlled source zone of potential volcanism extending through the repository site, resulting in comparatively high probabilities of volcanic disruption. Alternatively, some structure models exclude the repository from volcanic source zones. For example, Crowe and Perry (1989) proposed the NNW-trending Crater Flat volcanic zone, with its eastern boundary located west of the repository site, resulting in comparatively low probabilities. Thus, wide variation in probability estimates is a direct result of the varying ways in which these source zones have been drawn. Part of this dichotomy may be resolved if the relationships between volcanic and structure are considered mechanistically and in light of mapped structural features of the YMR. In following, these relationships are discussed in terms of:

- Regional tectonic models of YM and surrounding geologic features
- Mechanistic relationships between crustal extension and magma generation
- Local structural controls on magma ascent.

4.4.5.1 Regional Tectonic Models

Yucca Mountain lies within the Basin and Range Province of the western North American Cordillera; a province characterized by spatially segregated regions of east-west extension between zones of northwest trending dextral strike-slip or oblique strike-slip faults. Coupled with the overall pattern of crustal extension and transtension are numerous small-volume volcanic fields. Within this tectonic framework, five viable tectonic models that describe the pattern of regional and local deformation around Yucca Mountain have been proposed in the geologic literature over the past two decades. These five models are:

- Deep detachment fault
- Moderate depth detachment fault
- Planar with internal block deformation and ductile flow of middle crust
- Pull-Apart Basin (Rhombochasm or Sphenochasm)
- Amargosa shear or Amargosa Desert Fault system

In a broad sense, these five models can be considered in two general categories of deformation. The first three are dominantly related to extensional deformation and the latter are dominantly related to strike-slip deformation. Moreover, the five models are not mutually exclusive. Locally

extensional-dominated deformation, within Crater Flat for example, can exist within a larger region of trans-tensional deformation related to a pull-apart basin.

Add paragraph on basic geology

In the deep detachment fault model, the Crater Flat -Yucca Mountain faults are envisioned as soling into the Bare Mountain Fault at the base of the seismogenic crust, approximately 15 km depth. The faults accommodate strain within the hanging wall of the Bare Mountain Fault. This model is extension dominant, but it is compatible with a regional strike-slip system in which the Crater Flat - Yucca Mountain domain has largely dip-slip faulting, similar to a pull-apart basin. In addition, the model respects the geologic constraints on the timing of deformation (variable dips of fault blocks with growth of tuff strata across faults that were active during tuff deposition), as well as the rollover in fault blocks. However, restored cross sections are more difficult to balance than with a moderate depth detachment fault.

The moderate depth detachment fault model (Young et al., 1992; Ferrill et al., 1995; Ofoegbu and Ferrill 1995) is similar to the deep detachment model, but the Crater Flat -Yucca Mountain faults sole into a detachment fault at 5-10 km depth (Figure x-sections). The detachment then terminates against the deeper, larger Bare Mountain Fault. The geometry of this model is the most reasonable for obtaining a balanced restored cross section of the upper crustal section. A moderate detachment fault also permits the largely dip-slip Crater Flat -Yucca Mountain domain to be part of a regional strike-slip system.

Figure x-sections. Two balanced cross sections across Bare Mountain, Crater

Flat, and Yucca Mountain (from Stamatakos et al., 1996). The cross sections differ in the depth of the detachment fault. High-angle normal faults at Yucca Mountain intersect this detachment at depths between 5 and 10 km. Such high-dilation tendency faults may serve as pathways for ascending magmas.

Both shallow and moderately deep detachment models may influence basaltic magmatic activity in two ways. First, faults that sole into the detachment may serve as conduits for magma ascent in the shallow crust, if these faults provide relatively low-energy pathways to the surface (McDuffie et al., 1994; Jolly and Sanderson, 1997). Second, extension dominate models result in large-scale density contrasts in the shallow crust. Dense PreCambrian and Paleozoic rocks dominate the upper crustal section west of the Bare Mountain fault. East of the Bare Mountain fault, extension results in the formation of a half-graben and the upper crustal section is dominated by tuffs and alluvium. This broad density contrast may influence rates of partial melting, a topic pursued in the next section.

Alternatively, the Crater Flat -Yucca Mountain faults can be interpreted as planar to the ductile middle crust. This is an extension dominant model; fault dips do not shallow with depth. This model, which serves as the conceptual basis for the USGS boundary element model, assumes that the surface geometry of faults and fault blocks cannot be used to constrain deformation at depth. Fault block deformation and ductile flow (and perhaps magma intrusion) at depth are assumed to compensate for variable fault block dips which would otherwise produce large triangular-shaped gaps in the subsurface.

The pull-apart-basin model envisions Crater Flat as a pull-apart basin formed in a releasing bend of

a north-northwest trending regional strike-slip system (Fridrich, 1996). The pull-apart basin is a half-graben with a well-defined western edge in the Bare Mountain Fault, the diffuse set of Crater Flat -Yucca Mountain faults to the east, and an eastern edge in western Jackass Flats. The regional strike-slip system remains hypothetical, buried beneath Amargosa Valley alluvium southeast of the southern end of the Bare Mountain Fault. The pull-apart model explains the vertical axis rotation of the southern reaches of Crater Flat -Yucca Mountain as crustal-scale block rotations within the overall regional dextral shear. This shear is related to diffuse boundary interactions between the North American and Pacific plates. The model explains the north-northeast arcuate trend of Quaternary volcanic centers of Crater Flat as an alignment along a Reidel shear within the basin.

In the rhombocasm version of the pull-apart model, the basin-bounding strike-slip fault trends north-northwest out of Crater Flat and concealed beneath the Timber Mountain-Oasis Valley calderas. In the sphenochasm version, the northern extent of the bounding strike-slip fault is pinned at the northern end of Crater Flat. Strike-slip deformation increases south and east from the pin point. In response, the basin fans open to the south and extension on basin bounding normal faults like the Bare Mountain Fault increases southward.

The Amargosa Shear model is similar to the rhombochasm model, with Crater Flat representing a diffuse dextral shear zone along a major north-northwest trending crustal shear (e.g. Schweickert and Lahren, 1997). The shear zone extends northward along a hypothetical strike-slip fault extending north-northwest from Crater Flat beneath the Timber Mountain and Oasis Valley calderas. The lack of offset of these calderas is explained as diffuse detachment of the tuffs from underlying crust, in which offset is absorbed by horizontal faults within the tuff layers. The southern extension of the shear links with the Stewart Valley-State Line fault. Total length of the

fault and shear zones in greater than 250 km.

The Crater Flat shear zone includes the motion on faults within western Bare Mountain, the vertical axis rotation within southern Yucca Mountain, and the sites of volcanic activity in Crater Flat. The Quaternary cone alignment is believed to represent a Reidel shear oblique to the main shear axis. Based on a palinspastic reconstruction between southern Bare Mountain and the Striped Hills, this model calls for 30 km of right-lateral offset along the southern extension of this shear since the Miocene (post 11.5 Ma). This aspect of the model is suspect because of disparate apatite fission track ages for Bare Mountain and the Striped Hills suggest significantly different thermal histories in these two blocks since the Cretaceous.

Strike-slip dominated models have been used to infer an entirely different basis for distribution of volcanoes in the YMR than purely extensional models. For example, Schweickert, and Lahren, 1997 have envisioned a relatively uniform melt generation region beneath the YMR. In these circumstances, crustal structures, such as Reidel shears in pull-apart basins, allow these magmas to ascend to the surface. Fridrich (1996) also proposed that tensional structures control the ascent of magma through the crust and that volcanism will be limited to areas where these tensional structures exist. Some source zone models (e.g., Perry and Crowe, 1989) propose that YM lies outside of pull-apart basins, and therefore the probability of volcanism at YM is extremely low compared with Crater Flat. However, as noted above, the strike-slip fault on the eastern edge of the pull-apart has not ever been identified or is simply diffuse, greatly reducing the confidence with which such source zones for basaltic volcanism can be drawn accurately.

Elements of the above tectonic models are not mutually exclusive. For example, predominately

strike-slip deformation may given way to predominantly extensional deformation as regional shear results in rotation of the direction of maximum horizontal compressional stress relative to fault planes. Under these circumstances, it is appropriate to consider mechanistic relationships between crustal extension in the YMR and basaltic magma generation.

4.4.5.2 Mechanistic Relationships Between Crustal Extension and Magma Generation

There exists a direct link between tectonics and generation of basaltic magmas. In the Western Great Basin, extension and associated crustal deformation produce local changes in lithostatic pressure at the base of the crust. Such decreases in lithostatic pressure may result in partial melting in some areas of the mantle if mantle rocks in these areas are close to their solidus. Small decreases in lithostatic pressure moves these rocks above their solidus, inducing partial melting and eventually leading to the eruption of small-volume basaltic magmas. Thus, lateral changes in lithostatic pressure across the YMR may provide insight into areas of likely future volcanic activity.

Using a balanced cross section based on the moderately deep detachment fault model, crustal extension has resulted in large density differences in the upper 5–6 km of the crust in the YMR due to the displacement of Paleozoic and PreCambrian rocks across the Bare Mountain Fault, the formation of the Crater Flat basin, and subsequent deposition of ignimbrites and alluvium in Crater Flat (Figure density). The average density of a 5.6 km column of rock beneath Crater Flat and Bare Mountain can be calculated from this cross-section using average rock densities for the region (McKague, 1980; Howard, 1985). This difference in average density is 280 kg/m^3. Beneath this 5.6 km column, little density difference is expected because any faulting that occurs below 5.6 km

does not juxtapose rocks of significantly different densities. Given lithostatic pressure as

$$P_L = \int_0^h \rho(z) g \, dz$$

where g is gravity (9.8 m/s2), $\rho(z)$ is rock density at a given depth z, and h is the total depth, in this case 5.6 km, this density difference in the upper crust produces a lithostatic pressure difference between Bare Mountain and Crater Flat of approximately 15 Mpa. at a depth equivalent to the base of the Paleozoic section in Crater Flat. This lithostatic pressure estimate excludes topographic effects, because these effects attenuate rapidly with depth (ref).

Figure density. Comparison of density profiles beneath Bare Mountain (BM) and Crater Flat (CF). Profiles are constructed using a balanced cross-section (Ferrill et al., 1996) and density values from McKague (1980) and Howard (1985). Density differences are assumed to be negligible beneath 5.6 km.

Equation ** assumes that lithostatic pressure is a function of depth only, which is not strictly true where lateral changes in density exist in the crust. Lateral changes in density at the surface, such as those produced by topographic variation for the development of a basin, attenuate with depth because of changes in the magnitudes of horizontal stresses relative to vertical stress as a function of depth. In this case pressure is best estimated as:

$$P = -\frac{1}{3}\left(\sigma_{xx} + \sigma_{yy} + \sigma_{zz}\right)$$

where σ_{xx}, σ_{yy}, and σ_{zz} are the orthogonal normal stresses acting in the two horizontal and vertical directions, respectively.

Because of this attenuation, comparatively large-scale density variations are required to create lateral pressure changes in the mantle. Furthermore, lateral density contrast in the crust will cause lateral pressure changes in the crust and in the mantle only if the Moho discontinuity is not deflected as a result of isostatic compensation (Figure concept model). Isostatic compensation is not likely because the scale of features like Bare Mountain and Crater Flat is small compared to scale of features normally compensated for by isostasy (Anderson, 1989). What geophysical data exist (Brocher et al., 1996), support a flat Moho discontinuity in the region.

Figure concept model. Conceptual model of melt generation in response to crustal extension (a). Extension results in lateral density contrast in the crust which deflects iso-pressure surfaces downward, to P_1 from their initial depth P_o. This local decrease in pressure results in the partial melting of near-solidus mantle. A simple finite element model (b) indicates that pressure changes of 7 Mpa are expected at depths of 40 km in response to large density variations in the upper 5 km of the crust, using the bulk densities and values of Poisson's ratio, υ ,

indicated.

Large-scale crustal density variations necessary to produce pressure variation in the mantle at >40 km occur in the YMR, evinced by Bouguer gravity anomalies (Figure grav). The gravity map is dominated by large negative anomalies produced by Timber Mountain caldera, and positive gravity anomalies associated with the Funeral Mountains. A north-south trending area of largely negative gravity anomalies extends through Crater Flat and the Amargosa Desert, termed the Amargosa Trough by O'Leary (1996)

Figure grav. Bouguer anomaly map of the YMR. Data complied from numerous sources and obtained from the Geophysics Data Repository at Lawrence-Berkeley Laboratory.

These gravity data can be used to create an apparent density map, following the methods of Gupta and Grant (1984), and to infer changes in apparent lithostatic pressure, ΔP_L, at comparatively shallow depths. Construction of the apparent density, or ΔP_L, map from the gravity data requires several assumptions.

- The gravity data must be on a regular grid. In this case, the gravity data were interpolated on a regular grid using a minimum tension bicubic spline gridding algorithm.

- All density variation occurs due to lateral density variation between grid points. Density is taken to be constant between the surface and a depth, h, within each grid cell. Density

variations in the Earth below h are not considered to contribute to the gravity anomalies.

- The method assumes a horizontal ground surface. The YMR gravity data have been reduced to a Bouguer anomaly, meaning density variations produced by topography have been removed from the gravity map. Using this data set results in lower density variation than expected if topography is factored into the calculation. However, topographic effects have relatively short-wavelengths, do not produce significant pressure differences at depths of magma generation, and therefore may be neglected.

Using the notation of Gupta and Grant (1984), the gravity anomaly a point, $\Delta g(x,y)$, at the surface due to density variation at a point, $\Delta \rho(\xi,\eta,\zeta)$ beneath the surface, is:

$$\Delta g(x,y,0) = G\left\{\frac{\partial}{\partial z}\int_{-\infty}^{\infty}\int_{-\infty}^{\infty}\int_{0}^{h}\frac{\Delta\rho(\xi,\eta)\,d\zeta d\eta d\xi}{\sqrt{(x-\xi)^2+(y-\eta)^2+(z-\zeta)^2}}\right\}_{z=0}$$

Note that in this formulation density does not vary as a function of depth. All density variation is lateral and the amplitude of the gravity anomaly changes with depth of the anomalous mass only because of the change in distance from the mass anomaly to the gravity meter. Only the vertical component of the gravity anomaly is considered because this is measured by the gravity meter. Differentiating with respect to z gives

$$\Delta g(x,y,0) = G \int_{-\infty}^{\infty}\int_{-\infty}^{\infty}\int_{0}^{h} \frac{-\Delta\rho(\xi,\eta)\,d\zeta d\eta d\xi}{\left[(x-\xi)^2+(y-\eta)^2+\zeta^2\right]^{\frac{3}{2}}}$$

then integrating across depth

$$\Delta g(x,y,0) = G \int_{-\infty}^{\infty}\int_{-\infty}^{\infty} \frac{\Delta\rho(\xi,\eta)\,d\eta d\xi}{\sqrt{(x-\xi)^2+(y-\eta)^2}} - G \int_{-\infty}^{\infty}\int_{-\infty}^{\infty} \frac{\Delta\rho(\xi,\eta)\,d\eta d\xi}{\sqrt{(x-\xi)^2+(y-\eta)^2+h^2}}$$

which expresses the change in gravity in terms of the horizontal distance between the gravity meter and the density anomaly, and the average anomalous density, averaged between the surface and depth, h. Because all gravity variations are assumed to occur because of lateral variations in density, the relationship between gravity anomalies and apparent density anomalies can be expressed using a 2D Fourier transform of the gravity data. The 2d Fourier transform of the gravity field is given by:

$$\Delta g(u,v) = \int_{-\infty}^{\infty}\int_{-\infty}^{\infty} \Delta g(x,y,0) e^{i(ux+vy)}\,dy\,dx$$

where u and v are wavenumbers. Gupta and Grant(1984) developed a simple filter to relate density and gravity in the wavenumber domain, based on the wavelengths of anomalies:

$$\Delta\rho(u,v) = \frac{1}{2\pi G} \times \frac{\omega}{1-e^{-h\omega}} \times \Delta g(u,v)$$

where

$$\omega = \sqrt{u^2 + v^2}$$

The inverse Fourier transform then yields apparent density in the spatial domain:

$$\Delta\rho(x,y) = \frac{1}{2\pi G} \int_{-\infty}^{\infty}\int_{-\infty}^{\infty} \frac{\omega}{1-e^{-h\omega}} \Delta g(u,v)\, dv du$$

The change in lithostatic pressure across the map region is then

$$\Delta P_L(x,y) = \Delta\rho(x,y)\, gh$$

where g is now the average gravitational acceleration, $9.8\ m/s^2$, and h is the thickness of the crust within which all density changes are assumed to have occurred. Again, no significant density changes, in terms of overall change in lithostatic pressure, are assumed to occur at depths greater than h.

For $h = 5000\ m$, $\Delta\rho(x,y)$ varies from approximately -100 to +240 kg/m3 across the YMR (Figure Litho). The apparent density contrast across the Bare Mountain Fault in southern Crater Flat of 240-280 kg/m3 in excellent agreement with density contrasts obtained from the balanced cross section and measured density values in the region (Figure density). The most prominent feature of this map is the abrupt change in apparent density from high values west of the Bare Mountain Fault to predominately low values east of the Bare Mountain Fault. Although this change is most abrupt adjacent to the Crater Flat Basin, the apparent density map also reveals that this change persists south of Bare Mountain, in the Amargosa Desert, and north of Bare Mountain. The apparent density map shows that this change in density across the is a long-wavelength feature. Apparent density values remain low east of the Bare Mountain Fault for at least 50 km, and remain high west of the Bare Mountain Fault to the edge of the gravity map, 20 km from the fault (Figure Litho).

Figure Litho. Apparent density variation across the YMR, derived from gravity data. Change from the mean apparent density in the map area is contoured in kg/m3. Volcanoes tend to occur in areas of relatively low average density, east of the Bare Mountain fault.

Because the magnitude of lateral pressure change will attenuate as a function of depth, only long-

wavelength density variations in the crust will produce pressure changes in the mantle at depths of 40-100 km, the depth of magma generation in the YMR. The magnitude of pressure variations resulting from crustal density contrasts observed across the Bare Mountain Fault can be explored using finite element analysis. Based on a simplified geometric representation of the development of the basin, lateral pressure variations on the order of 7 Mpa are expected to occur at depths of 40 km (Figure concept model), attenuating to 2 Mpa at a depth of 80 km, and << 1 Mpa at 100 km. Mantle rocks at depths of 40-100 km are under average lithostatic pressures of 1000-3000 Mpa. Thus a change of 2-7 Mpa cross the density discontinuity represents a small fraction of the total pressure at that depth. This small difference reinforces the idea that extension and deformation of the magnitude observed in the YMR can only result in renewed magmatism if mantle rocks already are near their solidus (Figure concept model).

Observations of the distribution of volcanoes in the YMR suggests that these small pressure differences are sufficient. Plio-Quaternary volcanoes lie in the lower $\Delta P_L(x,y)$ areas east of the Bare Mountain fault, as expected if decreases in lithostatic pressure result in production of partial melts in the YMR. Nearly all of these volcanoes occur within the gravity low, which in part defines the Amargosa Trough (O'Leary, 1996) (Figure gravity). Topographically, Lathrop Wells cinder cone lies outside Crater Flat but, based on gravity data, is within the larger N-trending basin and at the margin of the prominent basement low in southernmost Crater Flat. Aeromagnetic anomalies (Langenheim et al., 1993) in the Amargosa Valley produced by buried Pliocene(?) basalts also lie within or at the margins of the southern extension of this basin. The easternmost of these buried basalts lies close to N-trending gravity anomaly demarcating the eastern edge of Amargosa Valley alluvial basin in this area.

These volcanoes erupted in areas of lower $\Delta P_L(x,y)$ than expected if eruptions occurred randomly throughout the map area. In fact, only one Plio-Quaternary volcano erupted where $\Delta P_L(x,y) > +2$ Mpa, and this volcano, Aeromagnetic Anomaly E (Table Litho) erupted in a high gravity gradient area along the southern projection of the Bare Mountain Fault. These observations suggest that long-wavelength density differences in the YMR, dominated by the Bare Mountain Fault and its extension south into the Amargosa Desert, are sufficient to produce pressure changes in the mantle that result in partial melting and volcanism.

Continued regional extension would result in depression of iso-pressure surfaces in areas of basin formation, such as on the footwall of the Bare Mountain fault, which may result in renewed partial melting. Such renewed partial melting can occur over a range of depths in the mantle simultaneously. Partial melting will tend to occur in areas where basaltic volcanism has occurred in the past because mantle rocks in these areas are likely close to their solidus, and therefore small decreases in pressure may reactivate partial melting. In contrast, some parts of the mantle in YMR is not near its solidus, and therefore extension will not result in magmatism in these areas because the pressure variations are not sufficient to produce melts.

Based this model of magma generation in response to extension, recurring Quaternary volcanism within vent clusters formed by Miocene and Pliocene basaltic volcanism occurs because mantle rocks beneath these regions are near their solidus and partially melt as a result of comparatively small amounts of extension. A given rate of extension will result in the greatest rate of change in mantle pressure directly beneath the lateral change in density in the crust, such as at the Bare

Mountain fault. Thus, with continuing extension, mantle in the region of this inflection has the greatest opportunity of producing partial melts as a result of a given amount of crustal extension. Therefore, episodes of basaltic volcanism may correlate with episodes of extension, resulting in renewed activity within basaltic vent clusters. Episodes of extension and basaltic volcanism may correlate temporally as well, because pressure variations in the mantle will likely equilibrate due to ductile flow over time. In other words, pressure changes in the mantle which result from crustal extension will be transitory.

Change in lithostatic pressure also affects magmatism because magmas ascend by buoyant rise. The buoyancy forces acting on the magma are equivalent to the hydrostatic pressure gradient, given by Lister and Kerr (1991) as:

$$P_h = \int_0^Z (\rho_{rock}(z) - \rho_{magma}) g dz$$

where ρ_{rock} and ρ_{magma} are density of rock and magma, respectively, g is gravitational acceleration and Z is the depth of magma generation. Rock density varies as a function of depth, most dramatically at the Moho discontinuity. Because the density of magma is typically less than that of mantle, but greater than most crustal rocks, a level of neutral magma buoyancy can exist in the crust. An isolated pod of magma above the level of neutral buoyancy will sink and a pod below the level of neutral buoyancy will rise. Magmas fed by conduits respond to the integrated hydrostatic pressure along the conduit but tend to have flow characteristics responding to the local

hydrostatic pressure. Thus, dikes will tend to propagate laterally above the level of neutral buoyancy (Lister and Kerr, 1991). The level of neutral buoyancy will be deeper in the crust in basins than beneath mountains. As Quaternary basalts in the YMR demonstrate, alkali basalts will not stagnate in the alluvial basins as they rise through them because the hydrostatic pressure is integrated over the depth from origination of the melt. However, longer dikes and dike swarms are expected to form in these alluvial basins than elsewhere because of the comparatively low lithostatic pressure. Thus, from the perspective of volcanic hazards analysis, understanding of the change in lithostatic pressure across the region can help constrain areas of likely melt generation and areas of likely dike propagation above the level of neutral buoyancy.

4.4.5.3 Local Structural Controls on Magma Ascent

Observations in the YMR indicate that there is a strong correlation on a local scale between structure and volcanism. These observations include the development of vent alignments (Smith et al., 1990; Connor et al., 1997) and occurrence of cinder cones along faults (Sections 4.4.1 and 4.4.4, Connor et al., 1997). These observations suggest that faults and related structures may influence magma ascent, at least on local scales, in the YMR, and the such influence should be considered on probabilistic volcanic hazard analysis of the proposed repository.

Igneous dikes transport basaltic magmas from the mantle to higher levels in the crust or to the surface. Propagating dikes, like hydraulic fractures, typically form perpendicular to the least principal stress, which is parallel to the principal horizontal stress in extensional terranes, because a fracture with this orientation requires the least amount of magma pressure to open (Stevens,

1911; Anderson, 1938).

Under some conditions, pre-existing faults or extension fractures will serve as pathways for magma instead of propagating a new dike fracture. Assuming that a pre-existing fault or extension fracture has no tensile strength, the pre-existing fracture is likely to dilate (i.e., capture magma) if the fluid pressure (P_f) exceeds the normal stress resolved on that fracture (Delaney et al., 1986; Reches and Fink, 1988; Jolly and Sanderson, 1997). The likelihood of dilation and capture is controlled by the magnitude of the three principal stresses (σ_1, σ_2, σ_3), P_f, and orientation of the pre-existing fracture in the stress field.

The ability of any fault or fracture to dilate during magma injection is directly related to the normal stress acting across the fracture. Assuming cohesionless faults, the relative tendency for a fault of a given orientation to dilate in a given stress state, dilation tendency, can be expressed by comparing the normal stress acting across the fault with the differential stress.

Dilation tendency of the fault is expressed as

$$T_d = \frac{(\sigma_1 - \sigma_n)}{(\sigma_1 - \sigma_3)},$$

where σ_1 and σ_3 are the maximum and minimum compressional stresses, respectively, and σ_n is the normal stress acting across the fracture. Faults with T_d greater than some threshold value, such

as 0.8, are considered to have a high-dilation tendency. A Schmidt plot of dilation tendency and fault poles indicates that in the YMR region, faults oriented 355°-085° with dips > 50° have high-dilation tendency.

In the YMR region, σ_1 is vertical, σ_2 is horizontal and oriented 028°, and σ_3 is horizontal and oriented 298°. The relative magnitudes of $\sigma_1:\sigma_2:\sigma_3$ are estimated to be 90:65:25. As a result of this stress pattern, steeply dipping N to NE-trending faults have a greater dilation tendency than faults of other orientations. Areas with higher concentrations of high dilation-tendency faults, therefore, may be more likely to be the sites of volcanic activity. Such high-dilation tendency faults may serve as conduits for magmas ascending through the crust over prolonged periods of time, resulting in the formation of cinder cone alignments (Conway et al., 1997).

Fault dip also influences a faults ability to transport magmas. McDuffie et al (1994) provide analytical results that indicate that the ability of a fault or fault zone to redirect ascending magma is highly dependent on the depth at which the fault zone is intersected and the dip of the fault zone. Particularly, their analysis suggests that only high-angle faults, with dips greater than 40-50°, are capable of dike capture at depths exceeding 1 km. At depths of 10 km, faults dipping at angles less than 70° due not likely provide low energy pathways to the surface compared to vertical dike propagation.

Steeply-dipping high-dilation tendency faults in the YMR include many faults that bound the YM block, such as the Solatario Canyon fault, which is located at the western edge of the repository site and which hosted dike injection approximately 10.6 Ma; the Ghost Dance Fault, which bisects

the repository from north to south, and the Bow Ridge fault, located east of the repository site. Some of these faults, particularly the Solatario Canyon Fault, likely extend to the detachment fault at depths of 5-10 km. Therefore, these faults have the potential as serving as low energy pathways for magma transport to the surface. The distribution of faults with relatively high-potential for acting as magma conduits can be inferred from geologic mapping. In areas of alluvial cover, gravity and magnetic data we provide the best indication of the distribution of these faults (e.g., Connor et al., 1996).

4.4.5.4 Summary

In summary, tectonic setting is important to consider in the volcanic hazard analysis on several scales. On regional scales, crustal extension results in changes in pressure in the mantle which can give rise to partial melting. Extension also results in the formation of dip-slip fault systems which may transect a large fraction of the crust and serve as conduits for magma rise. On local scales and at shallow depths, individual dikes may propagate along faults that have high-dilation tendencies and dike lengths may be in part controlled by local lithostatic pressure. Field investigations in the YMR have shown that all of these factors may operate in the YMR, partially controlling the distribution, and possibly the timing, of basaltic volcanism.

Additional Refs.

Brocher, T. 1996. Thoughts on the extensional models for the Basin and Range Province based on

crustal-scale seismic reflection profiles near Crater Flat and Yucca Mountain, Nevada. Geological Society of America, 1996 Annual Meeting, Abstracts with Programs, October 28-31, 1996, Denver, CO, p. A-125.

Connor, C.B., J.A. Stamatakos, D.A. Ferrill, and B.E. Hill. 1996. Integrating structural models into probabilistic volcanic hazard analyses: An example from Yucca Mountain, NV. Geological Society of America, 1996 Annual Meeting, Abstracts with Programs, October 28-31, 1996, Denver, CO, p. A-192.

Brocher T.M., P.E. Hart, W.C. Hunter, and V.E. Langenheim, 1996, "Hybrid-source reflection profiling across Yucca Mountain, Nevada: Regional Lines 2 and 3", USGS Open File Report 96-28., 100p.

McKenzie, D., and M. J. Bickle, *1988 J. Petrol.*, **29**, 625 (1988).

Ferrill, D.A., J.A. Stamatakos, S.M. Jones, B. Rahe, H.L. McKague, R.H. Martin, and A.P. Morris. 1996a. Quaternary slip history of the Bare Mountain fault (Nevada) from the morphology and distribution of alluvial fan deposits. *Geology* 24(6): 559–562.

Ferrill, D.A., G.L. Stirewalt, D.B. Henderson., J.A. Stamatakos, K.H. Spivey, and Wernicke., B.P., 1996b, "Faulting in the Yucca Mountain region", NUREG/CR-6401, CNWRA 95-017.

Fleck, R.J., B.D. Turrin, D.A. Sawyer, R.G. Warren, D.E. Champion, M.R. Hudson, and S.A. Minor. 1996. Age and character of basaltic rocks of the Yucca Mountain region, southern Nevada. *Journal of Geophysical Research* 100(B4): 8,205–8,227.

Frizzell, V.A. Jr., and J. Shulters. 1990. *Geologic Map of the Nevada Test Site, Southern Nevada*. U.S. Geological Survey Miscellaneous Investigations Map I-2046. Reston, VA: U.S. Geological Survey.

Gupta, V.K., and F.S. Grant, 1984. Mineral-exploration aspects of gravity and aeromagnetic surveys in the Sudbury-Cobalt area, Ontario, in W. J. Hinze (ed)., The Utility of Regional Gravity and Magnetic Anomaly Maps, Society of Exploration Geophysicists, Tulsa, OK, pp. 392-412.

Jolly, R.J.H., and D.L. Sanderson. 1997. A Mohr circle construction for the opening of a pre-existing fracture. Journal of Structural Geology, 19: 887-892.

Langenheim, V.E., K.S. Kirchoff-Stein, and H.W. Oliver. 1993. Geophysical investigations of buried volcanic centers near Yucca Mountain, southwest Nevada. *Proceedings of the Fourth Annual International Conference on High-Level Radioactive Waste Management.* La Grange Park, IL: American Nuclear Society: 1,840–1,846.

Langenheim, V.E., and D.A. Ponce. 1995. Depth to Pre-Cenozoic basement in southwest Nevada. *Proceedings of the Sixth Annual International Conference on High-Level Radioactive Waste Management.* La Grange Park, IL: American Nuclear Society: 129–131.

Lister, J.R. and R.C. Kerr, 1991. Fluid-mechanical models of crack propagation and their application to magma transport in dykes, Journal of Geophysical Research, 96: 10,049-10,077.

Ofoegbu, G.L. And D.A. Ferrill, 1995, " Finite Element Modeling of listric Normal Faulting", CNWRA 95-008.

O'Leary, D.W. 1996. Choosing a tectonic model for Yucca Mountain, Nevada. Geological Society of America, 1996 Annual Meeting, Abstracts with Programs, October 28-31, 1996, Denver, CO, p. A-192.

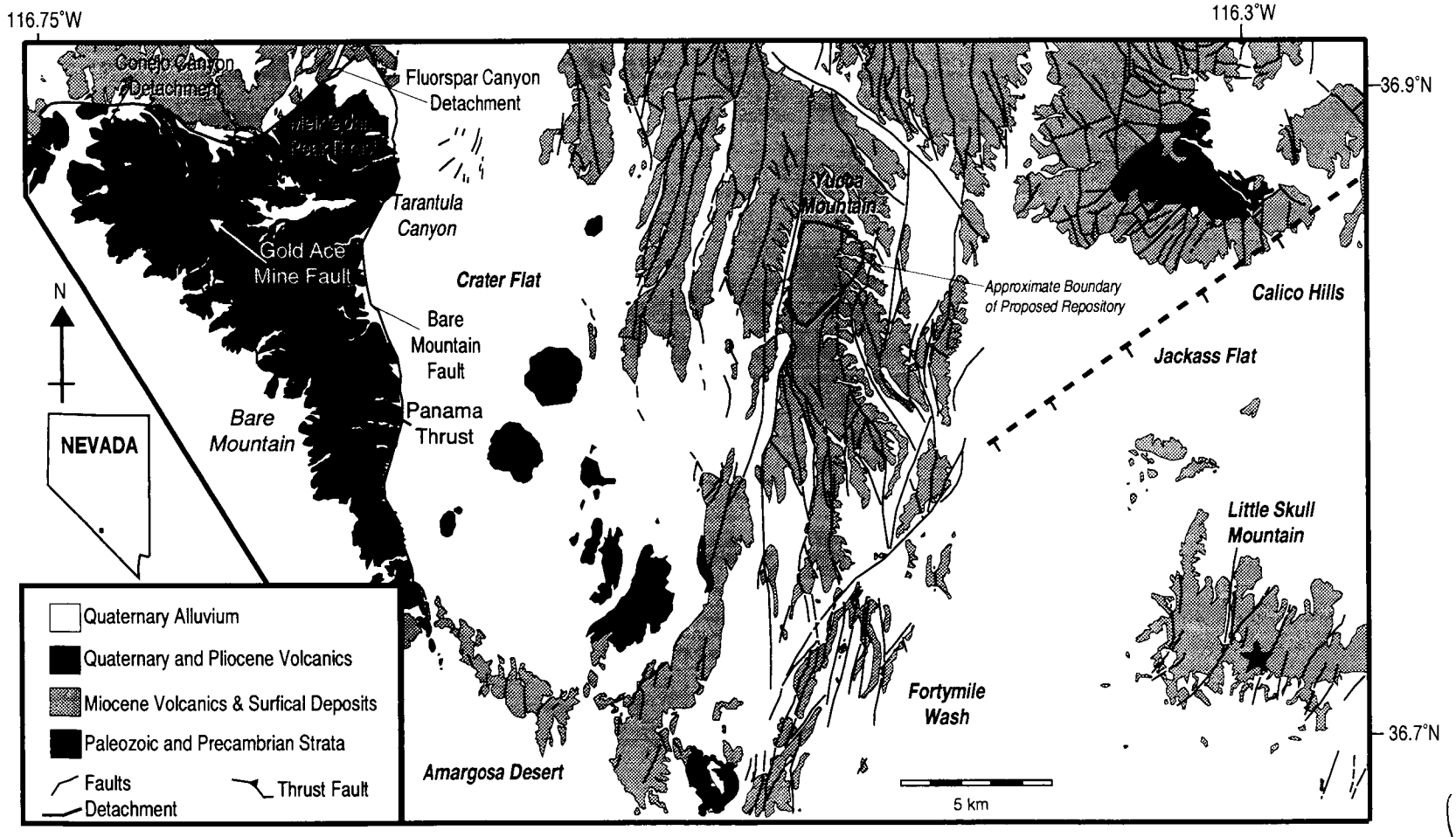
116.75°W
116.3°W
36.9°N
36.7°N
Conejo Canyon Detachment
Fluorspar Canyon Detachment
Tarantula Canyon
Yucca Mountain
Gold Ace Mine Fault
Crater Flat
Approximate Boundary of Proposed Repository
Calico Hills
Bare Mountain Fault
Jackass Flat
Panama Thrust
Bare Mountain
N
NEVADA
Little Skull Mountain
Fortymile Wash
Amargosa Desert
5 km
Quaternary Alluvium
Quaternary and Pliocene Volcanics
Miocene Volcanics & Surfical Deposits
Paleozoic and Precambrian Strata
Faults
Thrust Fault
Detachment

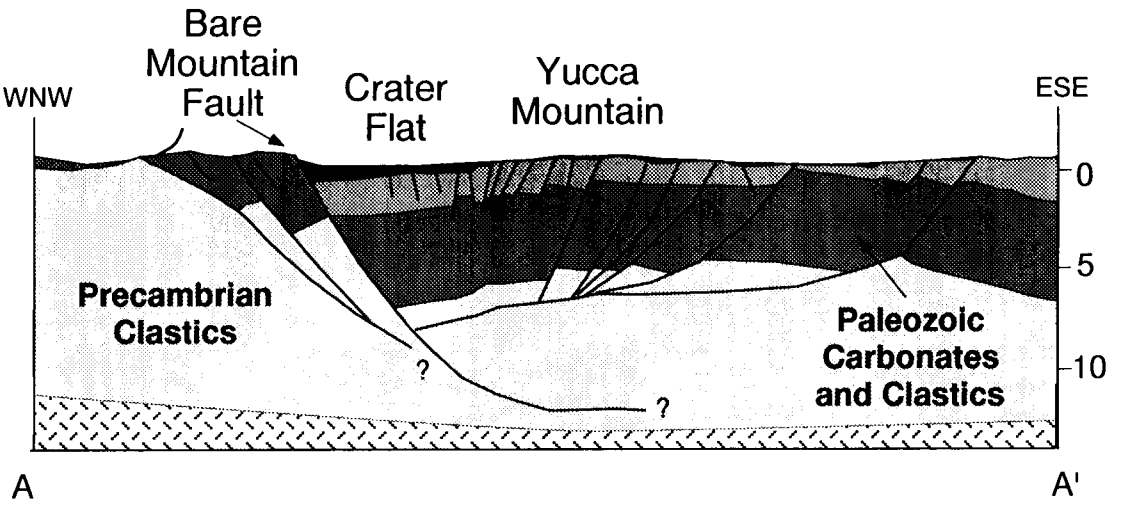
Bare
Mountain
Fault
Crater
Flat
Yucca
Mountain
WNW
ESE
0
5
10
Precambrian
Clastics
Paleozoic
Carbonates
and Clastics
?
?
A
A'

FINITE ELEMENT MODEL

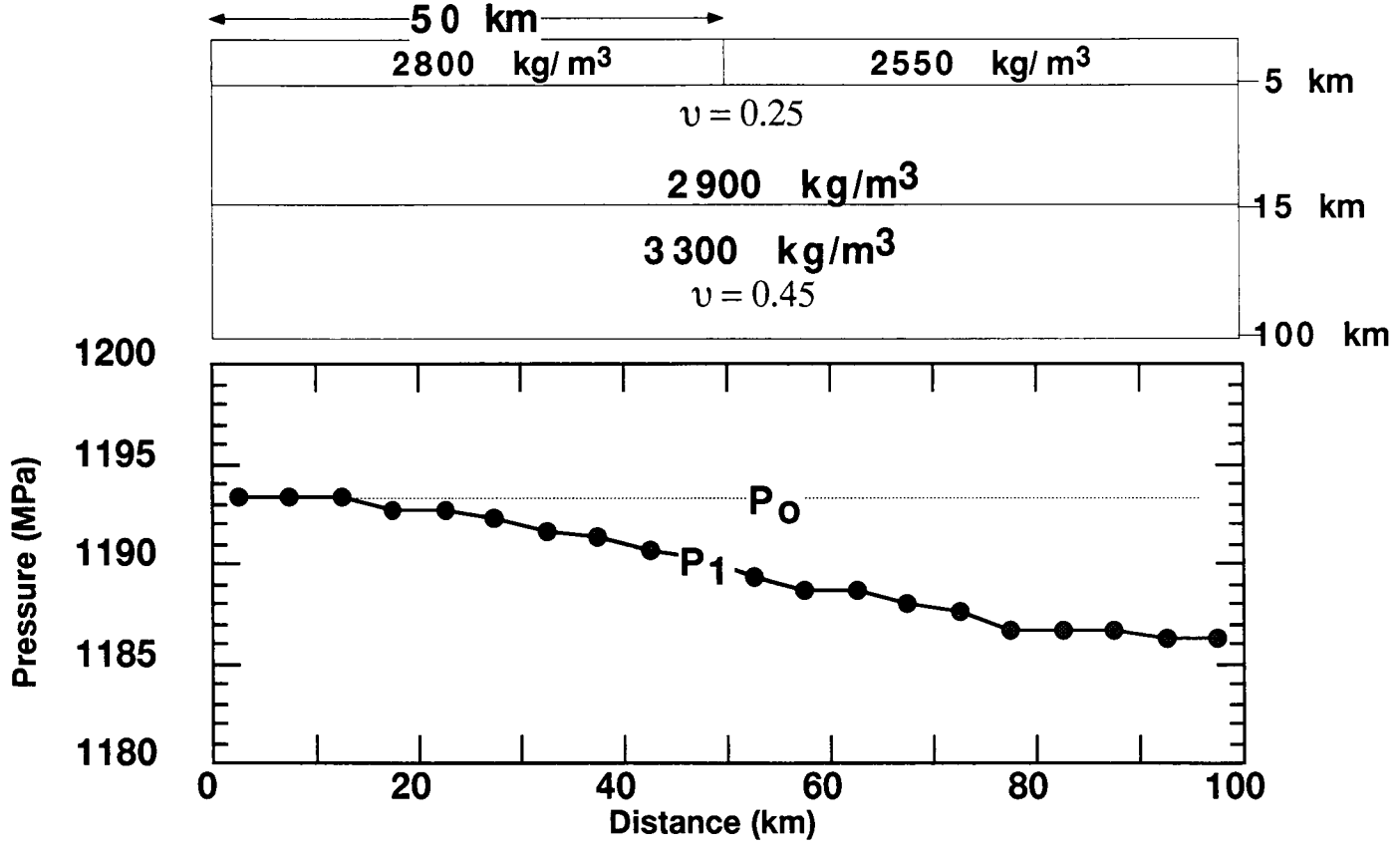

CC

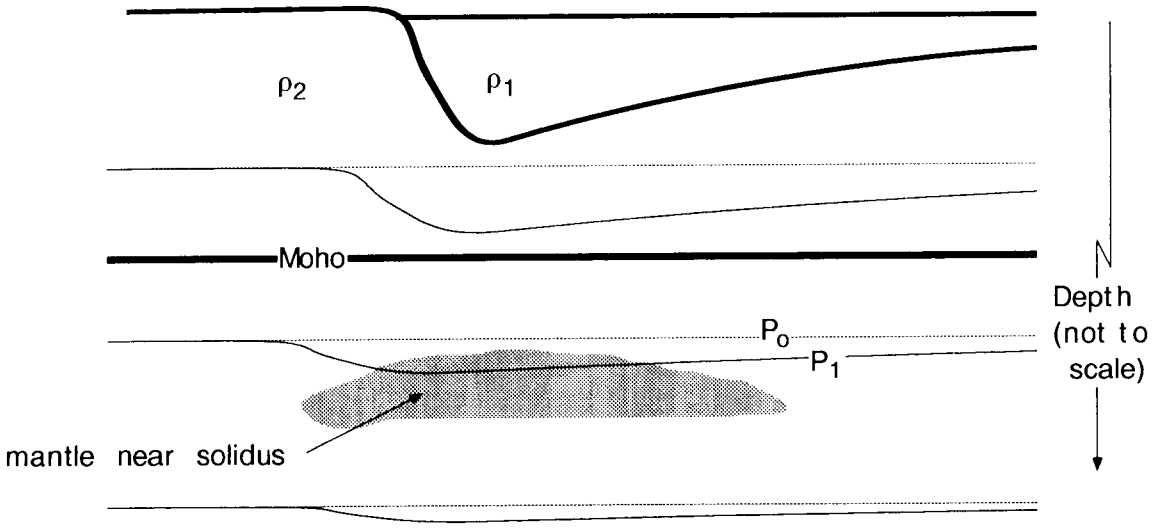
ρ2
ρ1
Moho
Depth
(not to
scale)
Po
P1
mantle near solidus

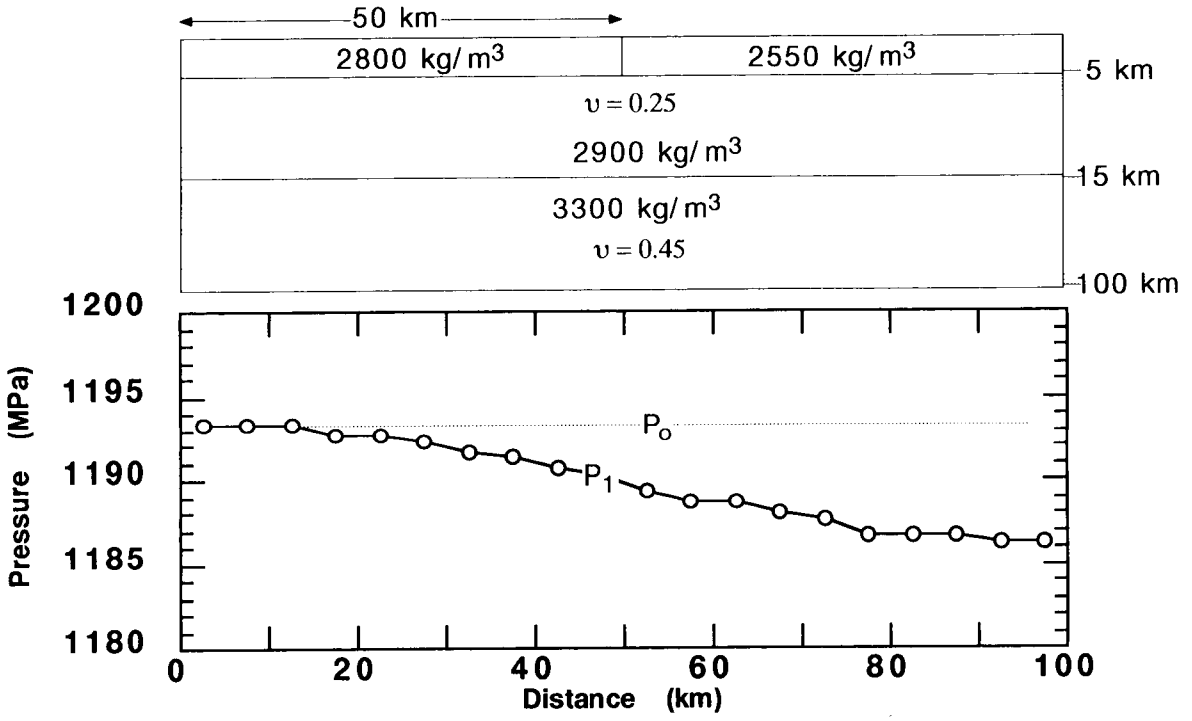
50 km
2800 kg/m3
2550 kg/m3
5 km
υ = 0.25
2900 kg/m3
15 km
3300 kg/m3
υ = 0.45
100 km
1200
1195
1190
1185
1180
Pressure (MPa)
Po
P1
0
20
40
60
80
100
Distance (km)

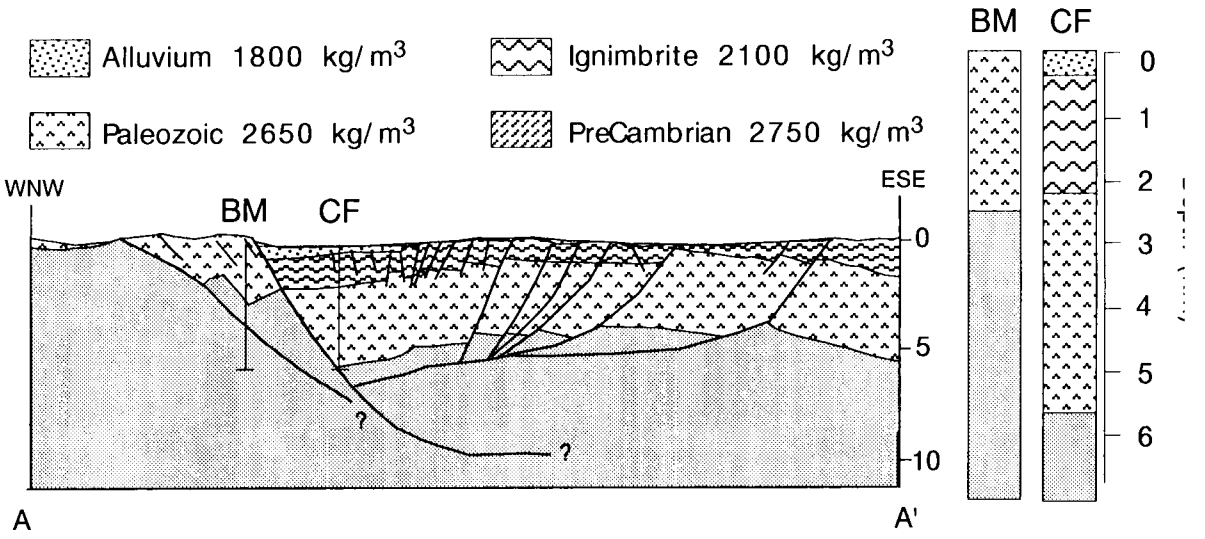
Alluvium 1800 kg/m3
Ignimbrite 2100 kg/m3
Paleozoic 2650 kg/m3
PreCambrian 2750 kg/m3
WNW
ESE
BM
CF
0
5
10
?
?
A
A'
BM
CF
0
1
2
3
4
5
6

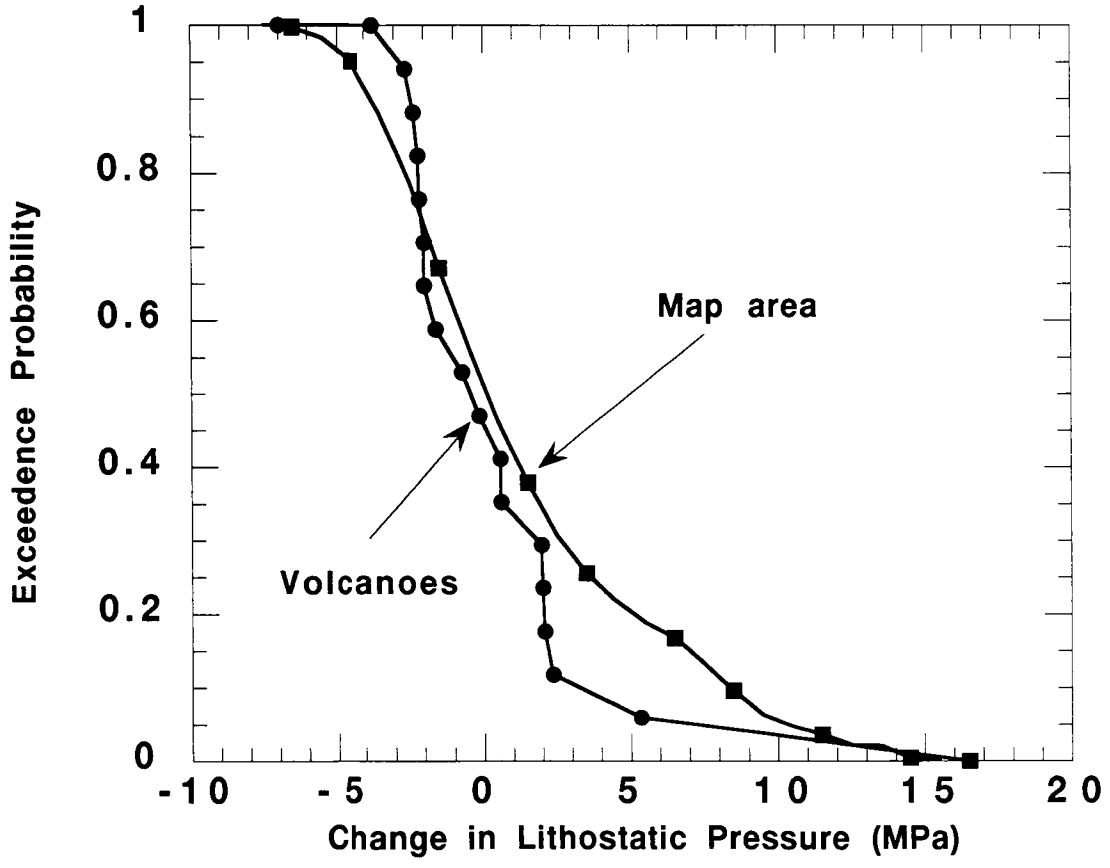
lithostatic pres / volc data
Exceedence Probability
1
0.8
0.6
0.4
0.2
0
-10
-5
0
5
10
15
20
Change in Lithostatic Pressure (MPa)
Map area
Volcanoes

Scientific Notebook — Chuck Connor CC
Project 20-1402-461 — October, 1997

The following true Basic code is used to calculate the probAbility of volcanism by area, incorporating tectonic controls,

written by Chuck Connor

Program

```
DIM x(23),y(23)
DIM  prob_dens(80000), litho_prob_dens(80000)
DIM repox(80000), repoy(80000), litho(80000),
litho_prob_dens_tot(80000)

LET h = 9000
LET gridx = 275.53
LET gridy = 223.25
LET grid_spacing = (275.53*223.25)^0.5


LET num_volcanoes = 3

LET north_angle = 28
!uniform random distribution
LET high_distribution = 10200
LET low_distribution = 100


! Lathrop Wells
LET x(1) = 543780.0
LET y(1) = 4060380.0

! black cone
LET x(2) = 538840.0
LET y(2) = 4074120.0

!Hidden Cone
```

Chuck Connor CC
October, 1997

LET x(3) = 523400.0
LET y(3) = 4112600.0

! crater flat 2
LET x(4) = 540420.0
LET y(4) = 4068780.0

! Amargosa B
LET x(5) = 553700.0
LET y(5) = 4052900.0

! Amargosa a2
LET x(6) = 546100.0
LET y(6) = 4053100.0

! Amargosa E
LET x(7) = 538300.0
LET y(7) = 4047200.0

!SW crater flat magnetic anomaly
LET x(8) = 535000.0
LET y(8) = 4067800.0

!the following cones have no apparent density estimates

! Amargosa Desert Anomaly C
LET x(9) = 547000.0
LET y(9) = 4042900.0

!Amargosa D
LET x(10) = 549400.0
LET y(10) = 4040000.0

!Thirsty Mtn

Chuck Connor CC
October, 1997

```
LET x(11) = 529520.0
LET y(11) = 4112150.0

!Buckboard Mesa
LET x(12) = 555180.0
LET y(12) = 4109200.0

OPEN #99: name "gauss.log", create newold
ERASE #99

OPEN #1: name "app_den.xyz"

DO while more #1
   LET counter = counter + 1

   INPUT #1: dum1$,dum2$,dum3$
    LET repox(counter) = val(dum1$)
    LET repoy(counter) = val(dum2$)
   LET mpa = val(dum3$)

    LET mpa = mpa*5000*9.8/1e6
    LET litho(counter) = 0.058824
    IF mpa < 2.3520 then LET litho(counter) = 0.11765
    IF mpa < 2.0580 then LET litho(counter) = 0.17647
    IF mpa < 2.0090 then LET litho(counter) = 0.23529
    IF mpa < 1.9600 then LET litho(counter) =  0.29412
    IF mpa < 0.59780 then LET litho(counter) = 0.35294
    IF mpa < 0.56840 then LET litho(counter) = 0.41176
    IF mpa < -0.14700 then LET litho(counter) = 0.47059
    IF mpa < -0.73500 then LET litho(counter) = 0.52941
    IF mpa < -1.6170 then LET litho(counter) = 0.58824
    IF mpa < -2.0090 then LET litho(counter) = 0.64706
    IF mpa < -2.0090 then LET litho(counter) = 0.70588
    IF mpa < -2.1560 then LET litho(counter) =  0.76471
    IF mpa < -2.2050  then LET litho(counter) = 0.82353
```

```
   IF mpa < -2.3520 then LET litho(counter) = 0.88235
   IF mpa < -2.6460 then LET litho(counter) = 0.94118
   IF mpa < -3.7534 then LET litho(counter) = 1.0000
   !let litho(counter) = 1.0
LOOP

PRINT "done reading file"

!FOR h = 5000 to 7000 step 2000

    MAT litho_prob_dens_tot = 0

   FOR i = 1 to num_volcanoes
      LET sum_ku = 0
       LET litho_sum_ku = 0

      FOR j = 1 to counter

            LET dist1 = ((repox(j) - x(i))/h)^2 + ((repoy(j)-y(i))/h)^2
           LET ku =  (1/(2*pi))*exp(-0.5*dist1)

          LET sum_ku = sum_ku + ku*(grid_spacing^2/(h^2*num_volcanoes))
         LET litho_sum_ku = litho_sum_ku +
ku*litho(j)*(grid_spacing^2/(h^2*num_volcanoes))


         LET litho_prob_dens(j) =
ku*litho(j)*(grid_spacing^2/(h^2*num_volcanoes))
           LET prob_dens(j) = ku*(grid_spacing^2/(h^2*num_volcanoes))

     NEXT j
        PRINT sum_ku, litho_sum_ku, sum_ku/litho_sum_ku
     PRINT

      FOR j = 1 to counter
```

```
        LET
litho_prob_dens_tot(j)=litho_prob_dens_tot(j)+litho_prob_dens(j)
*sum_ku/litho_sum_ku
            LET summer = summer +litho_prob_dens_tot(j)
      NEXT j
       PRINT summer
        !print sumone
       LET sumone = 0
       LET summer = 0
   NEXT i
    PRINT "done with kernel"
    OPEN #2: name "gauss.out", create newold
   ERASE #2
let n = 0
    FOR i = 1 to counter
let n = n + 1
if n = 20 then
        PRINT #2: repox(i), repoy(i),
1e6/grid_spacing^2*litho_prob_dens_tot(i)
let n = 0
end if
   NEXT i

     !for high_distribution = 5200 to 10200 step 1000
   !
     !let prob_with_dike = 0
   !
    !for j = 1 to counter
    !     call Dike (repox(j),repoy(j),
prob_dist,north_angle,high_distribution,low_distribution)
    !     let prob_with_dike = prob_with_dike +
litho_prob_dens_tot(j)*prob_dist
    !next j
    !print #99:"h = ";h
      !print #99: "high distribution = ";high_distribution
```

```
     !print #99:"probability with alignment intersection = ";prob_with_dike
   !
     !next high_distribution

    !next h
    !OPEN #2: name "gauss.out", create newold
   !ERASE #2
    !PRINT #2: 256,256
    !PRINT #2: 0,0
    !FOR j = 1 to 256
     !     PRINT #2: ymax-(j-1)*gridy;
   !NEXT j
    !FOR i = 1 to 256 step 1
     !     PRINT#2: (i-1)*gridx + xmin;
   !NEXT i
    !PRINT #2
    !
    !LET counter = 0
    !FOR j = 1 to 256
    !    FOR i = 1 to 256
    !        LET counter = counter + 1
     !          PRINT #2: litho_prob_dens_tot(counter);
    !
    !   NEXT i
    !    PRINT #2
    !NEXT j

   END

    SUB Dike (x_pt,
y_pt,prob_dist,north_angle,high_distribution,low_distribution)
        DIM rep_x(6), rep_y(6)

         !boundaries of the repository
```

```
LET n_repo = 6
 LET rep_x(1) = 548216
 LET rep_x(2) = 549658
 LET rep_x(3) = 549180
 LET rep_x(4) = 547827
 LET rep_x(5) = 547065
 LET rep_x(6) = 547393

 LET rep_y(1) = 4079714
 LET rep_y(2) = 4078510
 LET rep_y(3) = 4077130
 LET rep_y(4) = 4075864
 LET rep_y(5) = 4076802
 LET rep_y(6) = 4078484

 LET repo_center_x = 548500
 LET repo_center_y = 4078250


 IF north_angle = 0 then LET north_angle = 0.001
 LET north_angle = 90 - north_angle
  LET theta = north_angle*pi/180


  !        LET trial_dist = sqr((x_pt-repo_center_x)^2 + (y_pt -
repo_center_y)^2)  -3000
  !        IF trial_dist< high_distribution then

           !*************************
LET sumn = 0


 LET m1 = tan(theta)
 LET b1 = y_pt - m1*x_pt
 LET min_dist = 1e32
```

```
    CALL convex_hull(rep_x, rep_y, x_pt,y_pt,n_repo, pt_state$)

  IF pt_state$ = "true" then
   LET min_dist = 0

 ELSE                    !find distance to repo

   FOR i = 1 to n_repo

     IF i < n_repo then
        LET x1 = rep_x(i)
        LET y1 = rep_y(i)
        LET x2 = rep_x(i+1)
        LET y2 = rep_y(i+1)

     ELSE
        LET x1 = rep_x(i)
        LET y1 = rep_y(i)
        LET x2 = rep_x(1)
        LET y2 = rep_y(1)

     END IF

       LET m2 = (y2-y1)/(x2-x1)
      LET b2 = y2- m2*x2

     SET COLOR "red"

        LET x_intersect = (b1-b2)/(m2-m1)
       LET y_intersect = m1*x_intersect + b1


        IF (x_intersect => x1 and x_intersect <= x2) or (x_intersect <= x1
```

```
and x_intersect => x2) then

                LET dist_inter = sqr((x_pt-x_intersect)^2 + (y_pt-
y_intersect)^2)
              IF dist_inter < min_dist then
                LET min_dist = dist_inter
                LET inter_pt_x = x_intersect
                LET inter_pt_y = y_intersect
            END IF
          END IF


       NEXT i


    END IF

      IF min_dist = 0 then
        LET prob_dist = 1
       ELSE IF min_dist < low_distribution then
        LET prob_dist = 1
       ELSE IF min_dist > high_distribution then
        LET prob_dist = 0
    ELSE
          LET prob_dist = 0.5 * (high_distribution -
min_dist)/(high_distribution  -  low_distribution)
          PLOT x_pt,y_pt; inter_pt_x, inter_pt_y
            !print min_dist,x_pt,y_pt; x_intersect, y_intersect


    END IF

  END SUB

    SUB convex_hull(x_vert(), y_vert(), xpt,ypt,numvts, pt_state$)
```

```
LET pt_state$ = "false"

FOR curvt = 1 to numvts
   IF curvt = numvts then
      LET x1 = x_vert(curvt)
     LET x2 = x_vert(1)
      LET y1 = y_vert(curvt)
     LET y2 = y_vert(1)

 ELSE

      LET x1 = x_vert(curvt)
      LET x2 = x_vert(curvt + 1)
      LET y1 = y_vert(curvt)
      LET y2 = y_vert(curvt + 1)

 END IF

  WHEN error in          ! error when x2-x1 = 0
        LET m = (y2-y1)/(x2-x1)     !slope of line bet. vertices
       LET b = y1 - m*x1       !intercept of line

       LET ytest = m*xpt + b       ! point on line

        ! don't want points outside line segments: use
        ! the following tests

      IF x1 > x2 and y1 > y2 and ytest > ypt then EXIT FOR
      IF x1 > x2 and y1 < y2 and ytest > ypt then EXIT FOR
      IF x1 < x2 and y1 > y2 and ytest < ypt then EXIT FOR
      IF x1 < x2 and y1 < y2 and ytest < ypt then EXIT FOR

 USE
         !use this test instead if vertical line
```

```
            IF y2<y1 and xpt>x1 then EXIT FOR
            IF y2>y1 and xpt<x1 then EXIT FOR

        END WHEN

            !if the random point has passed the above tests for
             ! every line segment, the point lines within
           ! the selected area

           IF curvt = numvts then

              LET pt_state$ = "true"

         END IF

      NEXT curvt
  END SUB
```

Scientific Notebook
Project 20-1402-461

Chuck Connor CC
Nov. 1997

4.4.6 Acceptance Criteria 6

Probability models need to have explicitly determined uncertainties associated with calculated values in order to be meaningful. Uncertainty for reported probability values needs to incorporate both the precision of the model (e.g., influence of parameter uncertainty on the range of model results) and accuracy of the model (e.g., how well does the model predict the locations of volcanoes?). One of the difficulties inherent in the probabilistic volcanic hazard analysis of the proposed repository is that the few volcanoes in the YMR make it difficult to evaluate models in a quantitative way. Application of probability models in other volcanic fields (e.g., Condit and Connor, 1996) provides one method of evaluating probability models applied to the YMR. A second, equally important approach to model evaluation is to apply a range of models to estimate the probability of igneous events affecting the proposed repository and evaluate the sensitivity of probability estimates to this range of models. In the following, such a sensitivity analysis is performed for a range of models. Different models primarily involve different definitions of igneous events and the inclusion of more realistic, but often less well constrained, geologic processes in the analysis. These probability models are based on:

- Individual mappable eruptive units and vents
- Vents and vent alignments
- Vents and vent alignments with regional tectonic control
- Igneous Intrusions

In the following, annual probabilities of igneous events are calculated and compared using these models and a range of parameters.

4.4.6.1 Individual mappable eruptive units and vents

Individual mappable eruptive units and vents were used by Connor and Hill (1993; 1995) to estimate the probability of volcanic eruptions at the site. This definition of igneous events involves the fewest assumptions about volcanism, resulting in a straightforward sensitivity analysis.

Assuming that the probability of more than one event in a given year is small, the annual probability of volcanic eruptions within the repository boundary is given by:

$$P[\text{volcanic eruptions within repository boundary}] = 1 - \exp[-\lambda_r \lambda_t A_e]$$

where lt is the annual regional recurrence rate of volcanic vent formation, Ae is the effective repository area (Geomatrix, 1996), and lr is the spatial recurrence rate of volcanic eruptions at the repository, given a volcanic event in the region. Using a Gaussian kernel:

$$\lambda_r(x,y) = \frac{\Delta x \Delta y}{2\pi h^2 N} \sum_{v=1}^{N} \exp\left\{-\frac{1}{2}\left[\left(\frac{x-x_v}{h}\right)^2 + \left(\frac{y-y_v}{h}\right)^2\right]\right\}.$$

where x,y is a Cartesian coordinate within the repository boundary, xv,yv is the coordinate of the center of an igneous event, N is the number of such igneous events, h is a smoothing parameter (Section 4.4.4.3), and delx and dely define the area over which lr(x,y) is calculated. For the

following calculations, delx and dely = 1000 m, x,y is 548500.0, 4078500.0 and xv,yv are in UTM coordinates (Table ***). Based on the analysis in Section 4.4.4.2, a smoothing parameter, h $\geq$ 5 km, is appropriate for the Gaussian kernel. An effective repository area of 5.49 km is used in this analysis, based on the current repository design (figure CFBAS) and a 50 m buffer zone about the repository perimeter. The number of igneous events, N, depends on whether Pliocene and Quaternary or only Quaternary volcanoes are considered in the probability estimate.

Eight igneous events have occurred in the YMR during the Quaternary if these events are defined as individual mappable eruptive units and vents. Connor and Hill (1995) used this definition for igneous events and varied recurrence rates between five and ten volcanic events per million years (v/m.y.). Here, we model a range of 2 to 12 (v/m.y.), understanding that this range is based on limited data. A recurrence rate of more than 12 v/m.y. would signal a marked increase in activity compared to other volcanic fields. For example, recurrence rates in the Cima volcanic field, Ca, are on the order of 30 volcanoes per million years (Turrin et al., 1985). Comparable rates of basaltic volcanism have not occurred during the Plio-Quaternary in the YMR, with the possible exception of in the Greenwater range, in the southern YMR. Formation of less than 2 volcanic vents in the next one million years would signal a marked decrease in magmatism in the YMR. No evidence currently is available to suggest such a decrease is likely and assumption that such a decrease in regional recurrence rate will occur is not conservative for the volcanic hazard analysis.

Estimated probabilities using this model are sensitive to temporal recurrence rate of igneous events in the YMR, lt, and choice of h in the calculation of lr (x,y) (Figure model1). Based on these parameters, the annual probability of volcanic eruptions within the repository boundary is between 0.5 x 10^{-8} and 3.5 x 10^{-8}. Probabilities are slightly higher if the distribution of Quaternary

volcanoes are considered in estimation of lr, rather than the distribution of Plio-Quaternary volcanoes, because Quaternary volcanoes are, on average, located closer to the repository site. These values are quite close to those calculated by Connor and HIll (1995) using Epanechnikov kernel and nearest-neighbor estimators of spatial and spatio-temporal recurrence rate. Connor and Hill (1995) used Ae = 8 km^2, and estimated annual probabilities of volcanic disruption of the site between 1 x 10^{-8} and 5 x 10^{-8}.

Figure model1. Annual probability of volcanic eruptions within the repository boundary. Igneous events are defined as individual mappable eruptive units and vents. A Gaussian kernel is used with smoothing parameter, h, varying from 0 to 20 km. Analysis of existing vent distribution indicates h ≥ 5km is suitable for volcanic hazard analysis at the repository. Curves are shown for various regional recurrence rates of volcanic vent formation (lt = 2 x 10^{-6} v/yr, 8 x 10^{-6} v/yr, 12 x 10^{-6} v/yr), based on the distribution of Quaternary volcanoes (heavy lines) and Plio-Quaternary volcanoes (light lines). the effective repository area, Ae, is 5.49 km^2.

4.4.6.2 Vents and vent alignments

If igneous events are defined as vents and vent alignments, probability of volcanic eruptions within the repository boundary incorporates distance and direction of an igneous event, centered at a point, x,y, from the repository boundary. The probability of an igneous event centered at x,y is given by:

$$P_{x,y} = 1 - \exp\left(-\lambda_t \lambda_r\right)$$

where lt is the regional recurrence rate and lr is the spatial recurrence rate at point x,y, calculated using the Gaussian kernel (Eq. **). In practice, lr is calculated on a grid of points with map extent X,Y and grid spacing delx, dely. This probability is then weighted by the probability that an igneous event centered at x,y will result in a volcanic eruption within the repository boundary. For vent alignments in the YMR, the spacing of vents along the alignments is small compared to the size of the repository (Section 4.4.4.3). Vent alignment length is defined as the distance between the centers of the first and last vents on the alignment. Therefore, the probability of that an igneous event centered at x,y will result in vent alignment intersection with the repository boundary, and subsequent volcanic eruption within the repository boundary is:

$$P_L = \begin{cases} 1, x,y \in A_e \\ \frac{1}{2}\left[\frac{l_{max} - l_r}{l_{max} - l_{min}}\right], l_{min} \le l_r \le l_{max} \\ 0, \; l_r > l_{max} \end{cases}$$

where l_{min} and l_{max} are the minimum and maximum alignment half-lengths, respectively, and lr is the distance from x,y to the nearest repository boundary along the direction of the alignment. For this analysis it is assumed that vent alignments are oriented 028°, perpendicular to the direction of

minimum compressional stress in the YMR. Experimentation indicates that choosing a range of values of alignment orientation between 020° and 035° has negligible affect on probabilities of volcanic eruptions within the repository boundary. Probabilities are sensitive to l_{max}, which is varied over a range of values in the following analysis. Probabilities are not sensitive to the selection of l_{min}, which for the following calculations is 100 m. As indicated in Eq. ***, 50 percent of all igneous vents are individual vents rather than vent alignments in this model. The probability of volcanic eruptions within the repository boundary is then:

$$P[\textit{volcanic eruptions within the repository boundary}] = \sum_{i=1}^{X}\sum_{j=1}^{Y} P_{x,y}(x_i,y_j) \cdot P_L(x_i,y_j)$$

where xi, yj are on a rectangular grid of extent X,Y and grid spacing delx, dely.

Annual Probability of volcanic eruptions within the repository boundary were calculated using 5200 m $\leq l_{max} \leq$ 10200 m, and h = 5 and 7 km (Figure prob2). Based on nearest-neighbor vent and vent alignment distances in the YMR, h $\geq$ 7 km is reasonably conservative (Figure kernel model). Using the three Quaternary igneous events, Lathrop Wells, Quaternary Crater Flat, and the Sleeping Butte alignment, results in annual probabilities of volcanic eruptions within the repository boundary between 1 x 10^{-8} and 3 x 10^{-8}, assuming a regional recurrence rate of 3 v/m.y. Using a recurrence rate of 5 v/m.y. results in annual probabilities of up to 6 x 10^{-8}.

Figure prob2. Annual probability of volcanic eruptions within the repository boundary. Igneous events are defined as vents and vent alignments. A Gaussian kernel is used with smoothing parameter, h, of 5 and 7 km (labeled lines) and is

based on the distribution of three Quaternary igneous events. Analysis of existing vent distribution indicates h ≥ 7 km is suitable for volcanic hazard analysis at the repository. Vent alignment half-length, lmax, varied between 5200 and 10200 m, roughly changing probability estimates by a factor of two. Probabilities are calculated using lt = 3 x 10^{-6} /yr.

4.4.6.3 Vents and vent alignments with tectonic control

The above probability estimates may be modified to incorporate additional geologic controls on volcanism. Tectonism in the YMR has led to regional variations in crustal density that may cause variation in rates of partial melting across the YMR (Section 4.4.5.2). These variations are most apparent across the Bare Mountain Fault. Plio-Quaternary basaltic volcanism clusters east of this fault, in areas of anomalously low crustal density. In contrast, basaltic volcanism is apparently absent since the mid-Miocene west of the Bare Mountain Fault and its southern extension into the Amargosa Desert. Standard Gaussian kernel functions do not take into account these geologic details. As a result, the standard Gaussian kernel (i.e, Eq. ***) may overestimate probabilities of volcanic eruptions in some areas, for example on Bare Mountain, and underestimate probabilities elsewhere in the YMR.

The standard Gaussian kernel model developed above may be modified to incorporate variation in crustal density by developing a weighting function which takes crustal density into account. The model for basaltic volcanism in extensional environments developed in Section 4.4.5.2 relates pressure gradients in the mantle to regional changes in in crustal density caused by extension. However, pressure gradients in the mantle are likely transitory and small, thus only mantle rocks already close to their solidus will partially melt as a result of extension. As illustrated in Figure

concept model, partial melting will tend to occur where partial melting has occurred previously and near to the active, graben-bounding faults, where slip in the crust will result in the greatest pressure change in the mantle.

Direct evidence of pressure change in the mantle can only be inferred conceptually with the assistance of simple numerical models of mantle stresses (Figure concept model). However, the weighting function can be estimated from the frequency of volcanic eruptions as a function of crustal density. The distribution of this function, $f_T(x,y)$, is defined based on average crustal densities in the upper 5 km of the crust, at the locations of existing volcanoes, derived from application of the density filter to the gravity data set (Figure ft distribution). The Gaussian kernel is then modified to estimate the recurrence rate of volcanism at x,y:

$$K_g(x_i, y_j) = \exp\left\{-\frac{1}{2}\left[\left(\frac{x_i - x_v}{h}\right)^2 + \left(\frac{y_j - y_v}{h}\right)^2\right]\right\}$$

$$Q_v = \frac{\sum_{i=1}^{X}\sum_{j=1}^{Y} K_g(x_i, y_j)}{\sum_{i=1}^{X}\sum_{j=1}^{Y} f_T(x_i, y_j) \cdot K_g(x_i, y_j)}$$

$$\lambda_r(x,y) = \frac{\Delta x \Delta y}{2\pi h^2 N} \sum_{v=1}^{N} Q_v f_T(x,y)\, \mathrm{K}_g(x,y).$$

Introduction of the ratio Qv assures that the integral of the modified Gaussian kernel for a single volcano over a large map extent X,Y relative to the smoothing parameter, h, will be unity (Eq. ***). However, the probability will be redistributed based on crustal density variations in the vicinity of the volcano.

Figure ft distribution. The weighting function, $f_T(x,y)$ is derived from average crustal densities at Plio-Quaternary volcanoes. These densities are estimated from regional gravity data.

Comparison of the modified and standard kernels is made by contouring lr(x,y) across the YMR, using the distribution of Quaternary vents and vent alignments and h = 9000 m. As previously, N=3 in this model, including Quaternary Crater Flat, Lathrop Wells and Sleeping Butte as the three Quaternary igneous events. In Figure **standardmod**, lr(x,y) is contoured across the map region using equation ***. Given an igneous event in the region, there is a 68 percent chance that the igneous event will occur within this map area. The Sleeping Buttes alignment lies NNW of the mapped region (Figure YMRBAS). Larger values of lr(x,y) indicate areas where igneous events are most likely to be centered. The largest values occur in southern Crater Flat because of the proximity of Lathrop Wells and the Quaternary Crater Flat alignment. In this area, lr(x,y) varies between 8 x 10^{-4} volcanic events per square kilometer (v/km^2) and 2 x 10^{-4} v/km^2.

Figure standardmod. The spatial recurrence rate (v/km^2) is contoured in the area of Yucca Mountain, using the Gaussian kernel function (Eq. *). In this model, h= 9000 m, and N= 3, based on the number of Quaternary igneous events. The contour interval is 2 x 10^{-4} v/km^2. Other symbols are as in Figure CFBAS.**

Figure **modifiedmod** is based on the modified kernel (Eq. ***-***) using the same parameters as used in the standard kernel calculation (N=3, h= 9000m), but weighting the kernel using crustal densities derived using equations ***-***. Use of the modified kernel reduces the area of the lr(x,y) surface at, for example, the 2 x 10^{-4} v/km^2 contour, and increases the amplitude of the surface. The lr(x,y) surface also becomes asymmetric as a result of application of the modified kernel function. Values of lr(x,y) are greatest in southern Crater Flat, exceeding 1.2 x 10^{-3} v/km^2, and decrease abruptly near the Bare Mountain Fault. Probability values decrease less abruptly on the eastern boundary of Crater Flat because crustal densities change less rapidly on the eastern edge of the basin. This more gradual change in lr(x,y) on the eastern edge of the basin is consistent with the proposed model linking crustal extension and basaltic volcanism (Figure concept).

Figure modifiedmod. The spatial recurrence rate (v/km^2) is contoured in the area of Yucca Mountain, using the modified Gaussian kernel function (Eq. *) to incorporate tectonic control on the probability estimate. In this model, h= 9000 m, and N= 3, based on the number of Quaternary igneous events. The contour interval is 2 x 10^{-4} v/km^2. Other symbols are as in Figure CFBAS.**

The annual probability of volcanic eruptions within the repository boundary increases when the

modified kernel function is used. Annual probability of volcanic eruptions within the repository boundary were calculated using 5200m $\leq l_{max} \leq$ 10200m, and h = 7 km (Figure prob3). Using the three Quaternary igneous events, Lathrop Wells, Quaternary Crater Flat, and the Sleeping Butte alignment results in annual probabilities of volcanic eruptions within the repository boundary between 3 x 10^{-8} and 5.5 x 10^{-8}, assuming a regional recurrence rate of 3 v/m.y. Including Pliocene volcanoes in the estimation of lr(x,y) decreases the annual probability at the repository because many Pliocene volcanoes are located in the Amargosa Desert. Annual probabilities based on the modified kernel distribution and Plio-Quaternary volcanoes vary between 1.5 and 3 x 10^{-8}, comparable to the annual probabilities estimated using the standard kernel and the distribution of Quaternary vents and vent alignments.

Figure prob3. Annual probability of volcanic eruptions within the repository boundary. Igneous events are defined as vents and vent alignments. A modified Gaussian kernel is used with smoothing parameter, h= 7 km, based on the distribution of three Quaternary igneous events. Analysis of existing vent distribution indicates h $\geq$ 7 km is suitable for volcanic hazard analysis at the repository. Vent alignment half-length, l_{max}, varied between 5200 and 10200 m, roughly changing probability estimates by a factor of two. Probabilities are calculated using lt = 3 x 10^{-6} /yr. Curves are shown calculated using Plio-Quaternary events, N=12, and the modified Gaussian kernel, and Quaternary events, N=3, and the standard Gaussian kernel for comparison.

The regional recurrence rate of vent and vent alignment formation is poorly constrained in the

YMR. Varying regional recurrence rate of of igneous events between 1 and 5 v/m.y. results in nearly one order of magnitude variation in the annual probability of volcanic eruptions within the repository boundary. Using the modified kernel model, h=7 km, and 5200 m $\leq l_{max} \leq$ 10200 m, annual probability of volcanic eruptions within the repository varies between 1 x 10^{-8} and 9 x 10^{-8} (Figure recurrence_rates).

Figure recurrence_rates. **Annual probability of volcanic eruptions within the repository boundary using regional recurrence rates of lt = 1 x 10^{-6} /yr to 5 x 10^{-6} /yr. Igneous events are defined as vents and vent alignments. A modified Gaussian kernel is used with smoothing parameter, h= 7 km, based on the distribution of three Quaternary igneous events.**

4.4.6.4 Igneous Intrusions

The probability of igneous intrusions, such as dike swarms, intersecting the repository is greater than the probability of volcanic eruptions within the repository, because igneous intrusions must have greater areas than evinced by vent alignments and may occur with greater frequency. However, the recurrence rate of igneous intrusions and their geometry are so poorly constrained by available data that these parameters are not estimated and the probability of dike intersection with the repository is not calculated. Based on analogy with the San Rafael volcanic field, probabilities of igneous intrusion into the repository boundary may be 2 to 5 times the probability of volcanic eruptions within the repository boundary, but such an estimate is highly speculative.

4.4.6.5 Summary

Annual probability of volcanic eruptions within the repository boundary vary between 1 x 10^{-8} and 1 x 10^{-7} based on a range of models. This range accounts for varying definitions of igneous events and uncertainty in parameter distributions used to estimate probability. Annual probabilities are generally between 1 x 10^{-8} and 3 x 10^{-8} for igneous events defined as individual mappable units and vents. This definition of igneous events requires the fewest assumptions about underlying parameter distributions but also neglects some features of vent distribution that are important in the YMR. In particular, the formation of vent alignments is not considered in this model explicitly. However, defining igneous events as vents and vent alignments results in a similar range of probability estimates for the annual probability of volcanic eruptions within the repository boundary, 1 x 10^{-8} and 6 x 10^{-8}. Although recurrence rates are lower using this definition of igneous events, the area affected by individual events in greater. The distribution of alignment length and regional recurrence rate of these igneous events introduces the greatest uncertainties into these probability models. Incorporating regional crust density variation into this model results in a model more closely linked to geologic processes. Experimentation with kernel models modified by additional geologic data is new. Based on the crustal density models and similar models presented previously (Hill et al., 1996; Connor et al., 1996), the annual probability of volcanic eruptions within the repository boundary is between 1 x 10^{-8} and 9 x 10^{-8}. Probabilities of intersection of igneous intrusions with the repository are likely higher, but cannot be confidently estimated from available geologic data. Finally, it is noted that this range of probability values, 1 x 10^{-8} to 1 x 10^{-7}, arises from the application of a variety of models and a range of parameter distributions. Nothing in the above analysis suggests that this range of probabilities has central tendency, that the

mean or median of this range of probabilities is significant, or that high or low values in this range are more or less likely. This situation arises because, at least at the current time, it is not feasible to assign likelihood to the accuracy of these models in a meaningful way.

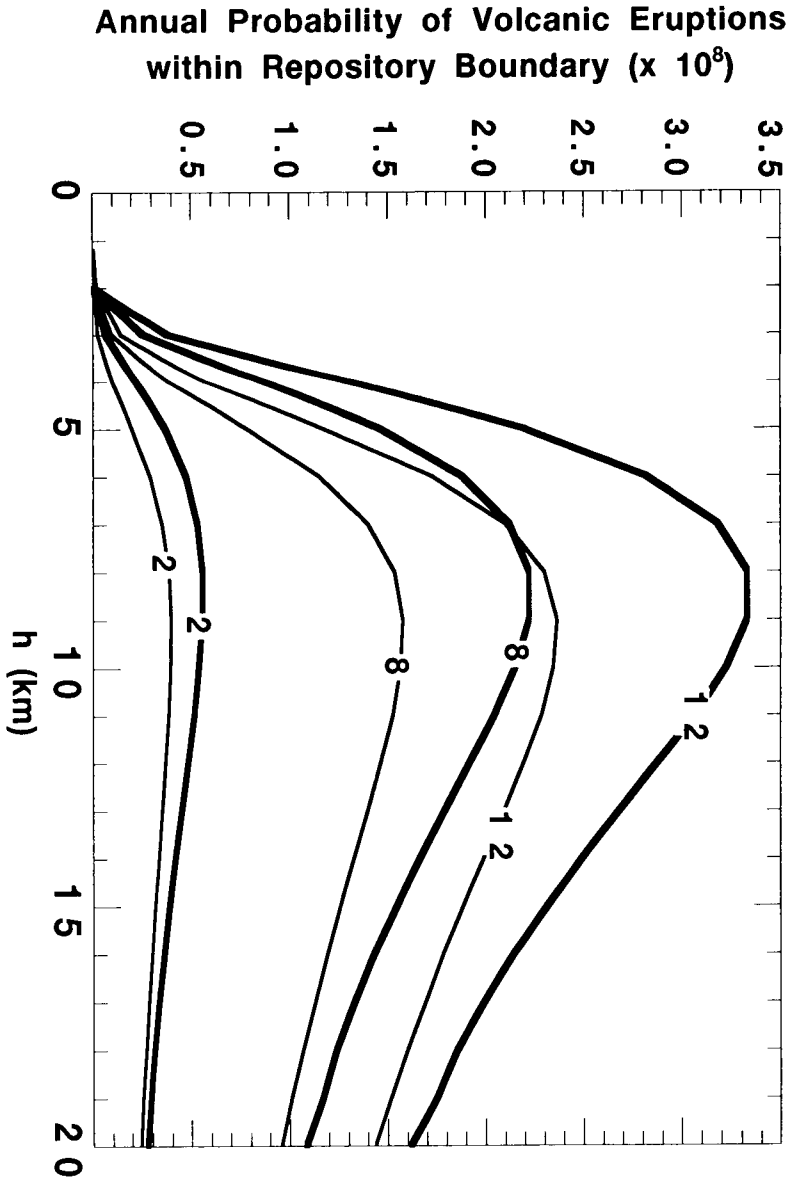
Annual Probability of Volcanic Eruptions
within Repository Boundary (x 10^8)
0.5
1.0
1.5
2.0
2.5
3.0
3.5
0
5
10
15
20
h (km)
2
2
8
8
12
12

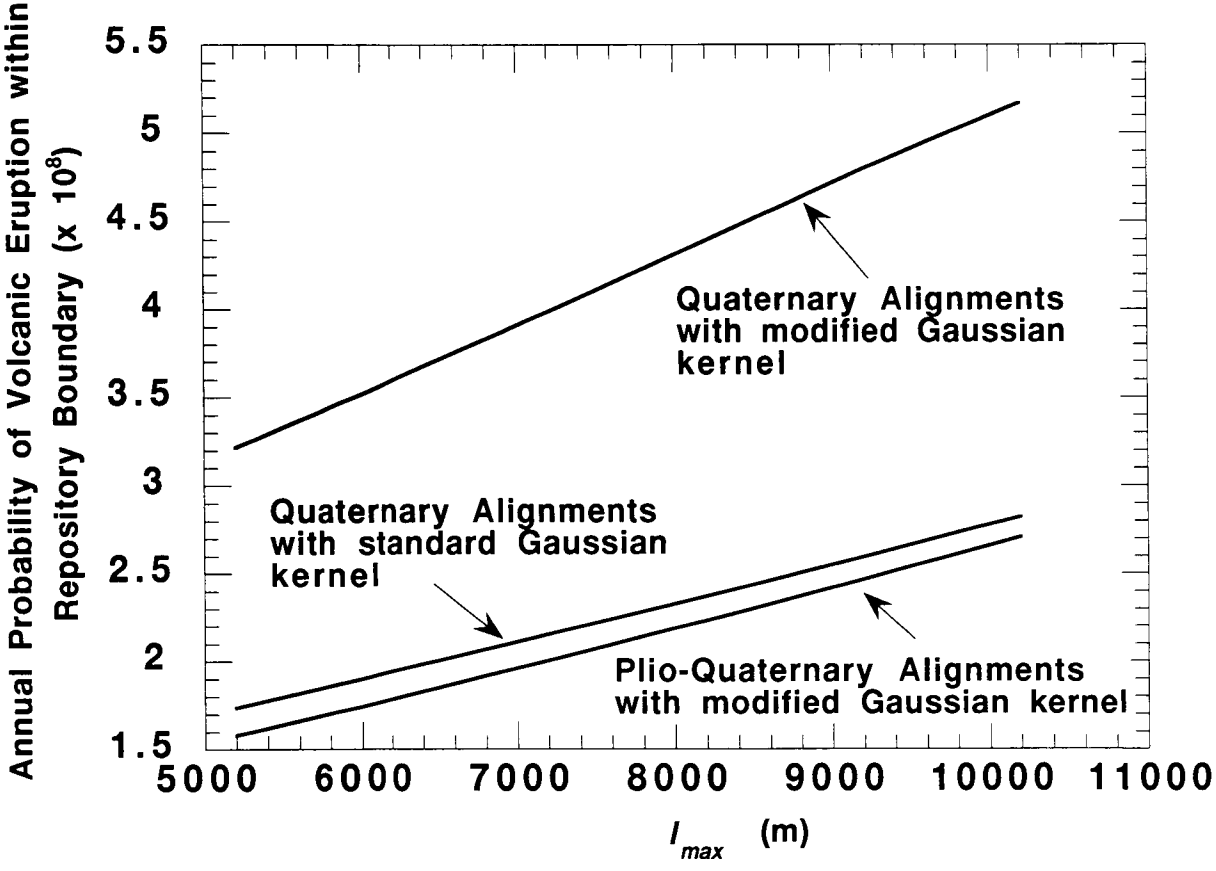
Annual Probability of Volcanic Eruption within Repository Boundary (x 10^8)
5.5
5
4.5
4
3.5
3
2.5
2
1.5
5000
6000
7000
8000
9000
10000
11000
l_max (m)
Quaternary Alignments with modified Gaussian kernel
Quaternary Alignments with standard Gaussian kernel
Plio-Quaternary Alignments with modified Gaussian kernel

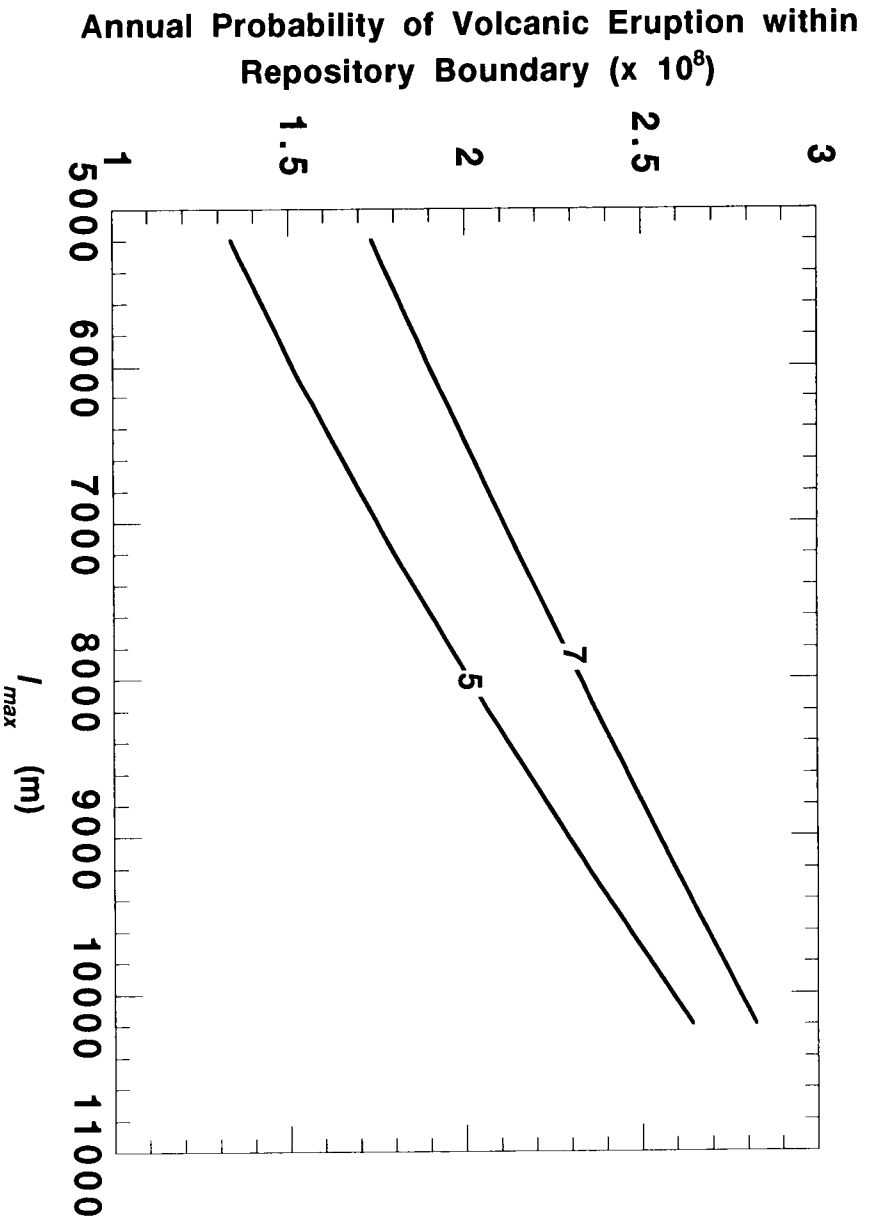
Annual Probability of Volcanic Eruption within Repository Boundary (x 10^8)
1
1.5
2
2.5
3
5000
6000
7000
8000
9000
10000
11000
l_{max} (m)
5
7

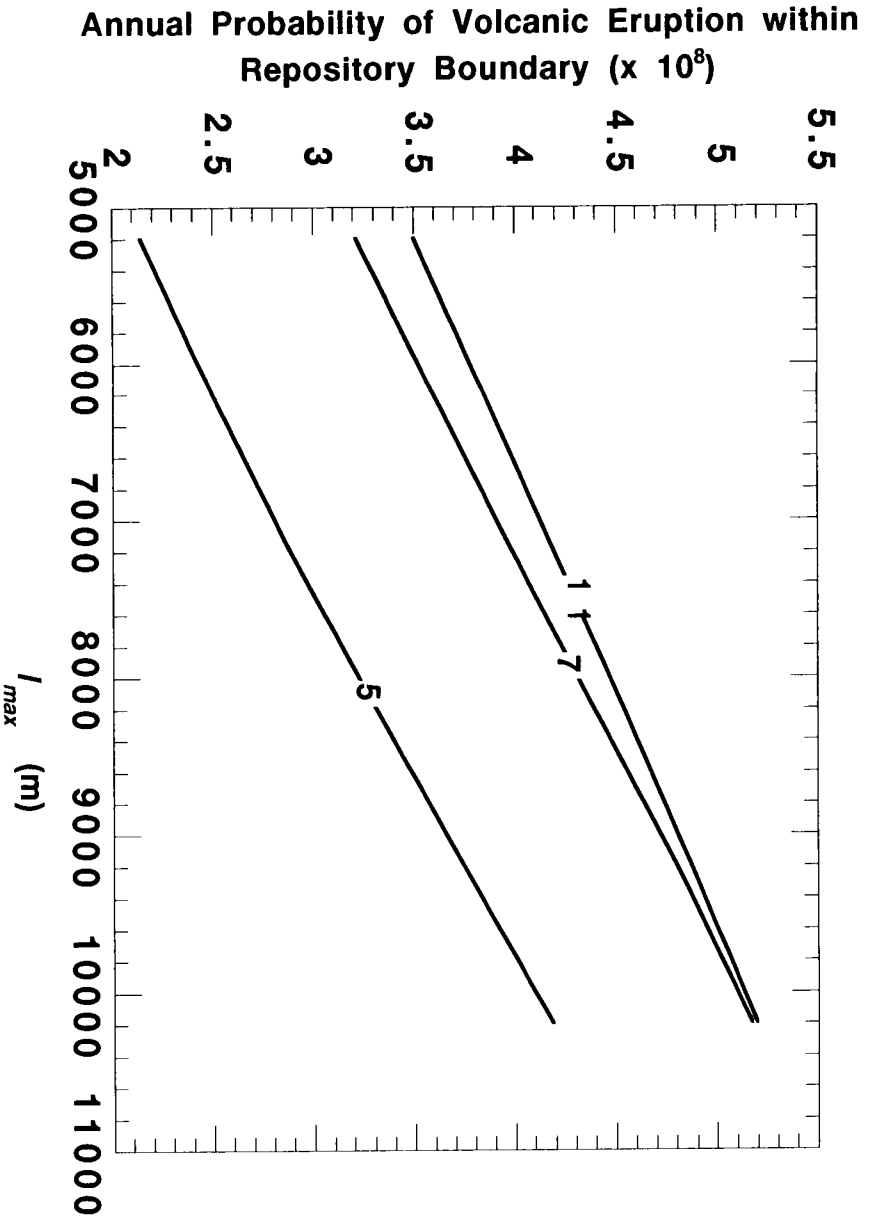
Annual Probability of Volcanic Eruption within Repository Boundary (x 10^{8})
2
2.5
3
3.5
4
4.5
5
5.5
5000
6000
7000
8000
9000
10000
11000
l_{max} (m)
1
7
5

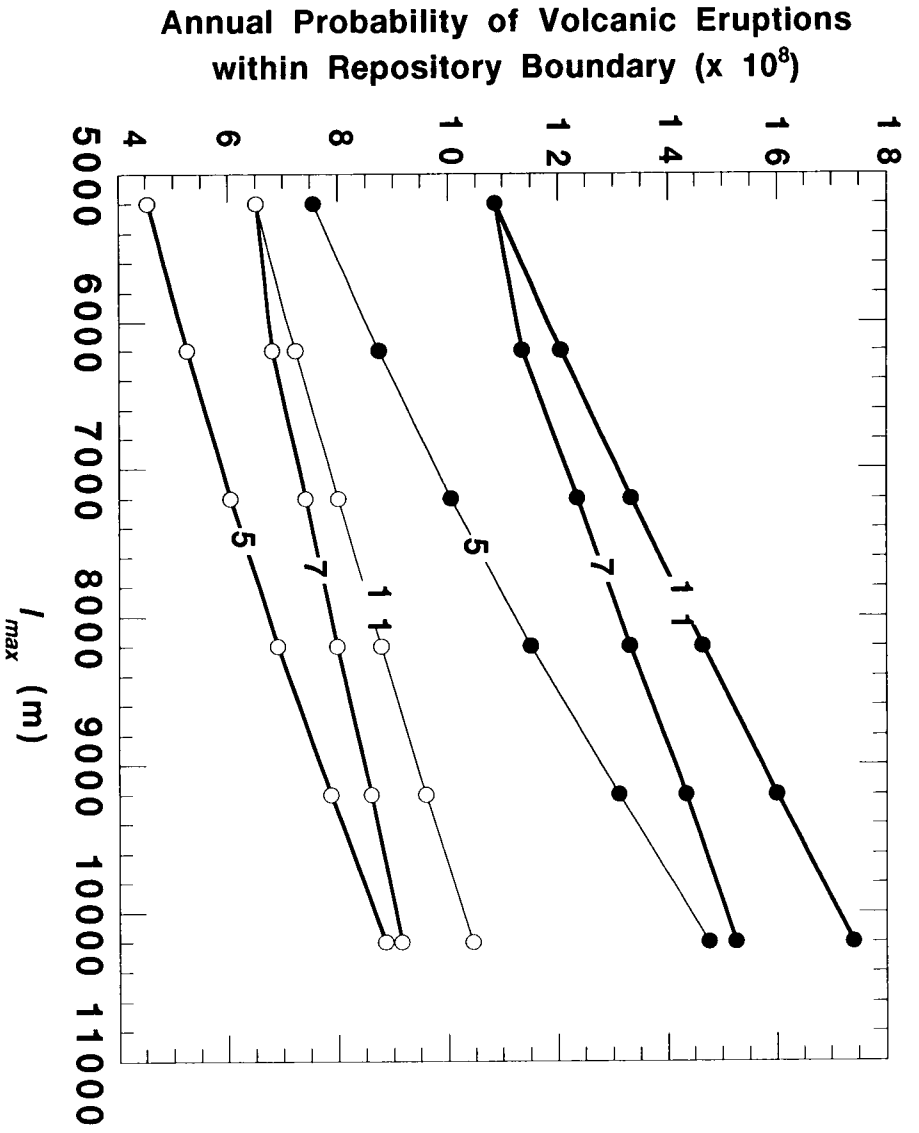
Annual Probability of Volcanic Eruptions
within Repository Boundary (x 10^8)
4
6
8
10
12
14
16
18
5000
6000
7000
8000
9000
10000
11000
l_{max} (m)
5
7
11
5
7
11

(22)

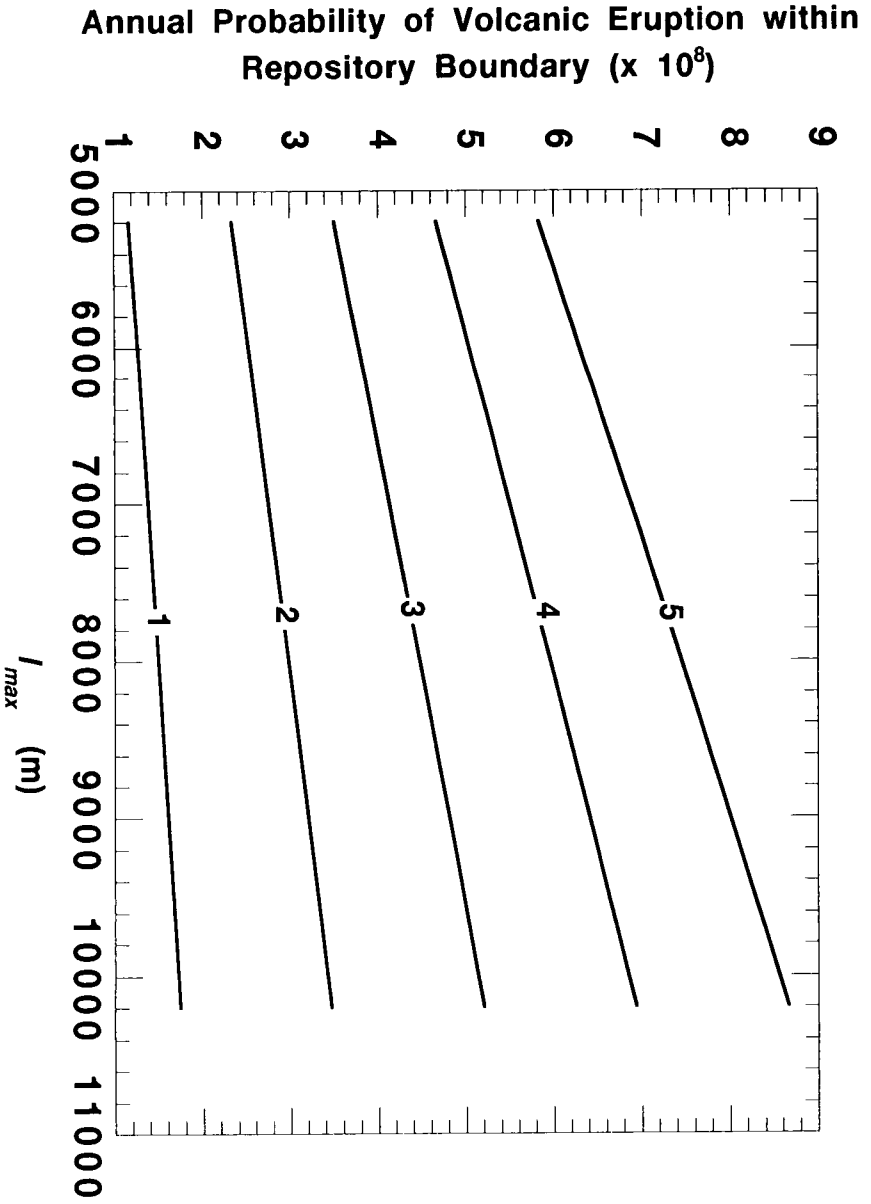
Annual Probability of Volcanic Eruption within Repository Boundary (x 10^8)
1
2
3
4
5
6
7
8
9
5000
6000
7000
8000
9000
10000
11000
l_{max} (m)
1
2
3
4
5

pp

	lmax (km)	h=5 km	h = 7 km	h = 9 km	h = 11 km	5 km 3 v/m	7 km 3 v/m	9 km 3 v/m	11 km 3 v/m
0	5200.0	0.015100	0.021700	0.022400	0.021700	4.5300e-08	6.5100e-08	6.7200e-08	6.5100e-08
1	6200.0	0.017500	0.024100	0.024100	0.022700	5.2500e-08	7.2300e-08	7.2300e-08	6.8100e-08
2	7200.0	0.020100	0.026640	0.026840	0.024677	6.0300e-08	7.9920e-08	8.0520e-08	7.4031e-08
3	8200.0	0.023000	0.029260	0.029120	0.026600	6.9000e-08	8.7780e-08	8.7360e-08	7.9800e-08
4	9200.0	0.026200	0.031980	0.031420	0.028650	7.8600e-08	9.5940e-08	9.4260e-08	8.5950e-08
5	10200	0.029500	0.034800	0.033750	0.030500	8.8500e-08	1.0440e-07	1.0125e-07	9.1500e-08

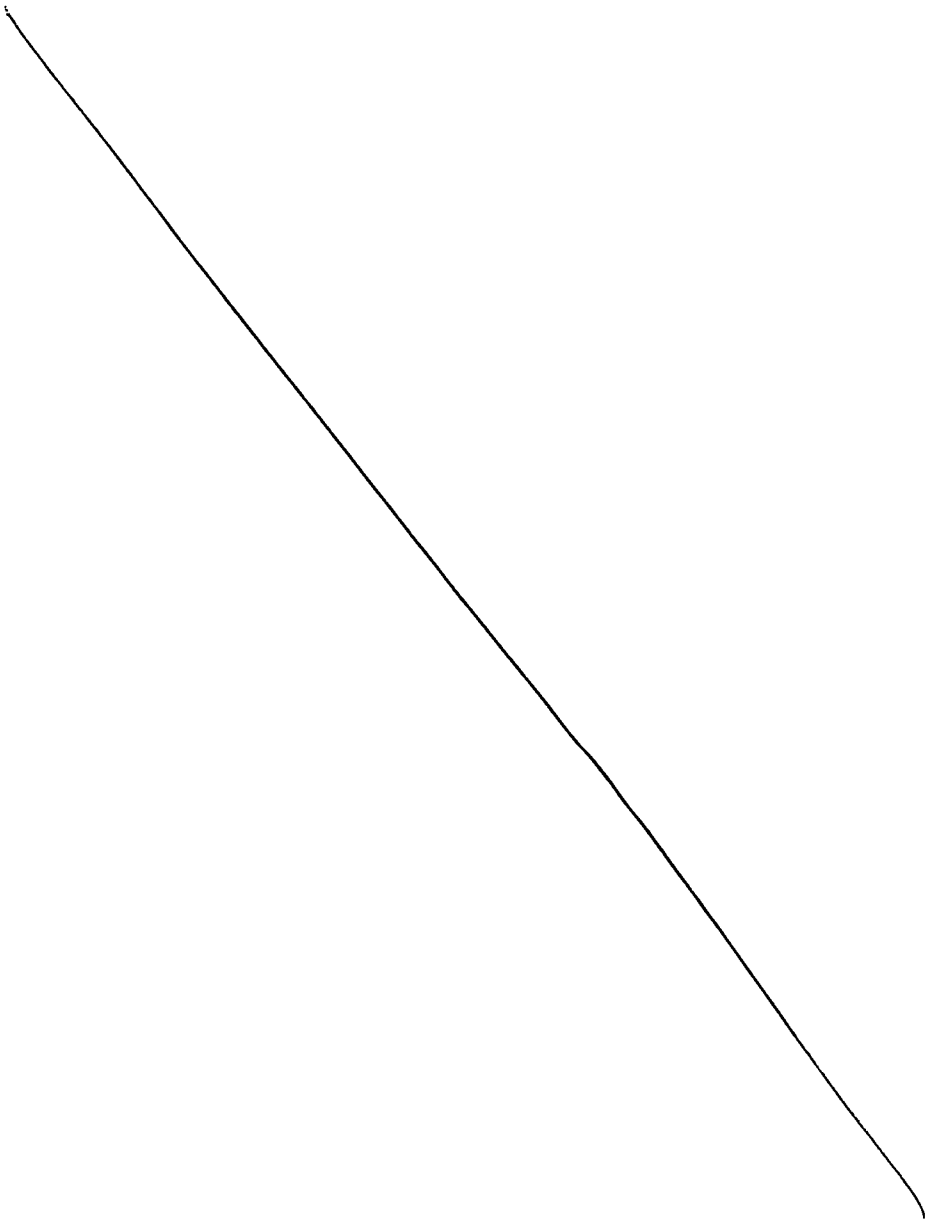

	5 km 5 v/m	7 km 5 v/m	9 km 5 v/m	11 km 5 v/my	N
0	7.5500e-08	1.0850e-07	1.1200e-07	1.0850e-07	
1	8.7500e-08	1.2050e-07	1.2050e-07	1.1350e-07	
2	1.0050e-07	1.3320e-07	1.3420e-07	1.2338e-07	
3	1.1500e-07	1.4630e-07	1.4560e-07	1.3300e-07	
4	1.3100e-07	1.5990e-07	1.5710e-07	1.4325e-07	
5	1.4750e-07	1.7400e-07	1.6875e-07	1.5250e-07	

dC

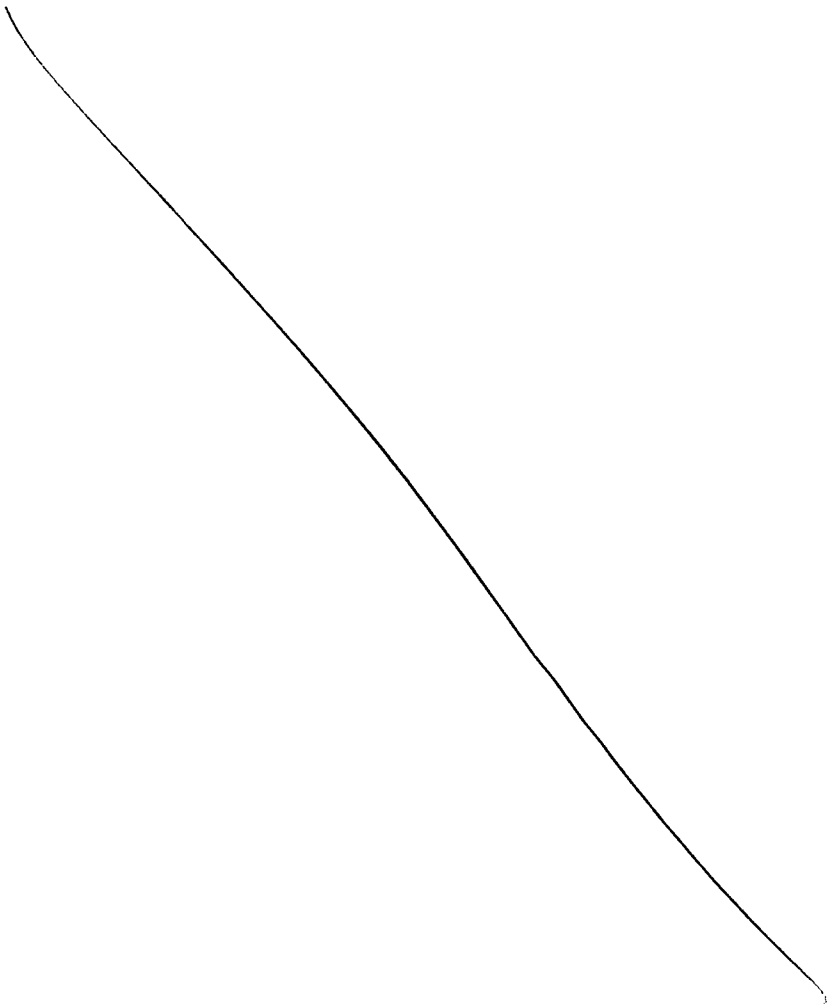

	A	h=11km,Q,litho	h=5,Q,litho	h=7,Q,litho	h=5,Q,notlitho	h=7,Q,no litho	h=5,PQ,litho
0	5200.0	0.011650	0.0071320	0.010710	0.0044480	0.0057811	0.0029600
1	6200.0	0.012810	0.0083100	0.011969	0.0051800	0.0064630	0.0035342
2	7200.0	0.013970	0.0096090	0.013278	0.0059900	0.0071653	0.0041893
3	8200.0	0.015120	0.011020	0.014634	0.0068750	0.0078951	0.0049337
4	9200.0	0.016230	0.012477	0.015991	0.0078160	0.0086422	0.0057330
5	10200	0.017320	0.013956	0.017235	0.0088128	0.0094080	0.0065761

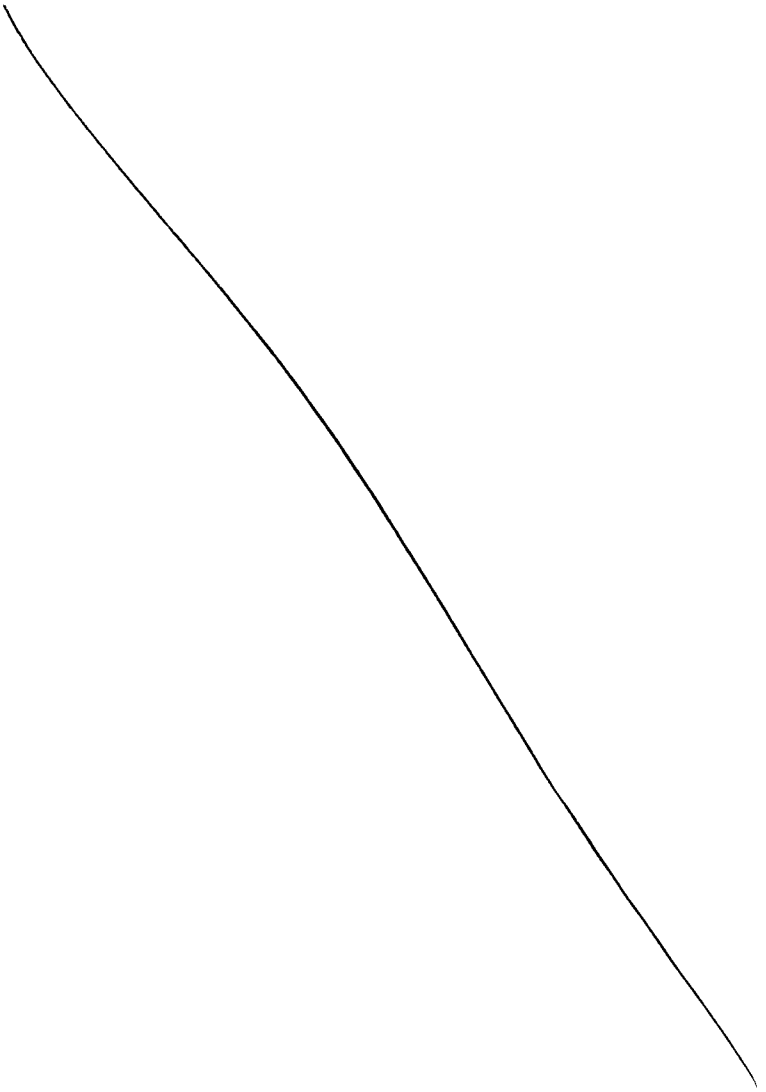

	h=7,PQ,litho
0	0.0052641
1	0.0059437
2	0.0066666
3	0.0074347
4	0.0082202
5	0.0090150

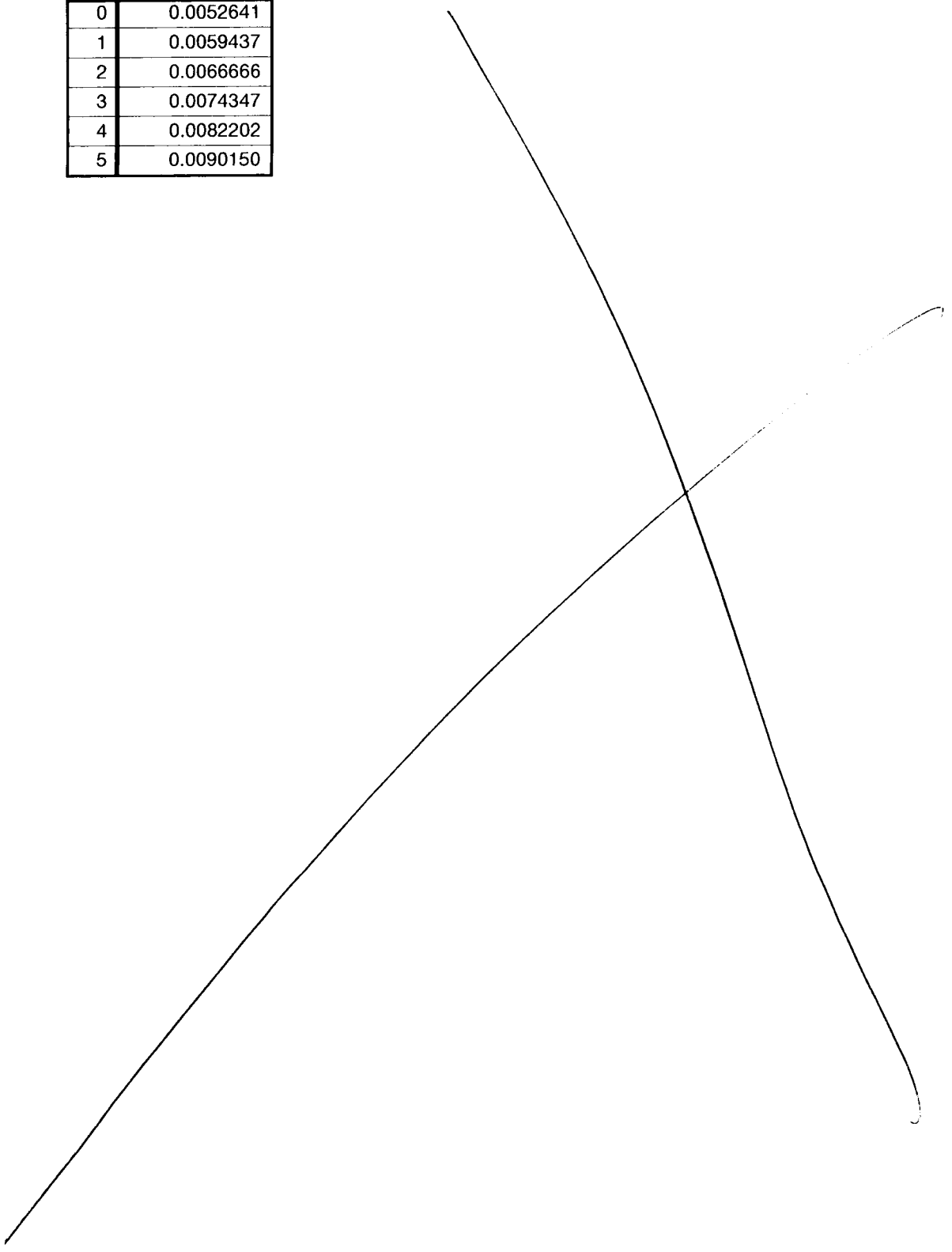

	A	volcanoes/km2	C	D	E	F	G	H
0	1.0000	0.0000	0.0000	0.0000	0.0000	0.0000	0.0000	0.0000
1	2.0000	2.1000e-06	1.1550e-05	1.3860e-10	2.3100e-11	9.2400e-11	0.0000	0.0000
2	3.0000	2.0700e-05	0.00011385	1.3662e-09	2.2770e-10	9.1080e-10	5.7000e-05	0.00031293
3	4.0000	8.5700e-05	0.00047135	5.6562e-09	9.4270e-10	3.7708e-09	0.00019700	0.0010815
4	5.0000	0.00017700	0.00097350	1.1682e-08	1.9470e-09	7.7880e-09	0.00033200	0.0018227
5	6.0000	0.00026100	0.0014355	1.7226e-08	2.8710e-09	1.1484e-08	0.00042700	0.0023442
6	7.0000	0.00031800	0.0017490	2.0988e-08	3.4980e-09	1.3992e-08	0.00048200	0.0026462
7	8.0000	0.00034800	0.0019140	2.2968e-08	3.8280e-09	1.5312e-08	0.00050490	0.0027719
8	9.0000	0.00035800	0.0019690	2.3628e-08	3.9380e-09	1.5752e-08	0.00050500	0.0027724
9	10.000	0.00035500	0.0019525	2.3430e-08	3.9050e-09	1.5620e-08	0.00048900	0.0026846
10	11.000	0.00034600	0.0019030	2.2836e-08	3.8060e-09	1.5224e-08	0.00046500	0.0025529
11	12.000	0.00033200	0.0018260	2.1912e-08	3.6520e-09	1.4608e-08	0.00043600	0.0023936
12	13.000	0.00031700	0.0017435	2.0922e-08	3.4870e-09	1.3948e-08	0.00040700	0.0022344
13	14.000	0.00030100	0.0016555	1.9866e-08	3.3110e-09	1.3244e-08	0.00037800	0.0020752
14	15.000	0.00028500	0.0015675	1.8810e-08	3.1350e-09	1.2540e-08	0.00035100	0.0019270
15	16.000	0.00027000	0.0014850	1.7820e-08	2.9700e-09	1.1880e-08	0.00032500	0.0017843
16	17.000	0.00025600	0.0014080	1.6896e-08	2.8160e-09	1.1264e-08	0.00030200	0.0016580
17	18.000	0.00024200	0.0013310	1.5972e-08	2.6620e-09	1.0648e-08	0.00028100	0.0015427
18	19.000	0.00022900	0.0012595	1.5114e-08	2.5190e-09	1.0076e-08	0.00026500	0.0014549
19	20.000	0.00021700	0.0011935	1.4322e-08	2.3870e-09	9.5480e-09	0.00024500	0.0013451
20	25.000							
21	30.000							
22	35.000							
23	40.000							

	I	J	K
0	0.0000	0.0000	0.0000
1	0.0000	0.0000	0.0000
2	3.7552e-09	2.5034e-09	6.2586e-10
3	1.2978e-08	8.6522e-09	2.1631e-09
4	2.1872e-08	1.4581e-08	3.6454e-09
5	2.8131e-08	1.8754e-08	4.6885e-09
6	3.1754e-08	2.1169e-08	5.2924e-09
7	3.3263e-08	2.2175e-08	5.5438e-09
8	3.3269e-08	2.2180e-08	5.5449e-09
9	3.2215e-08	2.1477e-08	5.3692e-09
10	3.0634e-08	2.0423e-08	5.1057e-09
11	2.8724e-08	1.9149e-08	4.7873e-09
12	2.6813e-08	1.7875e-08	4.4689e-09
13	2.4903e-08	1.6602e-08	4.1504e-09
14	2.3124e-08	1.5416e-08	3.8540e-09
15	2.1411e-08	1.4274e-08	3.5685e-09
16	1.9896e-08	1.3264e-08	3.3160e-09
17	1.8512e-08	1.2342e-08	3.0854e-09
18	1.7458e-08	1.1639e-08	2.9097e-09
19	1.6141e-08	1.0760e-08	2.6901e-09
20			
21			
22			
23			

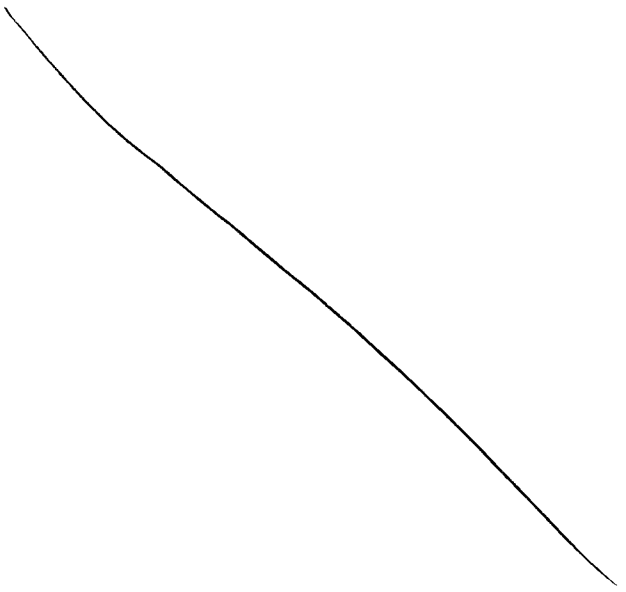

CC

Scientific Notebook
Project 20-1402-461

Chuck Connor
April 1998

Technical Comment: Anomalous Strain Accumulation in the Yucca Mountain Area, Nevada

Wernicke et al. (1) use GPS measurements to document crustal strain rates across Yucca Mountain (YM) that greatly exceed those inferred from the geologic record. These geodetic results raise several important issues concerning how regional strain patterns govern the time scales of volcanic, seismic, faulting, and hydrogeologic processes. Given the implications for YM, which is under consideration as a possible site for the disposal of high-level radioactive waste, the ramifications of the GPS results with respect to geologic hazards need clarification. In particular, several alternatives to the suggestion by *Wernicke et al.* that anomalous GPS strain rates indicate volcanic and seismic hazards at the site were previously underestimated by one order of magnitude warrant consideration.

First, the implications for volcanic hazards cannot be simply interpolated from GPS strain data. Rather, we see three alternative interpretations consistent with high GPS strain rates: (a) the current strain rates observed by *Wernicke et al.*, although high for the Basin and Range, are not anomalous compared to average Quaternary strain rates for the YM region, (b) the last 100-150 ka has been a period of anomalously high strain but this has not resulted in a one order of magnitude increase in recurrence rate of volcanism, or (c) Lathrop Wells volcano formed during a brief episode of anomalous strain which is not manifested by concurrent fault displacements. In the latter interpretation, episodically high regional recurrence rates of volcanism are permissible, but Lathrop Wells volcano loses its significance as a potential precursor to the formation of a new vent cluster.

Of the more than 100 radiometric age determinations of Lathrop Wells basalts, the most recent high precision $^{40}Ar/^{39}Ar$ dates indicate an age of 80 ka *(2)*. Compilations of $^{40}Ar/^{39}Ar$ and K/Ar dates give an age of 131-141 ka *(3)*. These data do not support the 10 ka age cited by *Wernicke et al.*

Available faulting data (Figure 1) are inconsistent with the notion that Lathrop Wells volcano is part of a current episode of anomalously high strain. Although of low resolution, these data provide a record of deformation that extends prior to the eruption of Lathrop Wells volcano. They do not delineate the onset of a continuing episode of anomalous high strain rate since 150 ka. Rather, they suggest a paucity of large fault displacements (>60 cm) since 50 ka.

Current estimates of recurrence rates of volcano or vent alignment formation in the YM region are 2-5 $\times$ 10^{-6}/yr (*5*). If these rates have been underestimated by one order of magnitude (*1*), the regional recurrence rate during this episode of anomalous strain would be 2-5 $\times$ 10^{-5}/yr. Using 3 x 10^{-5}/yr, the probability that a new volcano would not have formed during the last 80 ka is about 10%, and during the last 130 ka is about 2%. Because a new volcano has not formed, these low probabilities diminish the argument that volcanic recurrence rates since the formation of Lathrop Wells have been underestimated by one order of magnitude.

Therefore, interpretations (a) and (b) are consistent with current volcanic hazard estimates (*5*) that incorporate clustering and structural controls (*6*). We estimated the probability of volcanic eruptions through the proposed repository, given that a new volcano forms in the region, to be approximately 2 $\times$ 10^{-2} or less, using a range of parameters in Epanechnikov and Gaussian kernel models constrained by fault controls on volcano distribution *(5)*. These values are up to two orders of magnitude greater than average rates of volcanism in the Western Great Basin, mainly because of the recent and clustered basaltic volcanism around YM. This probability model predicts higher rates of volcanic activity between Lathrop Wells volcano and the proposed repository, and throughout southern Crater Flat, than elsewhere in the region precisely because it accounts for tectonic controls on

volcanism (Figure 2). Using regional recurrence rates of volcanic events of 2-5 $\times 10^{-6}$/yr and probability density functions for alignment length yields probabilities of volcanic disruption of the proposed repository between 10^{-8}/yr and 10^{-7}/yr. Increasing recurrence rate by one order of magnitude (interpretation c) gives an upper bound on volcanic eruptions at the site of 10^{-6}/yr, or 10^{-2} in a 10^{4}/yr performance period. These high recurrence rates imply a deterministic understanding of the link between rates of extension and rates of volcanism. *Wernicke et al.* offer an intriguing possibility that such a link might be found in monitorable strain, but the equally critical resolution of episodic events in the geologic record and the processes that drive them currently does not exist.

Second, higher strain rates do not require a 10 $\times$ increase in the number or size of earthquakes. Moreover, the dichotomy between the higher strain rates derived from GPS measurements and lower rates derived from paleoseismic results (in this case mainly derived from trenching studies) is not unexpected. Strain rates derived from each of these two techniques essentially represent end-member values. Trenching studies capture only that portion of crustal extension evident from known, large faults. An additional component of extension likely remains undetected on hidden faults, populations of small faults, or aseismic features such as extension fractures. Several recent studies show that longer term (i.e., 10^{6} yr), geologically derived slip rates exceed those predicted from trenching results *(7)*. In contrast, strain rates derived from GPS data can be expected to include an elastic part that is stored in rock as elastic strain energy and an inelastic part partitioned among several processes such as fracture dilation and slow aseismic slip on pre-existing faults and fractures.

Because extension may be accommodated by small faults and fractures, the most profound impact of the GPS results may be on local and regional groundwater flow in both the saturated and

unsaturated zones. For example, a component of extension could be accounted for by dilation of existing fractures. A set of vertical fractures or joints spaced 2 m apart, each dilating 0.5 mm in the next 10 k.y. could account for half of the extensional strain predicted by the GPS results. Such dilation would likely alter the groundwater flow regime, including flow already noted along fast pathways into the repository (*8*). As is the case for volcanism, however, a mechanistic relationship between strain and flow properties currently does not exist.

In conclusion, a one order of magnitude change in hazard rates does not necessarily follow the observations of *Wernicke et al.* These data, however, provide an important new perspective on the neotectonics of the YM site. The 1982 Nuclear Waste Policy Act calls for a strategy of defense-in-depth represented by a mandate for multiple barriers against release of radioactive materials into the accessible environment. In the defense-in-depth approach three separate systems - the stability of the waste form, the engineered barrier system, and the geologic system - are each called upon to contribute to waste isolation and mitigation of risks to the public health and safety for 10^4 to 10^5 years. We see the most important contribution of *Wernicke et al.* is the new insights they provide on the possible time scales across which tectonic processes operate. The challenge is to evaluate how these processes affect hazards to each of the multiple barriers at YM and risk to public health and safety.

C. B. Connor, J. A. Stamatakos, D. A. Ferrill, and B.E. Hill

Center for Nuclear Waste Regulatory Analyses

Southwest Research Institute

6220 Culebra Rd.

San Antonio, Texas 78238

1. B. Wernicke, J. L. Davis, R. A. Bennett, P. Elósegui. M.J. Abolins, R.J. Brady, M.A. House, N.A. Niemi, and J.K. Snow, *Science* **279**, 2096 (1998).

2. M.T. Heizler, T.I. Wilch, and J. Stroud, *EOS Transactions of the American Geophysical Union.* **78(46)**, p. F771 (1997).

3. D.B. Turrin, D Champion and R.J. Fleck, *Science* **253** (1991). D.B. Turrin, D.E. Champion, R.J. Fleck, G.H. Curtis, R.E. Drake, *K-Ar Ages and Paleomagnetic Directions from the Lathrop Wells Volcanic Center, Southwestern Nevada: An Evaluation of Polycyclic Volcanism*, U.S. Geological Survey Open-File Report 98-44 (1998).

4. I.G. Wong, J.C. Stepp. *Probabilistic Seismic Hazard Analyses for Fault Displacement and Vibratory Ground Motion at Yucca Mountain, Nevada, Final Report, Volume 2, Appendices,* Milestone SP32IM3, WBS Number 1.2.3.2.8.2.6 (1998). U.S. Geological Survey, *Seismotectonic Framework and Characterization of Faulting at Yucca Mountain, Nevada*, Edited by John W. Whitney (1996). L. Anderson, oral communication (1997). For earthquake events that overlap in time in two or more parallel trenches across the same fault the displacements were averaged.

5. C.B. Connor, B.E. Hill, *Journal of Geophysical Research* **100,** 10,107-10,125 (1995). U.S. Nuclear Regulatory Commission, *Issue Resolution Status Report: Igneous Activity* (1998). B.E. Hill, C.B. Connor, J.S. Trapp, *NRC High-Level Radioactive Waste Program Annual Progress Report: Fiscal Year 1996*, NUREG/CR-6513, pp. 2.1-2.32 (1997).

6. Past volcanism near YM has clustered in time and space and this clustering has a profound impact on estimates of probability of volcanic eruptions at YM *(5).* In addition, vent alignments are common features of volcanic activity near YM and there is ample evidence from this volcanic field and others that vent alignments, especially where correlated with faults, can reactivate after long periods of time. For example, the Quaternary Crater Flat alignment (Figure 2) includes magnetic anomalies interpreted to be produced by basalts with normal and reversed remanent magnetizations buried by up to 150 m of alluvium. C.B. Connor, S. Lane-Magsino, J. A. Stamatakos, R. H. Martin, P. C. LaFemina, B. H. Hill, and S. Lieber. *EOS, Transactions of the American Geophysical Union.* **78**: pp. 73, 77-78 (1997). E.I. Smith, T.R. Feuerbach, and J.E. Faulds, *Proceedings of the International Topical Meeting on High-Level Radioactive Waste Management, vol. 1* (American Nuclear Society/American Society of Civil Engineers, Las Vegas, pp. 18-90 (1991). C.B. Connor, J. A. Stamatakos, D.A. Ferrill, B.E. Hill, S.B.L. Magsino, P. LaFemina, and R.H. Martin, *EOS Transactions of the American Geophysical Union.* **77(46)**, p. F20 (1996). F.M. Conway, D.A. Ferrill, C.M. Hall, A.P. Morris, J.A. Stamatakos, C.B. Connor, A.N. Halliday, C.D. Condit, *Journal*

of Geophysical Research **102**, 815 (1997).

7. D.A. Ferrill. J.A. Stamatakos, S.M. Jones, B. Rahe, H.L. McKague, R.H. Martin, and A.P. Morris, *Geology* **24**, 559 (1996). J.A. Stamatakos, C.B. Connor, R.H. Martin, *Journal of Geology* **105**, 319 (1997).

8. J.T. Fabryka-Martin, A.L. Flint, D.S. Sweetkind, A.V. Wolfsberg, S.S. Levy, G.J.C. Roemer, J.L. Roach, L.E. Wolfsberg, and M.C. Duff, *Evaluation of Flow and Transport Models of Yucca Mountain Based on Chlorine-36 Studies For FY97*, Los Alamos National Laboratory, LA-CST-TIP-97-010.

Figure 1. Fault displacements plotted as a function of age with their associated uncertainties for the trenching results from the YM region *(4)*. Faults are BM - Bare Mountain, BR - Bow Ridge, FW - Fatigue Wash, PC - Paintbrush Canyon, SC - Solitario Canyon, SCR - Stage Coach Road, and WW - Windy Wash. Cumulative displacement of all faults (black circles) derived from the faulting data shown.

Figure 2. Current probability models based on the distribution and timing of past volcanic events reflect patterns in tectonics of the site. Here, the probability distribution for locations (centers) of volcanic eruptions or developing volcano alignments is contoured as expected events $\times 10^4/km^2$, given a volcanic event in the region. This map is based on the distribution of Quaternary volcanoes (black) and long

wavelength gravity variation, which in turn reflects basin development and extension (*8,12*). Even though based on few Quaternary volcanic events, the basic features of probability maps like this one are consistent across a wide range of model assumptions, account well for the distributions of Pliocene(?) volcanoes and vent alignments (gray), and reinforce the notion that tectonic features strongly influence patterns of volcanic activity. Miocene basalt outcrops are outlined; proposed repository is shown in green. Map projection is UTM, NAD 83 and coordinates are in meters.

9 of 17

SCIENTIFIC NOTEBOOK 115E

BY

Charles B. Connor

SCIENTIFIC NOTEBOOK 115E

BY

Charles B. Connor

Southwest Research Institute
Center for Nuclear Waste Regulatory Analyses
San Antonio, Texas

SCIENTIFIC NOTEBOOK

CHUCK CONNOR

PROJECT

IGNEOUS ACTIVITY

PROJECT NUMBER 20-1402-461

July, 1998 - Nov,1998

PARTS IN THIS NOTEBOOK:

Scientific Notebook
20-1402-461

August. 1998
Chuck Connor CC

Summary of CNWRA workshop on the consequences of volcanic activity

August 5, 1998

Summary

Probabilities of volcanic disruption of the site (10^{-7} /yr) are significant enough to require estimation of the consequences of volcanism for repository performance (NRC, 1998). A workshop on the consequences of volcanic activity for repository performance was held at the CNWRA July 27-July 31 with a limited number of attendees from NRC and CNWRA. The goal of this workshop was to improve consequence models of volcanic disruption of the proposed repository for use in risk analysis. Specific goals were:

- Review current CNWRA approaches to evaluating the consequences of volcanism
- Identify areas that have received sufficient investigation and those areas that require additional investigation
- Where necessary, develop strategies for evaluating the consequences of volcanism

The workshop included CNWRA staff, NRC Staff and three consultants that are recognized experts in the areas of analytical and numerical modeling of mechanics of volcanic eruptions, volcanic eruption dynamics, and health effects of volcanic eruptions. Summaries of consequence models of volcanic disruption of the repository were prepared by the three consultants (attached). Sparks and Woods prepared a report on the physical aspects of volcanic disruption of the repository. Baxter prepared a report on human exposure to the contaminated tephra deposit resulting from an eruption through the repository. Major conclusions from the workshop were:

The styles of basaltic volcanic eruptions currently used in CNWRA performance

assessment (PA) models are reasonable based on the geochemistry and physical volcanology of past eruptions. Experiments can be performed to augment and verify the physical properties of Yucca Mountain region magmas if this subissue is considered to be controversial.

Mechanics of the interaction between the repository and an intruding magmatic dike are not currently understood in sufficient detail. Current PA models may significantly underestimate the extent of repository disruption and the number of canisters affected by a single igneous event. Therefore, magma-repository interaction should be investigated using physical analog experiments, analytical calculations, and numerical models. These investigations should provide relevant information about the phenomenology of volcanic eruptions through the repository block, the number of canisters affected by volcanic eruptions, and the transient and long-term conditions waste canisters would be subjected to during and subsequent to volcanic eruptions.

Models of eruption dynamics and tephra dispersion currently in use at the CNWRA provide a valid approach to characterize the main features of ash and waste dispersion by strombolian and violent strombolian volcanic eruptions.

A study into the ways waste could be incorporated into basaltic magma during potential eruptions is necessary because this process may have a profound effect on the subsequent distribution of waste in the tephra deposit. The current CNWRA model of waste incorporation into the basaltic magma is physically unrealistic. In addition, alternative models for the dispersion of fine particles (< 50μm) should be investigated.

PA models of dose to a critical group resulting from a contaminated tephra blanket can benefit significantly from recent experience measuring air particulate concentrations following the 1980 eruption of Mount St. Helens and the 1995-present eruption of

Soufriere Hills, Montserrat. Additional experiments are required to measure particulate concentrations on basaltic tephra deposits, such as the tephra deposits from the 1995 eruption of Cerro Negro, Nicaragua. Particular attention should be paid to the differences between mass loading and particle counts because these differences may substantially affect calculated dose.

Workshop participants concluded that current approaches to assessing the consequences of volcanic activity may result in significant underestimation of risk. The number of waste packages affected by volcanism could be one to two orders of magnitude greater than assumed in current models, potentially resulting in larger releases (by direct transport to the surface and into hydrologic environment) than previously realized. More accurate assumptions about the distribution of waste in the ascending magma may increase waste concentration in the tephra deposit at the critical group location. Mass loading and exposure to contaminated waste resuspended from the tephra blanket may be greatly underestimated in current risk models. Nevertheless, risk estimates can be improved substantially through investigations designed to address the thermo-fluid-dynamics of magmas in the repository, the effects of these magmatic conditions on canisters, and resuspension of ash during realistic human activities. Workplans for FY99 and FY00, will be developed by the meeting participants during the next several weeks to address these major areas of concern.

The following report was prepared for 20-1402-461 by Andrew Woods and Steve Sparks as a follow up to this meeting and was submitted on October 12.

Report on Scoping Calculations for magma-repository interaction at Yucca Mountain, Nevada

Andrew W Woods and Stephen Sparks
Centre for Environmental and Geophysical Flows,
University of Bristol, Bristol, BS8 1TW

October 12 , 1998

1. Introduction

This report follows from the earlier report prepared by Sparks and Woods during the visit to the SWRI July-August 1998. In this report we expand on the discussion about the interaction between magma ascending along a volcanic dike into a nuclear repository. In particular, we describe a series of simple calculations aimed at quantifying the activity which might result when a dike intersects the repository tunnels, thereby allowing magma to decompress rapidly. The report includes calculations of both water poor basaltic magma, assumed to incompressible, as one end-member model and water-rich basaltic magma ($\sim 2-3wt\%$) as the other end member model. As outlined in the earlier report, water-rich magma is more likely in volcanic activity at Yucca Mountain, but we include both sets of calculations for completeness. The calculations are rather simplified, but are aimed at providing leading order estimates of the flow conditions. A full numerical simulation, based on the full 3 dimensional time dependent equations would require a much more detailed and lengthy study, and we include a proposal for this below.

The report first compares the geometry of a dike and of the proposed tunnels, in order to establish the relative ease with which the path of the basaltic magma may change on intersecting the tunnel. We then consider the flow conditions associated with a low volatile content magma, illustrating that, for typical magma properties, there may be considerable acceleration of the flow once the dike intersects the tunnel. We then describe some calculations associated with the more complex behaviour of a volatile rich magma. In both cases we examine the potential for the flow to displace the cannisters along the tunnel.

2. Geometry of Tunnels and Dike

We assume that during the final stages before eruption, basaltic magma ascends in a linear dike of fixed width w, of order 1-2m. The magma is assumed to originate in an underlying sill, or horizontal lens, located at a depth $H \sim 5-10$ km below the surface with an overpressure relative to lithostatic pressure at that depth Δp, of magnitude $10^6 - 10^7$Pa (Touloukian et al, 1981; Bower and Woods, 1997). This overpressure is necessary to drive the tip of the dike upwards, and maintain the 1-2m wide flow path for the following magma, as well as in order to overcome the viscous resistance of the magma ascending behind the dike tip. Under typical conditions, field evidence and modelling studies indicate overpressures near the dike tip of order $10^6 - 10^7$ Pa and magma ascent speeds of order 1 m/s (Pollard, 1973; Lister, 1991).

The proposed repository tunnels are located a distance $D \sim 22$m apart, and have individual diameters of 5m. If the dike intersects a series of tunnels, at an angle θ to the axis of the tunnels (figure 1a), then, with a large number of tunnels, magma may be

diverted from a section $D/\sin\theta$ of the dike into each tunnel. This would correspond to a change in the cross-sectional area of the flow path associated with the magma in each tunnel from

$$wD/\sin\theta \sim 22/\sin\theta \tag{1}$$

in the dike to an area 19.6 m^2 in the tunnel. For angles in excess of about 45^o, the cross-sectional area of the flow path would only change by a factor 0.33 - 1.0 if the magma began to flow from the dike and into the tunnel (figure 2). It is therefore likely that the flow will be diverted into the tunnel since the reduction in cross-sectional area, and hence flow resistance, is small. Furthermore, no overpressure is required to keep the tunnel open, in contrast to the dike tip where an overpressure of order $10^6 - 10^7$ Pa is required to continue opening the crust (Lister, 1991; Pollard, 1973).

The proposed tunnels are located about 300m below the surface, where the lithostatic pressure due to the overlying rock is about 7 Mpa. Therefore, the pressure at the dike tip just prior to breaking through into the tunnel will be given by the sum of the background pressure and the overpressure necessary to drive the dike upwards. However, the pressure in the tunnels themselves will be close to atmospheric. Once the dike breaks through into the tunnel, there will be a sudden decrease in pressure at the flow front, and this is expected to lead to significant acceleration of the flow. We now present some simple calculations aimed at providing leading order estimates of the flow along the tunnels. We initially assume there is no backfill in the tunnels, but later in the report we assess the potential for backfill to arrest the flow.

3. Low Volatile Content Magma

First we consider the motion of basaltic magma containing no volatiles. In this case, the sudden decompression of the magma as it enters the tunnel does not lead to any significant exsolution of volatiles and the magma remains essentially incompressible. Following intersection of magma with the tunnel, the motion becomes controlled by the balance between the applied pressure driving the flow up the dike and the frictional resistance to motion either in the dike or in the tunnel. No overpressure is required at the flow front to drive magma along the tunnel.

We now develop a much simplified model which captures the key physical balances and provides a good order of magnitude estimate for the flow. The detailed geometry of the flow in the dike as it is diverted towards the tunnel entrances from the deep uniform upflow is complex and requires numerical solution.

3.1 Mass Conservation. If the flow is incompressible, then mass conservation requires that the net flux in the dike equals that in the tunnels. Figure 1b shows our assumptions con-

cerning the geometry of flow from the deep source through the dike and into the repository tunnels. We assume that flow is diverted into the tunnels as it rises up the dike from the uniform supply at the sill. We assume that the magma flows along a sector of a circle from the sill, where the flow width is $22/\sin\theta$, to the tunnel, where the flow width is 5m and θ is the angle of the dike to the axis of the tunnels as shown in figure 1a. The magma between adjacent flow sectors is assumed to be at rest (figure 1). From the geometry of figure 1b, it is seen that the angle of this circular sector is approximately

$$\phi \sim (D/\sin\theta - d)/(H - h) \tag{2}$$

where $d = 5m$ is the tunnel width, h is the depth of the tunnel below the surface, $h \sim 300$m, and H is the depth of the sill, $\sim 5 - 10$km. For these typical values, ϕ is small, ≤ 0.01. We deduce that the flow is approximately uniform and upward in the dike (figure 1b). Note that the model flow geometry allows for magma to be supplied from the entire length of the sill (figure 1b).

For a flow rate $Q(t)$ along each tunnel, there is an equal flux along that part of the dike feeding the tunnel. At depth z below the tunnel, the extent of the current across the dike which supplies a single tunnel is approximately $l(z) = D/\sin\theta - z\phi$ so that $5 \leq l \leq 22$ (figure 1b). The flow speed is thus

$$u = Q/(wl) \tag{3}$$

where w is the width of the dike, $\sim 1 - 2m$. In the tunnel, the flow speed depends on whether the flow occupies the entire cross-sectional area or spreads along the base of the tunnel. If the area of the tunnel occupied by the flow is A, then the speed is

$$u = Q/A \tag{4}$$

3.2 Momentum Conservation. We may now write down the equation of motion, balancing the inertia, the frictional resistance and the overpressure driving the flow. We have averaged the equations across the area of the dike supplying magma to a single tunnel, and work in terms of the volume flow rate Q along this area. In the dike the rate of change of the flow with time and space ($\frac{Du}{Dt} = \frac{\partial u}{\partial t} + u\frac{\partial u}{\partial z}$), is given by

$$\frac{\rho}{lw}\frac{dQ}{dt} + \frac{\rho\phi Q^2}{l^3w^2} = -\frac{\partial p}{\partial z} - \rho g - \frac{\rho F Q^2}{w^3 l^2} - \frac{12\mu Q}{w^3 l} \tag{5}$$

The terms on the right hand side correspond to the vertical pressure gradient (note z is measured downwards), the gravitational force, and the last two terms represent the

frictional resistance exerted by the walls of the dike. This has been written as the sum of the turbulent drag, where F depends on the roughness length of the dike, but has a value typically of about 0.01, and the viscous drag (cf. Wilson et al, 1980; Stasuik et al., 1993). In the calculations, the Reynolds number of the flow

$$Re = \frac{\rho F Q}{12\mu} \tag{6}$$

determines whether the viscous or turbulent drag dominates. Both terms are included in all our calculations in order to span the range of flows from fast turbulent flow to slow viscous flow (cf. Wilson et al., 1980). Note that for $\phi \leq 0.01$, the gradual acceleration of the flow up the conduit as it becomes focussed towards the tunnel entrances, which is represented by the second term on the left hand side of (5), is negligible compared to the turbulent resistance, and hence the total resistance to the flow. We therefore neglect this effect in the following analysis. This also in part justifies the simple model for the focussing of the flow along the dike.

In the tunnel, the flow satisifies the analogous balance between acceleration, driving pressure gradient and resistance (cf. 5)

$$\rho \frac{dQ}{dt}\frac{1}{A} = -\frac{\partial p}{\partial x} - \rho F_t \frac{Q^2}{A^{5/2}} - \frac{8\pi\mu Q}{A^2} \tag{7}$$

where x is the distance along the tunnel from the dike and F_t is the turbulent friction coefficient for the tunnel, $F_t \sim 0.01$. Note that in the following calculations the frictional resistance of the flow in the tunnel is found to be small in contrast to that in the dike, and so the results are not sensitive to the simple parameterisation of the turbulent and viscous friction given by the last two terms of (7).

We have assumed that the flow occupies the whole area of the tunnel. For this to be the case, the flux supplied from the dike should exceed the flux associated with a gravity driven slumping flow in the tunnel (e.g. Simpson, 1997); otherwise the magma may simply run along the floor of the tunnel driven by gravity. However, since the prediction that the frictional resistance of the flow in the tunnel is small compared to that in the dike, the flux of magma supplied at the top of the dike is insensitive to the particular flow regime in the tunnel. In fact, we will see that the flow rate calculations suggest that the flow in the tunnel includes a gravity driven leading front followed by a region in which the tunnel is filled with magma.

3.3 Rate of advance of magma along the tunnel

By integrating the equations for flow in the dike and the tunnel, along the length of the flow, and then combining the results, we can relate the overpressure in the sill to the

flow rate Q. If we specify that the length of magma in the tunnel at time t after dike-tunnel interaction occurs is

$$L(t) = \int_0^t \frac{Q}{A} dt \tag{8}$$

so that

$$\frac{dL}{dt} = \frac{Q}{A} \quad \text{and} \quad \frac{d^2L}{dt^2} = \frac{1}{A}\frac{dQ}{dt} \tag{9,10}$$

we obtain the governing equation for the rate of advance of magma along the tunnel

$$\Delta P = \rho A \frac{d^2L}{dt^2}\left(\frac{L}{A} + \frac{1}{w\phi} ln\left(\frac{D}{d\sin\theta}\right)\right)$$

$$+\rho A^2 \left(\frac{dL}{dt}\right)^2 \left(\frac{F_t(H-h)}{Dd\sin\theta w^3} + \frac{LF}{A^{5/2}}\right) + \mu A \frac{dL}{dt}\left(\frac{8\pi L}{A^2} + 12ln\left(D/d\sin\theta\right)\frac{1}{\phi w^3}\right) \tag{11}$$

Equation (11) describes how the flow accelerates along the tunnel until converging to a quasi-steady state in which the frictional forces balance the pressure gradient associated with the overpressure in the sill. This overpressure represents the combination of the pressure in the sill in excess of lithostatic pressure at the depth of the sill, plus the lithostatic pressure at the location of the tunnel which becomes available for driving flow once the dike has intersected the repository and the pressure ahead of the flow front falls to atmospheric pressure. The lithostatic pressure in the environment of the tunnel is produced by the overlying crust, of thickness 200-300m which produces a pressure of about 5-7 MPa. The effective overpressure associated with the sill is typically of order 1-10 MPa, so that we expect the net pressure difference driving the magma to lie in the range 5-20 MPa. In the model, we assume that the country rock at a depth of 200-300m is able to withstand an under-pressure of 5-20 MPa following the breakthrough of the dike into the tunnel, and that as the pressure of the magma in the dike decreases, the dike remains open.

3.4 Predictions. To illustrate the form of the flow and to estimate the rate of advance of magma along the tunnel, we have solved equation (11) numerically. Typical flow calculations are shown in figures 3(a,b) in which the velocity and position of the leading edge of the magma is shown as a function of time. These runs have been made for a combination of basalt magma viscosities, sill overpressures and dike widths as shown on the figure. The calculations identify that with a typical overpressure of 5-20 MPa, for basalt magma with viscosity 10 and 100 Pa s, and with a 1 or 2m wide dike the flow accelerates to speeds in the range 1-20 m/s as the magma invades the tunnel. This will result in magma flooding several hundred metres along the tunnel within several tens of seconds. Such high speeds

result from the sudden release of pressure at the flow front. This decrease in pressure then migrates backwards through the magma until a quasi-steady flow is established. The predictions depend on the assumption that the dike remains open as the pressure falls; if the dike were to partially close up as a consequence of falling pressure then the flow resistance would increase and the flow rate would fall. It would be interesting to study such effects further; the present calculations may be regarded as giving an upper bound on the flow rate given the initial geometry of the dike.

Drainage of the Dike. If for example, there are 100 tunnels which intersect the dike, and each tunnel has length 1000m and cross-sectional area 19.5 m^2, then the total volume of magma which can be diverted into the tunnel is about $2 \times 10^6 m^3$. This is comparable to the volume of magma in the dike at the time of intersection with the tunnels. However, it may be an order of magnitude smaller than the total volume of magma typically erupted during such activity. The presence of air in the tunnel will have little impact on the flow, since in order to produce a pressure comparable to the driving pressure, it must be compressed by a factor of 10-100, at which point over 90-99% of the tunnel will be flooded with magma.

Morphology of the Flow Front. For these flows, the leading edge of the current will be quite elongate, with the leading edge of the flow being driven by a viscous-gravity balance. Scaling of the viscous resistance on the base and sides of the tunnel identifies that the speed of a gravity driven flow scales as

$$u \sim \frac{\rho g d^3}{10 L_g \mu} \tag{12}$$

where the leading edge of the flow occupies a length L_g along the tunnel, producing a slope on the leading edge of the current d/L_g. In order that this gravity driven flow speed is comparable to the following flow which fills the whole tunnel section and has speed, u, the length L_g should scale as

$$L_g \sim \frac{\rho g d^3}{10 u \mu} \tag{13}$$

For viscosity μ in the range $10 \leq \mu \leq 100$ Pa s, and with $u \sim 1 - 10$ m/s (figure 3), equation (13) indicates that $L_g \sim 10 - 1000$m. Behind this slumping region, the whole tunnel is therefore likely to be filled with magma (figure 4). Note that for such flow speeds, the turbulent drag is of comparable magnitude to the viscous drag (i.e. intermediate Reynolds number). This, coupled with the cylindrical geometry leads to rather complex detailed dynamics of the leading front of the magma in the tunnel. However, the earlier calculations, in which it is assumed that the tunnel is filled with magma, provide a good

estimate for the rate of advance of the magma along the tunnel, especially once the flow has settled to quasi-steady conditions (figure 3).

3.5 Impact on Cannisters

The flow of relatively dense and viscous magma along the tunnels will have an important dynamical impact on the cannisters. The flow will be diverted around the cannisters, producing a strong drag force on the cannisters. While the cannisters are at rest, the viscous force on the cannisters per unit mass will scale as $\frac{10\mu u}{r^2}$ where r is the radius of the cannister. Note the factor 10 in the viscous frictional term is a simplification of the total viscous stress which results from the complex flow around a cylinder embedded in a larger cylinder; the actual coefficient which should be used here can only be found by detailed 3 dimensional analysis of the viscous flow, beyond the scope of the present initial calculations. The turbulent drag force scales as $\frac{\rho u^2 C_d}{r}$ where C_d the drag coefficient has value of order unity (Moody, 1944). The frictional force with the floor of the tunnel will tend to resist motion of the cannister, and this will have magnitude of order $g\lambda\rho_c$ per unit volume of cannister, where λ is the friction coefficient with the floor of the tunnel and $\rho_c \sim 7,800\text{kg/m}^3$ is the density of the cannister.

It is first of interest to calculate the minumum speed of magma required to displace the cannisters as a function of the drag coefficient between the tunnel and the cannister. This is found as the solution of the relation

$$\frac{\rho u^2 C_d}{r} + \frac{10\mu u}{r^2} = \lambda\rho_c g \tag{14a}$$

where the left hand side represents the net drag force and the right hand side is the frictional resistance to motion. Here d_c is the length of the cannister, $\sim 5m$, and r is the radius of the cannister, $r \sim 1\text{m}$ As shown in figure 5a, this relation predicts that the cannisters will be displaced if the flow speed is of order 1-5 m/s. For a sufficiently wide dike or low viscosity magma, the cannisters are therefore likely to be displaced along the tunnel.

If the cannister is displaced, then it will move along the tunnel with speed $v(t)$, according to the relation

$$\rho_c \frac{dv}{dt} = \frac{\rho(u-v)^2 C_d}{r} + \frac{10\mu(u-v)}{r^2} - \lambda\rho_c g \tag{14b}$$

(for $v < u$). Numerical solution of (14), illustrated in figure 5b, shows that the cannisters may be accelerated rapidly to a quasi-steady speed of order a few m/s, depending on the magma viscosity and speed.

4. Volatile Rich Magma

We consider the case in which basaltic magma contains 1-3 wt% water in solution at high pressure. The rational for this choice in the context of Yucca Mountain is that evolved continental basic magmas (such as the hawaiite ofLathrop Wells) are expected to have high water contents. As basaltic magma decompresses, the volatiles become supersaturated and are exsolved from solution. This leads to inflation of the mixture, a reduction in density and compressible flow. A full simulation of such a flow requires complex numerical solution of the compressible flow equations, accounting for the frictional resistance of the dike and tunnel walls, for the gravitational force in the vertical dike, for the expansion of the mixture of magma and exsolving volatiles and for the associated change in rheology (Woods, 1995 a,b). We propose that such a study could be carried out, by a post-doctoral researcher, over the course of the next nine months.

The calculations presented in section 3 for volatile free magma represent a lower bound on the possible intensity of such an event; with volatile exsolution the process will be much more explosive. Here we illustrate some of the features of such flows, and present some simplified outline calculations. However, we emphasize that the full physical picture is much more complex than the simple calculations we present, and that these only serve as a guide to the possible style and magnitude of activity. The only recorded event of this kind involved the intersection of a dike with a geothermal bore hole in Iceland which produced a small volcanic eruption at the surface (Larsen et al., 1979).

4.1 Density of Mixture and Exsolution. The density of a mixture of magma and volatiles has the form

$$\rho = \left(\frac{nRT}{P} + \frac{1-n}{\sigma} \right)^{-1} \tag{15}$$

where n is the mass fraction of exsolved volatiles, R the gas constant, T the temperature, P the pressure and σ the magma density. The exsolved gas content may be expressed in terms of Henry's law (cf. Sparks, 1978; Tait et al. 1989)

$$n = n_o - sP^{1/2} \tag{16}$$

where n_o is the total volatile content of the magma, and s is the saturation constant, which has a typical value 3×10^{-6} for water dissolved in basalt.

As the pressure falls, the gas volume fraction

$$\phi = \frac{nRT}{P} \left(\frac{nRT}{P} + \frac{1-n}{\sigma} \right)^{-1} \tag{17}$$

in the mixture gradually increases. Figure 6 illustrates how the gas volume fraction varies with height in the dike subject to lithostatic pressure. At depths comparable to the depth of the repository tunnel, the mixture is already quite vesicular, with a void fraction of 0.2-0.4. However, if this mixture decompresses further, then the void fraction continues to increase until, with a void fraction of order 0.6-0.8, the mixture will fragment into a dispersion of liquid fragments and the gas becomes the continuous phase (Woods, 1995b; Sparks, 1978).

4.2 Compressible flow dynamics. Once the magma is allowed to decompress into the tunnel, a very rapid explosion will follow in which the magma expands and exsolves volatiles as it erupts into the low pressure tunnel. The initial stages of this explosion are likely to be analogous to flow in a large shock tube once a high pressure volatile phase has been released behind a diaphragm. Although the flow geometry is more complex than the ideal shock tube situation, and will require more detailed numerical modelling, it is instructive to examine the initial expansion flow which would develop in the tunnel if magma were suddenly released at a pressure comparable to that at the dike tip. We assume the volatile phase remains in equilibrium with the magma as it decompresses, and that at short times, when the mixture speed is small, there is little frictional resistance on the flow; although an approximation, this should give an indication of the magnitude and scale of the initial flows (Woods, 1995a).

For this simplified situation, an expansion fan propagates backwards into the mixture, while the decompressed material advances into the tunnel, producing a compression wave. This compression wave leads to formation of a shock as the air ahead of the expanding mixture of gas and pyroclasts is compressed. Three regions of flow then develop (Whitham, 1974). The expansion fan, which moves backwards into the decompressing material; a growing region of uniform flow of gas and pyroclasts which advances into the tunnel and a layer of compressed air ahead of the gas/pyroclast mixture. The leading edge of this compressed air is defined by a shock front, ahead of which the air is still and the pressure equals the initial atmospheric pressure (figure 7).

This simple wave can be quantified using the local equations for mass and momentum conservation in the tunnel

$$\frac{\partial \rho}{\partial t} + \frac{\partial}{\partial x}(\rho u) = 0 \tag{18}$$

and

$$\frac{\partial u}{\partial t} + u\frac{\partial u}{\partial x} = -\frac{1}{\rho}\frac{\partial p}{\partial z} \tag{19}$$

neglecting the frictional forces on the high speed flow in the tunnel. By combining these

equations, we obtain the conservation relations

$$\left(\frac{\partial}{\partial t} + (u \pm a)\frac{\partial}{\partial z}\right)(u \pm c) = 0 \tag{20}$$

where $a(p)$ is the speed of sound of the mixture, given by

$$a(p) = \left(\frac{\partial \rho}{\partial p}\right)^{-1/2} \tag{21}$$

and $c(p)$ is given by

$$c(p) = \int_{p_o}^{p} \frac{dp}{\rho}\left(\frac{\partial \rho}{\partial p}\right)^{1/2} \tag{22}$$

where p_o is the initial pressure of the magma-volatile mixture. Using the defintions for $\rho(p)$ and $n(p)$ given above, we can then find the values of the isothermal speed of sound, $a(p)$, and the function $c(p)$.

The expansion fan associated with the magma-volatile mixture is solved by following characteristics $C+$ given by $\frac{dx}{dt} = u + a$ on which $u + c$ is constant and characteristics $C-$ given by $\frac{dx}{dt} = u - a$ on which $u - c$ is constant. This predicts a region of increasing speed, $0 < u < V$, between the $C-$ characteristics $dx/dt = -c$ and $dx/dt = V - c$. Ahead of this, there is a region of uniform pressure, and speed, V, up to the $C+$ characteristic $dx/dt = V + c$ where the contact surface between the fragmented volcanic material and the original air in the tunnel is located (figure 7). Ahead of this surface, the compressed air advances down the tunnel behind a shock wave of speed U. Both U and V are given in terms of p, the pressure of the uniformly advancing region of gas and pyroclasts which forms ahead of the expansion fan,

$$V = \frac{5a_a(p - p_a)}{7p_a(1 + 6(p - p_a)/7p_a)^{1/2}} \tag{23}$$

and

$$U = a_a(1 + 6(p - p_a)/7p_a)^{1/2} \tag{24}$$

where a_a and p_a are the speed of sound and initial pressure of the air in the tunnel.

In figure 8 we illustrate how the pressure drop across the shock wave, and the speed of the advancing mixture of volcanic gas and pyroclasts varies with the volatile content of the magma. It is seen that for 2-3 wt% volatiles, the pressure of the shock wave becomes about 8-9 times atmospheric pressure. The mixture of pyroclasts and air, which follow

behind the shock with this pressure, then advances with a speed up to 150 m/s. Such speeds are typical of the speeds of strombolian explosion jets formed by decompression of volatile-rich basaltic magma into the atmosphere (Blackburn et al., 1976; Sparks et al,, 1997). If such a shock wave impacts a cannister, then the flow will be reflected and deflected around the cannister, leading to an increase in pressure. Although this increase in pressure requires more detailed modelling, the simple theory of reflected shock waves indicate that the pressure may increase by up to a factor of 8 for very strong shocks (Whitham, 1974). The pressure force associated with such a shock on an area of order 4 m^2, comparable to the cross-sectional area of the cannister, is of order 10^7N. This is 10-100 times larger than the frictional resistance between the cannister and the floor of the tunnel and may therefore launch the cannister into motion (figure 8).

Although this model is simplified, and neglects some of the detailed processes leading to fragmentation of the magma and of the frictional resistance of the mixture before fragmentation, the predictions do provide some initial estimates for the potential magnitude of the initial stages of an explosive eruption into a tunnel. As the eruption develops, and the pressure builds up in the tunnel, an increasing mass of material will flow into the tunnel. When the pressure becomes sufficiently large, the flow into the tunnel will remain unfragmented, and the dynamics will evolve towards the water poor flow scenario described earlier. However, this transition is very complex and requires numerical simulation. Furthermore, after the initial stages of the flow, the interaction between the tunnel and the dike which supplies the magma, is extremely complex. We envisage that initially the decompression wave and fragmentation surface will migrate downwards into the dike, but that subsequently, as the tunnel fills with magma and the pressure increases, the fragmentation surface will rise back into the tunnel. In order to examine this in more detail, we propose to develop a series of analogue experiments. These will allow us to explore the complex flow interactions associated with such a volatile explosive flow in a confined geometry.

5. Effect of Backfill in Tunnel

5.1 Tunnel doors Open. Backfill may have an important effect on retarding eruption of magma into the tunnel from the dike. In the case that the tunnel doors open to the atmosphere, the flow may be able to drive the backfill along the tunnel if it can overcome the frictional resistance between the backfill and the tunnel walls. We denote the effective coefficient of sliding friction for the backfill to be λ_s, and the mass of the backfill to be m_b per unit length of the tunnel. Thus, when in motion, the backfill produces a frictional resistance $\lambda_s m_b g$ per unit length of the tunnel. If the total extent of the backfill along the

tunnel floor is B then this leads to a pressure decrease across the backfill ΔP_b given by

$$\Delta P_b = \lambda_s m_b g B/A \tag{25}$$

where A is the area of the tunnel. We take the density of the backfill, measured as mass per unit volume in the tunnel, to be about 2000kg/m^3, based on estimates that the porosity of the backfill is about 30%. For $B \sim$ 1km, then $\Delta P_b \sim 10\lambda_s$ MPa. This pressure loss depends on the coefficient of sliding friction of the backfill in the tunnel.

The effect of this pressure loss is readily included in the calculations of section 3 by subtracting this pressure from the effective overpressure calculated in section 3. This leads to a reduced value for the overpressure available to drive magma along the dike and tunnel. It is this net overpressure which should then be used in equation (11). Comparing the frictional resistance with the overpressures of 5-20 MPa calculated in section 3, we deduce that with a relatively low value of the friction coefficient, the backfill will not be able to arrest the flow, although the smaller driving pressure would result in a slower flow. However, with a larger effective coefficient of sliding friction, the backfill could arrest the flow.

5.2 Closed Tunnel It is worth noting that with a closed tunnel door, able to withstand pressures in excess of 20 MPa backfill would provide an effective means of arresting the flow of magma down the tunnel.

6. Discussion and Proposed Experimental Program

The above calculations provide some preliminary insights into the potential interaction of high pressure magma and a repository tunnel. The modelling, although simple, has identified that, under typical flow conditions, for both volatile-free and volatile-rich magma, the intersection of a dike and a repository tunnel leads to relatively high speed flows along the tunnel. Many of these flows appear to be capable of displacing the cannisters along the tunnel, possibly leading to cannister-cannister impacts, and other damage. In addition to this mechanical impact, the magma is very hot, and may therefore lead to heating and thermal damage to the cannister.

In order to underpin and develop more physical insight into these theoretical calculations, we propose to build a laboratory analogue model of a dike intersecting a repository tunnel to illustrate and investigate the flow regimes which may develop. There is considerable expertise in Bristol in developing and running such analogue experiments, and the post-doctoral researcher, Dr Anne Marie LeJeune, an expert in such flow modelling, is available to work full-time on the project for 9 months from early 1999.

We propose to run the experiments in a specially built perspex test cell, as illustrated schematically in figure 9. The dike is modelled as the thin gap between two vertical glass

plates, and there is a horizontal glass tube issuing from one of the side plates to represent the tunnel. The base of the model dike will be connected to a pressurised source of fluid, while the upper part of the dike will be connected to a vacuum chamber of prescribed pressure. The tunnel will be separated from the dike by a diaphragm which can be broken remotely via an electric current. The end of the tunnel will be connected to a second vacuum chamber. A series of pressure sensors will be embedded in the model dike and model tunnel to record the evolution of the flow with time. In addition, each experiment will be video-recorded using high speed video/photography in order to monitor the flow. In order to simulate both low volatile and high volatile content magmas, two experimental fluid systems will be used. First, golden syrup, whose properties are well known, and which behaves as a viscous liquid will be used as an analogue for a low volatile content magma. Second, a mixture of pine-resin and acetone will be used to model high volatile content magma. Acetone is soluble in pine-resin at high pressure, but as the pressure falls, the acetone comes out of solution and forms a gaseous phase. This is directly analogous to the exsolution of water from a decompressing magma. By adjusting the pressures in the model dike and the tunnel independently using the two vacuum chambers, we will be able to simulate the pressure conditions which arise just before the dike intersects a tunnel. On breaking the diaphragm at this point, we will be able to follow the flows which develop as magma is drawn into the low pressure tunnel.

To complement this experimental study, we also propose that a series of more detailed numerical models of the explosive decompression of magma in the repository tunnels be carried out. This could be performed by a second post-doctoral research assistant who could interact with the experimental work, developing a model both of the experimental system and the full-scale magma -tunnel system. We therefore propose that a second theoretical researcher work on this project for the following nine months, in order to develop more accurate quantitative predictions for the flow evolution.

7. Summary

The calculations presented in this report are much simplified compared to the real volcanic flows which would develop following the intersection of magma in a dike and a repository tunnel. However, the calculations do provide some important leading order information about the potential magnitude and impact of such flows. Two main sets of calculations have been presented.

First, the motion of relatively volatile poor magma along the tunnels has been calculated. This identifies that for typical flow conditions, with pressures of 5-20 MPa driving the flow, the magma will advance along the tunnel at speeds in the range 1-20 m/s, thereby filling the tunnel (500m long) with magma in several tens of seconds. Such flows have the

power to displace the cannisters down the tunnel. Impacts between cannisters and with the tunnel walls may then lead to considerable damage to the cannisters. The thermal impact of the cannisters being embedded in magma, which occurs on a longer time scale and may lead to breakage of the cannisters, also merits analysis.

Second, the motion of a volatile rich magma was examined. In particular, the dynamics of an expansion wave propagating down a tunnel was analysed. This model was simplified by neglecting friction and assuming equilibrium exsolution of volatiles; the model predicts that a shock wave develops in the air ahead of the expanding magma-volatile mixture, with the pressure jump across the shock being up to 8-9 atmospheres. The fragmented magma-volatile mixture following the shock moves with speeds of order 100-150 m/s and also has a pressure of 8-9 atmospheres, equal to that behind the shock. Simple estimates suggest that impact and reflection of the shock on the plane surface of the cannisters may then produce pressures as large as 5-6 MPa. Once the shock wave reaches the end of the tunnel, it is reflected and the pressure in the tunnel gradually builds up. This flow could lead to considerable damage to cannisters in the tunnel; calculations suggest that such a shock wave impacting the cannister may produce sufficient force to launch the cannister into motion.

We propose from these simple calculations that a more complete study be carried out including both (i) a nine-month experimental study, using an analogue system, to model the complex dynamics of the flow and (ii) a complementary nine-month theoretical study of the compressible flow of a decompressing and exsolving magma coupled with the complex dike-tunnel geometry. This would help understanding of both the analogue experimental results and their connection with the possible magmatic flows in the tunnel.

References.

Blackburn, E., Wilson, L., and Sparks, RSJ., Mechanisms and dynamics of strombolian activity, J Geol Soc. Lond., 132, 429-440

Bower, S and Woods, A, 1997, Control of magma volatile content and chamber depth on the mass erupted during explosive volcanic eruptions, J Geophys. Res. 102, 10273-10290

Larsen, G., Gronvold, K., Thorarinson, S., 1979, Volcanic eruption through a geothermal borehole at Namafjall, Iceland, Nature, 278, 707-710.

Lister J, 1991, Steady solutions for feeder dikes in a density stratified lithosphere, Earth Planet Sci Lett., 107, 233-242

Moody, L., 1944, Friction factors in pipe flow, ASME Trans., 66, 671.

Phillips, J., Lane S.N., Lejeune, A., Hilton, M., 1995, Gum rosin-acetone system as analogue to the degassing of hydrated magma s, Bull Volc., 57, 263-268

Pollard, D.D., 1973, Equations for stress and displacement fields around pressurized ellip-

tical holes in elastic solids, Mathematical Geology, 5, 11-25
Simpson, J., 1997, Gravity Currents, Cambridge
Stasuik, M., Jaupart, C and Sparks, RSJ., 1993, On the variations of flow rate in non-explosive eruptions, Earth Planet Sci Lett, 114, 505-516
Sparks, RSJ, 1978, The dynamics of bubble formation and growth in magma s, a review and analysis, J Volc Geoth Res, 3, 1-37
Sparks, RSJ, et al., 1997, Volcanic plumes, Wiley.
Tait, S. Jaupart, C and Vergniolle, S., 1989, Pressure, gas content and eruption periodicity of shallow crystallising magma chambers, Earth Planet Sci Lett, 92, 107-123
Touloukian, Y, Judd, W., Roy, R., 1981, Physical properties of rocks and minerals, Vol 1., McGraw Hill, New York , 548pp
Whitham, G, 1974, Linear and Non Linear Waves, Wiley.
Wilson, L., Sparks, RSJ and Walker, GPL, 1980, Explosive volcanic eruptions V -the control of conduit geometry, Geo J Roy Astr Soc.,
Woods, AW, 1995a, A model of a Vulcanian explosion, Nucl Eng Design, 155, 345-357
Woods, A.W. 1995b, The dynamics of explosive volcanic eruptions, Rev Geophys, 33, 495-530

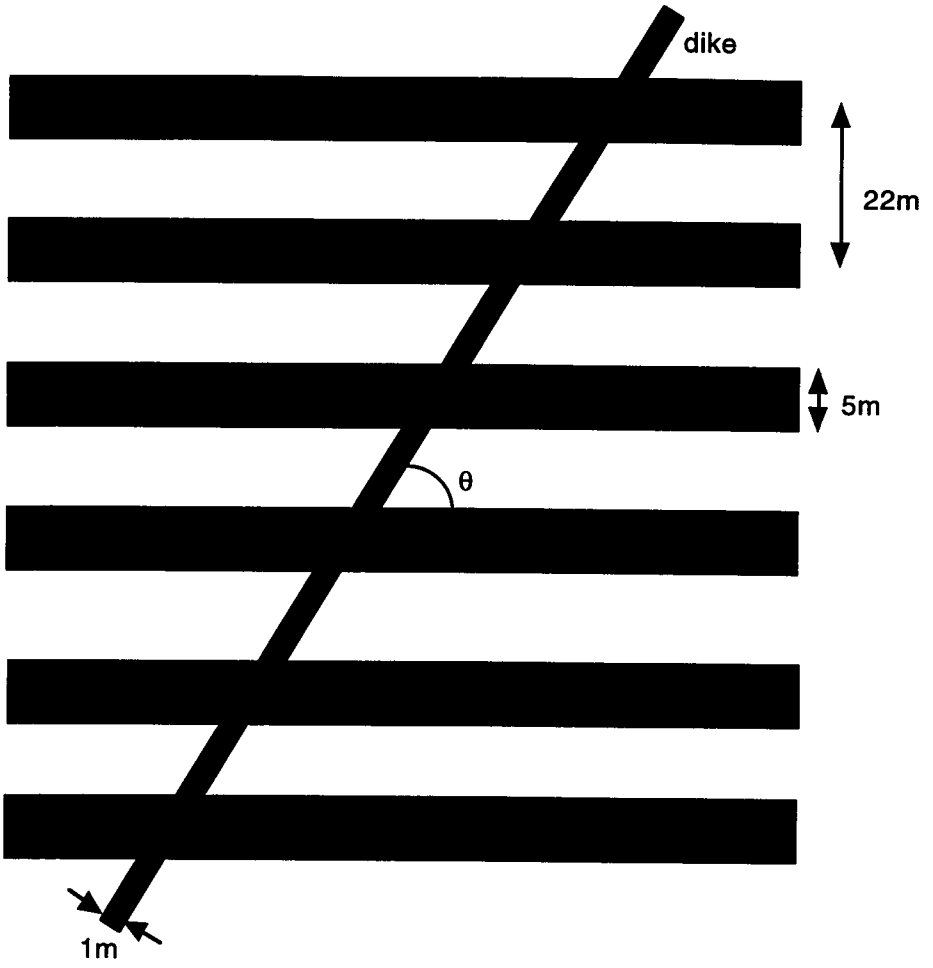

Figure 1 a Top view of geometry of tunnels and dike

b. side view of the diversion of the flow in dike towards the tunnels

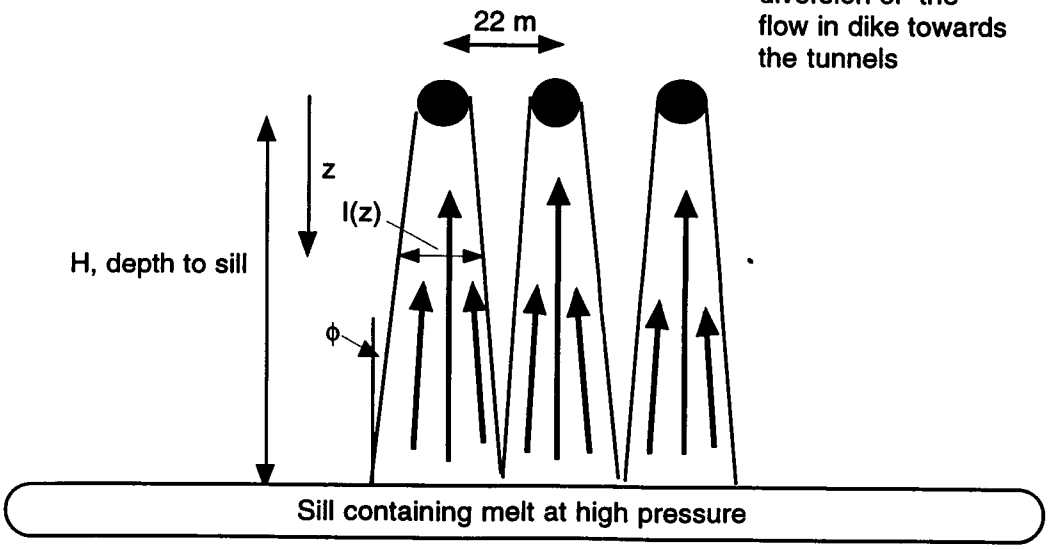

cc

2

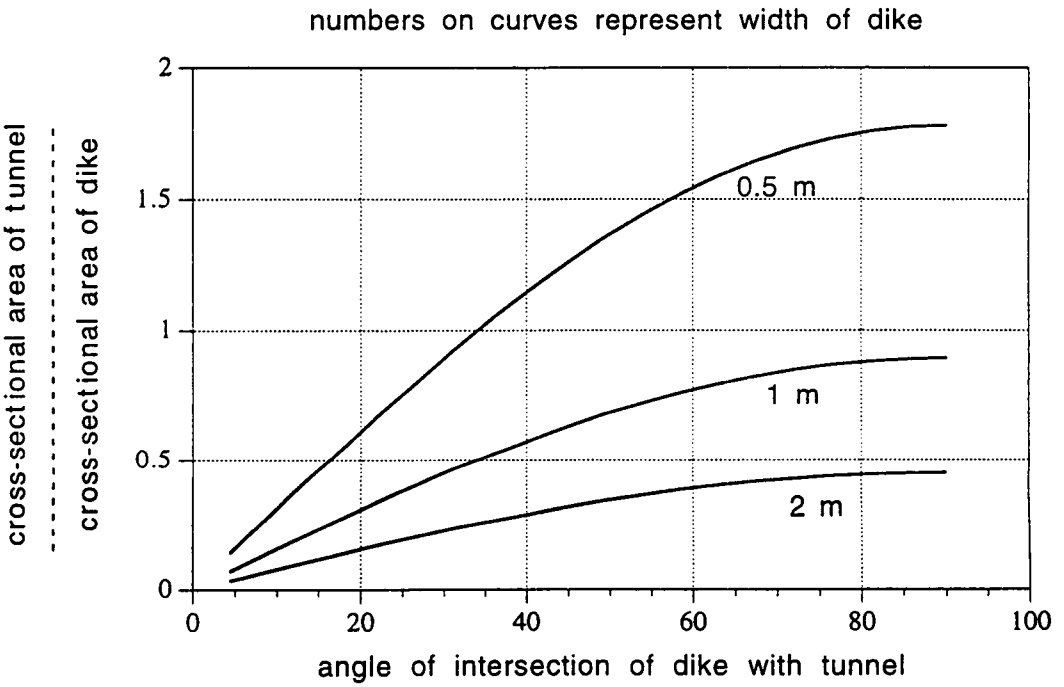
numbers on curves represent width of dike
cross-sectional area of tunnel
cross-sectional area of dike
2
1.5
1
0.5
0
0.5 m
1 m
2 m
0
20
40
60
80
100
angle of intersection of dike with tunnel

Numbers on curves correspond to
magma viscosity and dike width

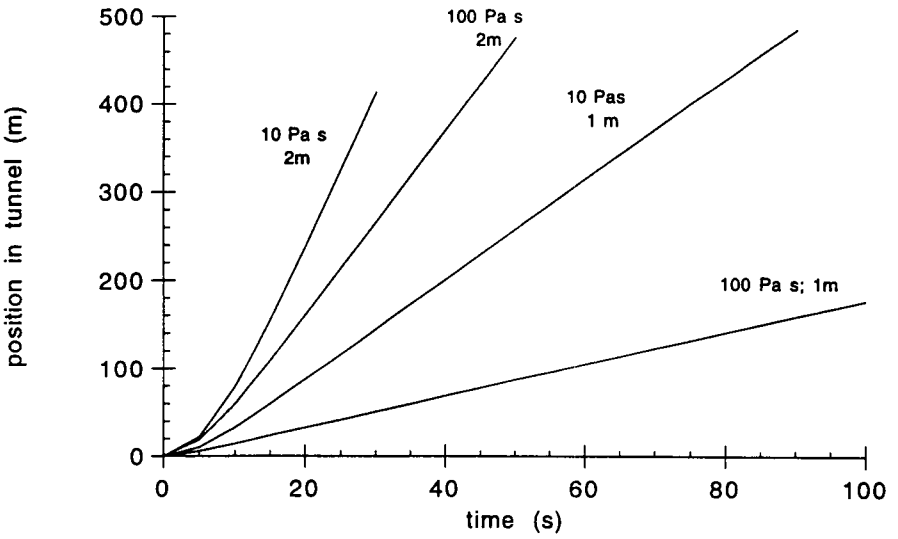

numbers on the curves represent
magma viscosity and dike width

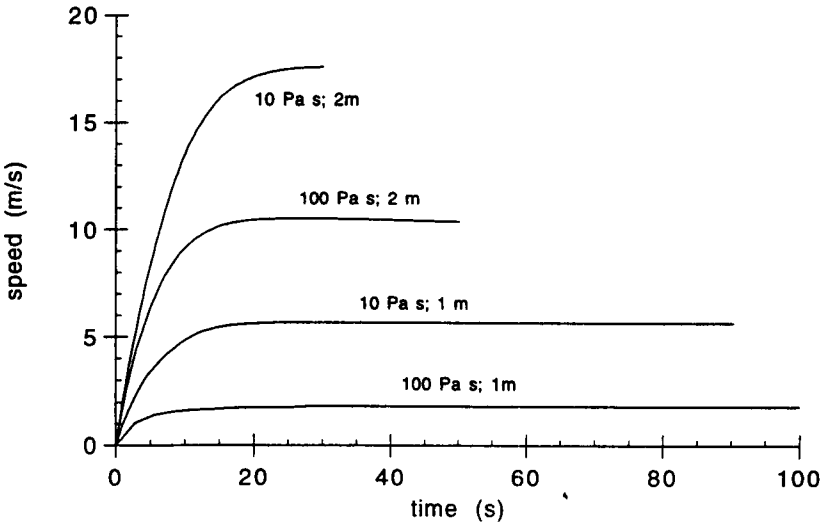

Main part of flow fills
the entire area of tunnel

nose of current extends
some distance along floor

Figure 4 Anatomy of the spreading current of lava

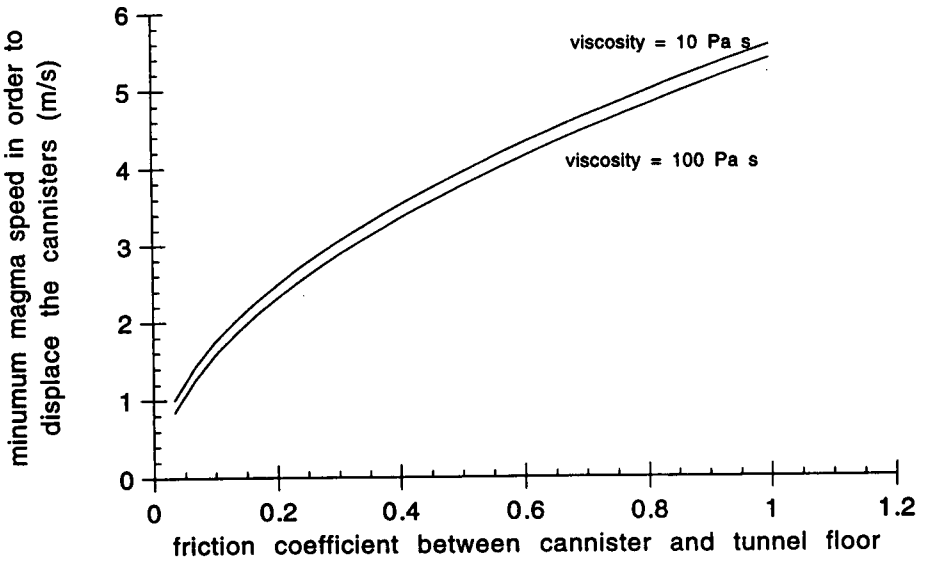
minumum magma speed in order to displace the cannisters (m/s)
viscosity = 10 Pa s
viscosity = 100 Pa s
0
1
2
3
4
5
6
0
0.2
0.4
0.6
0.8
1
1.2
friction coefficient between cannister and tunnel floor

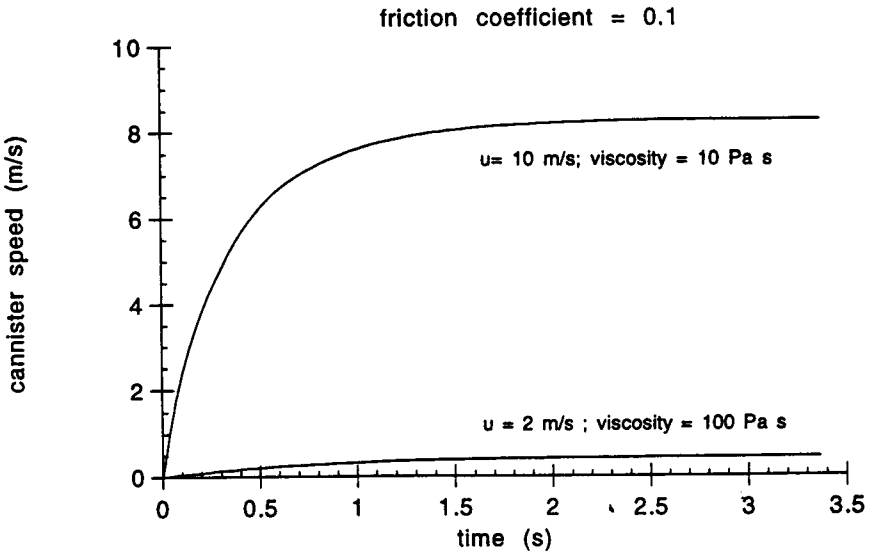
friction coefficient = 0.1
cannister speed (m/s)
u= 10 m/s; viscosity = 10 Pa s
u = 2 m/s ; viscosity = 100 Pa s
0
2
4
6
8
10
0
0.5
1
1.5
2
2.5
3
3.5
time (s)

cc

6

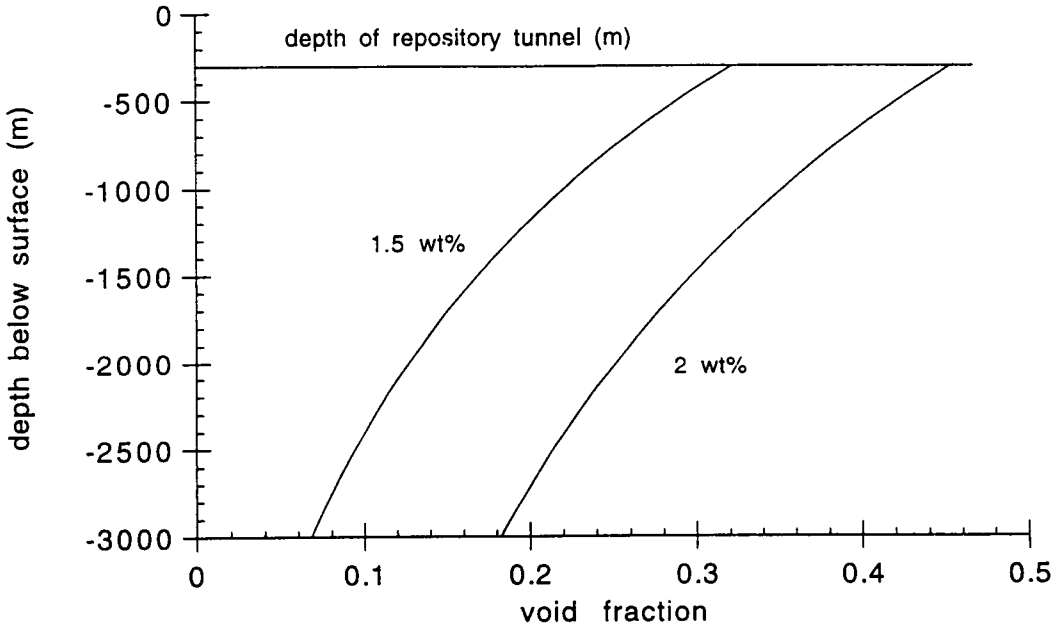
depth of repository tunnel (m)
1.5 wt%
2 wt%
depth below surface (m)
0
-500
-1000
-1500
-2000
-2500
-3000
0
0.1
0.2
0.3
0.4
0.5
void fraction

cc

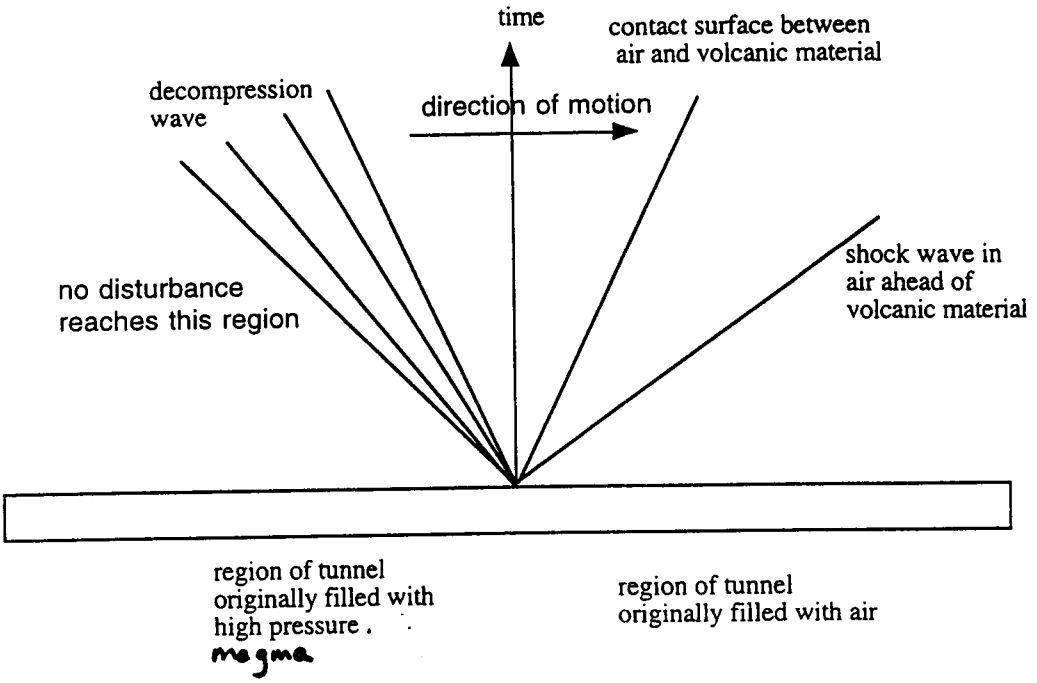
time
contact surface between
air and volcanic material
decompression
wave
direction of motion
no disturbance
reaches this region
shock wave in
air ahead of
volcanic material
region of tunnel
originally filled with
high pressure .
magma
region of tunnel
originally filled with air

7

8

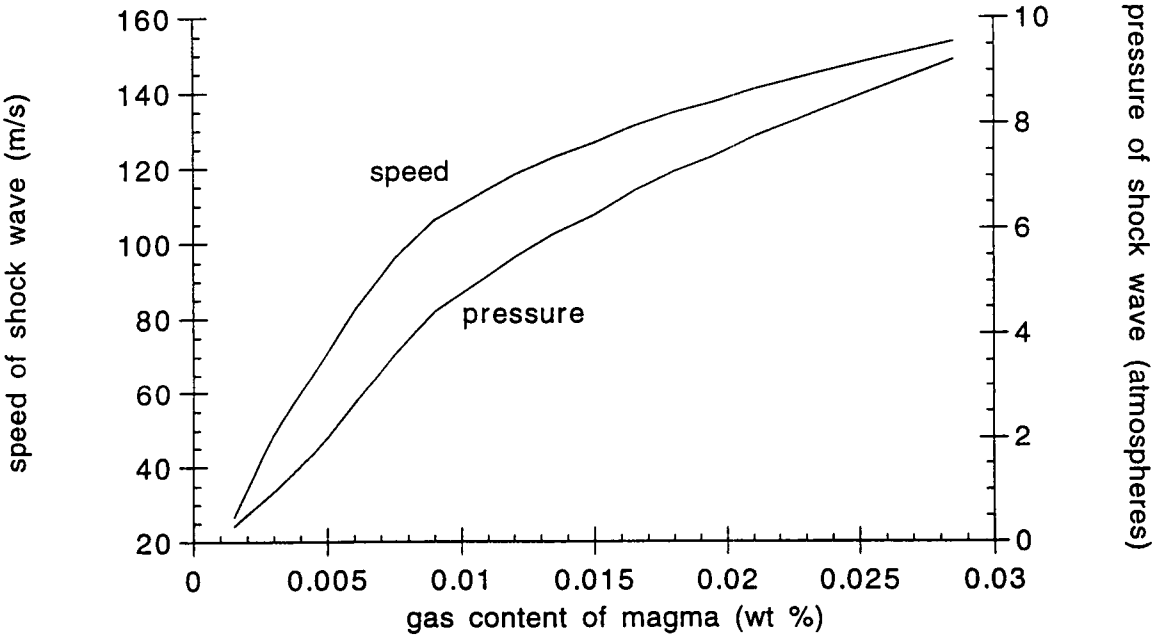
speed of shock wave (m/s)
160
140
120
100
80
60
40
20
speed
pressure
0
0.005
0.01
0.015
0.02
0.025
0.03
gas content of magma (wt %)
10
8
6
4
2
0
pressure of shock wave (atmospheres)

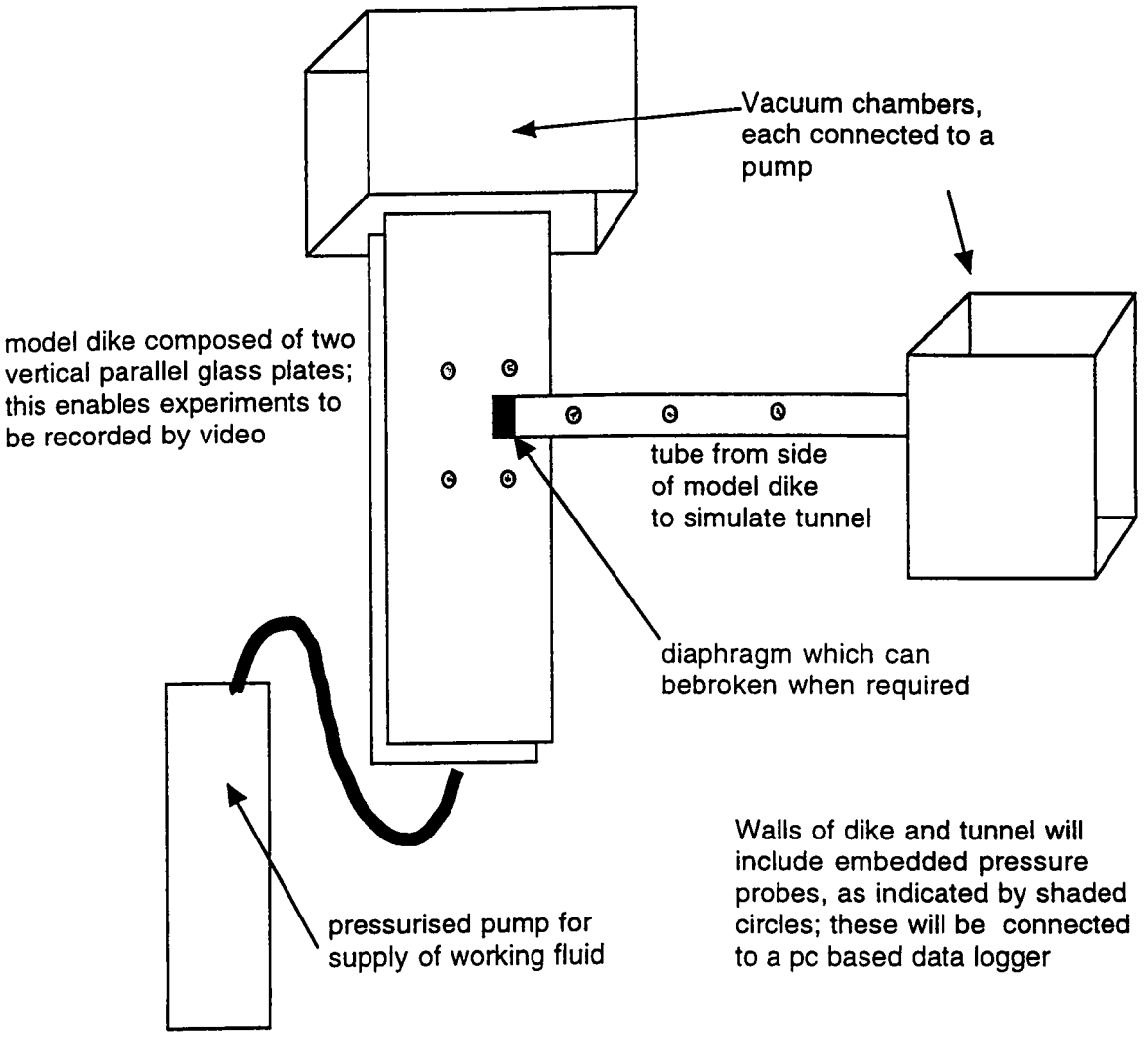
Vacuum chambers, each connected to a pump
model dike composed of two vertical parallel glass plates; this enables experiments to be recorded by video
tube from side of model dike to simulate tunnel
diaphragm which can bebroken when required
pressurised pump for supply of working fluid
Walls of dike and tunnel will include embedded pressure probes, as indicated by shaded circles; these will be connected to a pc based data logger

9

Scientific Notebook
Project 20-1402-461

July, 1998
Chuck Connor

The following is a review of a paper by Newhall and Hobblitt to be submitted to some hjournal (not yet determined). The review is included here because it summarizes many of the ideas related to PHVA used by the DOE and mutually exclusive versus non-mutually exclusvie models in probability trees.

Review of Newhall and Hoblitt - Probability trees for volcanic crises

Review by Chuck Connor (October 21, 1998)

Detailed comments:

1. Risk should not be (and cannot be) reported as a probability, since risk has units - like deaths per year, or dollars lost. Since risk is only meaningful in terms of these units (and of course a probability does not have units). You run into trouble with this at P(8|7) and P(9|8) and these branches do not belong in the event tree because these branches represent a risk rather than a hazard. It is much more useful to stick with the hazard (stop at P(7|6) in the case of your tree). Then go on to show how quantification of hazard provides an important basis for risk assessment.

2. I think this statement is too strong. Aren't you proposing prob. trees as a way to bridge the gap between the volcanic hazard analysis and the needs and questions of officials? But probability trees are not the cure-all - there will still be plenty of specific questions unanswered.

3. Based on A. Cornell's definitions, logic tree refers to the probability of probability models being right. In other words, for lahars I'll assign a 60 % weight to Iverson's numerical simulation of lahar reach and a 40 % weight to K. Scott's model based on his mapping experience at a specific volcano. This is much different than what you have - which is an event tree.

4. I am not sure why you are focusing in on expert elicitation here. This is one approach to assessing hazard (usually done when time and money are in short supply - like a volcano crisis; or as a method of avoiding data collection). Event trees can be used to support this style of analysis - but they are also more general as discussed at the end of the paper.

5. Value and vulnerability are redundant. Note that (as I mentioned in (1) above) risk has a magnitude (lives, dollars) and therefore is never a probability.

6. a. I think the section on Bayes theorem and uncertainty analysis should be presented here rather than at the end of the paper - since these are part of the general concept - also see comment 17.

b. There are clearly situations where the branches of the event tree are not conditional. For

example, wind direction is not conditional on the eruption occurring - but needs to be folded into the analysis probabilistically (as you do later in the paper). Independence is ok in the tree, which occurs if $P(A|B)\cdot P(B) = P(B|A)\cdot P(A)$

7. This paragraph is similar to many in the paper in that some generalizations are made about how to approach a specific problem on a specific branch of the tree. Is this necessary - after all - this is not a volcanology textbook. I think the paper can be shortened a lot by sticking with the structure of the tree, rather than glossing over the volcanology that is the underpinnings for this assessment.

8. Make sure you are consistent. P(1) is the probability of onset of volcanic unrest, not the probability of volcanic unrest in a given year. Once unrest has begun, P(1) is no longer relevant to the hazard analysis.

9. This section illustrates that it is tough to draw the distinction between process and empirical models. For example, I would say that inferring magma ascent from hypocenters is definitely an empirical approach, but you have chosen to pout it in the process section.

I would say that a true process model would take probability distributions of basic magma properties, like volume, fluid pressure, and volatile content, and from these basic properties derive a probability of eruption. I am not sure how the conceptual model you discuss could ever evolve into a process model that results in a probability value without this type of progression.

10. Wouldn't a process model as I described above make the difference between P(3|2) and P(4|3) transparent?

11. Do you think that there is a good case for more explosive eruptions following longer repose intervals (a la Santorini)?

12. A lot of empirical information in the process section!

13. These sections (P(5|4) and P(6|5) are interesting because the data used to derive these - largely what has happened in the past, will be much better known than the likely magnitude of the current eruption. So in practice, these empirical probabilities are not going to be very conditional.

14. The statement on page 24 about the probabilities summing to more than 1 is wrong and this is very important to the whole idea and use of probability trees. I think what you want to say is summarized by the following, which could be used in the general concept section, but which I have only developed for the sector problem.

Assume that the probability P(6|5) in sector A is P(A) and the probability P(6|5) in sector B is P(B). Then the probability that flows (falls) will occur in both sectors is

$$P(A \cap B) = P(A|B)\,P(B)$$

and if the events P(A) and P(B) are independent then this probability is equivalent to:

$$P(A \cap B) = P(B|\ A)\ P(A)$$

So independence implies that

$$P(A \cap B) = P(A)\ P(B)$$

Then the probability of flows (falls) in either sector A or sector B or both is:

$$P(A \cup B) = P(A) + P(B) - P(A \cap B)$$

where the intersection of the probability of A and the probability of B is subtracted because otherwise this intersection is incorrectly counted twice (resulting in probabilities greater than 1).

The probability that no flows (falls) will occur in sectors A or B is

$$1 - P(A \cup B)$$

Multiple sectors can be considered by thinking of $A \cup B$ as a single event

$$P(D) = P(A \cup B)$$

$$P(C \cup D) = P(C) + P(D) - P(C \cap D) = P(A \cup B \cup C)$$

Dispensing of P(D) results in an equation like this:

$$P(A \cup B \cup C) = P(A) + P(B) + P(C) - P(A \cap B) - P(B \cap C) - P(A \cap B) + P(A \cap B \cap C)$$

which gives the probability of a flow (fall) in one of the three sectors or some combination of the three sectors. This kind of formulation is used to calculate the probability of an "or gate" , in other words the union of events, on a probability tree. For example:

$P(A) = 0.75$

$P(B) = 0.85$

$P(C) = 0.65$

$P(A \cap B) = P(A|B)\ P(B) = 0.637$

$P(A \cup B) = 0.963$

$P(A \cup B \cup C) = 0.987$

This is extended to multiple sectors, e.g.:

$$P(A1 \cap A2 \cap ... \cap An) = P(An \mid A1 \cap A2 \cap ... \cap An\text{-}1) \cdot P(An\text{-}1 \mid A1 \cap A2 \cap ... \cap An\text{-}2)$$

$$\cdot \ldots \cdot P(A2 \mid A1) \cdot P(A1)$$

No matter how many sectors you add, the probability, of course, does not exceed unity. For very rare events, an upper bound on the probability can be approximated by the sum of the probabilities, because:

$$P(A1 \cup A2 \cup \ldots \cup An) \leq P(A1) + P(A2) + \ldots + P(An)$$

This approximation is useful for long term forecasting (the left hand side of your event tree) but will yield errors for high probability events. Also

$$P(A1 \cup A2 \cup \ldots \cup An) = P(A1) + P(A2) + \ldots + P(An)$$

only for mutually exclusive events, because for these events:

$$P(An \cap Am) = \varnothing$$

So, on your event tree, the probabilities of VEI 1 - 5 are mutually exclusive (e.g., $P(VEI2 \cap VEI3) = 0$ and these probabilities for explosion magnitude sum to 1. In contrast, the probabilities for eruption phenomena do not sum to one because these probabilities are not mutually exclusive.

I realize this nomenclature is a little formal but I think it can really help with evaluation of the probability trees in general.

15. This statement is fundamental and should be made much earlier - like in the general concept section. I have seen very complicated event trees - leaving the probability of anything bad happening very small! You could point out that many outcomes are terrible, and that it is reasonable to integrate across this terrible outcomes to determine their total probability. Also, this integration changes as you progress done the tree.

16. Any statement about expert elicitation in volcanology should include a mention (at least!) That consensus is not always right (sometimes it's not even close), that expert elicitation is not a substitute for data, and that expert elicitation is most valuable when it is treated as a very dynamic process - prob. distributions change continuously. Rather, it is a tool to explore variation in likely outcomes and to understand the origins of this variation.

17. The discussion of Bayes theorem is good but an example would help. This is important because it is very easy to misuse Bayes theorem - and it's a confusing approach to most people the first few times they hear it. Also, Bayes' theorem is a lot easier to apply to a logic tree than to an event tree. Expert elicitation should not be viewed as a consensus-building process. Here's how I think it can be applied at the simplest level.

C = an event, for example, eruption occurs given volcanic unrest.

B = an event, for example, earthquake frequency predicts the volcanic eruption

The goal is to calculate the probability P(C|B) - the probability of the volcano will erupt when the earthquake frequency says it will.

then P(B|C) is the probability that earthquake frequency correctly predicts the eruption. In other words, if the volcano is going to erupt, the level of earthquake activity will correctly forecast this eruption with probability P(B|C). This probability can be a function of earthquake frequency:

$C = 1 - \exp[-t/500]$

where t is the number of earthquakes per day.

In addition, a given level of earthquakes may incorrectly forecast an eruption some large percentage of the time. In other words, the level of earthquakes may reach some high level and then the unrest subsides without an eruption. This might be a constant or sum function.

$P(B|C^c) = 0.5$, in this example 50 percent of all forecasts based on earthquake frequency will be incorrect.

The prior information is that P(C) = 0.30, historically, 30% of the time the volcano in a state of unrest will erupt. So, suppose the current level of seismicity is 500 earthquakes per day:

$$P(C|B) = [P(B|C) \cdot P(C)\ ] / [P(B|C) \cdot P(C) + P(B|C^c) \cdot P(C^c)] = 0.35$$

So, the probability of eruption based on earthquake frequency is 35 percent. I think this kind of specific example will help show the use and limitations of the Bayesian approach.

General comment:

The concept of the probability tree and its application to volcanic crises becomes a lot more powerful if you introduce logic trees in addition to the event trees (Figure 1 and 8). Each transition probability in the event tree can be supported by a logic tree. The transition probabilities in the logic tree are determined by the weight assigned to individual approaches (i.e., empirical vs. process), the weight assigned to different methods, data and parameter distributions. These logic trees are the vehicle used to incorporate expert judgement and identify the areas where different data interpretations result in different hazards (and ultimately different risks).

I have included several examples of how I think this works. Consider the transition probability

between unrest with magmatic intrusion and magmatic eruption P(3|2) (Figure 1, attached). The logic tree provides a path from the observation that the volcano is in a state of unrest to the probability of eruption based on the relative weights assigned to monitoring techniques, models, and observations. The first decision in the logic tree is to evaluate the weight to assign to empirical data versus process models. This weighting is based on expert judgement and probably varies considerably among volcanologists. On the logic tree, empirical and process weights are mutually exclusive: P(empirical) $\cap$ P(process) = $\varnothing$ and P(empirical) + P(process) = 1.0. Each of these branch into disciplines, sub-disciplines, sub-sub-disciplines and eventually counter-cultures in the case of most Italian volcanoes. For each of these transition probabilities, the same rules apply, the weights are mutually exclusive and sum to one. The relative weights assigned to each of these transitions is largely a matter of the faith placed in any particular method or class of methods as an eruption tool. This remains true no matter how complicated the logic tree becomes.

In contrast, the final probability transitions (right side of the tree) are based on data and parameter distributions. The way to think of these transitions is "given that method X is an effective way to forecast volcanic eruptions, an eruption will occur with probability Y, given that the measured value of X is Z. For example, the expert volcanologist or group might recognize a relationship between the frequency of earthquakes (or the S/Cl ratio, or the SO2 flux, or the rate of change in deformation) and the probability of eruption, such as suggested in comment 17 on application of Bayes theorem. Alternatively these transition probabilities might be very abrupt. If the S/Cl ration is 10, the volcano will erupt. Two important things to note are (1) the relative weight assigned to

these methods has already been determined a previous branches, and (2) if the data or parameters is not measured (empirical) or estimated (process) then the branch does not exist. Finally, probabilities of eruption are determined for each branch. Note that these probabilities are not mutually exclusive - the sums of the probabilities will not equal one. However, multiplied through by the relative weight assigned to each method, the total probabilities equal one or less.

This logic tree makes the decision process used to estimate the transition probability P(3|2) transparent. I have assigned weights to the logic tree as an example to demonstrate this transparency (Figure 2, attached). These weights might be assigned by some volcanologist working on the scene and more than likely would not be agreed to by everyone. This example volcanologist is an empiricist and places no weight on process models to tell him about the probability of eruptions - so the process branch conveniently disappears. Four monitoring disciplines are on the empirical branch of this tree and this example volcanologist weights the seismic data most heavily, with gas and deformation data playing second fiddle and past eruption behavior of the volcano given low weight (the volcanologist does not have a lot of faith in these data). Each of these disciplines are divided into sub-areas (or methods) for which data are currently available at the volcano and each of these methods is assigned a mutually exclusive weight. For each of these methods, the chance of eruption - based on the current observations and past experience are evaluated in some way. Ideally this is very quantitative, but in practice it is not. Instead, assigning these probabilities are based on (i) educated guesses based on experience, (ii) data compilations and this and analogous volcanoes, and (iii) conceptual models (e.g., if the

RSAM shows exponential increase, the volcano is very likely to erupt). The total probabilities are the chance of eruption based on these transition probabilities, weighted by the previous transition probabilities. These sum to the probability of eruption — P(3|2).

In the example, there is about a one in four chance of eruption based on this example analysis. In this case, it is clear that the transition probability is as high as it is because of the gas data. Each of the gas methods give higher probabilities of eruption than other methods, and the overall transition probability would be much higher if this volcanologist placed more weight on the significance of the data compared to seismic or deformation methods. It is also easy to see what it takes to change the P(3|2) transition probability. For example, suppose that overnight the seismicity shallows and the frequency of earthquakes increases abruptly - sending the chances of eruption based on this information along to about 90 percent. No change in the over data sets is observed because these data have not been collected overnight. Based on this tree, the overall probability increases to 56 percent. Since these seismic data are new compared to the other data, the volcanologist may wish to assign a higher relative weight to the new data. Through making the logic tree, it is very easy to explore and discuss the conditions that lead to conclude that the probabilities of eruption are high or low.

In an expert elicitation (formal or informal) during volcanic unrest, each expert volcanologist would need to create such a logic tree, and defend the branches and the transition probability s/he estimates for each branch. Ideally, this would make the reasons for variation in the estimated

transition probability P(3|2) quite clear.

The logic tree I developed above is really only appropriate for a very well monitored volcano. A few things about calculating transition probabilities using alternative approaches become clear from considering a less well monitored volcano. Suppose that at some volcano four pieces of data are available: (i) RSAM measurements show high, rapidly fluctuating values but no clear trends; (ii) COSPEC measurements show a large increase in degassing over the last week, (iii) one soil Rn station also shows an increase, and (iv) a overflight of the crater shows a lot of new deformation along the crater walls, including areas of new degassing.

One way to think of this information is that these observations are all independent. If this were the case, then eruption probabilities could be assigned based on each piece of date. For example, the seismic group may place to probability of eruption, P[A], during the next week at 0.2 based on the RSAM data; the Cospec group - P[B] = 0.5; soil gas group - P[C] = 0.4; overflight group - P[D] = 0.5. If we simply look at the overall transition probability as the union of these probabilities (or gate) the transition probability is 0.88, much high than the probabilities suggested by any one of the groups.

The reason this transition probability would be wrong to use is that there is a high degree of cross-correlation between the four pieces of data. Estimates of probability based on the Rn soil gas data and the COSPEC data contain significant cross-correlation because both data sets respond strongly to increase in total mass flow. Conversely, each of the data sets contain some

independent information. The COSPEC data are specific to SO2, which usually shows the greatest increases when magma is exsolving gas in the shallow subsurface; the Rn soil data shows that distributed degassing is occurring along structural weaknesses in the edifice of the volcano. To cast this interdependence probabilistically, $P(B \cap C)$ has to be estimated. Say

$$P(B \cap C) = P(B|C)P(C) = 0.35$$

then

$$P(B \cup C) = .4 + .5 - .35 = 0.55$$

This result indicates that because the SO2 flux has been observed, the radon soil gas data is adding little to the estimate of the probability of eruption - but it is adding to the confidence in the estimate.

Similarly, you might conclude that a significant fraction of the seismic energy release summarized by the RSAM also went into the crater deformation observed during the overflight. For example, $P(A \cap D) = 0.19$, then

$$P(A \cup D) = 0.5 + 0.2 - 0.19 = 0.51$$

As occurred with the gas data, this result indicates that because the crater deformation has been observed, the RSAM data is adding little to the estimate of the probability of eruption - but it is adding to the confidence in the estimate. Finally, there is some cross-correlation expected between the gas data and the deformation data because mass flow should increase as a result of deformation. Nevertheless, the gas data do provide a lot of information about the involvement of magma that does not necessarily flow from the deformation data). Thus the volcanologists working on the scene also need to estimate:

$$P(A \cup D) \cap P(B \cup C) = 0.35$$

then the probability of eruption is

$$0.55 + 0.51 - 0.35 = 0.71.$$

To summarize, the gathering of different data sets resulted in four estimates of the probability of eruption. These estimates are not independent, because a significant fraction of the observed variation in each of the four data sets cross-correlates with other data sets. The volcanologists need to estimate this intersection in order to estimate the probability. If the cross-correlation is considered to be total, then the estimated probability of eruption will be equal to the largest value predicted using any one data set. If the cross-correlation is not total (usually the case since we normally think it is a good idea to go out an get multiple data sets) then the probability estimate

will always be higher than the probability estimated by any one method. That is, because deformation is occurring and SO2 is high, there is a higher probability estimated than would be estimated from any one of these data sets alone.

This result is very different than the one estimated from the logic tree in which methods receive a relative weight - the approach used in Figure 1 and the approach used in the Yucca Mountain PVHA. The logic tree for this same problem might look like figure 3 (attached). Note that this gives a diluted probability (0.37). This is one of the problems with all trees. In this case, it is clear that more models (or more outcomes in the case of an event tree) reduces the probability of a specific outcome.

Hope these ramblings help!

Cc

Scientific Notebook
Project 20-1402-461

August, 1998
Chuck Connor

The following article was prepared using overhead funds. The article is included in this scientific notebook because it summarizes significant elements of our real-time geophysical techniques used in NRC projects.

REAL-TIME GEOPHYSICS USING LINUX

by

Laura Connor and Charles B. Connor

Center for Nuclear Waste Regulatory Analyses
Southwest Research Institute
6220 Culebra Rd., San Antonio, TX, 78238, USA

draft of August 24, 1998

accepted by
Linux Journal

Information potentially subject to copyright protection was redacted from pages -1- through -14 of this scientific notebook.. The redacted material is from the reference information listed on p. -1- of this scientific notebook..

Information potentially subject to copyright protection was redacted from pages -1- through -14 of this scientific notebook.. The redacted material is from the reference information listed on p. -1- of this scientific notebook..

Information potentially subject to copyright protection was redacted from pages -1- through -14 of this scientific notebook.. The redacted material is from the reference information listed on p. -1- of this scientific notebook..

Information potentially subject to copyright protection was redacted from pages -1- through -14 of this scientific notebook.. The redacted material is from the reference information listed on p. -1- of this scientific notebook..

Information potentially subject to copyright protection was redacted from pages -1- through -14 of this scientific notebook.. The redacted material is from the reference information listed on p. -1- of this scientific notebook..

Information potentially subject to copyright protection was redacted from pages -1- through -14 of this scientific notebook.. The redacted material (Figures 1 through 9) is from the reference information listed on p. -1- of this scientific notebook..

Information potentially subject to copyright protection was redacted from pages -1- through -14 of this scientific notebook.. The redacted material (Figures 1 through 9) is from the reference information listed on p. -1- of this scientific notebook..

Information potentially subject to copyright protection was redacted from pages -1- through -14 of this scientific notebook.. The redacted material (Figures 1 through 9) is from the reference information listed on p. -1- of this scientific notebook..

Information potentially subject to copyright protection was redacted from pages -1- through -14 of this scientific notebook.. The redacted material (Figures 1 through 9) is from the reference information listed on p. -1- of this scientific notebook..

Information potentially subject to copyright protection was redacted from pages -1- through -14 of this scientific notebook.. The redacted material (Figures 1 through 9) is from the reference information listed on p. -1- of this scientific notebook..

Information potentially subject to copyright protection was redacted from pages -1- through -14 of this scientific notebook.. The redacted material (Figures 1 through 9) is from the reference information listed on p. -1- of this scientific notebook..

Information potentially subject to copyright protection was redacted from pages -1- through -14 of this scientific notebook.. The redacted material (Figures 1 through 9) is from the reference information listed on p. -1- of this scientific notebook..

Information potentially subject to copyright protection was redacted from pages -1- through -14 of this scientific notebook.. The redacted material (Figures 1 through 9) is from the reference information listed on p. -1- of this scientific notebook..

Information potentially subject to copyright protection was redacted from pages -1- through -14 of this scientific notebook.. The redacted material (Figures 1 through 9) is from the reference information listed on p. -1- of this scientific notebook..

Scientific Notebook
Project 20-1402-461

August, 1998
Chuck Connor

A significant issue in volcanic hazards assessment for the high-level waste repository is the integrity of the canister during heating by magma in the drifts. The following summarizes preliminary calculations about heating of canisters in the drifts.

Heating of the Canister by Submersion in Magma

Heating of the canister by submersion in magma may result in the failure of the canister. Preliminary calculations by Barnard (1998) suggest that canister failure will occur around 800 °C, but the behavior of canister materials at high temperatures is currently poorly known because high temperature tests have not been performed on actual canister materials and because final canister design is not agreed upon. The temperatures in the canister at times following the intrusion of magma into the repository tunnels are calculated and compared to the rate of cooling of the magma in the tunnel.

A simple approach to modeling approach is to assume that the canister is suddenly submerged in the convecting magma. Heat transfer with the canister will follow the equation (Carslaw, 1921):

$$\frac{\partial T}{\partial t}=\frac{\alpha}{r}\frac{\partial}{\partial r}\left(r\frac{\partial T}{\partial r}\right) \qquad (1)$$

where T is temperature, t is time, α is the thermal diffusivity, and r is radius, with initial conditions:

$$T(r,t=0)=T_i \qquad (2)$$

and a convective boundary condition at the surface of the canister, at $r = r_o$:

$$-k\frac{\partial T}{\partial r}=h_o(T-T_o) \qquad (3)$$

White (1984), following Schneider (1955), gives the solution to this heat transfer equation as:

$$\theta_c = \frac{T - T_o}{T_i - T_o} = C_1 e^{-\beta_1^2 \alpha t / r_o^2} \quad (4)$$

along the centerline of the cylinder and

$$\theta = \theta_c J_o(\beta_1 r / r_o) \quad (5)$$

off the centerline of the cylinder, for all times greater than:

$$t > 0.2 r_o^2 / \alpha \quad (6)$$

In this formulation J_o is a Bessel function of the first kind. Equation 4 may also be written using Bessel functions, but here is written using Heisler coefficients, C_1 and β_1 for the centerline formula. These coefficients depend on the Biot number:

$$Bi = h_o r_o / k$$

and are tabulated in White (1984). Approximation of heat transfer in this way only results in errors at short times (equation 6) after immersion.

Thermophysical properties of the *canister* are taken from Manteufel (1997). These are:

thermal conductivity K = 50 W/m °K
bulk density ρ = 7800 kg / m^3
heat capacity Cp = 450 J/kg °K
thermal diffusivity $\alpha = 1.4 \times 10^{-5}$ m^2/s

These are bulk properties of the canister, for which design specifications have not been finalized. The canister will be a cylinder approximately 5 m long and 1.2 m in diameter.

Thermophysical properties of the *magma* (McBirney, 1984) are:

thermal conductivity K = 1.25 W/m °K

Scientific Notebook
Project 20-1402-461

August, 1998
Chuck Connor

bulk density $\rho = 7800$ kg / m^3
heat capacity Cp = 1041 J/kg °K
thermal diffusivity $\alpha = 4.4 \times 10^{-7}$ m^2/s

and thermophysical properties of the *wall rock* (Manteufel ,1997) are:

thermal conductivity K = 2.1 W/m °K
bulk density $\rho = 2200$ kg / m^3
heat capacity Cp = 930 J/kg °K
thermal diffusivity $\alpha = 1.0 \times 10^{-6}$ m^2/s.

Temperature of the canister as a function of radial distance calculated at 30 min increments is shown in Figure 1. The initial canister temperature is assumed to be 250 °C and the magma temperature is 1100 °C and does not change for the duration of the calculation (infinite reservoir). For this calculation, it is assumed that high Biot numbers persist for the duration of heating (Bi = 50, $\beta_1 = 2.35$, and $C_1 = 1.65$). This implies a high heat transfer coefficient between the magma in the tunnel and the canister wall. However, the heat transfer coefficient may be strongly reduced by formation of a basalt crust on the outer pack. Using a very low Biot number (Bi = 0.1, $\beta_1 = 0.44$, and $C_1 = 1.02$) results in much slower heating of the canister and produces much lower temperature gradients inside the canister because the heat flux into the canister is so strongly limited by h_o (Figure 2).

The same equations can be used to calculate rate of cooling of the magma inside the tunnel, neglecting latent heat of crystallization and the heating of the wall rock, or flow in the tunnel (which I realize I will need to get back to). Here, the heat transfer coefficient is given by

$$h_o = \frac{3.5k}{D}$$

where D is the hydraulic diameter of the tunnel. This gives Bi = 1.75 ($\beta_1 = 1.5$, and $C_1 = 1.3$). For the 5-m-diameter tunnel, temperatures remain near 1100 °C for more than 20 days (Figure 3), indicating that there is plenty of time to completely heat the canisters and resulting in their failure.

Figure 1: Temperature profiles inside the canister in near perfect thermal contact with a convecting magma at 1100 °C (Bi = 50; Ti = 250 C, Tf = 1100 °C for a 1.2 m diameter canister). The canister is assumed to be infinite in length, which is a reasonable approximation for a

cylinder 5 x longer than in diameter. Temperature profiles for times between 2 and 4 hr are shown.

Figure 2: Temperature profiles inside the canister in poor thermal contact with a convecting magma at 1100 °C (Bi = 0.1; Ti = 250 C, Tf = 1100 °C for a 1.2 m diameter canister). Temperature profiles for times between 1 and 4 days are shown.

Figure 3: Temperature profile inside a magma-filled tunnel for 20, 30, 40, and 50 days.

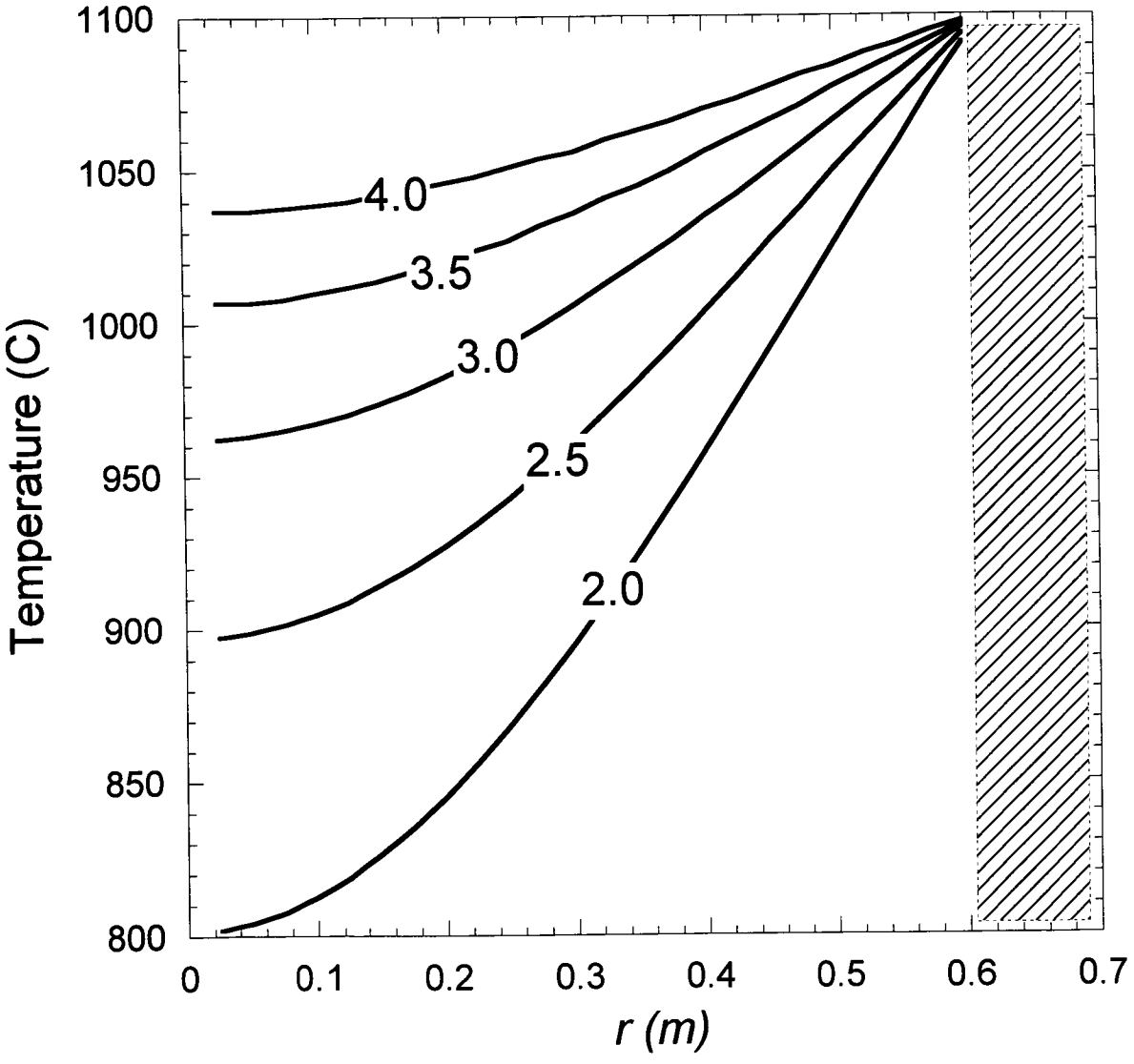
1100
1050
1000
950
900
850
800
Temperature (C)
4.0
3.5
3.0
2.5
2.0
0
0.1
0.2
0.3
0.4
0.5
0.6
0.7
r (m)

Figure 1

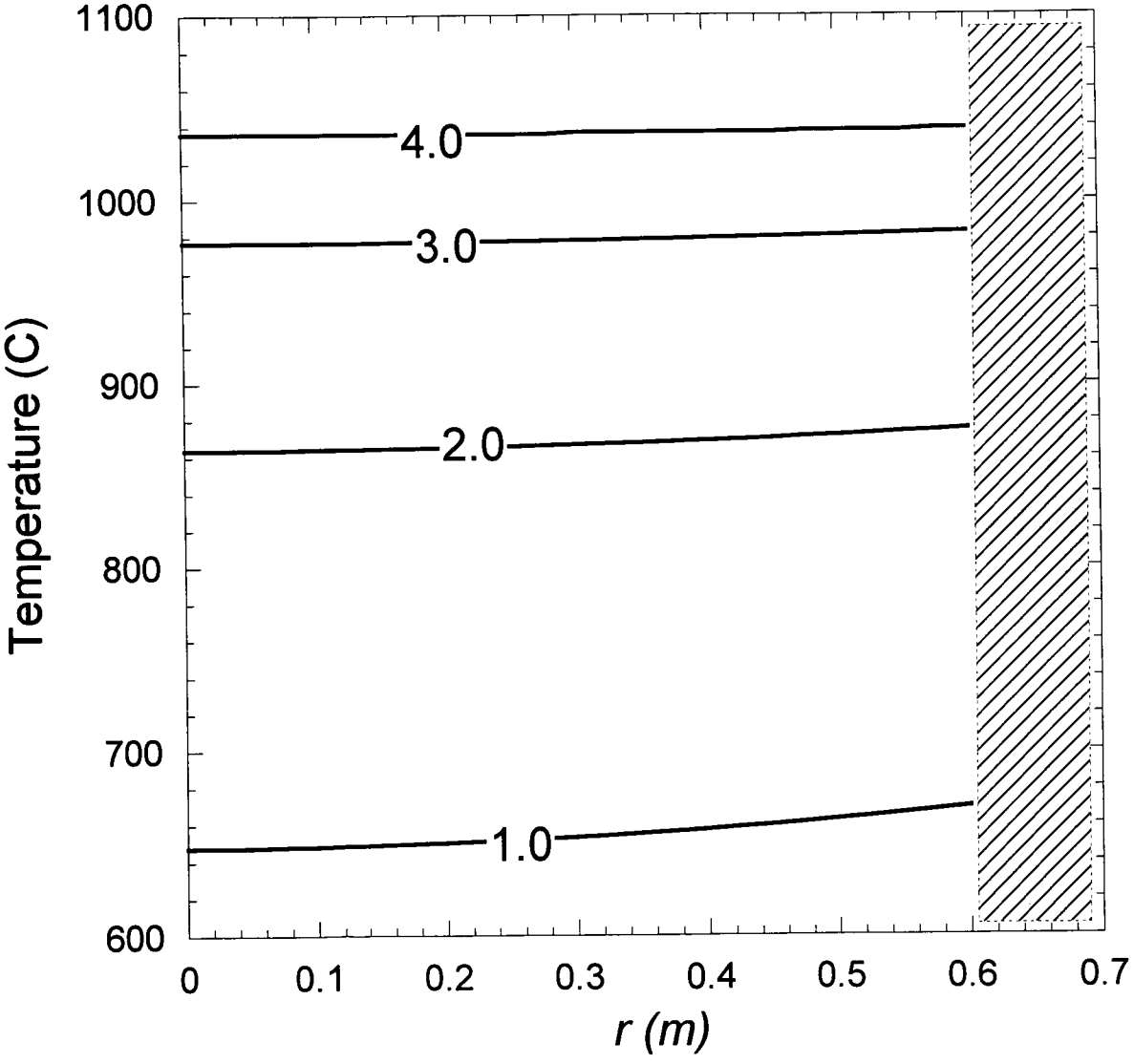
1100
1000
900
800
700
600
Temperature (C)
4.0
3.0
2.0
1.0
0
0.1
0.2
0.3
0.4
0.5
0.6
0.7
r (m)

Figure 2

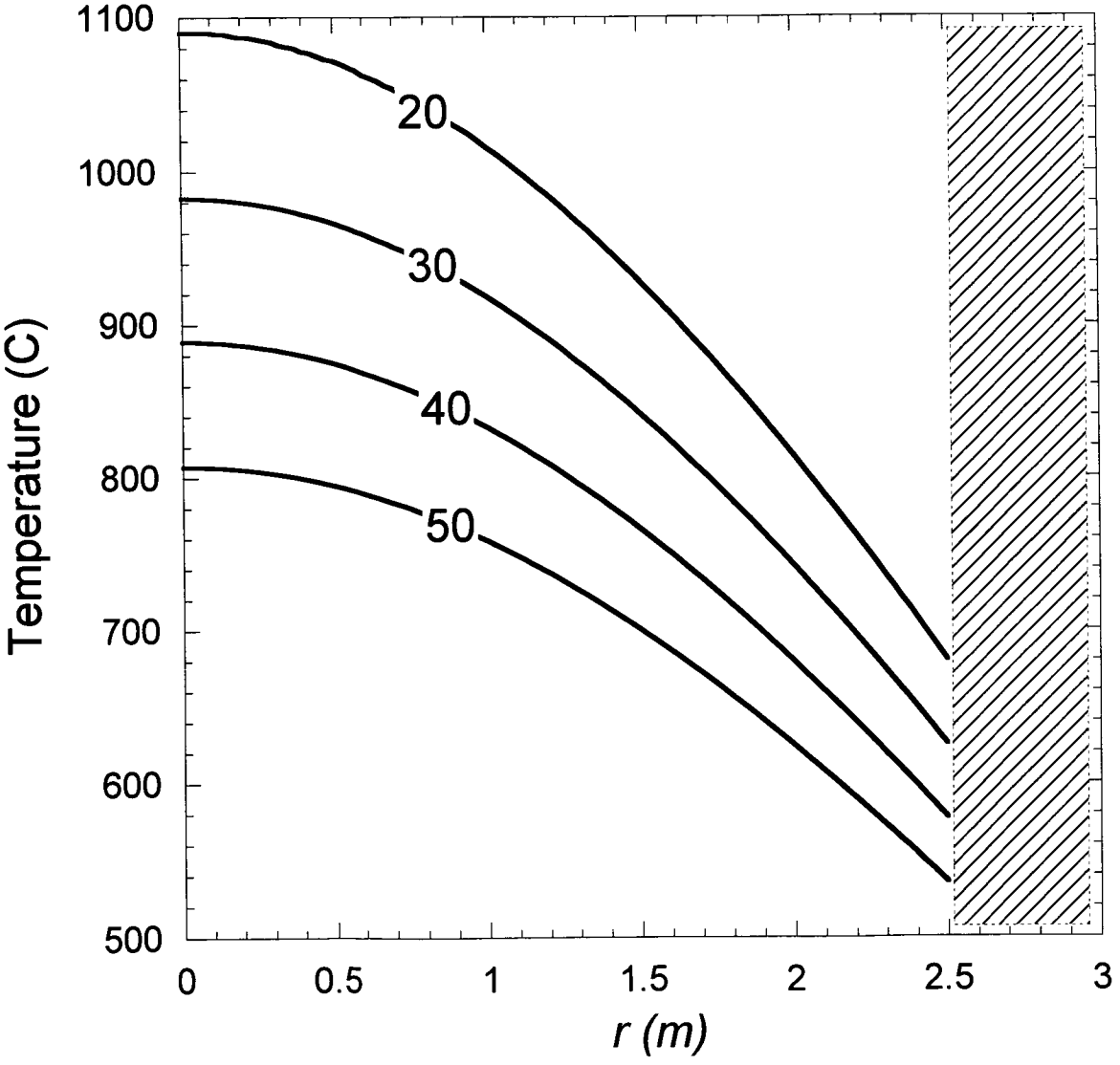
1100
1000
900
800
700
600
500
Temperature (C)
20
30
40
50
0
0.5
1
1.5
2
2.5
3
r (m)

Figure 2

Scientific Notebook
20-1402-461

Sept. 1998
Chuck Connor

The following Mathematica script is used to calculate the the cooling of magma in the tunnel. Text has been added to clarify the script.

k is the bulk thermal conductivity of the magma (W/mK)
k=1.25;

Ti is the initial magma temperature (C)
ti = 1100;

tf is the final temperature (wall rock temperature)
tf = 250;

alpha is the thermal diffusivity (m2/s)
alpha = 4.4 10^(-7);

h0 is the heat transfer coefficient between the tunnel walls and the magma
h0 = 100;

r0 is the radius of the tunnel - or canister (meters)
r0 = 2.5

Bi is the Biot number
bi=h0*r0/k

b1 and c1 are the Heisler coefficients. They must be looked-up in a table in order to be used - based on the Biot number. Here the table in White, F.M., 1984, Heat Transfer, page 178 is used.

b1=1.5
c1 =1.3;

```
tstar1 =alpha*(480 * 3600)/r0^2
thetc1= c1*Exp[-(b1^2)*tstar1];
joe1 =                  tf +(ti-tf)thetc1*BesselJ[0,b1*r/r0];
gj1 = Plot[joe1,{r,0,r0}]

tstar2 =alpha*(720 * 3600)/r0^2
thetc2= c1*Exp[-(b1^2)*tstar2];
joe2 =                  tf +(ti-tf)thetc2*BesselJ[0,b1*r/r0];
gj2 = Plot[joe2,{r,0,r0}]
```

```
tstar3=alpha*(960 * 3600)/r0^2
thetc3= c1*Exp[-(b1^2)*tstar3];
joe3 =                  tf +(ti-tf)thetc3*BesselJ[0,b1*r/r0];
gj3 = Plot[joe3,{r,0,r0}]

tstar4 =alpha*(1200 * 3600)/r0^2
thetc4= c1*Exp[-(b1^2)*tstar4];
joe4 =                  tf +(ti-tf)thetc4*BesselJ[0,b1*r/r0];
gj4 = Plot[joe4,{r,0,r0}]

gjy=Show[gj1,gj2, gj3, gj4]

stmp = OpenWrite["temp4.txt", FormatType ->OutputForm]
Do[
Write [ stmp,
            N[Evaluate[r],4],
                  "  ",
            N[Evaluate[joe1],4],
            "  ",
                  N[Evaluate[joe2],4],
            "  ",
                  N[Evaluate[joe3],4],
            "  ",
            N[Evaluate[joe4],4]
                        ],
      {r,0,r0,0.025}]

Close[stmp]
```

CC

Scientific Notebook
20-1402-461

Oct 1998
Chuck Connor

If all or most of the magma is redirected into the tunnels, it is worth considering conditions after the initial high-speed magma injection. In the following I have calculated the fluid pressures in the tunnel required to initiate vertical fracturing above the conduit using some (possibly serious) simplifying assumptions.

The Kirsch solution solves for the compressive stresses near a conduit or tunnel:

$$\sigma_{rr} = \frac{\sigma_1 + \sigma_2}{2}\left(1 - \frac{a^2}{r^2}\right) + \frac{\sigma_1 - \sigma_2}{2}\left(1 - \frac{4a^2}{r^2} + \frac{3a^4}{r^4}\right)\cos 2\theta$$

$$\sigma_{\theta\theta} = \frac{\sigma_1 + \sigma_2}{2}\left(1 + \frac{a^2}{r^2}\right) - \frac{\sigma_1 - \sigma_2}{2}\left(1 + \frac{3a^4}{r^4}\right)\cos 2\theta$$

$$\tau_{r\theta} = -\frac{\sigma_1 - \sigma_2}{2}\left(1 + \frac{2a^2}{r^2} - \frac{3a^4}{r^4}\right)\sin 2\theta$$

where

a is the conduit or tunnel radius
r is the distance from the center of the conduit ($r \leq a$)
θ varies from 0 deg in the direction of σ_1 and 90 deg in the direction σ_2
σ_1 is the greatest principle compressive stress, in the case of a conduit $\sigma_1 = \sigma_{\text{max, hort.}}$
σ_2 is the least principle compressive stress, in the case of a conduit $\sigma_2 = \sigma_{\text{min, hort}}$
σ_{rr} is the radial compressive stress
$\sigma_{\theta\theta}$ is the tangential compressive stress
$\tau_{r\theta}$ is the shear stress

So, tangential compressive stress is minimum along the σ_1 axis at the tunnel wall and is:

$$\sigma_{\theta\theta}=3\sigma_2 - \sigma_1$$

and the tangential compressive stress is at a maximum along the axis at the tunnel wall and is:

$$\sigma_{\theta\theta}=3\sigma_1 - \sigma_2$$

The magnitudes of displacements are also derived from the Kirsch solution assuming elastic behavior and are:

$$u_{rr}=\frac{\sigma_1+\sigma_2}{4G}\frac{a^2}{r} + \frac{\sigma_1-\sigma_2}{4G}\frac{a^2}{r}\left[4(1-\nu)-\frac{a^2}{r^2}\right]\cos 2\theta$$

and

$$u_{\theta\theta}= - \frac{\sigma_1-\sigma_2}{4G}\frac{a^2}{r}\left[2(1-2\nu)+\frac{a^2}{r^2}\right]\sin 2\theta$$

where

u_{rr} is the radial outward displacement
$u_{\theta\theta}$ is the tangential displacement
G is the shear modulus (aka modulus of rigidity)
ν is Poisson's ratio

for a typical host rock, Lister and Kerr (1990) use $G = 1 \times 10^{10}$ Pa (but Pollard, 1987 argues for a much lower value - 1×10^9 Pa , and $\nu = 0.25$.

If the magma pressure in the conduit is p_f, then an additional stress of magnitude p_f is added everywhere around the conduit wall. In order for a new tensile fracture to form, the tensile stress along the $\sigma 1$ axis (where tangential compressive stress is minimum) must equal the uniaxial tensile strength of the rock, T_o, and

$$p_f = T_o + 3\sigma_2 - \sigma_1$$

where

p_f is the fluid pressure in the conduit (adding a $-p_f$ tensile stress everywhere on the conduit wall)
T_o is the tensile strength of the rock. Note that if the rock is already jointed then the effective tensile strength is reduced by some factor.

For a horizontal tunnel in NTS tuff trending perpendicular to the regional maximum horizontal compressive stress at 300 m depth:

$\sigma 1 = \rho gh = 2600 \times 9.8 \times 300 = 7.6 \times 10^6$ Pa
$\sigma 2 = 5.5 \times 10^6$ Pa.(in the YMR $\sigma 1{:}\sigma 2{:}\sigma 3 = 90{:}65{:}25$.)
$To = 1 \times 10^6$ Pa
and
$p_f = 9.9 \times 10^6$ Pa to form a vertical fracture along the length of the roof of the tunnel trending perpendicular to the regional maximum horizontal compressive stress.

For a horizontal tunnel in NTS tuff trending perpendicular to the regional minimum horizontal compressive stress at 300 m depth:

$\sigma 1 = \rho gh = 2600 \times 9.8 \times 300 = 7.6 \times 10^6$ Pa
$\sigma 2 = 2.1 \times 10^6$ Pa.
$To = 1 \times 10^6$ Pa
and
$p_f = -2.5 \times 10^5$ Pa to form a vertical fracture along the length of the roof of the tunnel trending perpendicular to the regional minimum horizontal compressive stress. The negative value for p_f in this case means that tensile fractures will likely already exist in a tunnel trending perpendicular to the regional minimum horizontal compressive stress (roughly N25E in the YMR); therefore the magma will not need excess fluid pressure to form these fractures.

Note that sill formation is less likely because $\sigma 1 \gg \sigma 2$ in YM at repository depths and in order to propagate the horizontal fracture $p_f > \sigma 1 + To$.

The next question is what kinds of magma driving pressures are required to open a conduit to the surface along the length of the tunnel. Pollard (1987) uses the relationship:

where

$$\frac{t}{l} \approx \frac{P-S}{G/(1-\nu)}$$

t is the dike thickness
l is the dike length (in this case equal to the length of the tunnel)
P-S is the driving pressure
G is the shear modulus
ν is Poisson's ratio

Assume that the tunnel is1 km long, G is 1×10^9 Pa, and $\nu = 0.25$. For a one-meter-wide dike to propagate to the surface, the driving pressure (P-S) = 1.3×10^6 Pa. This result is highly dependent on a value of G, which could be as high as 1×10^{10} Pa, indicating that 1×10^6 Pa.< (P-S) < 1×10^7 Pa. This suggests that a fluid pressure of at least 3 MPa is needed to form a 1-m-wide dike along the length of the tunnel trending perpendicular to the least horizontal compressive stress and at least 5-6 MPa is needed to form a 1-m-wide dike along the length of the tunnel trending perpendicular to the maximum horizontal compressive stress, but these fluid pressures might need to be one order of magnitude higher depending on the value assumed for the shear modulus.

These overpressures are, naturally enough, on the same order as those required to initiate dike propagation from great depth and are greater than or comparable to the overpressures required to initiate hydrofracturing of the tunnel roof based on the Kirsch solution. This suggests that if (i) most or all of the magma in the dike is redirected into the tunnels, and (ii) a flow path into the repository is reestablished after the initial disruption associated with rapid magma acceleration in the tunnels and drainage of the dike, then dike injection may be initiated vertically above the tunnel along its entire length. For YM tunnels, vertical hydrofracturing in the tunnel roof is much more likely to occur in N-S trending tunnels but fluid pressures needed to initiate hydrofracturing in E-W -trending tunnels may also be reached. Given the comparatively shallow depth of the tunnels, exsolution of volatiles within the tunnel may also increase the fluid pressure available to inject a one-meter-wide dike to the surface.

Scientific Notebook
20-1402-461

Nov. 1998
ChuckConnor

"Entires into Scientific Notebook No. 115E for the period _July, 1998_____ to _Nov., 1998____ have been made by _Chuck Connor
Nov. 4, 1998

"No original text entered into this Scientific Notebook has been removed."

SCIENTIFIC NOTEBOOK
115E

SCIENTIFIC NOTEBOOK 115E

BY

Charles B. Connor

Southwest Research Institute
Center for Nuclear Waste Regulatory Analyses
San Antonio, Texas

SCIENTIFIC NOTEBOOK 115E

CHUCK CONNOR

PROJECT

IGNEOUS ACTIVITY

PROJECT NUMBER 20-1402-462

October 1999 - January 2000

PARTS IN THIS NOTEBOOK:

Testing PVHA_YM
Complete Listing of PVHA_YM

Scientific Notebook
20-1402-461
Inititals: CC

Chuck Connor
Feb 5,1999

Testing PVHA_YM

A complete listing of the PVHA_YM code is included in the following pages of this notebook.

The SRD for PVHA_YM is included following this listing

General tests of the PVHA_YM html document

1. All hot links in the PVHA_YM document have been tested and verified to operate correctly

2. All source code is included directly in the PVHA_YM html document

3. All instructions are included in the PVHA_YM html document

4. Hot keys described in the PVHA_YM html document are found to operate as advertized.

5. A description of the methods is included in the PVHA_YM html document

6. Shown to function correctly using Netscape browser version 4.5 for Linux, 4.6 for windows, and Explorer for Windows

Testing Applet Prob1Graph

1) functions with data sets 1,2,3,4,5 - if another integer is added the map is blank. Data sets are the data sets described in the text. If a noninteger is added, the code rounds to the nearest integer. If that integer corresponds to a valid data set, then that data set is plotted, otherwise the map is blank. The map is drawn blank for negative and 0 entries in the data set field. This is acceptable.

2) changing the Easting and Northing changes the probability as anticipated. See math calculations in the following. Entering 0 or negative number results in a blank graph. This is acceptable.

3. Hmin functions as advertized. Entering a number less the 0 (not reasonable) causes default of hmin to zero value, this is acceptable.

4. Hmax functions as advertized. Entering a number less than hmin results in a default value slightly greater than hmin. This result is acceptable. Hmax tested with input up to 2e9 and works correctly.

5. Effective area tested with numerous values and appears to work correctly. Entering 0 or negative effective area results in blank graph.

6.Time interval tested with numerous values and appears to work correctly. Entering 0 or negative effective area results in blank graph.

7. Recurrence rate tested with numerous values and appears to work correctly. Entering 0 or negative effective area results in blank graph. Using a very high recurrence rate results in a probability = 1 for h, this is correct.

Testing Applet Prob2Graph

Note: results the same as for Prob1Graph

1) functions with data sets 1,2,3,4,5 - if another integer is added the map is blank. Data sets are the data sets described in the text. If a noninteger is added, the code rounds to the nearest integer. If that integer corresponds to a valid data set, then that data set is plotted, otherwise the map is blank. The map is drawn blank for negative and 0 entries in the data set field. This is acceptable.

2) changing the Easting and Northing changes the probability as anticipated. See math calculations in the following. Entering 0 or negative number results in a blank graph. This is acceptable.

3. Hmin functions as advertized. Entering a number less the 0 (not reasonable) causes default of hmin to zero value, this is acceptable.

4. Hmax functions as advertized. Entering a number less than hmin results in a default

value slightly greater than hmin. This result is acceptable. Hmax tested with input up to 2e9 and works correctly.

5. Effective area tested with numerous values and appears to work correctly. Entering 0 or negative effective area results in blank graph.

6.Time interval tested with numerous values and appears to work correctly. Entering 0 or negative effective area results in blank graph.

7. Recurrence rate tested with numerous values and appears to work correctly. Entering 0 or negative effective area results in blank graph. Using a very high recurrence rate results in a probability = 1 for h, this is correct.

Testing Applet ProbMap1

1) functions with data sets 1,2,3,4,5 - if another integer is added the map is blank. If a noninteger is added, the code rounds to the nearest integer. If that integer corresponds to a valid data set, then that data set is plotted, otherwise the map is blank. The map is drawn blank for negative and 0 entries in the data set field. This is acceptable.

2) the number of contours is drawn correctly. If a noninteger 0, or negative number is added, the map simply does not update. An error message appears in the java console or at the bottom of the netscape window if an invalid number is entered. The program does not crash. This is acceptable.

3) The smoothing factor changes the map distribution appropriately (see tests for the math in the following). Negative and zero values for the smoothing factor result in a blank map. This is acceptable.

4) The X and Y grid dimensions were tested using values from 2 to 256 and functions correctly. Program is very slow at 256 x 256 grid point calculations. Also tested with unequal values of X and Y grid dimension and shown to function correctly. At large X and Y grid dimensions (256 x 256) label density is a bit high. If negative number or zero is entered, the map does not update and an error message appears in the bottom of the browser window and in the java console. The is acceptable.

5) Min, and Max easting and northing values are found to function correctly. Invalid entries result in an error message. Note, theses values only change the grid, not the map dimensions, use the hot keys to change the map dimensions. This is acceptable.

Testing Applet ProbMap2

Note: results identical to ProbMap1

1) functions with data sets 1,2,3,4,5 - if another integer is added the map is blank. If a noninteger is added, the code rounds to the nearest integer. If that integer corresponds to a valid data set, then that data set is plotted, otherwise the map is blank. The map is drawn blank for negative and 0 entries in the data set field. This is acceptable.

2) the number of contours is drawn correctly. If a noninteger 0, or negative number is added, the map simply does not update. An error message appears in the java console or at the bottom of the netscape window if an invalid number is entered. The program does not crash. This is acceptable.

3) The smoothing factor changes the map distribution appropriately (see tests for the math in the following). Negative and zero values for the smoothing factor result in a blank map. This is acceptable.

4) The X and Y grid dimensions were tested using values from 2 to 256 and functions correctly. Program is very slow at 256 x 256 grid point calculations. Also tested with unequal values of X and Y grid dimension and shown to function correctly. At large X and Y grid dimensions (256 x 256) label density is a bit high. If negative number or zero is entered, the map does not update and an error message appears in the bottom of the browser window and in the java console. The is acceptable.

5) Min, and Max easting and northing values are found to function correctly. Invalid entries result in an error message. Note, theses values only change the grid, not the map dimensions, use the hot keys to change the map dimensions. This is acceptable.

Testing the Math

coordinates of volcanoes:

Scientific Notebook
20-1402-461
Inititals: CC

Chuck Connor
Feb 5,1999

Lathrop: 543780, 4060380

Hidden Cone: 523400, 4112600

Red Cone: 537580, 4071880

Repo: 548500, 4078500

using the cursor (hot key c) these coordinates are also ided by the mapping applets.

Distance Lathrop - Repo = 18.72 km
Distance Hidden Cone - repo = 42.34 km
Distance Red Cone- repo = 12.77 km

the above distances check, using a gaussian kernel and smoothing factor = 40 km,

ku1 = 0.1426
ku2 = 0.09089
ku3 = 0.15124

so lambda(s) using a gaussian kernel, smoothing distance = 40 km, and data set 4 = 8e-05, this is correct

using A = 8, lambda(t) = 10e-06, and t = 10,000, lambda(s) = 8e-05

P = 6.4e-05 -> same answer determined by Prob1Graph code

on ProbMap1, 8e-05 is what plots at repo location for smoothing factor = 40 km

For Epanechnikov kernel (Prob2Graph, ProbMap2), and smoothing factor = 40 km, data set = 4:

ku1 = 0.49718
ku2 = 0
ku3 = 0.5717

using A = 8, lambda(t) = 10e-06, and t = 10,000, lambda(s) = 2.2e-04

Chuck Connor
Feb 5,1999

P = 1.78e-04 -> same answer as the Prob2Graph code
of ProbMap2, 2.2e-04 plots at the repo location for smoothing factor = 40 km.

The following plots illustrate these results

Additional tests were performed by calculating maps at different smoothing intervals

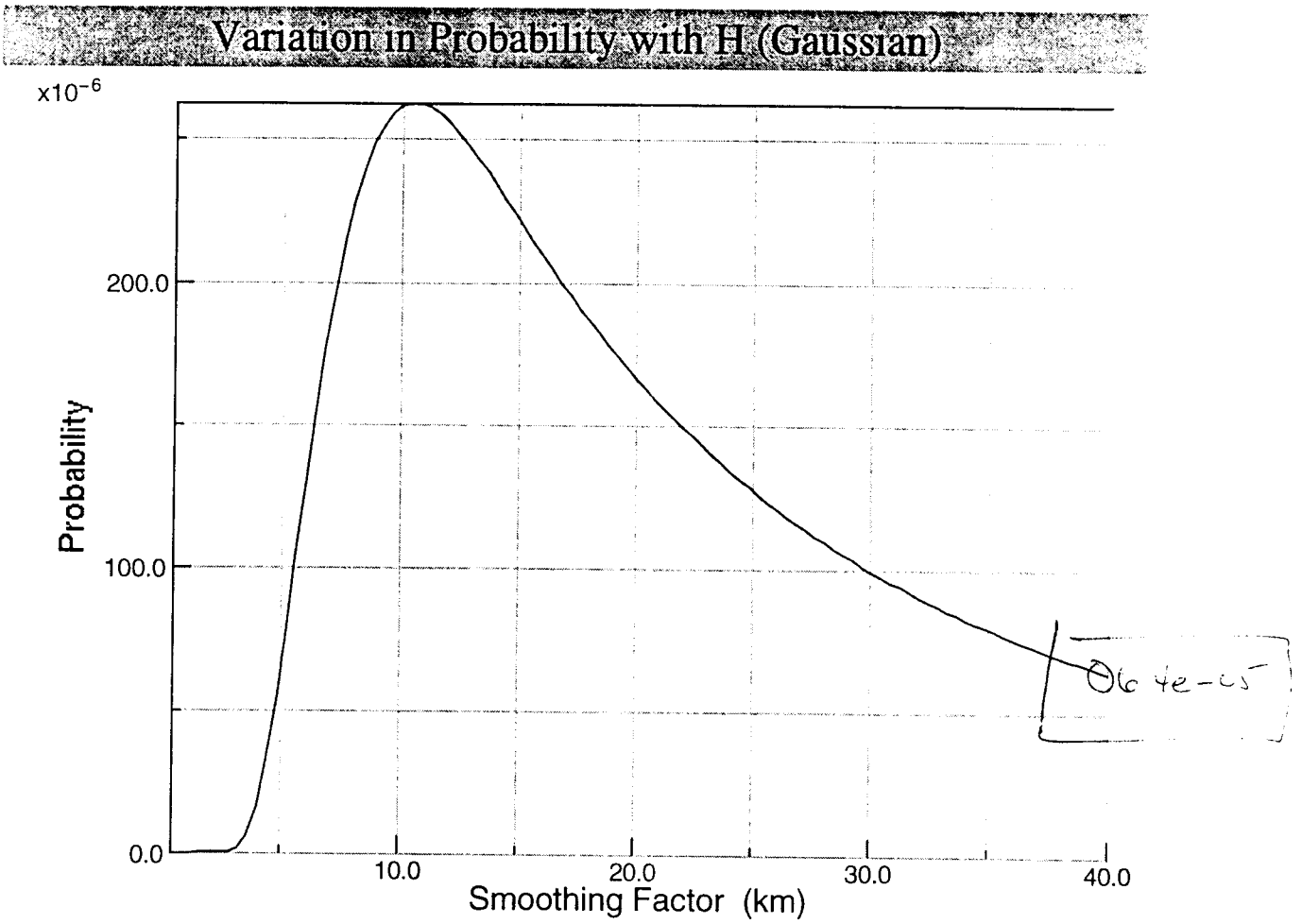
Variation in Probability with H (Gaussian)
x10⁻⁶
200.0
100.0
0.0
Probability
10.0
20.0
30.0
40.0
Smoothing Factor (km)
Data Set (1–5)
4
Calculate
Easting
548500.0
Northing
4078500.0
hmin
0.0
hmax
40.0
Effective Area
8.0
Time Interval
10000.0
Recurrence Rate
10.0e–6

Gaussian Probability Map

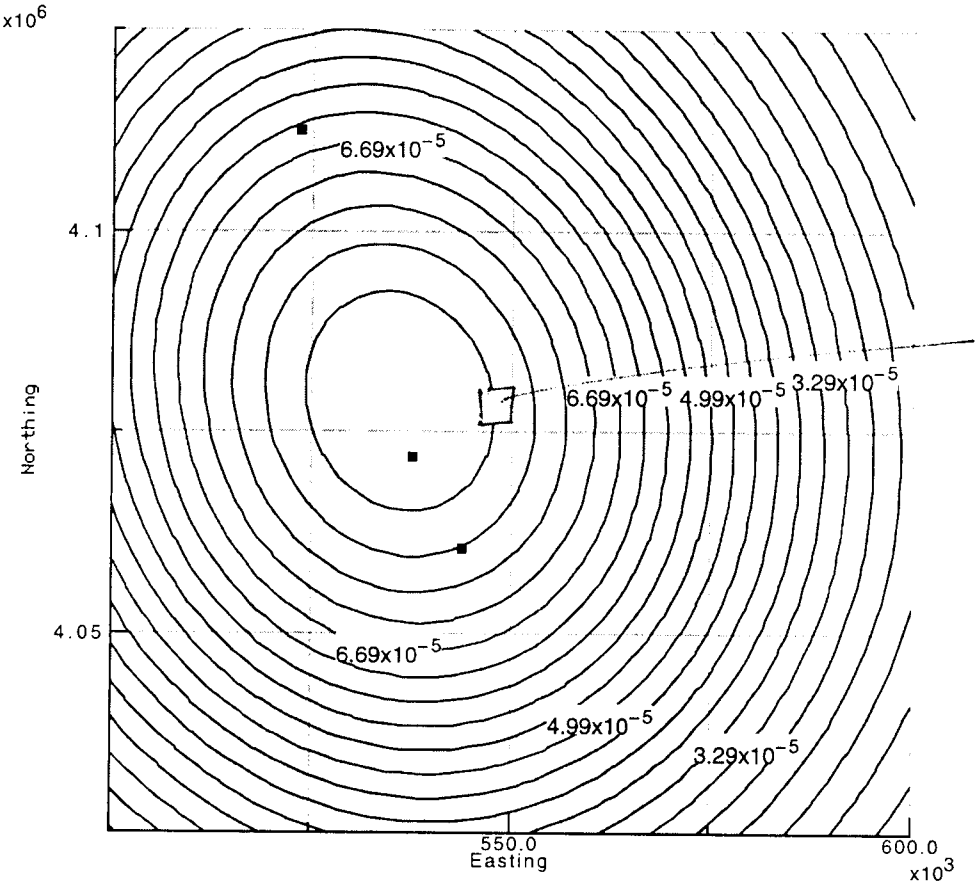

Data Set (1–5)	4	Calculate	
Number of Contours	20	Smoothing Factor (km)	40.0
X grid dimension	50	Y grid dimension	50
Minimum Easting	500000.0	Maximum Easting	600000.0
Minimum Northing	4025000.0	Maximum Northing	4125000.0

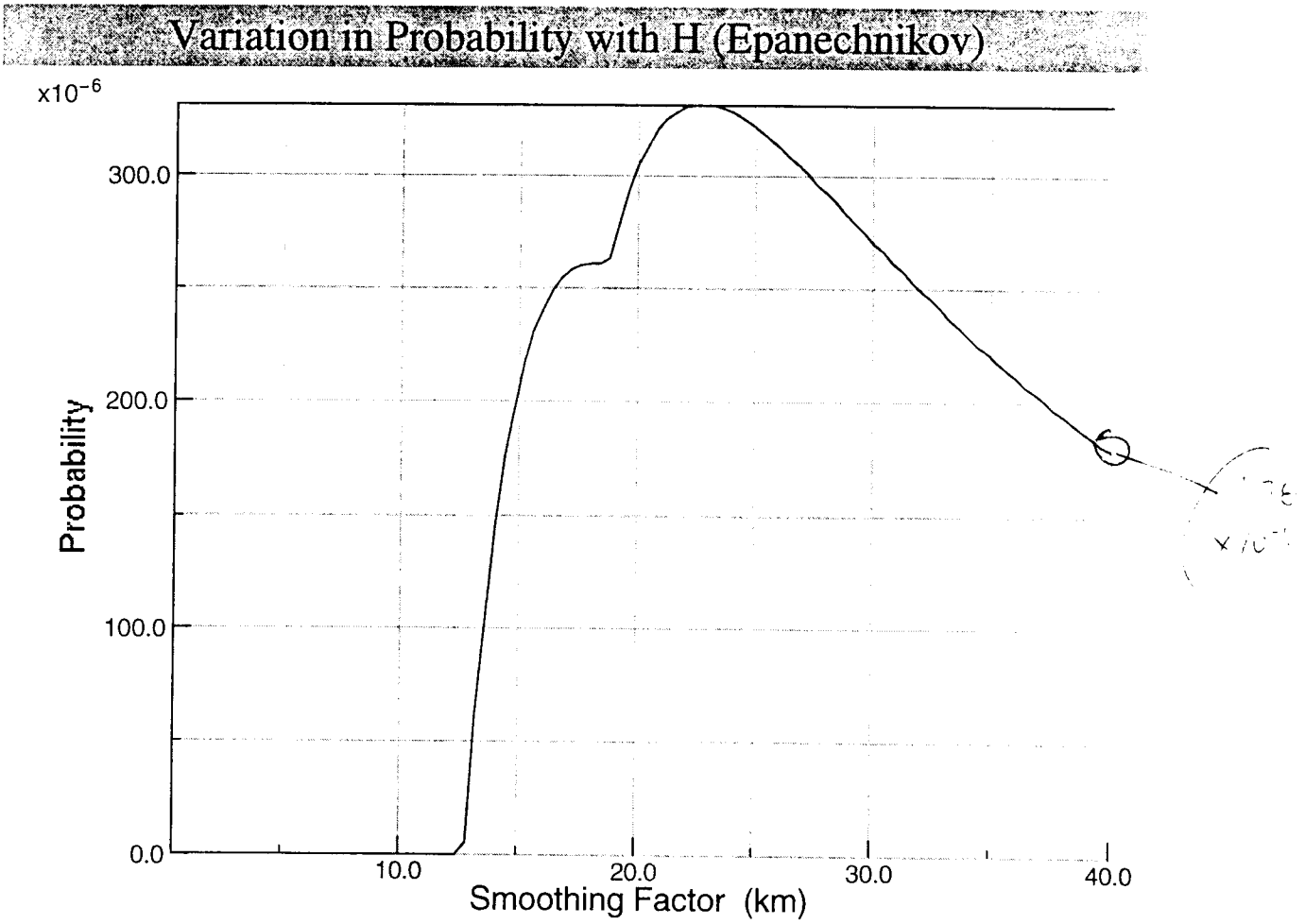

Data Set (1–5)	4	Calculate	
Easting	548500.0	Northing	4078500.0
hmin	0.0	hmax	40.0
Effective Area	8.0	Time Interval	10000.0
Recurrence Rate	10.0e-6		

Epanechnikov Probability Map

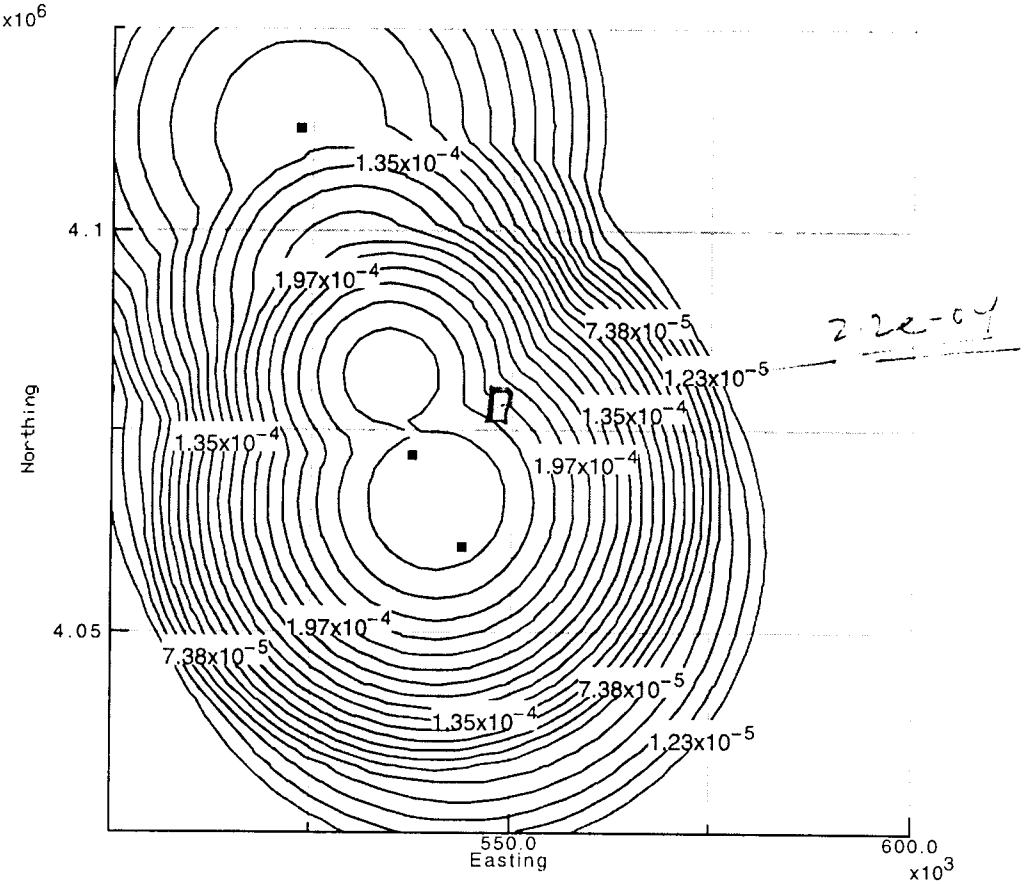

2.2e-04

Data Set (1–5)	4	Calculate	
Number of Contours	20	Smoothing Factor (km)	40
X grid dimension	50	Y grid dimension	50
Minimum Easting	500000.0	Maximum Easting	600000.0
Minimum Northing	4025000.0	Maximum Northing	4125000.0

PVHA_YM version 1.0 - Probabilistic Volcanic Hazard Assessment Methods for a Proposed High-Level Radioactive Waste Repository at Yucca Mountain, Nevada

---

Prepared for

Nuclear Regulatory Commission

Contract NRC-02-97-009

Prepared by

Charles B. Connor

Center For Nuclear Waste Regulatory Analyses

San Antonio, Texas

February, 2000

Abstract

The assessment of long-term performance of the proposed high-level radioactive waste repository at Yucca Mountain, Nevada, requires the use of mathematical models to consider the probability of disruptive scenarios. Volcanism is one important disruptive scenario to consider in site evaluation. The purpose of the PVHA_YM software is to provide and document mathematical models developed to assist staff in the probabilistic volcanic hazards assessment (PVHA) of the Yucca Mountain site.

PVHA_YM includes java applets that can be used to estimate the probability of a volcanic event

occurring within a effective area about the repository using kernel density estimators to smooth the point pattern map distribution of previous volcanic events in the region. Two types of kernel density estimators are included: Gaussian and Epanechnikov. These density estimators are used to estimate the probability of volcanic events at the site, and to plot conditional probability maps of the location of volcanic events, given a volcanic event in the magmatic system. Articles are provided that provide an overview of basaltic volcanism, summarize the application of kernel density estimators to the Yucca Mountain PVHA, and illustrate their application in analogous volcanic fields.

Table of Contents

Acknowledgments

This report was prepared to document work performed by the Center for Nuclear Waste Regulatory Analyses (CNWRA) for the U.S. Nuclear Regulatory Commission (NRC) under Contract No. NRC-02-97-009. The activities reported were performed on behalf of the U.S. NRC Office of Nuclear Material Safety and Safeguards, Division of Waste Management. This report is an independent product of the CNWRA and does not necessarily reflect the views or regulatory position of the NRC.

The author thanks the following individuals for their contributions to CNWRA research on PVHA at Yucca Mountain: Britt Hill, John Stamatakos, David Ferrill, Peter LaFemina, Michael Conway, Goodluck Ofoegbu, Ron Martin, Budhi Sagar, John Trapp, Chris Condit. Britt Hill compiled the data presented in the Data Table. The class "graph" used in PVHA_YM is modified from code developed and freely distributed by Leigh Brookshaw, under the GNU licensing agreement. Technical reviews were performed by Peter La Femina, Randy Folck, and H. Lawrence McKague. Programmatic review was

performed by Wesley Patrick. The efforts of all of these individuals are gratefully acknowledged.

Quality of Data, Analyses and Code Development

Data: No CNWRA-generated original data are contained in this report. Sources for other data should be consulted for determining the level of quality for those data.

Codes: The PVHA code Version 1.0, including the java applets ProbGraph1, ProbGraph2, ProbMap1, and ProbMap2, has been developed following the procedures described in the CNWRA Technical Operating Procedure (TOP) - 18, Development and Control of Scientific and Engineering Software, which implements the quality assurance (QA) guidance contained in CNWRA QA manual.

return to top
return to Table of Contents

Overview of PVHA_YM

The purpose of this document is to present codes and procedures used by Center for Nuclear Waste Regulatory Analyses (CNWRA) staff to perform a probabilistic volcanic hazard assessment (PVHA) for the proposed high-level radioactive waste repository at Yucca Mountain, Nevada. Volcanic hazards at the proposed Yucca Mountain site stem from the proximity of Yucca Mountain to small-volume basaltic volcanoes [Figure 1, Map showing the distribution of volcanoes in the area].

This document includes several articles that describe the geologic and statistical basis for the PVHA. The PVHA relies on the distribution and ages of these basaltic volcanoes as indictors of the expected rate of volcanic activity and the expected distribution of future volcanic events in the Yucca Mountain region.

Four computer programs (java applets) are used to estimate the probability of volcanic eruptions at the site using Gaussian and Epanechnikov kernels, and to create maps of the probable distribution of future volcanic events using the same two kernels. Complete listings of the source codes, and instructions in the use of these codes, are provided.

return to top
return to Table of Contents

Definition of Volcanic Events

It is crucial to define volcanic events explicitly in PVHA. In this PVHA for the Yucca Mountain site, we have limited our definition of a volcanic event to extrusive eruptions that result in the formation of basaltic vents as indicated by cinder cones, spatter mounds, and / or lava flows. A complete compilation of basaltic vents in the Yucca Mountain region is provided in the Data Table. Estimates of the probability of dike injection, without volcanic activity, are not considered explicitly in this PVHA.

Even using this restricted definition, it is possible to define volcanic events in various ways. Individual vents can be considered to be volcanic events, or closely spaced and similarly aged vents can be grouped together. Furthermore, only cones younger than a specific age might be included in the analysis as volcanic events. Therefore, the following data sets were defined:

Data set 1 includes known Miocene through Quaternary vents mapped in the Yucca Mountain region, including several magnetic anomalies, assumed to be Miocene or younger in age, that have not been drilled. See the data table for details. This data set does not include some petrologically distinct basalts of Miocene age, such as the 11.2 Ma Solitario Canyon dike. Number of volcanic events is 47 in data set 1. An average regional reccurence rate for this data set is approximately 5e-06 events per year. See the Data Table for details.

Data set 2 includes all known Pliocene - Quaternary vents mapped in the Yucca Mountain region, including several magnetic anomalies, assumed to be Miocene or younger in age, that have not been drilled. Several closely spaced vents have been grouped, and are treated as single volcanic events. For example, the two Little Cones are treated as a single volcanic event in this data set. Number of volcanic events is 20 in data set 2. An average regional recurrence rate for this data set is approximately 6e-06 volcanic events per year. See the Data Table for details.

Data set 3 includes all known Quaternary vents mapped in the Yucca Mountain region. Magnetic anomalies are not included in this data set. Number of volcanic events is 8 in data set 3. An average regional recurrence rate for data set 3 is 8e-06 volcanic events per year. See the Data Table for details.

Data set 4 includes three events. These are the Quaternary Crater Flat volcano alignment , taken as centered on Red Cone, the Sleeping Butte alignment, taken as centered on Hidden Cone, and Lathrop Wells. An average recurrence rate for this data set is 3e-06 volcanic events per year. See the Data Table for details.

Data set 5 includes all of the vent locations reported in the Data Table. Number of volcanic events is 64 in data set 5. An avarge recurrence rate for this data set is 6e-06 volcanic events per year.

return to top
return to Table of Contents

Basis for the PVHA

The Geologic and statistical basis for the PVHA for the Yucca Mountain site is provided in Connor and Hill [1995] and Connor et al. [2000] (see Articles). Briefly, kernel density estimators are used to estimate a probability surface directly from the location and timing of past, discrete volcanic events. As a result, kernel estimators are sensitive to patterns, such as vent clustering, commonly observed in basaltic volcano distributions. Furthermore, the resulting probability surfaces do not have the abrupt changes in probability that must be introduced in spatially homogeneous Poisson models. Thus, the kernel methods eliminate the need to define zones of volcanic activity a priori.

Two types of kernel density functions are provided: Gaussian and Epanechnikov kernels.

The Gaussian kernel is defined as:

$$ki = 2\ pi\ exp[-1/2\ (di/h)^2]$$

where di is the distance from the point s to the ith volcano and h is the smoothing parameter.

The Epanechnikov kernel is defined as:

$$ki = (2/pi)[1 - (di/h)^2],\ if\ (di/h)^2 < 1\ and$$

$$ki = 0,\ otherwise$$

In each case, the spatial recurrence rate of volcanic events in the 1 x 1 km area about the point s, given a volcanic event in the system is given by:

$$lambda(s) = 1/(nh^2)\ Sum\ \{from\ i=1\ to\ n\}\ ki.$$

The probability of a volcanic events within the area of the repository site is then:

$$P[N=>1] = 1 - exp[-t\ lambda(t)\ sum\ \{over\ area\ a\}lambda(s)\ ]$$

where t is the time interval of interest, lambda(t) is the temporal recurrence rate of volcanic events in the magmatic system, and a is the effective area, an area within which a volcanic event might occur and disrupt the repository.

Assuming that lambda(s) does not vary on the scale of the repository:

$$P[N=>1] = 1 - exp[-t\ lambda(t)\ a\ lambda(s)\ ]$$

These techniques have been tested using the recurrence rates of volcanism and patterns of volcanic activity in other volcanic fields. In particular, these models have been tested in the Springerville volcanic field, Arizona [See Articles]. An introduction to basaltic volcanic fields is given in Connor and Conway [2000] (see Articles).

return to top
return to Table of Contents

Applets

PVHA_YM calculations are performed using the following java applets.

ProbGraph1: calculates the probability of a volcanic event in an effective area about the repository, given a temporal recurrence rate, time interval of interest, and selected data set. Estimate uses a Gaussian kernel and plots probability as a function of the smoothing parameter.

ProbGraph2: calculates the probability of a volcanic event in an effective area about the repository,

given a temporal recurrence rate, time interval of interest, and selected data set. Estimate uses an Epanechnikov kernel and plots probability as a function of the smoothing parameter.

ProbMap1: calculates the probability surface for the Yucca Mountain region using a selected data set and smoothing parameter. Estimate uses a Gaussian kernel and plots the conditional probability of a volcanic event within a 1 x 1 km area, given an event in the magmatic system.

ProbMap2: calculates the probability surface for the Yucca Mountain region using a selected data set and smoothing parameter. Estimate uses an Epanechnikov kernel and plots the conditional probability of a volcanic event within a 1 x 1 km area, given an event in the magmatic system.

return to top
return to Table of Contents

Articles

Two articles are included in this document that describe the development of kernel density estimators and their application to the CNWRA PVHA for Yucca Mountain. These articles are:

> Connor et al., 2000, Geologic Factors controlling patterns of small volume basaltic volcanism: Application to a volcanic hazards assessment at Yucca Mountain, Nevada
>
> Connor and Hill, 1995, Three nonhomogeneous Poisson models for the probability of basaltic volcanism: Application to Yucca Mountain, Nevada

Application of PVHA techniques to analogous basaltic volcanic fields, for the purposes of validating the use of density kernels in PVHA, is described in:

> Condit and Connor, 1996, Recurrence rates of basaltic volcanism: An example from the Springerville volcanic field, Arizona.

An introduction to basaltic volcanic fields is provided in:

> Connor and Conway, 2000, Basaltic volcanic fields.

The intent of this article is to provide background on the nature of basaltic volcanic fields, their physical characteristics, evolution, and origins.

return to top
return to Table of Contents

Code Limitations

PVHA_YM contains codes used to estimate probabilities of volcanic events within the area of the proposed Yucca Mountain repository. Nevertheless, a complete PVHA analyses for the proposed repository can not be accomplished using PVHA_YM alone. For example, Connor et al. [2000] (See Articles) showed that geologic structure plays an important role in controlling the distribution of basaltic volcanism in the Yucca Mountain region. The affect of geologic structure is to increase the probability of volcanic disruption of the site. The influence of geologic structure is not incorporated in version 1.0 of PVHA_YM. Furthermore, volcanic events may effect a larger area than represented by a single vent. In basaltic volcanic fields, volcanic events may be defined as volcanic alignments, with length and orientation. For example, in Data set 4, the Quaternary Crater Flat alignment is treated as a single volcanic event. The areal dimension of volcanic events is not incorporated explicitly in version 1.0 of PVHA_YM, although the effective area parameter may be changed to help illustrate the influence of event area on probability estimates.

return to top
return to Table of Contents

Source Codes for PVHA_YM

PVHA_YM is written in HTML and Java.

To View the HTML source in your web browser, simply choose View Source from the menu at any time.

The java applets are organized in the following fashion:

Hestimate.java is the calculation engine for the probability graphs

Restimate.java is the calculation engine for the probability maps

Prob1Graph.java calculates a Gaussian probability graph, calling Hestimate.java

Prob2Graph.java calculates an Epanechnikov probability graph, calling Hestimate.java

ProbMap1.java calculates a Gaussian probability map calling Restimate.java

ProbMap2.java calculates an Epanechnikov probability map calling Restimate.java

These routines use classes in the "graph" package, including:

ContourProb.java plots the volcano locations and repository outline, as well as the underlying contours

Volcano.java contains the volcano location data sets used by the above applets

The graphing in PVHA_YM utilizes the Java2D Graph package version 2.4, written and freely distributed under the GNU licensing agreement by Leigh Brookshaw. The Graph class library is a package of Java classes designed to facilitate plotting data using Java applets. This graphing package is currently available at:

http://www.sci.usq.edu.au/staff/leighb/graph/

```
import java.io.*;
import java.math.*;
/*
**************************************************************************
**
**    Class  Hestimate
**
**************************************************************************
**
by Chuck Connor
Center for Nuclear Waste Regulatory Analyses
Southwest Research Institute
6220 Culebra Rd
San Antonio Texas. 78238-5166, USA
cconnor@swri.edu

Created: September, 1999

Purpose:
 *Class to estimate the spatial recurrence rate
 * aka the spatial weighting factor or spatial
 * intensity, for a given volcano distribution
 * originally written in TrueBasic by Chuck Connor (1993)
 * translated to Java by Chuck Connor (1999)
 *
 * Contact
 * Chuck Connor
 * CNWRA, Southwest Research Inst.
 * 6220 Culebra Rd
 * San Antonio, Tx, 78238-5166, USA
 * e-mail: cconnor@swri.org
 *
 * For more details about the algorithm used in this
 * class, see Connor and Hill, 1995, Journal of
 * Geophysical Research, 100 (B6) 10,107-10,125.
**************************************************************************
 **/

public class Hestimate {
    public double repox, repoy, nvolcanoes;

    /** where repox and repoy are the coordinates of the
        point for which the calculation is done (assumed to be
        in Universal Transverse Mercator coordinates / meters),
        nvolcanoes is the number of volcanoes
    **/

    public Hestimate(double repox, double repoy, int nvolcanoes) {

        this.repox = repox;
        this.repoy = repoy;
        this.nvolcanoes = nvolcanoes;


    }

    public double gaussh (double []vs, double smoothing_factor) {

        /** This method calculates the value of lambda
            for a given smoothing factor (h) using a gaussian
            kernel function.
```

```
            Pass this method the single dimensional array s,
            containing the point locations of the volcanoes in Universal
            Transverse Mercator coordinates (meters). The format of
            array s is: x1,y1,x2,y2,x3,y3,....,xn,yn. Also pass the value
            of the smoothing factor, also assumed to have unis of
            meters.

            The method returns the value of lambda in units
            ************   1/ km^2 ****************
            about the point repox,repoy,for the given data
            set, and smoothing factor (h).

        **/

        // let h be the smoothing factor in km

        double h = smoothing_factor;
        double dist1, dist2;
        double kuu, sumn;
        double lambda;

        int i;

        // make sure the summation is now zero
        sumn = 0.0;

double xcenter = repox/1000.0;
double ycenter = repoy/1000.0;

        for (i = 0;  i< 2*nvolcanoes; i+=2) {

            // for each volcano calculate distance^2 to repox,repoy (now converted t
            dist1 = (xcenter - vs[i]/1000.0)* (xcenter - vs[i]/1000.0) + (ycenter- v
            dist2 = dist1/(h*h);

            // use the Gaussian kernel
            kuu = 1/(2*Math.PI) * Math.exp(-0.5*dist2);
                sumn +=  (1.0/(h*h))* kuu;
                }
        //estimate lambda in 1/km^2
        lambda = sumn/(double) nvolcanoes;

        return lambda;
    } // end of the method gaussh

    public double epanh (double []vs, double smoothing_factor) {

        /** This method calculates the value of lambda
            for a given smoothing factor (h) using an
            Epanechnikov kernel function.

            Pass this method the single dimensional array s,
            containing the point locations of the volcanoes in Universal
            Transverse Mercator coordinates (meters). The format of
            array s is: x1,y1,x2,y2,x3,y3,....,xn,yn. Also pass the value
            of the smoothing factor, also assumed to have unis of
            meters.

            The method returns the value of lambda in units
            ************   1/ km^2 ****************
```

```
            about the point repox,repoy,for the given data
            set, and smoothing factor (h).

        **/

        // let h be the smoothing factor in km

        double h = smoothing_factor;
        double dist1, dist2;
        double kuu, sumn;
        double lambda;

        int i;

        // make sure the summation is now zero
        sumn = 0.0;

        double xcenter = repox/1000.0;
        double ycenter = repoy/1000.0;

        for (i = 0;  i< 2*nvolcanoes; i+=2) {

            // for each volcano calculate distance^2 to repox,repoy (now converted t
            dist1 = (xcenter - vs[i]/1000.0)* (xcenter - vs[i]/1000.0) + (ycenter- v
            dist2 = dist1/(h*h);

            // use the Epanechnikov kernel
            if (dist2 < 1.0) {
                kuu = (2.0/Math.PI)*(1.0 - dist2);
                sumn +=  (1.0/(h*h))* kuu;
            }
        }
        //estimate lambda in 1/km^2
        lambda = sumn/(double) nvolcanoes;

        return lambda;
    } // end of the method epanh

}
```

User: cconnor
Host: oso
Class: oso
Job: stdin

```
import java.io.*;
import java.math.*;
/*
**************************************************************************
**
**    Class  Restimate
**
**************************************************************************
**
by Chuck Connor
Center for Nuclear Waste Regulatory Analyses
Southwest Research Institute
6220 Culebra Rd
San Antonio Texas. 78238-5166, USA
cconnor@swri.edu

Created: September, 1999

Purpose:
 *Class to estimate the spatial recurrence rate
 * aka the spatial weighting factor or spatial
 * intensity, for a given volcano distribution
 * results to be plotted on a map
 * originally written in TrueBasic by Chuck Connor (1993)
 * translated to Java by Chuck Connor (1999)
 *
 * Contact
 * Chuck Connor
 * CNWRA, Southwest Research Inst.
 * 6220 Culebra Rd
 * San Antonio, Tx, 78238-5166, USA
 * e-mail: cconnor@swri.org
 *
 * For more details about the algorithm used in this
 * class, see Connor and Hill, 1995, Journal of
 * Geophysical Research, 100 (B6) 10,107-10,125.
**************************************************************************
 **/


public class Restimate {
    public double smoothing_factor, nvolcanoes;

    /** where smoothing_factor is given in kilometers,
        nvolcanoes is the number of volcanoes
    **/

    public Restimate(double smoothing_factor, int nvolcanoes) {

        this.smoothing_factor = smoothing_factor;
        this.nvolcanoes = nvolcanoes;


    }

    public double gaussh (double []vs, double x, double y) {

        /** This method calculates the value of lambda
            for a given smoothing factor (h) using a gaussian
            kernel function.
```

```
            Pass this method the single dimensional array vs,
            containing the point locations of the volcanoes in Universal
            Transverse Mercator coordinates (meters). The format of
            array s is: x1,y1,x2,y2,x3,y3,....,xn,yn. Also pass location for
            which the estimate is made (x,y) also in units of Universal
            Transverse Mectator coordinates (meters).

            The method returns the value of lambda in units
            ************   1/ km^2 ***************
            about the point x,y,for the given data
            set, and smoothing factor (h).

        **/

        // let h be the smoothing factor in km

        double h = smoothing_factor;
        double dist1, dist2;
        double kuu, sumn;
        double lambda;

        int i;

        // make sure the summation is now zero
        sumn = 0.0;

double xcenter = x/1000.0;
double ycenter = y/1000.0;

        for (i = 0;  i< 2*nvolcanoes; i+=2) {

            // for each volcano calculate distance^2 to repox,repoy (now converted t
            dist1 = (xcenter - vs[i]/1000.0)* (xcenter - vs[i]/1000.0) + (ycenter- v
            dist2 = dist1/(h*h);

            // use the Gaussian kernel
            kuu = 1/(2*Math.PI) * Math.exp(-0.5*dist2);
                sumn +=  (1.0/(h*h))* kuu;
                }
        //estimate lambda in 1/km^2
        lambda = sumn/(double) nvolcanoes;

        return lambda;
    } // end of the method gaussh

    public double epanh (double []vs, double x, double y) {
            /** This method calculates the value of lambda
            for a given smoothing factor (h) using an Epanechnikov
            kernel function.

            Pass this method the single dimensional array vs,
            containing the point locations of the volcanoes in Universal
            Transverse Mercator coordinates (meters). The format of
            array s is: x1,y1,x2,y2,x3,y3,....,xn,yn. Also pass location for
            which the estimate is made (x,y) also in units of Universal
            Transverse Mectator coordinates (meters).

            The method returns the value of lambda in units
            ************   1/ km^2 ***************
            about the point x,y,for the given data
            set, and smoothing factor (h).
```

```
        **/


        // let h be the smoothing factor in km

        double h = smoothing_factor;
        double dist1, dist2;
        double kuu, sumn;
        double lambda;

        int i;

        // make sure the summation is now zero
        sumn = 0.0;

        double xcenter = x/1000.0;
        double ycenter = y/1000.0;

        for (i = 0;  i< 2*nvolcanoes; i+=2) {

            // for each volcano calculate distance^2 to repox,repoy (now converted t
            dist1 = (xcenter - vs[i]/1000.0)* (xcenter - vs[i]/1000.0) + (ycenter- v
            dist2 = dist1/(h*h);

            // use the Epanechnikov kernel
            if (dist2 < 1.0) {
                kuu = (2.0/Math.PI)*(1.0 - dist2);
                sumn +=  (1.0/(h*h))* kuu;
            }
        }
        //estimate lambda in 1/km^2
        lambda = sumn/(double) nvolcanoes;

       return lambda;
    } // end of the method epanh

}
```

User: cconnor
Host: oso
Class: oso
Job: stdin

```
import java.awt.*;
import java.applet.*;

import graph.*;
import graph.Volcano;
/*
**************************************************************************
**
**                        Applet Prob1Graph
**
**************************************************************************

by Chuck Connor
Center for Nuclear Waste Regulatory Analyses
Southwest Research Institute
6220 Culebra Rd
San Antonio Texas. 78238-5166, USA
cconnor@swri.edu

Created: October, 1999

Based on code originally written in TrueBasic by C Connor, 1992-1994
Graphics portion of this code modified from code written by Leigh Brookshaw

Purpose:

**
**    This program calculates the probability of volcanic eruptions
**    in a given area
**    given input parameters using an Gaussian kernel.
**************************************************************************
*
* This applet uses the Hestimate class
* and plots the result.
*
**************************************************************************/

public class Prob1Graph extends Applet {

    G2Dint graph          = new G2Dint();   // Graph class to do the plotting
    Axis xaxis;
    Axis yaxis;
    DataSet data;
    Volcano volcano = new Volcano();

    TextField repoxinput     = new TextField(10);       // repository xlocation
    TextField repoyinput   = new TextField(10);      //repository y location
    TextField hmininput    = new TextField(10);      // min h input
    TextField hmaxinput      = new TextField(10);      // max h input
    TextField areainput      = new TextField(10);      // effective area input
    TextField timeinput      = new TextField(10);      // time interval input
    TextField recurinput      = new TextField(10);      // recurrence rate input
    TextField vdatainput      = new TextField(2);      // data set to plot

    Button plot           = new Button("Calculate"); // Button to plot it.


    public void init() {
        Label title = new Label("Variation in Probability with H (Gaussian)",
                                Label.CENTER);
        Panel panel             = new Panel();
```

```
GridBagLayout gridbag  = new GridBagLayout();
GridBagConstraints  c  = new GridBagConstraints();
Font font              = new Font("Helvetica",Font.PLAIN,14);

title.setFont(new Font("TimesRoman",Font.PLAIN,24));


setLayout(new BorderLayout() );
add("North",title);
add("Center",panel);

repoxinput.setText(getParameter("XLOC"));
repoyinput.setText(getParameter("YLOC"));
hmininput.setText(getParameter("HMIN"));
hmaxinput.setText(getParameter("HMAX"));
areainput.setText(getParameter("AREA"));
timeinput.setText(getParameter("TIME"));
recurinput.setText(getParameter("RECUR"));
vdatainput.setText(getParameter("DATASET"));

panel.setLayout(gridbag);

Label repoxlabel   = new Label("Easting");
Label repoylabel = new Label("Northing");
Label hminlabel = new Label("hmin");
Label hmaxlabel   = new Label("hmax");
Label arealabel   = new Label("Effective Area");
Label timelabel   = new Label("Time Interval");
Label recurlabel   = new Label("Recurrence Rate");
Label vdatalabel    = new Label("Data Set (1-5)");

repoxlabel.setFont(font);
repoylabel.setFont(font);
hminlabel.setFont(font);
hmaxlabel.setFont(font);
arealabel.setFont(font);
timelabel.setFont(font);
recurlabel.setFont(font);
vdatalabel.setFont(font);
repoxinput.setFont(font);
repoxinput.setBackground(Color.lightGray);
repoyinput.setFont(font);
repoyinput.setBackground(Color.lightGray);
hmininput.setFont(font);
hmininput.setBackground(Color.lightGray);
hmaxinput.setFont(font);
hmaxinput.setBackground(Color.lightGray);
areainput.setFont(font);
areainput.setBackground(Color.lightGray);
timeinput.setFont(font);
timeinput.setBackground(Color.lightGray);
recurinput.setFont(font);
recurinput.setBackground(Color.lightGray);
vdatainput.setFont(font);
vdatainput.setBackground(Color.lightGray);
plot.setFont(font);
plot.setBackground(Color.cyan);

 /*
 ** First row of the GridBag contains the plot
 */
```

```
c.weightx = 1.0;
c.weighty = 1.0;
c.gridwidth = 4;
c.gridwidth=GridBagConstraints.REMAINDER;
c.fill   =  GridBagConstraints.BOTH;

gridbag.setConstraints(graph,c);

/*
** Second row of the gridBag contains the function input and the
** plotit button
*/
c.fill   =  GridBagConstraints.NONE;
c.weightx=0.0;
c.weighty=0.0;
c.gridheight=1;

c.gridwidth=1;
c.anchor = GridBagConstraints.EAST;
gridbag.setConstraints(vdatalabel,c);

c.anchor = GridBagConstraints.WEST;
gridbag.setConstraints(vdatainput,c);

c.fill = GridBagConstraints.WEST;
c.gridwidth=GridBagConstraints.REMAINDER;

gridbag.setConstraints(plot,c);

 /*
 ** Third row contains the
 */
c.gridwidth=1;
c.anchor = GridBagConstraints.EAST;
gridbag.setConstraints(repoxlabel,c);

 c.anchor = GridBagConstraints.WEST;
 gridbag.setConstraints(repoxinput,c);

c.anchor = GridBagConstraints.EAST;
gridbag.setConstraints(repoylabel,c);

 c.anchor = GridBagConstraints.WEST;
 c.gridwidth=GridBagConstraints.REMAINDER;
 gridbag.setConstraints(repoyinput,c);

 /*
 ** Fourth row contains the
 */
 c.gridwidth=1;
 c.anchor = GridBagConstraints.EAST;
 gridbag.setConstraints(hminlabel,c);

 c.anchor = GridBagConstraints.WEST;
 gridbag.setConstraints(hmininput,c);

 c.anchor = GridBagConstraints.EAST;
 gridbag.setConstraints(hmaxlabel,c);

 c.anchor = GridBagConstraints.WEST;
 c.gridwidth=GridBagConstraints.REMAINDER;
```

```
 gridbag.setConstraints(hmaxinput,c);

 /*
 ** Fifth row contains the area and time interval of the grid
 */

 c.gridwidth=1;
 c.anchor = GridBagConstraints.EAST;
 gridbag.setConstraints(arealabel,c);

 c.anchor = GridBagConstraints.WEST;
 gridbag.setConstraints(areainput,c);

 c.anchor = GridBagConstraints.EAST;
 gridbag.setConstraints(timelabel,c);

 c.anchor = GridBagConstraints.WEST;
 c.gridwidth=GridBagConstraints.REMAINDER;
 gridbag.setConstraints(timeinput,c);


 /*
 ** Sixth row contains the recurrence rate of the grid
 */
 c.gridwidth=1;

 c.anchor = GridBagConstraints.EAST;
 gridbag.setConstraints(recurlabel,c);

 c.anchor = GridBagConstraints.WEST;
 c.gridwidth=GridBagConstraints.REMAINDER;
 gridbag.setConstraints(recurinput,c);

 // display the fields
panel.add(graph);
panel.add(vdatalabel);
panel.add(vdatainput);
panel.add(plot);

panel.add(repoxlabel);
panel.add(repoxinput);
panel.add(repoylabel);
panel.add(repoyinput);
panel.add(hminlabel);
panel.add(hmininput);
panel.add(hmaxlabel);
panel.add(hmaxinput);
panel.add(arealabel);
panel.add(areainput);
panel.add(timelabel);
panel.add(timeinput);
panel.add(recurlabel);
panel.add(recurinput);

//label the graph axes
xaxis = graph.createXAxis();
xaxis.setTitleText("Smoothing Factor  (km)");
xaxis.setTitleFont(new Font("Helvetica",Font.PLAIN,18));
xaxis.setLabelFont(new Font("Helvetica",Font.PLAIN,14));
```

```
        yaxis = graph.createYAxis();
        yaxis.setTitleText("Probability");
        yaxis.setTitleFont(new Font("Helvetica",Font.PLAIN,18));
        yaxis.setLabelFont(new Font("Helvetica",Font.PLAIN,14));


        data = new DataSet();

        xaxis.attachDataSet(data);
        yaxis.attachDataSet(data);
        graph.attachDataSet(data);

        graph.setDataBackground(new Color(230,240,240));
        graph.setBackground(new Color(240,250,250));

        plot();

    }



    void plot() {

        double repox, repoy, hmin, hmax, area, timeint, recur;
        int kount;
        int j;
        int setnum;
        double d[] = new double [200];
        boolean error = false;

        try {
            repox = Double.valueOf(repoxinput.getText()).doubleValue();
        } catch(Exception e) {
            this.showStatus("Error with x-location");
            System.out.println("x-location error "+e.getMessage());
            return;
        }

        try {
            repoy = Double.valueOf(repoyinput.getText()).doubleValue();
        } catch(Exception e) {
            this.showStatus("Error with y-location!");
            System.out.println("y location error "+e.getMessage());
            return;
        }
        try {
            setnum = Double.valueOf(vdatainput.getText()).intValue();
        } catch(Exception e) {
            this.showStatus("Illegal data set value: enter an integer!");
            System.out.println("Dataset error "+e.getMessage());
            return;
        }

        try {
            hmin = (Double.valueOf(hmininput.getText()).doubleValue());
        } catch(Exception e) {
            this.showStatus("Error with min smoothing factor");
            System.out.println("min smoothing factor error "+e.getMessage());
            return;
        }
        // illegal for hmin to be negative
```

```
if (hmin < 0.0) hmin = 0.0;

try {
    hmax = Double.valueOf(hmaxinput.getText()).doubleValue();
} catch(Exception e) {
    this.showStatus("Error with max smoothing factor");
    System.out.println("max smoothing factor error "+e.getMessage());
    return;
}

//illegal for hamx to be less than hmin
if (hmax < hmin) hmax = hmin+ 0.01;

try {
    area = Double.valueOf(areainput.getText()).doubleValue();
} catch(Exception e) {
    this.showStatus("Error with effective area");
    System.out.println("Effective area error "+e.getMessage());
    return;
}
// illegal for area to be negative
if (area < 0.0) area = 0.0;

try {
    timeint= Double.valueOf(timeinput.getText()).doubleValue();
} catch(Exception e) {
    this.showStatus("Error with time interval");
    System.out.println(" time interval error "+e.getMessage());
    return;
}
// illegal for timeint to be negative
if (timeint < 0.0) timeint = 0.0;

try {
    recur= Double.valueOf(recurinput.getText()).doubleValue();
} catch(Exception e) {
    this.showStatus("Error with recurrence interval");
    System.out.println(" recurrence interval error "+e.getMessage());
    return;
}
// illegal for recurto be negative
if (recur < 0.0) recur = 0.0;

//the volcano data set is determined from setnum
volcano.setVolcanoset(setnum);

// instantiate the volcanodata set
volcano.getVolcanoes();

Hestimate lambda1 = new Hestimate(repox, repoy, Volcano.nvolcanoes);

j =0;
int kountmax = 100;

for (kount=1; kount <= kountmax; kount++, j+=2) {
    try {

        d[j] = hmin + (hmax-hmin)/((double)kountmax) *(double)kount;
        d[j+1] = 1- Math.exp(-area*timeint*recur*lambda1.gaussh(Volcano.vs,
        System.out.println("h = " + d[j]);
        System.out.println("lambda = " + d[j+1]);
```

```
            } catch (Exception e) {error = true;}

        }


        data.deleteData();

        try {
            data.append(d,kountmax);
        } catch(Exception e) {
            this.showStatus("Error while appending data!");
            System.out.println("Error while appending data!");
            return;
        }


        graph.repaint();
    }



    public boolean action(Event e, Object a) {

        if(e.target instanceof Button) {
            if( plot.equals(e.target) ) {
                plot();
                return true;
            }
        }


         return false;
    }

}
```

User: cconnor
Host: oso
Class: oso
Job: stdin

```
import java.awt.*;
import java.applet.*;

import graph.*;
import graph.Volcano;
/*
**************************************************************************
**
**                        Applet Prob2Graph
**
**************************************************************************
**
by Chuck Connor
Center for Nuclear Waste Regulatory Analyses
Southwest Research Institute
6220 Culebra Rd
San Antonio Texas. 78238-5166, USA
cconnor@swri.edu

Created: October, 1999

Based on code originally written in TrueBasic by C Connor, 1992-1994
Graphics portion of this code modified from code written by Leigh Brookshaw

Purpose:

**
**    This program calculates the probability of volcanic eruptions
**    in a given area
**    given input parameters using an Epanechnikov kernel.
**************************************************************************
*
* This applet uses the Hestimate class
* and plots the result.
*
**************************************************************************/

public class Prob2Graph extends Applet {

    G2Dint graph          = new G2Dint();    // Graph class to do the plotting
    Axis xaxis;
    Axis yaxis;
    DataSet data;
    Volcano volcano = new Volcano();

    TextField repoxinput      = new TextField(10);        // repository xlocation
    TextField repoyinput    = new TextField(10);       //repository y location
    TextField hmininput    = new TextField(10);       // min h input
    TextField hmaxinput      = new TextField(10);       // max h input
    TextField areainput      = new TextField(10);       // effective area input
    TextField timeinput      = new TextField(10);       // time interval input
    TextField recurinput      = new TextField(10);       // recurrence rate input
    TextField vdatainput      = new TextField(2);       // data set to plot

    Button plot           = new Button("Calculate"); // Button to plot it.


    public void init() {
        Label title = new Label("Variation in Probability with H (Epanechnikov)",
                                Label.CENTER);
        Panel panel             = new Panel();
```

```
GridBagLayout gridbag  = new GridBagLayout();
GridBagConstraints  c  = new GridBagConstraints();
Font font              = new Font("Helvetica",Font.PLAIN,14);

title.setFont(new Font("TimesRoman",Font.PLAIN,24));


setLayout(new BorderLayout() );
add("North",title);
add("Center",panel);

repoxinput.setText(getParameter("XLOC"));
repoyinput.setText(getParameter("YLOC"));
hmininput.setText(getParameter("HMIN"));
hmaxinput.setText(getParameter("HMAX"));
areainput.setText(getParameter("AREA"));
timeinput.setText(getParameter("TIME"));
recurinput.setText(getParameter("RECUR"));
vdatainput.setText(getParameter("DATASET"));

panel.setLayout(gridbag);

Label repoxlabel   = new Label("Easting");
Label repoylabel = new Label("Northing");
Label hminlabel = new Label("hmin");
Label hmaxlabel   = new Label("hmax");
Label arealabel   = new Label("Effective Area");
Label timelabel   = new Label("Time Interval");
Label recurlabel   = new Label("Recurrence Rate");
Label vdatalabel    = new Label("Data Set (1-5)");

repoxlabel.setFont(font);
repoylabel.setFont(font);
hminlabel.setFont(font);
hmaxlabel.setFont(font);
arealabel.setFont(font);
timelabel.setFont(font);
recurlabel.setFont(font);
vdatalabel.setFont(font);
repoxinput.setFont(font);
repoxinput.setBackground(Color.lightGray);
repoyinput.setFont(font);
repoyinput.setBackground(Color.lightGray);
hmininput.setFont(font);
hmininput.setBackground(Color.lightGray);
hmaxinput.setFont(font);
hmaxinput.setBackground(Color.lightGray);
areainput.setFont(font);
areainput.setBackground(Color.lightGray);
timeinput.setFont(font);
timeinput.setBackground(Color.lightGray);
recurinput.setFont(font);
recurinput.setBackground(Color.lightGray);
vdatainput.setFont(font);
vdatainput.setBackground(Color.lightGray);
plot.setFont(font);
plot.setBackground(Color.cyan);

 /*
 ** First row of the GridBag contains the plot
 */
```

```
c.weightx = 1.0;
c.weighty = 1.0;
c.gridwidth = 4;
c.gridwidth=GridBagConstraints.REMAINDER;
c.fill   =  GridBagConstraints.BOTH;

gridbag.setConstraints(graph,c);

/*
** Second row of the gridBag contains the function input and the
** plotit button
*/
c.fill   =  GridBagConstraints.NONE;
c.weightx=0.0;
c.weighty=0.0;
c.gridheight=1;

c.gridwidth=1;
c.anchor = GridBagConstraints.EAST;
gridbag.setConstraints(vdatalabel,c);

c.anchor = GridBagConstraints.WEST;
gridbag.setConstraints(vdatainput,c);

c.fill = GridBagConstraints.WEST;
c.gridwidth=GridBagConstraints.REMAINDER;

gridbag.setConstraints(plot,c);

 /*
 ** Third row contains the
 */
c.gridwidth=1;
c.anchor = GridBagConstraints.EAST;
gridbag.setConstraints(repoxlabel,c);

 c.anchor = GridBagConstraints.WEST;
 gridbag.setConstraints(repoxinput,c);

c.anchor = GridBagConstraints.EAST;
gridbag.setConstraints(repoylabel,c);

 c.anchor = GridBagConstraints.WEST;
 c.gridwidth=GridBagConstraints.REMAINDER;
 gridbag.setConstraints(repoyinput,c);

 /*
 ** Fourth row contains the
 */
 c.gridwidth=1;
 c.anchor = GridBagConstraints.EAST;
 gridbag.setConstraints(hminlabel,c);

 c.anchor = GridBagConstraints.WEST;
 gridbag.setConstraints(hmininput,c);

 c.anchor = GridBagConstraints.EAST;
 gridbag.setConstraints(hmaxlabel,c);

 c.anchor = GridBagConstraints.WEST;
 c.gridwidth=GridBagConstraints.REMAINDER;
```

```
 gridbag.setConstraints(hmaxinput,c);

 /*
 ** Fifth row contains the area and time interval of the grid
 */

 c.gridwidth=1;
 c.anchor = GridBagConstraints.EAST;
 gridbag.setConstraints(arealabel,c);

 c.anchor = GridBagConstraints.WEST;
 gridbag.setConstraints(areainput,c);

 c.anchor = GridBagConstraints.EAST;
 gridbag.setConstraints(timelabel,c);

 c.anchor = GridBagConstraints.WEST;
 c.gridwidth=GridBagConstraints.REMAINDER;
 gridbag.setConstraints(timeinput,c);


 /*
 ** Sixth row contains the recurrence rate of the grid
 */
 c.gridwidth=1;

 c.anchor = GridBagConstraints.EAST;
 gridbag.setConstraints(recurlabel,c);

 c.anchor = GridBagConstraints.WEST;
 c.gridwidth=GridBagConstraints.REMAINDER;
 gridbag.setConstraints(recurinput,c);

 // display the fields
panel.add(graph);
panel.add(vdatalabel);
panel.add(vdatainput);
panel.add(plot);

panel.add(repoxlabel);
panel.add(repoxinput);
panel.add(repoylabel);
panel.add(repoyinput);
panel.add(hminlabel);
panel.add(hmininput);
panel.add(hmaxlabel);
panel.add(hmaxinput);
panel.add(arealabel);
panel.add(areainput);
panel.add(timelabel);
panel.add(timeinput);
panel.add(recurlabel);
panel.add(recurinput);

//label the graph axes
xaxis = graph.createXAxis();
xaxis.setTitleText("Smoothing Factor  (km)");
xaxis.setTitleFont(new Font("Helvetica",Font.PLAIN,18));
xaxis.setLabelFont(new Font("Helvetica",Font.PLAIN,14));
```

```
        yaxis = graph.createYAxis();
        yaxis.setTitleText("Probability");
        yaxis.setTitleFont(new Font("Helvetica",Font.PLAIN,18));
        yaxis.setLabelFont(new Font("Helvetica",Font.PLAIN,14));


        data = new DataSet();

        xaxis.attachDataSet(data);
        yaxis.attachDataSet(data);
        graph.attachDataSet(data);

        graph.setDataBackground(new Color(230,240,240));
        graph.setBackground(new Color(240,250,250));

        plot();

    }



    void plot() {

        double repox, repoy, hmin, hmax, area, timeint, recur;
        int kount;
        int j;
        int setnum;
        double d[] = new double [200];
        boolean error = false;

        try {
            repox = Double.valueOf(repoxinput.getText()).doubleValue();
        } catch(Exception e) {
            this.showStatus("Error with x-location");
            System.out.println("x-location error "+e.getMessage());
            return;
        }

        try {
            repoy = Double.valueOf(repoyinput.getText()).doubleValue();
        } catch(Exception e) {
            this.showStatus("Error with y-location!");
            System.out.println("y location error "+e.getMessage());
            return;
        }
        try {
            setnum = Double.valueOf(vdatainput.getText()).intValue();
        } catch(Exception e) {
            this.showStatus("Illegal data set value: enter an integer!");
            System.out.println("Dataset error "+e.getMessage());
            return;
        }

        try {
            hmin = (Double.valueOf(hmininput.getText()).doubleValue());
        } catch(Exception e) {
            this.showStatus("Error with min smoothing factor");
            System.out.println("min smoothing factor error "+e.getMessage());
            return;
        }
        // illegal for hmin to be negative
```

```
if (hmin < 0.0) hmin = 0.0;

try {
    hmax = Double.valueOf(hmaxinput.getText()).doubleValue();
} catch(Exception e) {
    this.showStatus("Error with max smoothing factor");
    System.out.println("max smoothing factor error "+e.getMessage());
    return;
}
//illegal for hamx to be less than hmin
if (hmax < hmin) hmax = hmin+ 0.01;

try {
    area = Double.valueOf(areainput.getText()).doubleValue();
} catch(Exception e) {
    this.showStatus("Error with effective area");
    System.out.println("Effective area error "+e.getMessage());
    return;
}
// illegal for area to be negative
if (area < 0.0) area = 0.0;

try {
    timeint= Double.valueOf(timeinput.getText()).doubleValue();
} catch(Exception e) {
    this.showStatus("Error with time interval");
    System.out.println(" time interval error "+e.getMessage());
    return;
}
// illegal for timeint to be negative
if (timeint < 0.0) timeint = 0.0;

try {
    recur= Double.valueOf(recurinput.getText()).doubleValue();
} catch(Exception e) {
    this.showStatus("Error with recurrence interval");
    System.out.println(" recurrence interval error "+e.getMessage());
    return;
}
// illegal for recurto be negative
if (recur < 0.0) recur = 0.0;


//the volcano data set is determined from setnum
volcano.setVolcanoset(setnum);

// instantiate the volcanodata set
volcano.getVolcanoes();

Hestimate lambda1 = new Hestimate(repox, repoy, Volcano.nvolcanoes);

j =0;
int kountmax = 100;

for (kount=1; kount <= kountmax; kount++, j+=2) {
    try {

        d[j] = hmin + (hmax-hmin)/((double)kountmax) *(double)kount;
        d[j+1] = 1- Math.exp(-area*timeint*recur*lambda1.epanh(Volcano.vs, d
        System.out.println("h = " + d[j]);
        System.out.println("lambda = " + d[j+1]);
```

```
            } catch (Exception e) {error = true;}

        }


        data.deleteData();

        try {
            data.append(d,kountmax);
        } catch(Exception e) {
            this.showStatus("Error while appending data!");
            System.out.println("Error while appending data!");
            return;
        }


        graph.repaint();
    }



    public boolean action(Event e, Object a) {

        if(e.target instanceof Button) {
            if( plot.equals(e.target) ) {
                plot();
                return true;
            }
        }


         return false;
    }

}
```

```
import java.awt.*;
import java.applet.*;

import graph.*;
import graph.ContourProb;
import graph.Volcano;
/*
**************************************************************************
**
**                        Applet ProbMap1
**
**************************************************************************

by Chuck Connor
Center for Nuclear Waste Regulatory Analyses
Southwest Research Institute
6220 Culebra Rd
San Antonio Texas. 78238-5166, USA
cconnor@swri.edu

Created: November, 1999

Based on code originally written in TrueBasic by C Connor, 1992-1994
Graphics portion of this code modified from code written by Leigh Brookshaw

Purpose:

applet ProbMap1 calculates the conditional probability of a new
volcano forming within a 1 km  x 1 km region, given that a new
volcano forms in the region

This applet uses the Restimate class to estimate
probability and contours the results

This applet uses the Volcano class to select data sets

This applet uses the ContourProb class to plot the map

**************************************************************************
This code was prepared as a result of work performed at the Center for
Nuclear Waste Regulatory Analyses (CNWRA) for the US Nuclear Regulatory
Commission (NRC) under contract NRC-02-97-009. This code is an independent
product of the CNWRA and does not necessarily reflect the views or
regulatory position of the NRC.
**************************************************************************/

public class ProbMap1 extends Applet {

    ContourProb graph         = new ContourProb();   // Graph class to do the plotti
    Axis xaxis;
    Axis yaxis;
    DataSet data;
    Volcano volcano = new Volcano();

    TextField cinput     = new TextField(4);       // Number of contours
    TextField xinput     = new TextField(4);       // X grid dimension
    TextField yinput     = new TextField(4);       // Y grid dimension
    TextField xmininput  = new TextField(10);      // Minimum x value input
    TextField xmaxinput  = new TextField(10);      // Maximum x value input
    TextField ymininput  = new TextField(10);      // Minimum y value input
    TextField ymaxinput  = new TextField(10);      // Maximum y value input
```

```
TextField vdatainput     = new TextField(2);       // data set to plot
TextField sfinput      = new TextField(4);       // smoothing factor input
Button plot           = new Button("Calculate"); // Button to plot it.

public void init() {
    Label title             = new Label(
                                    "Gaussian Probability Map",Label.CENTER);
    Panel panel             = new Panel();
    GridBagLayout gridbag   = new GridBagLayout();
    GridBagConstraints  c   = new GridBagConstraints();
    Font font               = new Font("Helvetica",Font.PLAIN,14);

    title.setFont(new Font("TimesRoman",Font.PLAIN,25));

    setLayout(new BorderLayout() );
    add("North",title);
    add("Center",panel);

    // Data from .html
    vdatainput.setText(getParameter("DATASET"));
    sfinput.setText(getParameter("SMOOTH"));
    cinput.setText(getParameter("CONTOURS"));
    xinput.setText(getParameter("XGRID"));
    yinput.setText(getParameter("YGRID"));
    xmininput.setText(getParameter("XMIN"));
    xmaxinput.setText(getParameter("XMAX"));
    ymininput.setText(getParameter("YMIN"));
    ymaxinput.setText(getParameter("YMAX"));

    panel.setLayout(gridbag);
    /*
    ** create labels for all the text input fields
     */
     Label clabel     = new Label("Number of Contours");
     Label xlabel     = new Label("X grid dimension");
     Label ylabel     = new Label("Y grid dimension");
     Label xminlabel  = new Label("Minimum Easting");
     Label xmaxlabel  = new Label("Maximum Easting");
     Label yminlabel  = new Label("Minimum Northing");
     Label ymaxlabel  = new Label("Maximum Northing");
     Label vdatalabel     = new Label("Data Set (1-5)");
     Label sflabel    = new Label("Smoothing Factor (km)");
     /*
     ** Set the fonts and colors to use
     */
     clabel.setFont(font);
     xlabel.setFont(font);
     ylabel.setFont(font);
     vdatalabel.setFont(font);
     sflabel.setFont(font);
     xminlabel.setFont(font);
     xmaxlabel.setFont(font);
     yminlabel.setFont(font);
     ymaxlabel.setFont(font);

     cinput.setFont(font);
     cinput.setBackground(Color.lightGray);
     xinput.setFont(font);
     xinput.setBackground(Color.lightGray);
     yinput.setFont(font);
     yinput.setBackground(Color.lightGray);
```

```
vdatainput.setFont(font);
sfinput.setBackground(Color.lightGray);
sfinput.setFont(font);
vdatainput.setBackground(Color.lightGray);
xmininput.setFont(font);
xmininput.setBackground(Color.lightGray);
xmaxinput.setFont(font);
xmaxinput.setBackground(Color.lightGray);
ymininput.setFont(font);
ymininput.setBackground(Color.lightGray);
ymaxinput.setFont(font);
ymaxinput.setBackground(Color.lightGray);
plot.setFont(font);
plot.setBackground(Color.cyan);


/*
** First row of the GridBag contains the plot
*/
c.weightx = 1.0;
c.weighty = 1.0;
c.gridwidth = 4;
c.gridwidth=GridBagConstraints.REMAINDER;
c.fill   =  GridBagConstraints.BOTH;

gridbag.setConstraints(graph,c);


/*
** Second row of the gridBag contains the function input and the
** plotit button
*/
c.fill   =  GridBagConstraints.NONE;
c.weightx=0.0;
c.weighty=0.0;
c.gridheight=1;

c.gridwidth=1;
c.anchor = GridBagConstraints.EAST;
gridbag.setConstraints(vdatalabel,c);

c.anchor = GridBagConstraints.WEST;
gridbag.setConstraints(vdatainput,c);

c.fill = GridBagConstraints.WEST;
c.gridwidth=GridBagConstraints.REMAINDER;

gridbag.setConstraints(plot,c);

/*
** Third row contains the Number of contours and smoothinf factor
*/
c.gridwidth=1;
c.anchor = GridBagConstraints.EAST;
gridbag.setConstraints(clabel,c);

c.anchor = GridBagConstraints.WEST;
gridbag.setConstraints(cinput,c);

c.anchor = GridBagConstraints.EAST;
gridbag.setConstraints(sflabel,c);
```

```
c.anchor = GridBagConstraints.WEST;
c.gridwidth=GridBagConstraints.REMAINDER;
gridbag.setConstraints(sfinput,c);

/*
** Fourth row contains the grid dimensions
*/
c.gridwidth=1;
c.anchor = GridBagConstraints.EAST;
gridbag.setConstraints(xlabel,c);

c.anchor = GridBagConstraints.WEST;
gridbag.setConstraints(xinput,c);

c.anchor = GridBagConstraints.EAST;
gridbag.setConstraints(ylabel,c);

c.anchor = GridBagConstraints.WEST;
c.gridwidth=GridBagConstraints.REMAINDER;
gridbag.setConstraints(yinput,c);

/*
** Fifth row contains the x range of the grid
*/

c.gridwidth=1;
c.anchor = GridBagConstraints.EAST;
gridbag.setConstraints(xminlabel,c);

c.anchor = GridBagConstraints.WEST;
gridbag.setConstraints(xmininput,c);

c.anchor = GridBagConstraints.EAST;
gridbag.setConstraints(xmaxlabel,c);

c.anchor = GridBagConstraints.WEST;
c.gridwidth=GridBagConstraints.REMAINDER;
gridbag.setConstraints(xmaxinput,c);


/*
** Sixth row contains the y range of the grid
*/

c.gridwidth=1;
c.anchor = GridBagConstraints.EAST;
gridbag.setConstraints(yminlabel,c);

c.anchor = GridBagConstraints.WEST;
gridbag.setConstraints(ymininput,c);

c.anchor = GridBagConstraints.EAST;
gridbag.setConstraints(ymaxlabel,c);

c.anchor = GridBagConstraints.WEST;
c.gridwidth=GridBagConstraints.REMAINDER;
gridbag.setConstraints(ymaxinput,c);

// display the fields
panel.add(graph);
```

```
        panel.add(vdatalabel);
        panel.add(vdatainput);

        panel.add(plot);
        panel.add(clabel);
        panel.add(cinput);
        panel.add(sflabel);
        panel.add(sfinput);
        panel.add(xlabel);
        panel.add(xinput);
        panel.add(ylabel);
        panel.add(yinput);
        panel.add(xminlabel);
        panel.add(xmininput);
        panel.add(xmaxlabel);
        panel.add(xmaxinput);
        panel.add(yminlabel);
        panel.add(ymininput);
        panel.add(ymaxlabel);
        panel.add(ymaxinput);

        //label the graph axes
        xaxis = graph.createXAxis();
        xaxis.setTitleText("Easting");

        yaxis = graph.createYAxis();
        yaxis.setTitleText("Northing");

        // set the graph colors
        graph.setDataBackground(new Color(230,240,240));
        graph.setBackground(new Color(240,250,250));
        graph.setContourColor(Color.black);
        graph.setLabelledContourColor(Color.red);

        // set the label interval
        // default condition -> contours not labelled
        graph.setLabelLevels(5);
        graph.setDrawLabels(false);

        // since its a map, make it square
        graph.square = true;

        plot();

    }


// the plot class does the work of creating the array to contour
// and interpeting the parameters from input

void plot() {
    int levels;
    int nx;
    int ny;
    int i, j;
    int setnum;
    double xmax;
    double xmin;
    double ymax;
    double ymin;
    double x, y;
```

```
int count = 0;
boolean error = false;
double smoothing_factor;

try {
    graph.setNLevels( Integer.parseInt(cinput.getText()) );
} catch(Exception e) {
    this.showStatus("Error with number of contour levels!");
    System.out.println(
                        "Number of contour levels error "+e.getMessage());
    return;
}

try {
    nx   = Integer.parseInt(xinput.getText());
    ny   = Integer.parseInt(yinput.getText());

} catch(Exception e) {
    this.showStatus("Error parsing grid dimensions!");
    System.out.println(
                        "Error parsing grid dimensions! "+e.getMessage());
    return;
}

try {
    xmax = Double.valueOf(xmaxinput.getText()).doubleValue();
    xmin = Double.valueOf(xmininput.getText()).doubleValue();
} catch(Exception e) {
    this.showStatus("Error with X range!");
    System.out.println("X range error "+e.getMessage());
    return;
}

try {
    ymax = Double.valueOf(ymaxinput.getText()).doubleValue();
    ymin = Double.valueOf(ymininput.getText()).doubleValue();
} catch(Exception e) {
    this.showStatus("Error with Y range!");
    System.out.println("Y range error "+e.getMessage());
    return;
}

try {
    setnum = Double.valueOf(vdatainput.getText()).intValue();
} catch(Exception e) {
    this.showStatus("Illegal data set value: enter an integer!");
    System.out.println("Dataset error "+e.getMessage());
    return;
}
try {
    smoothing_factor  = Double.valueOf(sfinput.getText()).doubleValue();
} catch(Exception e) {
    this.showStatus("Illegal smoothing factor");
    System.out.println("smoothing factor  error "+e.getMessage());
    return;
}

// Smoothing factor must be positive real number
if (smoothing_factor <= 0.0) smoothing_factor = 0.01;

if(xmin>=xmax || ymin>= ymax ) {
```

```
            this.showStatus("Error with Grid range!");
            System.out.println("grid range error! ");
            return;
        }
        if( nx < 2 || ny < 2 ) {
            this.showStatus("Error with Grid dimensions!");
            System.out.println("grid dimension error!");
            return;
        }

        graph.setRange(xmin,xmax,ymin,ymax);

        //the volcano data set is determined from setnum
            volcano.setVolcanoset(setnum);

            //array is the grid to plot
        double array[] = new double[nx*ny];

        this.showStatus("Calculating Grid Values!");
        count = 0;

        // instantiate the volcanodata set
        volcano.getVolcanoes();

        // instaniate lambda1 - a new instance of Restimate
        Restimate lambda1 = new Restimate(smoothing_factor, Volcano.nvolcanoes);

        // fill the array
        for(j=0; j<ny; j++) {
            y = ymin + j*(ymax-ymin)/(ny-1);
            for(i=0; i<nx; i++) {
                x = xmin + i*(xmax-xmin)/(nx-1);
                try {

                    // use the gaussian method in Restimate
                    array[count++] = lambda1.gaussh(Volcano.vs, x,y);
                } catch(Exception e) {
                    array[count++] = 0.0;
                    error = true; }
            }
        }

        //instantiate graph with array and array dimensions
        graph.setGrid(array,nx,ny);

        this.showStatus("Calculating Contours!");

        graph.repaint();
    }

    //keep track of Calculate events
    public boolean action(Event e, Object a) {

        if(e.target instanceof Button) {
            if( plot.equals(e.target) ) {
                plot();
                return true;
            }
        }
        return false;
    }
```

```
import java.awt.*;
import java.applet.*;

import graph.*;
import graph.ContourProb;
import graph.Volcano;
/*
**************************************************************************
**
**                        Applet ProbMap2
**
**************************************************************************

by Chuck Connor
Center for Nuclear Waste Regulatory Analyses
Southwest Research Institute
6220 Culebra Rd
San Antonio Texas. 78238-5166, USA
cconnor@swri.edu

Created: November, 1999

Based on code originally written in TrueBasic by C Connor, 1992-1994
Graphics portion of this code modified from code written by Leigh Brookshaw

Purpose:

applet ProbMap2 calculates the conditional probability of a new
volcano forming within a 1 km  x 1 km region, given that a new
volcano forms in the region, using an epanechnikov kernel

This applet uses the Restimate class to estimate
probability and contours the results

This applet uses the Volcano class to select data sets

This applet uses the ContourProb class to plot the map

**************************************************************************
This code was prepared as a result of work performed at the Center for
Nuclear Waste Regulatory Analyses (CNWRA) for the US Nuclear Regulatory
Commission (NRC) under contract NRC-02-97-009. This code is an independent
product of the CNWRA and does not necessarily reflect the views or
regulatory position of the NRC.
**************************************************************************/

public class ProbMap2 extends Applet {

    ContourProb graph         = new ContourProb();   // Graph class to do the plotti
    Axis xaxis;
    Axis yaxis;
    DataSet data;
    Volcano volcano = new Volcano();

    TextField cinput     = new TextField(4);       // Number of contours
    TextField xinput     = new TextField(4);       // X grid dimension
    TextField yinput     = new TextField(4);       // Y grid dimension
    TextField xmininput  = new TextField(10);      // Minimum x value input
    TextField xmaxinput  = new TextField(10);      // Maximum x value input
    TextField ymininput  = new TextField(10);      // Minimum y value input
    TextField ymaxinput  = new TextField(10);      // Maximum y value input
```

```
TextField vdatainput     = new TextField(2);      // data set to plot
TextField sfinput     = new TextField(4);      // smoothing factor input
Button plot          = new Button("Calculate"); // Button to plot it.

public void init() {
    Label title            = new Label(
                                    "Epanechnikov Probability Map",Label.CENT
    Panel panel            = new Panel();
    GridBagLayout gridbag  = new GridBagLayout();
    GridBagConstraints  c  = new GridBagConstraints();
    Font font              = new Font("Helvetica",Font.PLAIN,14);

    title.setFont(new Font("TimesRoman",Font.PLAIN,25));

    setLayout(new BorderLayout() );
    add("North",title);
    add("Center",panel);

    // Data from .html
    vdatainput.setText(getParameter("DATASET"));
    sfinput.setText(getParameter("SMOOTH"));
    cinput.setText(getParameter("CONTOURS"));
    xinput.setText(getParameter("XGRID"));
    yinput.setText(getParameter("YGRID"));
    xmininput.setText(getParameter("XMIN"));
    xmaxinput.setText(getParameter("XMAX"));
    ymininput.setText(getParameter("YMIN"));
    ymaxinput.setText(getParameter("YMAX"));

    panel.setLayout(gridbag);
    /*
    ** create labels for all the text input fields
     */
     Label clabel    = new Label("Number of Contours");
     Label xlabel    = new Label("X grid dimension");
     Label ylabel    = new Label("Y grid dimension");
     Label xminlabel = new Label("Minimum Easting");
     Label xmaxlabel = new Label("Maximum Easting");
     Label yminlabel = new Label("Minimum Northing");
     Label ymaxlabel = new Label("Maximum Northing");
     Label vdatalabel    = new Label("Data Set (1-5)");
     Label sflabel    = new Label("Smoothing Factor (km)");
     /*
     ** Set the fonts and colors to use
     */
     clabel.setFont(font);
     xlabel.setFont(font);
     ylabel.setFont(font);
     vdatalabel.setFont(font);
     sflabel.setFont(font);
     xminlabel.setFont(font);
     xmaxlabel.setFont(font);
     yminlabel.setFont(font);
     ymaxlabel.setFont(font);

     cinput.setFont(font);
     cinput.setBackground(Color.lightGray);
     xinput.setFont(font);
     xinput.setBackground(Color.lightGray);
     yinput.setFont(font);
     yinput.setBackground(Color.lightGray);
```

```
vdatainput.setFont(font);
sfinput.setBackground(Color.lightGray);
sfinput.setFont(font);
vdatainput.setBackground(Color.lightGray);
xmininput.setFont(font);
xmininput.setBackground(Color.lightGray);
xmaxinput.setFont(font);
xmaxinput.setBackground(Color.lightGray);
ymininput.setFont(font);
ymininput.setBackground(Color.lightGray);
ymaxinput.setFont(font);
ymaxinput.setBackground(Color.lightGray);
plot.setFont(font);
plot.setBackground(Color.cyan);


/*
** First row of the GridBag contains the plot
*/
c.weightx = 1.0;
c.weighty = 1.0;
c.gridwidth = 4;
c.gridwidth=GridBagConstraints.REMAINDER;
c.fill  =  GridBagConstraints.BOTH;

gridbag.setConstraints(graph,c);


/*
** Second row of the gridBag contains the function input and the
** plotit button
*/
c.fill  =  GridBagConstraints.NONE;
c.weightx=0.0;
c.weighty=0.0;
c.gridheight=1;

c.gridwidth=1;
c.anchor = GridBagConstraints.EAST;
gridbag.setConstraints(vdatalabel,c);

c.anchor = GridBagConstraints.WEST;
gridbag.setConstraints(vdatainput,c);

c.fill = GridBagConstraints.WEST;
c.gridwidth=GridBagConstraints.REMAINDER;

gridbag.setConstraints(plot,c);

/*
** Third row contains the Number of contours and smoothinf factor
*/
c.gridwidth=1;
c.anchor = GridBagConstraints.EAST;
gridbag.setConstraints(clabel,c);

c.anchor = GridBagConstraints.WEST;
gridbag.setConstraints(cinput,c);

c.anchor = GridBagConstraints.EAST;
gridbag.setConstraints(sflabel,c);
```

```
c.anchor = GridBagConstraints.WEST;
c.gridwidth=GridBagConstraints.REMAINDER;
gridbag.setConstraints(sfinput,c);

/*
** Fourth row contains the grid dimensions
*/
c.gridwidth=1;
c.anchor = GridBagConstraints.EAST;
gridbag.setConstraints(xlabel,c);

c.anchor = GridBagConstraints.WEST;
gridbag.setConstraints(xinput,c);

c.anchor = GridBagConstraints.EAST;
gridbag.setConstraints(ylabel,c);

c.anchor = GridBagConstraints.WEST;
c.gridwidth=GridBagConstraints.REMAINDER;
gridbag.setConstraints(yinput,c);

/*
** Fifth row contains the x range of the grid
*/

c.gridwidth=1;
c.anchor = GridBagConstraints.EAST;
gridbag.setConstraints(xminlabel,c);

c.anchor = GridBagConstraints.WEST;
gridbag.setConstraints(xmininput,c);

c.anchor = GridBagConstraints.EAST;
gridbag.setConstraints(xmaxlabel,c);

c.anchor = GridBagConstraints.WEST;
c.gridwidth=GridBagConstraints.REMAINDER;
gridbag.setConstraints(xmaxinput,c);


/*
** Sixth row contains the y range of the grid
*/

c.gridwidth=1;
c.anchor = GridBagConstraints.EAST;
gridbag.setConstraints(yminlabel,c);

c.anchor = GridBagConstraints.WEST;
gridbag.setConstraints(ymininput,c);

c.anchor = GridBagConstraints.EAST;
gridbag.setConstraints(ymaxlabel,c);

c.anchor = GridBagConstraints.WEST;
c.gridwidth=GridBagConstraints.REMAINDER;
gridbag.setConstraints(ymaxinput,c);

// display the fields
panel.add(graph);
```

```
        panel.add(vdatalabel);
        panel.add(vdatainput);

        panel.add(plot);
        panel.add(clabel);
        panel.add(cinput);
        panel.add(sflabel);
        panel.add(sfinput);
        panel.add(xlabel);
        panel.add(xinput);
        panel.add(ylabel);
        panel.add(yinput);
        panel.add(xminlabel);
        panel.add(xmininput);
        panel.add(xmaxlabel);
        panel.add(xmaxinput);
        panel.add(yminlabel);
        panel.add(ymininput);
        panel.add(ymaxlabel);
        panel.add(ymaxinput);

        //label the graph axes
        xaxis = graph.createXAxis();
        xaxis.setTitleText("Easting");

        yaxis = graph.createYAxis();
        yaxis.setTitleText("Northing");

        // set the graph colors
        graph.setDataBackground(new Color(230,240,240));
        graph.setBackground(new Color(240,250,250));
        graph.setContourColor(Color.black);
        graph.setLabelledContourColor(Color.red);

        // set the label interval
        // default condition -> contours not labelled
        graph.setLabelLevels(5);
        graph.setDrawLabels(false);

        // since its a map, make it square
        graph.square = true;

        plot();

    }


// the plot class does the work of creating the array to contour
// and interpeting the parameters from input

void plot() {
    int levels;
    int nx;
    int ny;
    int i, j;
    int setnum;
    double xmax;
    double xmin;
    double ymax;
    double ymin;
    double x, y;
```

```
int count = 0;
boolean error = false;
double smoothing_factor;

try {
    graph.setNLevels( Integer.parseInt(cinput.getText()) );
} catch(Exception e) {
    this.showStatus("Error with number of contour levels!");
    System.out.println(
                        "Number of contour levels error "+e.getMessage());
    return;
}

try {
    nx   = Integer.parseInt(xinput.getText());
    ny   = Integer.parseInt(yinput.getText());

} catch(Exception e) {
    this.showStatus("Error parsing grid dimensions!");
    System.out.println(
                        "Error parsing grid dimensions! "+e.getMessage());
    return;
}

try {
    xmax = Double.valueOf(xmaxinput.getText()).doubleValue();
    xmin = Double.valueOf(xmininput.getText()).doubleValue();
} catch(Exception e) {
    this.showStatus("Error with X range!");
    System.out.println("X range error "+e.getMessage());
    return;
}

try {
    ymax = Double.valueOf(ymaxinput.getText()).doubleValue();
    ymin = Double.valueOf(ymininput.getText()).doubleValue();
} catch(Exception e) {
    this.showStatus("Error with Y range!");
    System.out.println("Y range error "+e.getMessage());
    return;
}

try {
    setnum = Double.valueOf(vdatainput.getText()).intValue();
} catch(Exception e) {
    this.showStatus("Illegal data set value: enter an integer!");
    System.out.println("Dataset error "+e.getMessage());
    return;
}
try {
    smoothing_factor  = Double.valueOf(sfinput.getText()).doubleValue();
} catch(Exception e) {
    this.showStatus("Illegal smoothing factor");
    System.out.println("smoothing factor  error "+e.getMessage());
    return;
}
// Smoothing factor must be positive real number
if (smoothing_factor <=  0.0) smoothing_factor = 0.01;

if(xmin>=xmax || ymin>= ymax ) {
    this.showStatus("Error with Grid range!");
```

```
            System.out.println("grid range error! ");
            return;
        }
        if( nx < 2 || ny < 2 ) {
            this.showStatus("Error with Grid dimensions!");
            System.out.println("grid dimension error!");
            return;
        }

        graph.setRange(xmin,xmax,ymin,ymax);

        //the volcano data set is determined from setnum
            volcano.setVolcanoset(setnum);

            //array is the grid to plot
        double array[] = new double[nx*ny];

        this.showStatus("Calculating Grid Values!");
        count = 0;

        // instantiate the volcanodata set
        volcano.getVolcanoes();

        // instaniate lambda1 - a new instance of Restimate
        Restimate lambda1 = new Restimate(smoothing_factor, Volcano.nvolcanoes);

        // fill the array
        for(j=0; j<ny; j++) {
            y = ymin + j*(ymax-ymin)/(ny-1);
            for(i=0; i<nx; i++) {
                x = xmin + i*(xmax-xmin)/(nx-1);
                try {

                    // use the epanechnikov  method in Restimate
                    array[count++] = lambda1.epanh(Volcano.vs, x,y);
                } catch(Exception e) {
                    array[count++] = 0.0;
                    error = true; }
            }
        }

        //instantiate graph with array and array dimensions
        graph.setGrid(array,nx,ny);

        this.showStatus("Calculating Contours!");

        graph.repaint();
    }

    //keep track of Calculate events
    public boolean action(Event e, Object a) {

        if(e.target instanceof Button) {
            if( plot.equals(e.target) ) {
                plot();
                return true;
            }
        }
        return false;
    }
}
```

```
package graph;

import java.awt.*;
import java.applet.*;
import java.net.URL;
import java.util.*;
import java.io.InputStream;
/*
**************************************************************************
**
**    Class  ContourProb
**
**************************************************************************
**
by Chuck Connor
Center for Nuclear Waste Regulatory Analyses
Southwest Research Institute
6220 Culebra Rd
San Antonio Texas. 78238-5166, USA
cconnor@swri.edu

Created: December, 1999

Graphics portion of this code modified from code written by Leigh Brookshaw

Purpose: this applet provides contouring capability to the ProbMap classes
that call it. This applet also draws the volcano locations and the
location of the proposed YM repository.

**************************************************************************
**
** This class extends the interactive graphics class to incorporate
** contours.
**
**************************************************************************/


public class ContourProb extends G2Dint {

/*
**************
**
** Constants
**
*************/

/*
**   The minimum length of a curve before it gets a label
*/
         static final int MINCELLS = 30;
/*
**   Default number of contour levels
*/
         static final int NLEVELS = 12;


/**********************
**
** Protected Variables
**
**********************/
```

```
/**
 *   Dimension of the contour grid in the X direction
 */
     protected int nx;
/**
 *   Dimension of the contour grid in the Y direction
 */
     protected int ny;
/**
 *   Vector array containing the Contour curves.
 *   Each index in the array contains curves at a given
 *   contour level
 */
     protected Vector curves[];

/**
 *   If set the class calculates the contour levels based on
 *   the data minimum and maximum. Default value <i>true</i>.
 */
     protected boolean autoLevels;
/*
 *   If true the contour levels are calculated in
 *   logarithmic intervals
 */
     protected boolean logLevels;
/*
 *   If true the limits of the plot are the limits of the
 *   data grid not the limits of the contours!
 */
     protected boolean gridLimits;
/*
 *   The array of contour levels
 */
     protected double levels[];
/**
 *   The label for each contour level
 */
     protected TextLine labels[];
/**
 *   Font to use in drawing Labels
 */
     protected Font labelfont;
/**
 *   Color to use in drawing Labels
 */
     protected Color labelcolor;
/**
 *   Style to use in drawing Labels. TextLine.SCIENTIFIC or
 *   TextLine.ALGEBRAIC.
 */
     protected int labelStyle;
/**
 *   Precision to use in drawing Labels.
 */
     protected int labelPrecision;

/**
 *   Number of Significant figures to use in drawing Labels.
 */
     protected int labelSignificant;
```

```
/**
 *   Which levels will get labels. If it is equal to 1 every level
 *   gets a label, equal to 2 every second level etc. If it is equal to 0
 *   no labels are displayed.
 */
    protected int labelLevels;
/**
 *   If false labels are not drawn
 */
    protected boolean drawlabels;
/**
 *   If true the labels will be calculated for each
 *   contour level. These might not look all that hot.
 */
    protected boolean autoLabels;
 /**
  *  Color to draw non labelled contour line
  */
    protected Color contourColor;
 /**
  *  Color to draw labelled contour line
  */
    protected Color labelledColor;

/**
 *   The data grid, a 2D array stored in linear form.
 *   It is assumed that [0,0] is the bottom left corner
 *   and the data is ordered by row.
 */
    protected double grid[];

/**
 *   The X minimum limit of the data grid
 */
    protected double xmin;
/**
 *   The X maximum limit of the data grid
 */
    protected double xmax;
/**
 *   The Y minimum limit of the data grid
 */
    protected double ymin;
/**
 *   The Y maximum limit of the data grid
 */
    protected double ymax;
/**
 *   The minimum value of the grid values
 */
    protected double zmin;
/**
 *   The maximum value of the grid values
 */
    protected double zmax;

  /**
   * Boolean value if true Contours will not be calculated
   */
     public boolean noContours = false;
```

```
/*
*****************
**
** Constructors
**
****************/

  /**
   * Instantaite the class
   */
     public ContourProb() {

           grid = null;
           xmin = 0.0;
           xmax = 0.0;
           ymin = 0.0;
           ymax = 0.0;
           zmin = 0.0;
           zmax = 0.0;

           nx = 0;
           ny = 0;

           levels = new double[NLEVELS];
           labels = new TextLine[NLEVELS];

           autoLevels  = true;
           logLevels   = false;
           gridLimits  = false;
           autoLabels  = true;
           labelfont   = new Font("Helvetica",Font.PLAIN,12);
           labelcolor  = Color.blue;
           labelLevels = 1;
           labelStyle       = TextLine.ALGEBRAIC;
           labelPrecision   = 2;
           labelSignificant = 3;
           drawlabels = true;

           contourColor  = null;
           labelledColor = null;

           curves = null;

     }

/*
************
**
** Methods
**
***********/
  /**
   *  Load the grid to contour from a URL. There are 2 formats for the data
   *  optionally the limits of the grid can be parsed.<BR>
   *  <PRE>
   *  The expected format of the data
   *           1st Number:   nx
   *           2nd Number:   ny
   *           nx*ny numbers following
   *
   *  Optionally
```

```
*           1st Number:   nx
*           2nd Number:   ny
*           3rd Number:   xmin
*           4th Number:   xmax
*           5th Number:   ymin
*           6th Number:   ymax
*           nx*ny numbers following
*  </PRE><BR>
*  If xmin, xmax, ymin, ymax are not specified they are assumed
*  to be [1.0,nx,1.0,ny]
*
* @param file URL of the file to load
* @return <i>true</I> of the load was successful.
*
*/
 public boolean loadGrid( URL file) {
        byte b[] = new byte[50];
        int nbytes = 0;
        int max  = 100;
        int inc  = 100;
        int n    = 0;
        double data[] = new double[max];
        InputStream is = null;
        boolean comment    = false;
        int c;

        try {
              is = file.openStream();

              while( (c=is.read()) > -1 ) {

                  switch (c) {

                      case '#':
                                 comment = true;
                                 break;
                      case '\r': case '\n':
                                 comment = false;
                      case ' ': case '\t':
                               if( nbytes > 0 ) {
                                  String s = new String(b,0,0,nbytes);
                                  data[n] = Double.valueOf(s).doubleValue();
                                  n++;
                                  if( n >= max ) {
                                      max += inc;
                                      double d[] = new double[max];
                                      System.arraycopy(data, 0, d, 0, n);
                                      data = d;
                                  }

                                  nbytes = 0;
                               }
                               break;
                     default:
                                  if( !comment ) {
                                       b[nbytes] = (byte)c;
                                       nbytes++;
                                  }
                                  break;
                  }
```

```
            }

          if (is != null) is.close();
      } catch(Exception e) {
        System.out.println("Failed to load Grid from file ");
        e.printStackTrace();
        if (is != null) try { is.close(); } catch (Exception ev) { }
        return false;
      }

      if(n < 1 ) {
         System.out.println("Failed to load Grid from file ");
         return false;
       }

      nx = (int)(data[0] + 0.5);
      ny = (int)(data[1] + 0.5);

      if( n == nx*ny+6 ) {
          xmin = data[2];
          xmax = data[3];
          ymin = data[4];
          ymax = data[5];

          grid = new double[nx*ny];
          System.arraycopy(data, 6, grid, 0, nx*ny);
      } else
      if( n == nx*ny+2 ) {
          xmin = 1.0;
          xmax = (double)(nx);
          ymin = 1.0;
          ymax = (double)(ny);

          grid = new double[nx*ny];
          System.arraycopy(data, 2, grid, 0, nx*ny);
      } else {
          System.out.println("Error loading grid, Wrong number of points ");
          grid = null;
          return false;
        }

      zrange();
      calcLevels();

      detachCurves();
      curves = null;

      return true;

    }

  /**
   *  Set the range of the grid
   * @param xmin Minimum X value
   * @param xmax Maximum X value
   * @param ymin Minimum Y value
   * @param ymax Maximum Y value
   */


    public void setRange(double xmin,double xmax,double ymin,double ymax) {
```

```
            if( xmin >= xmax || ymin >= ymax ) return;

            this.xmin = xmin;
            this.xmax = xmax;
            this.ymin = ymin;
            this.ymax = ymax;
    }

 /**
  *  Return the range of the grid
  * @return An array contining xmin,xmax,ymin,ymax.
  */
    public double[] getRange() {
            double d[] = new double[4];
            d[0] = xmin;
            d[1] = xmax;
            d[2] = ymin;
            d[3] = ymax;

            return d;
     }
 /**
  *  return the dimensions of the grid
  * @return An array containing the number of columns, number of rows.
  */
    public int[] getDim() {
            int i[] = new int[2];

            i[0] = nx;
            i[1] = ny;

            return i;
     }

 /**
  *  Return the grid
  * @return An array of size nx by ny contining the data grid.
  */
    public double[] getGrid() { return grid; }

 /**
  * Manually set the contour levels.
  * @param levels An array containing the contour levels
  * @param nl The number of contour levels in the arrray
  */
    public void setLevels(double levels[], int nl) {
          int i;
          if( levels == null || nl <= 0 ) return;

          detachCurves();
          curves = null;

          autoLevels = false;

          this.levels = new double[nl];

          System.arraycopy(levels,0,this.levels,0,nl);

          labels = new TextLine[nl];
          for(i=0; i<labels.length; i++) {
            labels[i] = new TextLine( String.valueOf( (float)levels[i] ) );
```

```
        }
    }
/**
 * Manually set the Contour labels.
 * @param labels An array containing the labels.
 * @param nl Number of labels in the Array.
 */
   public void setLabels(TextLine labels[], int nl) {
         if( labels == null || nl <= 0 ) return;

         autoLabels = false;
         this.labels = new TextLine[nl];

         System.arraycopy(labels,0,this.labels,0,nl);
   }

/**
 * Set the font to be used with All the labels
 * @param f Font
 */
   public void setLabelFont(Font f) {
         labelfont = f;
   }

/**
 * Set the Color to be used with all the labels.
 * @param c Color
 */
   public void setLabelColor(Color c) {
         labelcolor = c;
   }

/**
 *  Set the grid to be contoured.
 * @param grid Array of values
 * @param nx   Number of columns
 * @param ny   Number of rows
 */
   public void setGrid(double grid[],int nx,int ny) {
      this.grid = grid;
      this.nx   = nx;
      this.ny   = ny;

      zrange();
      calcLevels();

   }
/**
 * Delete all the Contours
 */
   public void deleteContours() {
        if(curves == null) return;
        detachCurves();
        curves = null;
   }
/**
 * Detach contours so that they will not be plotted.
 */
   public void detachContours() {
        if(curves == null) return;
        detachCurves();
```

```
    }
  /**
   * Attach contours so that they will be plotted.
   */
    public void attachContours() {
         if(curves == null) return;
         attachCurves();
    }

  /**
   * Set the contour's color.
   * @param c Color
   */
    public void setContourColor(Color c) { contourColor = c; }
  /**
   * Set the labelled contour's color.
   * @param c Color
   */
    public void setLabelledContourColor(Color c) { labelledColor = c; }

  /**
   * Return the contour levels.
   * @return An array containing the contour levels
   */
    public double[] getLevels() { return levels; }
  /**
   * If true the limits of the plot will be the grid limits.
   * If false the limits of the plot will be the contours.
   * @param b boolean
   */

    public void setLimitsToGrid(boolean b) { gridLimits = b; }
  /**
   *  Set the contour levels that are to have labels.
   * <pre>
   *    if 0 no labels are drawn
   *    if 1 every level gets a label
   *    If 2 every 2nd level gets a label
   *    etc.
   * </pre>
   */
    public void setLabelLevels(int i) {
         if(i<=0) labelLevels = 0;
         else     labelLevels = i;
       }

  /**
   * If true contour levels are calculated on a log scale.
   * @param b boolean
   */
    public void setLogLevels(boolean b) {
              logLevels = b;

              if( zmin <= 0.0 || zmax <= 0.0 ) logLevels = false;
            }

  /**
   * Set the number of contour levels.
   * @@param l Number of contour levels
   */
    public void setNLevels(int l) {
```

```
        if(l <= 0) return;

        levels = new double[l];

        calcLevels();

        detachCurves();
        curves = null;
    }

 /**
  * If true contour levels are calculated automatically.
  * @param b boolean
  */
    public void setAutoLevels(boolean b) {
              autoLevels = b;
            }
 /**
  * If true contour levels are not labeled.
  * @param b boolean
  */
    public void setDrawLabels(boolean b) {
              drawlabels = b;
            }

 /**
  * Set the label style, either TextLine.SCIENTIFIC or
  * TextLine.ALGEBRAIC.
  * @param s Style
  */
    public void setLabelStyle(int s) {
                labelStyle = s;
                calcLabels();
}

 /**
  * Get the label style, either TextLine.SCIENTIFIC or
  * TextLine.ALGEBRAIC.
  * @return style
  */
    public int getLabelStyle() { return labelStyle; }

 /**
  * Set the label precision.
  * @param s Precision
  */
    public void setLabelPrecision(int p) {
                labelPrecision = p;
                calcLabels();
    }

 /**
  * Get the label precision.
  * @return precision
  */
    public int getLabelPrecision() { return labelPrecision; }

 /**
  * Set the label significant figures.
  * @param s number of significant figures
  */
```

```
    public void setLabelSignificance(int s) {
                labelSignificant = s;
                calcLabels();
    }

  /**
   * Get the number of significant figures for labels.
   * @return number of significant figures
   */
    public int getLabelSignificance() { return labelSignificant; }


  /**
   *   Add extra events to the G2Dint event handler.
   *
   *   If 'l' is pressed repaint without the labels
   *   If 'L' is pressed repaint with the labels.
   */
    public boolean keyDown(Event e, int key) {
          if(xaxis==null || yaxis==null) return false;

          if( super.keyDown(e,key) ) return true;

          switch ( key ) {

          case 'l':
                    drawlabels = false;
                    repaint();
                    return true;
          case 'L':
                    drawlabels = true;
                    repaint();
                    return true;
          }

          return false;
    }

/*
*********************
**
** Private Methods
**
*******************/

/*
**  calcLevels()
**              Calculate the contour levels
*/
    private void calcLevels() {
      int i;
      int l;

      if(!autoLevels) return;

      if(levels == null) levels = new double[NLEVELS];
      labels = new TextLine[levels.length];
      // Nice label steps not implemented yet
      //levelStep();
```

```
        if( logLevels ) {
           double inc = Math.log(zmax-zmin)/
                        (double)(levels.length+1);
           try {
              for(i=0; i<levels.length; i++) levels[i] = zmin +
                           Math.pow(Math.E,(double)(i+1)*inc);
            } catch (Exception e) {
              System.out.println("Error calculateing Log levels!");
              System.out.println("... calculating linear levels instead");
              logLevels = false;
              calcLevels();
            }
         } else {
           double inc = (zmax-zmin)/(double)(levels.length+1);
           for(i=0; i<levels.length; i++) levels[i] = zmin + (double)(i+1)*inc;
         }
      }
/*
**  calcLabels()
**              Calculate the labels
*/
      private void calcLabels() {
         int i;
         if( !autoLabels ) return;

         if(levels==null || levels.length <= 0) return;

         labels = new TextLine[levels.length];


         for(i=0; i<labels.length; i++) {
              labels[i] = new TextLine();
              labels[i].parseDouble(levels[i],
                       labelSignificant,labelPrecision,labelStyle);
         }
      }

/*
**    zrange()
**            Calculate the range of the grid
*/

      private void zrange() {
         int i;

         zmin = grid[0];
         zmax = grid[1];
         for( i=0; i<grid.length; i++) {

              zmin = Math.min(zmin,grid[i]);
              zmax = Math.max(zmax,grid[i]);

         }

         System.out.println("Data range: zmin="+zmin+", zmax="+zmax);

         if(zmin == zmax) {
            System.out.println("Cannot produce contours of a constant surface!");
          }

         if(zmin <= 0 || zmax <= 0) logLevels = false;
```

```
    }
/*
**   paintFirst(Graphics g, Rectangle r)
**        before anything is painted calculate the contours.
*/

     public void paintFirst(Graphics g, Rectangle r) {

        //System.out.println("paintFirst called");



        if( curves == null && !noContours ) {
                                  calculateCurves();
                                  calcLabels();
                               }

        setContourColors();

        if(gridLimits && !userlimits ) {
          if( xaxis != null ) {
               if(xaxis.minimum > xmin ) xaxis.minimum = xmin;
               if(xaxis.maximum < xmax ) xaxis.maximum = xmax;
             }

          if( yaxis != null ) {
               if(yaxis.minimum > ymin ) yaxis.minimum = ymin;
               if(yaxis.maximum < ymax ) yaxis.maximum = ymax;
             }
        } else
        if( dataset.isEmpty() ) {
          if( xaxis != null ) {
               xaxis.minimum = xmin;
               xaxis.maximum = xmax;
             }

          if( yaxis != null ) {
               yaxis.minimum = ymin;
               yaxis.maximum = ymax;
             }
        }


     }

 /**
 *  Set the colors for the contour lines
 */
     private void setContourColors() {
       int i;
       int j;
       Vector v;

       if(curves == null ||
          (contourColor==null && labelledColor==null) ) return;

       for(i=0; i<curves.length; i++) {
           setContourColors(curves[i],null);
       }
```

```
        if(contourColor != null) {
           for(i=0; i<curves.length; i++) {
               setContourColors(curves[i],contourColor);
           }
        }

        if(labelledColor != null) {
           for(i=0; i<curves.length; i++) {
               if(i%labelLevels == 0) {
                  setContourColors(curves[i],labelledColor);
               }
           }
        }



      }

   /**
   *  Set the colors for the contour lines
   */
       private void setContourColors(Vector v, Color c) {
         int i;
         DataSet d;

         if(v == null) return;

         for(i=0; i<v.size(); i++) {
             d = (DataSet)(v.elementAt(i));
             if(d != null) d.linecolor = c;
         }

      }
/*
**    attachCurves()
**        Attach all the curves to the graph and to the axes
*/
      private void attachCurves() {
         int i;
         if(curves == null) return;

         for(i=0; i<curves.length; i++) attachCurves(curves[i]);

      }
/*
**    attachCurves(Vector v)
**        Attach all the curves from a given level to the graph and to the axes
*/

      private void attachCurves(Vector v) {
         int j;
         if(v == null) return;
         for(j=0; j<v.size(); j++) {
               attachDataSet((DataSet)(v.elementAt(j)));
               if(xaxis != null)
                        xaxis.attachDataSet((DataSet)(v.elementAt(j)));
               if(yaxis != null)
                        yaxis.attachDataSet((DataSet)(v.elementAt(j)));
            }
      }
/*
```

```
**    detachCurves()
**                Detach All the curves from the graph and the axes.
*/
      private void detachCurves() {
         int i;
         if(curves == null) return;

         for(i=0; i<curves.length; i++) detachCurves(curves[i]);
      }
/*
**    detachCurves()
**                Detach all the curves from a given level from
**                the graph and the axes.
*/
      private void detachCurves(Vector v) {
         int j;
         if(v == null) return;
         for(j=0; j<v.size(); j++) {
               detachDataSet((DataSet)(v.elementAt(j)));
               if(xaxis != null)
                        xaxis.detachDataSet((DataSet)(v.elementAt(j)));
               if(yaxis != null)
                        yaxis.detachDataSet((DataSet)(v.elementAt(j)));
             }
      }

/*
**    paintLast(Graphics g, Rectangle rect)
**          Last thing to be done is to draw the contour labels if required.
*/
    public void paintLast(Graphics g, Rectangle rect) {
        int i, j;
        int points;
        int index;
        Vector v;
        DataSet ds;
        double point[] = new double[2];
        int  repoxmax, repoymax;
        int x;
        int y;
        Color current = g.getColor();
        Rectangle r = new Rectangle();
        Rectangle vmark   = new Rectangle();
        Rectangle repomark   = new Rectangle();
        Color volcolor = Color.black;
        Color repocolor = Color.yellow;
        Volcano volcano = new Volcano();

        // draw the repository outline
        g.setColor(repocolor);
        repomark.x = xaxis.getInteger(547198.0);
        repoxmax = xaxis.getInteger(549655.0);
        repomark.y = yaxis.getInteger(4080229.0);
        repoymax = yaxis.getInteger(4076079.0);

        repomark.width = repoxmax - repomark.x;
        repomark.height = repoymax - repomark.y;

         g.fillRect(repomark.x, repomark.y, repomark.width, repomark.height);

         // draw the volcano locations
```

```
g.setColor(volcolor);
vmark.width = 5;
vmark.height = 5;
volcano.getVolcanoes();
for (i=0; i < Volcano.nvolcanoes*2; i+=2) {
    x = xaxis.getInteger(Volcano.vs[i]  );
    y = yaxis.getInteger(Volcano.vs[i+1]);
    vmark.x = x - vmark.width/2;
    vmark.y = y - vmark.height/2;
    g.fillRect(vmark.x, vmark.y, vmark.width, vmark.height);
}

if( xaxis == null || yaxis == null || labels == null ||
    labelLevels == 0 || !drawlabels || curves == null ) {
    super.paintLast(g,rect);
    return;
}



      for(i=0; i<levels.length; i++) {
         if( labels[i] != null && !labels[i].isNull() &&
             i%labelLevels == 0 ) {
            labels[i].setFont(labelfont);
            labels[i].setColor(labelcolor);
            v = curves[i];
            for(j=0; j<v.size(); j++) {
                ds =  (DataSet)(v.elementAt(j));
                points = ds.dataPoints();
                index = (int)(Math.random()*(double)MINCELLS);
                while ( points > MINCELLS ) {
                     point = ds.getPoint(index);
                     x = xaxis.getInteger(point[0]);
                     y = yaxis.getInteger(point[1]);

                     r.width  = labels[i].getWidth(g);
                     r.height = labels[i].getAscent(g);
                     r.x = x - r.width/2;
                     r.y = y - r.height/2;

                     //     System.out.println("X = "+point[0] +  " Y =  " +
                     g.setColor(DataBackground);
                     g.fillRect(r.x, r.y, r.width, r.height);

                     g.setColor(current);

                     labels[i].draw(g, r.x, r.y+r.height,
                                    TextLine.LEFT);

                     points -= MINCELLS;
                     index += MINCELLS;
                }
             }
         }
      }


      super.paintLast(g,rect);


   }
```

```
/*
**   calculateCurves()
**        Calculate the contours and attach them to the graph and axes.
*/

     protected void calculateCurves() {
          int i;
          int j;
          double data[];
          double xscale = (xmax-xmin)/(double)(nx-1);
          double yscale = (ymax-ymin)/(double)(ny-1);

          IsoCurve isocurve;


          isocurve = new IsoCurve(grid,nx,ny);


          if( curves != null) {
                               detachCurves();
                               curves = null;
                             }
          if( zmin == zmax ) return;

          curves = new Vector[levels.length];


          for(i=0; i<levels.length; i++) {
              System.out.println("Calculating Contours: level="+levels[i]);
              isocurve.setValue(levels[i]);

              curves[i] = new Vector();

              while( (data = isocurve.getCurve()) != null ) {
                for(j=0; j<data.length; ) {
                   data[j] = xmin + data[j]*xscale;
                   j++;
                   data[j] = ymin + data[j]*yscale;
                   j++;
                 }

                try {
                  curves[i].addElement(new DataSet(data, data.length/2));
                } catch (Exception e) {
                  System.out.println("Error loading contour into DataSet!");
                  System.out.println("...Contour Level "+levels[i]);
                }
              }

              attachCurves(curves[i]);

              //repaint();
            }


     }


}
```

```
package  graph;
import java.io.*;

/*
**************************************************************************
**
**    Class  Volcano
**
**************************************************************************
**
by Chuck Connor
Center for Nuclear Waste Regulatory Analyses
Southwest Research Institute
6220 Culebra Rd
San Antonio Texas. 78238-5166, USA
cconnor@swri.edu

Created: December, 1999

Purpose: this class includes datasets 1-5 and defines these data
sets as static variables to be used by other applets in PVHA_YM

**************************************************************************

public class Volcano {

    protected static int volcanoset;
    public static int nvolcanoes;
    public static double [] vs;

    /*   public static int nvolcanoes2;
    public static double [] vs2;
    */


    static {
        volcanoset = 0;
    }

    public void getVolcanoes() {
        switch (volcanoset) {
        case 1:

            // first volcano dataset
            // includes 47 miocene to quaternary volcanic events
            nvolcanoes = 47;
            vs = new double [nvolcanoes*2];

        // Lathrop Wells
            vs[0] = 543780;
            vs[1] = 4060380;

            // Little Black Peak
            vs[2] = 522120;
            vs[3] = 4110340;

            // Hidden Cone
            vs[4] = 523400;
            vs[5] = 4112600;

            // Northern Cone
```

```
vs[6] = 540350;
vs[7] = 4079360;

// Black Cone
vs[8] = 538840;
vs[9] = 4074120;

// Red Cone
vs[10] = 537580;
vs[11] = 4071880;

// Little Cone 1
vs[12] = 535200;
vs[13] = 4069360;

// Little cone 2
vs[14] = 535480;
vs[15] = 4069560;

//Buckboard Mesa 1
vs[16] = 555180;
vs[17] = 4109200;

// Buckboard Mesa 2
vs[18] = 555500;
vs[19] = 4108500;

// Crater Flat a
vs[20] = 540330;
vs[21] = 4070050;

//Crater Flat b
vs[22] = 540420;
vs[23] = 4068780;

//Crater Flat c
vs[24] = 540360;
vs[25] = 4068440;

// Crater Flat d
vs[26] = 540680;
vs[27] = 4068820;

//Crater Flat e
vs[28] = 540700;
vs[29] = 4068260;

//Crater Flat f
vs[30] = 540300;
vs[31] = 4071600;

//magnetic anomalies
// AAB
vs[32] = 553700;
vs[33] = 4052900;

//AAA 1
vs[34] = 546100;
vs[35] = 4055100;

//AAA 2
```

```
    vs[36] = 546100;
    vs[37] = 4053100;

    //AAA 3
    vs[38] = 544500;
    vs[39] = 4051400;

    //AAC
    vs[40] = 547000;
    vs[41] = 4042900;

    // AAD
    vs[42] = 549400;
    vs[43] = 4040000;

    // AAE
    vs [44] = 538300;
    vs[45] = 4047200;

    // SW Crater Flat
    vs[46] =535000;
    vs[47] =4067800;

    //Thirsty Mesa 1
    vs[48] = 529520;
    vs[49] = 4112150;

    // Thirsty Mesa 2
vs[50] =529480;;
vs[51] =4112040;

//Thirsty Mesa 3
vs[52] =529540;
vs[53] =4111680;

// Nye Canyon N
vs[54] =604680;
vs[55] =4094260;

// Nye Canyon Middle
vs[56] =602170;
vs[57] =4088960;

//Nye Canyon S 1
vs[58] =600950;
vs[59] =4085920;

// Nye Canyon S 2
vs[60] =600550;
vs[61] =4085450;

//Nye canyon ring dike
vs[62] =599160;
vs[63] =4085820;

//Nye Canyon scarp canyon vent
vs[64] =597930;
vs[65] =4082470;

//Frenchman Flat Ue5I
vs[66] =595260;
```

```
vs[67] =4080980;

// Frenchman Flat Ue5K
vs[68] =593520;
vs[69] =4081480;

//Yucca Flat UE1h
vs[70] =582980;
vs[71] =4095280;

//Yucca Flat UE1j
vs[72] =582440;
vs[73] =4096580;

// Yucca Flat UE6d
vs[74] =583740;
vs[75] =4093400;

// Rocket Wash
vs[76] = 536100;
vs[77] = 4109100;

// Paiute Ridge 1
vs[78] = 592400;
vs[79] = 4106800;

// Paiute Ridge 2
vs[80] = 592800;
vs[81] = 4105900;

// Paiute Ridge 3
vs[82] = 593400;
vs[83] = 4105500;

// Paiute Ridge 4
vs[84] = 594800;
vs[85] = 4107900;

// Paiute Ridge 5
vs[86] = 595800;
vs[87] = 4106300;

// Pahute Mesa 1
vs[88] = 548900;
vs[89] = 4133300;

// Pahute Mesa 2
vs[90] = 554100;
vs[91] = 4134500;

// Pahute Mesa 3
vs[92] = 562400;
vs[93] = 4132700;


break;
case 2:

    //second volcano data set
    // includes pliocene and Quaternary
    // little cones considered 1 event
```

```
      // buckboard considered 1 event
      // 5 amargosa anomalies included
      // plio crater flat events e and f not included

 nvolcanoes = 20;
 vs = new double [nvolcanoes*2];

 // Lathrop Wells
     vs[0] = 543780;
     vs[1] = 4060380;

     // Little Black Peak
     vs[2] = 522120;
     vs[3] = 4110340;

     // Hidden Cone
     vs[4] = 523400;
     vs[5] = 4112600;

     // Northern Cone
     vs[6] = 540350;
     vs[7] = 4079360;

     // Black Cone
     vs[8] = 538840;
     vs[9] = 4074120;

     // Red Cone
     vs[10] = 537580;
     vs[11] = 4071880;

     // Little Cone 1
     vs[12] = 535200;
     vs[13] = 4069360;

     //Buckboard Mesa
     vs[14] = 555180;
     vs[15] = 4109200;

     // Crater Flat a
     vs[16] = 540330;
     vs[17] = 4070050;

     //Crater Flat b
 vs[18] = 540420;
 vs[19] = 4068780;

 //Crater Flat c
 vs[20] = 540360;
 vs[21] = 4068440;

 // Crater Flat d
 vs[22] = 540680;
 vs[23] = 4068820;

 //Crater Flat e
 vs[24] = 540700;
 vs[25] = 4068260;

 //magnetic anomalies
 // AAB
```

```
vs[26] = 553700;
vs[27] = 4052900;

//AAA 1
vs[28] = 546100;
vs[29] = 4055100;

//AAA 2
vs[30] = 546100;
vs[31] = 4053100;

//AAA 3
vs[32] = 544500;
vs[33] = 4051400;

//AAC
vs[34] = 547000;
vs[35] = 4042900;

// AAD
vs[36] = 549400;
vs[37] = 4040000;

// AAE
vs [38] = 538300;
vs[39] = 4047200;

break;
case 3:

    // The third volcano data set
    // includes all known Quaternary vents
    // mapped in the Yucca Mountain region.
    // Magnetic anomalies are not included in this data set.

    nvolcanoes = 8;
    vs = new double [nvolcanoes*2];

    // Lathrop Wells
    vs[0] = 543780;
    vs[1] = 4060380;

    // Little Black Peak
    vs[2] = 522120;
    vs[3] = 4110340;

    // Hidden Cone
    vs[4] = 523400;
    vs[5] = 4112600;

    // Northern Cone
    vs[6] = 540350;
    vs[7] = 4079360;

    // Black Cone
    vs[8] = 538840;
    vs[9] = 4074120;

    // Red Cone
    vs[10] = 537580;
    vs[11] = 4071880;
```

```
    // Little Cone 1
    vs[12] = 535200;
    vs[13] = 4069360;

    // Little Cone 2
    vs[14] = 535480;
    vs[15] = 4069560;

    break;
case 4:

    // The fourth volcano data set
    // includes three events.
    // These are the Quaternary Crater Flat volcano alignment,
    // taken as centered on Red Cone,
    // the Sleeping Butte alignment,
    // taken as centered on Hidden Cone,
    // and Lathrop Wells volcano.

nvolcanoes = 3;
vs = new double [nvolcanoes*2];

// Lathrop Wells
vs[0] = 543780;
vs[1] = 4060380;

// Hidden Cone
vs[2] = 523400;
vs[3] = 4112600;

// Red Cone
vs[4] = 537580;
vs[5] = 4071880;

break;

case 5:

    // fifth  volcano dataset
    // includes all vent locations reported in Data Table
    // some basalt outcrops with unknown vent locations
    // are not included

    nvolcanoes = 64;
    vs = new double [nvolcanoes*2];

    // Lathrop Wells
    vs[0] = 543780;
    vs[1] = 4060380;

    // Little Black Peak
    vs[2] = 522120;
    vs[3] = 4110340;

    // Hidden Cone
    vs[4] = 523400;
    vs[5] = 4112600;

    // Northern Cone
    vs[6] = 540350;
```

```
vs[7] = 4079360;

// Black Cone
vs[8] = 538840;
vs[9] = 4074120;

// Red Cone
vs[10] = 537580;
vs[11] = 4071880;

// Little Cone 1
vs[12] = 535200;
vs[13] = 4069360;

// Little cone 2
vs[14] = 535480;
vs[15] = 4069560;

//Buckboard Mesa 1
vs[16] = 555180;
vs[17] = 4109200;

// Buckboard Mesa 2
vs[18] = 555500;
vs[19] = 4108500;

// Crater Flat a
vs[20] = 540330;
vs[21] = 4070050;

//Crater Flat b
vs[22] = 540420;
vs[23] = 4068780;

//Crater Flat c
vs[24] = 540360;
vs[25] = 4068440;

// Crater Flat d
vs[26] = 540680;
vs[27] = 4068820;

//Crater Flat e
vs[28] = 540700;
vs[29] = 4068260;

//Crater Flat f
vs[30] = 540300;
vs[31] = 4071600;

//magnetic anomalies
// AAB
vs[32] = 553700;
vs[33] = 4052900;

//AAA 1
vs[34] = 546100;
vs[35] = 4055100;

//AAA 2
vs[36] = 546100;
```

```
      vs[37] = 4053100;

      //AAA 3
      vs[38] = 544500;
      vs[39] = 4051400;

      //AAC
      vs[40] = 547000;
      vs[41] = 4042900;

      // AAD
      vs[42] = 549400;
      vs[43] = 4040000;

      // AAE
      vs [44] = 538300;
      vs[45] = 4047200;

      // SW Crater Flat
      vs[46] =535000;
      vs[47] =4067800;

      //Thirsty Mesa 1
      vs[48] = 529520;
      vs[49] = 4112150;

     // Thirsty Mesa 2
vs[50] =529480;;
vs[51] =4112040;

//Thirsty Mesa 3
vs[52] =529540;
vs[53] =4111680;

// Nye Canyon N
vs[54] =604680;
vs[55] =4094260;

// Nye Canyon Middle
vs[56] =602170;
vs[57] =4088960;

//Nye Canyon S 1
vs[58] =600950;
vs[59] =4085920;

// Nye Canyon S 2
vs[60] =600550;
vs[61] =4085450;

//Nye canyon ring dike
vs[62] =599160;
vs[63] =4085820;

//Nye Canyon scarp canyon vent
vs[64] =597930;
vs[65] =4082470;

//Frenchman Flat Ue5I
vs[66] =595260;
vs[67] =4080980;
```

```
// Frenchman Flat Ue5K
vs[68] =593520;
vs[69] =4081480;

//Yucca Flat UE1h
vs[70] =582980;
vs[71] =4095280;

//Yucca Flat UE1j
vs[72] =582440;
vs[73] =4096580;

// Yucca Flat UE6d
vs[74] =583740;
vs[75] =4093400;

// Rocket Wash
vs[76] = 536100;
vs[77] = 4109100;

// Paiute Ridge 1
vs[78] = 592400;
vs[79] = 4106800;

// Paiute Ridge 2
vs[80] = 592800;
vs[81] = 4105900;

// Paiute Ridge 3
vs[82] = 593400;
vs[83] = 4105500;

// Paiute Ridge 4
vs[84] = 594800;
vs[85] = 4107900;

// Paiute Ridge 5
vs[86] = 595800;
vs[87] = 4106300;

// Pahute Mesa 1
vs[88] = 548900;
vs[89] = 4133300;

// Pahute Mesa 2
vs[90] = 554100;
vs[91] = 4134500;

// Pahute Mesa 3
vs[92] = 562400;
vs[93] = 4132700;

// basalt of sleeping butte 1
vs[94] = 525700;
vs[95] = 4112100;

//basalt of sleeping butte 2
vs[96] = 524300;
vs[97] = 4113600;

// Solitario canyon
```

```
        vs[98] = 546800;
        vs[99] = 4082400;

        // Miocene basalt of SW crater flat 1
        vs[100] = 536400;
        vs[101] = 4064000;

        // Miocene basalt of SW Crater Flat 2
        vs[102] = 534700;
        vs[103] = 4066500;

        // basalt of VH-2
        vs[104] = 537900;
        vs[105] = 4072950;

        // basalt of Kiwi Mesa
        vs[106] = 568940;
        vs[107] = 4078740;
        vs[108] = 568820;
        vs[109] = 4079000;

        // basalt of NE Amargosa Desert
        vs[110] = 563300;
        vs[111] = 4046500;

        // beatty basalt
        vs[112] = 525300;
        vs[113] = 4085600;
        vs[114] = 527400;
        vs[115] = 4085200;
        vs[116] = 514800;
        vs[117] = 4090800;

        // grapevine
        vs[118] = 476400;
        vs[119] = 4101800;
        vs[120] = 476800;
        vs[121] = 4102700;
        vs[122] = 477900;
        vs[123] = 4106600;

        // southern Death Valley
        // Cinder Hill
        vs[124] = 523900;
        vs[125] = 3977100;
        // Shoreline Butte
        vs[126] = 526200;
        vs[127] = 3973700;


        break;

        default:
            nvolcanoes = 1;
            vs = new double[nvolcanoes*2];
            vs[0] = 0.0;
            vs[1] = 0.0;
        }
    }

    public void setVolcanoset( int n) {
```

```
        volcanoset = n;
    }
}
```

Locations and Age Determinations for Basalts in the Yucca Mountain Region

Compiled by B. E. Hill

Compilation of K-Ar and Ar/Ar dates for post-11 Ma basaltic rocks of the YMR. Units and sample numbers as reported by authors. Wgtd mean corresponds to weighted mean on n samples and 1-sigma best estimated errors (Taylor, 1990), multiplied by the square root of the mean square of the weighted deviates (MSWD) if MSWD > 1 (e.g., Fleck et al., 1996). Average is average ± 1 standard deviation of reported dates. Unkn. is unknown, unpub. res. is unpublished research, and pers. comm. is personal communication.
Coordinates for vent locations in Universal Transverse Mercator meters, Zone 11, North American Datum 1927. Vent locations determined by cited authors and field observations (B. Hill, unpub. res., 1993-1996)

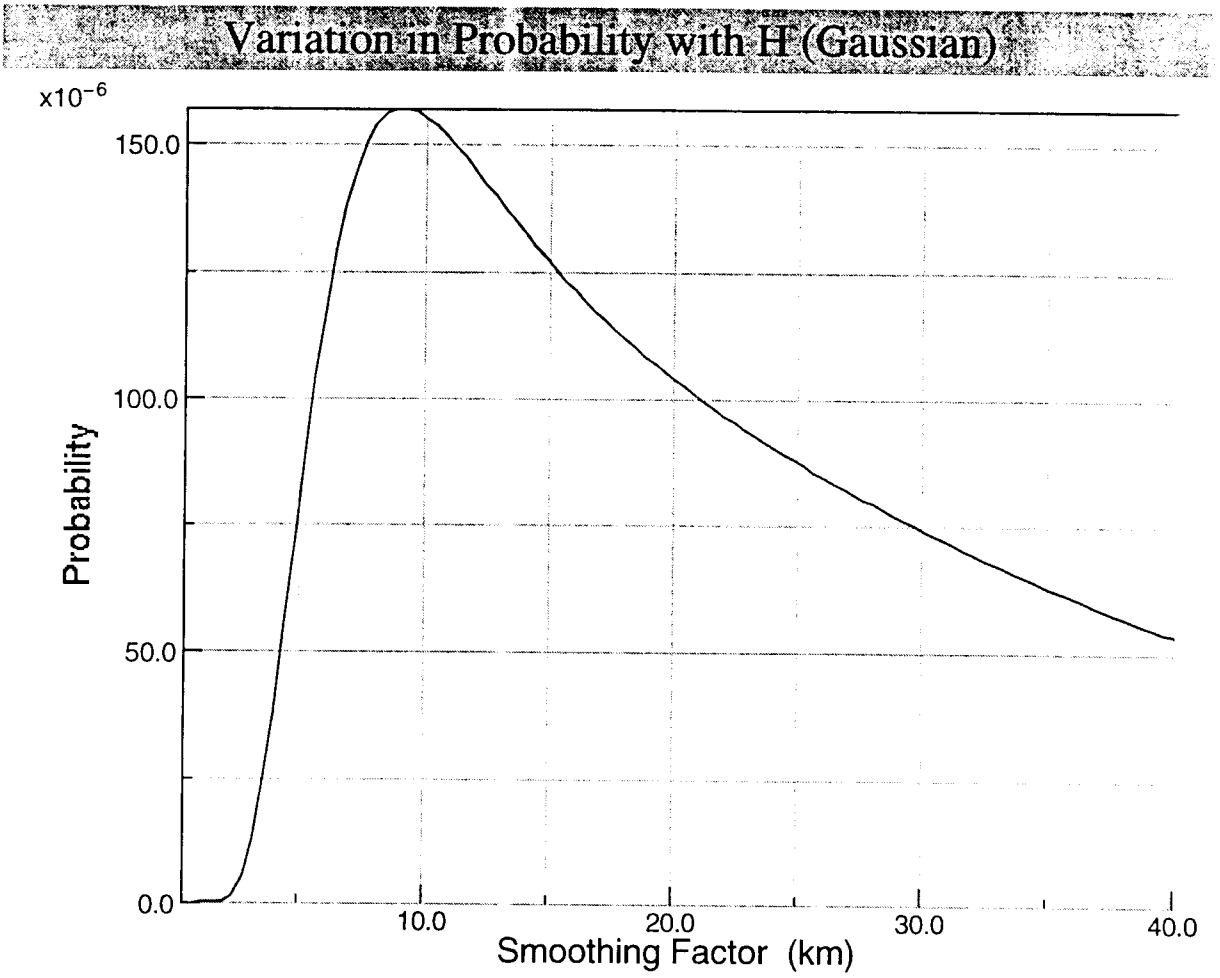

Data Set (1–5)	1	Calculate	
Easting	548500.0	Northing	4078500.0
hmin	0.0	hmax	40.0
Effective Area	8.0	Time Interval	10000.0
Recurrence Rate	10.0e–6		

About the Gaussian Probability Graph

This graph shows the probability of volcanic events within some area about a point, and within some time interval given a reccurance rate for volcanic events in the region. A Gaussian kernel density estimator is used for this calculation. To estimate probability at the center, x,y, of some small area (the effective area), use the Gaussian kernel:

$$ki = 2\ pi\ exp[-1/2\ (di/h)^2]$$

where *di* is the distance from the point x,y to the *ith* volcano and h is the smoothing parameter. Then recurrence rate of volcanic events in the 1 x 1 km area about the point x,y, given a volcanic event in the system is given by:

$$lambda = 1/(nh^2)\ Sum\ \{from\ i=1\ to\ n\}\ ki.$$

See Connor and Hill [1995] and Connor et al. [2000] for further explanation and tips on estimating appropriate smoothing factors. The graph shows the change in probability as a function of the smoothing factor.

Probability is calculated using Poisson's equation:

$$P[N=>1] = 1 - exp[-t\ lambda(t)\ sum\ \{over\ area\ a\}lambda(s)]$$

where t is the time interval for which probability is estimated, *lambda(t)* is the regional reccurance rate of volcanic events, a is the effective area, and *lambda(s)* is the spatial reccurance of volcanism calculated using the Gaussian kernel.

Various data sets can be selected that vary the definition of volcanic event.

Description of parameters for the Gaussian Probability Graph

Data Set:

The data set to use in the analysis is selected using an integer 1 - 5.

Data set 1 includes known Miocene through Quaternary vents mapped in the Yucca Mountain region, including several magnetic anomalies, assumed to be Miocene-Quaternary in age, that have not been drilled. See the data table for details. This data set does not include some petrologically distinct basalts of Miocene age, such as the 11.2 Ma Solitario Canyon dike.

Data set 2 includes all known Pliocene - Quaternary vents mapped in the Yucca Mountain region, including several magnetic anomalies, assumed to be Miocene-Quaternary in age, that have not been drilled. Several closely spaced vents have been grouped, and are treated as single volcanic events. For example, the two Little Cones are treated as a single volcanic event in this data set.

Data set 3 includes all known Quaternary vents mapped in the Yucca Mountain region. Magnetic anomalies are not included in this data set.

Data set 4 includes three events. These are the Quaternary Crater Flat volcano alignment , taken as centered on Red Cone, the Sleeping Butte alignment, taken as centered on Hidden Cone, and Lathrop Wells.

Data set 5 includes all vent locations reported in the Data Table.

Easting and Northing:

Defines the coordinates of the point for which calculations are made. Default is within the repository boundary. Coordinates are entered in Universal Transverse Mercator coordinate system (North American Datum, NAD83) in meters.

hmin, hmax:

The range of smoothing parameters for which probabilities are estimated, in kilometers. Default is 0 and 40 kilometers, respectively. hmax must be greater than hmin, and hmin must be equal to or greater than 0.

Effective Area:

The area about the point, defined by the Easting and Northing, over which probability is estimated, in square kilometers. Default is 8 square kilometers. The effective area should include the area of the repository, plus the area within which a volcanic eruption may occur and disrupt the repository (see

Connor and Hill, 1995). Effective Area must be a real number greater than 0.

Time Interval:

The time interval for which the probability estimate is made, in years. Default is 10,000 yr. Time Interval must be a real number greater than 0.

Recurrence Rate:

The recurrence rate of volcanic events in the magmatic system, in units of volcanic events per year. Default is 10.0e-6 volcanic events per year. Note: the recurrence rate should be varied with the definition of volcanic event (Data set) used in the analysis. The Recurrence Rate must be a real number greater than 0.

Hot Keys

Hot keys can change some of the features of the map or graph.

Note: if hot keys do not appear to function, ***left click*** the mouse once in the map or graph window.

A ***left click and drag*** of the mouse will zoom in on the selected area

r - redraw the map or graph using the current parameters

R - redraw the map or graph showing the entire data range

l - plot the map with contour labels *(applying several times will change label locations, only applies to contour plots)*

L - plot the map without contour labels *(only applies to contour plots)*

c - open another window to show the coordinates of the cursor

m - change the map or graph scale

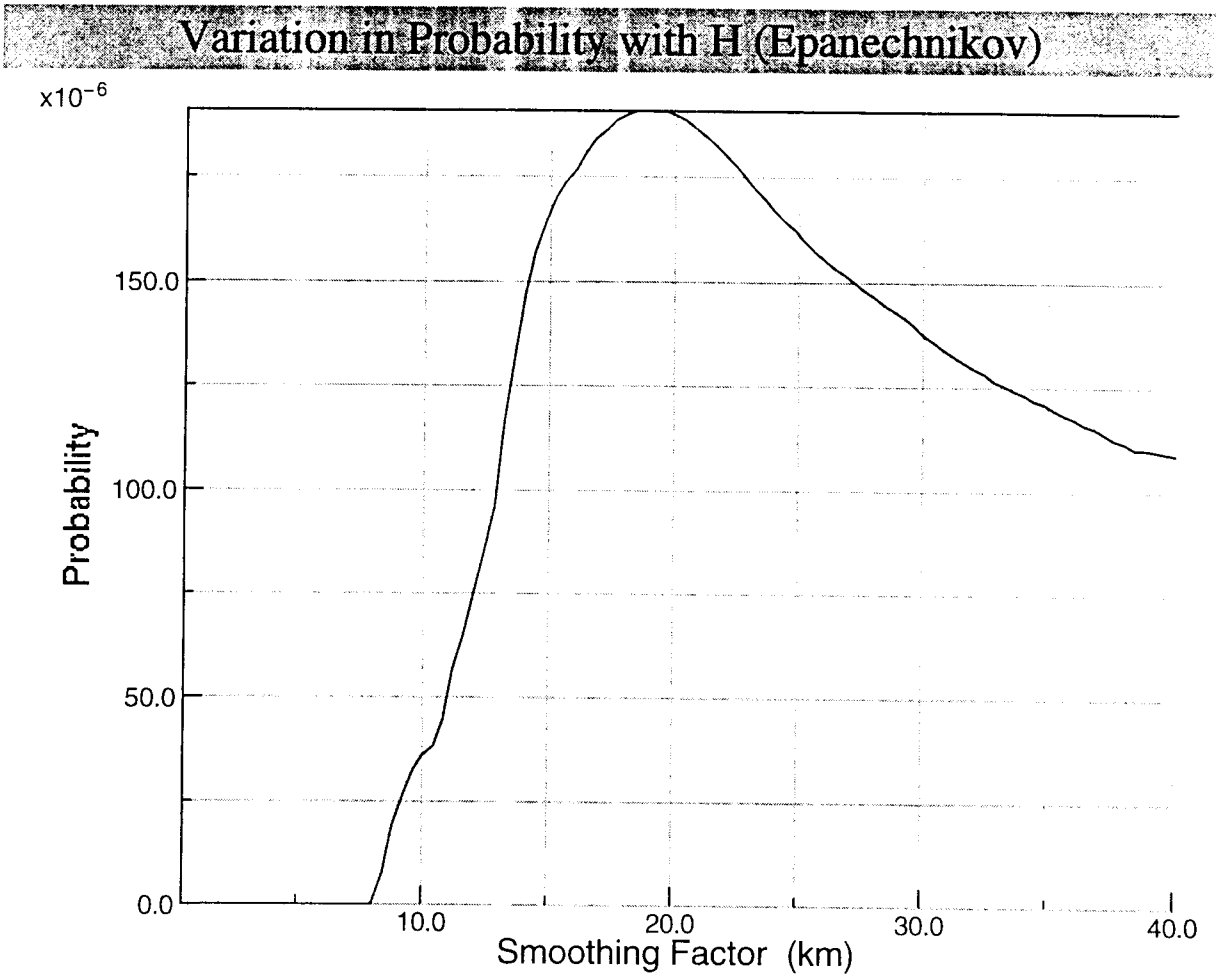

Data Set (1–5)	1	Calculate	
Easting	548500.0	Northing	4078500.0
hmin	0.0	hmax	40.0
Effective Area	8.0	Time Interval	10000.0
Recurrence Rate	10.0e–6		

About the Epanechnikov Probability Graph

This graph shows the probability of volcanic events within some area about a point, and within some time interval given a reccurance rate for volcanic events in the region. A Epanechnikov kernel density estimator is used for this calculation. To estimate probability at the center, *x,y*, of some small area (the effective area), use the Epanechnikov kernel:

$$ki = (2/pi)[1 - (di/h)^2], \text{ if } (di/h)^2 < 1 \text{ and}$$

$$ki = 0, \text{ otherwise}$$

where *di* is the distance from the point *x,y* to the *ith* volcano and *h* is the smoothing parameter. Then recurrence rate of volcanic events in the 1 x 1 km area about the point *x,y*, given a volcanic event in the system is given by:

$$lambda = 1/(nh^2) \text{ Sum } \{\text{from } i=1 \text{ to } n\} ki.$$

See Connor and Hill [1995] and Connor et al. [2000] for further explanation and tips on estimating appropriate smoothing factors. The graph shows the change in probability as a function of the smoothing factor.

Probability is calculated using Poisson's equation:

$$P[N=>1] = 1 - exp[-t \text{ lambda}(t) \text{ sum } \{\text{over area } a\}\text{lambda}(s)]$$

where *t* is the time interval for which probability is estimated, *lambda(t)* is the regional reccurance rate of volcanic events, *a* is the effective area, and *lambda(s)* is the spatial reccurance of volcanism calculated using the Epanechnikov kernel.

Various data sets can be selected that vary the definition of volcanic event.

Description of parameters for the Epanechnikov Probability Graph

---

Data Set:

The data set to use in the analysis is selected using an integer 1 - 5.

Data set 1 includes known Miocene through Quaternary vents mapped in the Yucca Mountain region, including several magnetic anomalies, assumed to be Miocene-Quaternary in age, that have not been drilled. See the data table for details. This data set does not include some petrologically distinct basalts of Miocene age, such as the 11.2 Ma Solitario Canyon dike.

Data set 2 includes all known Pliocene - Quaternary vents mapped in the Yucca Mountain region, including several magnetic anomalies, assumed to be Miocene-Quaternary in age, that have not been drilled. Several closely spaced vents have been grouped, and are treated as single volcanic events. For example, the two Little Cones are treated as a single volcanic event in this data set.

Data set 3 includes all known Quaternary vents mapped in the Yucca Mountain region. Magnetic anomalies are not included in this data set.

Data set 4 includes three events. These are the Quaternary Crater Flat volcano alignment , taken as centered on Red Cone, the Sleeping Butte alignment, taken as centered on Hidden Cone, and Lathrop Wells.

Data set 5 includes all vent locations reported in the Data Table.

Easting and Northing:

Defines the coordinates of the point for which calculations are made. Default is within the repository boundary. Coordinates are entered in Universal Transverse Mercator coordinate system (North American Datum, NAD83) in meters.

hmin, hmax:

The range of smoothing parameters for which probabilities are estimated, in kilometers. Default is 0 and 40 kilometers, respectively. hmax must be greater than hmin, and hmin must be equal to or greater than 0.

Effective Area:

The area about the point, defined by the Easting and Northing, over which probability is estimated, in

square kilometers. Default is 8 square kilometers. The effective area should include the area of the repository, plus the area within which a volcanic eruption may occur and disrupt the repository (see Connor and Hill, 1995). Effective Area must be a real number greater than 0.

Time Interval:

The time interval for which the probability estimate is made, in years. Default is 10,000 yr. Time Interval must be a real number greater than 0.

Recurrence Rate:

The recurrence rate of volcanic events in the magmatic system, in units of volcanic events per year. Default is 10.0e-6 volcanic events per year. Note: the recurrence rate should be varied with the definition of volcanic event (Data set) used in the analysis. The Recurrence Rate must be a real number greater than 0.

Gaussian Probability Map

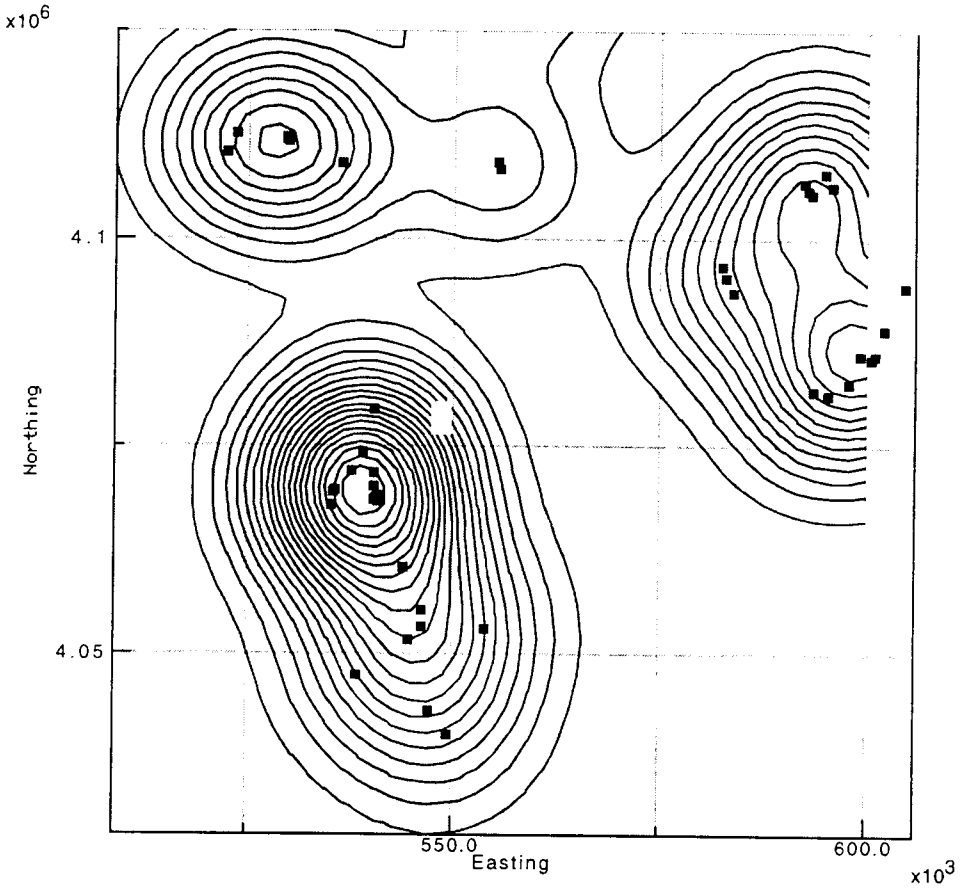

Data Set (1–5)	1	Calculate	
Number of Contours	20	Smoothing Factor (km)	8.0
X grid dimension	50	Y grid dimension	50
Minimum Easting	500000.0	Maximum Easting	600000.0
Minimum Northing	4025000.0	Maximum Northing	4125000.0

About the Gaussian Probability map

This is a conditional probability map plotted using a Gaussian kernel density estimator. The probability of a volcanic event within a 1 x 1 km area, given that a volcanic event occurs within the magmatic system, is contoured. To estimate probability at the center, x,y, of some small area (1 km^2) on this map, use the Gaussian kernel:

$$ki = 2\ pi\ exp[-1/2\ (di/h)^2]$$

where di is the distance from the point x,y to the ith volcano and h is the smoothing parameter. Then recurrence rate of volcanic events in the 1 x 1 km area about the point x,y, given a volcanic event in the system is given by:

$$lambda = 1/(nh^2)\ Sum\ \{from\ i=1\ to\ n\}\ ki.$$

The model will predict high probabilities close to existing volcanoes if the smoothing parameter, h, is chosen to be small. Conversely, probabilities will be more uniform across the region if a large value of h is chosen. See Connor and Hill [1995] and Connor et al. [2000] for further explanation and tips on estimating appropriate smoothing factors.

Various data sets can be selected that vary the definition of volcanic event. Volcanic events used in the analysis are shown as black rectangles on the map. The location of the proposed high-level radioactive waste repository is indicated by the yellow rectangle.

Map coordinates are given in Universal Transverse Mercator coordinate system (North American Datum, NAD83) in meters.

Description of parameters for the Gaussian Probability Map

Data Set:

The data set to use in the analysis is selected using an integer 1 - 5.

Data set 1 includes known Miocene through Quaternary vents mapped in the Yucca Mountain region, including several magnetic anomalies, assumed to be Miocene-Quaternary in age, that have not been drilled. See the data table for details. This data set does not include some petrologically distinct basalts of Miocene age, such as the 11.2 Ma Solitario Canyon dike.

Data set 2 includes all known Pliocene - Quaternary vents mapped in the Yucca Mountain region, including several magnetic anomalies, assumed to be Miocene-Quaternary in age, that have not been drilled. Several closely spaced vents have been grouped, and are treated as single volcanic events. For example, the two Little Cones are treated as a single volcanic event in this data set.

Data set 3 includes all known Quaternary vents mapped in the Yucca Mountain region. Magnetic anomalies are not included in this data set.

Data set 4 includes three events. These are the Quaternary Crater Flat volcano alignment , taken as centered on Red Cone, the Sleeping Butte alignment, taken as centered on Hidden Cone, and Lathrop Wells.

Data set 5 includes all vent locations reported in the Data Table.

Smoothing Factor:

The smoothing factor for the Gaussian kernel is equivalent to the standard deviation. Units of smoothing factor: kilometers. The Smoothing Factor must be a real number greater than 0.

Number of Contours:

Set the number of contours, drawn at equal intervals, on the map. Contour labels show probability of a volcanic event within a 1 x 1 km area, given a volcanic event within the magmatic system. Number of contours must be an integer greater than 0.

X and Y grid dimension:

Define the number of gridpoints in the the x and y directions for which conditrional probability estimates are made. Gridpoints are equally spaced between the minimum and maximum map dimensions. X and Y grid dimensions must be integers greater than 0.

Minimum and maximum Easting and Northing:

Defines the map area for which calculations are made. Coordinates are entered in Universal Transverse Mercator coordinate system (North American Datum, NAD83) in meters.

Epanechnikov Probability Map

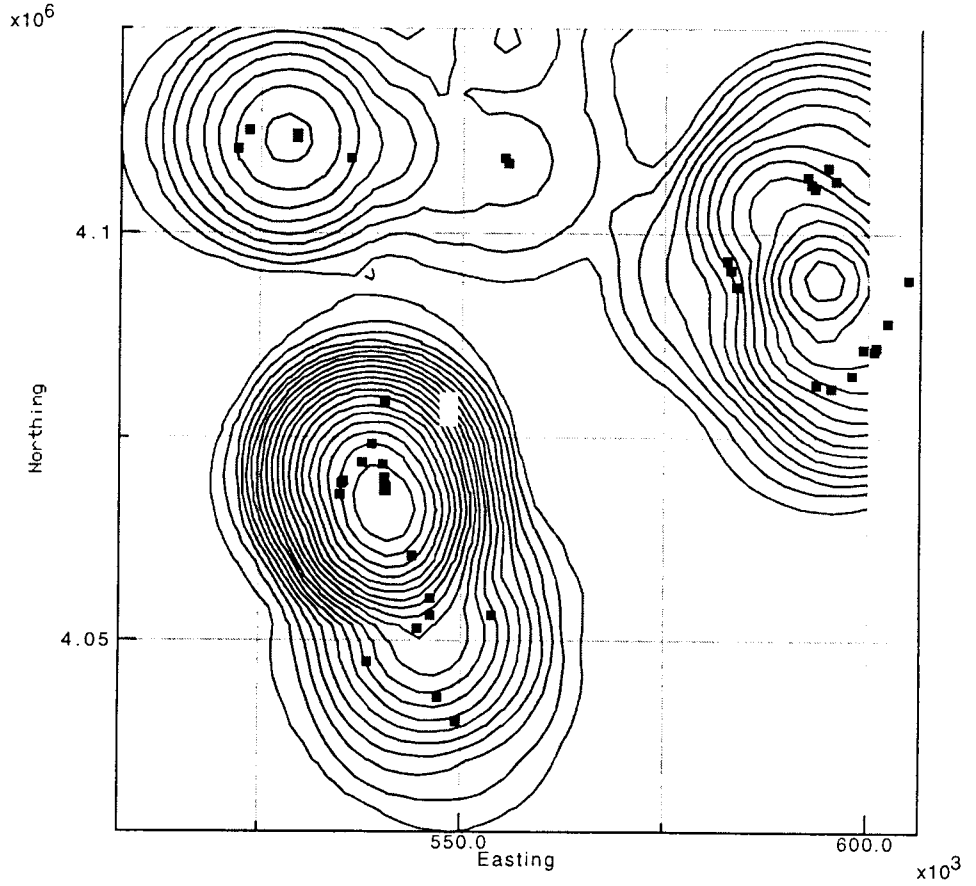

Data Set (1–5)	1	Calculate	
Number of Contours	20	Smoothing Factor (km)	18.0
X grid dimension	50	Y grid dimension	50
Minimum Easting	500000.0	Maximum Easting	600000.0
Minimum Northing	4025000.0	Maximum Northing	4125000.0

About the Epanechnikov Probability map

This is a conditional probability map plotted using an Epanechnikov kernel density estimator. The probabilty of a volcanic event within a 1 x 1 km area, given that a volcanic event occurs within the magmatic system, is contoured. To estimate probability at the center, x,y, of some small area (1 km^2) on this map, use the Epanechnikov kernel:

$$ki = (2/pi)[1 - (di/h)^2], \text{ if } (di/h)^2 < 1 \text{ and}$$

$$ki = 0, \text{ otherwise}$$

where di is the distance from the point x,y to the ith volcano and h is the smoothing parameter. Then recurrence rate of volcanic events in the 1 x 1 km area about the point x,y, given a volcanic event in the system is given by:

$$lambda = 1/(nh^2) \text{ Sum } \{\text{from } i=1 \text{ to } n\} ki.$$

Note that if no volcanoes are located within a distance h of the point x,y, then lambda = 0.

The model will predict high probabilities close to existing volcanoes if the smoothing parameter, h, is chosen to be small. Conversely, probabilities will be more uniform across the region if a large value of h is chosen. See Connor and Hill [1995] and Connor et al. [2000] for further explanation.

Various data sets can be selected to vary the definition of volcanic event. Volcanic events used in the analysis are shown as black rectangles on the map. The location of the proposed high-level radioactive waste repository is indicated by the yellow rectangle.

Map coordinates are given in Universal Transverse Mercator coordinate system (North American Datum, NAD83) in meters.

Description of parameters for the Epanechnikov Probability Map

Data Set:

The data set to use in the analysis is selected using an integer 1 - 5.

Data set 1 includes known Miocene through Quaternary vents mapped in the Yucca Mountain region, including several magnetic anomalies, assumed to be Miocene-Quaternary in age, that have not been drilled. See the data table for details. This data set does not include some petrologically distinct basalts of Miocene age, such as the 11.2 Ma Solitario Canyon dike.

Data set 2 includes all known Pliocene - Quaternary vents mapped in the Yucca Mountain region, including several magnetic anomalies, assumed to be Miocene-Quaternary in age, that have not been drilled. Several closely spaced vents have been grouped, and are treated as single volcanic events. For example, the two Little Cones are treated as a single volcanic event in this data set.

Data set 3 includes all known Quaternary vents mapped in the Yucca Mountain region. Magnetic anomalies are not included in this data set.

Data set 4 includes three events. These are the Quaternary Crater Flat volcano alignment , taken as centered on Red Cone, the Sleeping Butte alignment, taken as centered on Hidden Cone, and Lathrop Wells.

Data set 5 includes all vent locations reported in the Data Table.

Smoothing Factor:

The smoothing factor for the Gaussian kernel is equivalent to the standard deviation. Units of smoothing factor: kilometers. The Smoothing Factor must be a real number greater than 0.

Number of Contours:

Set the number of contours, drawn at equal intervals, on the map. Contour labels show probability of a volcanic event within a 1 x 1 km area, given a volcanic event within the magmatic system. Number of contours must be an integer greater than 0.

X and Y grid dimension:

Define the number of gridpoints in the the x and y directions for which conditrional probability estimates are made. Gridpoints are equally spaced between the minimum and maximum map dimensions. X and Y grid dimensions must be integers greater than 0.

Minimum and maximum Easting and Northing:

Defines the map area for which calculations are made. Coordinates are entered in Universal Transverse Mercator coordinate system (North American Datum, NAD83) in meters.

GEOLOGIC FACTORS CONTROLLING PATTERNS OF SMALL-VOLUME BASALTIC VOLCANISM: APPLICATION TO A VOLCANIC HAZARDS ASSESSMENT AT YUCCA MOUNTAIN, NEVADA

CHARLES B. CONNOR[1], JOHN A. STAMATAKOS[1], DAVID A. FERRILL[1], BRITTAIN E. HILL[1], GOODLUCK I. OFOEGBU[1], F. MICHAEL CONWAY[2], BUDHI SAGAR[1], and JOHN TRAPP[3]

1. Center for Nuclear Waste Regulatory Analyses, Southwest Research Institute, 6220 Culebra Rd, San Antonio, TX, 78238-5166, USA

2. Department of Physical Sciences, Western Arizona College, Yuma, AZ

3. U.S. Nuclear Regulatory Commission, Office of Materials Safety and Safeguards, Division of Waste Management, Washington, D.C.

Reference: Connor, C.B., J.A. Stamatakos, D.A. Ferrill, B.E. Hill, G.I. Goodluck, F.M. Conway, B. Sagar, J. Trapp, 2000, Geologic factors controlling patterns of small-volume basaltic volcanism: Application to a volcanic hazards assessment at Yucca Mountain, Nevada, Journal of Geophysical Research 105, 417-432.

User: cconnor
Host: oso
Class: oso
Job: stdin

User: cconnor
Host: oso
Class: oso
Job: stdin

THREE NONHOMOGENEOUS POISSON MODELS FOR THE PROBABILITY OF BASALTIC VOLCANISM: APPLICATION TO THE YUCCA MOUNTAIN REGION

CHARLES B. CONNOR and BRITTAIN E. HILL

Center for Nuclear Waste Regulatory Analyses, Southwest Research Institute, Bldg. 189

6220 Culebra Rd, San Antonio, Texas, 78238-5166, USA

Reference: Connor, C.B., and B.E. Hill, 1995, Three nonhomogeneous Poisson models for the probability of basaltic volcanism: Application to the Yucca Mountain region, Journal of Geophysical Research 100 (B6): 10,107-10,125.

RECURRENCE RATES OF VOLCANISM IN BASALTIC VOLCANIC FIELDS: AN EXAMPLE FROM THE SPRINGERVILLE VOLCANIC FIELD, AZ, USA

C.D. CONDIT

DEPARTMENT OF GEOSCIENCES, UNIVERSITY OF MASSACHUSETTS, AMHERST, MA, 01003

C.B. CONNOR

CENTER FOR NUCLEAR WASTE REGULATORY ANALYSES, SOUTHWEST RESEARCH INSTITUTE, SAN ANTONIO, TX, 78238

Reference: Condit, C.D., and C.B. Connor, 1996, Recurrence rates of volcanism in basaltic volcanic fields: An example from the Springerville Volcanic field, Az, USA, Geological Society of America, Bulletin 108, 1225-1241.

Basaltic Volcanic Fields

Charles B. Connor

Center for Nuclear Waste Regulatory Analyses, Southwest Research Institute, San Antonio, TX, USA

cconnor@swri.org

F. Michael Conway

Division of Math and Science, Arizona Western College, Yuma, AZ, USA

Reference: Connor, C.B., and F.M. Conway, 2000, Basaltic volcanic Fields, in: H. Sigurdsson, editor, Encyclopedia of Volcanoes, Academic Press, New York, 331-343.

List of Tables

No original data have been removed. Entries into SN 115E for the period October, 1999 to Jan 2000 have been made by C. Connor. Celia B Connor 2/10/00

11 of 17

SCIENTIFIC NOTEBOOK 115E

BY

Charles B. Connor

SCIENTIFIC NOTEBOOK
115E

BY

Charles B. Connor

Southwest Research Institute
Center for Nuclear Waste Regulatory Analyses
San Antonio, Texas

SCIENTIFIC NOTEBOOK 115E

CHUCK CONNOR

PROJECT

IGNEOUS ACTIVITY

PROJECT NUMBER 20-1402-461

Nov, 1998 - Jan, 1999

PARTS IN THIS NOTEBOOK:

cc

Scientific Notebook
Project 20-1402-461

Nov, 1998
Chuck Connor

The following paper was presented at the USGS seminar on volcanic hazards assessment.

An Application of PVHA: Cerro Negro volcano, Nicaragua

Chuck Connor, CNWRA, Southwest Research Inst., 6220 Culebra Rd., San Antonio, TX, 78238-5166, USA, e-mail: cconnor@swri.edu

cc

Scientific Notebook
Project 20-1402-461

Nov, 1998
Chuck Connor

The following paper was presented at the USGS seminar on volcanic hazards assessment.

A PVHA for Yucca Mountain, Nevada

Chuck Connor, CNWRA, Southwest Research Inst., 6220 Culebra Rd., San Antonio, TX, 78238-5166, USA, e-mail: cconnor@swri.edu

Information potentially subject to copyright protection was redacted from the hand written page numbers 4 through 6 of this scientific notebook. The redacted material is from the reference listed above.

Information potentially subject to copyright protection was redacted from the hand written pages 7 through 35 of this scientific notebook. The redacted material was a draft proposal prepared for NASA that was included in this notebook because it provides a good summary of the current status of measurements of fumarole degassing and plume dispersion. The author intended to use this information to develop more sophisticated models of radionuclide dispersion in eruption columns.

CC

Scientific Notebook
Project 20-1402-461

Nov, 1998
Chuck Connor

The following paper was reviewed for the Journal of volcanology and geothermal research

Review of: Whitehead et al., Rn-222 and Rn-220 in surface steam as a measure of downhole conditions....

Reviewed by: Chuck Connor, Nov 26, 1998

Regrettably, I cannot recommend this paper for publication. In its current form, this paper is unorganized, poorly written, and so disjointed that it becomes difficult to decipher the scientific content. The authors should attempt to collect additional data, reconsider their interpretations, then completely rewrite the paper before resubmitting it to a journal. That, said, the topic and what data are shown are worthy of eventual publication in JVGR and I encourage the authors to pursue a rigorous rewrite.

First some general comments:

(1) The paper needs a real introduction. The reader is left to discover that the authors explore the systematics of two decay-series to help characterize the Wairakei reservoir. An additional concern is assessment of public health and safety related to the release of these isotopes. Why not

start by clearly stating this? Figure 1, cited in the introduction should show the two main decay series discussed in the paper and the half-lives of species within these decay series. This will greatly help readers of the paper and serve to organize the following sections. Consider organizing the rest of the paper according to the decay series, rather than jumping around.

(2) The use of concentrations in the paper is suspect. How can you compare leachate concentrations from altered rocks to steam concentrations? This needs to be thought out more carefully and I suggest that additional leachate analyses be performed. I elaborate on this in the following.

(3) I am not sure what to make of the discussion of $^{220}Rn/^{222}Rn$ ratios in fumaroles and geothermal wells. The authors report low ratios in geothermal wells compared with some fumaroles. Does this difference occur because of the longer travel time of the steam in the geothermal wells, isolated from a Ra-224 source compared to the fumaroles, is there Ra in the fumaroles that is absent in the geothermal waters, or is it due to the relative abundance of Th-228 and Th-230 in the rock?

Rn-222 is sampling a volume extending outward < 1000 m from the well, Rn-220 is sampling a volume extending < 10 m from the well. Once the difference between Rn-220 concentrations in liquid and steam wells is accounted for, a direct correlation is observed between these isotopes.

There are three components of the transport (a) diffusion out of the rock matrix (slow), (b) advection in fractures (1-10 m /hr) , and (c) advection up the well (fast).

Does the higher Rn-220 in the water-dominated wells mean that the parents Ra-226 and Ra-224 are already in solution in the water-dominated wells? This idea is rejected by the authors because Ra absent in geothermal waters in the region. But Ra-226 and Ra-224 are present in adequate abundance in altered rocks in the area. Furthermore, the authors argue that differences in Th-230 and Th-232 concentration cannot account for this difference in $^{220}Rn/^{222}Rn$ ratio because the differences are too great.

So, the authors conclude that the observed isotopic compositions reflect diffusion. Alternatively, this difference could easily be related to the advection time in fractures, prior to entering the well. This assumes that the gas in the fractures is not necessarily in equilibrium with the gas produced by diffusion out of the rock matrix. This alterative should be discussed, since a major goal of the paper is to apply the isotope geochemistry to modeling the reservoir. A figure that illustrates these alternative models would help.

(4) Normally I don't comment on writing style - but the author's use of the passive voice is excessive and clouds the discussion.

Scientific Notebook
Project 20-1402-461

Nov, 1998
Chuck Connor

Some additional specific Comments:

p 2: More details about the well locations and the geology of the field (esp. The producing zones) is essential. Figure 2 of this paper should be a geologic map with the well locations superimposed. The liquid- and steam- dominated wells should be differentiated on the map, if possible, and structures which influence subsurface transport should be delineated. The purpose of this figure is to allow the reader to compare the results reported in Tables 1,3, and 5 with the geology of the well field, the proximity of wells to one-another, etc. For example, are the WK-59 and WK-79 results expected or unexpected considering the positions of, and local geologic structures about, these wells? The importance of the geology is evident at several points in the discussion. For example, a density of 2.5 kg l^{-1} is used to estimate the expected concentration of ^{222}Rn and used to normalize ^{222}Rn and ^{220}Rn concentrations observed in the wells. This is a critical calculation, used to interpret the Rn ratios in terms of steam and water transport, to discuss permeability variation, etc. Yet there is no discussion of actual rock density variation in the field. Down hole density data must exist and could provide a very useful benchmark. In a similar vein, lithology variations that may alter the radon source term are mentioned for the first time on page 14. Such surprises should be eliminated with a focused discussion of the geology early in the paper.

p 2-3. The last paragraph on page 2 and the first paragraph on page 3 are vague. It is unclear what you conclude about these earlier investigations. Reach some conclusion about this work. How

does your study improve on this work?

p 6: The choice of 10% reproducibility uncertainty is insufficiently supported, especially after saying that other studies showed reproducibility for similar systems at no better than 30%. Whatever is used should be noted in Table 1, which now only shows counting errors.

p 6: I found no later "internal consistency" that supported the guessed weight of leached solids.

p 6, sec 4.1: Table 1 does not show 220/222 ratios.

p 8. The downhole calculation of Rn-220 and Rn-222 needs better explanation. I think you should show the equations you use to make these calculations. This would be very useful to the reader. Also, since the activity coefficient for Rn will vary as a function of total pressure, I am not clear on how a simple application of Henry's Law is appropriate. Is it reasonable to assume that Rn water-steam partitioning follows equilibrium? Or, do you perform the calculation in a stepwise manner? In the second paragraph on page 8, you need to differentiate between radioactivity concentration and activity coefficient in the discussion of Henry's Law.

Similarly, show the procedure you used to estimate decay of Rn-220 during ascent (last paragraph on Page 8). It seems to me that this correction is intractable because of the possibility of multiple sources of the Rn-220 along the length of the well. Aren't these wells producing from

multiple fracture zones? What is the typical steam velocity in these wells (e.g., 1-10 m/s?)? On page 14, the possibility of Rn emanations from shallow laucustrine sediments is mentioned. How does this affect your downhole correction? Showing the equations explicitly will strengthen your case and add a useful dimension to the paper.

p 9-10, sec 4.3 (and elsewhere, e.g. top of page 11): It does not make sense to directly compare Rn and Ra isotope activity concentrations in different phases (rock, gas, and liquid).

p 10, 2nd paragraph: What does it mean to say that Rn-220 recharge by diffusion "should be complete" within 5 minutes? Yes, this is the time it takes for Rn-220 to reach radioactive equilibrium with its Ra-224 parent. But if it's diffusing out, it loses contact with the parent. Assuming a static system (no gas in or out except for diffusion from rock), the activity in the gas phase is a function of the rates of (i) production in the solid (i.e., parent activity), (ii) diffusion out of the solid, and (iii) decay. The authors seem to recognize this elsewhere, but this paragraph doesn't make sense to me, especially since diffusion rates aren't mentioned. Likewise, the comment about Rn-222 taking several weeks to reach equilibrium is confusing.

p 10: Are the values in Table 3 for liquid or gas?

p. 10: Local derivation versus transport in.

p 11: The "altered rock" values are actually for a leachate which removed an indeterminate amount of solid--not a bulk-rock analysis. This should be clear in the paper.

p 12. The section now titled "Unusual Th-230 and Th-232 concentrations cause the Rn emanation" indicates that the authors have discovered that the geothermal system is an open-system, or at least has behaved as an open system in the past. Parent isotopes are not only located in the 100 -1000 m zone about the wells but are transported into this region from elsewhere attached to colloids. The Th concentrations indicate that this has happened sometime in the last tens of thousands of years, and the Po-210 indicates that this open-system behavior is likely continuing.

p 13: I have great doubts about use of the concentrations from the leachate data in Table 2. First, it's only one sample. Second, as noted above, there is little (if any) basis for the assumed weight of solid represented. The use of activity ratios, however, is fine; there's just not much of it. Please note in Table 2 caption that these are 6 M HCl leachate data, not bulk rock.

Conclusions: The first sentence is not a "conclusion" as nothing is specifically concluded! Make clear that you are talking about colloid-facilitated Th transport--not in "solution."

See marginalia for additional comments.

CC

Scientific Notebook
Project 20-1402-461

Dec, 1998
Chuck Connor

Work is underway to investigate rio grande rift volcanic fields as possible analogs for Yucca Mountain region volcanism. The goal of using these volcanic fields as analogs is to look for correlations between crustal strain rate, and rates of basaltic volcanism, essentially as a test for the Wernicke model - i.e., a direct correlation. The following is a review of the basaltioc volcanic fields in southern New Mexico

Southern New Mexico Volcanic Fields

Three major basalt fields in New Mexico - the Potrillo volcanic field, McCartys flows, and Carrizozo volcanic field, represent an interesting history of the relationship between the Rio Grande rift structures and subsequent volcanism in the area, which has been compared to that of the East African rift system, the Ethiopian rift system and the Mid-Atlantic Ridge (Wright, 1963; McBirney and Gass, 1967; Aumento, 1968). The New Mexico volcanic fields are a result of a 40-my evolution of three overlapping stages of volcanic and tectonic activity:

The first, between 40 Ma - 29 Ma, is described as a modified Andean arc stage, characterized by early extension and calc-alkalic volcanism as the Farallon oceanic plate subsided under the American plate (Elston and Bornhorst, 1979). Calc-alkalic volcanic activity began with andesitic eruptions which became more felsic with time. Basaltic rocks began to appear around 35 Ma. Basaltic rocks became exceedingly common around 30 Ma, as the Pacific plate and North American plate collided. Tectonic and volcanic activity continued after the initial plate collision due to processes analogous to back-arc spreading.

Therefore, the second stage, from 30 Ma - 18 Ma is defined as a modified back-arc extension stage, characterized by the main stage of extension in the area and by eruptions of a) high-silica rhyolite and b) basaltic andesite and related rocks. With the inception of Basin and Range faulting, basaltic andesite became more abundant along the transition zone between the Basin and Range province and the Colorado plateau, while rhyolitic volcanism began to disappear.

The third stage, from 21 Ma - present, is defined by intraplate block faulting and predominantly basaltic volcanism. During intraplate block faulting, clusters of mid-Tertiary volcanic complexes that formed during the first stage became parts of mountain ranges or high plateaus (e.g. the San Juan mountains and the Mogollan plateau in central New Mexico). Meanwhile, deep fracturing associated with Basin and Range development led to the generation of alkali olivine basalt. Chapin (1979) defines a lull in magmatism between 20-13 Ma, followed by a slow and steady increase in volcanic activity since 13 Ma. Basaltic magmatism peaked 5 Ma as a result of accelerated crustal thinning from 8 to 3 Ma, while the most recent magmatic activity can attributed to recent reheating of the lower crust with the opening of the Rio Grande Rift (Padovani and Reid, 19*).

Today, the Potrillo volcanic field in south-central New Mexico, located on the western margin of the Rio Grande Rift, is a typical monogenetic volcanic field; it is predominantly made up of cinder cones and associated flows, but also contains maar volcanoes and shield cones. The Potrillo volcanic features are aligned along north-striking faults that are intersected by northwest-striking faults on which the volcanic units dip to the southeast (Hoffer, 1976). The Potrillo

volcanic field can be divided into three distinct basalt fields, namely the West Potrillo Basalt field to the west, the Santo Tomas- Black Mountain basalts to the east, and the central area containing the maar volcanoes and Aden-Afton basalts. The West Potrillo basalts are believed to be the oldest of the three fields, dated at **???**, while radiometric dates of 2.65 my have been obtained from Santo Tomas (Wood and Keinle, 1990). TheWest Potrillo Basalt field is structurally higher than the basalt fields to the east, and consists of more than 150 cinder cones, spatter cones, associated flows, and several small maars (Renault, 1970; Padovani and Reid, 19*). It is difficult to determine the thickness or total volume of the Potrillo basalts since much of the area has been covered by thick layers of sediment.

A total of six explosion craters, namely Kilbourne Hole, Hunt's Hole, the Potrillo maar, Mt. Riley, the Malpais maar, and Phillips Hole are found in the Potrillo volcanic region. (*The Aubele et al. paper claims 20 previously undiscovered maars - ??)* Three craters located in the central area of the Potrillo field - Kilbourne Hole, Hunt's Hole, and the Potrillo maar - are aligned north-south along the trace of the Fitzgerald-Robledo fault system which extends into northern Mexico (Padovani and Reid, 19*). These three maar craters were formed as a result of pyroclastic surges in the late Pleistocene which erupted through the alluvium and through a thin basalt flow originating from the Gardner cones to the south and extending to north of Kilbourne Hole (Hoffer, 1976a). The pyroclastic surge deposits of the maar ejecta blanketed the craters and formed elevated rims above the three craters. Padovani and Reid (19*) note that the Kilbourne Hole ejecta contain an abundance of varied crustal and mantle xenoliths, while the ejecta from Hunt's Hole contain none. **Why??**

Kilbourne Hole is the biggest and most famous of the Potrillo maars. The age of the the crater has been determined by K-Ar dating to be 0.103 ± 0.084 my (Denison, 1970?). Kilbourne Hole is nearly surrounded by a prominent rim of ejecta that rises about 140m above the center of the crater floor. Since 1907, there has been considerable debate over the formation of Kilbourne Hole, specifically whether or not subsidence played a role in the collapse of the crater wall following eruptive activity. Seager (1987) emphasizes that the Kilbourne Hole is a result of major subsidence of its tuff ring, in a caldera-like collapse, immediately after explosive activity. This contradicts previous popular belief that Kilbourne Hole formed simply as a result of explosive excavation, slumping, and erosion following phreatomagmatic explosions. Evidence to support a caldera-like collapse includes downfaulted strata of tuff-ring material at the base of inner wall of the crater and the relatively small volume of pyroclastic material in the maar rim and on the adjacent La Mesa plains to the east (Seager, 1987). The crater floor is up to 100 m lower than the surrounding La Mesa plains, which is clear evidence to support the idea of subsidence. Seager concludes that initially phreatomagmatic explosions constructed a ring of ejecta which subsequently subsided because the tuff ring could no longer be supported.

Hunt's Hole is located 8 km south of Kilbourne Hole and is smaller and shallower than its brother to the north.

why are there no xenoliths in Hunt's Hole basalt in contrast with Kilbourne?

Potrillo maar, located 3 km south of Hunt's Hole on the Mexican border, an elliptical crater with several cinder cones and basalt flows on its floor.

The Mt. Riley maar and Malpais maar are located in the West Potrillo Mountains. The

Mt. Riley maar has a nearly circular outline, and its rim dips 30-50 degrees away from the crater. The rim is composed of poorly sorted subangular basalt, scoria, hydroclastic lapilli tuff and tuff breccia, as well as mineral fragments including large crystals of feldspar, pyroxene, and olivine-enstatite (Seager, 1987; Hoffer, 1976). Bombs composed of similar olivine-enstatite aggregates are found in Kilbourne Hole, and inclusions of the same found at Potrillo maar. Parts of the rim have been buried by lavas from nearby cones to the north and west, and a thin layer of basalt covers the east and northeast floor of the Mt. Riley crater (Hoffer, 1976).

Malpais maar is a tuff ring formed by phreatomagmatic eruption of basaltic magma which Page (1973) describes in four stages. First, the initial steam eruptions produced air-fall and base-surge tuff currents which were deposited to create parallel-bedded tuffs. Second, cinder-spatter cones formed in the center of the crater, and erupted basaltic lava flows. The intrusion of dikes slowed the lava eruptions in the third stage, and finally, post-maar cones and associated lava flows were formed. The bedded tuffs that exist today are composed of ash, lapilli tuff, tuff-breccia, and a number of sedimentary structures including dunes, ripples, current crossbedding, lamilae, and bomb sag structures (Hoffer, 1976; Page, 1973). Younger lava flows occur on the flanks of smaller cinder cones on all sides of the maar ejecta except to the northwest where the ejecta are covered by the younger flows. This, Hoffer concludes, demonstrates that the maar formed before the extrusion of younger flows, and after the development of most of the cinder cones in the area.

The Aden Crater is a small shield volcano which has been dated at 0.53 ± 0.005 my by K-Ar dating. Today the crater is made up of a main sheild cone with a spatter rim; lava flows, tubes,

and channels; spatter cones, tumili and a fumerole (Kahn, 1987). The cone formed as a result of a series of events. First, a slightly sloping shield cone was formed by flows emerging from vents at the intersection of the Robledo fault and the Aden rift. An explosive phase followed and formed a spatter rampart around the top of the cone. As lava continued to issue from the central vent, it formed a lava lake at the top of the crater, with the spatter rim acting as a dam. Lava began to withdraw back into the vent, causing the western portion of the solidified lake surface to collapse. Finally, several small spatter cones were constructed with some minor explosive activity, followed by persisting fumerolic activity (Kahn, 1987; Wood and Keinle, 1990).

The McCartys volcanic field lies in east-central New Mexico, 350 km slightly northwest of the Potrillo basalt field, and contains four separate basalt flows - the Laguna basalts, the McCartys flows, the Paxton Springs flows, and a fourth flow with a highly irregular surface that Renault (1970) refers to as the Blocky flow.

The Carrizozo volcanic field is found 210 km slightly northeast of the Potrillo field, on the opposite side of the Rio Grande Rift. The Carrizozo is defined by two major eruptive periods - the Broken Back crater eruption, and the subsequent lower and upper Carrizozo flows (Renault, 1970).

Renault (1970) compares differentiation in the basaltic magmas from the Potrillo, McCartys, and Carrizozo volcanic fields, and attributes the variation of TiO_2 concentrations to structural setting. Although the differences in titanium concentration between similar basalts from the same volcanic field may result from mantle heterogeneity or differentiation of the magma, Renault finds a definite correlation between TiO_2 concentrations and the incumbent (?)

stress field influences in genetically different magmas. Stress distribution in block faulting states that upthrown blocks are under less compressive stress than downthrown blocks, so that the upthrown blocks would have more deeply penetrating fractures, like those associated with the uplifted blocks of Basin and Range development. Therefore, Renault argues, with pressure control on TiO_2 concentrations in the MgO-SiO_2-TiO_2 system, basalts erupted through upthrown blocks should be richer in titanium than basalts that are erupted through the adjacent downthrown blocks. Each of the three volcanic fields displays this relationship with respect to TiO_2 concentrations - the uplifted west Potrillo basalts and adjacent downdropped east Potrillo basalts, the Paxton Springs basalts compared with the other flows of the McCartys field, and the upper and lower flows of the Carrizozo field.

REFERENCES

Aubele, J.C., L. Crumpler, K. Loeber, A. Kudo.19*. Maare and Tuff Rings of New Mexico. New Mexico Geological Society, Special Publication Number 6. 109-114.

Cordell, Lindrith. 1975. Combined Geophysical Studies at Kilbourne Hole Maar, New Mexico. New Mexico Geological Society Handbook. 269-271.

(Same: Jackson and Bisdorf; 273-276, Hoover and Tippens, 277-78; O'Donnell et al, 279-280; Towle and Fitterman, 281.)

Hoffer, Jerry M. 1976. Geology of Potrillo Basalt Field, South-Central New Mexico. Circular 149, New Mexico Bureau of Mines and Mineral Resources; University of New Mexico.

Kahn, P.A. 1987. Geology of Aden Crater, Dona Ana County, New Mexico. M.S. Thesis, Univeristy of Texas at El Paso, .

Padovani, E.R., and M. Reid. 19*. Field guide to Kilbourne Hole maar, Dona Ana County, New Mexico. ?

Page, R.O. 1973. Stratigraphy of the Quaternary Malpais maar volcano, Dona Ana County, New Mexico. M.S. thesis, University of Texas at El Paso, 46 p.

Renault, Jacques. 1970. Major-element Variations in the Potrillo, Carrizozo, and McCartys Basalt Fields, New Mexico. Circular 113, New Mexico Bureau of Mines and Mineral Resources; University of New Mexico.

Seager, William R. 1987. Caldera-like collapse at Kilbourne Hole maar, New Mexico. New Mexico Geology, 9(4), 69-73.

cc

Scientific Notebook
Project 20-1402-461

Dec, 1998
Chuck Connor

Work is underway to investigate Rio grande rift volcanic fields as possible analogs for Yucca Mountain region volcanism. The goal of using these volcanic fields as analogs is to look for correlations between crustal strain rate, and rates of basaltic volcanism, essentially as a test for the Wernicke model - i.e., a direct correlation. The following is a review of the basaltic volcanic fields in southern New Mexico

Data were collected in the Portillo volcanic field during two days of field work to delineate the locations of buried lava flows and faults relative to the giant explosion craters - Kilbourne Hole and Hunt's Hole.

Several magnetic traverses, shown on the following pages, were made across the area to delinate magnetic anomalies. These traverses indicate the location of buried lava flows betwen the two craters. No obvious faults were identified.

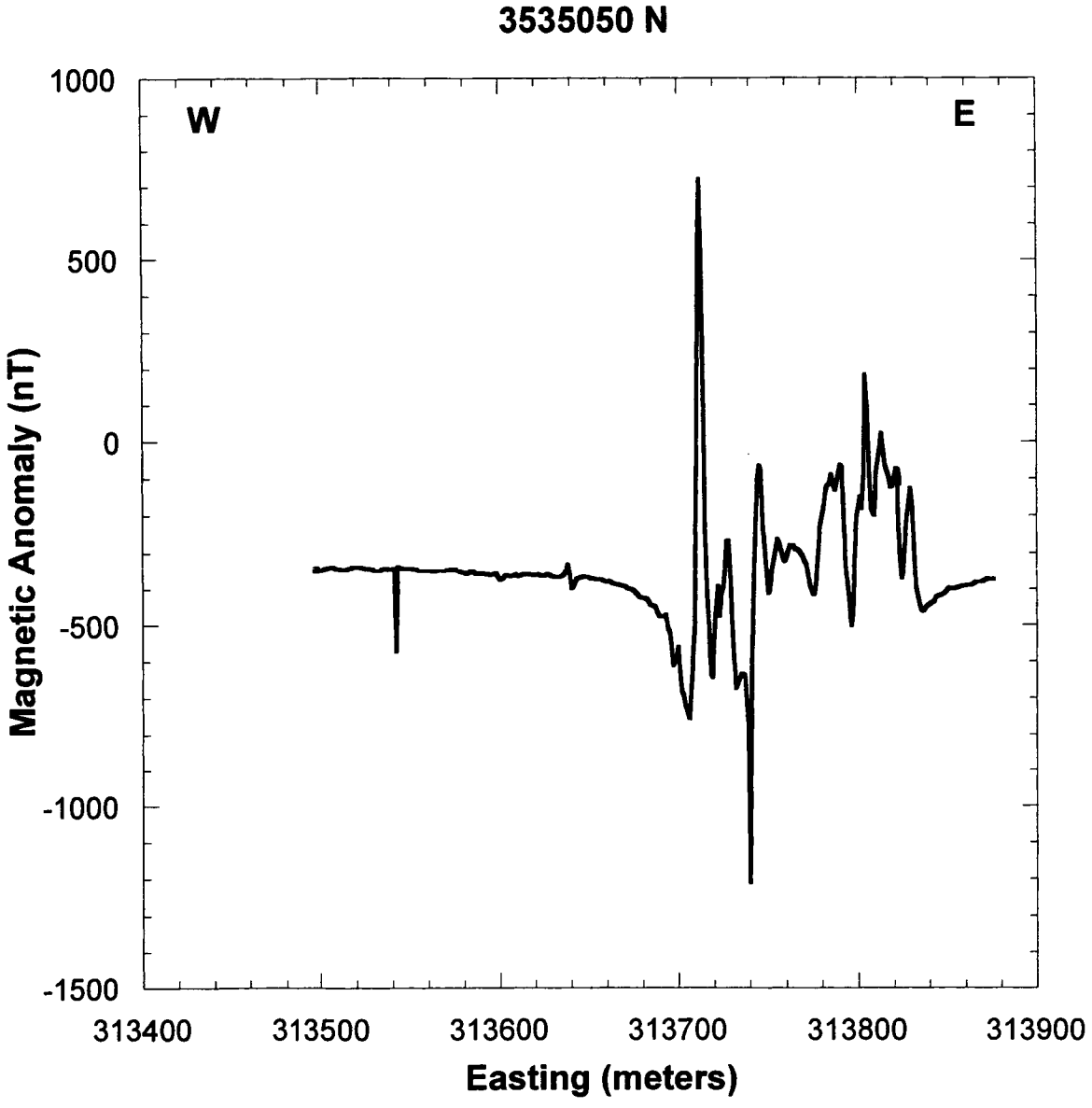
3535050 N
W
E
1000
500
0
-500
-1000
-1500
Magnetic Anomaly (nT)
313400
313500
313600
313700
313800
313900
Easting (meters)

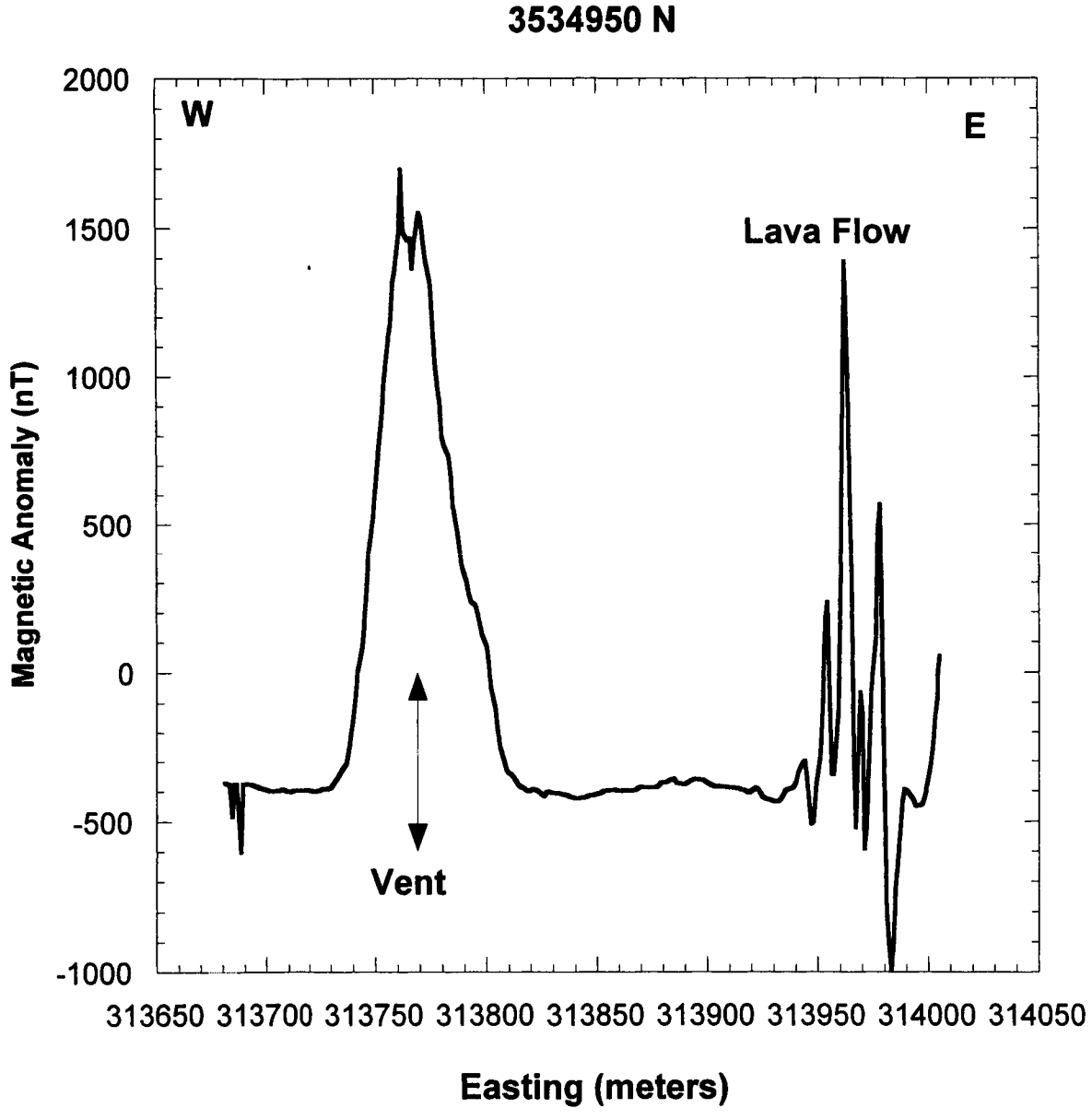
3534950 N
W
E
Lava Flow
Vent
Magnetic Anomaly (nT)
2000
1500
1000
500
0
-500
-1000
313650 313700 313750 313800 313850 313900 313950 314000 314050
Easting (meters)

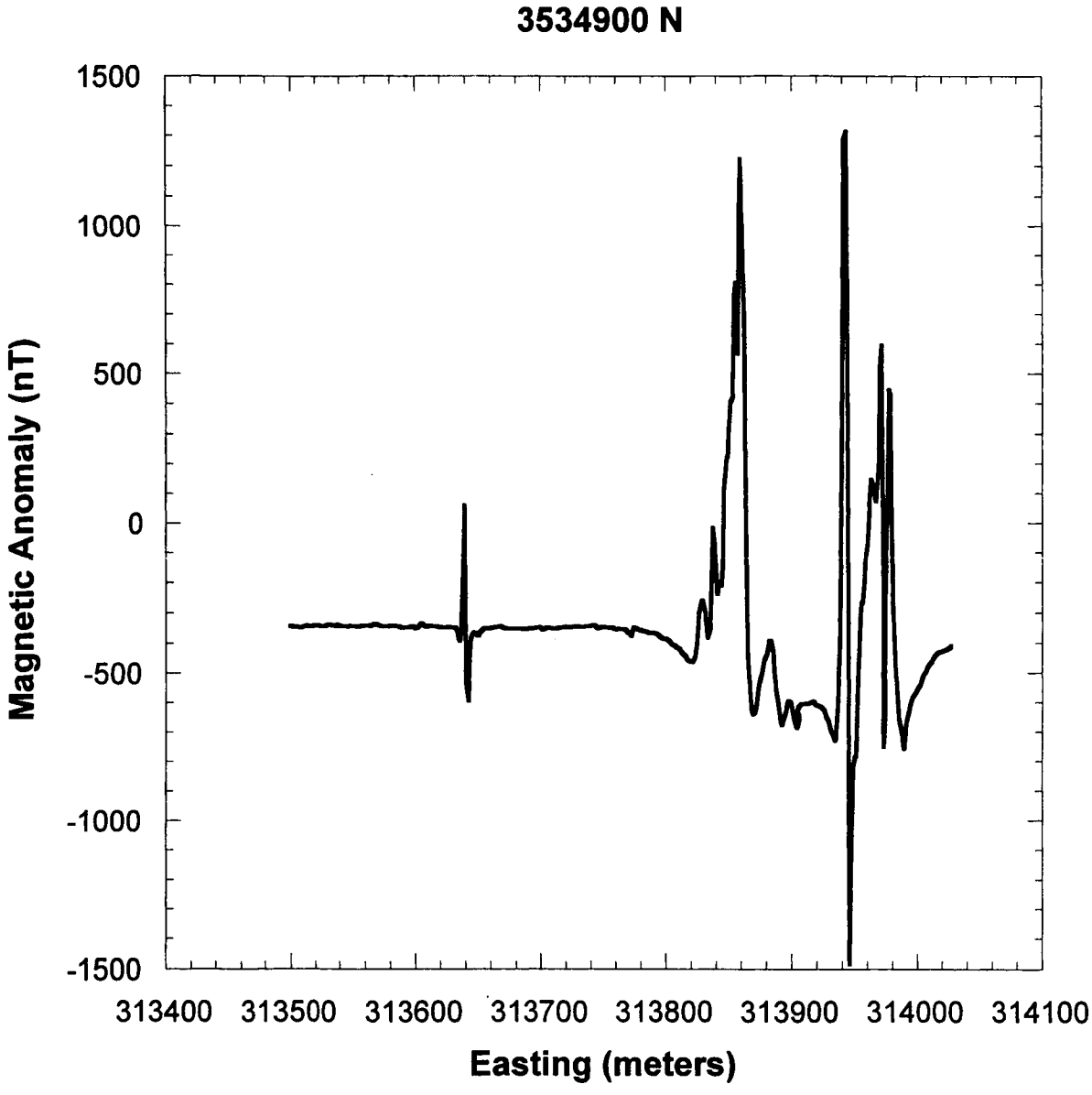
3534900 N
1500
1000
500
0
-500
-1000
-1500
Magnetic Anomaly (nT)
313400
313500
313600
313700
313800
313900
314000
314100
Easting (meters)

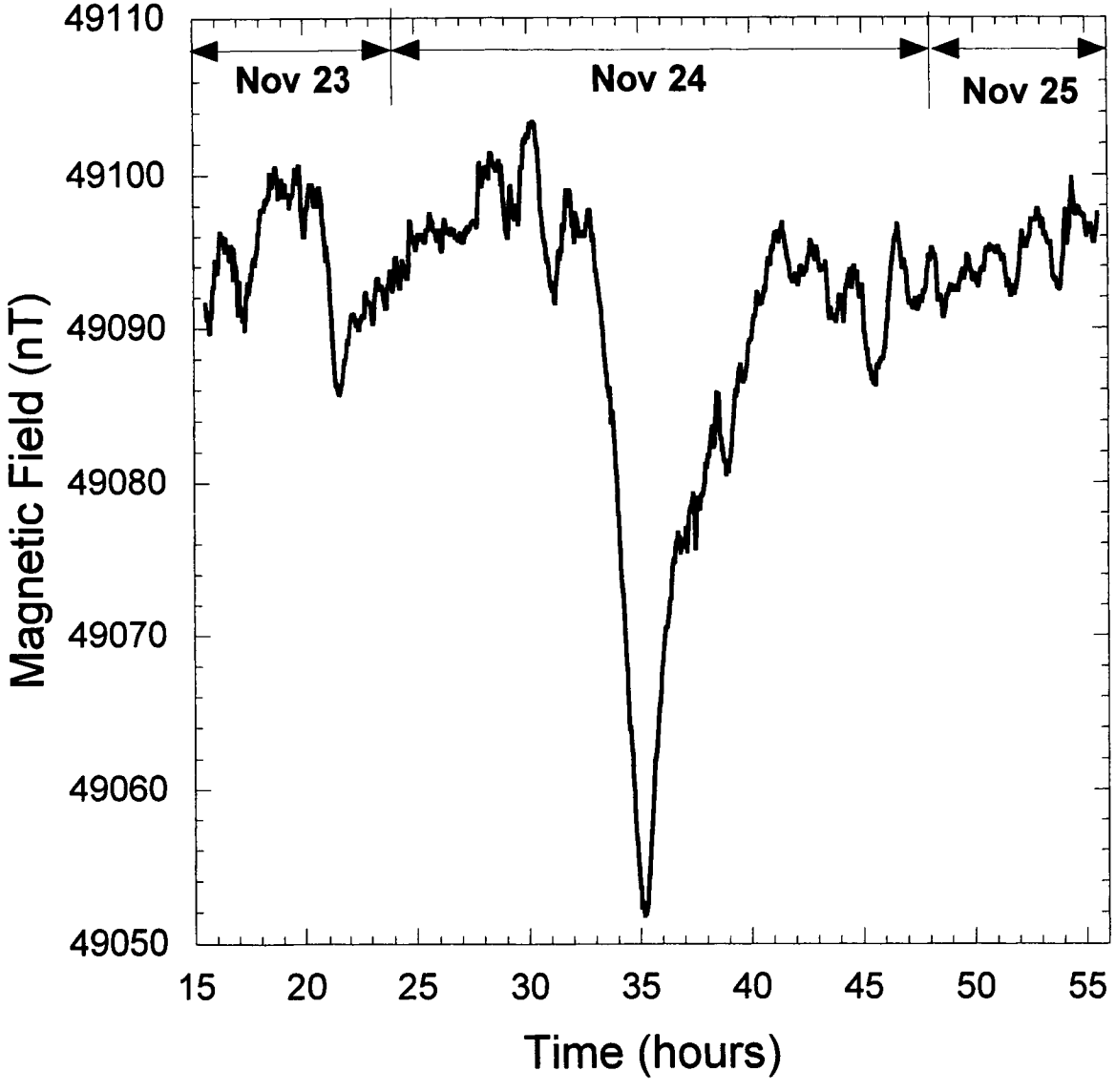
Nov 23
Nov 24
Nov 25
Magnetic Field (nT)
49110
49100
49090
49080
49070
49060
49050
15
20
25
30
35
40
45
50
55
Time (hours)

CC

Scientific Notebook
Project 20-1402-461

Jan, 1999
Chuck Connor

The following sow was prepared for the university of bristol/ cnwra work on magma-repository interactions

Statement of Work

The Center for Nuclear Waste Regulatory Analysis requires that analogue experimental and numerical models of repository - magma interaction be developed. These models will be used to identify the processes which occur during magma-repository interaction, and will enable calculation of pressure and flow conditions in a repository tunnel during injection of basaltic magma.

The analog experimental apparatus to model the ascent and break-through of magma into the repository will be used by Dr Anne Marie Le Jeune, to examine a range of flow conditions associated with both volatile rich and volatile poor magma intersecting the repository tunnel. A sequence of controlled experiments will be performed to examine the flow under a variety of possible analogue source conditions. The experimental study will provide pressure and flow speed data both in the model dike and model tunnel as the flow evolves. The experimental study will also provide high-speed video recording of the process of magma breakup as it decompresses, expands and the liquid films rupture. This will be used to develop a picture of the processes involved in magma-repository interaction; in particular, the propagation and reflection

of shock waves associated with the release of dissolved volatiles as the high pressure magma decompresses.

The numerical model will be developed in a hierarchial fashion, initially based on the assumption of homogeneous equilibrium flow of the magma-gas mixture along the repository tunnel. The model will account for the formation and propagation of shock waves, their reflection from the end-wall of the tunnel, and their subsequent interaction with the oncoming flow. The model will be able to predict the forces exerted on cannisters in the tunnel as they interact with the flow, and the gradual build up in pressure in the tunnel following magma breakthrough. The model will examine the sensitivity of the flows to the gas content of the magma, the fragmentation threshold for breakup of the liquid magma into a dispersion of liquid fragments, and the interaction of the flow in the tunnel with the flow in the feeder dike. The dike will be modeled as being elastic walled, and calculations will be performed for a range of dike widths. The numerical model will also be adapted for the experimental study, and the results of each component of the study will be compared.

The University of Bristol Centre for Environmental and Geophysical Flows will deliver results of the numerical and experimental simulations to the CNWRA no later than August 31 1999. This will be in the form of two reports describing the numerical and experimental work. The numerical report will delineate the model assumptions, the numerical technique, and the results of the analysis. The experimental report will describe the apparatus and experimental technique,

and will also describe the results of the experimental study. The reports will be delivered in hard copy and electronically. The numerical codes used to model the repository-magma interaction will also be delivered to the CNWRA. Because the numerical work involves the behaviour of basaltic magmas during intrusion into a proposed high-level radioactive waste repository, calculations must be included related to the conditions these magma flows will create at waste packages. We anticipate that development and application of these numerical and experimental models will require extensive interaction with CNWRA staff. Therefore, we require that the numerical modeler visit CNWRA for a period of at least four weeks, during which time the model will be installed on CNWRA computers, tested, compared with the results of physical analog experiments, and compared with natural analogues. We also require that the experimental modeler visit CNWRA for a period of at least twelve weeks during which time the experimental apparatus will be installed, tested, and a series of experiments performed.

cc

Scientific Notebook
Project 20-1402-461

Jan, 1999
Chuck Connor

The following proposal was prepared for NASA. It is included in this scientific notebook because many of the ideas I have delineated in this proposal will be applicable to NRC work in 20-1402-461. (It is a good summary of where we are, with respect to probabilistic modeling of plume dispersion).

1 Research Objectives

A fundamental goal of modern volcanology is to improve volcanic hazard assessments by integrating as much relevant information into these assessments as possible. Most often, volcanic hazard assessments are based on real-time or near real-time observations of volcanic activity, such as rates of seismic energy release or ground deformation. These data have been proven repeatedly to be excellent short-term indicators of the potential for volcanic eruptions. Yet a great deal of information about potential volcanic activity is also derived from the geologic and historic records. The geologic record, for example, often provides direct evidence of the range of eruption magnitudes, and particularly the maximum eruption magnitudes that have occurred at a volcano. During volcanic unrest and eruption crises, it is crucial to effectively link these different types of data, real-time observations and the geologic record, to estimate hazard and risk within reasonable uncertainties.

Most recently, attempts have been made to formalize hazard assessments by using expert

elicitation. In current implementations, such as during the extended volcanic crisis at Montserrat, a hazard event tree is constructed and probabilities for each branch of the tree (which represents the occurrence of an event) are estimated by a team familiar with the volcano and likely eruption outcomes. These event probabilities are conditional probabilities such as P[eruption | magma injection] and P[tephra fall > 10 cm | eruption]; the probability of an event depends conditionally on events associated with previous branches. Estimation of event probabilities is a difficult task, in which volcanologists are called upon to integrate and assess numerous, often disparate, data sets. Ideally, these data sets include the geologic record, real-time observations, and numerical models of potential volcanic activity. Because of the complexity of this task, volcanologists need tools to help them evaluate assumptions and uncertainties in their estimates of event probabilities.

We propose to investigate mechanisms for formally updating conditional probabilities using Bayesian methods. Improved estimates of conditional event probability distributions can be obtained by casting information derived from the geological and historical records as a prior probability distribution function (pdf), developing likelihood functions based on real-time data and expert interpretation of these data, and modifying the prior pdf using Bayes' theorem. Such Bayesian methods provide a systematic and logical algorithm for updating forecasts of volcanic hazards continuously as new information becomes available. Furthermore, Bayesian methods do not solely depend on the recurrence rate estimates that are central to Poisson models, which have high uncertainties, do not include real-time information, and, as a result, are nearly always

inadequate for hazards assessment during volcanic crises. Bayesian forecasting coupled with emerging techniques in numerical simulation of eruption phenomena, such as tephra dispersion, provide a powerful technique for incorporating complex and varied geological observations into hazard assessment models. Such a link is crucial for estimating transition probabilities. Thus, this project offers the Pacific Disaster Center (PDC) with a way of quantifying hazard estimates based on widely varying observations and data types.

In this study, we plan to focus on development of methods for estimating conditional probabilities for tephra (ash) dispersion and accumulation. We choose to focus on tephra dispersion and accumulation because this product of volcanic eruptions is among the most serious in terms of numbers of people affected in the circum-Pacific and the diversity of hazards resulting from tephra dispersion, including building collapse, disruption of facilities, aviation hazards, and secondary hazards associated with the remobilization of tephra blankets.

Before such an approach can be successfully implemented during a volcanic crisis, appropriate techniques for estimating the prior distribution and likelihood functions, central to Bayesian forecasting, need to be developed. Therefore, the project will be structured to: (i) explore alternative methods of estimating the prior distribution using numerical simulations to model geologic data; and (ii) develop techniques for rapidly folding likelihood functions into the analysis that are consistent with data types available to volcanologists during volcanic crises. Development of these methods comprises the central effort in this project. We plan to test and refine our approach by modeling tephra fall hazards at Colima volcano, Mexico (Figure 1). This

volcano produces a range of eruption types, has erupted frequently in the past (including most recent eruptions in 1991 and 1998), and hazards at Colima have been the topic of previous investigations by team members (e.g., Connor et al., 1993a; 1993b; Luhr and Prestegaard, 1988; Luhr and Carmichael, 1990; Clement et al., 1993). Of course, it is also possible that opportunities will arise to test our procedures at other circum-Pacific volcanoes as the project develops.

We anticipate that a tangible product of this research will be a computer code for practical application of Bayesian updating to real-time tephra hazards. After appropriate testing, we plan to assist PDC in the application of this code.

1.1 The Bayesian Method

Bayesian forecasting of tephra dispersion and accumulation relies on: (i) a model, M, that calculates tephra accumulation at a point, or over a region, based on stochastic parameters, $\mathbf{w}$, such as eruption rate, eruption duration, wind speed and direction; (ii) an estimate of the distributions of these parameters (or their moments) from past eruptions, based on best-fits of the observed tephra-stratigraphic section with the model; and (iii) updates of these parameters using the expert judgements of volcanologists, based on information available during volcanic crises. Alternative tephra dispersion models will be investigated to determine the most efficient model, where efficiency is based on the numbers and kinds of parameters that must be estimated, computational ease, and physical realism. Implementation of this approach is shown schematically in Figure 2 and discussed in detail in the following.

In Bayesian forecasting, we have a prior function p(**w**|**D**,*M*), where **w** is a vector of parameters that govern the dispersion and accumulation of tephra in model *M* and **D** is the geologic (or historical) data. Basically, estimate of the prior function will involve taking isolated measurements of tephra thickness and granulometry collected at sites around the volcano and estimating the joint pdfs of the parameter vector **w**. We plan to explore the possibility of simplifying this problem by estimating only the means and correlation matrix of **w**. In light of the numerous parameters comprising **w**, we plan to experiment with various techniques, including Monte Carlo simulation and direct inversion (e.g., Mackay, 1999) to optimize the fit.

Tephra accumulation based on these prior pdfs will be plotted as a complementary cumulative distribution (CCDF) function for a specific location or contoured, for example P[tephra thickness > 10 cm | eruption], across an entire region surrounding the volcano of interest. As such, hazard estimates based on prior distributions are useful to PDC because they can be calculated long before the onset of volcanic crises using a combination of geological and historical records, data from analogous volcanic systems, and reliable tephra dispersion models. The CCDF can be distributed by PDC to emergency managers for planning purposes (Figure 2).

Once new data become available (say at the initiation of a new eruption), a likelihood function, or a set of likelihood functions, f(**s** | **w**, *M*), will be developed from current information, such as wind speed and direction, and estimates of potential eruption magnitude and duration derived from real-time volcano monitoring. In this approach, the data vector **s** contains parameter estimates, derived by experts based on their real-time observations. For spatial hazard

assessments, such as tephra dispersion, remotely sensed data sets available to the PDC can be easily folded into the hazard assessment via the likelihood function. We plan to demonstrate this concept by using GOES data sets to estimate wind speed and direction, but the method can be extended to ASTER and differential SAR interferograms to estimate magma volumes. The likelihood functions allow experts working on the scene to fold these data types into their hazard estimates in a quantitative manner. Likelihood functions also provide a means of integrating expert judgement, based on previous experience at analogous volcanic systems, into the calculation of transition probabilities.

One role of the likelihood function is to incorporate shifts in the level of activity at the volcano. This is most critical when volcanic activity steps to a higher level than indicated by the geologic or historical records. Such nonstationary behavior is typical of many volcanic systems, which evolve petrologically or structurally through time, but is not well-treated by classical statistical approaches that rely solely on past recurrence rates to estimate probable outcomes.

The prior distribution is modified by the likelihood function to generate an improved model (posterior function) using Bayes' rule:

$$P(\mathbf{w} \mid \mathbf{s}, M) = [p(\mathbf{w}| \mathbf{D}, M)\, f(\mathbf{s} \mid \mathbf{w}, M)] / f(\mathbf{s}, M)$$

where:

$$f(\mathbf{s}, M) = \int p(\mathbf{w} \mid \mathbf{D}, M)\, f(\mathbf{s} \mid \mathbf{w}, M)\, d\mathbf{w}$$

In the most general case, we plan to estimate the mean and covariance matrix of the posterior

function, P(**w**|**s**,*M*). The relative importance of p(**w**|**D**,*M*) and f(**s**|**w**,*M*) in calculating P(**w**|**s**,*M*) is interesting to assess. At a volcano where little geologic work has been done prior to the onset of activity (e.g., Pinatubo before the 1991 eruption) the likelihood function, f(**s**|**w**,*M*) dominates the analysis. Conversely, consider a volcano with a long and well known history of activity but one that is not well-monitored (e.g., Cerro Negro, Nicaragua). At such a volcano, p(**w**|**D**,*M*) dominates the estimate of the posterior function.

1.2 Role of Geologic and Historical Records

In our approach, geological and/or historical records of tephra fall play a central role in estimation of the prior distribution, because these data are the best guide to possible outcomes of eruptive activity in the absence of information that can only be obtained during an eruption crisis. In a sense, it would be ideal if sufficient information existed to construct the CCDF for ash accumulation directly from the tephra-stratigraphy of the area of interest, without estimating parameters or using a numerical model. The geologic record of eruptive activity, however, is usually limited both in terms of the distribution of outcrops and of the types of volcanic events preserved. For example, tephra sections at many volcanoes in the circum-Pacific are limited to a handful of outcrops, where the tephra-stratigraphy is well exposed and preserved. These outcrops rarely correspond to the locations where hazards are most important to assess, such as population centers and critical (e.g., port, power plant) facilities. Therefore, expected tephra accumulation in most areas needs to be modeled, using tephra-stratigraphy as a control.

Furthermore, the geologic record is biased toward large, infrequent events that leave a distinctive geologic record. Smaller, generally more frequent, eruptions occasionally leave no discernable geologic record. In contrast, the historical record is very short at most circum-Pacific volcanoes and the historical record often poorly reflects the full range of activity a given volcano has experienced to date, and as noted previously, or may experience in the future.

The disparity between historical and geological records is particularly evident at Colima volcano, where there is nearly complete disjunction between the historical and the stratigraphic records. Dozens of explosive eruptions have been recorded in the last 400 years, but only a single scoria layer has been preserved in the geological record for that period. It is clear to us that the preserved sequence includes just a fraction of the eruptive events, biasing the geologic record toward large eruptions. Nevertheless, the style of eruptive activity may have also changed over time. Modeling these data and estimating parameter distributions that best fit the data can help resolve this disparity. For example, if complex, multi-modal parameter distributions are needed to model the historical and geological data sets together, nonstationary behavior in eruption style may be indicated. Alternatively, if comparatively simple parameter distributions model both historical and geological data sets, then the brevity of the historical record may account for the disparity. As this disjunction between geological and historical data sets is a classic situation, common at circum-Pacific volcanoes, a crucial activity in this work will be to formulate methods to reconcile geological and historical records through model fitting and parameter estimation.

1.3 Models of Tephra Dispersion and Deposition

The goal of modeling tephra dispersion and deposition using numerical simulations is to provide a path from the geological and historical records to parameters distributions and back to probabilistic estimates of tephra dispersion and accumulation (Figure 2). The first attempt to quantify the dispersion of ash in volcanic eruptions was by Suzuki (1983). Suzuki's (1983) model has been modified and applied to volcanic eruptions by Glaze and Self (1991) and Hill et al. (1998). Suzuki's model is empirical, the erupting column is treated as a line source reaching some maximum height governed by the energy and mass flow of the eruption. A linear decrease in the upward velocity of particles is assumed, resulting in segregation of tephra particles in the ascending column by settling velocity, which is a function of grainsize, shape, and density. Ash particles are removed from the column based on their settling velocity, the decreasing upward velocity of the column as a function of height, and a probability density function which attempts to capture some of the natural variation in the parameters governing particle diffusion out of the column. Dispersion of the ash that diffuses out of the column is modeled for a uniform wind field and is governed by the diffusion-advection equation with vertical settling. Thus, this model is empirical and relies on estimation of 19 parameters.

The more recent class of models (Woods 1988, 1995) concentrates on the bulk thermophysical properties of the column, defining a gas thrust region near the vent, and a convective region above, within which the thermal contrast between the atmosphere and the rising column results in the entrainment of air and buoyancy forces loft ash particles upward. In

contrast to Suzuki (1983), this class of models uses equations for the conservation of mass in the gas thrust:

$$\frac{d(uL^2\beta)}{dz} = \frac{uL}{8}\sqrt{\alpha\beta}$$

and convective:

$$\frac{d(uL^2\beta)}{dz} = 2\varepsilon\alpha uL$$

regions of the column, conservation of momentum:

$$\frac{d(u^2L^2\beta)}{dz} = (\alpha - \beta)gL^2$$

and conservation of energy:

$$\frac{d}{dz}(C_p\theta\beta uL^2) = C_aT\frac{d}{dz}(\beta uL^2) + \frac{u^2}{2}\frac{d}{dz}(\beta uL^2) - \alpha uL^2g$$

to model the development of the eruption column, where u, L, and β are column velocity, radius, and bulk density, respectively, air is entrained in the column based on an entrainment coefficient, ε (typically equal to 0.1), α is the ambient air density and z is vertical distance above the vent, C_p

is the bulk specific heat of the gas column (gas + entrained air + pyroclasts), θ is the temperature of the column C_a is the specific heat of air, and g is gravity. Bulk density and specific heat, in turn, depend on the initial gas fraction in the magma. These equations can be recast as three coupled differential equations and solved numerically for a given set of initial conditions.

A practical outcome of this physical approach is that the model requires fewer parameters and the parameters that need to be estimated are more easily derived from geologic data than parameters required in the Suzuki model. We plan to combine our existing eruption column code, with a near field gravity current model and a more distal wind-driven ash-fall model. For the first time, this will enable us to fit tephra-stratigraphic data by varying eruption intensity and meteorological parameters. The gravity spreading will follow models such as Bursik et al. (1991) and the wind-driven ash fall will follow from Glaze and Self (1991) and Woods and Bursik (1991). The transition from gravity to wind-driven spreading would occur when the cloud had spread sufficiently that the radial spreading velocity falls below the wind speed (as a first approximation). The actual issue of the transition from buoyancy to wind driven dispersal is still unresolved as a dynamical process, in that there is no detailed model of the transition, and so in part of this project we plan to explore new ways of developing such a model.

1.4 Role of Real-Time Observations

Development of the likelihood function is the most subjective part of the process but also the easiest to implement. We plan to show how to update likelihood functions automatically

using GOES data to constrain distributions of meteorological parameters. We will also provide structure for experts to input parameter distribution estimates as likelihood functions, based on their interpretations of current activity and previous experience at analogous volcanoes.

2 Expected Results

At the completion of the project, we plan to have a Bayesian forecasting tool that is tested, using data from Colima volcano, and ready to use by the PDC in volcanic hazard assessments around the Pacific Rim. Our Final Report will include the code, a manual for use of this code, and description of the modeling techniques and analysis for Colima volcano. Moreover, this project will be a pragmatic demonstration of methods of combining geologic data, current information, and expert judgement to improve hazard assessments. These Bayesian techniques should be generally applicable in a variety of hazard situations. We plan to present our results at scientific meetings and publish our approach and results in the peer reviewed literature.

3 Relevance of the Proposed Work

The PDC will benefit from this project in several specific ways. First, a tangible product of this project will be computer code for Bayesian forecasting of tephra dispersion, applicable to any volcano in the circum-Pacific. PDC and its clients can use results of these models to prepare better hazard assessments for emergency managers prior to volcanic crises, update possible outcomes of volcanic crises as new information becomes available, integrate and assess expert judgement quickly, and optimize resource allocations in response to volcanic crises. Second, because Bayesian forecasting techniques include a variety of data types, such as remotely sensed

and geologic field data, we will structure the Bayesian forecasting codes to be compatible with the PDC GIS environment. That is, our models will draw upon GIS data sets for development of prior and likelihood functions, and return forecasts that can be displayed and updated in a GIS environment. Third, the Bayesian forecasting methods developed in this project for tephra dispersion are equally valid for a variety of natural hazards. The experience gained in Bayesian forecasting of tephra dispersion may be applicable to forecasting of a variety of natural and human-induced hazards that fall under the purview of the PDC.

4 Detailed Work Plan

We plan to complete this project in one year. The following needs to be achieved to ensure successful completion of the project: (i) a numerical simulation algorithm must be developed; (ii) the best techniques for optimizing the fit of the numerical code to the data must be identified and implemented; (iii) software must be implemented for extracting meteorological information from GOES images; (iv) the technique needs to be tested using data previously gathered at Colima volcano; and (v) the software must be integrated as an application that supports the PDC GIS.

The project will be conducted in two phases. The first phase of the project will be devoted to development and refinement of the tephra dispersion code and identification and implementation of methods for optimizing the prior distribution based on geological and historical data sets. Assuming a June 1, 1999, start date, most of the work during Phase 1 will be conducted during the summer and fall. The project participants will meet at Southwest Research Institute (SwRI), in San Antonio Texas to discuss the form of the model and data. We invite PDC

staff to participate in all or part of the SwRI meeting to facilitate continuity with the PDC program. By December 1999, we plan to have working versions of all the algorithms used in the project, and plan to have developed prior functions for Colima volcano. This will complete the first phase of the project and a brief progress report will be submitted.

Second phase activities will primarily involve completing and testing the application. The application will be modular (c.f., Figure 2), written as a set of filters in ansii C (i.e., system independent). We will avoid development of costly GUI interfaces by structuring the application to integrate into a GIS environment that will handle display and database management. During the second phase, we also plan to refine our methods for estimating the likelihood functions, and revisit details of the numerical model, including testing model sensitivities. We plan one additional meeting at SwRI during Phase 2 (hopefully with the participation of PDC staff) and plan to submit our Final Report by June 1, 2000.

5 Role of Personnel

The Principal Investigator (PI) on this project will be Charles Connor (SwRI). Andrew Woods (University of Bristol), James Luhr (Smithsonian Institution), and Budhi Sagar (SwRI) will act as Co-Investigators. See Appendix A for brief resumes for these individuals. Connor will be primarily responsible for developing methods of estimating prior and likelihood functions, exploring various Bayesian forecasting techniques, developing and integrating the overall code. Connor also has extensive experience working at Colima and is a member of the Colima Science Committee for evaluation of volcanic hazards. Connor is active in probabilistic volcanic hazard

studies for the International Atomic Energy Agency and the U.S. Nuclear Regulatory Commission. Woods will be responsible for developing and implementing various tephra dispersion algorithms. Woods is co-director of the Centre for Geophysical and Environmental Flows and has extensive experience applying numerical models of volcanic phenomena to hazards assessment during volcanic crises. Woods will also participate in evaluation of Bayesian forecasting using volcanological data sets. Luhr, together with Carlos Navarro of the Colima Volcano Observatory, currently have a project underway to map tephra deposits around Colima volcano. Luhr (also a member of the Colima Science Committee) and Navarro will participate in the project by providing these data and assisting in evaluation of the effectiveness of our models for back- and forecasting tephra dispersion at Colima. Sagar has extensive experience in application of Bayesian analysis to geophysical and hydrogeologic problems. Sagar will participate in development of optimization methods for parameter estimation. In addition to these Investigators, a graduate student from the University of Bristol will participate in the development of algorithms and coding, working in San Antonio as a limited term employee of SwRI. A SwRI GIS specialist and computer programmer, Ron Martin, will participate in software development.

6 Data Requirements

GOES images and previously collected tephra-stratigraphic data from Colima volcano are required to complete this project.

7 Supporting Facilities

SwRI has extensive facilities to support this project. Coding, data analysis, and visualization will be conducted in the GIS lab at SwRI. The GIS lab includes a networked group of high performance Silicon Graphics, Inc. (SGI) and Sun workstations including a dual processor SGI Onyx2 Reality/Engine. Connected to the workstations are digitizers, plotters, printers, large hard-disk mass storage units, tape and CD-ROM units (drives and burners), and optical storage units. The GIS lab is connected to Windows NT and PowerMac workstations, and the internet via highspeed communication links. Major GIS visualization and mapping software in the SwRI GIS lab, and which will be utilized in this project, includes Earthvision, ArcInfo/ArcView, Erdas Imagine, Geosoft/ Montag and Generic Mapping Tools. Numerous C compilers and program development tool are currently available at SwRI. Data, programs, and text will be moved among the participating institutions (SwRI, Smithsonian, PDC, University of Bristol) using anonymous ftp sites.

All facilities required for the analysis of tephra-stratigraphy (not directly funded by this project, but an important ingredient) are available at the Smithsonian, including scanning electron microscope, microprobe, and petrographic microscopes. University of Bristol also has extensive computer capability and facilities for the physical analog modeling of eruption plumes.

8. References

Bursik, M.I., S.N. Carey, and RSJ Sparks. 1992. A gravity current model for the May 18, 1980 Mount St. Helens plume. Geophysical Research Letters 19: 1663-1666.

Clement, B.M., C. B. Connor, and G. Draper. 1993. Paleomagnetic estimate of the emplacement temperature of the long-runout Nevado de Colima volcanic debris avalanche deposit, Mexico, Earth and Planetary Science Letters, 120: 499-510.

Connor, C.B., S. Lane and B.M. Clement, 1993. Structure and thermal characteristics of the summit dome, March 1990 - March, 1991: Volcan Colima, Mexico. Geofisica

Internacional, 32: 643-657.

Connor, C.B, B.M. Clement, X. Song, S. Lane, and J. Thomas. 1993. Continuous monitoring of high-temperature fumaroles on an active lava dome, Volcan Colima, Mexico: Evidence of mass flow variation in response to atmospheric forcing. Journal of Geophysical Research 98: 19,713-19,727.

Glaze, L.S. and S. Self. 1991. Ashfall dispersal for the 16 September 1986 eruption of Lascar, Chile, calculated by a turbulent diffusion model. Geophysical Research Letters 18: 1237-1240.

Hill, B.E., C.B. Connor, M. Jarzemba, P.C. LaFemina, M. Navarro, and W. Strauch. 1998. The 1995 eruptions of Cerro Negro volcano, Nicaragua, and risk assessment for future eruptions. Geological Society of America, Bulletin 110: 1231-1241.

Luhr, J.F., and K.L. Prestegaard. 1988. Caldera formation at Volcan Colima, Mexico, by a large Holocene volcanic debris avalanche, Journal of Volcanology and Geothermal Research, 35: 335-348.

Luhr, J.F. and I.S.E. Carmichael. 1990. Petrologic monitoring of the cyclic eruptive activity at Volcan Colima, Mexico. Journal of Volcanology and Geothermal Research, 42: 235-260.

MacKay, D.J.C. 1999. Probable networks and plausible predictions - a review of Bayesian methods for supervised neural networks. Available at: http://wol.ra.phy.cam.ac.uk/mackay/index.html.

Suzuki, T. 1983. A theoretical model for the dispersion of tephra. (D. Shimozuru and I. Yokoyama, eds.) Arc Volcanism, Tectonics and Physics. Terra Scientific Publishing: Tokyo, 95-113.

Woods, A.W. 1988. The dynamics and thermodynamics of eruption columns. Bulletin of Volcanology 50: 169-191.

Woods, A.W. 1995. The dynamics of explosive volcanic eruptions. Reviews in Geophysics 33: 495-530.

Woods, A.W. and M.I. Bursik. 1991. Particle fallout, thermal disequilibrium and volcanic plumes. Bulletin of Volcanology 53: 559-570.

CC

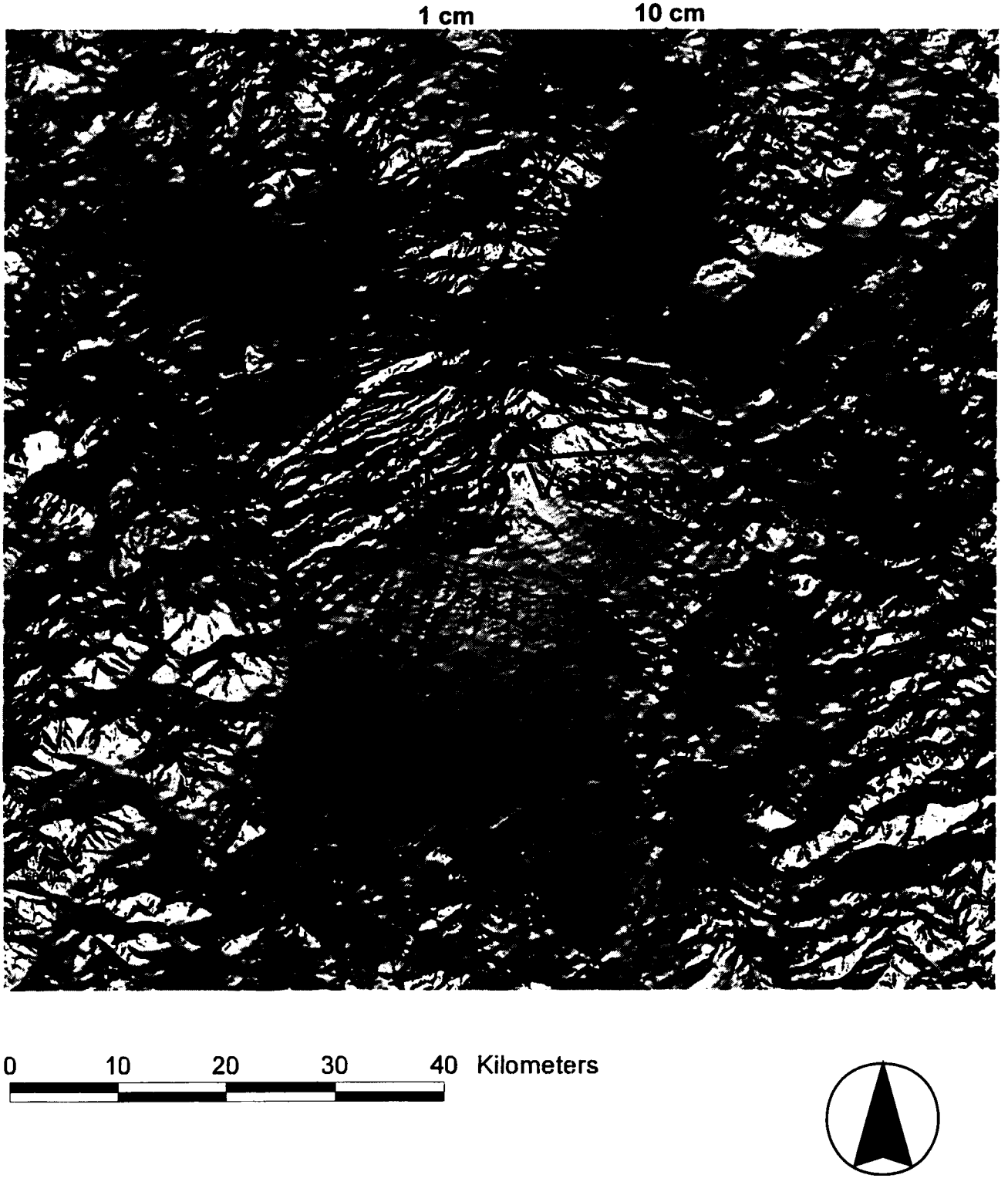

Figure 1. The objective of this project is to create a Bayesian forecast of probable ash accumulation (shown *schematically* as P[tephra > 1 m, 10 cm, 1 cm | eruption] > 95%), based on tephra stratigraphy (e.g., blue dots), real-time information, and numerical simulations. Results will be displayed in a GIS, shown here including shaded relief image of a digital elevation model with cultural data.

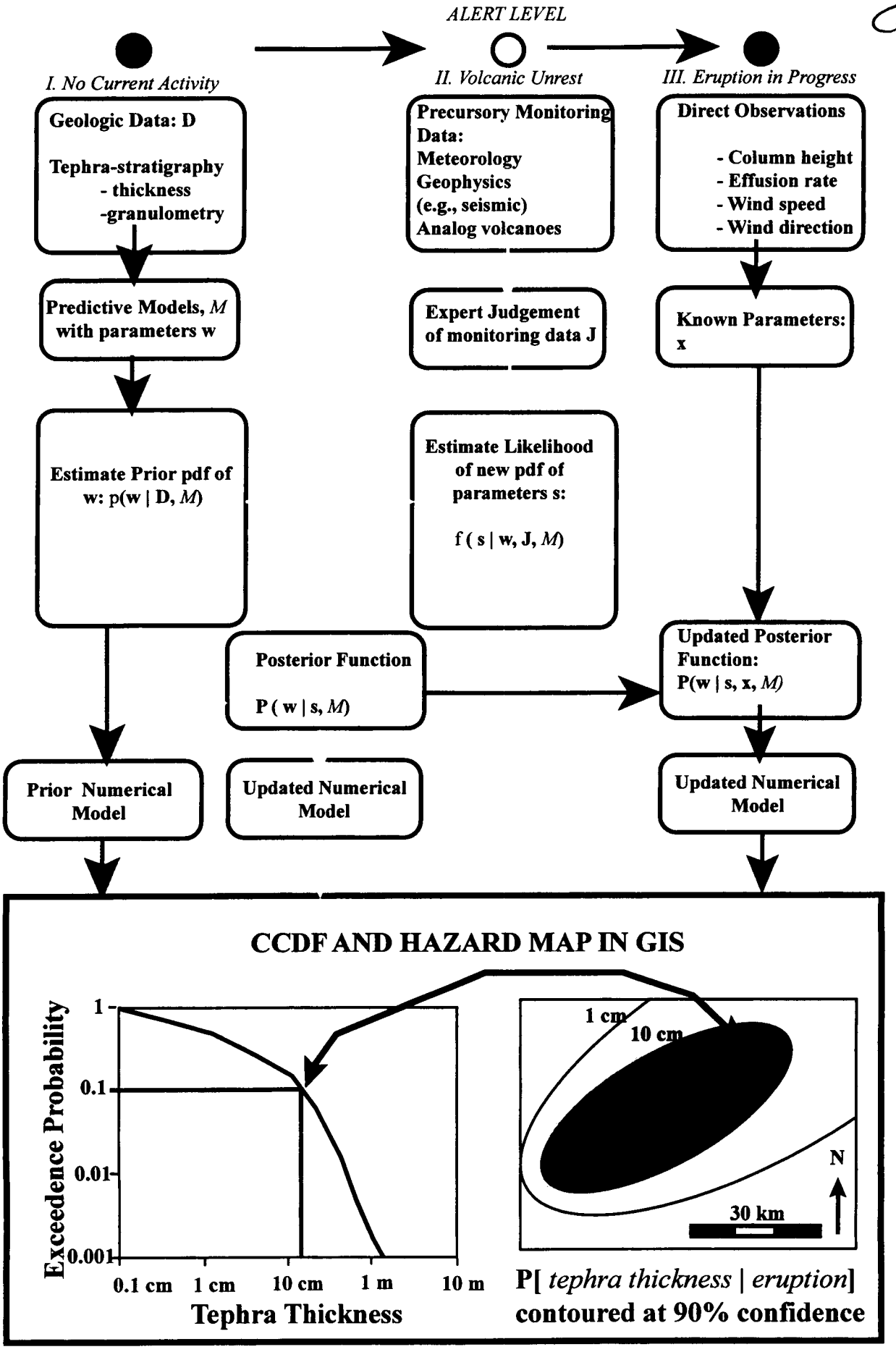

Figure 2. Flowchart showing the steps in Bayesian forecasting of tephra dispersion and accumulation.

Scientific Notebook
Project 20-1402-461

Jan, 1999
Chuck Connor

The following proposal was prepared for the SwRI ACR. It is included in this scientific notebook because many of the ideas contained within will be used to assess magnetic anomalies in the Potrillo volcanic field, an analog area for volcanism studies in the Yucca Mountain region. Also, if the proposed work is successful, we may use these techniques in the YM area as well.

Executive Summary

We propose to combine recent developments in differential global positioning systems (DGPS), cesium-vapor magnetometers, and unmanned aerial vehicle (UAV) technology to create a high-resolution map the geomagnetic field. To our knowledge, this research will be the first to map the geomagnetic field using a UAV. The automated survey design will enable us to map the geomagnetic field in higher resolution and more efficiently than possible using current industry techniques. The time is right to develop this concept because (i) industry is currently rethinking the practice of manned aerial magnetic surveys, given the human and economic costs associated with annual fatalities resulting from crashes during low altitude geomagnetic surveying, and (ii) industry is aware that higher resolution surveys, very important in the oil and minerals exploration business, will only be achieved through a dramatic improvement in surveying techniques. We are confident we can develop the survey tool industry is looking for by combining Division 9 experience in the testing and marketing of UAV technology and Division

20 experience in the development of high-resolution magnetic mapping techniques.

Therefore, the basic goals of this joint Division 9 and Division 20 IR & D project will be to:

- Integrate the magnetometer and DGPS onto the UAV platform, including bench testing

- Perform a geomagnetic survey near Kilbourne Hole, New Mexico, a test site we have previously visited that combines excellent geophysical anomalies with a remote, safe location in unrestricted air space for testing the system

- Develop a high-resolution magnetic map of the test site, coupled with a geophysical model based on the data and report that will serve as the basis of both a scientific publication and, in different form, a marketing tool

After making numerous contacts with geophysicists in the exploration business about this concept, we have concluded that IR & D funding is an appropriate vehicle for its development. Although the future role of UAVs in geophysical exploration is nearly uniformly accepted in industry, most individuals and companies have adopted a "show me" attitude toward development, primarily because these end-users are unable to assess how close we are to fielding a UAV that is a suitable geophysical platform. With a high resolution map in hand as demonstration of the concept, we hope to overcome this hesitation on the part of the geophysics

industry and establish SwRI in a lead position for future development.

The duration of this project will be one year, at which point the results of the project will be presented at scientific meetings, in the peer-reviewed literature, and to industry. As the project develops, we will also carefully assess the practicality to adding additional instrumentation, such as airborne gravity meters and gradiometers, electromagnetic instruments, and remote sensing acquisition systems commonly used in geophysical exploration.

1 INTRODUCTION

Geomagnetic surveys have been primary means of exploring and mapping earth resources for hundreds of years. This geophysical technique exploits variations in the Earth's ambient magnetic field to locate bodies of magnetic rock, such as ore bodies. More subtle changes in the magnetic properties of rocks at depth, for instance between alluvium (sand and gravel) filling a sedimentary basin and bedrock around the basin, are used in oil exploration to map buried geologic structures. Geomagnetic fields are also used to detect and map buried anthropogenic features, such as buried gas pipelines. The widely recognized utility of geomagnetic data creates demand for these surveys. For example, World Geosciences, Inc., reports that they flew 1.1 million kilometers of airborne geomagnetic survey lines for their clients in 1996-1997. Smaller geophysical contractors than World Geosicences are also flying more surveys than ever before. For example, PGS, a contractor operating in the Gulf of Mexico, flew 90,000 miles of

aerogeophysical surveys last year. With this increase in demand for airborne geomagnetic data, two central issues have emerged that the airborne geophysics industry is struggling to contend with:

- Flying airborne geophysical surveys is dangerous, and as a result, increasingly expensive

- There is an increasing need for very high-resolution airborne geomagnetic surveys, not easily achieved using traditional airborne surveying techniques because of the high speeds of fixed wing aircraft and the high expense of helicopter surveys

We propose to meet the challenge posed by these two issues by developing an unmanned aerial vehicle (UAV) geomagnetic mapping system. We plan to achieve this goal by combining Division 9 expertise in UAV technology with Division 20 expertise in automated techniques for high resolution geomagnetic mapping. In the following, the nature of these two issues, hazards and need for higher resolution surveys, is clarified. This analysis is followed by a detailed plan for development of the concept to a stage acceptable for marketing SwRI expertise in this technology to the geophysical exploration community.

1.1 Serious Safety Issues in Airborne Geophysics

The high demand for airborne geomagnetic data comes at a high cost. Serious problems exist in aviation safety in geophysics. Approximately 34 fatalities (likely an underestimate) have

occurred as a result of 15 crashes during geophysical surveys since 1994. There are no statistics on non-fatal accidents, even though these often result in very serious injuries. Average tangible cost to a company per fatality is on the order of $300,000. Estimated intangible costs, including liability settlements, are estimated to range from $1,000,000 to $50,000,000 per fatality. One company, High Sense, estimated the annual cost of its aviation safety program is $500,000, one tenth of the company's total annual revenue.

The International Aerogeophysical Safety Association (IAGSA) is a not-for profit association devoted to improving safety in airborne geophysics. IAGSA has tracked accident statistics since 1994. Most crashes during surveys involve controlled flight into ground. In other words, there was nothing wrong with the airplane when the crash occurred and the crash resulted from pilot error during low elevation surveys. Usually these accidents occur in areas of complex topography where pilots are asked to fly at low elevations to improve survey resolution. Nevertheless, some crashes have occurred over flat terrain. The second most common accident type is of unknown cause (in three of these cases the airplane was never found). A small fraction of the crashes involved mechanical failure of the aircraft.

The P.I.s on this proposal attended a conference on aviation safety in geophysics sponsored by the Society of Exploration Geophysicists last September, where several presentations were made by staff of the National Transportation Safety Board, aerogeophysical contractors (such as World Geosciences, High Sense and Geoterrex), and clients (such as BHP and Shell). Several

consistent themes emerged:

- The costs resulting from accidents are unacceptably high,

- Airborne geophysics is extremely risky - for example a representative from Royal Dutch Shell indicated that employees engaged in aerogeophysical work are 260 times more likely to experience a fatal accident that an employee engaged in seismic work and that the life expectancy of an employee working in aerogeophysics is remarkably low - 20 yr,

- The increased accident rate in the last several years results from a combination of increased work in airborne geophysics and increased price competition. The cost of aerogeophysical surveys (not including the costs of safety programs and accident compensation) has fallen about 30 percent in the last four years due to increased competition among contractors.

.

Representatives from the oil and minerals industries all expressed a great deal of interest in UAVs because of the potential for improving safety, but also all indicated that successful airborne geomagnetic surveys would have to be flown before they would be seriously interested in paying for UAV technology.

1.2 Need for Higher Resolution Geomagnetic Surveys

Although extremely important, safety is not the only issue that can be resolved for the airborne geophysics community by geomagnetic mapping using UAVs. Increasingly, end-users of airborne geomagnetic data require higher-resolution data sets to make their geological (and economic) decisions concerning exploration targets. The effect of this requirement is to call for more dense flight line spacing in target areas, and to drive the airplane flight level to lower elevations, because of the increase in magnetic anomaly amplitude with decreasing distance from the ground. Safety issues aside, the requirement of flying dense and monotonous survey patterns at low altitudes above the ground is ideal for an autonomous UAV.

In addition, quality control (QC) is a fundamental issue in high resolution airborne surveys. QC is frequently compromised in traditional airborne surveys because of cross-track error on survey lines and high flight speeds compared to the rate at which location of the sensor can be determined. As a result of imprecise geolocation, the repeatability of survey lines is often low and multiple surveys of the same area are required in order to achieve acceptable results. At worst, anomalies in the geomagnetic field produced by geolocation errors can be misinterpreted as exploration targets as a result of low QC.

The importance of high QC emerges most clearly when multiple flight level surveys are flown. Such surveys involve repeating the airborne surveys of a given geographic area at several (at least three) flight elevations in order to develop a 3D picture of the geomagnetic field. Van Niewenhause (1998) showed that traditional modeling techniques, using mathematical estimates

of the vertical gradient, develop serious errors that can reduce the accuracy of the resulting geologic models. These errors can be avoided with multi-level surveys because the vertical magnetic gradient can be determined from data directly, proving sufficiently high QC can be achieved at each level. Because magnetic gradients can be used to infer depth, volume and geometry, 3D mapping and interpretation of gradient data is a powerful new tool for geophysical investigations, but one which requires development of new survey techniques.

2 Proposed Solution

UAVs offer a solution to industry problems related to safety and survey resolution because automated UAVs:

- By definition do not put a flight crew at risk,
- Can be programmed to fly accurate flight lines and will not deviate from programmed flight, even on monotonous surveys such as multiple flight level surveys,
- Can fly at comparatively very low airspeeds, resulting in a density of sample points and accurate geolocation information.

SwRI staff are in an excellent, perhaps unique, position to implement UAV technology in

geophysics very rapidly. SwRI staff from Division 9 now have considerable experience in building, testing, and marketing UAV technology. The SwRI UAV that will be used on this project, described in detail in the following, provides an excellent platform for conducting high resolution surveys. This UAV has a flight speed of 30 miles per hour, extremely slow compared with conventional aircraft. As a result, high data density can be achieved without loss of accuracy. In tandem with experience in UAV technology, SwRI staff from Division 20 have considerable experience in developing new geomagnetic mapping technologies that integrate kinematic differential global positioning systems (GPS), with submeter geolocation accuracies, and in the production of very high resolution magnetic maps (see enclosures).

Thus, the basic goals of this joint Division 9 and Division 20 IR & D project will be to:

- Integrate the magnetometer and differential GPS onto the UAV platform

- Perform a geomagnetic survey at a test site we have previously visited (Kilbourne Hole, New Mexico) that combines excellent geophysical anomalies with a remote, safe location in unrestricted air space for testing the system

- Develop a high-resolution magnetic map of the test site, coupled with a geophysical model based on the data and report that will serve as the basis of both a scientific publication and, in different form, a marketing tool

In the following, specific technical issues related to development of the UAV as a geophysical platform are discussed and a project plan and budget are developed.

3 Technical Issues

Several technical issues need to be addressed in order to implement a UAV geomagnetic mapping system and to demonstrate its viability as a geophysical technique. These include the current state-of-the-art in UAV technology and high resolution geomagnetic mapping, and modifications to each that will be required in order to succeed in implementing the proposed concept.

3.1 Unmanned Aerial Vehicle Technology

This project has become practical because of the development of low-cost reliable UAVs at SwRI. These UAVs use GPS technology, sophisticated guidance software, and automated pilot instrumentation to guide an engine-powered parafoil (Figure 1). SwRI originally developed these UAVs in 1996-1997 for the U.S. military, which is experimenting with low-cost, expendable resupply vehicles. Several of these units have been delivered and SwRI is continuing to work with the US. Marine Corps to optimize the use of UAVs for their applications. In addition, NASA staff from the Johnson Space Flight Center have taken delivery of one SwRI UAV for use as part of the X-38 project, development of an autonomous crew return vehicle for the

International Space Station. This UAV is being used for parachute design and astronaut training. In total, SwRI has built five of these UAVs and continuously improved software and hardware designs based on this experience.

Figure 1 - UAV in flight

Several different types of UAVs are currently used and all share some common characteristics. First, personnel are never carried by UAVs. The purpose of UAV development is to leave scientists and other personnel on the ground, where they can concentrate on data collection and interpretation. This greatly reduces the risks associated with flying geophysical surveys. Second, UAVs are autonomous vehicles in the sense that they do not rely on instructions telemetered from the ground for navigation, unless instructed to do so. Instead, UAVs fly a pre-programmed flight path, navigating to waypoints using GPS. This autonomy greatly reduces the skill required to fly high QC flight lines. In fact, many of the people flying SwRI UAVs, Marine Corps personnel for example, are not pilots.

Although this UAV was originally developed for other applications, many characteristics that make them well-suited for geophysical surveys. Basic specifications of the UAV are:

- Payload 500 lbs (227 kg)
- Airspeed 30 mph (13 m/s)

- Maximum elevation 12,000 ft (3500 m)
- Maximum flight time 10 hrs
- Manual or pre-programmed flight control
- Complete flight data and geophysical data telemetry using 900 MHz spread spectrum radios
- 200 W 12 V DC power available for instrumentation
- Requirements for take of and landing: about 100 m of dirt road or pasture
- Easily shipped to study area (rather than flown to study area)

Of course some of the above specifications are interdependent, such as maximum payload and maximum flight elevation.

It is important to realize that we have accepted reduced performance of our UAV in order to achieve a high level of safety and low cost. For example, in the unlikely event of engine failure, the parafoil design ensures that the UAV will descend at a low velocity (about 2 m/s vertical). This means that onboard instrument packages have a high probability of surviving such an incident undamaged. Also, although we will only use UAV far from roads and developed areas at the New Mexico test area, the low descent velocity minimizes potential damage to ground facilities. Fixed wing UAVs, in contrast, fly at much greater velocities and descend very rapidly in the event of engine failure or loss of control. The parafoil design also provides for much greater payloads than fixed wing UAVs. The current SwRI UAV design enables us to mount

almost as much instrumentation as we want on the UAV. In contrast, fixed wing UAVs generally have extremely limited payload capacities. These features of the SwRI UAV make it an excellent experimental vehicle.

The cost of this safer design and increased payload is that the UAV cannot operate in a wide variety of weather conditions. For example, we do not fly the UAV when surface wind speeds exceed 15 mph. Although this is a serious limitation for some geophysical surveys, we do not view this as a particularly important draw back for our planned experiments. Follow-on experiments can incorporate UAV designs that include fixed wing UAVs, such as the Outrider biplane developed in part at SwRI and similar much more sophisticated (and expensive) UAVs capable of flying in adverse atmospheric conditions.

Some modification of UAV software is planned for this project. Specifically, the guidance software will be modified to include arc and vector flying. In arc and vector flying, the guidance software keeps the UAV on a survey line rather than flying toward a specific waypoint. Thus, arc and vector navigation significantly reduces cross track error compared to waypoint navigation.

3.2 Magnetometer Technology

The geophysics component of this project relies on the coupling of dependable cesium vapor magnetometers for measuring the magnitude (intensity) of the geomagnetic fields, and kinematic

differential GPS for geolocation.. The cesium-vapor magnetometer uses optical pumping to measure the magnetic field. As a result, this sensor is comparatively insensitive to its orientation, can collect magnetic field data at a rate of up to 50 Hz, and is extremely sensitive (precision of 0.1 nT). These features make the cesium-vapor magnetometer ideal for UAV survey designs.

Like an airplane or helicopter, the UAV itself produces a magnetic field that interferes with accurate measurements of the natural geomagnetic field. Our observations indicate that the magnetic field associated with the UAV exceeds 100 nT everywhere on the UAV. Although this value is very small compared to the intensity of magnetic fields produced by airplanes and helicopters, it is too high to allow mounting of the magnetometer directly on the UAV for high resolution geomagnetic mapping.

The standard technique in airborne surveys used to eliminate this interference is to mount the magnetometer in an aerodynamic "bird" and drop the bird away from the body of the airplane using a winch assembly (Figure 2). At distances of 50 - 100 feet, the magnetic anomaly associated with the airplane is sufficiently reduced (< 10 nT) to allow geomagnetic mapping of the Earth's natural field. We plan to use a similar assembly mounted on the UAV. The magnetometer will be lowered and raised using a winch mounted on the UAV, triggered by instructions from the ground station. The magnetometer bird, however, will not be lowered 50-100 ft, because the magnetic anomaly associated with the UAV is much less than that of an airplane. Our initial calculations indicate that the bird will need to be lowered approximately 20 feet from the UAV.

Figure 2 - magnetometer bird and winch

Alternatively, a magnetic compensation system could be mounted on the UAV that dampens out the magnetic field produced by the UAV. Such compensation systems use Hemholtz coils to dampen the magnetic field associated with the vehicle. Unfortunately, the magnitude of the magnetic anomaly at a given location on the UAV depends on the flight direction - therefore compensation systems are linked to the airplane guidance system and the magnitude of the compensating field induced by electrical current in the Hemholtz coil must be computer controlled. As a result, such compensation systems are expensive and rarely used. Consequently, we prefer the winch system.

3.3 Kinematic Differential GPS Technology

UAV geomagnetic mapping techniques will only be successful if the magnetometer sensor position can be easily determined with sufficient precision. One of the key issues in attaining sufficient precision involves the rapid processing and evaluation of differential GPS data. Although the differential GPS unit we plan to use has a reported one sigma error resolution of approximately 2 cm horizontal and 4 cm vertical, numerous conditions frequently encountered during collection of differential GPS data can dilute this precision. These conditions range from the occlusion of satellites to delays in telemetry of base station coordinates due to interfering

radio traffic. Our experience using this system suggests that the occurrence of such conditions can increase one sigma error to several meters or several tens of meters.

Such changes in precision have a negative impact on data gathering, particularly in a situation as dynamic as a UAV geomagnetic survey. We plan to process differential GPS data as the data are telemetered from the UAV and evaluate the quality of these data in real-time using several techniques. These techniques will include plotting of vertical and horizontal dilution of precision, vertical and horizontal standard deviation of position, and tracking related quality parameters. In total, approximately 21 quality parameters can be tracked simultaneously. The simplest approach to data handling is rejection of data of insufficient precision. Alternative approaches will also be explored, such as interpolation of data collected during GPS satellite occlusion.

A second critical issue in differential GPS data processing is accounting for the offset between the magnetometer sensor and the differential GPS antenna. This offset distance must be accounted for by data processing as the data are collected. The offset distance calculation is complicated by the fact that DGPS measurements and magnetic measurements will not occur simultaneously. Thus, velocity and direction must be considered in interpolation of the sensor position. We plan to modify software developed for ground surveys that will estimate sensor position and error in sensor position in real-time, based on these considerations.

In traditional airborne geomagnetic surveys, errors occasionally occur that introduce a systematic

bias between readings collected on adjacent survey lines. These errors are referred to as levelling errors and result from improper instrument drift or position corrections. We plan to minimize the introduction of similar errors in the UAV survey through use of accurate position information and drift corrections. Nevertheless, systematic bias between survey lines, both vertical and horizontal, will be assessed as part of post-processing for production of geomagnetic maps.

4 Field Area and Mapping

The Kilbourne Hole, New Mexico, site is located in a high desert area approximately 35 miles west of the western suburbs of El Paso (about a one hour drive on well-maintained dirt roads) and 30 miles north of the US-Mexico border (Figure 3). One of the P.I.s (Connor) visited this site over the Thanksgiving holidays in order to assess the viability of the site as a test area, both in terms of its physiography, geomagnetic anomalies, and suitability for testing the UAV.

Figure 3 - Kilbourne Hole location

Few places in the United States are as suitable as Kilbourne Hole for testing the UAV. Kilbourne Hole and a large surrounding area is in unrestricted airspace and on Bureau of Land Management land. The area around Kilbourne Hole is remarkably flat, with less than 200 ft of vertical elevation change across the entire area - and this elevation change is restricted to the rim of

Kilbourne Hole itself. There are no trees, paved roads, buildings or other structures, telephone or power lines, or any over type of obstruction to low level UAV flights in this entire region. The only vegetation in the area is low scrub-brush and sage. Several large ranches (in terms of area) are located near Kilbourne Hole and these ranchers would be consulted before overflights began.

At the same time, Kilbourne Hole is geologically complex and the resulting geomagnetic maps will be sufficiently interesting to be useful. Kilbourne Hole is a volcano formed approximately 16 thousand years ago (Poths et al., 1991). Lava flows in the area are highly magnetic, partially buried by alluvium, and cut by geologic faults. Kilbourne Hole was the site of airborne geomagnetic mapping in the mid-70's by the U.S. Geological Survey for evaluation as a possible geothermal resource (Cordell, 1975). Therefore it will be practical to compare the results of the UAV survey directly with traditional airborne magnetic survey results.

The survey itself will be conducted during a two week period. Personnel will drive to the site from San Antonio and stay in west El Paso (Sunnyland area) for the duration of the survey. The goal will be to survey a 10 km^2 area immediately south of Kilbourne Hole. This area has large amplitude magnetic anomalies and the surveys will result in an excellent map (Figure 4).

Figure 4 - Area south of Kilbourne Hole and magnetic anomalies.

The survey will include mapping at an elevation of 100 m above the ground surface on flight

lines spaced 100 m apart and stacked profiles across the area, surveying the same line at multiple levels above the surface. If these initial surveys are successful, the mapping will be repeated at several flight elevations to produce a complete multiple level survey.

In the unlikely event that surveys at Kilbourne Hole prove to be impractical for unforseen reasons, a alternative site at Fort Sumner, New Mexico is also available.

5 Benefits of this Research

The expected accomplishments of this research are:

- Development of the first UAV geophysical mapping system

- Demonstration of this system by constructing a high-resolution geomagnetic map

Through these accomplishments, we have the opportunity to capitalize on our preliminary successes in the areas of UAV and geophysics by merging these technologies to produce a new survey method that addresses critical issues in the geophysical exploration industry.

In addition, UAVs are very likely to revolutionize the way many types of geophysical data are

collected. In addition to geomagnetics, many types of electrical, electromagnetic and gravity data and remote sensing data collection systems could benefit from integration with UAV technology. Early SwRI research and development in this area should yield significant long-term benefits.

6 Project Plan

This project will be subdivided into four major tasks. These tasks are:

- Design of the geophysical platform for the UAV
- Implementation and bench testing of the platform design
- Survey
- Final Report Preparation

6.1 Task 1: Design of the Geophysical Platform for the UAV

Task 1 will begin with a complete reevaluation of the requirements of high-resolution geomagnetic surveys and the necessary modifications of the UAV for meeting these requirements. The final design of the system and performance requirements of the UAV

geomagnetic mapping system will be formulated as part of this task.

6.2 Task 2: Implementation and bench testing of the platform design

Task 2 involves implementation of hardware and software modifications for the survey. These modifications include hardware installation on the UAV, code modification to the UAV guidance system to include arc and vector navigation rather than waypoint navigation, and modification of currently used computer codes for real-time telemetry of geophysical data from the UAV to the ground station. This activity will be followed by bench testing of the components of the survey system. As part of Task 2, preliminary flights with the magnetometer bird will be performed at a test area in Floresville and any required modifications to the winch - magnetometer bird system will be performed.

6.3 Task 3: Survey

Task 3 involves preparation for field testing of the UAV geomagnetic mapping system in the New Mexico desert, performance of the actual survey, and tasks associated with evaluation of the flight and survey map preparation.

6.4 Task 4: Final Report

A final report will be submitted to the ACR summarizing the major accomplishments of this project. It is anticipated that the results of this project will also be presented at the Society of Exploration Geophysicists Meeting and published in geophysical journal, such as Leading Edge.

7 Project Schedule

A project duration of one year is planned. Figure 5 shows the planned project schedule by task. The project is geared so that field work will be conducted in October and early November, 1999. This time of year is excellent for meteorological conditions at the Kilbourne Hole site and is practical in terms of the availability of project personnel.

Figure 5. Schedule of task activities.

8 Personnel and Organization

Project participants will include Dr. Charles B. Connor (Principal Scientist, Division 20) and David Ogden (Principal Engineer, Division 9). Connor will be primarily responsible for telemetry and visualization of geophysical data from the UAV, survey design specifications, evaluation of data QC during the survey, interpretation of the geophysical data and map, and report preparation. Connor will be assisted by Division 20 PL-1 staff in these activities. Ogden

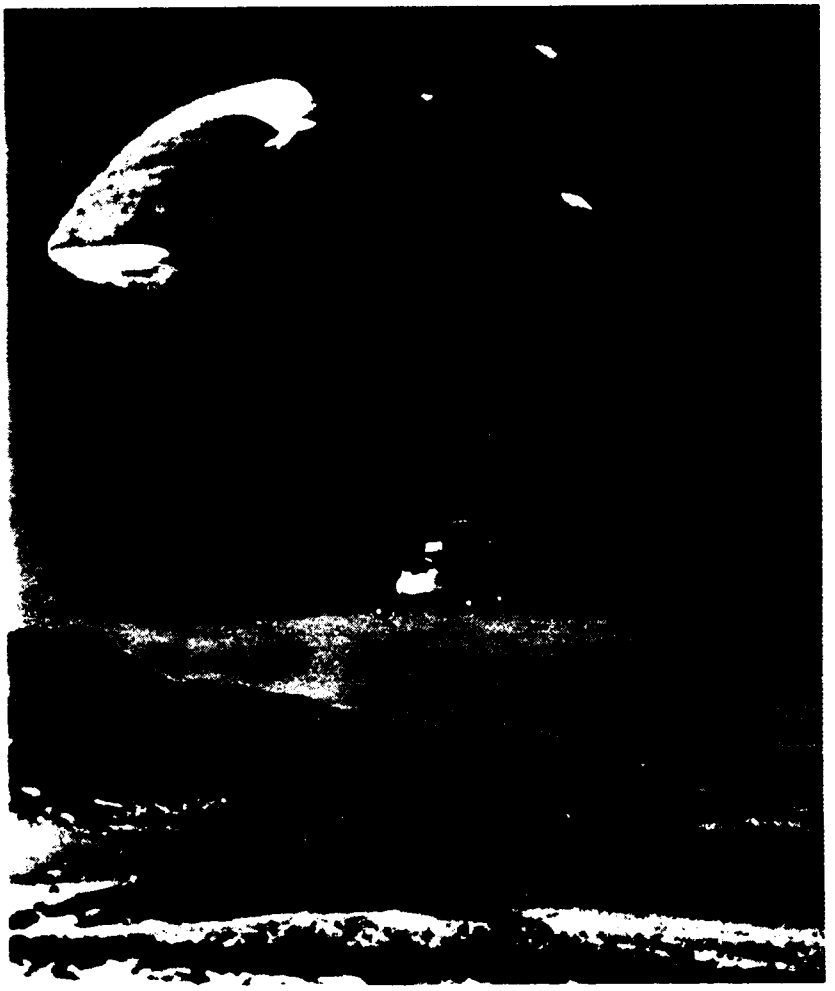

Figure 1. This SwRI UAV will be modified to carry the magnetometer bird and related components. The magnetometer bird will be lowered from the UAV using a winch installed at the position of the red box in this photo (see Figure 2).

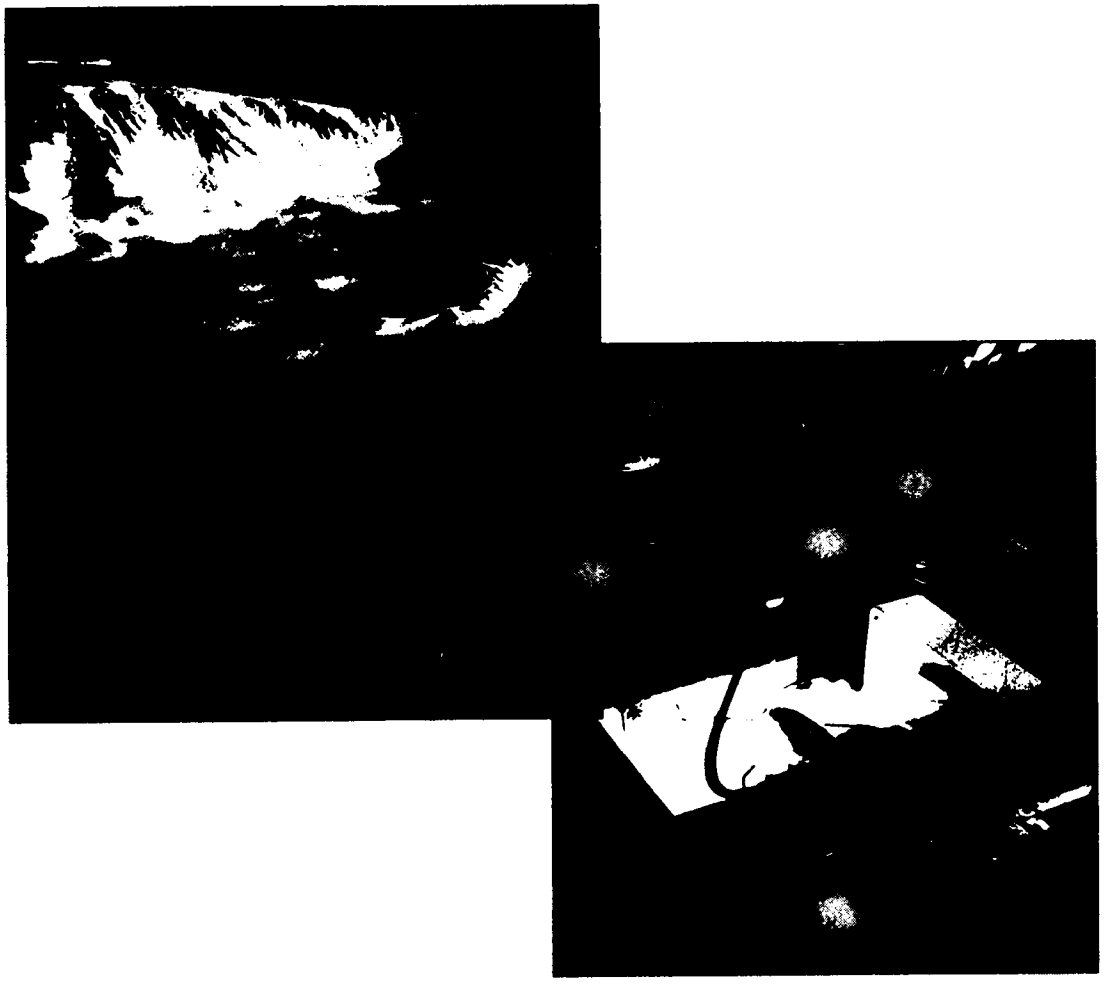

Figure 2. The magnetometer will be located in a bird (approximately 4 feet in length) and lowered from the UAV using a winch activated by commands radio-telemetered from the ground station. Data will be transmitted from the bird to the UAV via the winch cable and then telemetered to the ground station. Photos show the University of Texas Institute of Geophysics bird and winch mounted in a Twin Otter aircraft during a magnetic survey of the TransAntarctica Mountains. Photos by L. Connor.

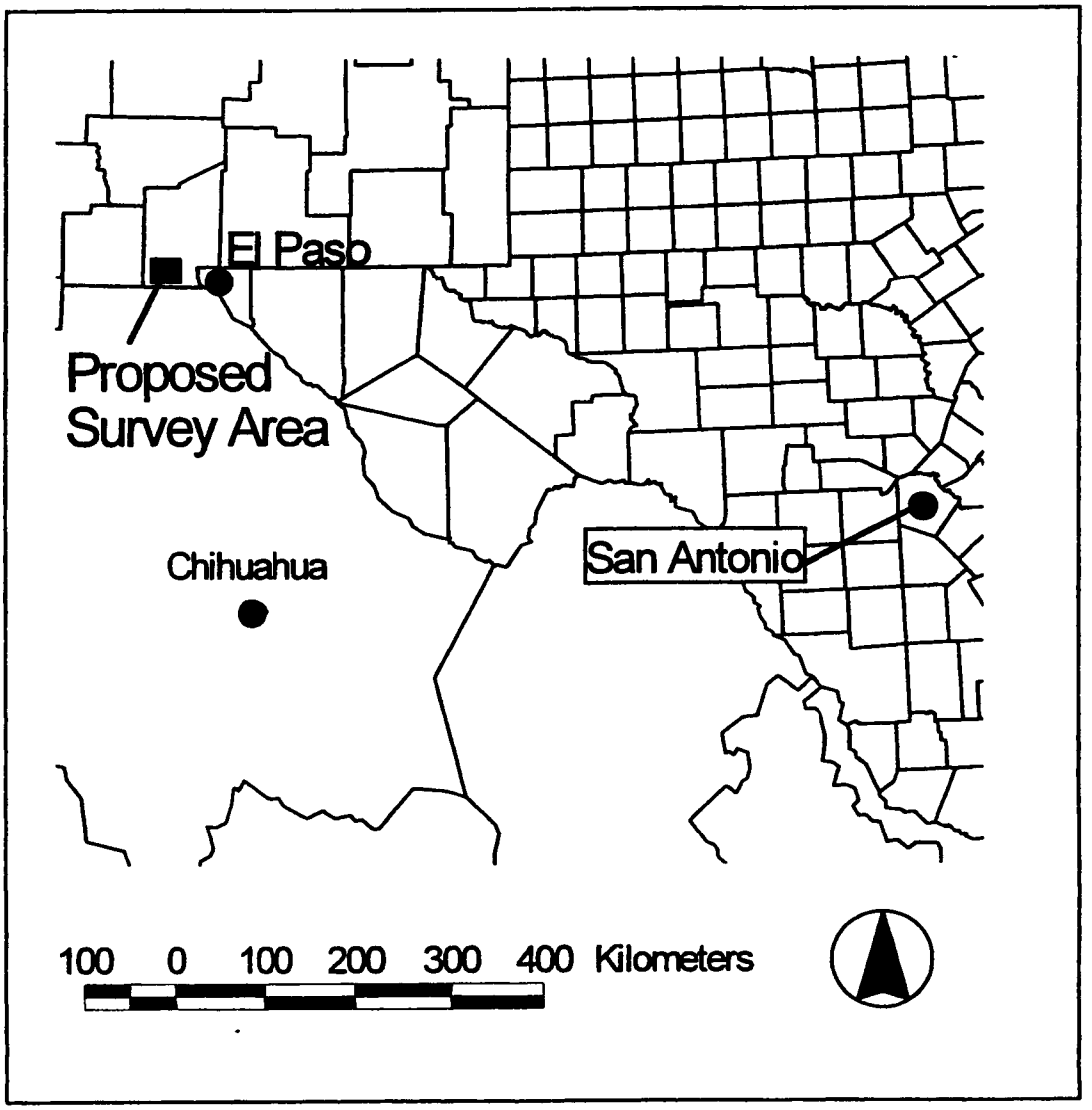

Figure 3. Kilbourne Hole location

cc

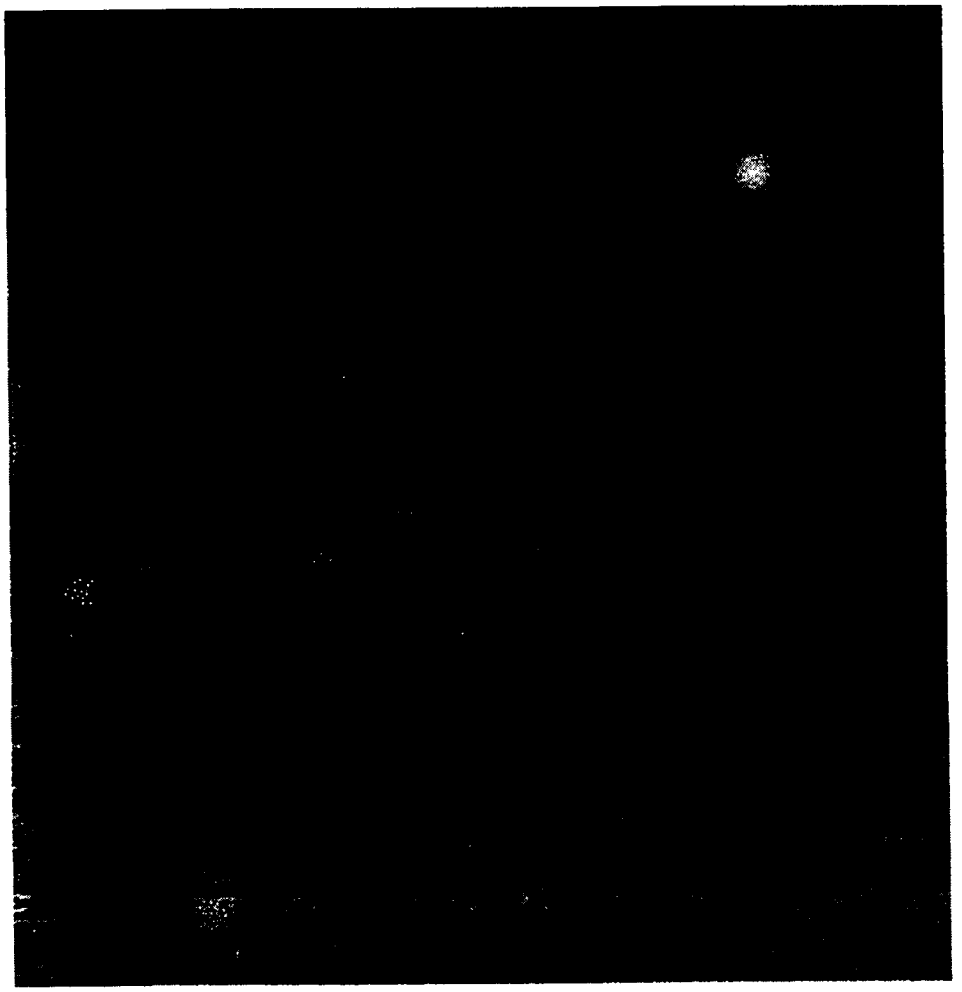

Figure 4. Two-meter resolution satellite image of the proposed survey area, Kilbourne Hole, New Mexico. Kilbourne and Hunt's holes are both volcanic explosion craters with buried basaltic lavas between them. The proposed survey area is approximately 10 km^2 and the entire image covers approximately 50 km^2. Note, change in image reflectance is due to a change in the illumination angle for the composite images.

Figure 5. The proposed survey area is flat, treeless, and completely undeveloped. This photo is taken looking north from near Hunt's Hole toward Kilbourne Hole (see Figure 4). The survey team is collecting ground magnetic measurements for the East–West profile shown in Figure 6. Photo by J. Connor.

cc

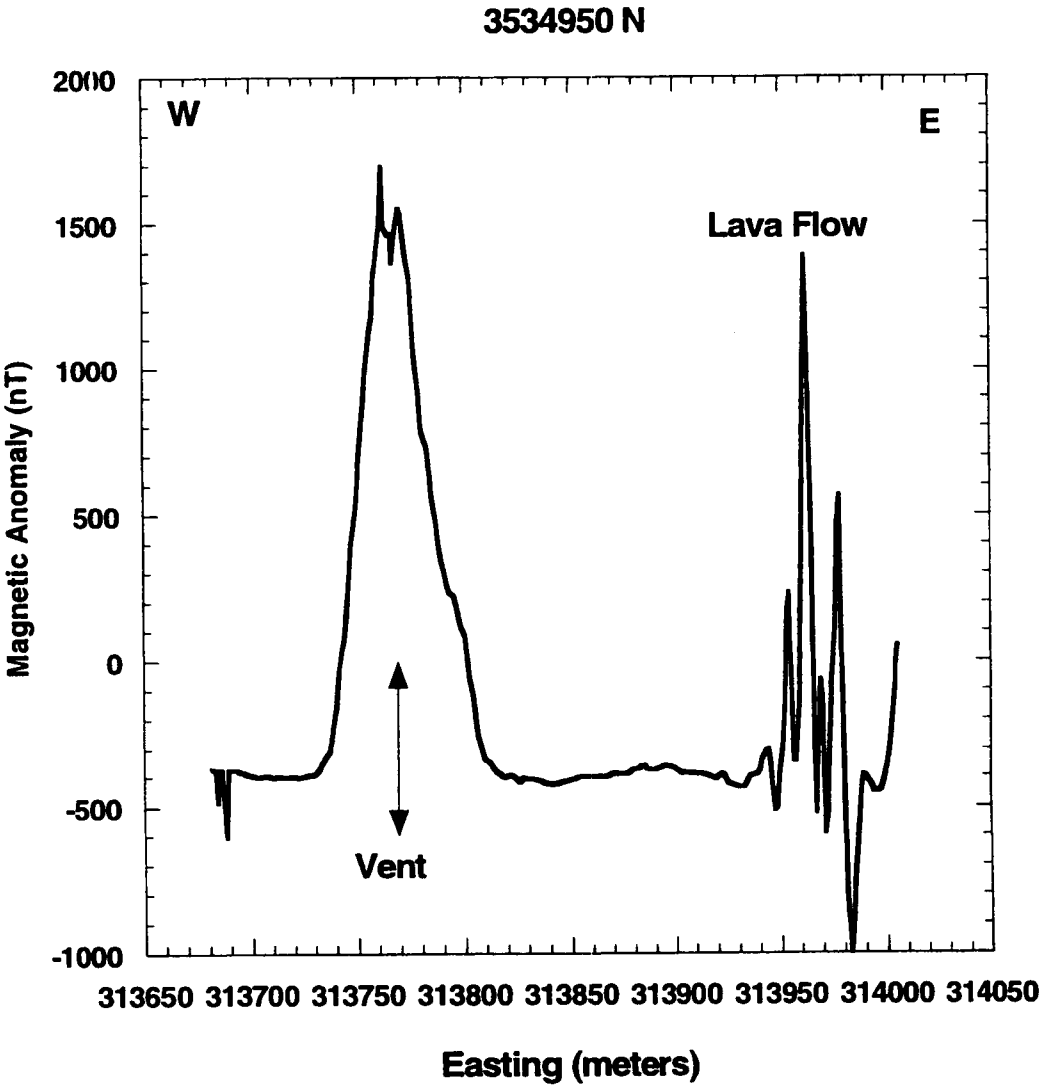

Figure 6. Magnetic data collected on a ground traverse within the proposed survey area during a preliminary survey in November, 1998. Note the large amplitude magnetic anomalies associated with buried vents and lava flows. The variable frequency and amplitude of these anomalies will provide an excellent test case for the UAV geomagnetic mapping system.

will lead the team for modification of the UAV, implementation of the winch system for the magnetometer, and all activities related to the UAV flight. Ogden will be assisted in these activities by Division 9 PL-1 staff. Approximate time commitments for these individuals will be: C. Connor (320 hrs), David Ogden (320 hrs), Division 9 PL-1 personnel (320 hr), Division 20 PL-1 personnel (320 hr), and a Division 9 technician (320 hrs).

9 Equipment Required

No capital equipment is required for this project. An existing UAV located in Division 9 will be modified for the project. The project will use cesium-vapor and proton-precession magnetometers, the DGPS system, laptop computer, and radio telemetry equipment owned by Division 20. Silicon graphics workstations and all related computer facilities needed for this project are available in Division 20. The magnetometer bird and winch system will be rented for the bench testing and survey portions of the project. All other equipment, such as cables, batteries, and data storage disks will be purchased on the project.

10 Proposal Cost

Daves section - I'll find out what the bird rental will be

Table 1 call out

11 Previous and Current IR & D Projects

Connor was awarded a Quick-Look grant in November, 1997, for using nonferrous all-terrain bicycles to perform magnetic surveys over comparatively large areas. A total of $10,296 were awarded to fund this quick-look proposal, which was completed in February, 1998 (La Femina and Connor, 1998. Developments resulting from this Quick-look proposal were used in work contracted from the U.S. Nuclear Regulatory Commission. Computer codes for visualization of geophysical data developed for this Quick-look will be modified for the UAV project.

12 Related Research

This proposal is a direct outcome of previous work on high-resolution ground magnetic surveys conducted by Division 20 staff (Connor et al., 1996; 1997; Stamatakos et al., 1997; Connor and La Femina, 1997). Clients sponsoring this previous work include the U.S. Nuclear Regulatory Commission, The International Atomic Energy Agency, and Brown and Root Environmental. Our work integrating kinematic differential GPS and magnetometers has received two national awards (GPS World, 1997; 1998).

13 References

Connor, C.B., and P.C. La Femina. 1997. *Final Report: Magnetic Survey of the Ujung*

Lemahabang Site, Muria Peninsula, Indonesia. San Antonio, TX: Center for Nuclear Waste Regulatory Analyses, Southwest Research Institute.

Connor, C.B., R.H. Martin, P.G. Hunka, J.A. Stamatakos, D.B. Henderson, and R.V. Klar. 1996. *Ground Magnetic Survey of the Little Cones*. CNWRA 96-002. San Antonio, TX: Center for Nuclear Waste Regulatory Analyses, Southwest Research Institute.

Connor, C.B., S. Lane-Magsino, J.A. Stamatakos, R.H. Martin, P.C. La Femina, B.E. Hill, and S. Leiber. 1997. Magnetic surveys help reassess volcanic hazards at Yucca Mountain, Nevada. *Eos, Transactions of the American Geophysical Union* 78(7): 73-78. Lead Article.

Cordell, L. 1975. Combined geophysical studies at Kilbourne Hole maar, New Mexico. *New Mexico Geological Society Guidebook*, 26th Field Conference, Las Cruces County: 269-272.

GPS World. 1997. Hunt for Hidden Volcanoes. *GPS World Showcase* August, 1997: 13.

GPS World. 1998. Geophysics by Bicycle. *GPS World Showcase* August, 1998: 12.

La Femina, P.C., and C.B. Connor. 1998. Final Report: The All Terrain Bicycle Geomagnetic Mapping System, submitted to the Advisory Committee on Research, Southwest Research Institute, February, 1998.

Stamatakos, J.A., C.B. Connor, and R.H. Martin. 1997. Quaternary basin evolution and basaltic volcanism of Crater Flat, Nevada, from detailed ground magnetic surveys of the Little Cones. *Journal of Geology* 105: 319-330.

Poths, J., E.Y. Anthony, M. Whitelaw, and J. Hoffer. 1991. He surface exposure dates and paleomagnetism of the Quaternary Potrillo volcanic field, Rio Grande rift, south central New Mexico, *Eos, Transactions of the American Geophysical Union* 72: 577.

Van Niewenhause, R. 1998. State-of-the-art in Gulf of Mexico airborne geophysics. Presented at : Society of Exploration Geophysicists Annual Meeting, New Orleans, September 24-26.

Scientific Notebook
Project 20-1402-461

Jan, 1999
Chuck Connor

The following is a trip report for a talk in Kiel Germany and work on volcanic hazards assessment in Vienna.

Summary of the Kiel Meeting

Connor visited GeoMar, a Research Institute in Kiel Germany, and lectured on volcanic hazard analysis of the Yucca Mountain site. Hans Schmincke, a volcanologist a GeoMar, was particularly interested in this topic because he has participated in the volcanic hazard analysis for the Mulheim- Karlach Nuclear Power Plant, located in the Eifel volcanic field, south of Bonn. Schmincke testified as a "friend of the court" and evaluated volcanic hazard studies performed by Colenco and other groups. Schmincke has worked in the Eifel area since about 1970.

Unfortunately, all of the volcanic hazard studies performed by Colenco and others are confidential. Schmincke, however, did not view these studies favorably. Currently, the plant is shutdown. According to Schmincke, this was primarily due to the seismic hazard at the site but volcanic hazards played a significant role in this decision. Briefly, the site is located about 15 km from the Lacher See phreato-magmatic crater, formed during an eruption 12,000 B.P. Lacher See is part of a predominantly basaltic volcanic field located in the Rhine Graben. This eruption was of a very large magnitude, approximately equivalent in magnitude to the 1992 eruption of Mt. Pinatubo. The main effect of the eruption on the site was related to ashfall. Ash dammed the

Rhine river south of the site, causing extensive flooding upstream. The site was submerged under approximately 20 m of water for an unknown period of time.

There is now talk in Germany of reopening the debate about the power plant. Essentially, the idea according to Schmincke is that the utilities will shutdown several older plants, and in exchange bring the Mulheim-Karlach plant on line. Schmincke suggested that we jointly pursue funding for a complete volcanic hazard analysis - using the techniques developed for Yucca Mountain and the large data sets he has collected during the last 30 yr. Schmincke indicated that he would inquire about obtaining federal (German) funding for this project. I indicated that U.S. funding was not likely available. Nonetheless, I am curious about the potential for NRC funding for the volcanic hazard analysis since it would be very good experience, increase our international "exposure", and the hazard problems are quite similar to Yucca Mountain issues. Such a project might involve hiring a German post-doc to work in San Antonio on the Eifel hazard study.

Summary of the IAEA Meeting

Connor attended a meeting at the International Atomic Energy Agency, Vienna, to review progress on the characterization of the Muria site and volcanic hazard analysis. The meeting also was attended by Mulyanto Soderjibroto, Sutikno Bronojioto, Antonio Godoy (as a consultant to the IAEA, Georgio Pasquare (University of Milano), Alexander McBirney (University of

Oregon), and Leonello Serva (Chief of the geologic hazard division, ANPA, National Agency for the Protection of the Environment, Italy). The meeting spanned four days (Tuesday-Friday, November 10-13).

Presentations were made that summarized work in the last 18 months on the volcanic hazard assessment of the Muria site, a proposed nuclear power plant in central Java. In his opening remarks, Mulyanto Soderjibroto commented that Indonesia remains committed to their nuclear program. He indicated that President Habibi was a long time supporter of the Indonesia nuclear program, but also indicated that during the last six months, especially since the "unfortunate accident" in which 500 people were killed during rioting, Habibi has been less interested in long term development. Overall, the tone of the meeting was subdued as it was clear that the future of the nuclear program in Indonesia is very uncertain.

Several issues arose during the course of the meeting with regard to CNWRA involvement in the project. First, Mulyanto offered to fund the entire volcanic hazard analysis for the site as a CNWRA project. Unfortunately, Mulyanto also made it clear that only one answer on site suitability was appropriate at this point. Alternative plans were formed as follows:

1) IAEA has already set aside funds for procurement of SPOT digital elevation data. I suggested that CNWRA select the appropriate images and do some initial processing in ERDAS and Arc/Info. This accomplishes two things. First, CNWRA becomes more integrated into the

project. Second, it provides us with an outstanding data set. Ron Martin indicated to me that less than 40 hrs would be required to select the data sets and do some initial processing.

2) Two Indonesian geoscientists may come to CNWRA for training in development of volcanological databases, GIS, and some instruction on volcanic hazard assessment. IAEA will provide funding to cover their expenses and provide the CNWRA with $5,000 to cover our costs associated with hosting these geologists.

3) CNWRA involvement was discussed in terms of providing technical support for the Indonesian volcanic hazard assessment, following this training. This technical support would include providing computer programs for use in hazard modeling and instruction on their use. This support would not involve writing a report on the volcanic hazards of the Muria site. We need to reach some conclusions about how to license software like ASHPLUME and PVHAview to organizations interested in performing these kinds of analyses.

Field studies were performed during the last 18 months following IAEA recommendations cover topics relatd to: maars, gas emissions, lava flows, pyroclastic flows, lahars and petrology-geochemical analyses. Clarification is also carried out regarding the stratigraphic sequence at the Ujung Lemah Abang (ULA) site. Topics discussed and specific recommendations made during the meeting are summarized in the following.

(1) Maars. NTT staff presented new data on the geology of the maars indicating clearly that these eruptions included a magmatic component. This is determined from the occurrence of juvenile bombs and a small lava flow in one of the maars. Second, new age determinations were presented. These age data are preliminary Ar/Ar dates, showing an age of 0.5 +/- 0.2 Ma, considerably older than previously thought. Additional age and geochemical data will be gathered.

(2) Gas Emissions. New information about gas emissions were presented by NTT. These data confirm that gas emissions in the Muria area have a magmatic component. Data from other areas, including nearby gas fields, were collected and these indicate no magmatic component. Therefore the Muria gas emissions are considered to be anomalous.

(3) Lava Flows. Field studies at the site concentrated on the origin of lava flows at ML-1, ML-2, ML-3, and LG-3. It was concluded that outcrops in the vicinity of ML-2 are lava flows. Some debate continues about the nature of the lava block in the LG-3 borehole. The magnetic survey of the site indicates that continuous outcrops of lava are not present in the site vicinity. Instead, isolated blocks of lava are present throughout much of the site area. One interpretation of these blocks is that they are transported to the site vicinity by lahars or mudflows. However, an alternative interpretation is that these blocks are the eroded remnants of lava flows. This idea is supported by the similarity between textures observed at LG-3 and those observed in outcrops in the area of ML-2. To summarize, there is no doubt that mudflows and/or lahars occur in the site

vicinity. There is some debate about the occurrence of lava flows in the site vicinity based on alternative interpretations of LG-3. A preliminary Ar/Ar age determination for the ML3 lava flow gives an age of 0.75 +/- 0.2.

(4) Lahars. Volcanic debris flows found on the north and northwest flank of Muria volcano are considered to be lahars. Lahars occur throughout the study area on the northwest flank of Muria volcano. New stratigraphic analyses show that these lahars are older than the sequence of pyroclastic flows and lava flows mapped in the Muria summit area. Mudflows are differentiated from lahars based on the occurrence of juvenile ash in the matrix of the deposit. Therefore, mudflows, also occur in the area that are not necessarily associated with volcanic eruptions. Interpretations vary, but this may be the case with the deposits observed in the LG-3 borehole.

(5) Site Volcano Stratigraphy. In addition, field work in the site vicinity indicates that the stratigraphy of the site may be related to a volcanic center separate from the Young Muria center. The primary reason for development of this idea is that the site stratigraphy is tilted slightly, dipping to the south toward the Young Muria volcano. Wide ranging discussions about this included suggestions that a older volcanic center may be located off the current Java coast or that tectonism had tilted this stratigraphic sequence subsequent to its deposition. There is also a suggestion from preliminary age determinations that this stratigraphic sequence represents older eruptions and cannot be associated with Young Muria volcano. If so, it may be that volcanic

products from Young Muria have not reached the site.

(6) Based on comparison with the Italian potassic volcanoes it is clear that the Young Muria volcano is close to the maximum repose for this type of volcano. However, potassic volcanoes do reactivate after periods of repose on the order of 400-300 ka. Use of these analogous volcanic systems suggests that the possibility of reactivation of Young Muria cannot be completely discounted.

Recommendations

(1) Radiometric dating of maars, lava flows, and the LG-3 lava block is a priority. At least ten additional age determinations are planned.

(2) Major and trace element geochemistry for a stratigraphic sequence of the Muria volcano is important in order to look for petrogenetic similarities or differences among the different episodes. Particular care should be taken to collect samples from the phreatomagmatic craters and compare these to young Muria geochemistry. It is recommended that 30-40 samples be analyzed and that these analyses all be performed in the same laboratory. Geochemical analysis should also be performed on the same samples used for radiometric dating. Rock samples for radiometric age dating and geochemical analysis will be collected by Prof. Pasquare and the NTT team in March or April, 1999.

(3) Nannofossils in the sediments underlying the ULA stratigraphic sequence should be used to clarify the ages of these sediments.

4) No geophysical information is available on the Young Muria volcanic systemt o indicate the potential for volcanic eruptions in the next one hundred years. Geophysical information that could be used to make this assessment includes: (i) micro-seismic monitoring; (ii) seismic tomography, (iii)deformation measurements to document long-term strain. As a first step to rectify this situation, microseismic data recorded previously by NTT should be reviewed. It should be determined whether or not these data are sufficient to perform a seismic tomographic analysis on the subsurface structure of the volcano, with the specific goal of searching for low velocity zones that maybe associated with the presence of partial melt.

5) It is recommended that additional work be done to locate the vent for the ML-1, ML-2, and ML-3 lava flows. This will assist in the probability analysis. On shore geophysical data (aeromagnetics, gravity, or other data sets) should be reviewed to assist in this analysis.

6) It is recommended that work now begin on the probabilistic volcanic hazard assessment. This analysis should concentrate on two separate activities. The first involves modeling the probability of new vent formation on the flanks of Muria volcano. The second task involves the modeling of geophysical flows from the Young Muria central vent, including lava flows, pyroclastic flows and lahars using digital elevation data.

7) A site visit to Karimun Java Islands near the Muria Peninsula is important in order to determine the geology of these islands and their relationship to the site geology. Off-shore geophysical data should also be reviewed in order to determine if eroded volcano products and source areas may be present.

A workshop is planned to summarize the status of this work in 2000. At this workshop, new geological data will be summarized and the probabilistic analysis will be presented. In addition, discussions about publications have resulted in the idea of an overall summary of these activities.

Problems Encountered

NONE

Scientific Notebook
Project 20-1402-461

Jan, 1999
Chuck Connor

The following is a set of experiments for TH and IA KTIs I have proposed

Proposed Natural Analog Experiment at Parícutin Volcano

1 Introduction

Thermohydrologic models are being used to predict normal performance of the proposed high-level radioactive waste repository and to predict the thermal conditions that may exist within and near the repository following igneous activity. These models are used by DOE to support findings in the viability assessment and will form part of the technical basis for the license application. In addition, new methods in electrical resistance tomography and electromagnetics are being used by DOE and its contractors to monitor thermohydrologic processes. These geophysical methods are used to track redistribution of moisture and temperature gradients within rock masses, such as tunnel walls, that are not otherwise observable. Although important to understanding both the normal performance of the repository and its behavior following potential disruption, tests of these models and methods are complex and difficult. For this reason, DOE and its contractors have devised several large scale heater tests to further our understanding of thermohydrologic processes that may operate within Yucca Mountain. Although laudable, these large scale tests are of short duration and the experimental designs themselves may significantly alter the thermohydrologic conditions of interest.

We propose to test both numerical thermohydrologic models and investigate the utility of electrical geophysical methods in monitoring thermal systems using a natural analog: the cooling Parícutin basaltic cinder cone in Mexico. There are several advantages to using Parícutin as a natural analog to test the thermohydrologic models that are applied in both the Thermal Effects and Igneous Activity KTIs.

- Because Parícutin formed during a single period of activity, the thermal history of the volcano is extremely well known. Pyroclastic ejecta was deposited on the cone at 600-700 °C continuously during the 1943-1946 phase of the eruption, building a 350-m-tall cinder cone. Unlike other volcanoes or large geothermal systems, no other source of heat has affected the cone since its formation 50 yr ago. Thus, a long term thermohydrologic experiment is well underway at Parícutin.

- The volcanic activity at Parícutin created a very well-sorted, coarse-grained deposit consisting of low density basaltic pyroclasts. This lack of internal heterogeneity makes the cone an ideal medium for assessing thermohydrologic models. In contrast to the

cinder cone, cooling vents on the lava flows surrounding the cinder cone are much hotter. These lavas are low porosity, low permeability basalts with abundant glass. Like all lava flows, these are variably fractured, producing a bulk thermal and hydrologic conductivities quite close to those observed in welded tuff. Experiments on both the cone and at cooling lava vents can be conducted to resolve the effectiveness of thermohydrologic models under these varied conditions.

- The geometry of the cone has radial symmetry, greatly simplifying the numerical thermohydrologic models that will be developed. In addition, the comparatively small size and geometry of the cone allows us to place sensors around the cooling rock, rather than simply above the cooling rock, which is the case in nearly all other natural analog systems.

- The Parícutin cinder cone is a very easy place to work The volcano is located 40 km from the city of Uruapan and is easily reached by car. The cone and surrounding area is not vegetated and access to all of the thermal areas is straightforward.

In the following, background information about Parícutin, the planned field experiments, and anticipated results are described.

2 Background on Parícutin

Parícutin formed as a result of eruptive activity that commenced in 1943 and continued through 1952. Details of the Parícutin eruption are summarized by Wilcox (1954) and Luhr and Simkin (1993). The Parícutin eruption began in February, 1943, when hot gases and pyroclastic rocks began erupting from a small fissure in a cultivated field. This pyroclastic activity was preceded by several weeks of seismic activity that was reported to increase in intensity and frequency up until the initiation of the eruptive phase (Wilcox, 1954). Although the eruption lasted nine years, most of the central cone was built in the first year of activity, during which time pyroclastic activity was fairly steady (Segerstrom, 1950). During October, 1943, a series of new vents formed on a NE -trending line. These vents, located NE and SW of the main cone, were the sites of vigorous explosive and effusive activity, and were alternately active and quiescent until the end of eruptive activity in 1952. According to Wilcox (1954), new satellite vents continued to form as late as 1947. Lava flow effusion ceased at Parícutin in February, 1952 and pyroclastic activity declined gradually until it also ceased in March, 1952. The cinder cone is now approximately 350 m in height and lava flows from the volcano cover an area of about 24 km2. The two youngest satellite vents, Taqui northeast of the main cone and Ahaun southwest of the main cone, remain visible above the lava flows and are currently the sites of high-temperature fumaroles. The nine year Parícutin eruption produced approximately 1.3 km^3 of lava and 0.7 km3 of tephra and a total volume of 1.32 km^3 (dense rock equivalent) (McBirney et al., 1987).

Wilcox (1954) reports that xenoliths of gabbro, quartz monzonite, and Tertiary silicic tuffs were common in the eruptive products during the first two years of activity. Parícutin lies on a section of Quaternary basalts of unknown thickness, but likely on the order of several hundred meters thick (Williams, 1950); the thickness of the underlying Tertiary silicic tuffs is also unknown, but is estimated by Williams (1950) to be over 300 m thick the Parícutin region, based on exposures along the Cupatitzio river about 30 km from Parícutin.

Parícutin continues to degas today, forty-one years after the cessation of eruptive activity. This degassing is extremely weak compared with that observed at many quiescent composite volcanoes, but is also quite sustained, with low mass flow fumaroles remaining stable since at least 1983 (McClelland et al., 1987). Connor (1989) mapped fumaroles and soil Hg anomalies around the main crater and Ahuan vent, located SW of the main crater, and the Taqui vent, located NE of the main crater.

2.1 Current Thermal-hydrology of the Cinder Cone

The main cinder cone is composed entirely of angular, nonwelded scoria. Individual scoria fragments are ash to block-sized and typically have porosities of 30-50 percent, giving the overall deposit a porosity of 50-70 percent. The bulk thermal and hydraulic conductivities of Parícutin cinder cone have not been determined. Measurements at similar cinder cones yield thermal conductivities of 0.1 - 0.25 W/m°K and permeability of approximately 1×10^{-10} m^2.

Ground temperatures on the cone vary from ambient to 150 C. The highest temperature areas are located on the cone rim and occur along short, discontinuous fractures in the scoria that are approximately 1 -2 m in length with apertures of 1-2 cm. Thermocouples can be inserted to depths of 10-20 cm within these fractures. In cool weather, steam is visible rising from these fractures on the cone rim. This pattern of thermal areas concentrated on the cone rim is common to virtually all young cinder cones and is so common because conductive cooling of the homogeneous scoria is the dominant heat transfer process in these cones. Condensation and vaporization zones develop about the hot interior of the cone, which initially has a uniform temperature and cools very slowly due to the low thermal conductivity of the scoria. This, combined with the radial symmetry of the cone, creates an excellent setting for developing techniques to monitor and model thermohydrologic processes.

2.2 Current Thermal-hydrology of the Lava Flows and Lava Vents

High-temperature fumaroles at Parícutin are restricted to the Ahuan and Taqui lava vents. Lava flows erupted from these vents until 1952. Consequently, the lava flows in this area are up to 50 m thick. The basaltic lavas are dense aa flows, with glassy textures and very low matrix porosity

and permeability. The lava flows are fractured and water vapor, where present on the cooling lava flows, flows along these fractures.

Temperatures at the Ahuan vent have been monitored intermittently since 1983. During this period, temperatures have decreased from a maximum of 473 °C, recorded in November, 1983, and temperatures have dropped steadily since that time. In 1993, temperatures in four fumaroles at the Ahuan vent were measured at three minute intervals for three days. The highest temperatures recorded during this field work were about 220 °C and daily temperature variations were approximately 40 °C. These fumaroles are located in a zone that measures approximately 100 m by 50 m. The fumaroles do not have a large condensable phase although flow is audible in these fumaroles. These comparatively high temperature fumaroles are surrounded by low-temperature fumaroles (40 - 85 °C) that cover a broad zone around the Ahuan vent, extending into some of the surrounding lava flows. These fumaroles emit water vapor.

A single self-potential electrical traverse across the Ahuan vent , made by Connor in 1983, identified a 1.2 volt anomaly. This is a very large electrical anomaly and, although quite preliminary, indicates the presence of a localized zone of groundwater vaporization in the high temperature zone beneath the vent. This test also provides a strong indication that electrical methods will be successful at delineating thermal zones in the subsurface at Paricutin.

A second zone of higher temperature fumaroles is located at the Taqui vent, on the NE flank of the main cone. Fumarole temperatures of up to 280 °C were identified at the Taqui vent in 1993.

3 Experiments and Anticipated Results

Three types of data will be collected during field work at Paricutin.

- Near-surface soil properties including: temperature, moisture content, hydraulic conductivity
- Electromagnetic experiments, principally transient electromagnetic soundings
- Electrical resistance tomography

Together, these data types can provide a comprehensive, 3D picture of temperature and moisture distributions within the cinder cone and at the Ahuan vent. The data gathered in these experiments will be modeled using thermohydrologic codes such as Multiflo. Together with the well-known boundary conditions on the temperature of these deposits at the time of their eruption, the time elapsed since the eruption and the geometry of the system, these data will provide an excellent test of the thermohydrologic model assumptions, as well as provide an increased understanding of the resolution of the geophysical methods. Thus, using Parícutin as a

natural analog enables us to efficiently test these methods under conditions similar to those expected at the repository.

It is expected that these field tests will require several weeks of field work at Parícutin to complete. Therefore, we plan a total of three field trips to Parícutin. The first, to be conducted this spring will be a reconnaissance trip of several days duration to finalize the survey design and make simple, preliminary measurements. The second trip will be two weeks in duration and the team will conduct experiments on the cinder cone and only preliminary measurements at the Ahuan vent. Numerical modeling will be performed following these experiments and a second major field campaign will be conducted. This field work will concentrate on the Ahuan vent and possibly additional work will be done on the cone, if the numerical modeling indicates further field work will be useful.

Results of this project will be directly incorporated into the Thermal Effects and Igneous Activity IRSRs and we anticipate presenting the results at scientific meetings and in journal articles.

CC

Scientific Notebook
Project 20-1402-461

Jan, 1999
Chuck Connor

The following abstract was presented at the Fall AGU

Guidelines for Probabilistic Hazard and Risk Assessments for Nuclear Facilities

CB Connor and B.E. Hill (Center for Nuclear Waste Regulatory Analyses, Southwest Research Institute, 6220 Culebra Rd, San Antonio, TX, 78238; 210-522-6649; e-mail: cconnor@swri.org)

Nuclear facilities are constructed at very high cost and require extremely high standards of safety. Ideally, such facilities should only be located in areas of very low geologic risk. Nevertheless, nuclear facilities are built or planned within volcanically active regions around the world. These facilities include: the proposed high-level radioactive waste repository at Yucca Mountain, Nevada; INEL facilities, Idaho; the existing Metzamor nuclear power plant, Armenia; the proposed Muria power plant, Indonesia; and numerous others. The safety requirements of these facilities are such that it is imperative to develop consistent methodologies for hazard and risk assessment of low probability, but potentially high consequence volcanic events. Suggested guidelines for such assessments include: (i) evidence of Holocene activity within nearby magmatic systems requires a deterministic assessment of hazards; (ii) evidence of Quaternary activity nearby magmatic systems requires a probabilistic assessment that depends on conservative estimates of both the recurrence rate and nature of volcanic activity; (iii) the capability of volcanoes affecting site safety can be determined from the geologic history of the magmatic system, numerical simulations, and data from analogous volcanoes; (iv) some volcanic hazards (e.g., tephra fall) can be mitigated by design, but others (e.g., pyroclastic flows) often

cannot be mitigated and should be used as criteria for site rejection; (v) hazard analyses should be based on a freely disseminated and geologically accurate database; and (vi) for existing facilities, monitoring programs and response plans should be developed. Hazard assessments are best quantified using complimentary cumulative probability distributions. Risk estimates should consider integrated expected radiation dose to an individual or group, in addition to more traditional measures of risk, because deleterious effects of contaminated volcanic deposits persist long after the cessation of volcanic activity.

12 of 17

SCIENTIFIC NOTEBOOK 115E

BY

Charles B. Connor

SCIENTIFIC NOTEBOOK
115E

BY

Charles B. Connor

Southwest Research Institute
Center for Nuclear Waste Regulatory Analyses
San Antonio, Texas

Project 20-1402-461

SCIENTIFIC NOTEBOOK
IA 20-14-2-461
115E

Chuck Connor
May 20, 1999

The following input was provided as part of C. Connor activities on the Natioanl Research

Council panel to assess the USGS volcanic hazards program. Two figures are attached

Information potentially subject to copyright protection was redacted from pages 1 through 43 (numbered bottom left). The redacted material is from the information listed above. No additional information is know.

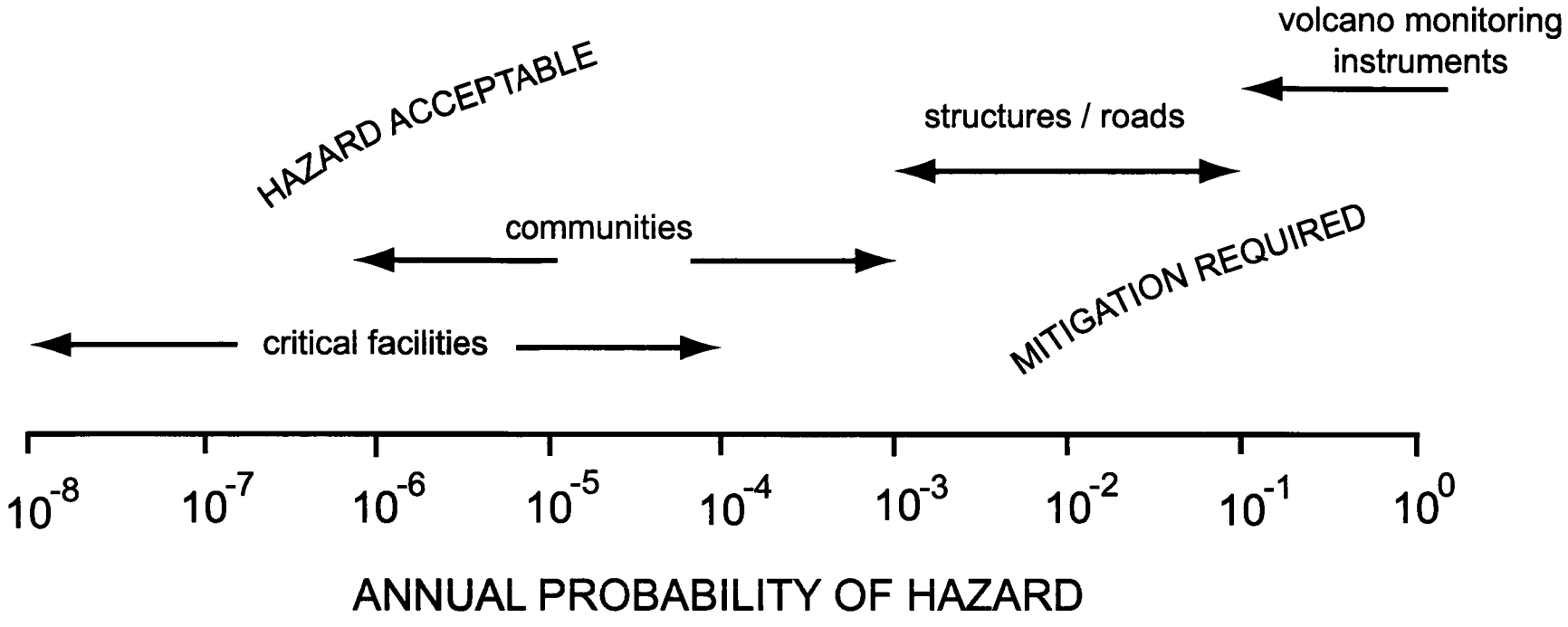
volcano monitoring instruments
HAZARD ACCEPTABLE
structures / roads
communities
MITIGATION REQUIRED
critical facilities
10^{-8} 10^{-7} 10^{-6} 10^{-5} 10^{-4} 10^{-3} 10^{-2} 10^{-1} 10^{0}
ANNUAL PROBABILITY OF HAZARD

Do you assume magma chamber @ this depth for math. convenience? No evidence that magma chambers @ this shallow depth in Yucca Mountain magmatic system. ac 8/18/9

Numerical study of magma-repository interactions: working document

Onno Bokhove
School of Mathematics, Bristol

ac 8/18/9

1 Introduction

drifts

We consider the problem of volcanic melt and volatile flow along a dike from a magma chamber into a series of repository tunnels filled with air (Woods and Sparks 1998). The mixture of melt and volatiles moves upward under an overpressure, of order $10^6 - 10^7\ Pa$ relative to the lithostatic pressure in a magma chamber at depth H, of order $5 - 10\,km$ below the surface. The questions to be broached include: how fast and how violent does the melt-volatile mixture enter and fill the repository tunnels, how do rarefaction waves travel back into the magma after such tunnels open up, and how do shock waves reflect against the end wall of the tunnel? We examine the interaction between the melt-volatile flow and air-filled tunnels in an idealized fixed geometry, in which a dike of fixed width w, of order $1 - 2m$, and finite extent is considered following the sketch in Fig. 1(a). The dike is filled with a melt-volatile mixture and intersects a tunnel at a certain time. Thereafter the magma-repository interaction begins.

This working document is organized as follows. A model of gas dynamics for volatile-rich magma and air is stated in section 2. There, scalings for the model equations are introduced and assessed to develop a dimensionless model of the process. The model is simplified as being one-dimensional flow along the dike and tunnel, see the sketch in Fig. 1(b). Corner effects at the entrance of the tunnel are thus simplified by considering geometries with smooth dike-tunnel transitions. Numerical schemes for solving the one-dimensional equations are reviewed in section 3 and several numerical tests are presented. In section 4 magma-repository interactions are described. The discussion in section 5 outlines and comments on future work.

2 Volatile rich-melt model

2.1 Two fluid model: melt-volatiles and air

We consider a model for two compressible fluids in which a two-phase fluid of melt, containing 1-3% volatiles in solution at high pressure, encounters a tunnel filled with air (following Woods and Sparks 1998). The two-phase mixture of melt and volatiles (e.g. water) in solution is modelled in a simplified way as a single fluid with an isothermal equation of state for the density ρ as function of pressure p. (In the analogue laboratory experiment the melt-volatile mixture is replaced by a gum-rosin-acetone (GRA) two-phase fluid.)

The compressible equations of motion for the melt-volatile mixture are

$$\begin{aligned} \frac{\partial \mathbf{u}}{\partial t} + (\mathbf{u}\cdot\nabla_3)\,\mathbf{u} + \frac{1}{\rho}\nabla_3 p &= -g\hat{\mathbf{z}} + \mu\mathbf{F}, \\ \frac{\partial \rho}{\partial t} + \nabla_3\cdot(\rho\mathbf{v}) &= 0, \end{aligned} \tag{1}$$

or is this $\mu\nabla^2 u$?

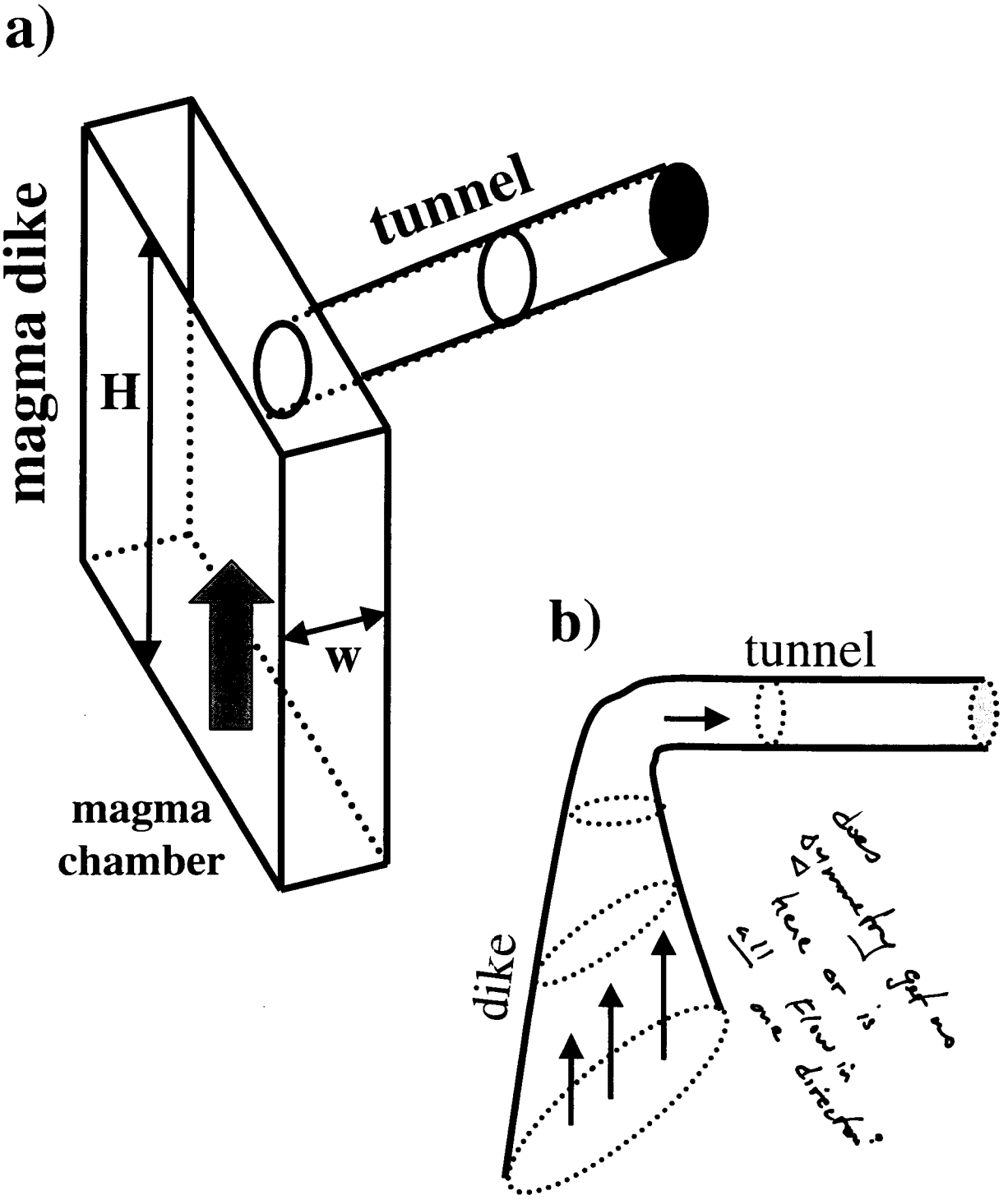

Figure 1: (a) Sketch of the idealized and experimental configuration of a volcanic dike and a repository tunnel. When the membrane, depicted at the beginning of the tunnel as a grey area, is removed, the dike-repository fluid interaction starts. (b) Sketch of a simplified configuration in a tube model of the flow in dike and tunnel. The flow in this model depends only on a smooth coordinate following dike and tunnel with a smooth connection between the two; the varying area of cross sections is also taken into account.

with three-dimensional velocity $\mathbf{u}$ and gradient $\boldsymbol{\nabla}_3$, gravity g, vertical unit vector $\hat{\mathbf{z}}$, and dimensionless forcing $\mathbf{F}$ with friction parameter μ. The isothermal equation of state of the melt-volatile fluid is

$$\rho(p) = \left(\frac{n(p)\, R_v\, T}{p} + \frac{1 - n(p)}{\sigma} \right)^{-1} \tag{2}$$

with $n(p)$ the mass fraction of exsolved volatiles, $R_v \approx 462\, J\,(kg\,K)^{-1}$ the mixture's gas constant, fixed temperature $T = 1000 - 1200\, K$, and melt density $\sigma \approx 2500\, kg\, m^{-3}$. The exsolved gas content $n(p)$ obeys Henry's law

$$n(p) = n_0 - s\, p^{\beta} \tag{3}$$

where $n_s = s\, p^{\beta}$ is the mass fraction of volatiles in solution. The total volatile content $n_0 = 1 - 3\%$ and $s \approx 3 * 10^{-6}\, Pa^{-1/2}$ is the saturation constant. The exponent $\beta \approx 0.5$ for a basaltic fluid. The single fluid with equation of state (2) and Henry's law (3) is a first approximation to the complicated physics of the two-phase melt-volatile mixture. In case of supersaturation the mass fraction $n(p)$ may be argued to become time dependent (Woods 1995). For typical volcanic parameters, the values $\rho(p)$ and sound speed $a(p) = \sqrt{\partial p / \partial \rho}$ have been drawn in Fig. 2. As $p \to p_c$ the sound speed $a(p) \to \infty$. All volatiles are in solution for a slightly lower pressure $p_i = (n_0/s)^{1/\beta}$ and the mixture is then incompressible. Typical parameter values for the GRA fluid are found in Fig. 2 and are deduced in part from "Figure 3", where pressure is plotted versus the mass fraction n_s of acetone in solution, in Phillips et al. (1995).

The compressible equations of motion for air are

$$\begin{aligned} \frac{\partial \mathbf{u}_a}{\partial t} + (\mathbf{u}_a \cdot \boldsymbol{\nabla}_3)\mathbf{u}_a + \frac{1}{\rho_a} \boldsymbol{\nabla}_3 p_a &= -g\, \hat{\mathbf{z}}, \\ \frac{\partial \rho_a}{\partial t} + \boldsymbol{\nabla}_3 \cdot (\rho_a\, \mathbf{u}_a) &= 0, \\ c_p \left(\frac{\partial T_a}{\partial t} + (\mathbf{u}_a \cdot \boldsymbol{\nabla}_3)\, T_a \right) &= \frac{\beta_a\, T_a}{\rho_a} \left(\frac{\partial p_a}{\partial t} + (\mathbf{u}_a \cdot \boldsymbol{\nabla}_3)\, p_a \right) \end{aligned} \tag{4}$$

with three-dimensional air velocity, pressure and density differentiated from the basaltic fluid with subscript $(\cdot)_a$, thermal expansion coefficient β_a, gas constant $R = 287.04\, J\,(kg\,K)^{-1}$ and ideal gas law

$$p_a = \rho_a\, R\, T_a. \tag{5}$$

The two fluids described by (1) and (4) meet at an interface $G(\mathbf{x}, t) = 0$ with $\mathbf{x} = (x, y, z)^T$ which is assumed to move with the flow:

$$\frac{\partial G}{\partial t} + (\mathbf{u} \cdot \boldsymbol{\nabla}_3)\, G = 0. \tag{6}$$

In reality, the behaviour of the two fluids may be more complicated when mixing occurs. One effect is that the two-phase fluid decomposes as the melt fragments separate from the volatiles at the interface.

In the three-dimensional or simplified two-dimensional geometry, no-normal flow boundary conditions are imposed at dike and tunnel walls but we will simplify the dynamics to one-dimensional flow along the dike and tunnel in section 2.3. Hydrostatic overpressure and absorbing-generating boundary conditions are used in the magma chamber at the bottom of the dike. Initial conditions will be simplified to a shock-tube problem in which a membrane or diaphragm between dike and tunnel is removed instantly. The initial conditions in the dike will be hydrostatic plus an overpressure associated with dike tip migration and atmospheric pressure in the tunnel, and the flow starts at rest.

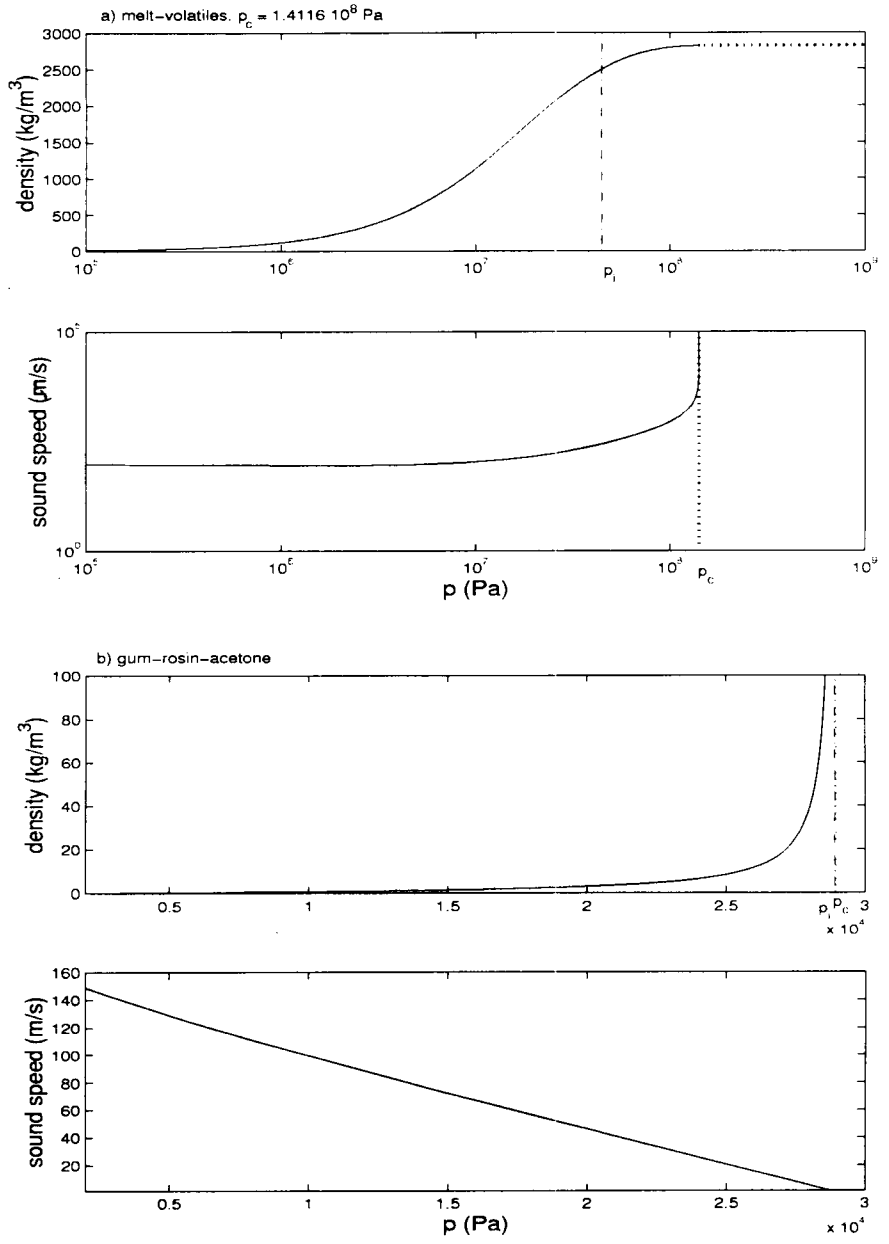

Figure 2: Idealized equation of state for: (a) volcanic melt-volatile with $T = 1000\,K, \sigma = 2500\,kg\,m^{-3}, n_0 = 2\%, s = 3 * 10^{-6}\,Pa^{-1/2}, R_v = 462\,J\,(kg\,K)^{-1}, \beta = 0.5$. (b) GRA with $T = 293\,K, \sigma = 1080\,kg\,m^{-3}, n_0 = 20\%, s = 6.749 * 10^{-5}\,Pa^{-1/2}, R_v = 482\,J\,(kg\,K)^{-1}, \beta = 0.7782$. (i) Density and (ii) sound speed are drawn versus pressure. A critical pressure p_c of GRA is defined when $\rho \to \infty$.

2.2 Non-dimensionalization

Numerical integration is simpler when using numerical values close to unity. So, by considering the melt-volatile equations of motion and state, the following scalings for various parameters are suggested:

$$\begin{aligned} p &= P_0\, p', \quad \rho = \rho_0\, \rho', \quad t = (L/U)\, t', \quad \mathbf{x} = L\, \mathbf{x}', \\ \mathbf{u} &= U\, \mathbf{u}, \quad n(p) = n_0\, n'(p'), \quad \sigma = \rho_0\, \sigma' \end{aligned}$$

with $P_0 = n_0\, R_v\, T\, \rho_0$ and $U^2 = P_0/\rho_0$. Upon dropping the primes, the dimensionless (scaled) melt-volatile equations read

$$\begin{aligned} \frac{\partial \mathbf{u}}{\partial t} + \mathbf{u} \cdot \boldsymbol{\nabla}_3 \mathbf{u} + \frac{1}{\rho}\, \boldsymbol{\nabla}_3 p &= -\frac{1}{F_l}\, \hat{\mathbf{z}} - \nu\, \mathbf{F}, \\ \frac{\partial \rho}{\partial t} + \boldsymbol{\nabla}_3 \cdot (\rho\, \mathbf{v}) &= 0, \end{aligned} \tag{7}$$

with equation of state

$$\rho(p) = \left(\frac{n(p)}{p} + \frac{1 - n_0\, n(p)}{\sigma} \right)^{-1} \tag{8}$$

and Henry's law

$$n(p) = 1 - \epsilon\, p^{\beta}. \tag{9}$$

The Froude number $F_l = P_0/(\rho_0\, g\, L)$, friction number $\nu = \mu\, L/\sqrt{P_0/\rho_0}$, and $\epsilon = s\, {P_0}^{\beta}/n_0$. A cursory examination of Fig. 2(a) around pressures of $10^6\ Pa$ suggests that values of $\rho_0 \approx 100\, kg\, m^{-3}$ are reasonable for the volcanic fluid while values of $\rho_0 \approx 1\, kg\, m^{-3}$ are valid for the GRA fluid. Length scale L is chosen to be somewhere between the radius and length of the tunnel.

2.3 One- and two-dimensional gas dynamics

Consider a system of curvilinear coordinates ξ_i $(i = 1, 2, 3)$ with scale factors h_i (Batchelor 1967). An infinitesimal cube in such a coordinate system then has sides $h_i\, d\xi_i$ and volume $d\tau$ given by $(d\tau)^2 = \sum_{i=1}^{3} (h_i\, d\xi_i)^2$.

In the dike-repository system a representative $\xi_1(x, y, z)$-coordinate may be identified with corresponding cross-section $A(\xi_1)$, normal to ξ_1-isolines, as is illustrated in Fig. 3a. A one-dimensional system, obtained by averaging over cross-sections and by neglecting cross-sectional flows, is readily derived from (1) by considering mass and momentum density $\rho\, u_1$ conservation in a control volume $(h_1\, A(\xi_1)\, d\xi_1)$. One finds (e.g. Whitham 1974):

$$\begin{aligned} \frac{\partial(\rho\, A\, u_1)}{\partial t} + \frac{1}{h_1} \frac{\partial}{\partial \xi_1} \left(\rho\, A\, u_1^2 + p\, A \right) &= -\nu\, \rho\, F_1 + p\, \frac{1}{h_1} \frac{\partial A}{\partial \xi_1} - \frac{1}{F_l}\, \rho\, A\, \frac{1}{h_1} \frac{\partial z(\xi_1)}{\partial \xi_1}, \\ \frac{\partial(\rho\, A)}{\partial t} + \frac{1}{h_1} \frac{\partial}{\partial \xi_1} \left(\rho\, A\, u_1 \right) &= 0, \end{aligned} \tag{10}$$

where u_1 is the ξ_1-component of the velocity, etc. Corner effects at the tunnel's entrance are simplified by considering geometries with smooth dike-tunnel transitions (cf. Fig. 1(b)) . In essence we follow the flow along the (dashed-dotted) centerline $\xi_1 = 0$ in Fig. 3(a).

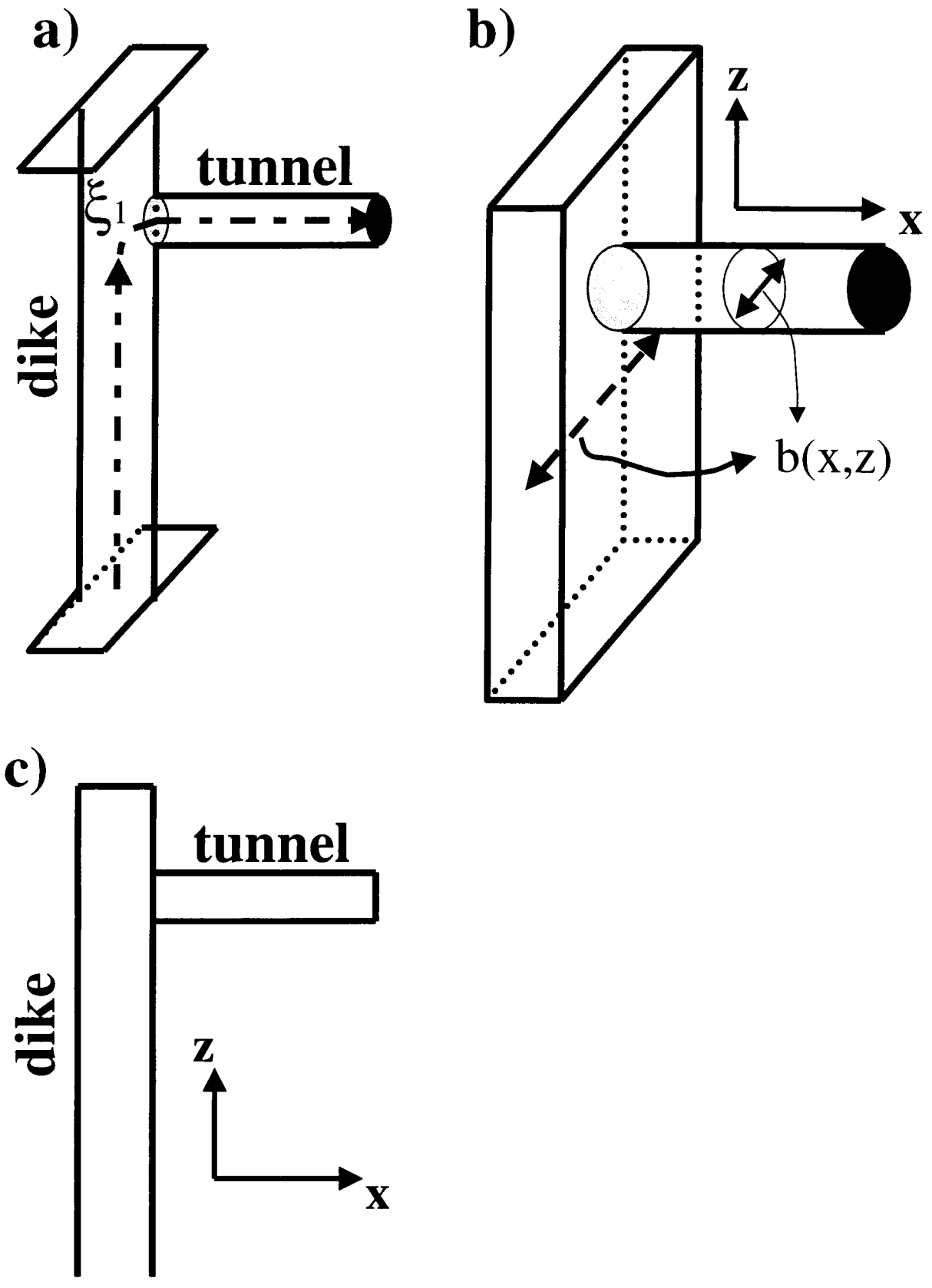

Figure 3: Schematics of dike and tunnel for: (a) one-dimensional flow and (b,c) two-dimensional flow. In (a) the effective one-dimensional coordinate is indicated by the dashed-dotted coordinate-line $\xi_1 = 0$, while the effective two-dimensional domain in a vertical plane is given in (c).

? where is Eq 11 ?

3 Numerical schemes

Essentially non-oscillatory finite-difference numerical schemes developed by Shu and Osher (1989) and, in convex form, by Liu and Osher (1998) have been used to discretise (10) and (11) on a uniform grid. These schemes are explicit and can be higher order in spatial and temporal discretization. We use second and third order schemes in space and time.

Consider a hyperbolic system with additional forcing, dissipative and/or geometric terms $\mathbf{F}$

$$\begin{aligned} \mathbf{q}_t + \sum_{k=1}^{d} \mathbf{f}_k(\mathbf{q})_{x_k} = \mathbf{q}_t + \mathcal{L}(\mathbf{q}) &= \mathbf{F} \\ \text{with initial condition } \mathbf{q}(\mathbf{x},0) &= \mathbf{q}_0(\mathbf{x}), \end{aligned} \tag{12}$$

where $\mathbf{q} = (q_1, \ldots, q_n)^T, \mathbf{x} = (x_1, \ldots, x_d)$. On the computational grid $\mathbf{x}_j = j\,\Delta\mathbf{x}$ and $t_n = n\,\Delta t$, and $\mathbf{q}_j^n$ is the computed approximation of the exact solution $\mathbf{q}(\mathbf{x}_j, t_n)$. We continue our description of the algorithms for simplicity in one spatial dimension, where we have $\mathbf{q}_t + \mathbf{f}(q)_x = \mathbf{F}$. Non-uniform grids may be transformed to uniform ones under a smooth transformation $\xi = \xi(x)$. This is of interest when we wish to model the flow far in the dike on a coarse grid and the flow around the entrance of the tunnel and the flow in the tunnel on a fine grid in order to enhance the resolution of shock waves in and around the tunnel. The numerical methods are still appropriate in this curvilinear framework (Shu 1997), and we find $\mathbf{q}_t + \xi_x\, f(\mathbf{q})_\xi = \mathbf{F}$.

The (convex) essentially non-oscillatory (CENO/ENO) schemes considered are conservative and their discretisation has the form

$$\frac{dq}{dt} = q_j^n - \lambda\,(\hat{f}_{j+1/2} - \hat{f}_{j-1/2}), \tag{13}$$

with $\lambda = \Delta t/\Delta x$, for an appropriate higher-order flux $\hat{\mathbf{f}}$ such that $L(q) = \mathcal{L}(q) + O((\Delta x)^m)$ (if no confusion arises vector notation is dropped). Either a second-order total variation diminishing (TVD) Runge-Kutta time discretisation,

$$\begin{aligned} q^{(1)} &= q^n + \Delta t\,[L(q^n) + F^n] \\ q^{n+1} &= \frac{1}{2}\left(q^n + q^{(1)} + \Delta t\,[L(q^{(1)}) + F^{(1)}]\right) \end{aligned} \tag{14}$$

or a third order one is used,

$$\begin{aligned} q^{(1)} &= q^n + \Delta t\,[L(q^n) + F^n] \\ q^{(2)} &= \frac{1}{4}\left(3\,q^n + q^{(1)} + \Delta t\,[L(q^{(1)} + F^{(1)}]\right) \\ q^{n+1} &= \frac{1}{3}\left(q^n + 2\,q^{(2)} + 2\,\Delta t\,[L(q^{(2)}) + F^{(2)}]\right), \end{aligned} \tag{15}$$

following Shu and Osher (1989).

The discretisation in two dimensions on a regular grid is a line-by-line extension of the one-dimensional (C)ENO algorithm.

3.1 ENO

The ENO algorithm for finite differences was developed by Shu and Osher (1989) (see also the review of Shu 1997). The ENO calculation of higher-order flux $\hat{f}_{j+1/2}$ in one dimension is based on the use of adaptive

"stencils", that is the use variables on r grid points left and s grid points to the right of grid point j. A higher-order interpolating formula is constructed at each time step by using information from surrounding grid points such that discontinuities are avoided except that at least one upwind gridpoint is present in each stencil.

Systems of hyperbolic equations are decomposed into characteristic form, using left $\mathbf{R}^{-1}$ and right $\mathbf{R}$ eigenvector matrices, of the form:

$$\mathbf{q}_t + \mathbf{A}\,\mathbf{q}_x = 0, \tag{16}$$

where $\mathbf{A}$ is the eigenvalue matrix. This matrix is locally taken to be constant before the ENO interpolation calculates the fluxes at the cell edges. The flux $\hat{f}_{j+1/2}$ of the system in flux conservative form is found by projecting back from eigenvector space using the right eigenvector matrix. Roe-averaged quantities (Shu and Osher 1989) are used to calculate variables at the cell edge $j+1/2$ from the variables at finite-difference points j and $j+1$:

$$\begin{aligned} u_{j+1/2} &= \frac{u_j\sqrt{\rho_j} + u_{j+1}\sqrt{\rho_{j+1}}}{\sqrt{\rho_j} + \sqrt{\rho_{j+1}}} \\ \rho_{j+1/2} &= \frac{1}{2}(\rho_j + \rho_{j+1}). \end{aligned} \tag{17}$$

Projection of the fluxes and variables onto the space of eigenvectors and back is computationally expensive. The convex ENO (CENO) scheme avoids this characteristic decomposition but introduces more numerical dissipation (particularly in regions with high gradients).

3.2 CENO

So far, a standard second-order local lax-Friedrichs flux (LLF2) given by

$$\begin{aligned} \hat{f}^{LLF2}_{j+1/2} &= \frac{1}{2}\Big(f(q_{j+1}) + f(q_j) - \alpha_{j+1/2}\,(q_{j+1} - q_j)\Big) + \\ &\quad \frac{1}{4}\,m\Big[\Delta_+ f(q_j) + \alpha_{j+1/2}\Delta_+ q_j, \Delta_- f(q_j) + \alpha_{j+1/2}\Delta_- q_j\Big] - \\ &\quad \frac{1}{4}\,m\Big[\Delta_+ f(q_{j+1}) - \alpha_{j+1/2}\Delta_+ q_{j+1}, \Delta_- f(q_{j+1}) - \alpha_{j+1/2}\Delta_- q_{j+1}\Big] \end{aligned} \tag{18}$$

is used in CENO with

$$\Delta_\pm p = \pm\,(p_{j\pm1} - p_j) \tag{19}$$

and the canonical minmod wave limiter $m[\cdot,\cdot]$ is defined as

$$m(x,y) = \begin{cases} (\operatorname{sign} x)\min(|x|,|y|) & \text{if } x\,y > 0, \\ 0 & \text{otherwise.} \end{cases} \tag{20}$$

For a scalar equation, dissipation $a_{j+1/2}$ is the maximum of $|f'(q)|$ in cell j and $j+1$. For a system the largest eigenvalue (as an upper bound of the largest local eigenvalue) fixes $a_{j+1/2}$ for all components at the cell edge $j+1/2$ between adjacent cells j and $j+1$.

Higher-order extensions of convex ENO are found in Liu and Osher (1998).

3.3 Gravity

The forcing terms $\mathbf{F}$ may generate artificial dynamics when the hyperbolic part of the system and the forcing terms are not discretized in a similar manner. The gravity term ρ/F_l (or dimensionally $\rho\, g$) in the vertical momentum density equation (or $(\chi/F_l)\,\partial z/\partial\xi_1$ in (10)) can in general not be captured in flux form.When a flow starts in hydrostatic balance and at rest, some caution is required to avoid artificial flows. Neither ENO nor CENO automatically remedy this caveat in general, even though the discretisation is second or higher order. Several fixes may be implemented to stabilize initial conditions of rest before a perturbation is encountered.

3.4 Interfacial dynamics

One dimension

In one dimension the interface between melt-volatiles on one and air on the other side is given by a Lagrangian particle at $x = x_i(t)$. The particle dynamics is given by

$$\begin{aligned} \frac{dx_i}{dt} &= u_i, \\ \frac{du_i}{dt} &= -\frac{1}{\rho}\frac{\partial p}{\partial x}\bigg|_{x=x_i(t)} = -\frac{1}{\rho_a}\frac{\partial p_a}{\partial x}\bigg|_{x=x_i(t)}. \end{aligned} \tag{21}$$

Both velocity $u_i(t) = u(x = x_i(t), t)$ and pressure are continuous across the interface, while density is generally not.

The discretisation around the interface is chosen to be mixed Eulerian and Lagrangian. Two finite-volume (i.e. finite-rod) cells are introduced around $x_i(t)$. They are updated or moved, when $x_i(t)$ passes a grid point at a next time step, such that conservation of mass and (locally) momentum is maintained, although formal higher-order accuracy may be lost during updates. The length of these rods is chosen to lie between $(1/2)\,\Delta x$ and $(3/2)\,\Delta x$ with Δx the spacing between grid points. Variables at grid points next to the interface are determined by interpolation using the information of the variables in finite-volume cells and at adjacent grid points.

3.5 Numerical tests

To develop and test the numerical codes, the basaltic fluid flows (1) and air (4) flows are first considered in separation before the interface dynamics is added. In all these three cases, the two separate codes and the combined code, specific simulations in one-dimension are compared with exactly solvable (stationary) shock and shock tube solutions.

3.5.1 1D melt-volatile

Stationary shock

The stationary shock solution of (10) (with scale factor $h_1 = 1, \xi_1 = x, g = \nu = 0$) follows directly from momentum density and mass conservation across the discontinuity. If the pressures left and right of a stationary shock are given by p_l and p_r, then the velocities are $u_l = \rho_r\, u_r/\rho_l$ and

$$u_r = \sqrt{\frac{\rho_l}{\rho_r}\frac{(p_l - p_r)}{(\rho_l - \rho_r)}},$$

respectively. We start with values $\rho_l = \rho(p = 5 * 10^6\, Pa)\, kg\, m^{-3}$ and $\rho_l = \rho(p = 10^5\, Pa)\, kg\, m^{-3}$ and a discontinuity at $x = 1.25\, m$.

The stack plots in Fig. 4 and hereafter should be interpreted as follows. The initial profile of density or velocity is plotted versus space. Subsequent profiles of density and velocity, arising after subsequent time-intervals, are plotted in the same graph but the value on the vertical axis is shifted upward each time by a specified amount; in other words it is "stacked". Stack plots thus become density or velocity plots versus space and time. Sometimes the vertical axis is denoted as time axis but I prefer to display the amplitude of the variable.

The CENO simulation is seen, in the stack plots of Fig. 4(a), to shed an acoustic wave to adjust to a stationary numerical shock solution, while ENO appears to be perfect (see Fig. 4(b)) in that the steepness of the wave is determined by one grid spacing only and that no adjustment occurs. For shocks moving into still fluid ahead of the shock both ENO and CENO schemes show an acoustic wave adjustment.

Shock tube

The shock tube solution of (10) (with scale factor $h_1 = 1, \xi_1 = x, g = \nu = 0$ and) with pressure $5 * 10^6\, Pa$ on the left and $10^5\, Pa$ on the right is obtained by matching a shock to a backward propagating rarefaction wave (similar calculations are found in Whitham 1974). Boundary conditions in this configuration are chosen to be open. The simplest implementation of such opne boundary conditions, which suffices in this case, is to define variables on extra "ghost" grid points outside the domain based on the value of variables at the last interior grid point. Looking at the density evolution in Fig. 5, we see that a rarefaction wave is travelling to the left, moving away from the discontinuous initial condition. This smooth rarefaction wave connects to a forward (i.e. to the right) propagating shock wave, which is apparent in the numerical solution as a steep density change of about $50\, kg\, m^{-3}$. The steepness of the shock wave is limited by the grid size and the numerical scheme. In particular, the CENO simulation is seen to be more dissipative than the ENO simulation, in Fig. 5, but both simulations are otherwise similar. A comparison of numerical and exact solution still needs to be done.

4 Magma-repository interactions

4.1 Curved dike-tunnel channel in one dimension

Melt-volatiles

We consider the one-dimensional dike-tunnel flow-tube model with a geometry as sketched in Fig. 1(b). To be precise, a top stretch of $100\, m$ of vertical dike (for $\xi_1 < 100\, m$) with a constant cross-sectional area of $A = 22\, m^2$ is connected to a $100\, m$ tunnel with a constant cross-sectional area of $A = 25\, m^2$ (for $[100 + (\pi/2)\, R]\, m < \xi_1 < [200 + (\pi/2)\, R]\, m$). The connection between dike and tunnel is a 90^o arc of radius $R = 5\, m$ and the cross-sectional area of this arc between dike and tunnel varies linearly as function of the coordinate line ξ_1 in the center of the flow tube (see Fig. 3(a)) from dike to tunnel values. The equations of motion are given by (10). Gravity is thus a function of ξ_1 and influences the flow in dike and arc but not in the repository tunnel. The initial pressure at $\xi_1 = 0$ is $\sigma\, g\, h = 2500 * 10 * 400\, Pa$ plus overpressure $10^7\, Pa$ and in the dike and arc above up to the membrane the initial pressure is hydrostatic.

In Fig. 6 and Fig. 7 numerical CENO simulations of this one-dimensional melt-volatile shock-tube problem are shown in the form of stack plots of density and velocity of the basaltic fluid. The membrane at $\xi_1 =$

$[100 + (\pi/2)\, R]\, m$ is broken at time zero. Thereafter a rarefaction wave travels downward (to the left in the figures) into the dike and a small shock wave travels to the tunnel end where it reflects into a larger shock wave which eventually leaves the domain downward (to the left in the figures).

The large density and pressure changes between the initial and reflected shock may be a cause of concern. The initial shock wave is small with pressure jump of about $7 * 10^5\, Pa$ while the reflected shock wave has a pressure jump of about $75 * 10^5\, Pa$, that is about ten times larger than the initial shock wave. The force on a canister caused by a passing shock wave is plotted versus time in Fig. 8. The force is this change in pressure Δp times the cross-sectional area of a canister, $\Delta p \times \pi R_c^2$ with R_c the radius of a canister. The dashed-dotted line is the force due to the forward propagating shock and the solid line is the force due to the reflected shock. The initial high negative force for $t < 0.5\, s$ is an artefact of the way we have evaluated the pressure jump across a shock wave and should be ignored.

5 Discussion

Scoping numerical calculations of volcanic basaltic melt-volatile flow in a volcanic dike-tunnel system have been performed. The strategy has been to model a simplified flow in one dimension along the curvilinear flow-tube channel in Fig. 1(b) by averaging the flow across dike and tunnel cross-sections and by neglecting any Reynolds-stress terms.

Two shock-capturing numerical schemes have been used to calculate the one-dimensional compressible gas dynamics derived in (10) with equation of state (2) and Henry's law (3). Both an essentially non-oscillatory (ENO) numerical scheme and a convex essentially non-oscillatory (CENO) scheme have been used to compute one-dimensional basaltic flow. These two codes have been developed in order to check one against the other. They were tested by comparing the numerical (C)ENO solutions with exact stationary shock and shock tube solutions, although the latter exact implicit solution still needs evaluation. These comparisons were good even although discontinuities associated with the shock are smeared due to finite resolution and numerical dissipation.

Simulation of basaltic flow that suddenly enters the repository tunnel from a volcanic dike —a shock tube problem— shows a weak-amplitude shock wave propagating to the end of the tunnel. There it reflects to become a large-amplitude shock wave propagating back into the tunnel and then into the dike down towards the magma chamber.

The real flow transition from dike to tunnel is probably slower than in the presented one-dimensional simulation because the real flow around the tunnel entrance will be three-dimensional and vertical as well as horizontal pressure gradients will develop around the tunnel entrance. Two-dimensional simulations in a vertical plane could model at least part of these pressure gradients. Alternatively, in the one-dimensional model we may vary the cross-sectional area A and/or the length of the link or connection between dike and tunnel in order to incorporate some of the expected delays in the flow around the tunnel entrance.

Research in the immediate future will consist of one-dimensional simulations of the melt-volatile-air and gum-rosin-acetone systems including the interface dynamics, and a comparison with the analogue gum-rosin-acetone experiments. Simulations of the basaltic-air system will be performed for various values of the volatile content n_0, the overpressure in the magma chamber, friction, and the length of the link between dike and tunnel in order to assess the strength of the shock wave that reflects off the end of the tunnel.

Further numerical validation of the codes will be performed by comparing numerical simulations for compressible air flow in separation and together with the basaltic flow with exact shock and shock-tube solutions in linear geometry with constant cross-sectional area. An exact shock-tube solution for combined

basaltic and air flow, which exists, should give an idea of the strength of the forward propagating shock as function of the initial pressure difference at the membrane at the time the basaltic flow enters the tunnel. Since the density variation on each side of the propagating interface and shock is rather weak, we may be able to calculate approximate values of the strength of the shock that reflects at the tunnel wall. The question is whether this strong reflected shock is able to push canisters into the dike. Finally, the developed numerical codes will be carefully documented so that they can be used as forecasting tool of magma-repository fluid interactions.

The simulations shown in this report could benefit from local adapative mesh refinement and grid adaptation around shocks and interfaces. The development of these numerical refinements falls outside the scope of the present project and in one dimension a brute-force increase of the resolution suffices.

Eventually, it may be necessary to include supersaturation effects and even more of the physics of the two-phase fluid. Thereafter it may be of interest to develop two-dimensional simulations in order to assess how the fluid behaves around the tunnel entrance. This can be done at first for the melt-volatile fluid only, following (11), and later also for the basaltic fluid and air in which case we will have to model the interface dynamics.

Acknowledgements The numerical work benefitted significantly from research of the (first) author performed under a EC MAST-III Surf and Swash Zone Mechanics grant received by Professor D.H. Peregrine, who also kindly suggested involvement in the present project. Dr. A. Rogerson's assistance in the initial development of the ENO numerical (shallow-water) dynamics codes is gratefully acknowledged.

References

Batchelor, G.K., 1988: *Fluid Dynamics.* Cambridge University Press, 615 pp.

Lamb, H., 1932: *Hydrodynamics.* Dover, Toronto, 508 pp.

Liu, X.-L. & Osher, S., 1998: Convex ENO high order multi-dimensional schemes without field by field decomposition on staggered grids. *J. Comp. Phys.* **142**, 304–330.

Phillips, J.C., Lane, S.J., Lejeune, A.M., and Hilton, M., 1995: Gum rosin-acetone system as an analogue to the degassing behaviour of hydrated magmas. *Bull. Volc.* **57**, 263–268.

Shu, C-W., 1997: Essentially non-oscillatory and weighted non-oscillatory schemes for hyperbolic conservation laws. NASA Langley research Center. 77 pp.

Shu, C-W. & Osher, S., 1988: Efficient implementation of essentially non-oscillatory shock-capturing schemes. *J. Comp. Phys.* **7**, 439–471.

Shu, C-W. & Osher, S., 1989: Efficient implementation of essentially non-oscillatory shock-capturing schemes II. *J. Comp. Phys.* **83**, 32–78.

Whitham, G.B., 1974: *Linear and nonlinear waves.* John Wiley, Toronto, 636 pp.

Wilson, L., Sparks, R.S.J., Huang, C.T., and Watkins, N.D., 1980: Explosive volcanic eruptions, IV, The control of magma properties and conduit geometry on eruption column behaviour. *Geophys. J. R. Aston. Soc.* **63**, 117–148.

Woods, A.W., 1995: The dynamics of explosive volcanic eruptions. *Reviews of Geophysics* **33**, 495–530.

Woods, A.W. and Sparks, S., 1998: *Report on scoping calculations for magma-repository interaction at Yucca mountain.* Centre for Environmental and Geophysical Flows, University of Bristol, Bristol, 24 pp.

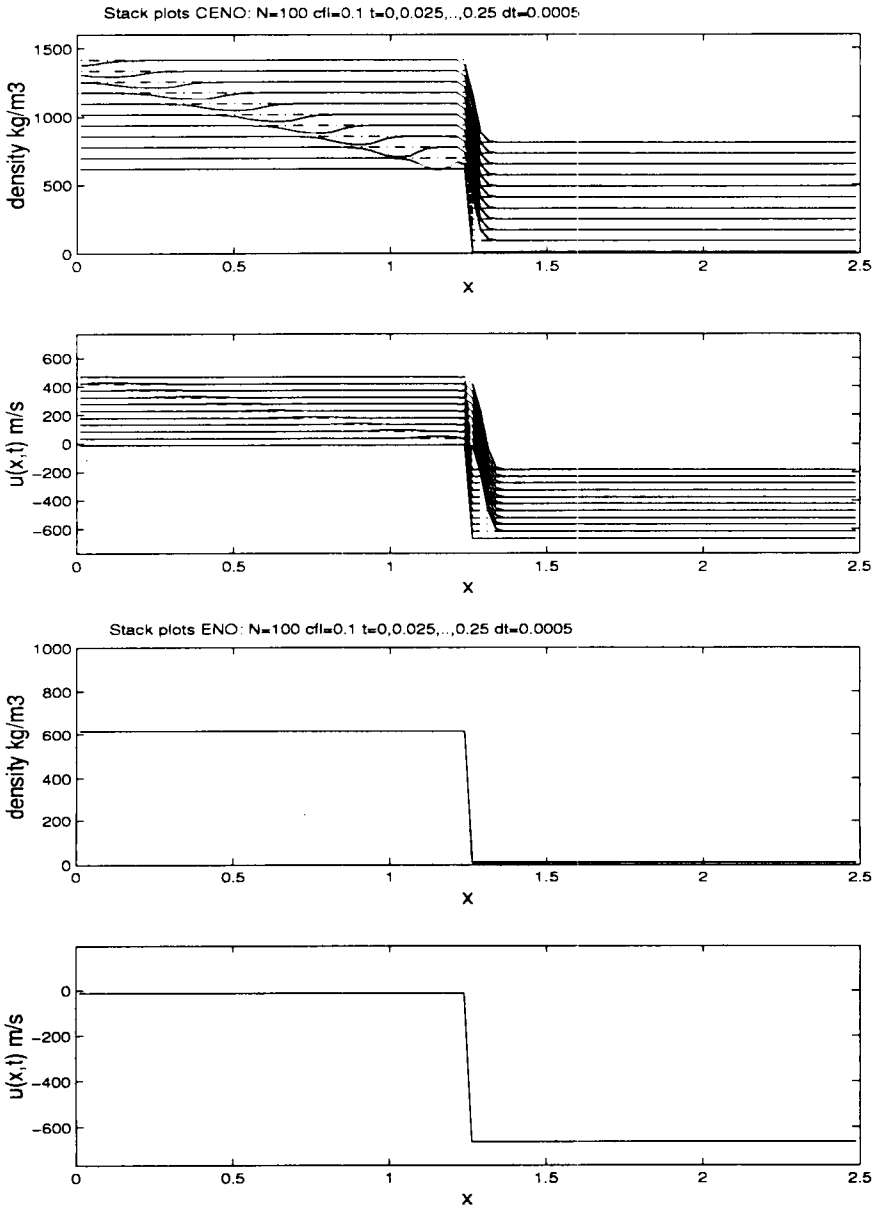

Figure 4: Stationary shock test for melt-volatile flow: (a) CENO code, density and velocity (stack plots with offset $0.8\,\rho_0 = 80\,kg\,m^{-3}$ in ρ and $0.2\,U = 48.06\,m/s$ in u. Lenght scale $L = 5\,m$.) and (b) ENO code, density and velocity. Dashed-dotted lines indicate the exact and solid lines the numerical solution. Time spacing is $0.025\,s$.

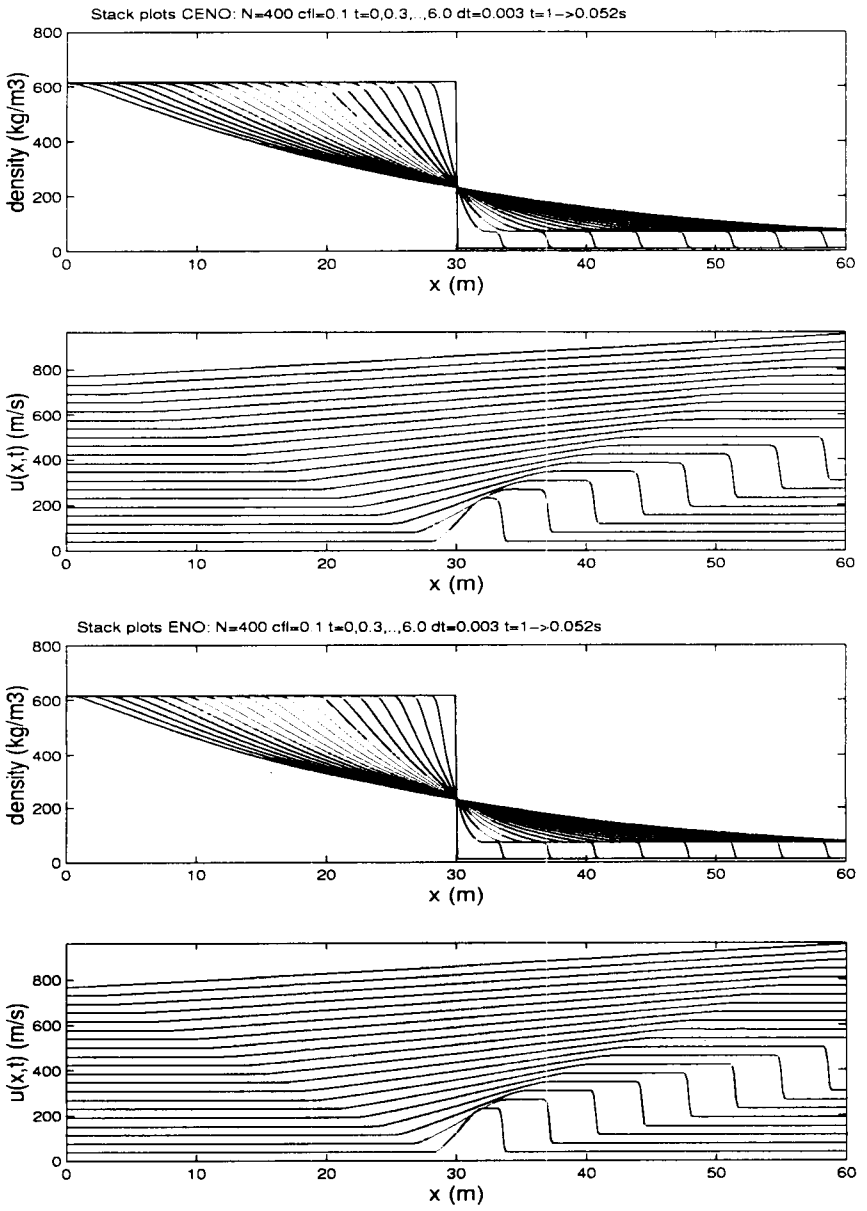

Figure 5: Shock tube tests for melt-volatile flow with open extrapolating boundary conditions: (a) CENO code, density and velocity and (b) ENO code, density and velocity. (Stack plots have offset $0.2\,U = 38.45\,m/s$ in u. $L = 5\,m$.)

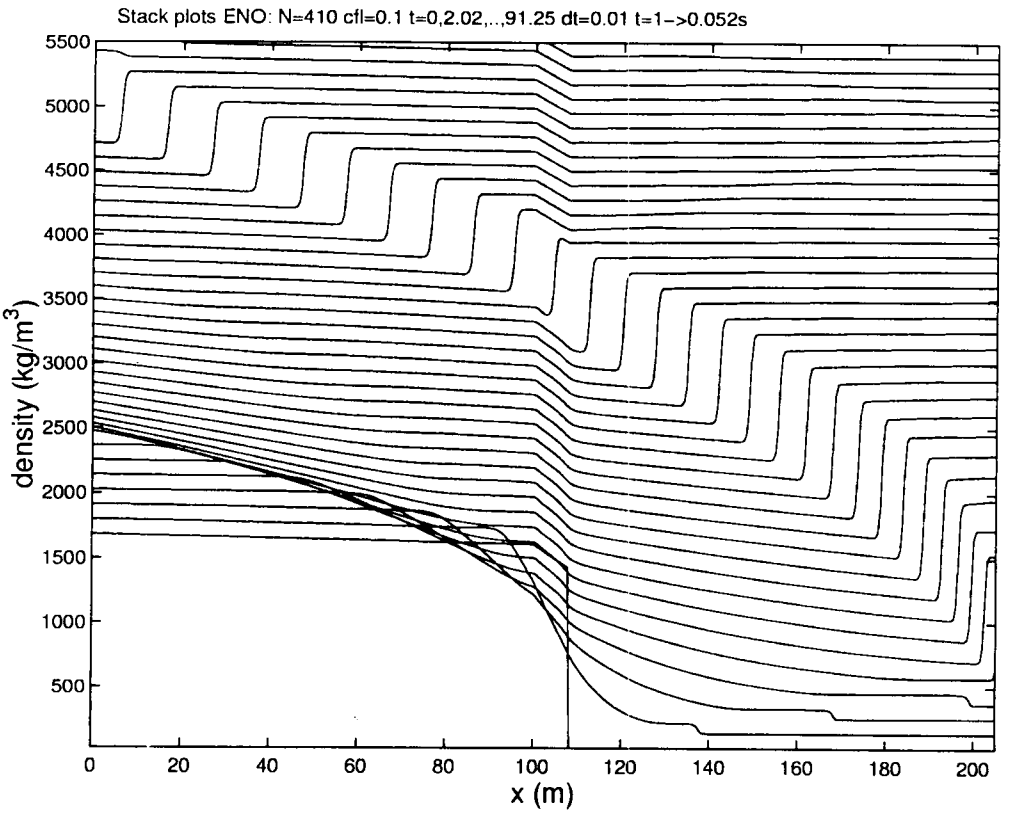

Figure 6: Stack plots (every $0.1054\,s$) of density are given for a magma-repository shock tube problem with melt-volatile flow. For $\xi_1 < 100\,m$ we are in the vertical dike, for $100\,m < \xi_1 < (100 + (\pi/2)\,R)\,m$ we are in the 90^o arc of $R = 5\,m$ radius, and for $(100 + (\pi/2)\,R)\xi_1 <= (200 + (\pi/2)\,R)\,m$ we are in the horizontal repository tunnel. Initial pressure is $2 * 10^7\,Pa$ at $\xi_1 = 0$ and hydrostatic above, i.e. in dike and arc, and $10^5\,Pa$ in the repository. The repository tunnel is closed at $(200 + (\pi/2)\,R)\,m$ and the dike at $\xi_1 = 0$ has open boundary conditions. $\rho_0 = 100\,kg\,m^{-3}$, $L = 5\,m$, and the offset is $120\,kg\,m^{-3}$.

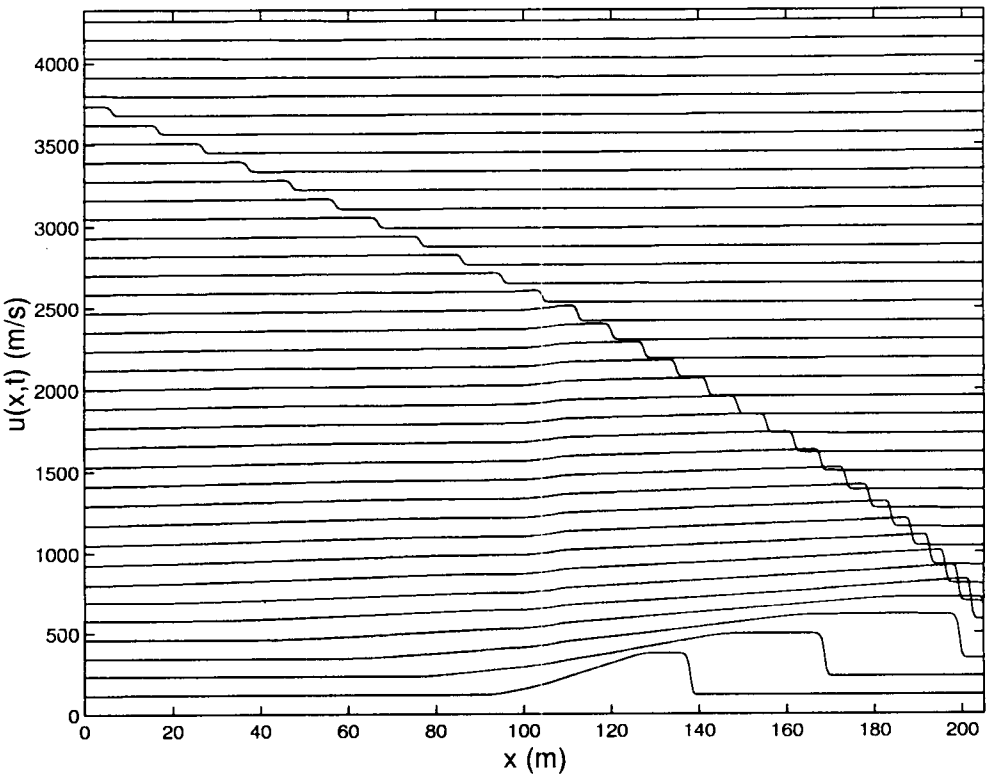

Figure 7: Stack plot of velocity of a dike-repository shock tube problem. See caption of previous figure. The offset is $115.35\,m/s$.

Volcano Hazards

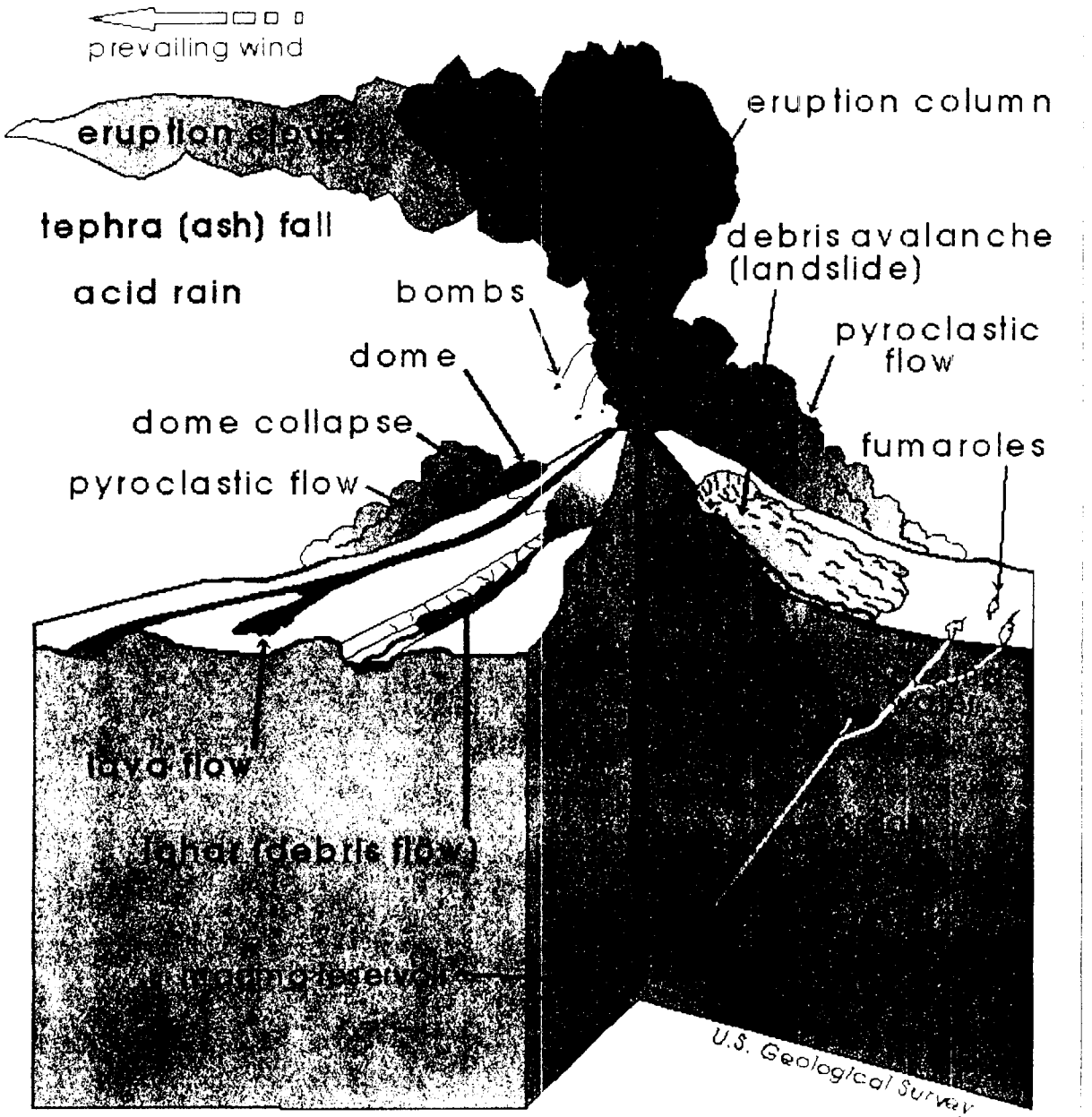

USGS

Topinka, USGS/CVO, 1998, Modified from Myers and Brantley, 1995, USGS Open-File Report 95-231

Cascade Eruptions During the Last 4,000 Years

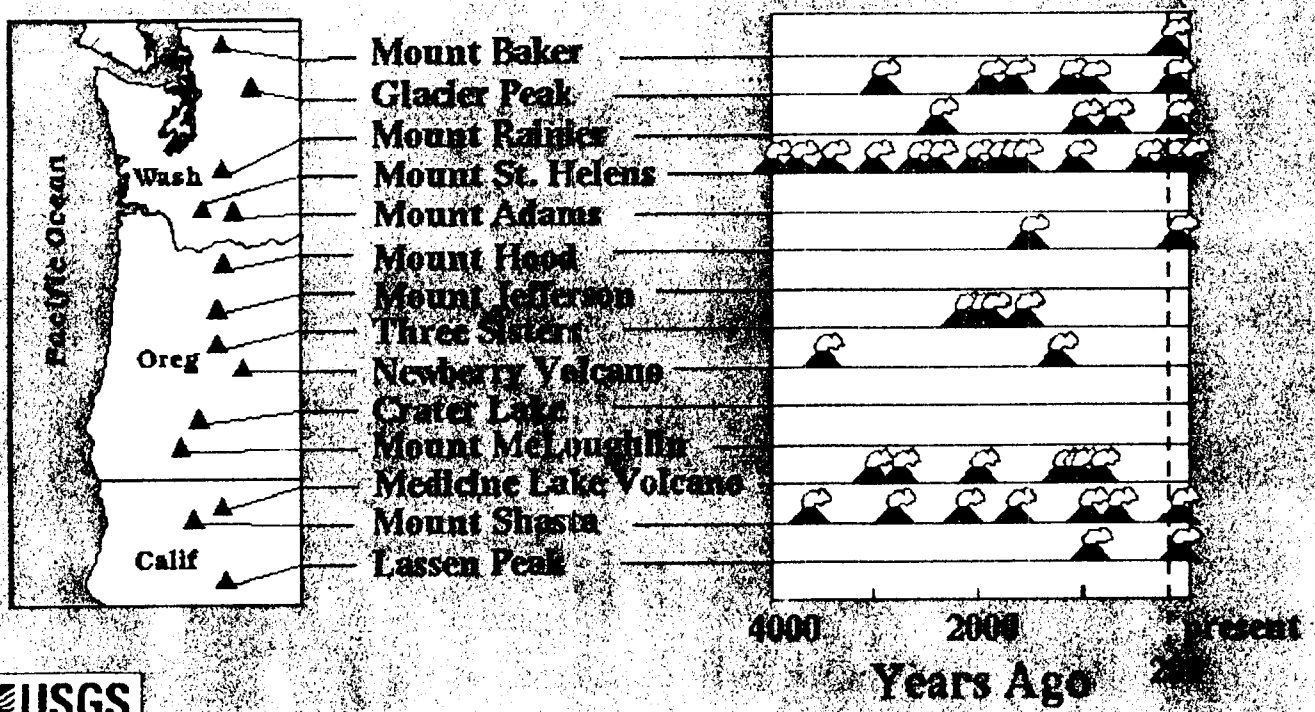

USGS

Graphic by: Bobbie Myers, USGS Open-File Report 94-585

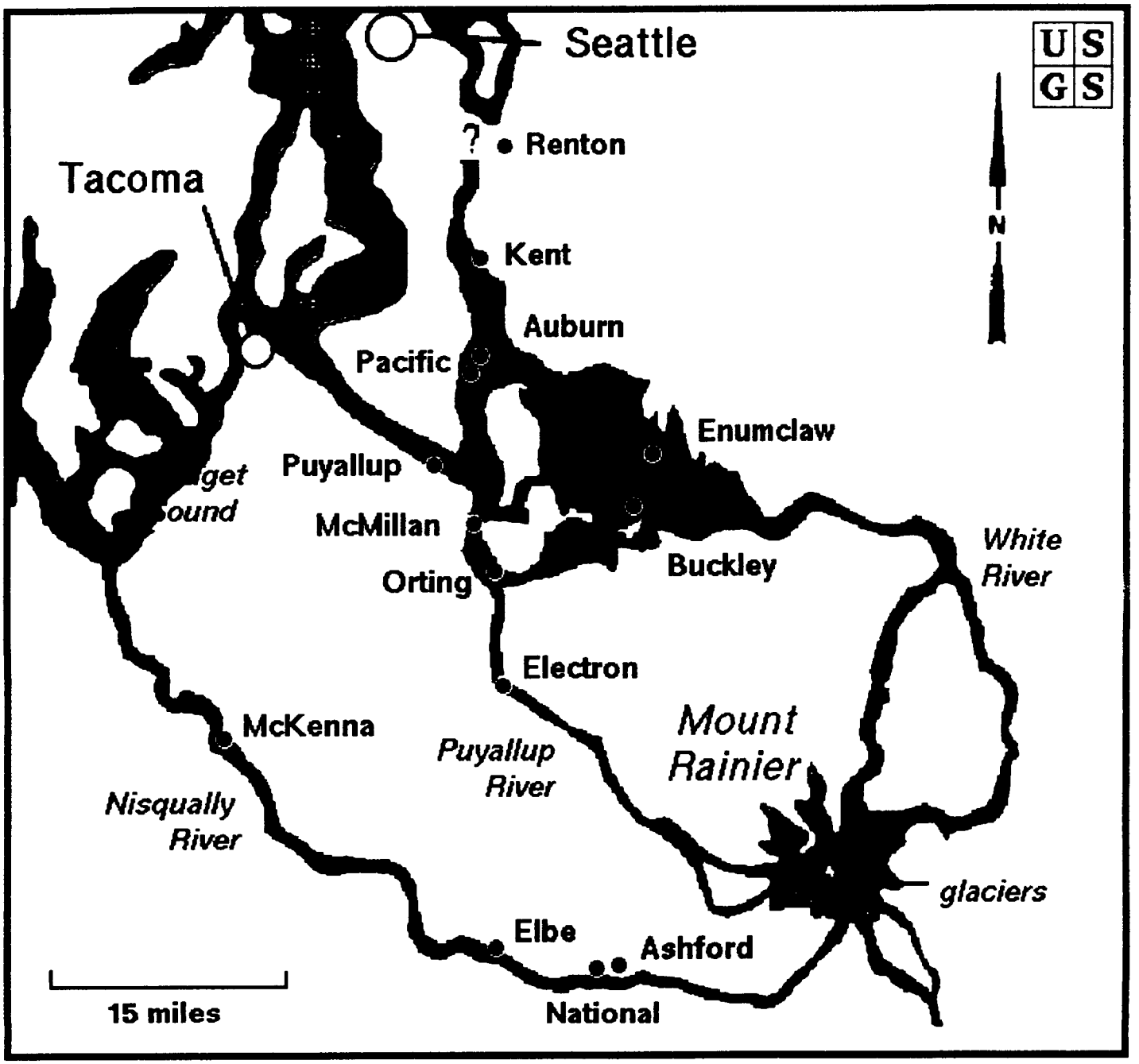
Seattle
USGS
?
Renton
Tacoma
N
Kent
Auburn
Pacific
Enumclaw
Puyallup
McMillan
Orting
Buckley
White River
Electron
McKenna
Mount Rainier
Puyallup River
Nisqually River
glaciers
Elbe
Ashford
National
15 miles

SCIENTIFIC NOTEBOOK
IA 20-14-2-461
115E

Chuck Connor
May 30, 1999

The following was submitted as part of National Research Council review of the USGS volcanic hazards program

Information potentially subject to copyright protection was redacted from pages 1 through 6 (center, bottom of pages). The redacted material is from the information listed above. No additional information is known.

Scientific Notebook
20-1402-461
IA KTI

Chuck Connor
Initial:
June 14, 1999

Heat Transfer through the cinder cone

We modeled heat conduction through the cinder cone using a finite difference approximation to the heat transfer equation in a cylindrical coordinate system (Figure **a). Heat conduction through the interior of the cone is described by:

$$\frac{1}{r}\frac{\partial T}{\partial r}+\frac{\partial^2 T}{\partial r^2}+\frac{\partial^2 T}{\partial k^2}=\frac{1}{\alpha}\frac{\partial^2 T}{\partial t^2}$$

where r and k are radial and vertical coordinates, respectively, T is temperature, t is time, and α is the bulk thermal diffusivity of the cinder cone. The finite difference approximation of temperature at time $t + \Delta t$ for a point in the cone interior is given by solving:

$$\frac{1}{\Delta r^2}\left[\left(1-\frac{1}{2i}\right)T_4-2T_1+\left(1+\frac{1}{2i}\right)T_2\right]+\frac{1}{\Delta k^2}\left[T_5-2T_1+T_3\right]=\frac{1}{\alpha\Delta t}\left[T_1^{t+\Delta t}-T_1\right]$$

explicitly, where T_1 - T_5, Δr and Δk are geometric terms defined in figure **a, Δt is the time step. The main difference between this finite difference approximation and Cartesian models is the need to track change in the cell volume with distance from the cone centerline. This is accommodated using i, the node number in the positive r-direction, such that $r = i\Delta r$ Heat transfer at the surface of the cone is modeled as a convective boundary, using a constant heat transfer coefficient, h_o, bulk thermal conductivity of the cone, k_c, and constant atmosphere temperature, T_o. The finite difference approximation to the heat transfer equation at the convective boundary in the positive r-direction is:

$$\frac{1}{\Delta r^2}\left[2T_4-2T_1\right]+\frac{2h_o\Delta r}{k_c}\left(1+\frac{1}{2i}\right)\left[T_0-T_1\right]+\frac{1}{\Delta k^2}\left[T_5-2T_1+T_3\right]=\frac{1}{\alpha\Delta t}\left[T_1^{t+\Delta t}-T_1\right]$$

in the positive k-direction:

$$\frac{1}{\Delta r^2}\left[\left(1+\frac{1}{2i}\right)T_4-2T_1+\left(1+\frac{1}{2i}\right)T_2\right]+\frac{2\left[T_3-T_1\right]}{\Delta k^2}+\frac{2h_o\Delta k}{k_c}\left[T_o-T_1\right]=\frac{1}{\alpha\Delta t}\left[T_1^{t+\Delta t}-T_1\right]$$

in both positive *k*- and *r*- directions:

$$\frac{1}{\Delta r^2}\left[2T_4-2T_1\right]+\frac{2h_o\Delta r}{k_c}\left(1+\frac{1}{2i}\right)\left[T_0-T_1\right]+$$
$$\frac{2[T_3-T_1]}{\Delta k^2}+\frac{2h_o\Delta k}{k_c}\left[T_0-T_1\right]=\frac{1}{\alpha\Delta t}\left[T_1^{t+\Delta t}-T_1\right]$$

and so on.

Pure insulating boundary conditions, e.g.,

$$q''=-k_c\frac{dT}{dr}=0$$

where q'' is heat transfer per unit area, are assumed to exist along the centerline of the cone and at the cone base. Along the cone centerline:

$$\lim_{r\to 0}\left(\frac{1}{r}\frac{\partial T}{\partial r}\right)=\frac{\partial^2 T}{\partial r^2}$$

and the finite difference approximation to the radial heat conduction equation becomes:

$$\frac{4\left[T_2-T_1\right]}{\Delta r^2}+\frac{\left[T_3-2T_1+T_5\right]}{\Delta k^2}=\frac{1}{\alpha\Delta t}\left[T_1^{t+\Delta t}-T_1\right]$$

along the cone centerline.

For the models presented here, h_o= 10 and To= 0 °C throughout the simulations. The parameters

k_c and α are constant over the domain of the cinder cone but are varied between simulations. The thermal diffusivity, α, was varied between 1 $\times 10^{-6}$ m^2/s and 1 $\times 10^{-7}$ m^2/s and the bulk thermal conductivity, k_c, was varied between 0.2- 2.0 W/m°K. These values for k_c and α are reasonable approximations to observed bulk cinder cone propoerties (Connor et al., 1997). The initial cinder cone temperature is varied between 100 °C and 600 °C both between simulations and over the domain of the cinder cone to mimic the deposition of pyroclasts at different temperatures during various phases of activity. A cone profile through Cone I at Tolabachik volcano was digitized and used for the cone geometry in the numerical simulations.

Results of the numerical simulation are summarized in Figures **b-***e. The first case investigated considers a uniform initial cone temperature of 300 C. This initial temperature corresponds to a both moderate scoria accumulation rate in the near-vent area and moderate eruption rate from the vent. Thus, pyroclasts are somewhat cooled, to the point of brittle fracture, as they accumulate in the cone. Using a high bulk thermal conductivity and thermal diffusivity for scoria, temperatures in a large fraction of the cone volume are < 100 C after 200 yr. At a point below the cone rim, the scoria temperatures drop below 100 C in the first 50 yr (Figure **b). In contrast, lower bulk thermal conductivities and thermal diffusivities show a high thermal gradient within the cone persists after 200 yr and a large fraction of the cinder cone remains at approximately 300 C (Figure **c).

A second set of models (Figures **d and **e) use nonuniform initial cone temperatures. It is assumed that early in the eruption a small scoria mound is built during low energy activity, resulting in an initial temperature of 600 C. This is followed by a higher energy phase of the eruption in which scoria transported to much higher levels in the atmosphere, fragmented, and deposited at initial temperatures of 100 C. This scenario is close to the sequence of events observed at several cinder cones during their formation, such as Tolbachik Cones I-III. At high heat transfer rates for scoria, the mantle of 100 C ash quickly cools in the near-surface and heats in the deeper part of the cone in response to the heat transfer from the early-formed hot spatter mound.

Basic conclusions from these numerical simulations are:

(1) In all cases, with a variety of initial temperature conditions and bulk thermal properties, cooling of the cinder cones is incomplete after 200 yr, in good agreement with our field observations.

(2) In all cases the maximum temperature gradient is perpendicular to topography near the surface. This means that the condensation / vaporization will occur in a thin zone parallel to

bedding within the cone as the cone cools. This is a good explanation for the formation of caliche layers along beds commonly observed in cinder cones.

3) The models show that a point below the cone rim cools relatively quickly, yet surface temperature measurements consistently reveal comparatively high temperatures along fractures at the cone rim. So heat advected from the interior of the cone to the cone rim by air circulation is required to sustain the observed surface temperatures. Nevertheless, the models indicate that it is not necessary to transport heat from deep in the cone to account for the temperatures we observe at the surface. In most cases, circulating air need not penetrate more than one half of the cone by volume. Furthermore, the temperatures we observe in the 300-500 C range at the surface do not require any additional heat source, such as a dike. Simple cooling of the cinder cone also accounts for the temperatures observed at Jorullo.

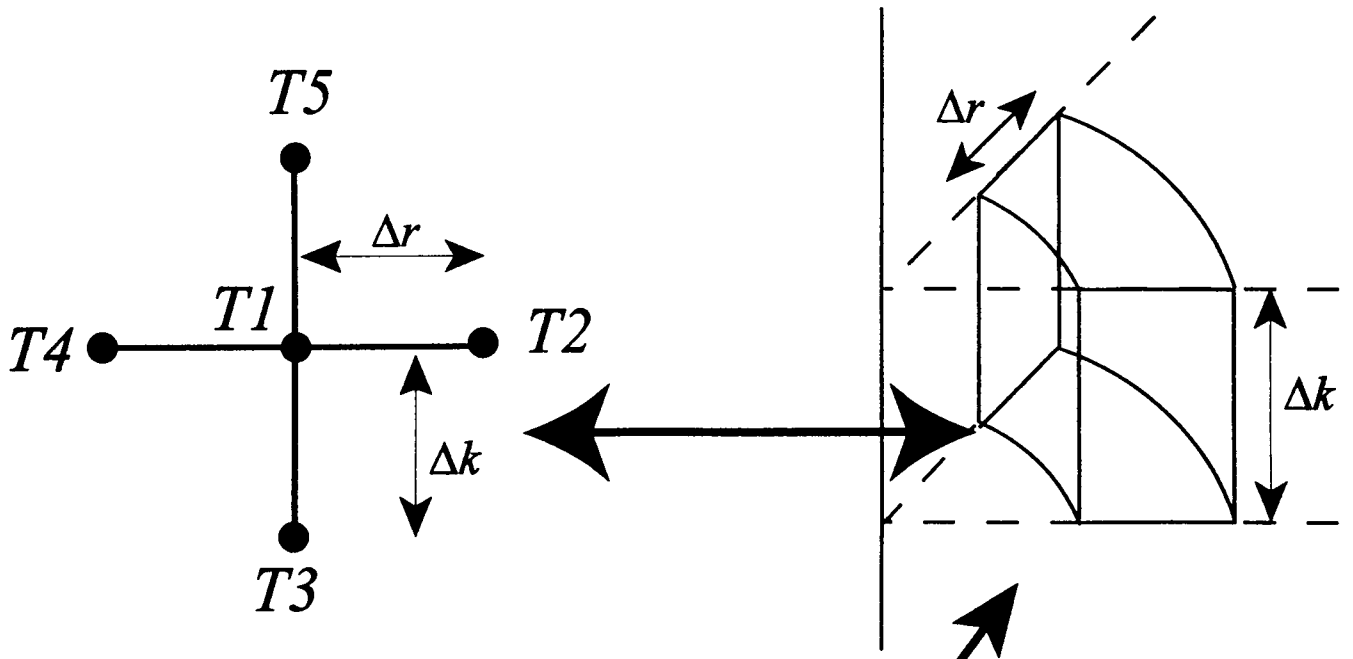

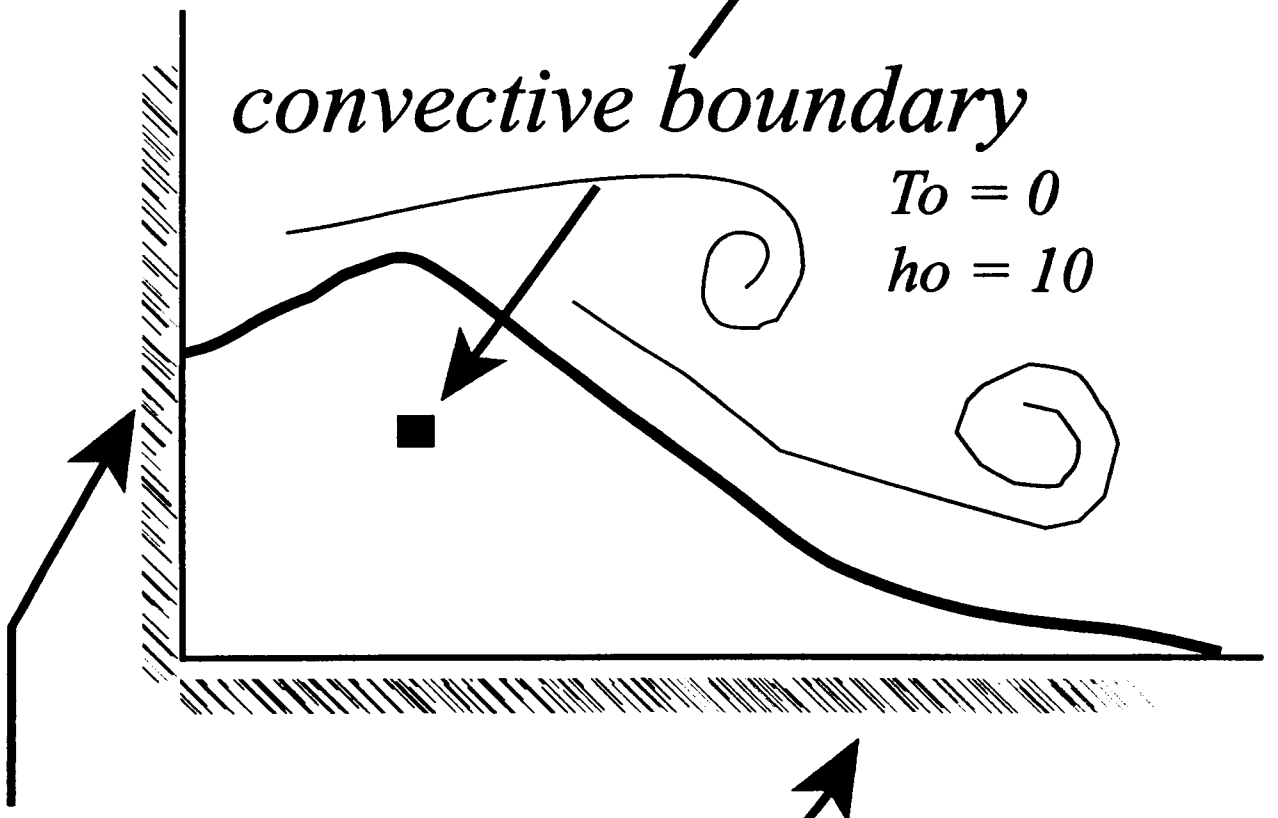

insulated boundary

$q'' = 0$

Cinder Cone Cooling Radial Heat Transfer Model

$t_0 = 300°C$

years elapsed = 200.008212
time steps = 12654
k = 0.10 W/mK
h =10.0
α = 1e-07 m²/s

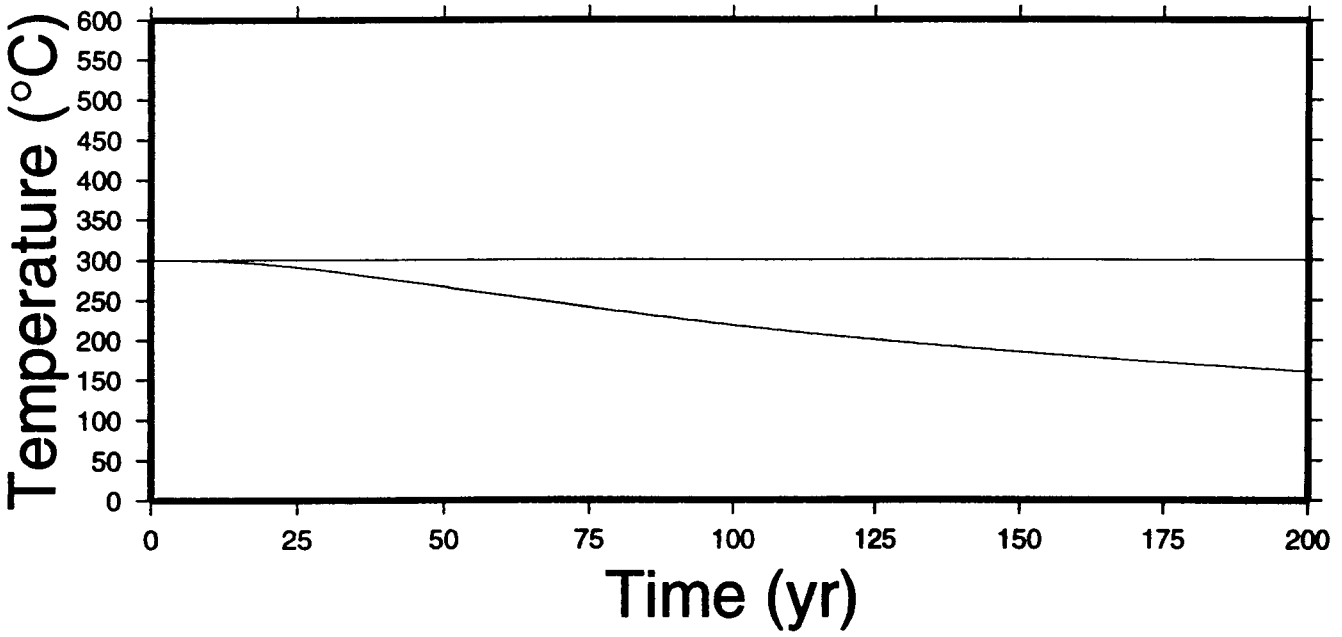

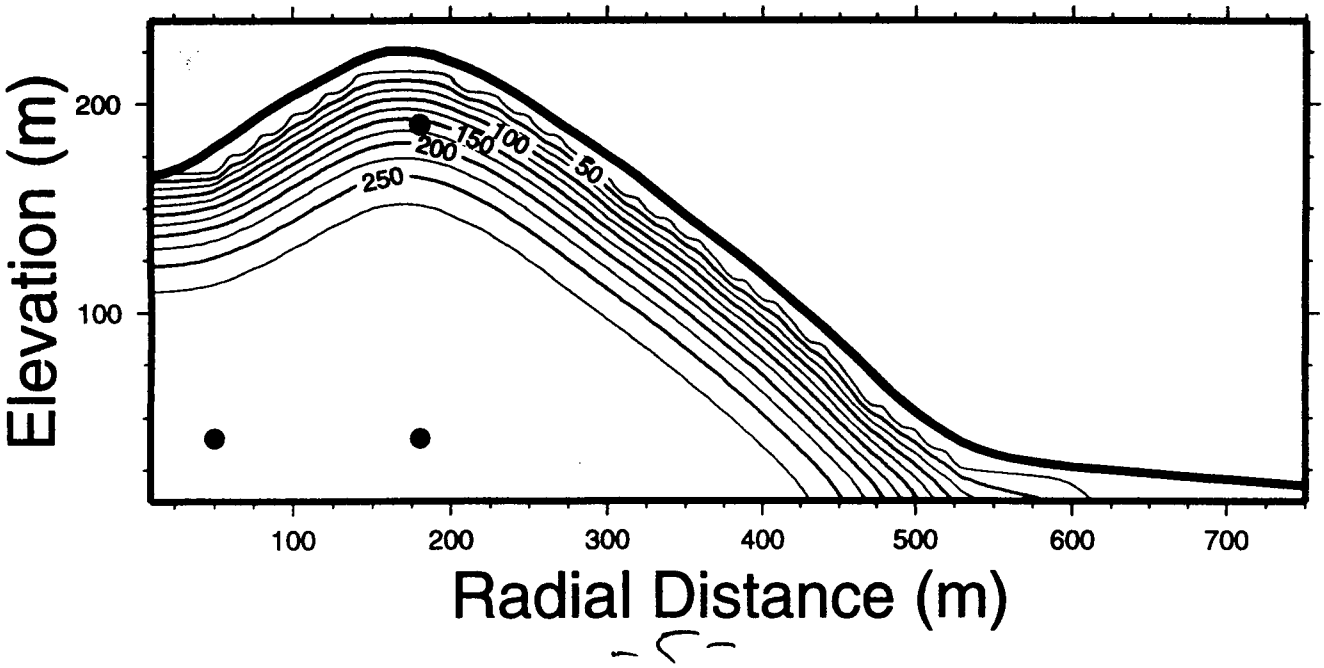

Cinder Cone Cooling Radial Heat Transfer Model

$t_0 = 300°C$

years elapsed = 200.003284
time steps = 12881
k = 1.0 W/mK
h =10.0
α = 1e-06 m²/s

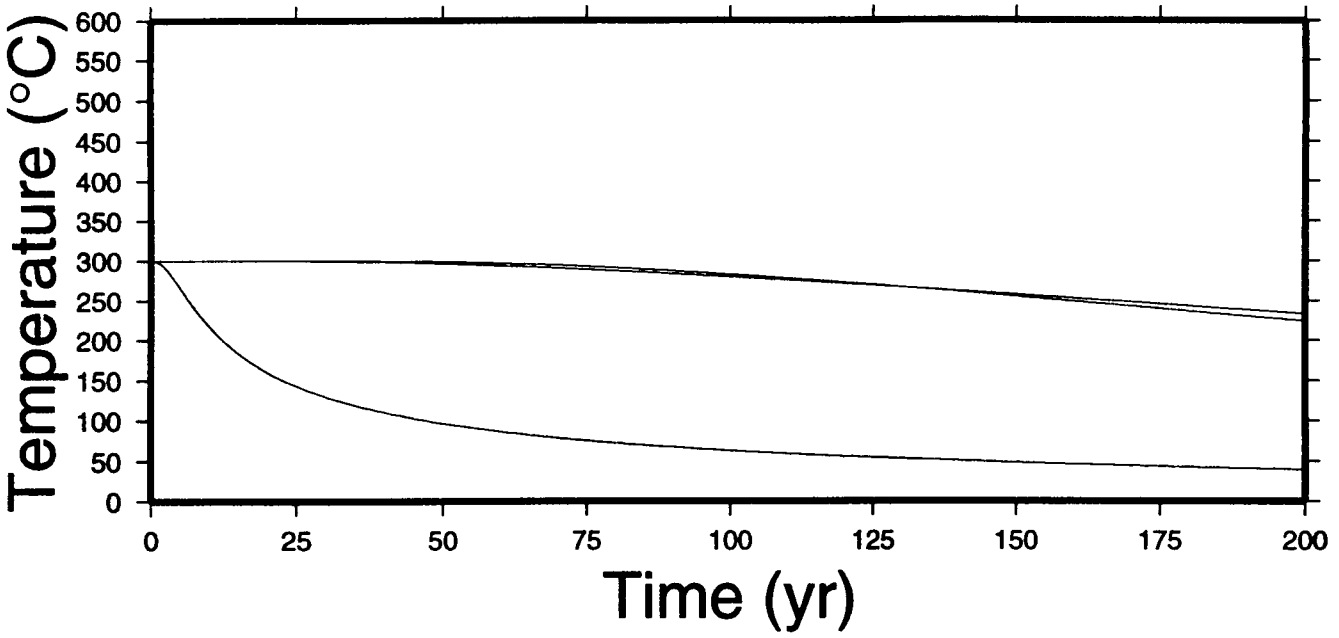

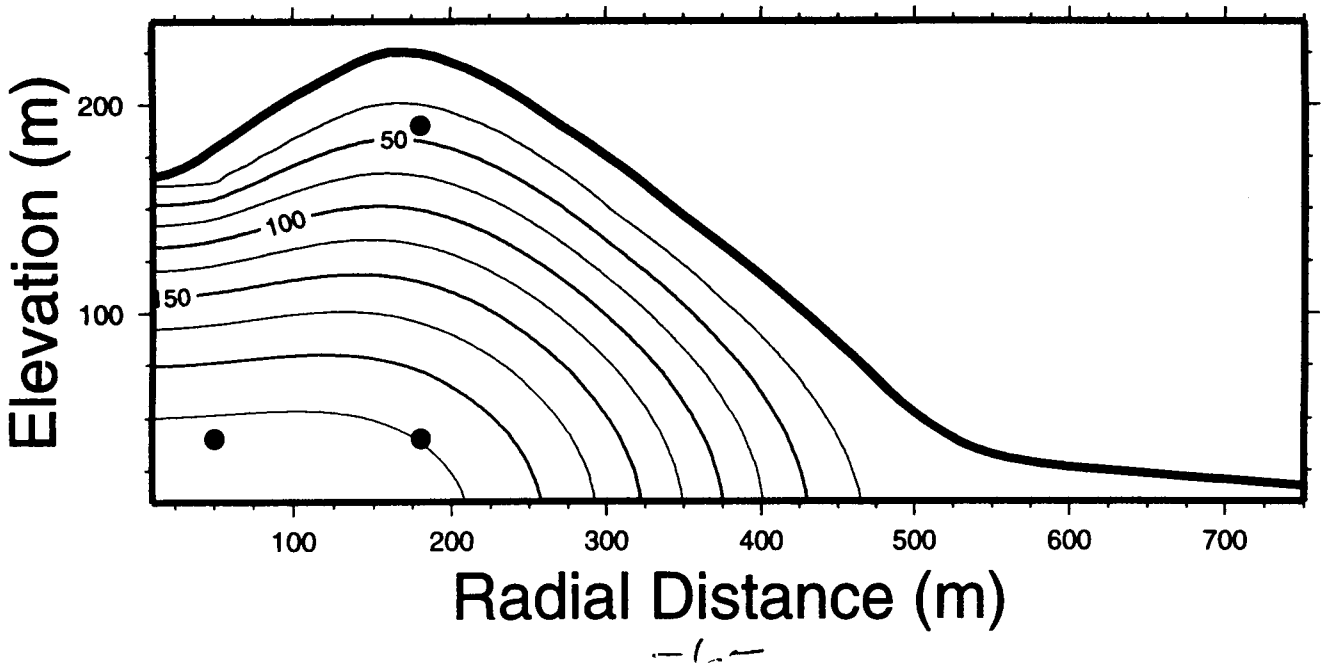

Cinder Cone Cooling Radial Heat Transfer Model

t_0 = 100/600

years elapsed = 200.008212
time steps = 12654
k = 0.1 W/mK
h =10.0
α = 1e-07 m²/s

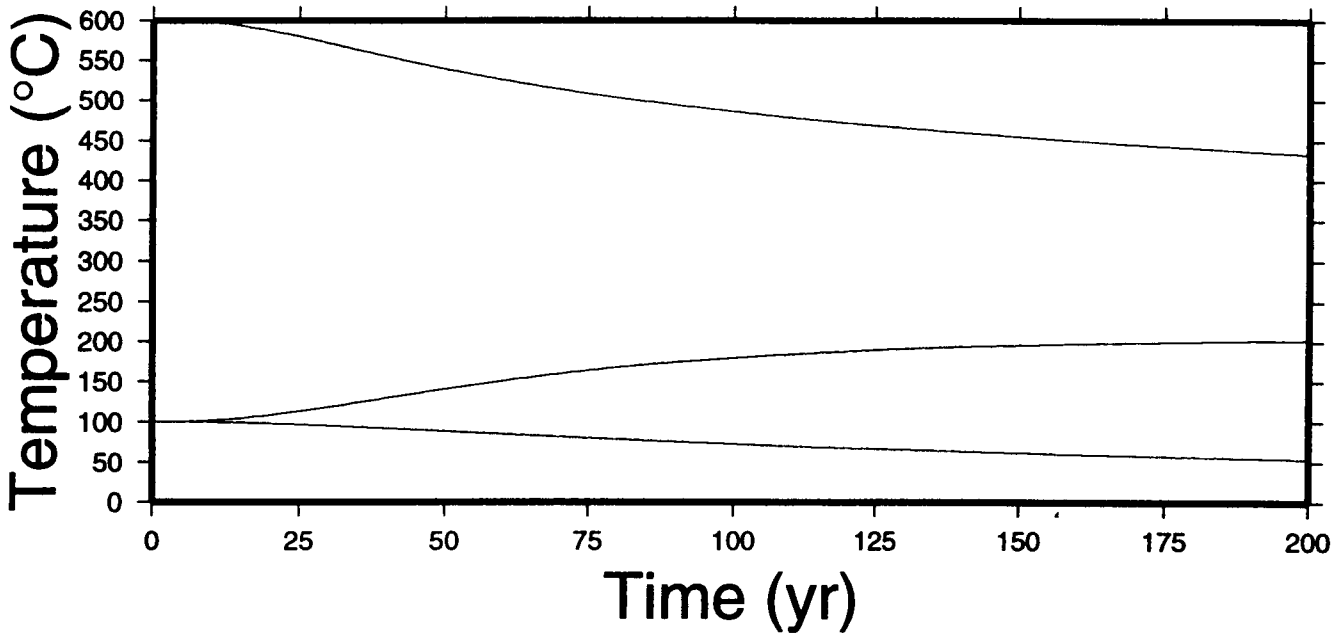

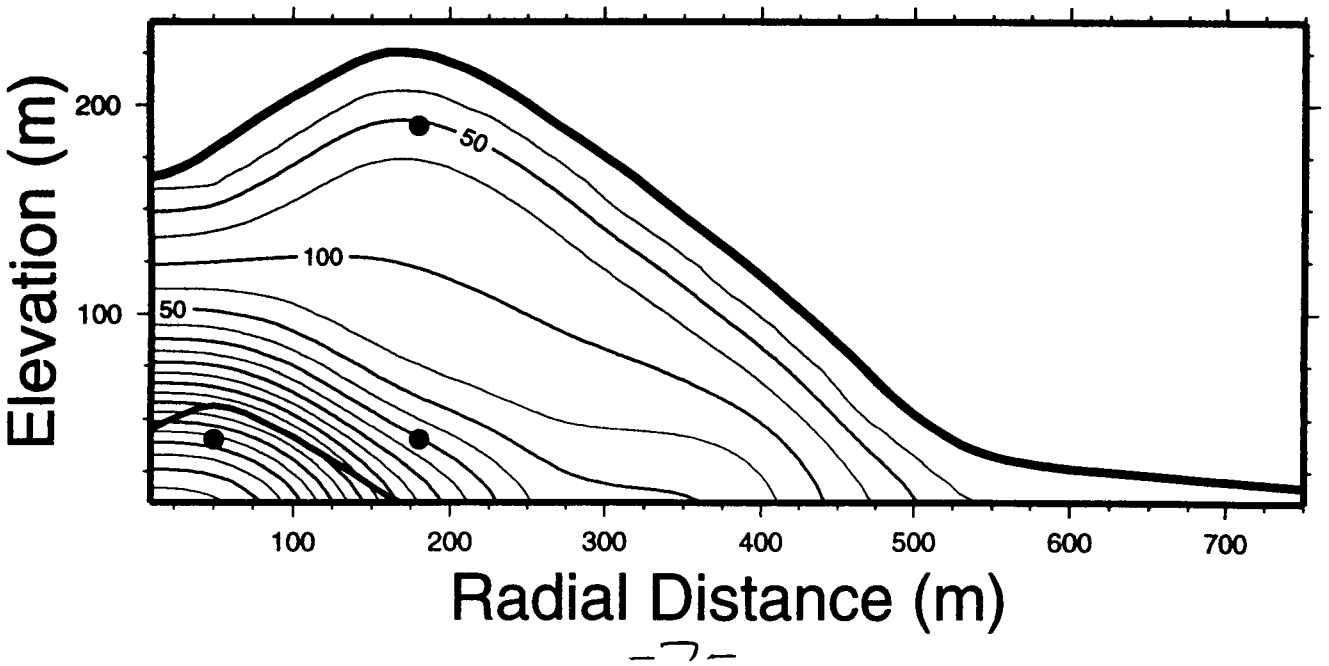

Cinder Cone Cooling Radial Heat Transfer Model

$t_0 = 100/600$

years elapsed = 200.003284
time steps = 12881
k = 1.0 W/mK
h =10.0
α = 1e-06 m²/s

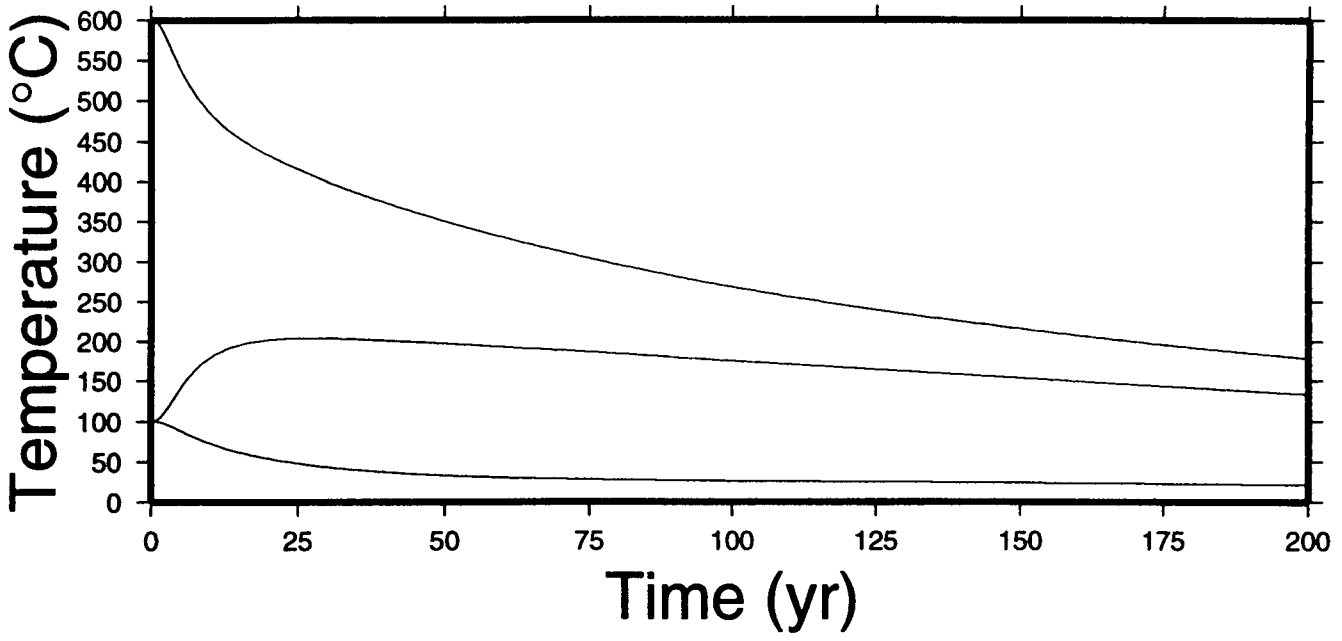

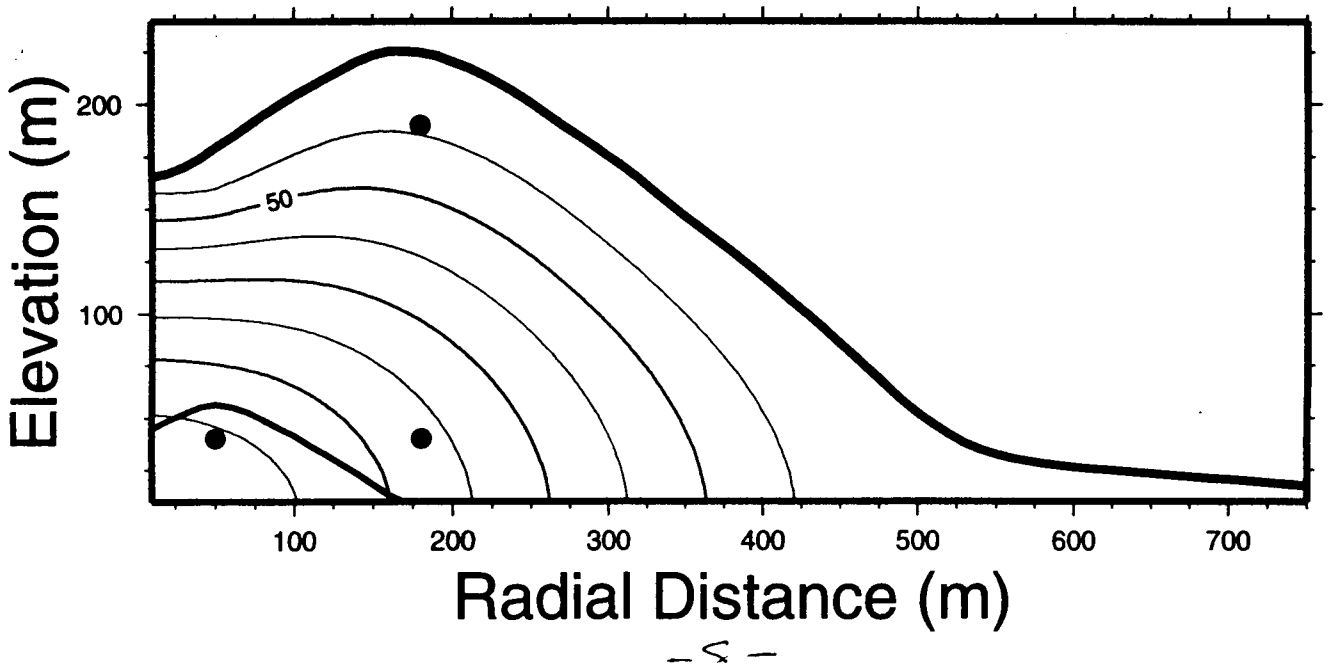

```
#! /bin/csh -f
#############################################################
#         runner.csh
#
#         This is a c- shell script to
#         run cinder cone cooling codes
#
#
#    Chuck Connor
#       Center for Nuclear Waste Regulatory Analyses
#       Southwest research Institute
#       6220 Culebra Rd
#       San Antonio, TX, 78238-5166, USA
#
#       April 30, 1999
#################################################################


    # define htc as the heat transfer coefficient between
    # the cinder cone surface and surrounding atmosphere
    set htc = 100.000

    #define td as the thermal diffusivity of the cinder cone
    # this is constant for the entire cinder cone
    set td = 1e-06

    # define cond as the bulk thermal conductivity of the cinder cone
    set cond = 1.000

    #num_it is the number of iterations (steps) in the cooling model
    set num_it = 126535


    #the first code to run, p1,  sets up the geometry of the cooling cone
    # source code is prof_read.c - list prof_read.c for
    # details of how geometry is formulated and syntax
    # p1 requires one input file and produces 2 output files

    #   p1 prof.dat c_boxes.txt c_temps.txt

    # the second code to run,  c1, calculates the radial heat transfer
    # list the source code c_heat.c for details

    c1 c_boxes.txt c_temps.txt c_out.xyz c_pro1.txt c_pro2.txt c_pro3.txt $htc $cond $td  $nu
+ m_it

    #c1 prints the total time elapsed in years to the file answ.out
    #get this value, store in $year, and delete the file
    set year = (`cat answ.out`)
    rm answ.out

    #The following are the GMT scripts to create the final figure

   # makecpt -Cno_green -T0/600/25 > cinder.cpt

    psbasemap
    xyz2grd c_out.xyz -Gc_out.grd -I10.0 -R10.0/10.0/750.0/240.0r
   # grdimage c_out.grd -JX6i/2.5i -X1.0i -Ccinder.cpt -P -K > test1.ps
    grdcontour c_out.grd -JX6i/2.5i -X1.0i -Ba100f25:"Radial Distance (m)":/a100f25:"Elevatio
+ n (m)":WSne -C25 -A50 -G3i/10 -S4 -P -K > test1.ps
     psxy -R -JX -O -P -Sc0.1i -G0 -W plot_xy.dat -K >> test1.ps
    psxy -R -JX -O -P -W3.0p profile.d -K >> test1.ps

    psxy -R/0/200/0/600 -JX6i/2.5i  -Ba25f25:"Time (yr)":/a50f50:"Temperature (@~\260@~C)":WS
```

```
+ ne -O  -Y4.0i -P c_pro1.txt -K >> test1.ps

      psxy -R -JX  -O -P c_pro2.txt -K >> test1.ps


      psxy -R -JX -O  -P c_pro3.txt -K  >> test1.ps


      # plot the headers
      # echo x-position y position font size tilt font shift

      echo "0.0 5.0   18 0.0 2 0 Cinder Cone Cooling Radial Heat Transfer Model " | pstext -R0/
+ 11/0/8.5 -Jx1i -O -K >> test1.ps

    echo "0.0  4.2  18 0.0 2 0  years elapsed = $year " | pstext -R0/11/0/8.5 -Jx1i -O -K >> te
+ st1.ps
      echo "0.0  3.9  18 0.0 2 0  time steps = $num_it " | pstext -R0/11/0/8.5 -Jx1i -O -K >> t
+ est1.ps

      echo "0.0  3.6  18 0.0 2 0  k = $cond W/mK " | pstext -R0/11/0/8.5 -Jx1i -O -K >> test1.p
+ s

      echo "0.0  3.3  18 0.0 2 0  h =$htc " | pstext -R0/11/0/8.5 -Jx1i -O -K >> test1.ps

      echo "0.0  3.0  18 0.0 2 0  @~a@~ = $td m@+2@+/s " | pstext -R0/11/0/8.5 -Jx1i -O >> test
+ 1.ps

      ghostview test1.ps
```

```
/*

  Program Name: prof_read.c
  Written by: Chuck Connor
  CNWRA
  Southwest Research Inst.
  6220 Culebra Rd
  San Antonio, TX, 78238-5166
  Phone: 210-522-6649
  E-mail: cconnor@swri.edu
  Date: April 6, 1999
  Language: Ansi C

  Purpose: This program calculates prepares input files for the program c_heat,
  a code used to model conductive cooling of cinder cones. The input to prof_read.c
  consists of a a file containing a single column of numbers. These numbers
  correspond to the elevation of the surface of the cinder cone with respect to
  the cone base elevation. The values progress from the innermost elevations -
  ie on the cone centerline, to eelevation values at thegreatest distance from the
  cone centerline


  Running this code:

  One input files are required to run this code. The name of the input file
  must be prof.dat <- short for cinder cone profile data. Ideally, this data
  set contains elevations that average variations in the radial geometry of
  the cone.



  ........................................
  .......++++++..........................
  ....++++++++++++.......................
  ++++++++++++++++++.....................
  ++++++++++++++++++++++.................
  ++++++++++++++++++++++++++.............
  ++++++++++++++++++++++++++++++.........
  1234++++++++++++++++++++++++++++++ .....

  ^                                      ^
  |                                      |

  first elevation point                  last elevation point in prof.dat

  The input data in prof.dat look like:
  ---------------------------------------
  165.00
  165.63
  167.04
  169.95
  174.19
  179.17
  184.18
  189.30
  194.73

  ---------------------------------------

  Each value in the above file corresponds to an
  elevation (in meters) above the base of the cone.
  The program assumes that the points (elevation values) are spaced at
  10 meter intervals in the horizontal (radial) direction.
```

```
  Two files are output by the code: c_boxes.txt and
  c_temps.txt. Each output file has the following
  structure:

  ........................................->  (last row filled)
  .......++++++.............................
  ....++++++++++++..........................
  ++++++++++++++++++++.....................->  (fifth row filled)
  ++++++++++++++++++++++...................
  ++++++++++++++++++++++++++++.............
  ++++++++++++++++++++++++++++++++.........->  (second row filled)
  1234++++++++++++++++++++++++++++++++ .....->  (first row filled)
  In the above figure a + means the element is part of the
  body and a . means the element is part of the atmosphere

  Data in c_boxes is either 1 or 0, 1 if the element is
  part of the body and 0 if the element is part of the
  atmosphere

  Data in c_temps is 0 if the element is part of the
  atmosphere and nonzero if the element is part of
  the body. Values in c_temps are in degree C.
  ____________________________________________________
  Data in c_boxes.txt has the following form:

  1
  1
  1
  1
  0
  0
  0
  ____________________________________________________
  The corresponding data set in c_temps.txt  has
  the following form:

  300
  300
  300
  300
  0
  0
  0

  ____________________________________________________

*/

#include <math.h>
#include <stdio.h>
#include <stdlib.h>

void main (int argc, char *argv[])
{

  /* file f1 will contain the raw profile data
     - results of the analysis, f2 is an input file which containes 1's
     and 0's -
     each followed by a carriage return. Each 1 indicates that the node is
     part of the cinder cone (scoria) and each 0 indicates that the node
     is part of
     the atmosphere. file f3 contains initial temperature data for each node in
     file f2.
```

```
  */
  FILE *f1, *f2, *f3;

  int t[101][26], tbox[101][26];

  int r, k, iele;

  double p;
  double ele;

  if (argc != 4) {
    printf("Usage: infile outfile1 outfile2 \n");
    printf(" \n");
    printf("where infile: input file containing the elevation data \n");
    printf("      outfile1: output file containing 0 and 1 (or box file) \n");
    printf("      outfile2: output file containing the temperature data \n");
    printf("list code for additional details \n");
    printf(" \n");
    exit (1);
  }


  /* open / create the data files */

  if ((f1 = fopen (argv[1], "r")) == NULL) {
    printf ("cannot read file %s \n", argv[1]);
    exit(1);
  }

  if ((f2 = fopen (argv[2], "w")) == NULL) {
    printf ("cannot create file %s \n", argv[2]);
    exit(1);
  }

  if ((f3 = fopen (argv[3], "w")) == NULL) {
    printf ("cannot create file %s \n", argv[3]);
    exit(1);
  }

  for (r = 0; r < 101; r++) {

    /* read the elevation data as doubles from the
       f1 file - then round to the nearest 10s of meters
       and print the result - just to check it out
    */
    fscanf ( f1, "%le", &ele);
    iele = (modf(ele/10.0, &p) < .5) ? (int)floor(ele/10.0) : (int)ceil(ele/10.0);
    printf("%f %d\n", ele, iele);


    /* perform some simple filters on iele
       if iele is negative - correct this error
       making iele = 0

       if iele is greater than 22  -> the cone
       rim is 220 m high and too close to the top edge of the model space
       so trim it
    */
    if (iele < 0) iele = 0;
    if (iele > 22) iele = 22;


    for (k = 0; k < 26; k++) {
```

```
      if (k <= (int) floor(iele/3.0) && r < 50) {
        tbox[r][k] = 1;
        t[r][k] = 600;
      }

      else if (k <= iele) {
        tbox[r][k] = 1;
        t[r][k] = 100;
      }

      else {
        tbox[r][k] = 0;
        t[r][k] = 0;
      }

    } /* next k */

  } /*next r */


  /* print the results to files to be
     read by the programm c_heat.exe */

  for (k = 0; k < 26; k++) {
    for (r = 0; r < 101; r++) {
      fprintf (f2, "%d \n", tbox[r][k]);
      fprintf (f3, "%d \n", t[r][k]);

    } /*next rcount */
  } /* next kcount */

} /*end */
```

```
/*

Program Name: c_heat.c Written by: Chuck Connor CNWRA Sothwest
Research Inst.  6220 Culebra Rd San Antonio, TX, 78238-5166 Phone:
210-522-6649 E-mail: cconnor@swri.edu Date: March 24, 1999 Language:
Ansi C

Purpose: This program calculates the solution to the time-transient
heat conduction equation in radial coordinates using finite differences, based
on the math formulations in Carslaw (1921, Introduction to the mathematical
theory of conduction of heat in solids, MacMillian and Co., London).

My inital reason for writiing this code is to model conductive
cooling of cinder cones.

Assumptions: The code is written with the assumption that the boundary
conditions at r = 0 (centerline) and k = 0 (base) of the model are completely
insulating.

The body radiating heat is submersed in a convecting fluid (ie the atmosphere)
At r = large number and k = large number it is assumed that temperature is
constant and t = 0.

The initial temperature conditions of the body and the body geometry
depend on input files contributed by the user.

Running this code:

Two input files are required to run this code. The names
of these files are fixed in the current version: c_boxes.txt and
c_ temps.txt. Each file contains an array of 2525 elements and each
element is separated by a carriage return. These correspond to a 101 x 25
array of numbers - the radial section of the body geometry and surrounding
space (atmosphere).

Both of these arrays are filled by sarting at the bottom centerline,
continuing radially outward, advancing to the next level up, going radially
outward on the second level, etc, as follows

.........................................->  (last row filled)
.......++++++.............................
....++++++++++++.........................
++++++++++++++++++++.....................->  (fifth row filled)
++++++++++++++++++++++++.................
++++++++++++++++++++++++++++++...........
++++++++++++++++++++++++++++++++++.....->  (second row filled)
1234++++++++++++++++++++++++++++++++++ .....->  (first row filled)


In the above figure a + means the element is part of the
body and a . means the element is part of the atmosphere

Data in c_boxes is either 1 or 0, 1 if the element is
part of the body and 0 if the element is part of the
atmosphere

Data in c_temps is 0 if the element is part of the
atmosphere and nonzero if the element is part of
the body.

_____________________________________________________
Data in c_boxes.txt has the following form:
```

```
 1
 1
 1
 0
 0
 0
```

The corresponding data set in c_temps.txt has the following form:

```
 300
 300
 300
 300
 0
 0
 0
```

The output file has the following form:
x,y,temperature -> where x and yare in meters
and temperature is in degrees C.

```
10.000000 10.000000 299.999741
10.000000 20.000000 299.998945
10.000000 30.000000 299.995819
10.000000 40.000000 299.984382
10.000000 50.000000 299.945242
10.000000 60.000000 299.820439
10.000000 70.000000 299.451223
10.000000 80.000000 298.442636
10.000000 90.000000 295.911887
10.000000 100.000000 290.112126
10.000000 110.000000 278.047511
10.000000 120.000000 255.417737
10.000000 130.000000 217.411512
10.000000 140.000000 160.680772
10.000000 150.000000 86.004600
10.000000 160.000000 0.021496
10.000000 170.000000 0.000000
10.000000 180.000000 0.000000
10.000000 190.000000 0.000000
10.000000 200.000000 0.000000
```

Notes on running program:

1) overflow and similar problems can occur if the thermophysical propoerties of the rock are poorly conditioned

2) the interior node temperatures can vary in the input file, but the atmosphere temperature has to be constant. If the atmosphere temperature is not 0 deg C, then t0 must be changed in addition to the input file.

```
*/

#include <stdio.h>
#include <stdlib.h>

void main (int argc, char *argv[])
{
```

```
/* file f1 will contain the output data
   - results of the analysis, f2 is an input file which containes 1's and 0's -
   each followed by a carriage return. Each 1 indicates that the node is
   part of the cinder cone (scoria) and each 0 indicates that the node is part of
   the atmosphere. file f3 contains initial temperature data for each node in
   file f2. */
FILE *f1, *f2, *f3, *f4, *f5, *f6, *f7;

/* matrix t contains the temperature data for each time step. */
double t[101][26];
/* matrix tbox contains geometrical information about the node, according to
   the following rules;

   tbox = 9: this is an interior cinder cone point
   tbox = 8: this is an inside corner
   tbox = 7: this is a flat edge
   tbox = 6: this is a flat edge
   tbox = 5: this is an inside corner
   tbox = 4: this is an outside corner

   Thus tbox is used to calculate heat transfer out of
   each box

*/
int tbox[101][26];

/* rn is the number of nodes in the radial direction- not taking into account the
   last node
   and kn is the number of nodes in the vertical direction
   - not taking into account the  last node (compare the
   dimensions of tbox and t to the values of rn and kn */
int rn = 100;
int kn = 24;

/* set up the thermo-physical parameters for the model */
/* t0 is the constant atmospheric temperature */
/* these parameters are all doubles */
double t0 = 0.0;

/* h0 is the heat transfer coefficient between the atmosphere and the cone */
double h0;

/* kond is the bulk thermo-conductivity of the cone */
double kond;

/* alpha is the thermo-diffusivity of the cinder cone
   alpha = thermal conductivity/ (density* heat capacity) */
double alpha;

/* set up the geometric parameters of the model */
/* these parameters are all integers */
/* 10 m between nodes */
double delz = 10.0;
/* let the step in the vertical = step in the horizontal */
double  delr = delz;

/* time step, delt - will be calculated
   to optimize the speed of the code */

double delt;

/* this is the total number of steps taken - time elaspsed */
long int num_steps;
```

```
  /* check for parameters and geometry that
     will lead to errors (numerical instabilities in the  solution */

  double sigma, bi, error;

  /* total years run is printed out to the file answ.out */
  double years_run;

  /* the following are book keeping variables */
  long int tott;
  int  k,i,j;
  int sumt;
  double d1,d2,dum1,dum2,dum3;
  double t1,t2,t3,t4,t5;
  int kcount, rcount;
  int loop_ct = 0;

  if (argc != 11) {
    printf("Usage: infile1 infile2 outfile1 outfile2 h0 kond alpha num_steps \n");
    printf(" \n");
    printf("where infile1: input file containing 0 and 1 (or box file) \n");
    printf("      infile2: input file containing the temperature data \n");
    printf("      outfile1: output temperature grid (x y z format) \n");
    printf("      outfile2: output temperature profile data \n");
    printf("      h0: heat transfer coefficient (cone -> atmosphere)  \n");
    printf("      kond: bulk thermal conductivity of cone (W/m C) \n");
    printf("      alpha: thermal diffusivity of cone (m*m/s) \n");
    printf("      num_steps: number of time steps in run \n");
    printf("list code for additional details \n");
    printf(" \n");
    exit (1);
  }

  if ((f2 = fopen (argv[1], "r")) == NULL) {
    printf ("cannot open file %s \n", argv[1]);
    exit(1);
  }

  if ((f3 = fopen (argv[2], "r")) == NULL) {
    printf ("cannot create file %s \n", argv[2]);
    exit(1);
  }


  if ((f1 = fopen (argv[3], "w")) == NULL) {
    printf ("cannot create file %s \n",argv[3]);
    exit(1);
  }

  if ((f4 = fopen (argv[4], "w")) == NULL) {
    printf ("cannot create file %s \n",argv[4]);
    exit(1);
  }

  if ((f5 = fopen (argv[5], "w")) == NULL) {
    printf ("cannot create file %s \n",argv[5]);
    exit(1);
  }

if ((f6 = fopen (argv[6], "w")) == NULL) {
    printf ("cannot create file %s \n",argv[6]);
    exit(1);
  }
```

```
  h0 = atof(argv[7]);
  kond = atof(argv[8]);
  alpha = atof(argv[9]);
  num_steps = atol(argv[10]);

  /* perform the calculations to make sure
     that the finite difference solution will be
     stable */


  bi = h0*delz/kond;
  error = 1.0/(2.0*(2.0+bi));
  delt = error*delz*delz/alpha;

  sigma = alpha*delt/(delz*delz);
  if (sigma > error) printf ("sigma is too big!   !!!!!!!\n" );
  printf ( "sigma =  %f \n",sigma);
  printf (" error = %f \n", error);

  /* let the user know that the time step
     has changed to maximize performance and
     achieve a stable solution */

  printf ("delt = %f \n",delt);
  years_run = delt*(double)(num_steps)/(3600.0*24.0*365.4);
  printf("total run time = %f yr\n", years_run);

if ((f7 = fopen ("answ.out", "w")) == NULL) {
    printf ("cannot create file answ.out \n");
    exit(1);
  }
fprintf (f7, "%f \n",years_run);

  /* read the data from the input files */
  for (kcount = 0; kcount <= kn; kcount++) {
    for (rcount = 0; rcount <= rn; rcount++) {
      fscanf(f2, "%d", &tbox[rcount][kcount]);
      fscanf(f3, "%lf", &t[rcount][kcount]);
    }
  }

  fclose (f2);
  fclose (f3);

  /* this is the main loop set. The outer loop steps through
     time and the second loop steps through vertical distance. The inner loop
     steps through the cone radius */

  for ( tott = 1; tott <= num_steps; tott ++ ) {
    for ( k = 1; k <= kn; k++ ) {
      for (i = 1; i <= rn; i++) {
        /* determine if it is an interior or exterior node - exterior nodes
           are in the atmosphere and no additional calculations are required
           interior nodes -> including those on the edges of the cone - are the
           topics of calculations */

        if (tbox[i][k] == 1) {


          /* sumt is calculated to determine how heat is diffused from the node - weather
             the node is an interior point, outside corner, etc. */
```

```
          sumt = tbox[i][k] + tbox[i][k+1]+tbox[i][k-1]+tbox[i+1][k]+tbox[i-1][k]+tbox[i+1][k
+ -1]+tbox[i+1][k+1]+tbox[i-1][k-1]+tbox[i-1][k+1];

          /* the following case select performs all of the heat transfer
             calculations for the interior points - using slightly different equations
             depending on the value of sumt. */

          switch (sumt) {

          case 9:
            /*interior point - 2d radial conduction equation for an interior
              point - depends on thermal diffusivity (alpha), radial distance step
              (delr), vertical distance step (delz), and time step (delt) - each of
              these steps is constant across the geometry and elapsed time.
            */
            d1 = 1.0-1.0/(2.0*(double)i);
            d2 = 1.0+1.0/(2.0*(double)i);
            dum1 = 1.0/(delr*delr) *(d1*t[i-1][k] - 2.0*t[i][k] + d2*t[i+1][k]);
            dum2 = 1.0/(delz*delz) * (t[i][k-1] - 2.0*t[i][k] + t[i][k+1]);
            dum3 = dum1 + dum2;

            t[i][k] = t[i][k] + delt*alpha*dum3;
            break;
          case 5:
          case 8:

            /* both case 5 and 8 are for a node that is an inside corner -
               2d radial conduction equation for an interior
               point - depends on thermal diffusivity (alpha), radial distance step
               (delr), vertical distance step (delz), and time step (delt) - each of
               these steps is constant across the geometry and elapsed time. One quadrant
               about the node is a convective boundary (atmosphere) and the solution
               also depends on sigma = alpha*delt/(delz*delz), air temperature (to),
               and Biot number (bi)
            */

            if (tbox[i+1][k+1] == 0){
              t1 = t[i][k];
              t2 = t[i+1][k];
              t5 = t[i][k+1];
              t3 = t[i-1][k];
              t4 = t[i][k-1];
            }
            else if (tbox[i-1][k+1] == 0) {
              t1 = t[i][k];
              t2 = t[i][k+1];
              t5 = t[i-1][k];
              t3 = t[i+1][k];
              t4 = t[i][k-1];
            }
            else printf ("error in geometry - case 8 - \n");


            t[i][k] = 4.0/3.0*sigma*(t3+t4+0.5*t2+0.5*t5+bi*t0) + (1.0-4.0*sigma - 4.0/3.0*si
+ gma*bi)*t1;
            break;
          case 6:
          case 7:

            /* both case 6 and 7 are for a node that is a flat edge (horizontal -
               or vertical). 2d radial conduction equation for an interior
               point - depends on thermal diffusivity (alpha), radial distance step
               (delr), vertical distance step (delz), and time step (delt) - each of
               these steps is constant across the geometry and elapsed time. Two quadrants
```

```
            about the node form a convective boundary (atmosphere) and the solution
            also depends on sigma = alpha*delt/(delz*delz), air temperature (to),
            and Biot number (bi)
          */

          if (tbox[i][k+1] == 0) {
            t1 = t[i][k];
            t3 = t[i][k-1];
            t4 = t[i-1][k];
            t2 = t[i+1][k];
          }
          else if (tbox[i-1][k] == 0) {
            t1 = t[i][k];
            t3 = t[i+1][k];
            t4 = t[i][k+1];
            t2 = t[i][k-1];
          }
          else if (tbox[i+1][k] == 0) {
            t1 = t[i][k];
            t3 = t[i-1][k];
            t4 = t[i][k+1];
            t2 = t[i][k-1];
          }
          else printf ("error in geometry - case 6 \n" );

          t[i][k]= 2.0*sigma*(t3+0.5*t2+0.5*t4+bi*t0) + (1.0-4.0*sigma - 2*sigma*bi)*t1;

          break;

        case 4:

          /* outside corner - 2d radial conduction equation for an interior
             point - depends on thermal diffusivity (alpha), radial distance step
             (delr), vertical distance step (delz), and time step (delt) - each of
             these steps is constant across the geometry and elapsed time. Three quadrants
             about the node form a convective boundary (atmosphere) and the solution
             also depends on sigma = alpha*delt/(delz*delz), air temperature (to),
             and Biot number (bi)
          */

          if (tbox[i+1][k-1]  == 1) {
            t1 = t[i][k];
            t2 = t[i+1][k];
            t3 = t[i][k-1];
          }
          else if (tbox[i-1][k-1] == 1) {
            t1 = t[i][k];
            t2 = t[i-1][k];
            t3 = t[i][k-1];
          }
          else printf ("problem with geometry - case 4 \n");


          t[i][k] = 2.0*sigma*(t2+t3+2.0*bi*t0) + (1.0-4.0*sigma - 4.0*sigma*bi)*t1;

        default:
          printf( "problem in node summation, sumt = %d \n", sumt);
        } /* end switch */

      }  /* end if */

    } /* end for - next (i) */
  } /* end for - next (k) */
```

```
    /* This next block takes care of r = 0
       this is an insulated boundary condition
       either within the cone tbox = 1 or iutside the
       cone tbox = 0
    */

    for (k = 1; k <= kn; k++) {

      if (tbox[0][k+1] == 1) {
        dum1 = 4.0*(t[1][k]-t[0][k])/(delr*delr);
        dum2 = (t[0][k-1] - 2.0*t[0][k] + t[0][k+1])/(delz*delz);
        t[0][k] = t[0][k] + delt*alpha*(dum1+dum2);
      }
      else {
        t1 = t[0][k];
        t3 = t[0][k-1];
        t2 = t[1][k];
        t4 = t2;
        t[0][k]= 2.0*sigma*(t3+0.5*t2+0.5*t4+bi*t0) + (1.0-4.0*sigma - 2.0*sigma*bi)*t1;

        /* EXIT FOR  */
        break;
      }
    } /* end for next k */


    /* use the ground as an insulator */

    for (i = 1; i <= rn; i++) {
      if (tbox[i][1] == 1) {
        t[i][0] = 2.0*sigma*(t[i][1]+ 0.5*t[i-1][0] + 0.5*t[i+1][0]) +  (1.0-4.0*sigma)*t[i][
+ 0];
      }
      else break;
    } /* next i */

    /* change the value at t(0,0) */

    t[0][0] = 2.0*sigma*(t[0][1] + t[1][0]) + (1.0-4.0*sigma)*t[0][0];

    loop_ct ++;

    if (loop_ct == 50) {
      /*  fprintf (f4, "%f %f %f %f \n", (double)(tott*delt/(3600.0*24*365.4)), t[1][1], t[5]
+ [5], t[10][10]); */
  fprintf (f4, "%f %f \n", (double)(tott*delt/(3600.0*24*365.4)), t[18][2]);
  fprintf (f5, "%f %f \n", (double)(tott*delt/(3600.0*24*365.4)), t[18][10]);
  fprintf (f6, "%f %f \n", (double)(tott*delt/(3600.0*24*365.4)), t[18][15]);
      loop_ct = 0;
    }

   }  /*next tott  */

  /* the following code is for spy glass transform output
  PRINT #1: rn,kn+2
  PRINT #1: 0,0
  FOR j = 1 to rn
      PRINT #1: j*delr;
  NEXT j
  FOR i = 1 to kn
      PRINT#1: i*delz;
  NEXT i
  PRINT
```

```
PRINT
MAT PRINT #1: t
*/


/* if not using spyglass - simply output
the code as a list */
  for (j=1; j <= rn; j++) {
    for (i = 1; i <= kn; i++) {
      fprintf (f1, "%f %f %f \n", (double)(j*delr), (double)(i * delz), t[j][i]);
    }
  }
  fclose (f1);
  printf ("done \n");
  exit(0);
}
```

Scientific Notebook
20-1402-461
IA KTI

Chuck Connor
Initial:
June 14, 1999

The following code was created to decimate a data file so that it can be read by the GM-SYS program. GM-SYS models gravity and magnetic data collected for varioua KTIs, including IA, SDS, and USFIC. Commonly, we collect individual profiles with many thousands of data points. For modeling, GM-SYS accepts a maximum of 500 data points. Therefore we filter the data sets, eliminating some fraction of the data set before importing it into GM-SYS

It is noted that other techniques exist, such as mid-mean or moving average techniques for decimating data sets. Because our sample density is so great, and changes in the magnetic field are so gradual, it makes little sense (little is gained) by implementing these more sophisticated techniques.

```
1
2    /*
3
4    Program Name: desimator.c
5    Written by: Chuck Connor
6                CNWRA
7                Sothwest Research Inst.
8                6220 Culebra Rd
9                San Antonio, TX, 78238-5166
10
11               Phone: 210-522-6649
12               E-mail: cconnor@swri.edu
13   Date: May 25, 1999
14   Language: Ansi C
15
16   Purpose: This program gets data in the form shown in the following and out
17   puts every nth reading  */
18
19   /* input data looks like
20
21   ....+....+....+....+....+....+
22   4058825 -306.9096
23   4058827 -306.6811
24   4058829 -306.4675
25   4058831 -306.2686
26   4058832 -306.0844
27   4058834 -305.9146
28   4058836 -305.759
29   4058838 -305.6176
30   4058840 -305.4899
31   4058842 -305.3761
32   4058843 -305.2756
33   4058845 -305.1884
34   4058847 -305.1143
35   4058849 -305.0529
36   4058851 -305.004
37
38   */
39
40   #include  <stdio.h>
41   #include  <stdlib.h>
42   #include  <string.h>
43   #include  <math.h>
44
45
46
47   void main(int argc, char *argv[])
48   {
49
50     FILE *f1, *f2;
51    int ct, tot_ct, tot_out;
52    char line[80];
53    int num_drop;
54
55   if (argc != 4) {
56   printf("Usage: infile outfile num \n"  );
57   printf(" \n");
58   printf("where infile: input file containing mag data \n"   );
59   printf("      outfile: output containing 1/12 mag data \n"   );
60   printf("      num: number of readings dropped for every reading kept\n"    );
61   printf(" \n");
62   exit (1);
63   }
64
65   if ((f1 = fopen (argv[1], "r")) == NULL) {
66      printf ("cannot open input file %c \n"  , argv[1]);
67      exit(1);
68   }
69
70   if ((f2 = fopen (argv[2], "w")) == NULL) {
71      printf ("cannot create output file %c \n"  , argv[2]);
72      exit(1);
73   }
74
```

```
75   num_drop  = atoi(argv[3]);
76    ct  = 1;
77    tot_ct  = 1;
78    tot_out  = 1;
79     while  ( fgets(line, 80, f1) != NULL )
80     { /*printf("%s\n", line);    */
81         ct++;
82         tot_ct++;
83
84         if (ct > num_drop) {
85         fputs(line, f2);
86         ct = 0;
87         tot_out++;
88         }
89     }
90     printf("Number of mag readings input: %d\n"   , tot_ct);
91     printf("Number of mag readings output: %d\n"   , tot_out);
92
93   printf  ("done \n");
94   }
```

Scientific Notebook
20-1402-461
IA KTI

Chuck Connor
Initial:
June 14, 1999

The following code was created to perform heading corrections to magnetic data files collected using the All-terrain bicycle geomagnetic mapping system (ATBGMS) techniques.

The code is tested using data from Kilbourne Hole, New Mexico. Peter La Femina rode the ATBGMS NE along a road and then returned on the same road (heading SW). Data, uncorrected, show an offset of about 30 nT due to the heading of the bicycle. This difference in heading is subtracted using the headingt code, as illustrated by "new test" below.

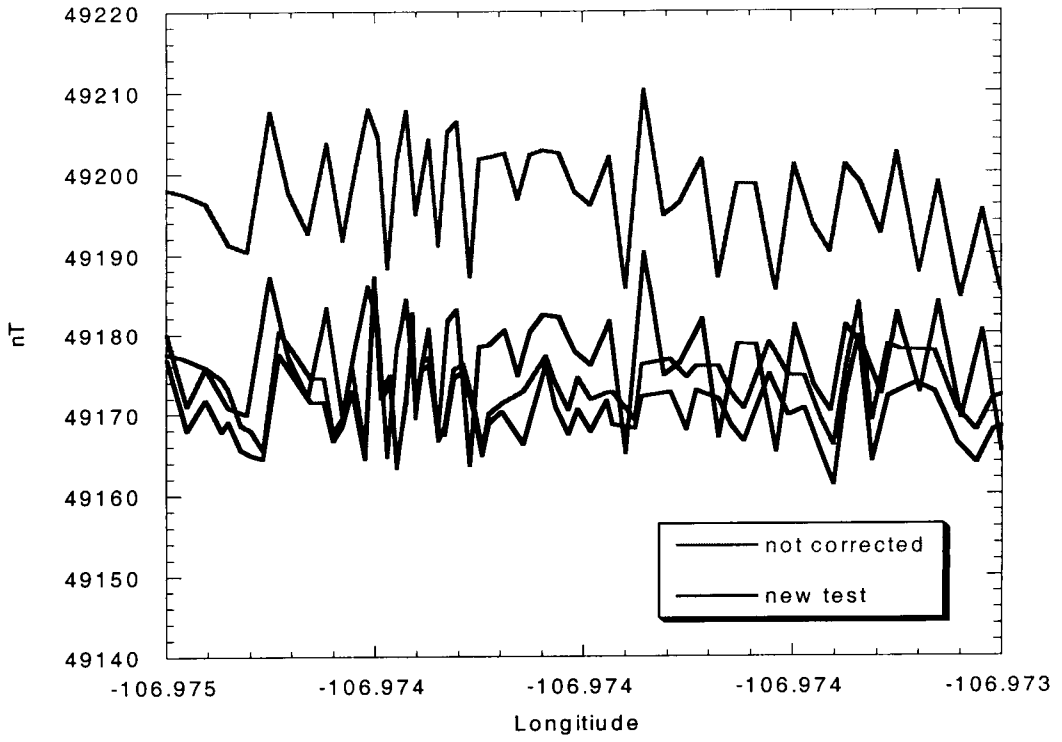

```
/* Written by: Laura Connor, Programmer
 *             SWRI - Div09
 * Last Modified: January 6, 1998
 *
 * Heading correction modified June 14, 1999 by C. Connor

 * Description:
       This code determines the heading at each magnotometer reading
       and adjusts the reading to eliminate directional variations.  A look-up
       table is used to determine the magnitude of the effect.
       The data for the loolkup table is generated by taking 36 magnotometer
       readings in the same spot, rotating 10 degrees after each reading.
       ADJUST COMPASS TO READ W.R.T. MAGNETIC NORTH.
       The data is recorded in a text file starting with 0 (magnetic north)
       and ending with 350 (for format see below). The file should only
       contain numbers, and no blank lines.

       Note: Program assumes headings are relative to Magnetic NORTH.

 * History: Written by Laura Connor, 12-97

 * Inputs: data file
          text file (for look up table) format:
             heading(degrees) mag-reading(nT)


 * Outputs: data file (with 'H' appended to input file name)

 * Data file format (input and output):
        easting northing mag-reading(nT) time(HH:MM:SS.SS)

 * Usage:
     heading <heading correction file> <input file>
 */

#include <stdio.h>
#include <stdlib.h>
#include <string.h>
#include <math.h>

#define PI 3.14159265358979323846

typedef struct {
  double heading;
  double mag;
} READING;

static READING headings[36];

double heading_correction (double h, double mag, int ct);

int main(int argc, char *argv[])
{
  double easting, northing, mag;
  double x2, x1, x, y2, y1, y;
  double theta, heading, cmag, hmag, baseH;
  int ret, ct, cnt, len, i, deg;
  char outfile[255], buf[255], *ext, time[12];
  FILE *in, *out, *head;

  printf("\n\nCOPYRIGHT  (January, 1998)  Southwest Research Institute\n"    );
  printf("\tAll rights reserved.\n\n"  );

  if (argc < 3)
  { fprintf(stderr,
     "Usage: %s <heading file> <input file>\n"   , argv[0]);
    return(1);
  }

  head = fopen(argv[1], "r");
  if (head == NULL)
  { fprintf(stderr,
            "Unable to open heading file: %s\n"   , argv[1]);
    return(1);
```

```
75      }
76
77      in = fopen(argv[2], "r");
78      if (in == NULL)
79      { fprintf(stderr,
80                "Unable to open input file: %s\n"  , argv[2]);
81        return(1);
82      }
83
84      len = strlen(argv[2]);
85
86      ext = strchr(argv[2], '.');
87      if (ext == NULL)
88      { fprintf(stderr, "No valid extension on input filename: %s\n"   ,
89                argv[2]);
90        return(1);
91      }
92      strcpy(buf, argv[2]);
93      for (i=0; i<len; i++)
94        if (buf[i] == '.') break;
95
96      strncpy(outfile, buf, i);
97      outfile[i] = 'H';
98      outfile[i+1] = '\0';
99      strcat(outfile, ext);
100
101     out = fopen(outfile, "w");
102       if (out == NULL)
103     { fprintf(stderr,
104               "Unable to open output file: %s\n"  , outfile);
105       return(1);
106     }
107     printf("Creating output file: %s\n"  , outfile);
108
109     ret =  fscanf(head, "%d %lf", &deg, &hmag);
110     if (ret == EOF) return(0);
111     if (ret != 2)
112     { fprintf(stderr, "Error inputing first data line from heading file.\n"   );
113       return(1);
114     }
115     if (deg)
116     { fprintf(stderr, "First degree reading should be zero.\n"  );
117       return(1);
118     }
119     headings[0].heading = 0.0;
120     headings[0].mag = 0.0;
121     printf("\nHeading corrections:\n" );
122     printf("%d %f %f\n", deg, headings[0].heading, headings[0].mag);
123     baseH = hmag;
124
125     ct = 1;
126     while (ret = fscanf(head, "%d %lf", &deg, &hmag), ret != EOF)
127     { if (ret != 2)
128       { fprintf(stderr, "Error inputing data line %d from heading file.\n"   ,
129                 ct+1);
130         return(1);
131       }
132       if (deg/10 != ct)
133       { fprintf(stderr, "['%d' Bad degree in heading file on line %d, expecting %d\n"    ,
134                 deg, ct+1, ct * 10);
135         return(1);
136       }
137       headings[ct].heading = PI * (double)deg / 180.0;
138       headings[ct].mag = hmag - baseH;
139       printf("%d %f %f\n", deg, headings[ct].heading, headings[ct].mag);
140       ct++;
141     }
142
143     ret = fscanf(in, "%lf %lf %lf %s", &easting, &northing, &mag, time);
144     if (ret == EOF) return(0);
145     if (ret != 4)
146     {  fprintf(stderr, "Error inputting first data line\n"  );
147        return(1);
148     }
```

```
149
150    /* printf("%.2f %.2f %.1f\n",easting, northing, mag); */
151    x2 = easting;
152    y2 = northing;
153
154    cnt = 1;
155    while (ret = fscanf(in, "%lf %lf %lf %s" , &easting, &northing, &mag, time),
156           ret != EOF)
157    {
158       cnt++;
159       /* printf("%.2f %.2f %.1f\n",easting, northing, mag); */
160       if (ret != 4)
161       { fprintf(stderr, "Error inputting data line %d.\n"  , cnt);
162         return(1);
163       }
164       x1 = easting;
165       y1 = northing;
166
167       x = x2 - x1;
168       y = y2 - y1;
169
170       if (!x && !y)
171          continue;
172       else if (!x)
173          theta = 1.570796327;  /* 90 degrees */
174       else if (!y)
175          theta = 0.0;
176       else
177          theta = atan(y/x);
178
179     /*  theta += .104719755;  6 degree correction for magnetic north */
180
181       if (x < 0.0)
182         heading = (y <= 0.0) ? 4.71238898 - theta : 4.71238898 + theta;
183       else  /* x > 0.0 */
184         heading = (y <= 0.0) ? 1.570796327 + theta : 1.570796327 - theta;
185
186       cmag = heading_correction (heading, mag, ct);
187       fprintf(out, "%.10f %.10f %.3f %s\n"  , easting, northing, cmag, time);
188       x2 = x1;
189       y2 = y1;
190    }
191    fclose(in);
192    fclose(out);
193    fclose(head);
194    printf("Done\n");
195    return(0);
196 }
197
198 double heading_correction (double h, double mag, int ct)
199 {
200    int i;
201
202    for (i = 0; i <= ct; i++)
203    { if (headings[i].heading > h)
204        return (mag - 0.5*headings[i-1].mag);
205    }
206    return 0.0;
207 }
```

Entries into S.N. 115E for May 20, 99 to

cc 8/18/00 ~~June 14, 99~~ August 18, 00 have been

made by C. Cann . Clark B Cann . 8/18/00

No original data have been removed

cc 8/18/00